



Giorgio Ronchi  
Foundation



---

*13<sup>th</sup> International Workshop on*

**Advanced Infrared  
Technology & Applications**

**PROCEEDINGS**

*September 29- October 2, 2015  
Area della Ricerca CNR  
Pisa, Italy*



**ISBN: 978-88-7958-025-0**

Published by: Pisa, CNR Research Area

© 2015 Institute of Science and Technologies “A. Faedo”  
National Research Council (CNR)

*Fondazione “Giorgio Ronchi”, Firenze  
CNR-ITC, Sez. di Padova  
CNR-IFAC “Nello Carrara”, Firenze  
CNR-ISTI “Alessandro Faedo”, Pisa*

*13<sup>th</sup> International Workshop on*

**Advanced Infrared  
Technology & Applications**

**PROCEEDINGS**

*Edited by: Laura Ronchi, Paolo Bison, Mario D’Acunto, Davide Moroni, Valentina Raimondi, Ovidio Salvetti, Xavier Maldague, Antoni Rogalski, Takahide Sakagami, Marija Strojnik*

## **General Chair**

L. Ronchi Abbozzo

## **Co-Chairs**

P. Bison, CNR-ITC, Padova, Italy  
M. D'Acunto, CNR-ISM, Rome, Italy  
X. Maldague, Laval University, Quebec, Canada  
D. Moroni, CNR-ISTI, Pisa, Italy  
V. Raimondi, CNR-IFAC, Firenze, Italy  
A. Rogalski, Military University of Technology, Warsaw, Poland  
T. Sakagami, Kobe University, Kobe, Japan  
M. Strojnik, CIO, Leon Gto, Mexico

## **Scientific Committee**

D. Balageas, ONERA, France  
C. Corsi, CREO, Italy  
E. Dereniak, Univ. of Arizona, USA  
C.T. Elliott, Heriot-Watt Univ., Scotland.  
C. Maierhofer, BAM, Germany  
C. Meola, Univ. of Naples, Italy  
G. Paez, CIO, Mexico  
I. Pippi, CNR-IFAC, Italy  
H. Rutt, Southampton University, UK  
O. Salvetti, CNR-ISTI, Italy  
J.L. Tissot, ULIS, Veurey Voroize, France  
V.P. Vavilov, Tomsk University, Tomsk, Russia  
H. Zogg, ETH, Zurich, Switzerland

## **Organizing & Technical Secretariat**

F. Pardini, CNR-ISTI, Italy  
A.M. Meriggi, Fondazione "Giorgio Ronchi", Firenze, Italy  
E. Ricciardi, C.O.C.E.S., Italy  
M. Tampucci, CNR-ISTI, Italy  
M. Volinia, Politecnico di Torino, Italy



# Table of Contents

*Session: Systems and applications in near-, mid- and far-infrared - Part I*

<b>C. Corsi</b>	2
<i>Infrared sensors' history in Italy</i>	
<b>Yingjie Ma, Yonggang Zhang, Yi Gu, Xingyou Chen, Li Zhou, Suping Xi, Hsby Li and Aizhen Li</b>	3
<i>Control the operating voltage and gain slope of InAlAs/InGaAs avalanche photodetectors</i>	
<b>Songmin Zhou, Bin Weng and Chun Lin</b>	6
<i>The PN junction width of HgCdTe conversed through ion implantation and ion beam etching</i>	

*Session: Systems and applications in near-, mid- and far-infrared - Part II*

<b>Michal Švantner, Zdeněk Veselý and Lukáš Muzika</b>	11
<i>Depth limits of flash-pulse IRNDT method for low- and high-diffusivity materials</i>	
<b>A. G. Unil Perera, Yan-Feng Lao, L. H. Li, S. P. Khanna and E. H. Linfield</b>	16
<i>Tunable hot-carrier photodectectors</i>	
<b>Zhizhong Bai, Chen J., Xu Zh., Zhou Y., Xu G. and Zhu H.</b>	20
<i>Investigation of High Quantum Efficiency Resonant Cavity Enhanced InAs/GaSb type II Superlattice Long Wavelength Infrared Detectors</i>	

*Session: Aerospace and industrial applications*

<b>Louis-Daniel Thérooux, Jean Dumoulin and Erick Merliot</b>	24
<i>Automatic installation of thermoplastic CFRP monitored by infrared thermography for pipelines</i>	
<b>Eric Johnson and Yong Kim</b>	28
<i>Thermographic Testing of Microwave Circulator Adhesive Bonds</i>	
<b>Donatella Guzzi, Cinzia Lastri, Vanni Nardino, Lorenzo Palombi, Ivan Pippi, Valentina Raimondi and Alessandro Barducci</b>	32
<i>Compressive sensing and its potential for infrared applications</i>	
<b>Daiki Shiozawa, Tsuyoshi Inagawa, Atsushi Akai and Takahide Sakagami (invited lecture)</b>	36
<i>Accuracy improvement of dissipated energy measurement and fatigue limit estimation by using phase information</i>	

<i>Session: Environmental monitoring - Part I</i>	
<b>Veronica Redaelli, Gaia Dominique Bariffi, Silvia Mazzola, Raffaella Rossi, Leonardo Nanni Costa and Fabio Luzi</b>	<b>41</b>
<i>Infrared thermography (IRT) in horses trained for endurance races</i>	
<b>Alessandro Bortolin, Paolo Bison, Gianluca Cadelano, Giovanni Ferrarini, Lei Lei and Xavier Maldague</b>	<b>45</b>
<i>Mapping the heat flux of an insulated small container by infrared thermography</i>	
<b>Susana Lagüela, Natalia Caparrini and Luján López</b>	<b>49</b>
<i>Evaluation of infrared thermography as standalone technique for detection of sediment-pollution in water</i>	
<b>Francesco Salamone, Ludovico Danza, Italo Meroni and Maria Cristina Pollastro</b>	<b>53</b>
<i>Design and optimization through thermography: nEMoS architecture</i>	
<b>Matteo Ghellere, Alice Bellazzi, Lorenzo Belussi and Italo Meroni</b>	<b>59</b>
<i>Urban monitoring from infrared satellite images</i>	
 <i>Session: Environmental monitoring - Part II</i>	
<b>M. Miguel Valero, Oriol Rios, Elsa Pastor and Eulàlia Planas</b>	<b>63</b>
<i>Automatic detection of wildfire active fronts from aerial thermal infrared images</i>	
<b>Fabio Sansivero and Giuseppe Vilardo</b>	<b>68</b>
<i>Advances in automated processing of thermal infrared images from Osservatorio Vesuviano TIR permanent surveillance network at Campi Flegrei (Pozzuoli, Italy)</i>	
<b>Atsushi Hashimoto, Ken-Ichiro Suehara and Takaharu Kameoka</b>	<b>72</b>
<i>Applications of infrared spectroscopic techniques to quality evaluation in agriculture and food process</i>	
<b>Barbara Bukowska-Belniak, Andrzej Leśniak and Daniel Kessler</b>	<b>76</b>
<i>Thermographical monitoring of leak processes in embankments</i>	
<b>Rebecca Whetton, Toby Waine and Abdul Mouazen</b>	<b>79</b>
<i>A practical approach to In-situ hyperspectral imaging of wheat crop canopies</i>	
<b>Marc-André Gagnon, Pierre Tremblay, Simon Savary, Marc Duval, Vincent Farley, Philippe Lagueux, Éric Guyot and Martin Chamberland</b>	<b>83</b>
<i>Airborne thermal infrared hyperspectral imaging for mineral mapping</i>	
 <i>Session: Advanced technology and materials - Part I</i>	
<b>Malgorzata Kopytko and Antoni Rogalski (invited lecture)</b>	<b>87</b>
<i>HgCdTe barrier infrared detectors</i>	
<b>Yoshifumi Ohbuchi, Nobuaki Nagatomo and Hidetoshi Sakamoto</b>	<b>91</b>
<i>Thermal image analysis of plastic deformation and fracture behaviors by thermo-video system</i>	
<b>Hai Zhang, Wolfgang Holub, Ulf Hassler and Xavier Maldague</b>	<b>95</b>
<i>Micro-laser Line Thermography and High Resolution X-ray Tomography on Micro-porosities: A Comparative Study of Experiments and Simulation</i>	

<b>Jianxin Chen, Zhicheng Xu, Yi Zhou, Fangfang Wang, Jiajia Xu and Li He</b>	<b>99</b>
<i>LWIR InAs/GaSb Superlattice Photodiodes with Different Barrier Structures</i>	
<i>Session: Biomedical applications - Part I</i>	
<b>Mario D'Acunto, Antonio Cricenti, Marco Luce, Davide Moroni and Ovidio Salvetti</b>	<b>103</b>
<i>NIR window and Near-Field detection of gold nanoshells</i>	
<b>Steffen Frahm, Carsten Dahl Mørch, Ole Kæseler Andersen and Lars Arendt-Nielsen</b>	<b>107</b>
<i>Temperature controlled laser stimulator for pain research</i>	
<b>Marco Gargano, Nicola Ludwig, Athos Trecroci, Damiano Formenti, Andrea Bosio, Ermanno Rampinini and Giampietro Alberti</b>	<b>111</b>
<i>Skin temperature dynamics during an incremental maximal test in elite male cyclists</i>	
<i>Session: Advanced technology and materials - Part II</i>	
<b>Alessandro Tredicucci (invited lecture)</b>	<b>114</b>
<i>Graphene-based devices for Terahertz photonics</i>	
<b>Elżbieta A Pieczyska, Maria Staszczak, Michał Maj, Katarzyna Kowalczyk-Gajewska, Dominik Kukla, Hisaaki Tobushi and Shunichi Hayashi</b>	<b>115</b>
<i>Infrared thermography analysis of thermomechanical shape memory polymer behavior – initial loading stage</i>	
<b>A. Amato, A.S. Aricò, M. Lo Faro, R. Montanini, S.A. Piccolo, A. Quattrocchi, G. Squadrito, S. Trocino and S.C. Zignani</b>	<b>119</b>
<i>Infrared thermography applied to solid oxide fuel cells at operating temperatures</i>	
<b>Mustafa Hostut, Yuksel Ergun, Sezai Elagoz, Abidin Kilic, Tunay Tansel and Atilla Aydinli</b>	<b>123</b>
<i>Electrical Performance of N-Structure T2SL Photodetectors</i>	
<b>Antonio Cricenti and Marco Luce</b>	<b>127</b>
<i>Infrared scanning near-field optical microscopy in material science and biology</i>	
<b>Pawel Madejczyk, Waldemar Gawron, Piotr Martyniuk, Artur Keblowski, Wioletta Pusz, Jaroslaw Pawluczyk, Malgorzata Kopytko, Antoni Rogalski and Jozef Piotrowski</b>	<b>129</b>
<i>The focus on engineering steps for high temperature HgCdTe photodiodes optimization.</i>	
<i>Session: Biomedical applications - Part II</i>	
<b>Chi-En Lee and Chung-Ming Chen</b>	<b>133</b>
<i>The automated marker-free longitudinal IR breast image registration algorithm</i>	
<b>Cuc Stanca, Prodan Doina, Sarosi Codruta, Saplontai Aniela, Silaghi-Dumitrescu Laura, Prejmerean Vasile and Moldovan Marioara</b>	<b>138</b>
<i>Degradation of some experimental dental composite materials</i>	
<b>Mihaela Streza, Dorin Dadarlat, Doina Prodan, Ioana Hodisan, Cristina Prejmerean and Stanca Boboia</b>	<b>142</b>
<i>Adhesion studies of dental sealants to enamel by using optical microscopy and lock-in infrared thermography</i>	

<b>Cristina Prejmerean, Doina Prodan, Mihaela Vlassa, Tinca Buruiana, Loredana Colceriu and Marioara Moldovan</b>	<b>147</b>
<i>Influence of composition and light curing modes upon the degree of conversion of dental composites evaluated by FTIR spectroscopy</i>	
<b>Bardia Yousefi, Julien Fleuret, Seyed Alireza Ghaffari, Simon Fréchet, Félix Labrie Larrivé, Marcelo Sung Ma Jo, Xavier Maldague and Raymon Watts</b>	<b>152</b>
<i>Unsupervised Automatic tracking of Thermal changes in Human Body</i>	
 <i>Session: Advanced technology and materials - Part III</i>	
<b>Marija Strojnik and Gonzalo Paez (invited lecture)</b>	<b>157</b>
<i>Propagation of thermal pulse in tissue</i>	
<b>Rosa De Finis, Davide Palumbo, Francesco Ancona and Umberto Galietti</b>	<b>162</b>
<i>New thermal method to assess endurance limit of stainless steels</i>	
<b>Changzhi Shi, Chun Lin, Yanfeng Wei, Lu Chen, Mingxing Zhu and Quanzhi Sun</b>	<b>167</b>
<i>Barrier Layer Induced Channeling Effect of As Ion-implantation in HgCdTe and Its Influences on Electrical Properties of p-n Junctions</i>	
<b>Konstantin Petrosyants and Igor Kharitonov</b>	<b>171</b>
<i>Analysis of temperature-current rise in modern pcb traces by means of thermography</i>	
<b>Valeri Kotelnikov and Elena Ryazanova</b>	<b>175</b>
<i>Method of 3d solar energy conversion</i>	
<b>Changzhi Shi, Chun Lin, Yanfeng Wei, Lu Chen, Mingxing Zhu and Quanzhi Sun</b>	<b>179</b>
<i>Influences of Ion Beam Current on Dopant Profiles and Barrier Layer Induced Channeling Effect in Arsenic Implanted HgCdTe Epilayer</i>	
 <i>Session: Biomedical applications - Part III</i>	
<b>Trabelsi Hedi, Elkadri Noomene and Sediki Ezeddine</b>	<b>183</b>
<i>Detection of abnormalities under skin tissue by thermography</i>	
<b>Maryam Asrar and Amin Al-Habaibeh</b>	<b>186</b>
<i>A comparison between Visual, Near-infrared and Infrared Images for the Detection of Veins</i>	
<b>Renée Lampe, Blumenstein Tobias, Varvara Turova and Ana Alves Pinto</b>	<b>190</b>
<i>Sensomotor waistcoat – a helpful tool for blind people and children with cerebral palsy to support space perception and improve body scheme</i>	
<b>Slokom Nesrine, Zghal Imen and Trabelsi Hedi</b>	<b>194</b>
<i>Detection and Quantification of Macular Edema from Optical Coherence Tomography Images</i>	
<b>Bushra Jalil, Ovidio Salvetti, Valentina Hartwig , L. Potì and A. L'Abbate</b>	<b>201</b>
<i>Infrared imaging to study hand skin microcirculation in healthy and systemic sclerosis volunteer</i>	
 <i>Session: Image processing and data analysis - Part I</i>	
<b>Simone Boccardi, Carosena Meola and Giovanni Maria Carlomagno</b>	<b>206</b>
<i>Measurements with a QWIP infrared camera: signal treatment and noise correction</i>	

<b>Piotr Hellstein and Mariusz Szwedo</b>	<b>210</b>
<i>IR3D Analysis - three-dimensional imaging in active thermography and non-destructive testing</i>	
<b>Gerhard Traxler and Amirreza Baghbanpourasl</b>	<b>214</b>
<i>Monitoring of the cross wedge rolling process by thermographY</i>	
<b>Olivier Janssens, Lothar Verledens, Raiko Schulz, Veerle Ongenae, Kurt Stockman, Mia Loccufier, Rik Van de Walle and Sofie Van Hoecke</b>	<b>220</b>
<i>Infrared and Vibration Based Bearing Fault Detection Using Neural Networks</i>	
 <i>Session: Non destructive test and evaluation - Part I</i>	
<b>Kwang-Hee Im, Je-Woung Park, In-Young Yang, Jeong-An Jung, David K. Hsu and Sun-Kyu Kim</b>	<b>224</b>
<i>Characterization of terahertz penetration and applications for composite materials</i>	
<b>Takahide Sakagami, Daiki Shiozawa, Yoshitaka Tamaki, Hiroki Ito, Akihisa Moriguchi, Tatsuya Iwama, Kazuyoshi Sekine and Teruya Shiomi</b>	<b>229</b>
<i>Nondestructive detection of corrosion damage under corrosion protection coating using infrared thermography and terahertz imaging</i>	
<b>Henrique Fernandes, Clemente Ibarra-Castanedo and Xavier Maldague</b>	<b>234</b>
<i>Carbon fiber composites inspection and defect characterization using active infrared thermography</i>	
<b>Eva Barreira, Elton Bauer, Niubis Mustelier and Vasco P. Freitas</b>	<b>242</b>
<i>Measurement of materials emissivity – Influence of the procedure</i>	
 <i>Session: Non destructive test and evaluation - Part II</i>	
<b>Fariba Khodayar, Saeed Sojasi and Xavier Maldague</b>	<b>246</b>
<i>Infrared Thermography and NDT: 2050 Horizon</i>	
<b>Rachael Tighe, Janice Dulieu-Barton and Simon Quinn</b>	<b>247</b>
<i>Stress based NDE using infrared thermography</i>	
<b>Hiroataka Tanabe, Yui Izumi, Takayuki Hibino, Tohru Takamatsu and Takahide Sakagami</b>	<b>251</b>
<i>Study on heat generation behaviors in Sonic-IR method</i>	
<b>Giovanni Ferrarini, Alessandro Bortolin, Gianluca Cadelano and Paolo Bison</b>	<b>255</b>
<i>Thermal response measurement of building insulating materials by infrared thermography</i>	
 <i>Session: Systems and applications for the cultural heritage - Part I</i>	
<b>Stefano Sfarra, Paolo Bison, Alessandro Bortolin, Gianluca Cadelano, Giovanni Ferrarini, Domenica Paoletti, Clemente Ibarra-Castanedo, Xavier Maldague and Fabio Peron</b>	<b>259</b>
<i>Solar loading thermography for architectural heritage surveys: plumb the depth by looking at the façade</i>	
<b>Iole Nardi, Stefano Sfarra, Dario Ambrosini, Donatella Dominici and Elisa Rosciano</b>	<b>263</b>
<i>Complementarity of terrestrial laser scanning and IR thermography for the diagnosis of cultural heritage: the case of Pacentro castle</i>	

<b>Fabrizio Clarelli, Gabriele Inglese and Paolo Bison</b>	<b>267</b>
<i>Thermography for depth profiling in cultural heritage</i>	
 <i>Session: Non destructive test and evaluation - Part III</i>	
<b>Paul Toasa and Thomas Ummenhofer</b>	<b>270</b>
<i>Lock-in thermography applied to real time crack detection in constructional steelwork</i>	
<b>Yui Izumi, Hirotaka Tanabe, Takayuki Hibino, Tohru Takamatsu and Takahide Sakagami</b>	<b>275</b>
<i>Development of new sonic-ir method using ultrasonic wave inputted through water</i>	
<b>Patrizia Aversa, Umberto Galietti, Vincenza Luprano, Davide Palumbo, Cristina Racioppo and Rosanna Tamborrino</b>	<b>279</b>
<i>Comparison between thermographic and heat flux meter technique: a case study</i>	
<b>Mohamed El Afi and Sougrati Belattar</b>	<b>283</b>
<i>Infrared thermography applied to characterization of a pipe internally and externally corroded</i>	
<b>Waldemar Swiderski</b>	<b>288</b>
<i>Detecting Defects in Marine Structures by Using Eddy Current Infrared Thermography</i>	
<b>Sofie Van Hoecke, Olivier Janssens, Raiko Schulz, Kurt Stockman, Mia Loccufier and Rik Van de Walle</b>	<b>291</b>
<i>Towards thermal imaging based condition monitoring in offshore wind turbines</i>	
 <i>Session: Systems and applications for the cultural heritage - Part II</i>	
<b>Stefano Sfarra, Eleni Cheilakou, Panagiotis Theodorakeas, Domenica Paoletti and Maria Kouli</b>	<b>296</b>
<i>An eye to the future, an eye to the past, thinking to a full-scale restoration process: physical and chemical ndt analysis in cooperation</i>	
<b>Anna De Falco, Tiziana Santini and Maurizio Sguazzino</b>	<b>300</b>
<i>Applications of the infrared thermography to the assessment of historic buildings: a case study in Pisa</i>	
<b>Marco Gargano, Nicola Ludwig and Elisabetta Rosina</b>	<b>304</b>
<i>Non destructive characterization of thermal and optical properties on high performances textiles</i>	
<b>Francesca Pietrarca, Mauro Mamelì, Sauro Filippeschi and Fabio Fantozzi</b>	<b>308</b>
<i>Non intrusive wall material recognition through active thermography and numerical modeling</i>	
<b>Lorenzo Palombi, Monica Galeotti, Emanuela Massa, Roberto Olmi, Marcello Picollo, Alessia Andreotti, Giovanni Bartolozzi, Marco Bini, Ilaria Bonaduce, Emma Cantisani, Massimo Chimenti, Maria Perla Colombini, Costanza Cucci, Ute Dercks, Laura Fenelli, Irene Malesci, Alessandra Malquori, Marco Montanelli, Annalisa Morelli, Sara Penoni, Louis David Pierelli, Cristiano Riminesi, Sara Rutigliano, Barbara Sacchi, Sergio Stella, Gabriella Tonini and Valentina Raimondi</b>	<b>313</b>
<i>The use of IR-based techniques in the PRIMARTE project: an integrated approach to the diagnostics of the cultural heritage</i>	

<i>Session: Astronomy and Earth observation</i>	
<b>Roberto Bonsignori</b> ( <i>invited lecture</i> )	<b>317</b>
<i>Satellite remote sensing of Earth thermal emission for weather, climate and ocean operational applications</i>	
<b>Marija Strojnik and Gonzalo Paez</b>	<b>318</b>
<i>Telescope array for extra-solar planet detection from far side of Moon</i>	
<b>Anum R. Barki, Kory J. Priestley and J. Robert Mahan</b>	<b>322</b>
<i>An Initiative to Include Coherence and Polarization in Earth Scene Identification</i>	
<b>Graham Ferrier</b>	<b>326</b>
<i>The Potential and Challenges in the use of field-based Fourier Transform InfraRed Spectroscopy for geological applications</i>	
 <i>Session: Image processing and data analysis - Part II</i>	
<b>Jonathan Gaspar, Michael Houry and Jean-Laurent Gardarein</b>	<b>330</b>
<i>Wide &amp; accurate thermal control of plasma facing component in fusion facility</i>	
<b>Qiong Zhang, Frank Ferrie and Xavier Maldague</b>	<b>334</b>
<i>A NSCT-based infrared-visible image fusion approach using fast iterativeshrinking compressed sensing</i>	
<b>Gian Marco Revel, Paolo Chiariotti, Edoardo Copertaro and Giuseppe Pandarese</b>	<b>340</b>
<i>Stationary Wavelet Transform denoising in Pulsed Thermography: influence of camera resolution on defect detection</i>	
 <i>Session: Non destructive test and evaluation - Part IV</i>	
<b>Paolo Bison, Alessandro Bortolin, Gianluca Cadelano, Giovanni Ferrarini, Lorenzo Finesso and Ravibabu Mulaveesala</b>	<b>344</b>
<i>Frequency modulated heating source in IR thermography</i>	
<b>Nobuhiro Shimoi and Carlos Cuadra</b>	<b>346</b>
<i>Comparison of natural frequencies of vibration for a bridge obtained from measurements with accelerometers and piezoelectric sensor</i>	
 <i>Session: Image processing and data analysis - Part III</i>	
<b>Gabriele Inglese</b>	<b>350</b>
<i>Perturbations of the heat transfer coefficient due to surface damages</i>	
<b>Nebi Gül and Ali Berkol</b>	<b>354</b>
<i>Improvement of predefined electrooptical system performance by a mathematical model for image intensifier tube</i>	
<b>Kai He, X. Wang, Chun Lin, Qinyao Zhang and Ruijun Ding</b>	<b>358</b>
<i>Numerical method for the capacitance of HgCdTe MIS structure and band-to-band tunneling effect on the low frequency behavior in high frequency C-V characteristics</i>	
 <b>Author Index</b>	 <b>363</b>

# PAPERS







# Infrared Sensors' History in Italy

Carlo Corsi\*

*Centro Ricerche Elettro Ottiche (CREO), L'Aquila, Italy*

Key Words: Infrared, Sensors ,Thermo-Vision, Innovation Technology, History

Infrared ,strategically important for future devices and systems ,after great developments in scientific aspects at the origins at the beginning of 1800 has been mainly confined to technological developments particularly in Sensors devices and systems. This has been true also in Italy where the developments of the first Thermopile by Leopoldo Nobili in 1829 and its application as Radiometer by Macedonio Melloni in 1833 originated a great growth of innovative technologies in materials, devices and systems (starting soon after the 2<sup>nd</sup> World War) in Italian Electronic Companies, mainly for military products, and Government Research Centers (CNR and Defense Labs), particularly in Tuscany Region and later on in Rome territory. More recently scientific aspects , especially in civil environmental and thermodynamics investigations , have also been strongly developed , mainly by Universities and CNR Labs.

A survey review and a deep analysis of the most relevant developments, particularly in R&D, appreciated on international stage will be done and reported underlying successes and failures.

# Control the operating voltage and gain slope of InAlAs/InGaAs avalanche photodetectors

Y. J. Ma<sup>1</sup>, Y. G. Zhang<sup>2,\*</sup>, Y. Gu<sup>3</sup>, X. Y. Chen<sup>4</sup>, L. Zhou<sup>5</sup>, S. P. Xi<sup>6</sup>, Hsby Li<sup>7</sup>, A. Z. Li<sup>8</sup>

State Key Laboratory of Functional Materials for Informatics, Shanghai Institute of  
Microsystem and Information Technology, Chinese Academy of Sciences  
865 Chang Ning Road Shanghai, 200050, China

(All authors have the same affiliation and mailing address)

<sup>1</sup>yjma@mail.sim.ac.cn, <sup>2,\*</sup>ygzhang@mail.sim.ac.cn, <sup>3</sup>ygu@mail.sim.ac.cn,  
<sup>4</sup>xychen@mail.sim.ac.cn, <sup>5</sup>lzhou@mail.sim.ac.cn, <sup>6</sup>spxi@mail.sim.ac.cn,  
<sup>7</sup>hsby@mail.sim.ac.cn, <sup>8</sup>azli@mail.sim.ac.cn

InGaAs/InAlAs SAM APDs with a p-type multiplication layer are reported. Wedge-shaped electric field profiles with different gradients and peak intensities confined in a thin InAlAs avalanche layer were realized. These devices showed optimum operating gains up to 40 in linear mode with low operating voltages <20 V, small gain slopes, and high-gain uniformity. Moreover, a reduced breakdown voltage temperature coefficient <6 mV/K in the temperature range of 200–350 K was observed, whereas the dark current showed a noticeable increase.

## Introduction

Focal plane arrays (FPAs) based on InGaAs avalanche photodetectors (APD) pixels is an attractive application prospective in infrared imaging systems which has been regarded as one of the 4th generation infrared detection systems [1]. For APD-FPA applications, low operating voltage, small gain-voltage slope and high APD pixel gain uniformity are highly preferred to improve the voltage compatibility for readout integrated circuits [2]. Thin multiplication layer is generally used to lower the operating voltage of APDs taking advantage of the carrier's 'dead-space effect' [3]. One possible route for reducing the gain-voltage slope might be tailoring of E gradient in the avalanche region.

In this work, we demonstrated the fabrication of separate absorption and multiplication (SAM) InAlAs/InGaAs APDs with low operating voltages less than 20 V, small gain slopes and high gain uniformity. A wedge-shaped E profile confined in the avalanche region was realized by a 0.3- $\mu\text{m}$ -thick p-type InAlAs multiplication layer doping to  $3 \times 10^{17} \text{ cm}^{-3}$ . By adjusting the doping concentration in InGaAs absorbers, the gradient of the E profile was moderately reduced, resulting in smaller

dark currents, a larger breakdown voltage ( $V_{\text{BR}}$ ) and larger M. These APDs showed optimum operating gains up to 40 in linear mode with a slightly increased dark current. A small temperature coefficient of  $V_{\text{BR}}$  of less than 6 mV/K was also observed. Those multiplication performances are attributed to the modified E profiles in the p-type avalanche region.

## Experimental Details

The InAlAs/InGaAs APD wafers were lattice-matched grown in a gas-source molecular beam epitaxy (GSMBE) system. Sample structures are shown in Fig. 1(a). Two APD wafers with identical growth parameters except for the absorption layer doping density were grown (denoted by APD-1 and APD-2). The doping densities in the absorbers of APD-1 and APD-2 were  $3 \times 10^{17}$  and  $6 \times 10^{16} \text{ cm}^{-3}$ , respectively. Top-illuminated square mesa diodes were fabricated using standard photolithography, wet chemical etching, Si<sub>3</sub>N<sub>4</sub> passivation and lift-off metallization techniques. No AR coating was applied. After processing, the top InGaAs contact layer in the photo sensitive area was removed by chemical etching. A 1550 nm laser diode with an output power of

5  $\mu\text{W}$  from a single-mode fiber was used as light source in the photocurrent measurements. The temperature dependent breakdown characteristics were measured by bonding the device into a TO-5 package and then mounting in an opened cycle liquid nitrogen cryostat.

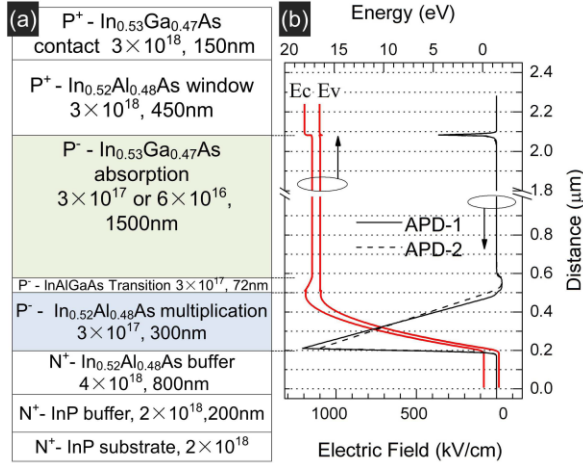


Fig. 1 (a) Epitaxial structure of APD-1 and APD-2. The doping concentration unit is  $\text{cm}^{-3}$ . (b) Calculated energy-band diagram across APD-1 at a bias of  $-16.5 \text{ V}$ , and corresponding E profiles for both APD-1 and APD-2.

## Results and Discussions

The simulated band alignments and E field distributions along the growth direction for the two APDs biased at  $-16.5 \text{ V}$  are shown in Fig. 1(b). It is seen that the E profile in the M region shows both wedge shape with high peak E field intensities. The gradient of the E profile and the E field peak intensity were reduced for APD-2 compared to APD-1. Fig. 2 shows the photo I-V, the dark I-V and the deduced M-voltage curves for the two APDs.  $V_{\text{BR}}$  of APD-1 and APD-2 was determined to be  $19.7$  and  $20.5 \text{ V}$ , with the dark currents of  $119.5$  and  $111.7 \text{ nA}$  at the bias of  $0.9V_{\text{BR}}$ , respectively. Those results indicate that a reduction of doping concentration in the p-type InGaAs absorber could help reduce dark current, increase  $V_{\text{BR}}$  and enhance M.

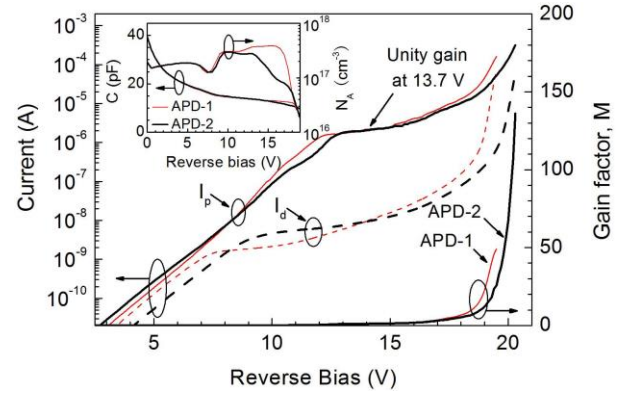


Fig. 2 Measured photocurrent  $I_p$  (solid lines) and dark current  $I_d$  (dash lines) at room temperature of APD-1 (thin lines) and APD-2 (bold lines), as well as their gain factor M versus reverse bias. Inset: measured C-V curves and the deduced  $N_A$  in the multiplication layer.

Fig. 3 shows the measured room-temperature multiplied spectral responses for APD-2 under reverse biases from  $13$  to  $20 \text{ V}$  using a Fourier transform infrared (FTIR) spectrometer adopting a globar source. The device showed a peak response at  $1.55 \mu\text{m}$  with a cutoff wavelength of  $\sim 1.75 \mu\text{m}$ . Inset of Fig. 3 shows the responsivity at  $\lambda = 1.55 \mu\text{m}$  as a function of reverse bias extracted from the spectral responses (scaling via the responsivity measured at unity gain). It is seen that the responsivity of APD-2 shows clear gain with increase of reverse bias which is similar to the photo I-V results shown in Fig. 2.

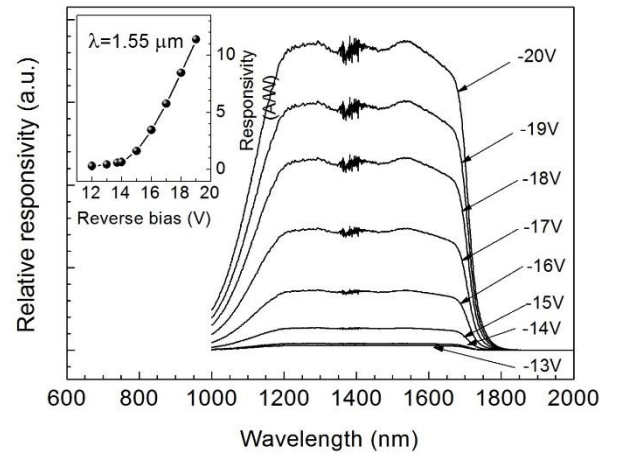


Fig. 3 Measured response spectra of APD-2 under different reverse biases at room temperature. Inset shows extracted bias voltage dependent responsivity of APD-2 from the measured spectra and calibrated photocurrent to  $1.55 \mu\text{m}$  light.

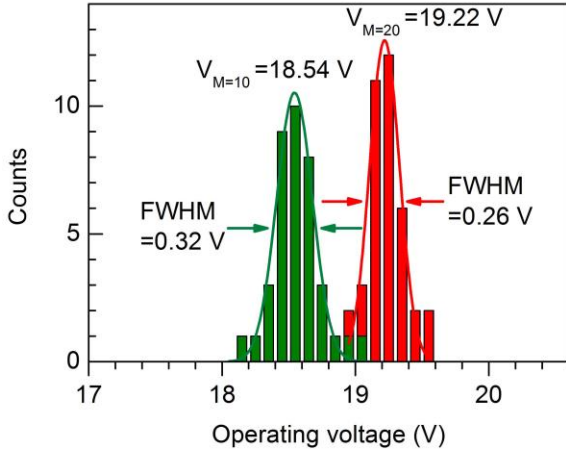


Fig. 4 Statistical distribution of  $V_{M=10}$  and  $V_{M=20}$  for APD-2.

Fig. 4 shows the statistical distributions of operating voltage at  $M=10$  ( $V_{M=10}$ ) and  $M=20$  ( $V_{M=20}$ ) for APD-2. Over 50 devices distributed uniformly on a 1 cm $\times$ 1 cm wafer were measured. Both  $V_{M=10}$  and  $V_{M=20}$  distributions can be fitted using a Gaussian function with mean values of 18.54 and 19.22 V and FWHMs of 0.32 and 0.26 V, respectively. The achieved high gain uniformity is mainly attributed to the excellent epitaxial layer uniformity and the reliable device processes.

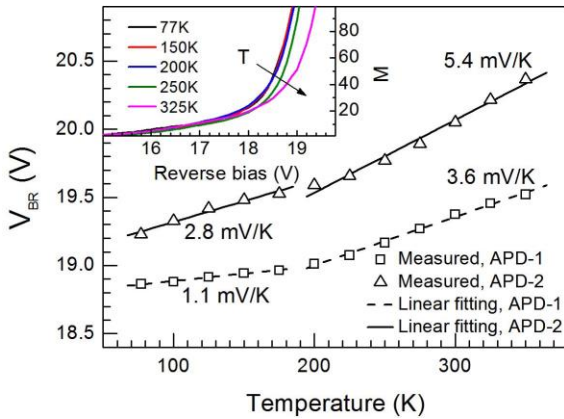


Fig. 5. Measured  $V_{BR}$  for APD-1 and APD-2 as a function of temperature. Dash and solid lines are linear fittings of  $V_{BR}$  for APD-1 and APD-2, respectively. Inset shows the M-reverse bias curves for APD-2 at different temperatures.

Fig. 5 shows the temperature dependent  $V_{BR}$  for APD-1 and APD-2 in temperature range of 77-350 K. Temperature coefficients of 1.1 and 3.6 mV/K for APD-1, and 2.8 and 5.4 mV/K for APD-2, at both low (77-180 K) and high (180-350 K) temperature regimes, respectively, were fitted by  $V_{BR}=(\Delta V_{BR}/\Delta T)\times T+V_0$ . The extracted

$\Delta V_{BR}/\Delta T$  are far smaller than that reported for thin multiplication layer InAlAs/InGaAs which were typically in the range of 15-40 mV/K. Such reduction is tentatively attributed to the much higher E peak intensities in the avalanche region than that in other works (typical 700~800 kV/cm). Carriers acquire the impact ionization threshold energy sooner at higher fields, scattering from fewer phonons on the way, and the temperature dependence of  $V_{BR}$  is, consequently, reduced. The observed different  $\Delta V_{BR}/\Delta T$  at temperature ranges of 77-180 K and 180-350 K are possibly a consequence of the different dominating scattering mechanisms at different temperature ranges for ternary alloys. Inset of Fig. 5 shows the M-reverse bias curves at different temperatures. It is seen that the M curves also showed weak temperature dependence for  $T<200$  K and increased temperature dependence for  $T>200$  K.

## Conclusion

In conclusion, we demonstrated the fabrication of SAM InAlAs/InGaAs APDs with a p-type multiplication layer. Wedge-shaped E profiles with different gradients and peak intensities confined in a thin InAlAs avalanche layer were realized. These APDs showed low operating voltages less than 20 V, small gain slopes and high gain uniformity with optimum operating gains up to 40 in linear mode. Moreover, reduced temperature coefficients of 3-6 mV/K in the temperature range of 200 to 350 K were also observed, whereas the dark current shows a noticeable increase. Those multiplication performances are attributed to the modified electric field profiles and are ideally suitable for FPA imaging applications.

## References

1. P. Martyniuk, J. Antoszewski, M. Martyniuk, L. Faraone, and A. Rogalski, Applied Physics Reviews **1** (2014) 041102.
2. W. R. Clark, A. Davis, M. Roland and K. Vaccaro, IEEE Photon. Technol. Lett. **18** (2006) 19-21.
3. R. J. McIntyre, IEEE T. Electron Dev. **46** (1999) 1623-1631.

# The PN junction width of HgCdTe conversed through ion implantation and ion beam etching

Zhou Songmin<sup>1</sup>, Weng Bin<sup>1,2</sup>, Li Hao<sup>1</sup>, Liu Dan<sup>1</sup>, Wei Yanfeng<sup>1</sup>, Ye Zhenhua<sup>1</sup>, Ding Ruijun<sup>1</sup>, He Li and Lin Chun<sup>\*1</sup>

<sup>1</sup> Shanghai Institute of Technical Physics, Shanghai 200083, P. R. China

<sup>2</sup> Shanghai Tech University, Shanghai 200083, P. R. China

**Abstract:** In this work, a novel junction width measurement method is proposed on LW HgCdTe. A serial of junctions were fabricated by B<sup>+</sup> implantation. There is a series of N-type pairs that distances are varied from 0mm to 10mm between every two junctions, which obtained by high resolution lithography. Current-voltage and Laser Beam Induced Current (LBIC) measurements are applied to determine the HgCdTe junction edge. The LBIC signal and current-voltage orrectification characteristic indicates the existence of a pn junction. The junction width of intrinsic doped HgCdTe was measured, and a significant 0.5mm horizontal expansion N-type region was observed. Moreover, the expansion width of junctions that converse by ion beam etching are also investigated.

**Key words:** HgCdTe, PN junction width, B ion implantation, ion beam etching

## Introduction

The maturity of infrared (IR) technologies enables detectors to be used for varying applications such as in the security, science or space sector. At the present time, the most commonly used material for infrared detection is the HgCdTe semiconductor. Because of its wide tuning range of bandgap, high quantum efficiency, and high operating temperature, HgCdTe is the most preferred material to fabricate infrared focal plane array (IRFPA) [1]–[3]. Ion implantation enables very precise control of the doping distribution depth and dose, it has been used as a means to obtain good quality photovoltaic detectors and widely used as standard process in planar HgCdTe photodiodes manufacturing. However, implantation introduces damages in the PN

junction. As a result, the Schocley-Read recombination rate and trap assistant<sup>1</sup> tunneling (TAT) probability increase. And the interstitial Hg that formed by implantation will diffuse into the side and inner layer [4][5]. The junction width after implantation is key parameter to these processing. The appropriate width and distance of PN junction are critical to achieve the highest performance of photodiodes. However, due to the narrow band gap of HgCdTe material, a significant band bending at the surface has been found. The results of traditional methods of junction profile measurement, such as differential Hall, capacitor-voltage (C-V) method and scanning probe microscopy (SPM), strongly depend on the surface condition of the samples. Therefore it is difficult to determine the junction width precisely and repeatedly.

---

\*chun\_lin@mail.sitp.ac.cn



There are few convenient techniques that can quickly and accurately measure the junction profile of each pixel for an HgCdTe infrared focal plane array. Recently, laser beam induced current (LBIC) imaging has been used in characterization of HgCdTe PN junction [6]–[8]. LBIC imaging can provide spatially resolved information about electrically active defects and localized non-uniformities in HgCdTe materials and devices used for infrared photovoltaic arrays [8][9].

In this paper, a novel junction width measurement method for planar PN junction in HgCdTe epilayer is proposed and demonstrated. The method is based on current-voltage and laser beam induced current (LBIC) measurements on a list of N-type pairs that formed through boron implantation and ion beam etching. The lateral size of junction is determined by current-voltage test results of series neighbor PN pairs. And LBIC signal of individual PN junctions is also designed in this method to identify the PN junction width.

The advantage of the method is the capability to determine the lateral expansion through a list PN junction pairs who are different distances between every pair junctions. The junction lateral expansion of B+ implanted intrinsic doped HgCdTe was measured by this new method. Moreover, junction width of samples with post-implant annealing and junction formed by ion beam etching were also investigated.

### Sample structure and measurement

Though the planar junction size has been designed, it is difficult to measure its real width because the N-type region would expand after implantation. The problem can be solved by transforming the measurement from single junction size to a number of pairs of neighboring PN junctions. A series of N-type pairs which are commonly adopted for the spreading resistance profiling (SRP) method is qualified for the transformation. In view of the property of HgCdTe, one column of N-type pairs whose distances varied from 0mm to 10mm between every two junctions, which obtained by high resolution lithography as shows in the Fig.1. The

width of N-type regions that were formed by ion implantation as design, and the distance increases from 0mm to 10mm between the two N-type regions of every pair. The pair of N-type regions is connective at first, as the distance increasing, they will isolate as N-P-N sandwich structure. Therefore the width resolution of this method could be as high as 0.5 $\mu$ m.

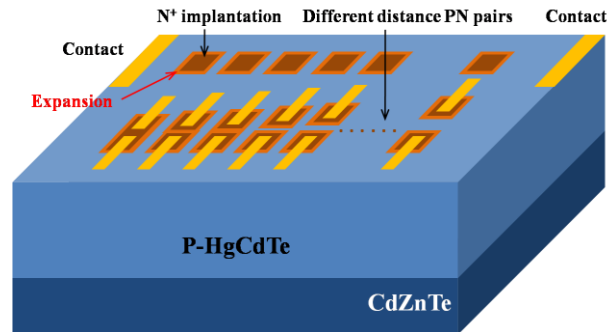


Fig.1. the schematic of the test structure

The current-voltage characteristics of every pair N-type regions are measured in this structure. When the characteristics result shows ohmic-contact, it indicates two N-type regions are connective. When the result shows rectification characteristics, it indicates two N-type regions are isolated. We can use these results and the distances of two pairs of N-type regions to calculate the junction width expansion.

At the same time, some single isolated N-type regions are also designed for LBIC test in Fig.1. As the peaks of LBIC signal locate at the lateral boundaries of the junction, the lateral junction sizes can be determined by the peak-to-peak spaces in LBIC signals.

The validity of the method is based on the presumption that all the junction profiles of the pixel arrays are identical. This presumption depends on the uniformity of the epilayer. Fortunately, it occurs to the HgCdTe epilayers grown by LPE.

### Experiment

The VHg-doped, P-type Hg<sub>1-x</sub>Cd<sub>x</sub>Te (x=0.230) layers were grown by liquid phase epitaxy on CdZnTe substrates. Numerous 50 $\mu$ m $\times$ 50 $\mu$ m pairs of N-type regions were fabricated by B+ ion implantation or ion beam etching with varied distance from 0mm to 10mm between every two junctions. The boron ion implantation process



was carried out at an implant energy of 120-150keV with an implant dosage of  $1-10 \times 10^{14} \text{cm}^{-2}$  at room temperature. The ion beam etch process was carried out with the argon flow rate of 10sccm about 5 minutes. After the implantation or etching process, a ZnS film with a thickness of 100nm was evaporated on the device as a passivation layer. Implanted N-type regions with gold contacts were fabricated for current-voltage characteristics. Two remote contacts on either side of the n-on-p junctions were also deposited with gold in preparation for LBIC measurements. Both LBIC and current-voltage measurement were carried out at liquid nitrogen temperature.

## Discussions

The current-voltage characteristics of every pair N-type regions are measured in this structure. The characteristic result shows as ohmic-contact that indicates the N-type pair is connective, and the rectification characteristic shows that the N-type pair is isolated. We can use these results and the distances of N-type regions to calculate the junction width.

The current-voltage characteristics of some N-type pairs induced by boron implantation in the structure are measured and showed in the Fig.2. In the Fig.2 (a), two junctions of different pairs that their distances are respective  $1\mu\text{m}$  and  $2\mu\text{m}$  are measured, and they show the rectification characteristics. The square line in the Fig.2 (a) is the result of two N-type regions whose distance is greater than  $50\mu\text{m}$ . The results obviously indicate that two PN junctions who are back-to-back and their N-type regions are isolated. Current-voltage characteristics of N-type pairs in different distances from  $0\mu\text{m}$  to  $10\mu\text{m}$  are showed in Fig.2 (b). When the distance is  $1\mu\text{m}$ , the result indicates ohmic-contact. It can infer that the N-type pair is connective. When their distances are not less than  $2\mu\text{m}$ , the results such as two back-to-back PN junctions in Fig.2(a) indicate that they are disconnected. It can easily infer that the N-type region is expanded about  $0.5\mu\text{m}$ .

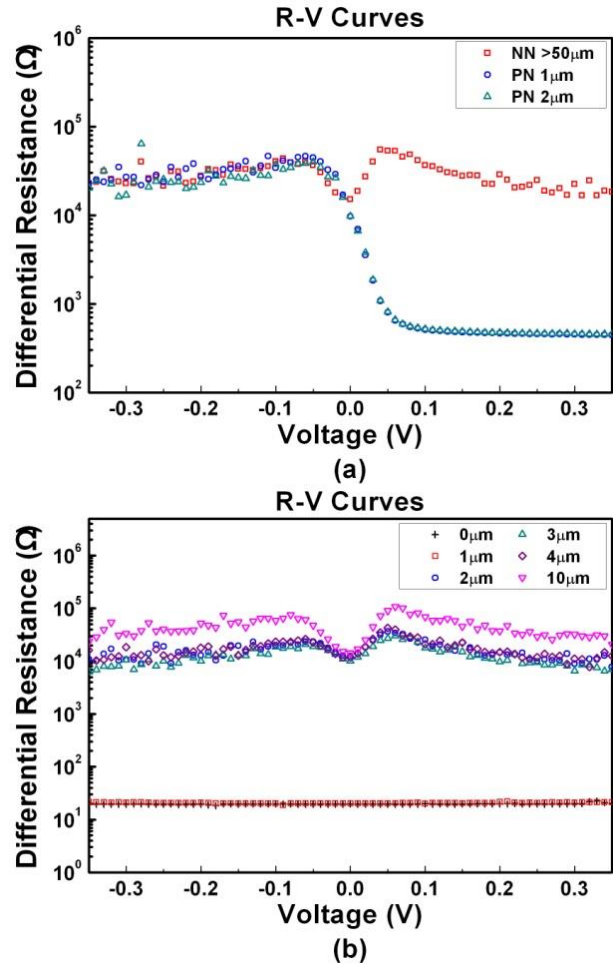


Fig.2. The differential resistance of N-type pairs and PN junctions converted by boron implantation, (a) the R-V curves of two PN junctions and a distance far than  $50\mu\text{m}$  N-type pair, (b) the R-V curves of different distance N-type pairs.

The LBIC signal of a pixel row whose N-type regions size and space are designed as  $50\mu\text{m}$  and  $150\mu\text{m}$  is illustrated in Fig.3. The LBIC signal showed in the Fig.3 is the very strong, a pair of signal peak and valley correspond to the opposite edges of N-type region. The period is about  $150\mu\text{m}$  that accord with design dimension. The N-type region size can be calculated from signal, it is equal to the peak-to-peak distance on the typical junction LBIC signal. The calculated size of N-type regions are showed in Fig.4. There are two junctions that their widths are  $49\mu\text{m}$  even smaller than design size, it may be due to measurement error caused by the motor step and the spot shape. Therefore, we can infer that the actual size of N-type region is  $50\mu\text{m}$ .

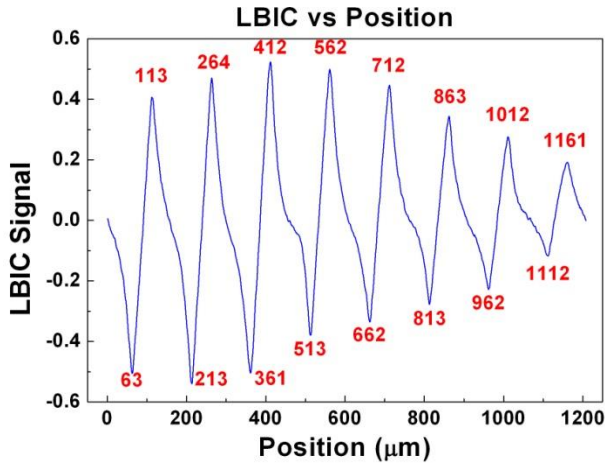


Fig.3. The LBIC signal of the pixel array, the design size and space of the N-type regions are respective  $50\mu\text{m}$  and  $150\mu\text{m}$ .

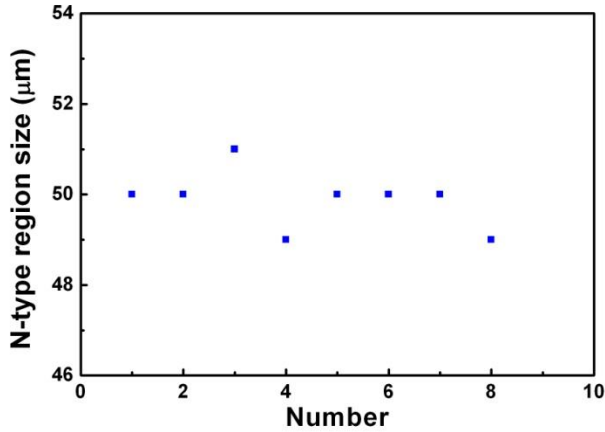


Fig.4. The lateral junction sizes vs. pixel number at different position that extract from LBIC signal.

The current-voltage characteristics of some N-type regions in the structure are measured and showed in the Fig.5. In the Fig.5 (a), two junctions of two pairs that distances are respective  $1\mu\text{m}$  and  $2\mu\text{m}$  are measured, and they show the rectification characteristics. Both square and cycle lines in the Fig.5 (a) are the results of N-type pairs that distances are greater than  $50\mu\text{m}$ . The results obviously indicate that two PN junctions of the pairs are back-to-back, so their N-type regions are isolated. Current-voltage characteristics of N-type region pairs that distances at  $0\mu\text{m}$  and  $10\mu\text{m}$  are showed in Fig.5 (b), both of their N-type regions are connective. It can easily infer that the N-type region is expanded greater than  $5\mu\text{m}$ .

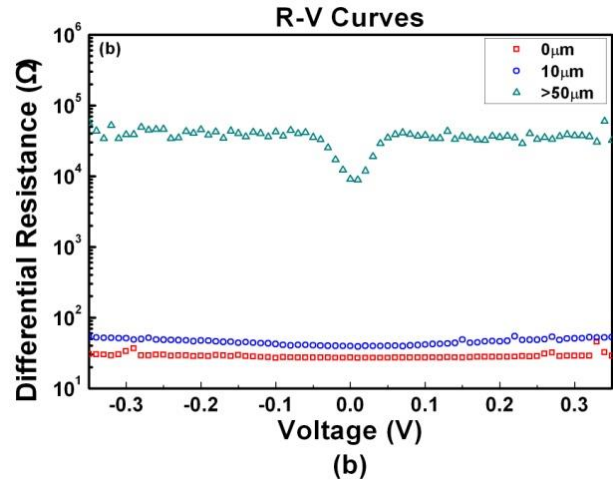
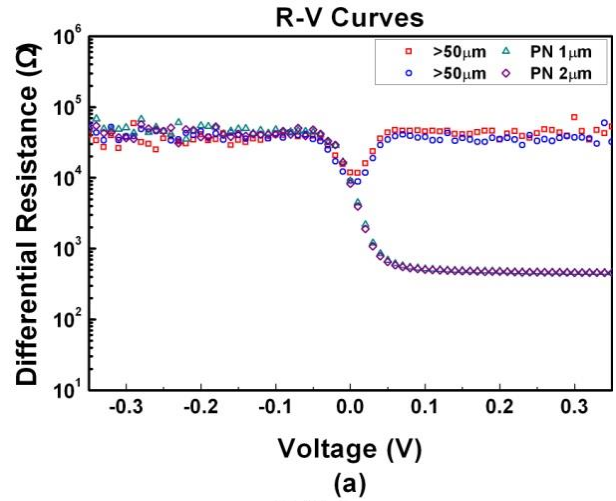


Fig.5. The differential resistance of N-type pairs and PN junctions converted by ion beam etching, (a) the R-V curves of two PN junctions and two N-type pairs of distances greater than  $50\mu\text{m}$ , (b) the R-V curves of different distances N-type pairs.

It has been widely accepted that the N-type region is formed by damages and defects (e.g. native point defects, interstitial Hg atoms and extended defects) caused by ion implantation process instead of the implanted B atoms. The ion implantation does not form the PN junction directly. At shallow layer near the surface the N region is formed by native point defects or complexes introduced by ion implantation. The interstitial Hg atoms are released from the damaged region and diffuse into the side and inner layer. In the intrinsic doped HgCdTe epilayer, the Hg vacancies are annihilated by the interstitial Hg atoms and the n type background is revealed. Therefore the boundary of implanted junction is beyond the implanted Boron distribution edge [4][5]. The results from our experiments confirm this assumption again. By

the method proposed in this paper, the lateral size of the implanted junction in the VHg-doped HgCdTe are  $1\mu\text{m}$  greater than the implanted dimension at liquid nitrogen temperature, which do not expand as much as the junction depth [10][11]. However to explore the mechanism of the junction expansion needs more effort and the more accurate experiments should be carried out.

## Conclusion

A novel method of junction width measurement in HgCdTe planar PN junction is proposed in this paper. In order to precisely measure the PN junction width, a series of N-type pairs that distance varied from 0mm to 10mm between every two junctions were fabricated by high resolution lithography. We can easily control the distance of N-type pairs by mask design and lithography. The width resolution of this method can as high as 0.5mm. By measuring the current-voltage characteristics of the N-type pairs, the junction width expansion can be extracted. The junctions that converted by boron implantation expanded about 0.5mm while those converted by ion beam etching expanded much greater than 5mm. In addition, the LBIC signal result that the actual size of N-type region is  $50\mu\text{m}$ . In the previous work, we report that the junction width expansion is about  $5\mu\text{m}$ . It must be due to measurement error that caused by the motor step of  $2\mu\text{m}$  and the spot shape about  $10\mu\text{m}$ . In this paper, the LBIC signal and the Current-Voltage characteristics results were confirmed each other. Furthermore, the new measurement is applicable to planar PN junction either HgCdTe or other materials.

## References

1. A. Rogalski, J. Antoszewski and L. Faraone, "Third-generation infrared photodetector arrays," *J. Appl. Phys.*, 105, 091101, 2009.
2. P. Norton, "HgCdTe infrared detectors," *Opto-Electron. Rev.*, 10, 159-174, 2002.
3. J. Wang, X. S. Chen, W. D. Hu, L. Wang, W. Lu, F. Q. Xu, J. Zhao, Y. L. Shi, and R. B. Ji, "Amorphous HgCdTe infrared photoconductive detector with high detectivity above 200 K," *Appl. Phys. Lett.*, 99, 113508-1-113508-3, 2011.
4. G. L. Destefanis, "Electrical Doping of HgCdTe by Ion Implantation and Heat Treatment," *J. Crystal Growth*, 86,700, 1988.
5. L. O. Bubulac, Defects, "Diffusion and Activation in Ion Implanted HgCdTe," *J. Crystal Growth*, 86,723, 1988.
6. W. D. Hu, X. S. Chen, Z. H. Ye, Y. G. Chen, F. Yin, B. Zhang, and W. Lu, "Polarity inversion and coupling of laser beam induced current in Asdoped long-wavelength HgCdTe infrared detector pixel arrays: Experiment and simulation," *Appl. Phys. Lett.*, 101, 181108-1-5, 2012.
7. D. A. Redfern, C. A. Musca, J. M. Dell, and L. Faraone, "Characterization of electrically active defects in photovoltaic detector arrays using laser beam-induced current," *IEEE Trans. Electron Devices*, 52(10), 2163-2174, 2005.
8. F. Yin, W. D. Hu, B. Zhang, Z. F. Li, X. N. Hu, X. S. Chen, and W. Lu, "Simulation of laser beam induced current for HgCdTe photodiodes with leakage current," *Opt. Quantum Electron.*, 41, 805-810, 2009.
9. F. X. Zha, M. S. Li, J. Shao, W. T. Yin, S. M. Zhou, X. Lu, Q. T. Guo, Z. H. Ye, T. X. Li, H. L. Ma, B. Zhang, and X. C. Shen, "Femtosecond laser-drilling-induced HgCdTe photodiodes," *Opt. Lett.*, 35, 971-973, 2010.
10. S. M. Zhou, C. Lin, H. B. Li, Y. F. Wei, Z. H. Ye, R. J. Ding and L. He, "Mercury Cadmium Telluride implanted junction profile measurement and depth control", *Proc. of SPIE Vol. 9070: 907031*, 2014.
11. H. B. Li, J. J. Xu, et al. "A novel junction profile measurement in HgCdTe epilayer by laser beam induced current," *Proc. Of SPIE 8193, 819331*, 2011.

# Depth limits of flash-pulse IRNDT method for low- and high-diffusivity materials

M. Švantner<sup>1</sup>, Z. Veselý<sup>2</sup>, L. Muzika<sup>3</sup>

<sup>1</sup> University of West Bohemia, Plzeň, Czech Republic, msvantne@ntc.zcu.cz

<sup>2</sup> University of West Bohemia, Plzeň, Czech Republic, zvesely@ntc.zcu.cz

<sup>3</sup> University of West Bohemia, Plzeň, Czech Republic

Infrared nondestructive testing (IRNDT) is an advanced experimental method for defects inspection, which is based on active thermography. IRNDT uses an external excitation of a tested material and a thermographic analysis for an analysis of its response. It allows to obtain information about the tested material surface and sub-surface defects or structural inhomogeneities. The flash-pulse is the IRNDT method, which uses a very short thermal excitation pulse by a flash-lamp. The method principles and parameters are introduced in the contribution. Experimental results are presented and depth-limits for an inspection of materials with low and high diffusivity are discussed.

## Introduction

Infrared thermography [1] is an analytical technique, for noncontact measurement of spatial and time distribution of the surface temperature fields. It is based on detection of objects radiation in the infra-red range, which is particularly dependent on temperature and thermo-optical properties of the measured surfaces [2]. Advantages of the infrared thermography include: it is a noncontact method; it records temperature fields; it can measure rotating objects or objects of very high temperatures. The main disadvantages are that it is influenced by the measured surface thermo-optical properties, ambient temperature or surrounding atmosphere properties. These relationships can make an accurate temperature measurement quite complicated [3] and should be taken into account at thermographic analysis.

The thermography can be classified as qualitative or quantitative and passive or active. The qualitative thermography evaluates infrared

radiation contrasts between individual components, different positions on a component or between a component and background. Important applications are: heat leaks diagnostics, electrical components inspections, surveillance of people etc. The goal of quantitative thermography is to evaluate an exact numerical value of temperature or temperature differences. It is useful in many technological applications, for example heat treatment control.

Both the qualitative or quantitative approaches can be based on the passive or active thermography. The temperature contrast or the temperature changes are of natural origin in the case of passive thermography. On the other hand, the external source and an excitation of analyzed objects are used in cases of active thermography. The excitation causes a temperature contrast connected with thermal properties local differences or local heat sources concentration for example. These differences can be quantified directly or used for some advanced evaluation.

## Infrared nondestructive testing

IRNDT is the inspection method, which is based on active thermography [4, 5]. The principle is based on changes of heat transfer conditions in the material due to the defects. The material can be exposed directly to a thermal source or using an internal heat source. If a direct heating (halogen or flash lamps, hot air etc.) is used then the heat flux in the material is affected by a presence of defects. Ultrasound, vibration, mechanical or electrical loading can be used for the internal excitation. Local heat sources then occur due to the loading interaction with material defects. The described processes result in material surface radiation response, which can be detected by an IR camera. An example of a lamp excitation principle is illustrated in fig.1.

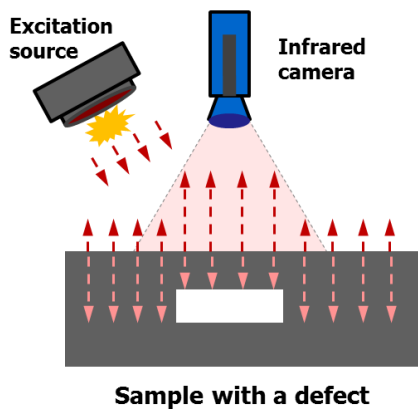


Fig.1. Schematic illustration of lamp excitation IRNDT principle in a reflection configuration.

Different excitation methods can be used based on a used excitation source, tested material properties or other requirements (inspection speed, inspection area, material loading limitation etc.). The basic excitation methods are continuous, pulsed and periodical loading. The response is detectable on a raw thermogram in the simplest case. However, advanced evaluation methods should be used in the most cases [6]:

- *Pulse thermography.* The excitation is applied for a very short time and the object cooling progress is analyzed.
- *Lock-In thermography.* Modulated periodical excitation of the analyzed object is used and

amplitude and phase of the response signal is analyzed.

- *Transient (Step) Thermography.* A heat pulse of longer times is used and the tested object time-thermal response is analyzed.

The excitation can be realized by different sources:

- *External heat excitation source:* halogen lamps (Transient, Lock-In), flash lamps (Pulse), laser contact heat, hot air etc.
- *Vibro-thermography:* stimulation of a measured object by vibrations (modulated high-power ultrasound signal). The vibrations cause friction and occurrence of local heat sources on discontinuity surfaces (cracks).
- *TSA - Thermal stress analysis:* periodical excitation by mechanical energy. Local heat sources occur due to the thermo-mechanical effects at stress concentrators (cracks etc.).
- *Other methods.* Electro-magnetic excitation for example.

High-speed cooled infrared cameras or bolometric cameras are applicable. Different excitation sources, IR cameras and evaluation methods can be combined in dependence on application requirements. IRNDT is used in many scientific or industrial applications, for example for solar cells inspection, aircraft components inspection, wind turbine blades inspection etc. An overview, state-of-the-art and trends of IRNDT are extensively described in [7] for example.

## Experimental procedure

We used flash-pulse IRNDT method in this work. The excitation by a flash lamp is applied for a very short time and the object cooling progress is then analyzed. The method is very fast, it is possible to estimate a defects depth and a thermal load of a tested sample is mostly low. Disadvantages are detectability dependence on defects geometrical orientation and limited inspection area. The method is very good suited for thin layers and near surface defects inspection.



The goal of this work was to evaluate depth limits of the flash-pulse method for materials with different thermal diffusivity. The excitation source was a 5 kJ flash lamp and the pulse length was from 3 to 25 ms. A high-speed IR camera SC7650 was used for the response detection. The recording frequency was 20-200 Hz. A carbon-epoxy composite sample, steel sample and aluminum based (duralumin) sample were tested.

The carbon-epoxy, steel and duralumin samples had the thermal diffusivity about 0.2, 4.8 and 50  $\text{m}^2/\text{s}$  respectively. All the samples were plates with drilled holes of different depths and diameters at the back side. The inspection was performed at the front side of the samples and the holes simulated defects at different depths from the surface. The carbon-epoxy sample was a 144x120 mm plate of the thickness 5.3 mm with 6 holes of diameter 30 mm in depths 1.3-3.8 mm. The steel sample was a 200x150 mm plate of the thickness 5.15 mm with 22 holes of diameter 1-10 mm in depths 0.8-4 mm. The duralumin sample was a 230x100 mm plate of the thickness 12.2 mm with 27 holes of diameters 3.2-11.6 mm in depths 0.7-8.3 mm. The steel and duralumin samples front side (the inspected side) was painted by a black high-emissivity colour. The experimental configuration was similar as it is shown in Fig.1.

Different methods were used for the measurements evaluation: Root model, e-model and Pulse-Phase method. The Root model and e-model use an analytical approximation of the measured signal. The Pulse-Phase method performs a Fourier Transform and gives a phase spectrum as a function of frequency. All the methods allow evaluation adjusting by additional parameters (evaluation time, approximation polynomial grade etc.). The final results were evaluated visually based on contrast of the expected defects to the full thickness material around. The evaluation procedure was adjusted for the best possible results for each of the measurements. Detectability of the defects depending on their depth, size and inspected material was analyzed.

## Results

Defects of all depths were detected in the carbon-epoxy sample. The defect in the depth 1.3 mm was found using 200 Hz IR camera sampling frequency, pulse length 5 ms and inspection time 4 s. The evaluation is shown in Fig.2.

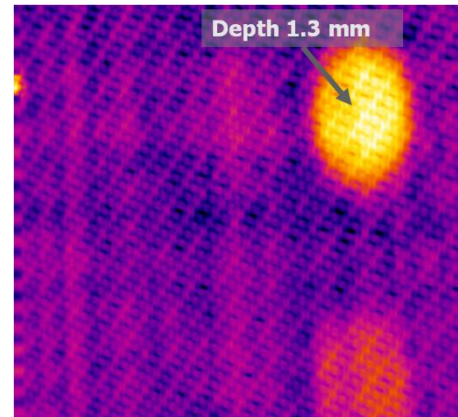


Fig.2. Flash pulse evaluation of the carbon-epoxy sample. Maximum defect depth 1.3 mm, IR camera sampling frequency 200 Hz, pulse length 5 ms, inspection time 4 s.

The pulse length and inspection time should be extended for defects detection at a greater distance from the surface. The pulse length 15 ms, inspection time 20 s and camera frequency 40 Hz were used for the detection of the defect in the depth 3.8 mm. The evaluation is shown in fig.3. Although the defect can be found, the detectability is significantly worst compared to the defects closer to the surface. The contrast is lower, defect boundary is blurred and a detected (visible) defects size does not correspond to the real size of the defect.

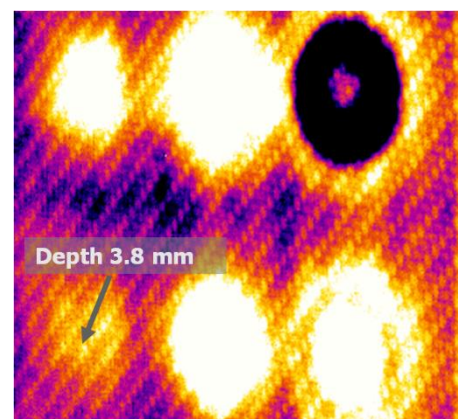


Fig.3. Flash pulse evaluation of the carbon-epoxy sample. Maximum defect depth 3.8 mm, IR camera sampling frequency 40 Hz, pulse length 15 ms, inspection time 20 s.

It is evident, that the detectability of defects deeper than 2.7 mm from the surface is limited. The defect in the depth 3.8 mm would be probably not found if it is smaller.

Suitable pulse length and camera frequency for steel sample inspection were from 3 to 5 ms and from 120 to 250 Hz respectively. The inspection time was from 0.1 to 8 s. Defects of diameter 10 mm were found in depths from 0.8 to 4.2 mm in the steel sample. Other defects in depth range from 0.14 to 3 mm and diameter range from 2.6 to 9 mm were also detected. However, the defects of a diameter under 2.3 mm were not indicated. These results confirm that the detectability can be limited in the case of small defects even if bigger defects can be indicated in the same or greater distance from the surface.

The duralumin sample was inspected by the IR camera sampling frequency in the range from 100 to 200 Hz, which is very similar to the parameters used for the steel sample testing. The pulse length was from 5 to 25 ms and the inspection time was from 2 to 5 s. Defects in depth 8 mm were not detected regardless of their size. Defects in depth about 5 mm were indicated if their size was greater than 8 mm. Defects in depth from 0.7 to 1.9 mm were found if their size was bigger than 4 mm.

It was shown that smaller defects in bigger depths can be found in duralumin compared to the carbon-epoxy sample. The maximum depth of detectable defects was similar in the steel and duralumin samples. However, the defects size in the steel sample was bigger than in the duralumin sample at similar depths. Contrast of indicated defects to the background was lower and their boundaries were more blurred compared to the carbon-epoxy or steel sample for all the visible defect depths. The dependence of detectability in different depths and inspection time demonstrates the depth estimation ability of the method.

## Conclusion

The results presented showed that the flash-pulse IRNDT is a usable inspection method for materials with low and high thermal diffusivity. Different flash-pulse evaluation methods (pulse-phase, e-model etc.) and parameters were tested. The experimental work continues on previous published results. It brings some new information regarding the used experimental set-up and tested materials.

The maximum inspection depth in the carbon-epoxy material with the diffusivity  $0.2 \text{ m}^2/\text{s}$  was about 4 mm. The depth-detectability was higher in the case of high diffusivity materials. The maximum inspection depth was about 5 mm in steel or duralumin samples, which had the diffusivity 4.8 and  $50 \text{ m}^2/\text{s}$  respectively. The maximum depth of detection can be reduced if a defect size is too small. The defect size should be generally bigger than their depth. However, orientation of the defects or material properties can influence the detectability in specific cases.

## Acknowledgements

The result was developed within the CENTEM project, reg. no. CZ.1.05/2.1.00/03.0088, cofunded by the ERDF as part of the Ministry of Education, Youth and Sports OP RDI programme and, in the follow-up sustainability stage, supported through CENTEM PLUS (LO1402) by financial means from the Ministry of Education, Youth and Sports under the "National Sustainability Programme".

## References

1. G. Gaussorgues: *Infrared Thermography*, Kluwer Academic Publisher, 1994.
2. M. F. Modest: *Radiative heat transfer*, 3rd Edition, Academic Press, 2013.
3. M. Švantner, P. Vacíková, M. Honner, Non-contact charge temperature measurement on industrial continuous furnaces and steel charge emissivity analysis, *Infrared Physics & Technology*, 61 (2013) 20–26.
4. X. Maldague: *Theory and Practice of Infrared Technology for Nondestructive Testing*, Wiley-Interscience, 2001.

5. H. T. Yolken, G. A. Matzkanin: Thermography for Nondestructive Evaluation (NDE), Nondestructive Testing Information Analysis Center, USA, 2001.
6. Švantner M., Veselý Z., Active thermography for materials non-destructive testing, Proc. of 23rd Int. Conf. on Metallurgy and Materials Metal 2014, Brno, Czech Republic, TANGER Ltd., pp.861-856.
7. Vavilov V.: Thermal NDT: historical milestones, state-of-the-art and trends, Quantitative InfraRed Thermography, 11:1 (2014) 66-83.



# Tunable hot-carrier photodetectors

A. G. Unil Perera<sup>1</sup>, Yan-Feng Lao<sup>1</sup>, L. H. Li<sup>2</sup>, S. P. Khanna<sup>2</sup>, and E. H. Linfield<sup>2</sup>

<sup>1</sup>Department of Physics and Astronomy, Georgia State University, Atlanta, GA 30303, USA

<sup>2</sup>School of Electronic and Electrical Engineering, University of Leeds, Leeds LS2 9JT, United Kingdom

A photodetector operating based on a hot-cold carrier energy transfer mechanism has been demonstrated. Hot carriers injected into a semiconductor structure interact with cold carriers and excite them to higher energy states. This enables a very long-wavelength infrared response up to 55  $\mu\text{m}$ , which is tunable by varying the degree of hot-hole injection.

## Introduction

The cut-off wavelength limit ( $\lambda_c$ ) in traditional photodetectors is determined by the activation energy of the semiconductor structure through the relationship:  $\lambda_c = hc/\Delta$ , [1] where  $\Delta$  is an internal work function defined as the energy difference between the Fermi level of the emitter and the valence-band (VB) edge of the barrier. [2] This spectral rule dominates device design and intrinsically limits the long wavelength response of the photodetector. Modifying the energy distribution of carriers, for example, by introducing hot-cold carrier interactions, can lead to a change in the response.

We report extending the spectral threshold wavelength into the very-long wavelength infrared (VLWIR) range by using a p-type graded-barrier GaAs/AlGaAs heterojunction photodetector. This result is explained as owing to energy transfer from hot carriers to cold carriers. [3] The detector experimental dark current can be fitted by a thermionic emission model [4] using the activation energies according to the designed values. The advantage of the hot-carrier mechanism is a new detection concept which separates the photoemission threshold from affecting the spectral response, allowing minimizing the detector noise by using a high activation threshold.

## Device structure

Semiconductor heterostructures based on p-type GaAs/Al<sub>x</sub>Ga<sub>1-x</sub>As were used to study the hot-carrier detection. As shown in Fig. 1 (a), they consist of three p-type GaAs regions ( $p = 1 \times 10^{19} \text{ cm}^{-3}$ ), i.e., an injector, absorber and collector, for which the VB alignment is schematically plotted in Figs. 1 (b). The injector provides a hot-hole reservoir upon photoexcitation. Holes surmounting the barrier are “hot” because of their excess energies relative to the band edge of the absorber.

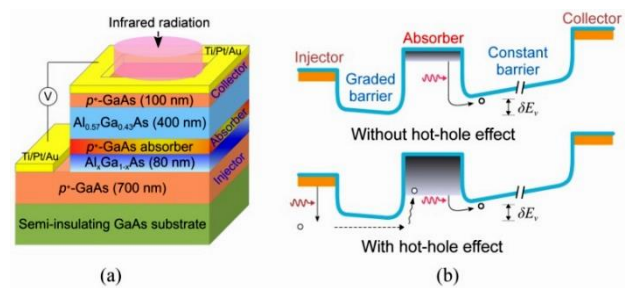


Fig. 1. (a) Schematic of the p-type GaAs/Al<sub>x</sub>Ga<sub>1-x</sub>As hot-hole photodetector structure. (b) Schematic valence-band diagrams (including band bending) under negative bias (positive polarity applied on the injector), with a comparison of hole photoexcitation and emission without (top) and with (bottom) hot-cold hole energy transfer.  $\delta E_v$  is the offset between the barriers below and above the p-GaAs absorber.

## Results and discussion

The photoresponse shown in Fig. 2 (b) was measured at 5.3 K. The most striking fact is that, a very long-wavelength infrared response is seen up to 55  $\mu\text{m}$ , whilst the conventional limit is only 3.9  $\mu\text{m}$  (shaded region) according to the internal work function (i.e.,  $\Delta$ ) of the absorber/constant barrier junction ( $\Delta = 0.32$  eV). The agreement between  $\lambda_c$  and  $\Delta$  in terms of  $\lambda_c = hc/\Delta$  is typically found to be good in a variety of detectors, and has been used as a guideline to tune spectral response through varying  $\Delta$ , and to determine band offsets. However, the observed VLWIR response threshold in this case does not agree with the value of  $\Delta$  given by  $\lambda_c = hc/\Delta$ .

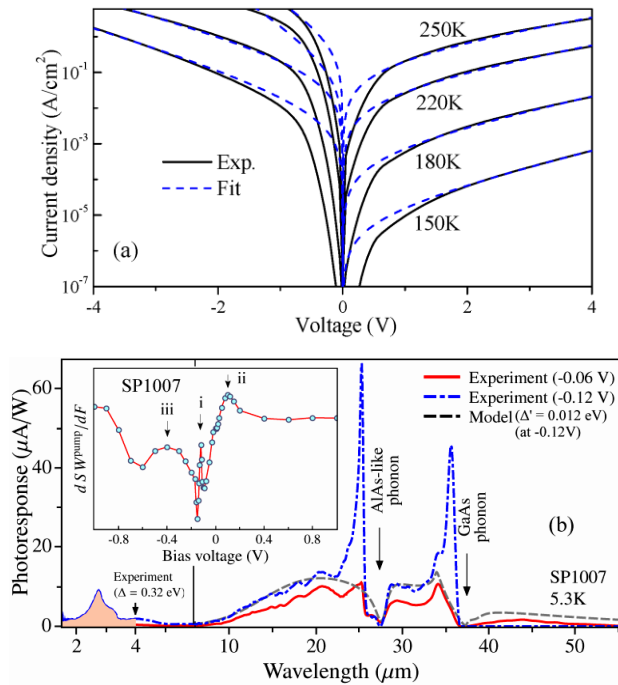


Fig. 2. (a) Experimental and theoretical dark current-voltage (I-V) characteristic; the fittings are based on the thermionic emission model, with active energies of 0.32 eV and 0.40 eV for reverse and forward biases, respectively. (b) Experimental photoresponse at 5.3 K, and the escape-cone model (dashed line) fit, with reduced threshold energy ( $\Delta'$ ) as 0.012 eV (103  $\mu\text{m}$  in wavelength). The marked arrows are associated with GaAs and AlAs-like phonons. Inset: Differential SWpump versus bias, showing distribution peaks (i, ii and iii).

In general the observed VLWIR response could be due to a bolometric effect, or an impurity-band/free-hole carrier based response. Possible optical transitions contributing to photon absorption by the p-type GaAs absorber in the

infrared range include the impurity band-to-valence band transition, and intra-/inter-valence band transitions, both of which are free-carrier type effects. Increasing the doping concentration shifts the absorption peak and broadens the absorption width, as a result of enhanced carrier scatterings, and the shifting/increasing of the Fermi level/free-carrier plasma frequency, respectively. The absorber, though, has a major effect on the bolometric response and impurity-band absorption. By measuring a control sample which contains the same GaAs absorber, we can exclude these two mechanisms as a cause of the VLWIR response. Additionally, the bolometric response, proportional to the temperature variation of the absorber upon photon absorption and the corresponding resistance change, monotonically increases with increasing bias. This effect contrasts with the strongly non-monotonically bias-dependent VLWIR response. As seen in Fig. 2 (b), the observed VLWIR response agrees well with a fitting value  $\Delta = 0.012$  eV (escape-cone model), although the design and Arrhenius plot gives  $\Delta = 0.32$  eV. Well explained features associated with GaAs and AlAs-like phonons show that the escape-cone model response with a value of 0.012 eV (103  $\mu\text{m}$ ) agrees well with measured response.

The hot-cold carrier energy transfer mechanism is in part supported by the differential photocurrent. The short-wavelength portion of light from either a Fourier transform infrared (FTIR) spectrometer, or from an external optical excitation source (denoted as the “pump”), is essential to generate photoexcited hot holes and establish the VLWIR response. The pump-excited holes with energies higher than all of the barriers can be described by a three-dimensional drift model, [5]

$$I_{ph}^{pu} = e \cdot v(F) \int_{\Delta}^{+\infty} N(\varepsilon) d\varepsilon \quad (1)$$

where  $dI_{ph}^{pu}$  is the pump current.  $N(\varepsilon)$  is the concentration of holes with energy  $\varepsilon$ . The electric field  $F$  is evaluated across the barrier regions. The drift velocity  $v(F)$  is associated with an empirical fitting parameter - the

mobility, which is dependent upon both the doped GaAs absorber and undoped AlGaAs barrier. Despite its simplicity, Eq. 1 accounts for the current-voltage characteristics reasonably well in most devices. Taking the derivative of  $I_{ph}$  with respect to  $F$  gives

$$\frac{dI_{ph}^{pu}}{dF} = e \cdot \frac{dv(F)}{dF} \int_{\Delta}^{+\infty} N(\varepsilon) d\varepsilon - e \cdot v(F) \frac{d\Delta}{dF} N(\Delta) \quad (2)$$

in which  $dI_{ph}^{pu}/dF$  is mainly determined by the image-force barrier lowering [2] and tilting of the graded barrier by applied bias. In the high-field region, the first term of Eq. 2 vanishes since  $v(F)$  approaches a constant saturation velocity. The energy distribution of holes is thus proportional to the differential  $I_{ph}^{pu}$ , which consists of photocarriers with different energies.  $I_{ph}^{pu}$  can be evaluated as being proportional to the spectral weight (SW) of the response, defined as

$$SW \propto \int_{\lambda_{min}}^{\lambda_{max}} R(\lambda) d\lambda \quad (3)$$

where  $R(\lambda)$  is the spectral responsivity. As seen in the inset of Fig. 2 (b), the differential  $SW$  displays three distribution peaks at -0.12, -0.40 and 0.10 V, which were confirmed by photocurrent-voltage characteristics measured using different optical excitation source. As a comparison, another sample, which does not display the VLWIR response peaks, only displays one differential  $SW$  peak at 0 V. In terms of hot-carrier spectroscopy, [6] the occurrence of distribution peaks is a sign of a hot-cold carrier interaction which leads to the excitation of cold carriers into higher energy states. With increasing negative bias, the slope of the graded barrier is reduced (towards a horizontal shape). An increase in the injection of hot holes and enhanced hot-cold interactions is then expected, which consequently leads to an increase in cold holes occupying higher energy states. This explains the distribution peak at -0.12 V. When the bias is further increased, the electric field is distributed uniformly throughout the structure. The lowering of the constant barrier by the image-force effect will facilitate

the escape of higher-energy cold holes over the barrier, which leads to another distribution peak at higher negative bias (-0.40 V). At high biases, the hot-hole related current is also high, which overwhelms the VLWIR radiation caused photocurrent. Observing the positive-bias hole distribution peak (0.10 V) is uncommon. A possible reason is the non-linear increase of photocurrent with bias due to the asymmetric band alignment. However, applying a negative bias leads to the optimum VLWIR response, which is much stronger than that under positive bias. The three distribution peaks rely on the structural details such as the graded barrier and the barrier offset. Ability to control these peaks should lead to tunability of the hot-hole photodetection.

The occurrence of the VLWIR response due to the hot-cold carrier interaction means that one can tune the degree of hot-hole injection to control this response. The experimental setup shown in Fig. 3 was used to demonstrate the tuning of the VLWIR response. A  $\lambda_{CO} = 4.5 \mu\text{m}$  (corresponding to 0.28 eV) long-pass filter is used to block the high-energy ( $> 0.28 \text{ eV}$ ) photons (from spectrometer) from being incident onto the sample. The generation of hot holes is enabled by sending an external high-energy light. The photocurrent, represented by the spectral weight of the response, at different excitation levels is shown in Fig. 4 (a). Fig. 4

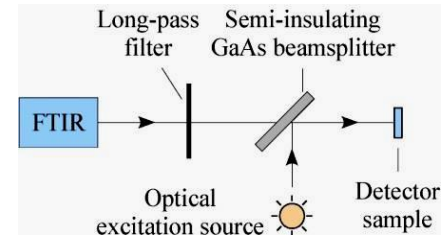


Fig. 3. Experimental apparatus, where the double-side polished semi-insulating GaAs wafer acts as a beamsplitter.

(b) shows the excitation power spectra. The variation of the VLWIR response (at -0.1 V) with the excitation power is plotted in Fig. 4 (c), indicating that the VLWIR response is enabled by increasing the excitation intensity,

demonstrating the response tunability varying the degree of hot-hole injection.

In addition to the bulk p-type doping absorber, nano structures, (e.g., quantum well and dot) can be used to enhance the hot-carrier effect due to the extended carrier lifetime through carrier confinement. Also, optical enhancements

including surface plasmon and cavity resonance can be used to further enhance the optical electric field. All these shall contribute to increased responsivity as well as an elevated operating temperature.

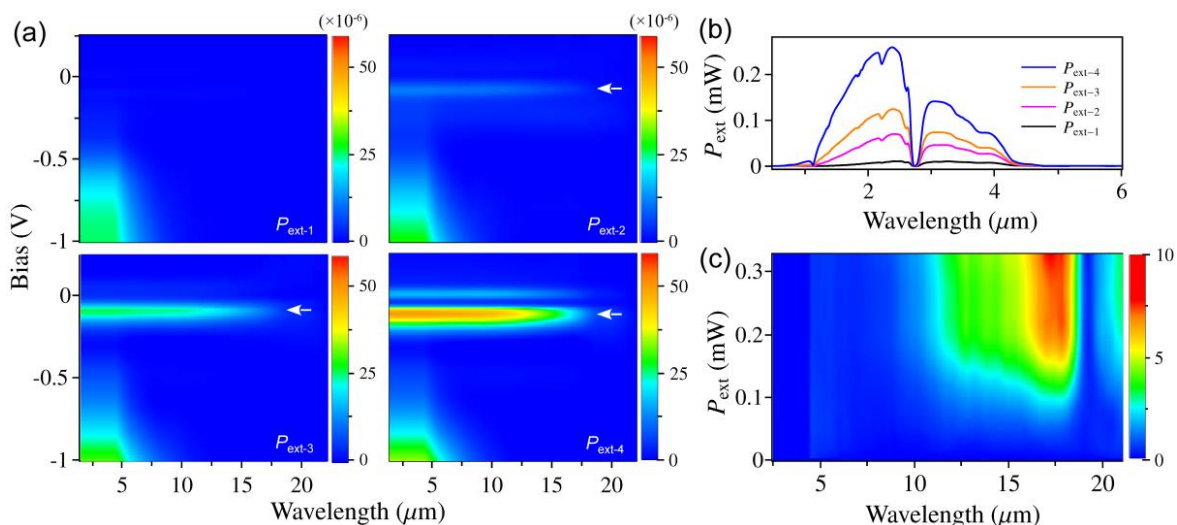


Fig. 4. (a) Spectral weights of response obtained using different intensities of optical excitation source. The left image in the first panel was obtained using  $P_{ext-1}$ , which is very similar to the case where the external optical source is fully blocked. (b) Power spectra of the excitation optical source (incident on the sample with an active area of  $260 \times 260 \mu\text{m}^2$ ). A quartz glass filter is used to enable spectra up to  $4.8 \mu\text{m}$  which ensures the excitation optical source is only used to excite hot holes. (c) The dependence of the VLWIR response (at  $-0.1 \text{ V}$ ) on the excitation power.

## Conclusion

To conclude, we have demonstrated a photodetector with response up to  $55 \mu\text{m}$ , which is tunable by varying the degree of hot-hole injection. This study shows the possibility of incorporating long-wavelength response in a short-wavelength detector. This work was supported in part by the US Army Research Office (grant no. W911NF-15-1-0018), and in part by the US National Science Foundation (grant no. ECCS-1232184).

## References

- [1] S. M. Sze, *Physics of Semiconductor Devices*. New York: John Wiley & Sons, 1981.
- [2] Y.-F. Lao and A. G. U. Perera, "Temperature-dependent internal photoemission probe for band parameters," *Physical Review B*, vol. 86, p. 195315, 2012.
- [3] Y.-F. Lao, A. G. U. Perera, L. H. Li, S. P. Khanna, E. H. Linfield, and H. C. Liu, "Tunable hot-carrier photodetection beyond the bandgap spectral limit," *Nat Photon*, vol. 8, pp. 412-418, 2014.
- [4] D. G. Esaev, M. B. M. Rinzan, S. G. Matsik, and A. G. U. Perera, "Design and optimization of GaAs/AlGaAs heterojunction infrared detectors," *J. Appl. Phys.*, vol. 96, pp. 4588-4597, 2004.
- [5] H. Schneider and H. C. Liu, *Quantum Well Infrared Photodetectors - Physics and Applications*, vol. 126 Berlin: Springer, 2007.
- [6] A. F. J. Levi, J. R. Hayes, P. M. Platzman, and W. Wiegmann, "Injected-Hot-Electron Transport in GaAs," *Physical Review Letters*, vol. 55, pp. 2071-2073, 1985.

# Investigation of High Quantum Efficiency Resonant Cavity Enhanced InAs/GaSb type II Superlattice Long Wavelength Infrared Detectors

Z. Bai<sup>1</sup>, J.Chen, Zh. Xu, Y. Zhou, G.Xu, H. Zhu

<sup>1</sup> Key Laboratory of Infrared Imaging Material and Detectors  
Shanghai Institute of Technical Physics, Chinese Academy of Sciences  
Shanghai 200083, China and baizz@mail.sitp.ac.cn

In this paper, we will present a new way to increase the quantum efficiency of Type-II InAs/GaSb superlattice infrared detectors. We introduce the resonant cavity enhanced structure which is commonly used in semiconductor lasers to InAs/GaSb type II superlattice infrared detector. We simulated the absorber layer absorption coefficient and InAsSb thickness, optimized the optical structure of superlattice resonant cavity by which the surface reflectance of detectors will reduce to zero. Resonant cavity enhanced InAs/GaSb type II superlattice infrared detectors with quantum efficiency of 51% at 10.3 $\mu\text{m}$  and 85% at 6 $\mu\text{m}$  were prepared. The quantum efficiency of superlattice detector is enhanced by the resonant cavity structure effectively.

## Introduction

Type-II InAs/GaSb superlattice (T2SL) is one of 2<sup>nd</sup> generation infrared detector material, it has some excellent properties for infrared detection, such as high absorption coefficients comparable to HgCdTe, high material uniformity, and reduced tunneling currents, suppressed Auger recombination rates[1, 2]. Recently, T2SL have garnered significant interest and are now considered to be a potential alternative to HgCdTe technology in the long wavelength infrared (LWIR) detection regime [3, 4]. But the free carrier absorption of GaSb substrate and minority carrier diffusion length greatly influenced the quantum efficiency of T2SL detectors, especially in long wavelength infrared detectors. There are some methods to increase the quantum efficiency of infrared detectors: increasing absorption layer thickness, doping absorption region, depositing anti-reflection coating, removing substrates [5-8].

In this study we created a new way to increase the quantum efficiency of superlattice infrared detectors without increasing the active layer

thickness and anti-reflection coating. We designed a resonant cavity enhanced T2SL infrared detector structure which is commonly used in semiconductor lasers. In these detectors, a photosensitive diode is placed inside a resonant optical cavity delimited by two mirrors. Incident infrared radiation forms a standing wave pattern inside the cavity at specific wavelengths depending on the cavity length [9]. In this paper, the absorption coefficient of InAs/GaSb absorption layer and InAsSb thickness were simulated, The spectral response of resonant cavity structure detectors were simulated and analyzed. Finally, a 10.3 $\mu\text{m}$  detector with resonant cavity structure was designed and prepared.

## Experiments

Type-II InAs/GaSb superlattice infrared detector structure of resonant cavity was designed by comsol software, the relationship between reflectance and absorption coefficient of InAs/GaSb absorption layer were simulated, the detector structure and InAsSb layer thickness were optimized. The spectral response of



resonant cavity structure devices were simulated and analyzed by which the surface reflectance of detectors will reduce to zero. A detector with resonant cavity structure was designed.

The superlattice materials were grown on (100) GaSb substrates using a molecular beam epitaxy (MBE) system equipped with As and Sb valved cracker sources. Thermal effusion cells are used as Ga and In sources. Si and Be are employed as n-type and p-type dopants, respectively. Prior to the growth, the surface oxides of the GaSb substrates were thermally desorbed, which was monitored by reflection high energy electron diffraction (RHEED). The growth temperature was set at around 400°C measured by a calibrated infrared pyrometer. The lattice-mismatch of the superlattices to GaSb substrates was tuned by fine designing the interface structures and growth process, such as IF layer thickness and composition.

The absorption region of the LWIR photodetectors is composed of 15ML InAs/7ML GaSb superlattices. InAsSb was grown as an etching stop layer (Fig. 1). The grown photodetector structures were processed into back illuminated single-element devices using standard optical lithography, inductive coupled plasma (ICP) dry etching, and E-beam evaporation of top and bottom Ti/Pt/Au ohmic contacts, thermal evaporation of indium bump, flip chip bonding to testing ROIC, chemical etching to remove GaSb substrate. Current-voltage (I-V), optical response measurements and blackbody response were performed at liquid nitrogen temperature (around 77K).

## Results and Discussion

### Simulation of resonant cavity structure

Figure 1 shows the cross-section of the proposed resonant cavity enhanced structure for LWIR InAs/GaSb type II superlattice infrared detectors. The cavity has two mirrors: Au mirrors and Semiconductor Air(S-A) interface mirrors. Between the two mirrors is the main body of the resonant cavity which contains a p-i-n photo detector. The absorber layer is 15ML

InAs/7ML LWIR InAs/GaSb superlattices. Be-doped superlattice works as the p-type contact, Si-doped superlattice works as the n-type contact. GaSb is the positive electrode. InAsSb is an important part of the cavity, it works as the etching stop layer and S-A interface material.

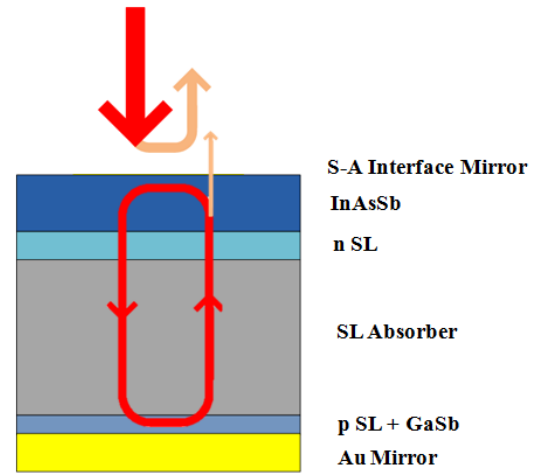


Figure 1 Cross-section structure of resonant cavity enhanced InAs/GaSb type II superlattice infrared detectors.

In this study the InAs/GaSb superlattices absorber layer thickness was set as 3 $\mu\text{m}$ . The detectors reflectance was studied by changing the absorption coefficient of absorption layer. The simulation was taken by calculating Maxwell equations in COMSOL software. Figure 2 shows simulated results, the detectors reflectance with different absorption coefficient of InAs/GaSb absorption layer shows different properties. The reflectance peak is at 12 $\mu\text{m}$  for all curves in Figure 2. When the absorption coefficient is 500 $\text{cm}^{-1}$ , the device reflectance is 30%, the reflectance peak is sharp and the Full Width Half Maximum (FWHM) is 1.1 $\mu\text{m}$ . When the absorption coefficient increases to 2000 $\text{cm}^{-1}$ , the device reflectance decreases to 0%. There is no reflected light when the absorption coefficient increases to 2000 $\text{cm}^{-1}$ . While the FWHM of the reflectance peak increases to 2 $\mu\text{m}$ . When the absorption coefficient increases to 5000 $\text{cm}^{-1}$ , the device reflectance increases to 12%, the reflectance peak becomes wider. Seen from the simulation results, an absorption coefficient of 2000 $\text{cm}^{-1}$  is enough for absorber layers to absorb

all the incident photons with this resonant cavity structure. Increasing absorption coefficient of absorber layers will not decrease devices reflectance, but increase devices absorption wavelength coverage.

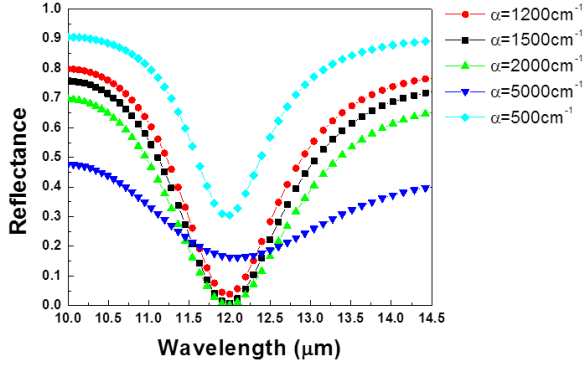


Figure 2 Simulated devices reflectance with different absorption coefficient of InAs/GaSb absorption layer of resonant cavity enhanced detectors.

Incident infrared radiation forms a standing wave pattern inside the cavity at specific wavelengths depending on the cavity length. In this study the InAs/GaSb superlattices absorber layer thickness was  $3\mu\text{m}$ , but the thickness of InAsSb layer was changed to modulate the response wavelength of the devices. Figure 3 shows the simulated devices reflectance of different InAsSb layer thickness of InAs/GaSb resonant cavity enhanced detectors. In this simulation the absorption coefficient was set as  $2000\text{cm}^{-1}$ . When the InAsSb layer thickness is  $900\text{nm}$ , the wavelength of reflectance peak is at  $11.75\mu\text{m}$ . When the InAsSb layer thickness is increasing the wavelength of reflectance peak is increasing. While the FWHM of the reflectance peak is constant. Changing the InAsSb thickness is a good way to design devices working wavelength.

To improve the external quantum efficiency of type-II InAs/GaSb superlattice infrared detectors, we designed a resonant cavity enhanced structure infrared detector. In this design, the 15ML InAs/7ML GaSb LWIR absorption layer thickness is  $3\mu\text{m}$ , the absorption coefficient is  $2000\text{cm}^{-1}$ , the InAsSb etching stop layer thickness is  $0.9\mu\text{m}$ . The

working wavelength is  $10.7\mu\text{m}$ . Figure 4 shows the absorptance spectrum of the designed resonant cavity enhanced InAs/GaSb type II superlattice infrared detector. According to the simulation results, the surface reflectance of superlattice detectors reduces to zero at the wavelength of  $10.7\mu\text{m}$ , the quantum efficiency of the detector is 100% at  $10.7\mu\text{m}$ . The FWHM of this absorptance peak is  $1\mu\text{m}$ . The quantum efficiency increases observably in certain wavelength.

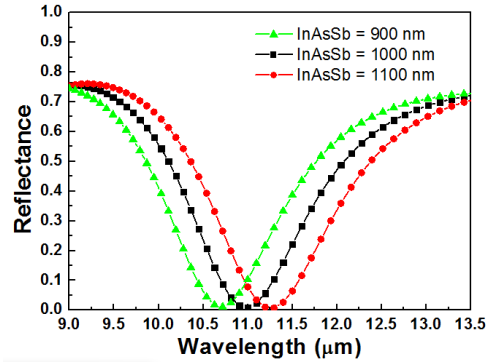


Figure 3 Simulated devices reflectance of different InAsSb etching stop layer thickness of InAs/GaSb resonant cavity enhanced detectors.

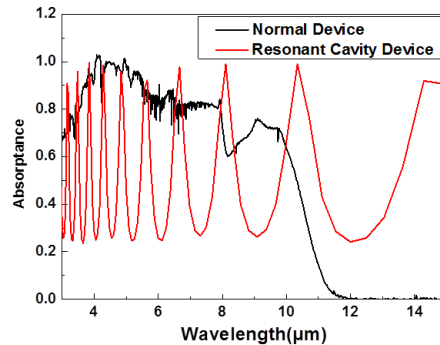


Figure 4 The absorptance spectrum of a simulated resonant cavity enhanced InAs/GaSb type II superlattice infrared detector.

### Quantum efficiency of resonant cavity structure detectors

Type-II InAs/GaSb superlattices detectors with optimized resonant cavity enhanced

structure has finally been prepared. Figure 5 shows the quantum efficiency spectrum of normal p-i-n structure and resonant cavity enhanced structure InAs/GaSb type II superlattice infrared detectors. There is 200 $\mu\text{m}$  GaSb substrate attached to normal p-i-n structure, which decreases the quantum efficiency of the detectors. Compared to the normal structure detectors the quantum efficiency of resonant cavity enhanced detector is evidently enhanced by resonant cavity structure at certain wavelength. The quantum efficiency of resonant cavity enhanced detector at 10.3 $\mu\text{m}$  wavelength is 51%, while the the normal structure detectors is only 10%. Resonant cavity structure with GaSb substrate removal extended the response wavelength about 0.5 $\mu\text{m}$  of the detectors. The highest quantum efficiency of resonant cavity detector is 85% (at 6 $\mu\text{m}$ ). This is one of the highest quantum efficiency ever reported. Calculated by the absorption coefficient, 3 $\mu\text{m}$  absorber layer thickness is not enough to get such quantum efficiency. The quantum efficiency of this detector is enhanced by the resonant cavity structure.

Compared to the simulation results (Fig.4 ), the quantum efficiency spectrum shape of the detector is consistent with the absorptance spectrum of simulated results. The peak of quantum efficiency spectrum (Fig.5) is one-to-one correspond to the peak of simulated absorptance spectrum(Fig.4). The difference of the 1<sup>st</sup> peak wavelength between simulated (at 10.7 $\mu\text{m}$ ) and experiment prepared (at 10.3 $\mu\text{m}$ ) is comes from the GaSb substrate removal process. In this process InAsSb was etched at the same time. The thickness of InAsSb reduced 100nm is calculate by the simulation results shown in figure 4.

Further work will conduct to improve the internal quantum efficiency, we will deeply study the intrinsic relationship between the absorption region thickness and diffusion length of the superlattice resonant cavity.

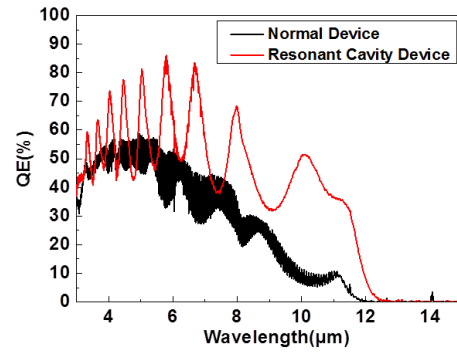


Figure 5 The quantum efficiency spectrum of normal and resonant cavity enhanced infrared detector.

## Conclusion

InAs/GaSb type II superlattice infrared detectors with resonant cavity enhanced InAs/GaSb structure have been designed. The optical structure of superlattice resonant cavity simulated and optimized by which the surface reflectance of detectors will reduce to zero. Detectors with quantum efficiency of 51% at 10.3 $\mu\text{m}$  wave length were prepared.

## References

1. D.L. Smith, C. Maihiot, Proposal for strained type II superlattice infrared detectors, *J. Appl. Phys.* 62, pp. 2545, 1987.
2. Rogalski, Material considerations for third generation infrared photodetectors, *Infra. Phys. Technol.* 50, pp. 240, 2007.
3. G.A. Sai-Halasz, R. Tsu, and L. Esaki , *Appl. Phys. Lett.*, Vol. 30,12, pp. 651 ,1977.
4. W. Tennant, *J. Electron. Mater.* Vol. 39, pp. 1030, 2010.
5. Binh-Minh Nguyen, D. Hoffman, Y. Wei, Pierre-Yves Delaunay, A. Hood, and M. Razeghi, *Appl. Phys. Lett.*, 90, 231108, 2007.
6. D. Hoffman, Binh-Minh Nguyen, Pierre-Yves Delaunay, A. Hood, and M. Razeghi, *Applied Physics Letters*, 91, 143507, 2007.
7. Pierre-Yves Delaunay, Binh-Minh Nguyen, D. Hofman, and M. Razeghi, *Appl. Phys. Lett.*, 91, 231106, 2007.
8. Bruce D. MacLeod and Douglas S. Hobbs, *SPIE* 6940-31, 2008.
9. F. Felder, M. Arnold, M. Rahim, C. Ebnetner, H. Zogg, *Appl. Phys. Lett.*, 91, 101102, 2007.



# Automatic installation of thermoplastic CFRP monitored by infrared thermography for pipelines

Louis-Daniel Th roux<sup>1</sup>, Jean Dumoulin<sup>1,2</sup> and Erick Merliot<sup>3</sup>

<sup>1</sup> LUNAM Universit , IFSTTAR, COSYS-SII, F-44340, Bouguenais, France

<sup>2</sup> INRIA/IRISA, I4S Team, Campus de Beaulieu, 35042 Rennes, France

<sup>3</sup> Universit  Paris-Est, IFSTTAR, COSYS-LISIS, F-77447, Marne-La-Vall e, France  
jean.dumoulin@ifsttar.fr

With ageing, resilience of pipelines network requires rehabilitation operations. Unfortunately, repairing those pipelines is costly and requires excavation which, depending on the location of the pipeline, can be problematic. For this reason, it was deemed pertinent to study and develop a repair method without having recourse to excavation: using CFRP reinforcement. This paper will concern mostly the study of the heating process of a prepreg thermoplastic solution, by experimental and numerical approaches, as well as the thermography inspection system.

## Introduction

Retrofitting with composite such as composite fiber reinforced polymer (CFRP) and thermoplastic has become a popular solution in civil engineering [1-4]. The REPTILES project is aimed at developing an automatic process that install prepreg thermoplastic CFRP on concrete. This requires an understanding of the thermal properties of the thermoplastic. To fully comprehend the gluing procedure, a prototype bench was conceived. The first part of this study was to obtain an estimation of thermal properties of the thermoplastic as well as the primer. A laboratory test bench was set-up by combining Infrared measurements with standards ones. This information allowed us to estimate the optimal heating process and to numerically simulate the approached solution. Finally, a series of tests were conducted on scale one planar prototype bench to validate the numerical simulations and to observe the practical problems encountered. The reinforcement process of a concrete pipeline includes many steps. This research focalizes on two particular steps of the process. First, a primer is applied on the concrete surface, filling cracks and fissure as well as making the whole surface even. Then, after 48 to 72 hours, the primer is solidified and the thermoplastic can be installed. The thermoplastic, which consist of

prepreg CFRP, must be heated to active the thermoplastic glue. While it is still hot, the thermoplastic must be pressured on the primer. The whole process must take place at a maximum speed of 10 cm per second.

## Active Infrared Thermography

Infrared Thermography serves two purposes in this project. First of all, it is used to monitor the heating temperature of the CFRP. After it was installed, thermography is used to detect any flaws in the bonding. For the thermoplastic to adhere to the primer, it must be heated at the melting temperature of the glue (at least 190  C). Knowing that environmental conditions may varies which could impact the heating process. Furthermore, movements during the installation process may cause variation in the distance between the CFRP and the lamps. In this regard, to make sure the temperature of the CFRP is neither too high nor too low, the heating process will have to be monitored by thermography.

To optimize the heating process and to control the quality of the gluing, a non-destructive system using two thermal infrared cameras was studied and designed. It can be considered that due to the CFRP gluing process and the control solution studied, we are in an active infrared thermography configuration.

## Heating source

To heat the CFRP to the required temperature, multiples heating methods are at our disposal. The first criterion is that it needs to be a contactless method. This is because the CFRP must be heated until the glue melt. If there is contact, the glue will adhere on the surface. Among the contactless methods, four have retained our attention; by induction, laser, plasma torch and lamp. Induction heating requires the component to be conductive enough and also requires specific adjustment for such CFRP sheet that could be difficult to set-up in real site. The use of plasma torch is not recommended since it can only heat a limited area. Laser heating by sweeping spot is also dismissed as the power required to heat could be potentially hazardous for the users. Finally, heating by infrared lamps was chosen since it is probably the safest and easy to set-up in the final system configuration as well as a potential efficient heating method.

The choice of the heating lamps spectral characteristics will depend on the radiative properties of CFRP sheet in function of the wavelength [5]. For an optimal heating, it is preferable to use a lamp that radiate in the spectrum where the absorptivity of the composite is at its highest. Our choice tumbled on the short-wave lamps as well as the fast-response-medium-wave. Such lamps radiate mostly in the spectral bandwidth ranging between 0 to 2  $\mu\text{m}$ .

## Laboratory characterization

To evaluate the thermal properties of the composite, various tests were conducted. Among those, differential scanning calorimetry (DSC) as well as scanning electron microscope (SEM) were conducted by the provider. The emissivity of the CFRP in function of the temperature is a parameter that must be known to efficiently and precisely measure the temperature. Since the emissivity is unknown, a characterization experiment in laboratory was also put into place. The experiment involve using a reference of know emissivity and temperature and compare its digital level measured with the one from the CFRP at the

same temperature [6]. To do this, the experimental setup consists of an aluminum support on which the top surface was painted. The paint used is of known emissivity and have a diffuse emissivity. Incrusted in the support is a shallow hole in which the CFRP is installed. The hole is covered in a PTFE tissue (film) that prevents the composite sheet to glue to the aluminum support. Multiples thermocouples coated in thermal grease are inserted in the aluminum support as well as on and bellow the CFRP sheets. The support is installed on a heating plate with an adjustable temperature.



Fig. 1. Photos of the experimental setup for emissivity characterization versus temperature of the composite.

Results obtained shows that for temperature over 100 °C the emissivity value is roughly between 0.8 and 0.85. In the heating phase, when the CFRP reach 190°C, a sudden rise in the emissivity can be seen. This change in emissivity correspond to the tipping temperature where the glue melt and can also be seen during the cooling process.

Another emissivity test was performed to evaluate the difference in emissivity between a CFRP sheet that is new (never melted before) and one that has been melted before. Results showed that for the unmelted CFRP sheet, the emissivity was lower than premelted CFRP.

## Numerical simulations

Numerical models were conceived to achieve multiple goals. The first is to be able to pre-test heating solutions, for different type of lamp with various spectral characteristics. It has also enabled us to better comprehend and predict the thermal behavior of the composite, thus optimizing both the heating and the control process. Using thermal properties presented obtained in the previous section, a model of the heating process was carried out. However, the only unknown parameter remaining was the heat source. Information about the size or emissivity of the filament was not given by the manufacturer. In this regard, complementary

experiments were realized to estimate such parameters and used to design and tune the model. CFRP thermal properties were measured in laboratory and were used in the numerical model. Finally, a 3D FEM numerical model with moving heating sources was realized and used to study the influence of various parameters in the design of the heating system.

### Full size experimentation

A full size prototype bench was conceived and built at Ifsttar, Nantes (see Figure 2). The setup consists of a one by four meters long table. The table was covered by a 32 mm cement layer over the whole surface. Since the concrete slab was very thin and yet had to cover 4 m<sup>2</sup>, we used fiber reinforced cement. The concrete was covered with a thin layer of primer (roughly 1 mm). The robot was guided by a conveyer belt and guided by rail on each side of the table. The installation roll was made of an aluminum tube with an additional layer in silicone. This material was adequate since it couldn't bond with the thermoplastic glue, was soft enough to adapt to small deformation (crack, cavity, etc) and was resistant to pressure and temperature elevation. The weight of the composite roll applied pressure on the silicon tube.

The CFRP sheets are placed on a conveyer that moves at a speed that can vary from roughly 0.1 cm/s to 10 cm/s. The lamps are fixed directly over the conveyer belt on which the composite sheet scrolls. Two infrared cameras (FLIR A35sc series) were placed on each side of the lamps and synchronized.

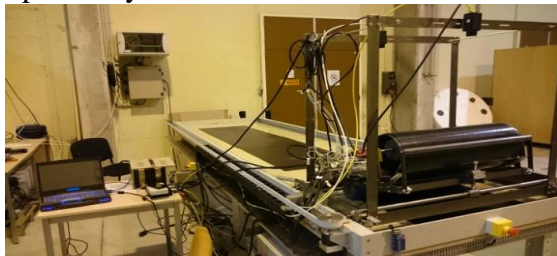


Fig. 2. Test bench.

The solution adopted for the heating system consisted in two short-wave (SW) lamps and two Fast Response Medium Wave (FRMW) lamps of a maximum inlet electrical power of 12 kW. The heating power was controlled by a dedicated application developed under LabVIEW. The

mean distance between active heating elements and CFRP sheet was round 4 cm. With this configuration, it was possible to melt the glue at a maximum speed of 7 cm/s.

### Results and discussion

Since the carbon sheet was very close to the lamps, any unevenness at the melting temperature induced radiative heat flux local spatial variation. Such effect can be seen in the shapes of the temperature profiles that show a deviation between experiments and simulations. We also notice that the sample that was already melted and then heated again was significantly warmer than a new sample. This observation is in accordance with the results obtained in the characterization section.

Images from the first thermal camera were compared with the results from the simulation of the numerical model (Figure 3). The order of temperature for speed of 5cm/s was compared and showed little difference between the theoretical and experimental temperature. This shows that the model is valid and could potentially be used to calculate the effect of various parameters.

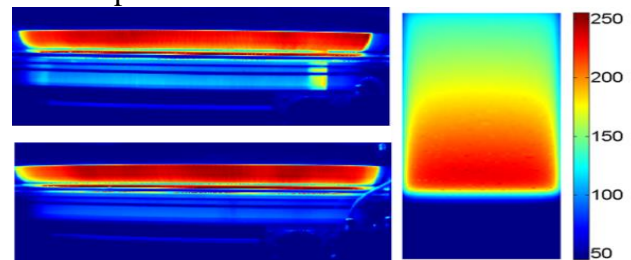


Fig. 3. Temperature in °C resulting from experiments (right) and numerical simulation (left) with a speed of 5 cm/s.

Thermal images from the second camera indicated that the heating was irregular, especially near the edge of the composite. Observation of the temperature field of the applied composite showed a lack of heating near the border of the composite for which the thermoplastic didn't melt. This was anticipated as the simulation showed similar results and illustrated in temperature profiles presented in Figure 4. The heating tubes were simply not large enough.

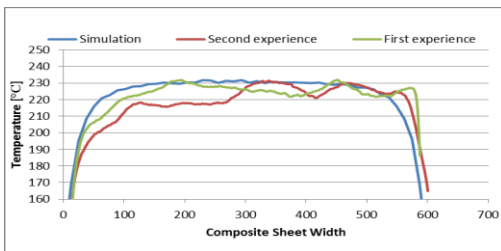


Fig. 4. Graph of the average temperature profile through time for both experimental test plotted versus the results of the simulation for a speed of 5 cm/s.

According to the manufacturer technical specifications, the lamps used have an effective heating area of only 50 cm, while the composite sheets are 60 cm large. This caused the sheets to glue incorrectly as would reveal the thermal images obtained by the second camera. This camera, monitoring the composite after application, revealed that a large lateral portion of the composite was not glued properly. This problem was noticed in many, if not all, of the tests we conducted. Each time, it was the left portion of the composite sheet that showed gluing problem. It was assumed that this issue was the results of an uneven pressure of the application roll.

Looking at the experimental temperature profile, it can be observed that results vary greatly from one sample sheet of CFRP to another. This is due to the fact that the sheets were very close to the lamps, thus any deformation in the sheets induced heating variations. Complementary experiments are required to achieve the validation of our model. For future work, we propose to use a static target that is also relatively flat and no too close to the heat lamp. It would be recommended to take an opaque target, so the infrared camera can be positioned behind the target sample. Knowing precisely the value of the thermal properties of the sample, by measuring the heat flux on the back of the sample, the net heat flux received by the sample could be calculated accurately.

The various experiments conducted in the framework of this study showed the extent and limitation of a heating and monitoring system. Implementation of the heating system that was initially planned showed that it was insufficient to heat the CFRP to the melting temperature at the nominal speed of 10 cm/s. However, a numerical model of the heating system was conceived and the experimental measure could be used to consolidate

various model parameters. Simulation results showed that the reached temperature should fulfill requirement by acting on the lamps specifications which leave room for unforeseen event.

## Conclusion

Even though the prototype had some success, there are still many issues that need to be solved. The main addressed problem is that the composite sheet temperature may remained below the crystallization temperature when applied on the primer. This was caused by the heat transfer from the composite sheet to the silicon roll. The series of tests conducted on the prototype also allowed validation of the finite element model. The temperature measurements are in accordance with the numerical simulation using similar parameters. This is important as it will be possible to optimize the final system.

## Acknowledgments

Authors wish to thanks OSEO FUI Reptiles for financial support; FREYSSINET, BOSTIK and PORCHER companies for their technical help; J-L Manceau, A. Grosseau and F. Blaineau for their technical help.

## References

1. L. Hollaway, J.-G. Teng, Strengthening and Rehabilitation of Civil Infrastructures Using Fibre-Reinforced Polymer Composites, Woodhead Publishing in Materials, 2008
2. X. Maldague, P. Moore, Nondestructive Testing Handbook: Vol 3 Third Edition, American Society for Nondestructive Testing, 2001
3. M. R. Valluzzi, E. Grinzato, C. Pellegrino, C. Modena, "IR thermography for interface analysis of FRP laminates externally bonded to RC beams", Materials and Structures, vol 42, pp.25–34, 2009.
  - A. Crinière, J. Dumoulin, C. Ibarra-Castaneda and X. Maldague, "Inverse model for defect characterization of externally glued CFRP on reinforced concrete structures: Comparative study of square pulsed and pulsed thermography", Quantitative InfraRed Thermography Journal, Taylor & Francis Editor, vol 11, pp 84-114, 2014. DOI: 10.1080/17686733.2014.897512.
4. R. Siegel, J. Howell, Thermal Radiation Heat Transfer: Fourth Edition, Taylor & Francis Editor, 1990
5. J. Dumoulin, Mesure du coefficient d'échange pariétal dans le cas d'un refroidissement par impact de jet, Msc Thesis, INSA de Toulouse, 1991.



# Thermographic Testing of Microwave Circulator Adhesive Bonds

E. C. Johnson, Y. M. Kim

The Aerospace Corporation, Los Angeles, CA, USA

The results of an effort to determine if IR imaging methods can be used to assess adhesive bond quality in a microwave circulator are reported. The circulator to be tested was of a somewhat standard three-port design, consisting of an aluminum housing that sandwiched two triangular ferrite slabs separated by a dielectric between potted magnets. The adhesive bondlines of interest were those between the ferrite and the aluminum housing. A testing scheme was developed whereby the aluminum housing was heated in a controlled fashion while an IR camera was used to monitor the thermal response of both ferrite triangles. As expected, it was found that if both ferrite triangles were properly bonded, a similar thermal response was observed. However, if one of the triangles had a partial or cracked adhesive bond, it resulted in a measurable thermal response difference.

## Introduction

A study was performed to see if IR imaging methods could be used to assess the adhesive bond quality in an assembled microwave circulator. The test article is depicted in Fig 1. It consists of two halves machined from an aluminum block that are bolted together to form the housing. The housing has ports on three sides, one of which is depicted in Fig. 1b. A potted magnet is present in both the top (Fig. 1a) and bottom halves of the device. The magnets sit beneath raised triangular membranes of aluminum that are evident when the halves are separated as in Fig. 1c. A ferrite triangle is glued to the center of each raised aluminum triangle and a dielectric triangle is glued to the ferrite triangle on the top half of

the device. When the two halves are bolted together, the result is an Al-ferrite-dielectric-ferrite-Al sandwich that can be seen through the ports (Fig. 1b). It is the bonds between these sandwiched components that are of interest for this study. For ease of discussion, each of these bondlines was assigned a number as depicted in Fig. 1d. In the as-built configuration, Bondlines 1, 2 and 4 consist of a thin layer of epoxy. There is no material in Bondline 3. This permits separation of the circulator halves so that tuning adjustments can be made. For the purposes of this study, the dielectric bondline was ignored.

## Approach for Assessing Bond Quality

The epoxy adhesive serves two purposes. First, it mechanically holds the ferrite and dielectric triangles in place and second, it heat sinks the ferrite to the aluminum. This second purpose coupled with the symmetry of the circulator housing provides a possible avenue for assessing the relative quality of the bonds. The plan was to heat the circulator in a controlled symmetrical fashion while using an IR camera to monitor the temperature of the ferrite triangles as viewed one of the ports. To accomplish this, the circulator was positioned on of a square of foam insulation board and a heated Al block was placed on its top surface as depicted in Fig. 2. A FLIR

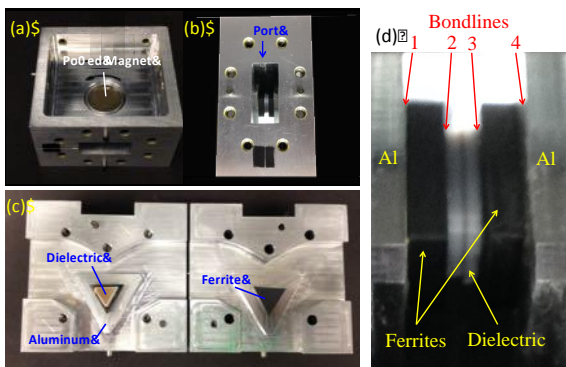


Fig. 1. Three-port circulator.

SC8200 IR imager was then used to monitor the change in the temperature of the block, the ferrite triangles and a position on the circulator housing.

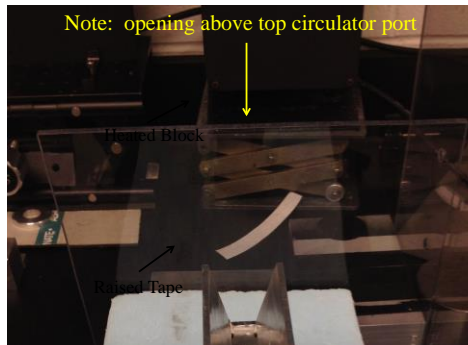


Fig. 2. Circulator positioned for test.

To achieve accurate temperature measurements on the aluminum surfaces of the heating block and the circulator housing, the region being monitored was coated with a layer of flat black paint. To minimize thermal radiance through the top port, the heating block was designed to leave it uncovered. To conduct a test, the circulator was removed from the foam board and placed on a thick plate of aluminum at room temperature long enough for thermal equilibrium to be achieved. During this time, the heated block was placed on a hot plate set at ~ 130 °F. The circulator was then placed back on the foam board. The raised tape on the board that can be seen in Fig. 2 ensured that the circulator was in the same position relative to the IR imager for each test. The IR imager was then keyed to start a 200 sec recording and the heated block was set on top of the circulator. For ease of discussion, the above test procedure will be referred to as the “ferrite thermal response test.” Sample frames from one of the tests recorded at 60 sec and 180 sec are depicted in Fig. 3.

### Initial Results

The imaging software permits one to outline multiple regions of interest (ROIs) on the image. In Fig. 3, there are four such ROIs indicated by colored and numbered boxes. The average temperature in these regions can then be plotted as a function of time for

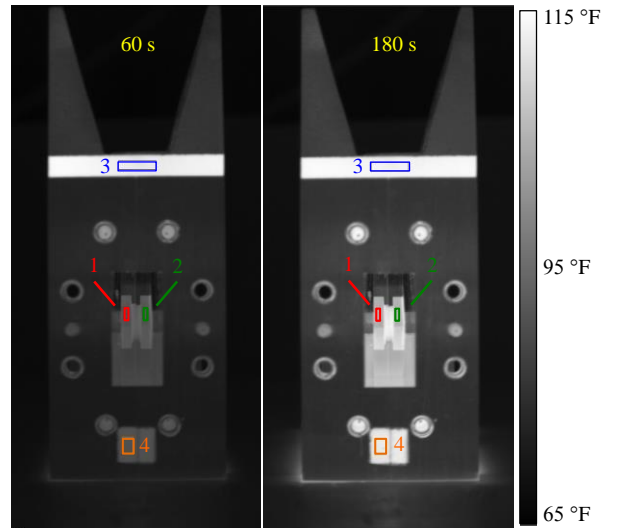


Fig. 3. Sample frames from the thermal response test.

the recorded interval as depicted in Fig. 4. Perusal of the ROI plots in this figure reveals the expected behaviors. The heating block was set on the circulator about 10 sec after recording was initiated. ROI 3 on the heating block started out warm from the hot plate and cooled throughout the recording. The heat moved downward through the circulator, heating first the ferrites (ROIs 1 & 2) and then the lower portion of the circulator housing (ROI 4). The ferrites, in this case, were similarly bonded and therefore exhibited nearly identical thermal behaviors. Following the initial test, the circulator was disassembled and the epoxy was removed from Bondline 4. It was then reassembled with a thin sheet of paper between the clean surfaces of Bondline 4 and subjected to a repeat ferrite thermal response test.

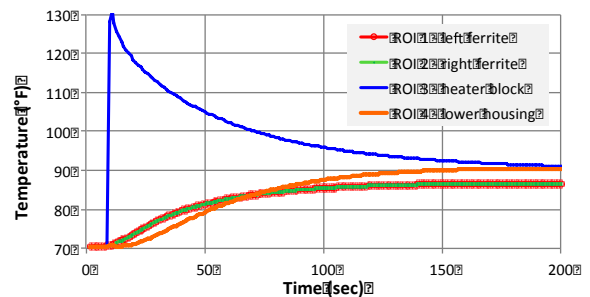


Fig. 4. ROI temperatures as a function of time.

The difference between the heating rates of the ferrite bonded to the aluminum and that isolated from the aluminum by the thin sheet of paper

was readily apparent. To bring this out, the temperature of the right ferrite,  $T_R$  was subtracted from that of the left ferrite,  $T_L$  at each point and then divided by the temperature span experienced by the ferrites during the test. The parameter,

$$\Delta T = \left[ \frac{T_L - T_R}{T_{max} - T_{min}} \right] * 100\% \quad (1)$$

was then plotted in Fig. 5 for each of the two aforementioned tests. For the condition labeled, Epoxy-Epoxy-clean-paper, where the right ferrite is effectively thermally uncoupled from the circulator housing,  $\Delta T$  rises to nearly 11% at about 25 sec. On the other hand, for the nearly symmetric condition labeled, Epoxy-Epoxy-clean-Epoxy,  $\Delta T$  remains below 1% for the entire test. This small, but finite, difference may have been, in part, due to the inherent asymmetry in the as-built configuration where the dielectric is bonded to the left ferrite (Bondline 2), but not the right ferrite (Bondline 3). To mitigate this asymmetry in some of the ensuing tests, a small dab of thermal paste (TP) was placed in Bondline 3.

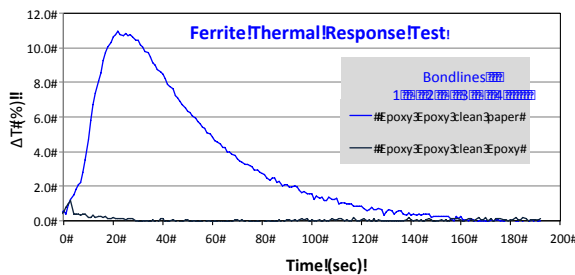


Fig. 5. The % difference between the left and right ferrite temperatures for the conditions noted.

### Additional Tests

Having established a quantitative approach for assessing the relative thermal bonding of the left and right ferrites, a series of ferrite thermal response tests were performed to demonstrate the sensitivity of the technique to various bond conditions.

Thermal Paste as a Bonding Agent - For these tests, TP was used to create the bonds. In preparation, Bondlines 1, 3 and 4 were cleared of bonding agents. The circulator was on loan,

and permission had not been obtained to remove the Epoxy in Bondline 2, so it remained as a small asymmetry in the tests. Ferrite thermal response tests were then performed for the bond conditions noted in the key for the  $\Delta T$  plots presented in Fig. 6. The first three represent nearly symmetrical conditions so that the  $\Delta T$  values remained small throughout the test. One might argue that, of these three tests, the  $\Delta T$  curve for the first rides slightly higher because Bondlines 2 and 3 have a more pronounced difference (Epoxy vs clean). The higher  $\Delta T$  values for Tests 4 and 5 reflect the significant difference in thermal bonding to the circulator housing for the left and right ferrites. Having paper in Bondline 4 provides the highest level of thermal isolation for the right ferrite and hence, the highest values for  $\Delta T$ .

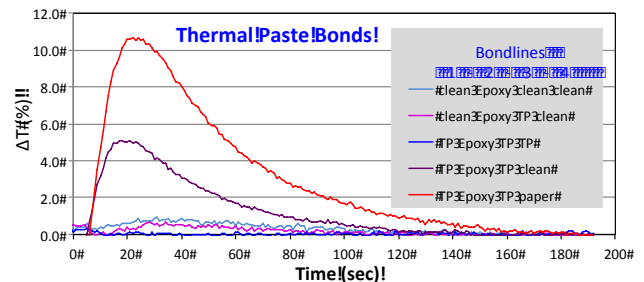


Fig. 6. Thermal response test results for TP bonds.

Epoxy as a Bonding Agent - For these tests, Epoxy was used to create the bonds. As before, Bondlines 1, 3 and 4 were cleared of bonding agents and Bondline 2 was left intact. Ferrite thermal response tests were then performed for the bond conditions noted in the key for the  $\Delta T$  plots presented in Fig. 7. The first four represent nearly symmetrical conditions so that the  $\Delta T$  values remained small throughout the test. Tests 4, 5 and 6 were for more asymmetric bond conditions and, hence, resulted in higher  $\Delta T$  values. Having paper in Bondline 4 again provided the highest level of thermal isolation for the right ferrite, resulting in the two highest  $\Delta T$  curves for Tests 5 and 6. Of these two curves, the highest is for the slightly more asymmetric condition where there is no bonding agent in Bondline 3. Finally, for Test 7 the Epoxy in Bondline 4 was cracked, but left in place. As one might expect, the resulting  $\Delta T$  curve reaches appreciable values, but the thermal connection

resulting from the contact condition between the cracked surfaces of the epoxy was enough to reduce these values to nearly half of those seen in Test 5, with paper in Bondline 4.

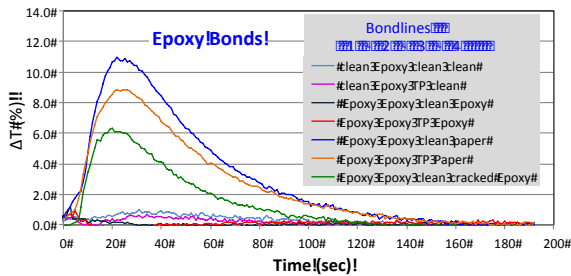


Fig. 7. Thermal response test results for TP bonds.

**Bond Size Variation Tests** - For the ensuing tests, the condition of Bondlines 1, 2 and 3 were held intact with Epoxy, Epoxy and TP, respectively. Bondline 4 was created using small pieces of Al foil that were carefully coated with mineral oil. The Al foil controlled the size of the bond while at the same time holding the “unbonded” area of the ferrite slightly away from the Al surface of the circulator. This prevented thermal shorting of the unbonded area of the ferrite. The results are presented in Fig. 8. Perhaps most notable is that the  $\Delta T$  curves for the 100% and 47% bond conditions exhibit a minimum at the point of highest absolute temperature difference between the left and right ferrites. This is simply a reflection of the fact that the oil coated Al foil conducts heat through the bondline better than the epoxy or thermal paste. As one would expect, the maximum absolute temperature difference increases monotonically as the size of the bonded area decreases. The change, however, is not proportional over the entire range. The change is nearly linear for the less than 50% bond conditions, but the 100% condition deviates from the line. It

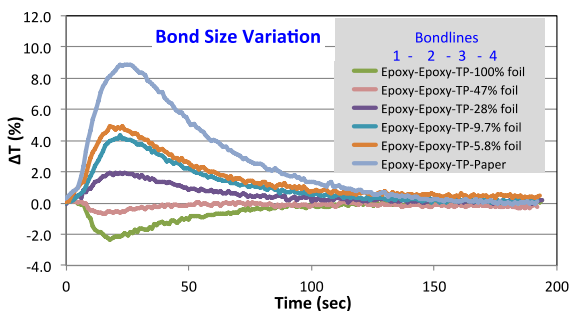


Fig. 8. Effect of bond size on  $\Delta T$ .

is not obvious that linear behavior should be expected, however, as factors in addition to uniform thermal conduction through the bond, such as convective cooling and geometrical variations, come into play during the thermal response test. One possibility is that the pressure exerted by the thin aluminum membrane is not uniform across the face of the ferrite when the circulator is assembled.

## Conclusions

The thermal symmetry of a microwave circulator was exploited to see if IR imaging methods could be used to assess the relative quality of two bonds between triangular pieces of ferrite and the aluminum housing. Accordingly, a methodology, dubbed the “ferrite thermal response test,” for introducing a uniform heat flux into the housing while monitoring the temperature of two ferrite pieces was developed. The methodology produces a measurement of the temporal variation in the temperature difference,  $\Delta T$ , between the two ferrites during the test. As expected the test proved sensitive to variations in the relative bond conditions. If one of the bonds was cracked or missing altogether it was clearly indicated. In addition,  $\Delta T$  increased monotonically as the percent area bonded for one of the ferrites was decreased while the other was maintained as a good bond. The test as devised provides a relative measurement, which has its limitations. For instance, one would expect similar results if both ferrites were totally bonded or totally unbonded. The ferrite thermal response test, however, may also prove useful as a means for monitoring the bond behavior for circulators subjected to various qualification environments such as thermal vacuum tests and burn-in.

## Acknowledgement

Support from the Aerospace Corporation’s Sustained Experimentation and Research for Program Applications program is gratefully acknowledged.



# COMPRESSIVE SENSING AND ITS POTENTIAL FOR INFRARED APPLICATIONS

D. Guzzi<sup>1</sup>, C. Lastri<sup>1</sup>, V. Nardino<sup>1</sup>, I. Pippi<sup>1</sup>, V. Raimondi<sup>1</sup>, A. Barducci<sup>2</sup>

<sup>1</sup> IFAC-CNR, Via Madonna del Piano 10, 50019, Sesto Fiorentino, Italy, d.guzzi@ifac.cnr.it

<sup>2</sup> SOFASI s.r.l., Viale Guidoni, 50100, Firenze, Italy, alessandro.barducci@sofasi.it

Compressive sensing (CS) allows the reconstruction of signals acquired at sampling frequency below the Nyquist rate relying on the assumption that the acquired signal is sparse (i.e. it exhibits a certain degree of correlation). The possibility of undersampling a signal without losing significant information is accomplished by means of a specific integral transformation. For radiometric and spectroscopic signals, this transformation is performed by an optical subsystem spatially modulating the light and by a single pixel detector. Due to these characteristics CS can lead to the development of devices characterized by a reduction in terms of mass, volume and memory budgets. CS theory can be applied to a wide range of optical instruments. After a brief theoretical background, the paper will describe some promising CS applications in the infrared spectral range.

## Introduction

Compressive sensing (CS) is a novel technique, belonging to the general field of signal compression, that allows the acquisition of signals at sampling frequency below the Nyquist sampling rate. This technique relies on the following assumptions: random sampling and high degree of correlation of the signal, the latter being referred in the literature as “sparsity”. A basic example of sparsity is constituted by a multidimensional signal (e.g. an image) with a strong average autocorrelation, such as an image with large areas of constant value. The image can still contain high spatial frequency components associated to regions of little extension showing image-edges or rapid radiometric variations; however, the image itself is redundant. A randomly sampled sparse signal conveys a greater information amount than the one predicted by the traditional sampling theory, regardless of the maximum frequency contained in its spectrum. The possibility of undersampling a signal without losing meaningful information can be made accessible to an instrument

through a specific integral transformation (IT). When optical signals are considered, such a transformation is performed by a subsystem - placed in front of the instrument’s focal plane - that spatially modulates the light. The calculation of an IT involves the weighted summation of signal samples taken in different spatial points of the signal domain, an operation called multiplexing. Therefore CS always includes a multiplexing scheme that implements the same mathematical transformation [1,2,3].

Until now, the standard approach to mitigate the redundancy of sampled signals has been the application of *a posteriori* compression algorithms that discard part of the collected data, depending on the signal quality to preserve. Lossless compression algorithms guarantee to maintain the original amount of information, but offer a small gain in terms of data reduction. On the contrary, during CS acquisitions the signal compression takes place before signal registration, i.e. during the sampling phase.

CS scheme reduces the number of detector pixels to one, since the sensing array is replaced by a one-pixel detector, but at the same time it requires the presence of a spatial light modulator that implements the multiplexing scheme. In any case, although CS requires additional components, the

reduction of detector pixels to one can introduce a meaningful simplification in the overall system architecture offering savings in terms of mass, volume, required memory for temporary data storage, bandwidth necessary for data transmission, and electrical power consumption.

CS theory can be applied in the development of different optical systems with applications in the spectral range from Ultraviolet (UV) to Far Infrared.

The aim of this paper is the description of the most promising applications of CS theory in the infrared range. After a brief theoretical background and the presentation of results obtained in the laboratory for hyperspectral imaging in the visible-near infrared range, an overview of infrared applications that could potentially benefit from the use of CS techniques will be performed pointing out possible trade-offs between application concepts and system configurations. Particular attention will be given to the simplification of the system architecture and to the typology of the employed devices.

## Theoretical background

The traditional sampling theory (e.g. the Nyquist-Shannon theorem) states a sufficient condition for an exact reconstruction of the original (analogue) signal from constant samples. In other words, Nyquist-Shannon theory does not exclude the existence of signals which can be sampled at a lower rate, yet permitting an error-free reconstruction of their analogue counterparts. The first example of such undersampling practice is constituted by the so-called bandpass sampling, a technique largely employed in telecommunication engineering for digitizing narrowband sources whose spectrum (Fourier Transform) vanishes outside a tiny spectral interval far from the origin. The bandpass sampling scheme is well suited to avoid aliasing when undersampling passband signals. This approach allows an important gain of sampling efficiency, but it can rarely

be applied to signals with spectral features typically originated by a natural source.

On the other end, CS relies on two principles: sparsity, a characteristic related to the signal of interest, and incoherence, a property related to the sensing process.

Sparsity expresses the idea that the “information rate” of a continuous time signal may be much smaller than suggested by its bandwidth, or that a discrete-time signal depends on a number of degrees of freedom which is comparably smaller than its finite length. CS exploits the fact that many natural signals are sparse or compressible in the sense that they have concise representations when expressed in the proper basis.

Incoherence can be related for example to the duality between time and frequency. As an incoherent signal have an extremely dense representation in its transformed domain, a signal that has a sparse representation is distributed in the acquisition domain. Mathematical theorems [4] related to undersampling and sparse signal recovery, suggest that “measurements” (the equivalent of Shannon’s “samples”) are obtained as the scalar product of the signal with pseudorandom sequences (e.g., Gaussian). The reconstruction process involves the determination of the sparsest signal that matches the available measurements using linear programming techniques.

## CS technique for Infrared applications

The application of CS theory to spectroscopy or to digital imaging can be regarded as an evolution of Multiplex Imaging (MI). The data of interest  $i(\xi)$  is connected to the measured datagram  $I(x)$  by an integral transformation. The datagram is a sparse representation of  $i(\xi)$  in order to be efficiently sampled. CS spectroscopy can be considered in its turn as an extension of earlier spectroscopic techniques such as Fourier Transform Spectroscopy.

Fig. 1 shows the schematics of the multiplexing optical layout included in CS spectrometer. The fundamental component is constituted by a Spatial light modulator (SLM) which performs the desired integral transform. The focal plane contains a single pixel or a low-resolution 2D detector (ideally a

single pixel detector) that integrates the optical signal.

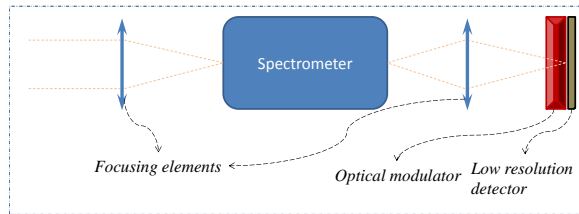


Fig. 1. Typical multiplexing optical layout included in a CS spectrometer. A spatial light modulator performs the required integral transform and feeds the detector.

Following this scheme, CS reduces the number of detector pixels to one or few pixels, since the array can be replaced in principle by a single-pixel detector. Due to these characteristics, CS could allow the development of instrument with a reduction in terms of mass, volume and memory budgets with respect to standard systems.

Compressive imaging is one of the first application as far investigated [6], while in the last years several studies were undertaken for investigating the application of CS to several fields of spectroscopy [7, 8, 9].

CS can be applied to the development of optical and 3D cameras that could benefit by the use of CS technologies in those Infrared spectral ranges where the production of 1D or 2D sensor arrays with large amount of element and uniform optical properties is particularly challenging. Outside the visible wavelengths, the responsivity of conventional cameras drops, therefore, a conventional camera could have problems in capturing images Infrared spectral range. CS, reducing the number of pixels of the camera to only one with a responsivity extended to Infrared, can solve the problem of the reduced sensitivity and performances in this spectral region.

A promising field of application is hyperspectral imaging. In the framework of the ITI-B project titled “Hyperspectral Passive Satellite Imaging via Compressive Sensing” a CS based hyperspectral imager prototype operating in the visible-near infrared range (350 nm – 1000 nm) has been

developed at CNR-IFAC [9]. The prototype was used to carry out several CS acquisitions and to test the performances of the developed hardware. Fig 2 shows a view of the prototype.

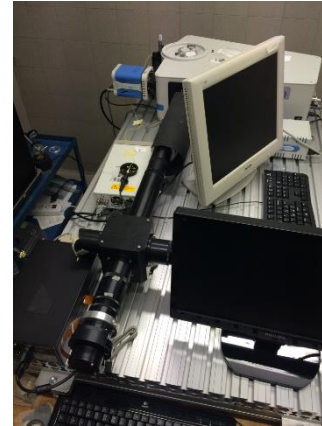


Fig. 2. View of the CS hyperspectral imager prototype.

Fig. 3 depicts an image extracted from a CS acquisition of a red laser source performed with a random Gaussian distribution.



Fig. 3 Image extracted from a CS acquisition.

The results demonstrated the feasibility of CS hyperspectral acquisition and the necessity of a CS hardware characterized by a very high optical quality in order to improve the performance of the entire CS system and of the reconstructed signals. Infrared hyperspectral imaging, which traditionally requires expensive and very large numbers of detector elements, can benefit from the application of CS theory, in particular in the Thermal Infrared (TIR) region where the signal is extremely sparse (i.e. the spectrum is slowly varying and flat). In this case, a trade-off between the number of pixels, the modulator speed and integration time could be necessary depending on the application field. For example CS hyperspectral imaging for Earth Observation [9] allows a reduction of the detector throughput, which is related to lower memory capacity, but it requires correspondently faster spatial light modulators.

As far as spectroscopy is concerned, CS is particularly interesting when applied to

measurements subject to physical limitation [10]. For example, many spectroscopy applications in near or Mid Infrared (MIR) rely on the use of photomultiplier arrays or detector materials with few number of detector elements. For these applications the CS scheme is particularly appealing, since it allows the signal reconstruction with a number of samples greater than the number of detector elements. As an example, CS could be used to develop a sensor for characterizing narrow band Near Infrared (NIR) sources [11, 12] with a reduced number of InGaAs detector elements.

Another promising application field is THz imaging. The reconstruction of THz images can benefit from CS since the latter permits to use significantly fewer measurements than a conventional raster-scan imaging technique [13].

## Conclusion

There are evidences that CS can be successfully applied not only for Infrared imaging, but also in Infrared spectroscopy. In particular space applications could benefit by the use of CS, since it could allow a reduction in terms of mass and volume as well as in the use of the required memory for temporary data storage. A saving is also expected in data transmission bandwidth, electrical power consumption during sampling, storage and transmission by applying CS technology in the Infrared spectral range.

## References

1. E. J. Candès. Compressive sampling, Proceedings of the International Congress of Mathematicians, Madrid, Spain, European Mathematical Society, 2006.
2. E. J. Candès, J. Romberg, T. Tao. Robust uncertainty principles: exact signal reconstruction from highly incomplete frequency information, *IEEE Trans. Inform. Theory*, Vol. 52, pp. 489 – 509, 2006.
3. A. Barducci, D. Guzzi, C. Lastrì, P. Marcoionni, V. Nardino, I. Pippi. Compressive

Sensing and Hyperspectral Imaging, Proceedings of the 9th International Conference on Space Optics (ICSO 2012), Topics 2 Spectrometers - Hyperspectral instruments, 2012.

4. E. Candès, J. Romberg. Sparsity and incoherence in compressive sampling, *Inverse Prob.*, Vol. 23, no. 3, pp. 969–985, 2007.
5. S. R. Gottesman, E. E. Fennimore. New family of binary arrays for coded aperture imaging, *Applied Optics*, Vol. 28, No. 20, 1989.
6. M. B. Wakin, J. N. Laska, M. F. Duarte, D. Baron, S. Sarvotham, D. Takhar, K. F. Kelly, R. G. Baraniuk. An Architecture for Compressive Imaging, Proceedings of the 2006 IEEE International Conference on Image Processing, Atlanta, GA (USA), 8-11 Oct. 2006.
7. M. E. Gehm, R. John, D. J. Brady, R. M. Willet, and T. J. Schulz. Single-shot compressive spectral imaging with a dual-disperser architecture, *Optics Express*, Vol. 15(21), pp. 14013 – 14027, 2007
8. O. Katz, J. M. Levitt, Y. Silberberg. Compressive Fourier Transform Spectroscopy, *Frontiers in Optics, OSA Technical Digest (Optical Society of America, 2010)*, paper FTuE3, 2010.
9. A. Barducci, D. Guzzi, C. Lastrì, V. Nardino, I. Pippi, V. Raimondi. Compressive Sensing for Hyperspectral Earth Observation from Space, *International Conference on Space Optics (ICSO)*, 2014.
10. D. J. Brady, M. E. Gehm, N. Pitsianis, X. Sun. Compressive sampling strategies for integrated microspectrometers, *Intelligent Integrated Microsystems*, Edited by Ravindra A. Athale, John C. Zolper, Proc. of SPIE Vol. 6232, 62320C, 0277-786X/06/\$15, doi: 10.1117/12.666124, 2006
11. P. Potluri, M. Gehm, M. Sullivan, D. Brady. Measurement-efficient optical wavemeters, *Optics Express*, Vol. 12, pp. 6219–6229, 2004
12. A. B. Hamza, D. J. Brady. Reconstruction of reflectance spectra using robust non-negative matrix factorization, *IEEE Transactions on Signal Processing*, Vol. 54, no. 9, pp. 3637 – 3642, 2006.
13. W. L. Chan, M. L. Moravec, R. G. Baraniuk, D. M. Mittleman. Terahertz imaging with compressed sensing and phase retrieval, *Optics Letters*, Vol. 33, No. 9, pp. 974-976, 2008.

# Accuracy improvement of dissipated energy measurement and fatigue limit estimation by using phase information

D. Shiozawa<sup>1</sup>, T. Inagawa<sup>1</sup>, A. Akai<sup>1</sup>, T. Sakagami<sup>1</sup>

<sup>1</sup> Kobe University, 1-1, Rokkodai Nada-ku, Kobe, Japna, shiozawa@mech.kobe-u.ac.jp

In this study, accuracy improvement technique of dissipated energy measurement based on phase information, which is called phase lock-in method, was suggest. This method utilizes a specific phase difference of energy dissipation. This phase difference is found when large dissipated energy is observed in staircase-like stress level tests. It is effective to use a phase lock-in method for removal noise component, such as thermoelastic temperature change due to harmonic vibration.

## Introduction

Fatigue limit estimation based on the dissipated energy measurement using infrared thermography has been getting an increasing attention in various industries<sup>(1)-(4)</sup>. Mechanism of energy dissipation in relation to fatigue damage initiation has not been investigated yet. The present author's group has investigated the mechanism of energy dissipation through AFM observation at crack initiation<sup>(5)</sup>. It was found from these results that energy dissipation was related to activity of slip band and estimated fatigue limit is corresponding to crack initiation stress level of the material. Most of study on dissipated energy has been discussed based on the mean temperature rise or irreversible component of heat generation due to energy dissipation. In this study, phase information of energy dissipation was investigated and was applied to the accuracy improvement of dissipated energy measurement for fatigue damage estimation.

## Measurement of dissipated energy and Phase analysis for dissipated energy

Reversible temperature change is observed on the specimen subjected to cyclic loading. This phenomenon is called as thermoelastic effect, and the thermoelastic temperature change  $\Delta T_E$

is formulated by thrmoeastic coefficient  $k$ , absolute temperature  $T$ , and sum of principal stresses  $\Delta\sigma$ .

$$\Delta T_E = -kT\Delta\sigma \quad (1)$$

In the actual case, temperature rise due to irreversible energy dissipation  $\Delta T_D$  occurs at the maximum tensile stress and at the maximum compressive stress. Thus, the measured temperature change  $T(t)$  on the surface includes  $\Delta T_E$  and  $\Delta T_D$ . The component of thermoelastic temperature change  $\Delta T_E$  is obtained as follows,

$$\Delta T_{E,\sin} = \frac{2}{N} \sum_{t=1}^N T(t) \sin(t) \quad (2)$$

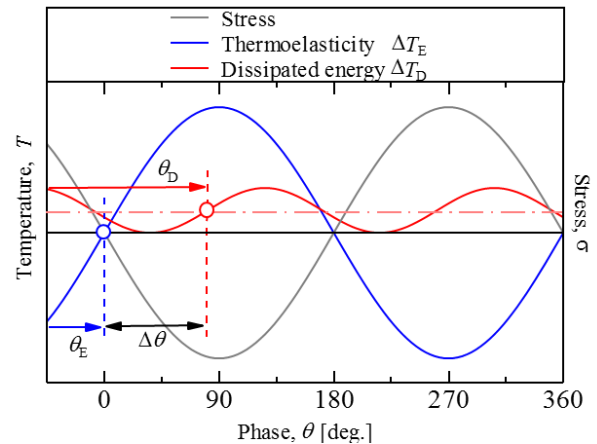


Fig. 1 Schematic illustrations of temperature change due to thermoelasticity and energy dissipation, and load signal.

$$\Delta T_{E,\cos} = \frac{2}{N} \sum_{t=1}^N T(t) \cos(t) \quad (3)$$

$$\Delta T_E = \sqrt{\Delta T_{E,\sin}^2 + \Delta T_{E,\cos}^2} \quad (4)$$

$\sin(t)$  is the reference signal made from cyclic loading, and  $\Delta T_{E,\sin}$  means the amplitude of temperature change which is synchronized with the reference signal.  $\Delta T_{E,\cos}$  means the amplitude of temperature change having the opposite phase to that of reference signal. The phase lag between thermoelastic temperature change and cyclic load  $\theta_E$  is caused by thermal diffusion.  $\theta_E$  is calculated as follows,

$$\theta_E = \tan^{-1} \left( -\frac{\Delta T_{E,\cos}}{\Delta T_{E,\sin}} \right) \quad (5)$$

The temperature change due to energy dissipation  $\Delta T_D$  can be obtained as the component having double frequency of the reference signal by lock-in algorithm, as follows,

$$\Delta T_{D,\sin} = \frac{2}{N} \sum_{t=1}^N T(t) \sin(2t) \quad (6)$$

$$\Delta T_{D,\cos} = \frac{2}{N} \sum_{t=1}^N T(t) \cos(2t) \quad (7)$$

$$\Delta T_D = 2\sqrt{\Delta T_{D,\sin}^2 + \Delta T_{D,\cos}^2} \quad (8)$$

$\Delta T_D$  means the amount of heat generation, so that it is presented as the range of temperature change. Dissipated energy  $q$  is calculated from  $\Delta T_D$ , density  $\rho$  and specific heat  $c$  of material.

$$q = \rho c \Delta T_D \quad (9)$$

The phase lag between temperature change due to energy dissipation and reference signal is calculated as follows,

$$\theta_D = \tan^{-1} \left( -\frac{\Delta T_{D,\cos}}{\Delta T_{D,\sin}} \right) \quad (10)$$

$\theta_D$  includes an influence of thermal diffusion. To remove the influence of thermal diffusion on phase information of energy dissipation, the phase difference  $\Delta\theta$  is defined as follows,

$$\Delta\theta = \theta_D - \theta_E \quad (11)$$

## Experimental set up

The material under test is JIS type 316L austenitic stainless steel. The cyclic axis loading with a frequency of 5 Hz was applied to the specimen by an electrohydraulic fatigue testing machine. In the staircase-like stress level test <sup>(1)</sup>, the applied stress amplitude was increased from 200MPa to 280MPa step by step. The temperature change on the specimen surface was measured by infrared thermography with a MCT array detector. The number of cycles for each step is 3100cycles, and each temperature measurement is performed by 1000 cycle loadings.

## Results and discussion

The changes of dissipated energy and phase difference in the staircase-like stress level test for stress ratio  $R=-1.0$  are shown in Fig. 2. It is found from Fig. 2 that dissipated energy increase significantly from  $\sigma_a=255$ MPa. The phase difference  $\Delta\theta$  shows unstable in the low stress level: from 200MPa to 250MPa. On the other hand, the phase difference shows the constant value (about 60 degree) at the high stress levels where the change of dissipated energy shows increasing. The experiments were carried out at least four times and the results show good

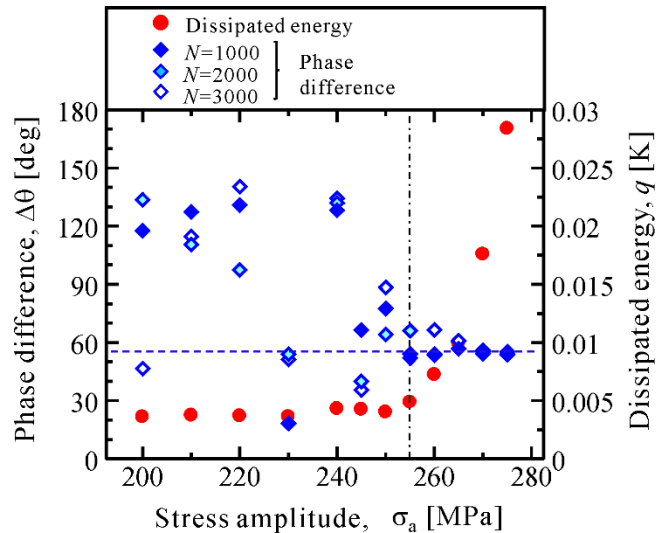


Fig. 2 change of dissipated energy and phase difference of energy dissipation for cyclic load .



repeatability. The estimated fatigue limit based on dissipated energy ( $\sigma'_w=254\text{MPa}$ ) coincided with the fatigue limit obtained by  $S$ - $N$  curve ( $\sigma_w=250\text{MPa}$ ).

The distribution of dissipated energy and phase difference at  $\sigma_a=265\text{MPa}$  are shown in Fig. 3. The area where dissipated energy shows high value coincides with the area where phase difference shows about 60 degree. To investigate the relationship between dissipated energy and phase difference, the histogram of phase difference is obtained.

The Relationship between the histograms of phase difference and the applied stress amplitude is shown in Fig. 4. The histograms for low stress level from 200 MPa to 250 MPa show two peaks. On the other hand, those for high stress level show a peak at 60 deg. As a result of analyzing the load signal measured from load cell, it becomes clear that there is non-linear component of load, except target component of load signal. This non-linear component is considered to be caused by harmonic vibration of electrohydraulic testing machine. The component of temperature change having double frequency and the phase difference of 140 degree is thermoelastic temperature change due to harmonic vibration of fatigue testing machine, so that it is not the component of energy dissipation. The component of temperature change having double frequency and the phase difference of 60 degree becomes dominant when applied stress is above fatigue limit. This component is considered to indicate the energy dissipation related to fatigue damage. Therefore, temperature change due to energy dissipation has a specified phase difference.

### Accuracy improvement of dissipated energy measurement

The conventional lock-in algorithm evaluates the component of temperature change having double frequency, which includes a thermoelastic temperature change due to harmonic vibration of fatigue testing machine and the dissipated energy related to fatigue damage. The new analytical technique is

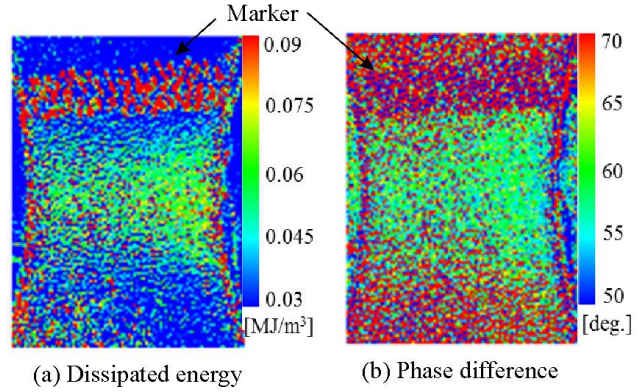


Fig. 3 Relationship between dissipated energy and phase difference. ( $\sigma_a=265\text{MPa}$ ,  $N=3000$  cycles).

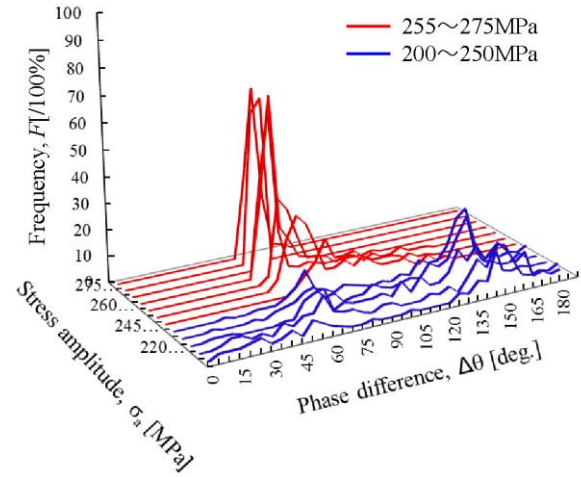


Fig. 4 Histogram of phase difference.

suggested by using that a temperature change due to energy dissipation has a specific phase difference. In this technique, which called as phase lock-in method, a staircase-like stress level test is conducted, and change of phase difference is measured. When change of phase difference shows constant value and the dissipated energy increases, this phase difference is determined as the specific phase difference of energy dissipation  $\Delta\hat{\theta}$ . The correlation value between the measured temperature change  $T(t)$  and the modified reference signal, which shifted by the specific phase difference  $\Delta\hat{\theta}$  and the phase lag of thermoelastic temperature change  $\theta_E$ , is calculated as follow,

$$\Delta\hat{T}_D = \frac{2}{N} \sum_{t=0}^N T(t) \cdot \sin \left\{ 2 \cdot \left( 2\pi \cdot t \cdot \frac{f_{\text{load}}}{f_{\text{meas}}} - (\theta_E + \Delta\hat{\theta}) \right) \right\} \quad (12)$$

where  $f_{load}$  and  $f_{meas}$  indicate load frequency and measurement frequency of thermal camera, respectively. When the correlation value is a minus value, it is set to 0.

The dissipated energy obtained by both methods in staircase-like stress level test is shown in Fig. 5. In this analysis, the specific phase difference  $\Delta\hat{\theta}$  was set to be 57 degree. It is found that the dissipated energy obtained by phase lock-in method at low stress level is smaller than that by conventional lock-in method. The estimated fatigue limit is 254 MPa for conventional lock-in method, and 251 MPa for phase lock-in method. The estimated fatigue limit by phase lock-in method coincides with fatigue limit by  $S-N$  curve, compared with that by conventional lock-in method.

The distributions of dissipated energy obtained by both methods are shown in Fig. 6. Applied stress amplitude is 255MPa for this measurement, and this stress amplitude is above and near fatigue limit. It is found that concentration of dissipated energy obtained by phase lock-in method at notch root is clearer than that by conventional lock-in method. The relationship between phase difference and dissipated energy shown in Fig 6(c) means that the components having the phase difference of 140 degree, which indicates temperature change due to harmonic vibration, is removed by phase lock in method.

## Conclusions

For the accuracy improvement of dissipated energy, phase lock-in method using the specific phase difference is suggested. Phase difference of energy dissipation is determined when the change of phase difference shows constant value and large dissipated energy is observed in staircase-like stress level test. It is effective to use a phase lock-in method for removal noise component, such as thermoelastic temperature change due to harmonic vibration of fatigue testing machine.

## Reference

1. G. La Rosa and A. Risitano, Thermographic methodology for rapid determination of the fatigue limit of materials and mechanical components, International Journal of Fatigue, Vol.22, 65-73, 2000.
2. J. -C. Krapez and D. Pacou, Termogarghy Detection of Damage Initiation during Fatigue Tests, Proceedings of SPIE, Vol.4710, 435-449, 2002.
3. Y. Irie, H. Inoue, T. Mori and M. Takao, Evaluation of Fatigue Limit of Notched Specimen by Measurement of Dissipated Energy, Transactions of the Japanese Society of Mechanical Engineers, Series A, Vol.76, No. 764, 410-412 2010.

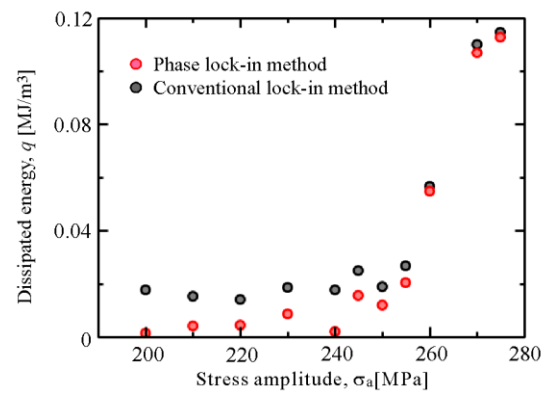
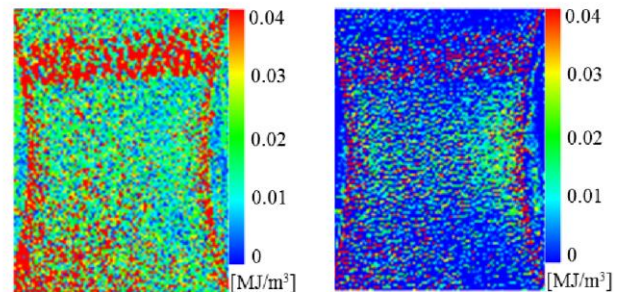
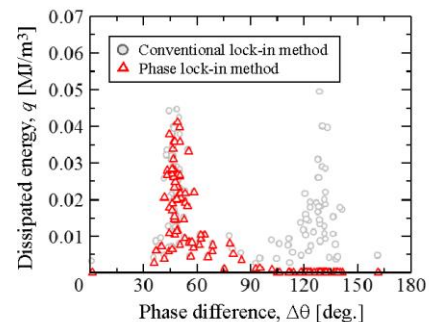


Fig. 5 Comparison between phase lock-in and conventional lock-in method for measurement of dissipated energy in staircase-like stress level test.



(a) Conventional lock-in method (b) Phase lock-in method



(c) Relationship between dissipated energy and phase difference

Fig. 6 Effect of phase lock-in method on the distribution of dissipated energy ( $\sigma_a=255$ MPa).



4. M. P. Luong, Infrared thermography of fatigue in metals, Proceedings of SPIE, Vol.1682, 222-233, 1992.
5. D. Shiozawa, K. Inaba, A. Akai and T. Sakagami, Experimental Study of Relationship Between Energy Dissipation and Fatigue Damage From

Observation of Slip Band by Atomic Force Microscope, Advance Materials research, Vol. 891-892, pp.606-611, 2014.

# INFRARED TERMOGRAPHY (IRT) IN HORSES TRAINED FOR ENDURANCE RACES

V. Redaelli<sup>1</sup>, G. D. Bariffi<sup>1</sup>, S. Mazzola<sup>2</sup>, R. Rossi<sup>1</sup>, L. Nanni Costa<sup>3</sup>, F. Luzi<sup>1</sup>

<sup>1</sup> Dept. VESPA, via G. Celoria, 10 – 20133 Milano - vereda@tin.it, gaiadominique.bariffi@studenti.unimi.it, raffaella.rossi@unimi.it, fabio.luzi@unimi.it

<sup>2</sup> Dept. DIVET, via G. Celoria, 10 – 20133 Milano – silvia.mazzola@unimi.it

<sup>3</sup> Dept. DISTAL, via G. Fanin, 46 – 40127 Bologna – leonardo.nannicosta@unibo.it

## Abstract

The aim of this study was evaluate the possibility of using the infrared thermography technique (IRT) to detect the work-related stress in 8 horses involved in training exercise (light, medium, strong) for endurance races Max temperature in left and right lacrimal caruncle by thermography and hearth rate were assessed before and after training with different intensity. Cortisol serum content was also determined on blood collected at training, Max temperature at lacrimal caruncle of left eye was significantly affected by intensity of training and time of measure while the other parameter were significantly influenced by the time of measure only. Max temperature in left and right lacrimal caruncle was positively and significantly correlated with the heart rate while positive but no significant relationship was found with the cortisol serum content.

## Introduction

During the last years Infrared Thermography (IRT) is largely widespread in veterinary medicine [5] [6] [7] [8] as non-invasive technique to measure superficial body temperature. IRT, together with other parameters, such as cortisol and heart rate, is often used to evaluate stress in horses during trials and competitions [1] [2] [3] [4] [10].

The aim of this study was evaluate the possibility of using the infrared thermography technique (IRT) to detect the work-related stress during training in horses endurance athletes.

## Materials and Methods

The trial took place at the farm *Società Agricola "La Bosana" Piozzano, Piacenza – Italy* and involved 8 horses with the same level of preparation for International Endurance Race (90 km MiPAAF). Horses were submitted to the same training program, fed with same diet and housed in the same paddock. Age, gender, cloak

and number of previous competitions of horses are reported in Table 1.

	<i>Year</i>	<i>Sex</i>	<i>Coat</i>	<i>Total competitions</i>
BR	2008	CM	Bay	6
BC	2008	CM	Bay	5
AR	2007	F	Bay	9
BT	2007	F	Gray	8
TA	2007	F	Bay	7
FD	2007	CM	Gray	13
OV	2001	CM	Gray	19
ZR	2006	F	Gray	11

Table 1: Description of horses included in the trial

Examined training work took place during three days in the week before competition. The training session was divided into two parts: in the first part horses gradually reached the maximum effort, while in the second part a cool-down phase was carried out. This procedure was followed during the three days of testing: one day with light work (1 hour at an average speed

of 19 km/hour), one day with medium (2 hours at an average speed of 16 km / hour) and one day with hard work (3 hours at an average speed of 20 km/hour). During tests the animals were not directly stricken by solar radiation

Heart rate assessment, thermographic measurements and blood sampling were carried out at one hour after morning's feeding immediately before training. At the end of training, horses were tied off the track and the previous measurements in the same orders were immediately done. The heart rate was measured via stethoscope for a period of 60 seconds. Thermographic videos were recorded by a thermocamera model AVIO G120EX, with a 320x240 uncooled microbolometer sensor was used. Videos were recorded at 10 fr / sec focusing on the following points (Figure 1):

- Lacrimal caruncle of Right/Left Eye
- Front Crown right / left
- Rear Crown right / left
- Front Pastoral right / left
- Rear Pastoral right / left
- Gluteal femoral muscle
- Longissimus dorsi muscle

Max temperature recorded on lacrimal caruncle measures in both eyes were considered in this study. Blood samples were collected before and after each training session on each horse involved in the trial by the farm's veterinarian. A part of 20 cl of blood taken from the jugular vein were placed in a portable refrigerator and stored at a temperature of about 4 °C, waiting to reach the laboratory, where samples were analysed (HeCo Vet C, Radim Diagnostics, Italy). The titration of the blood cortisol was performed by immunoassay ELISA technique. During the three hours training session, a pause took place after 2 hours 30 min when heart rate and IRT measures were carried out. No differences were found between measurements of IRT and heart rate recorded during the pause and at the end of the exercise. Thus, the former measurements were not considered in the data processed for statistical analysis.

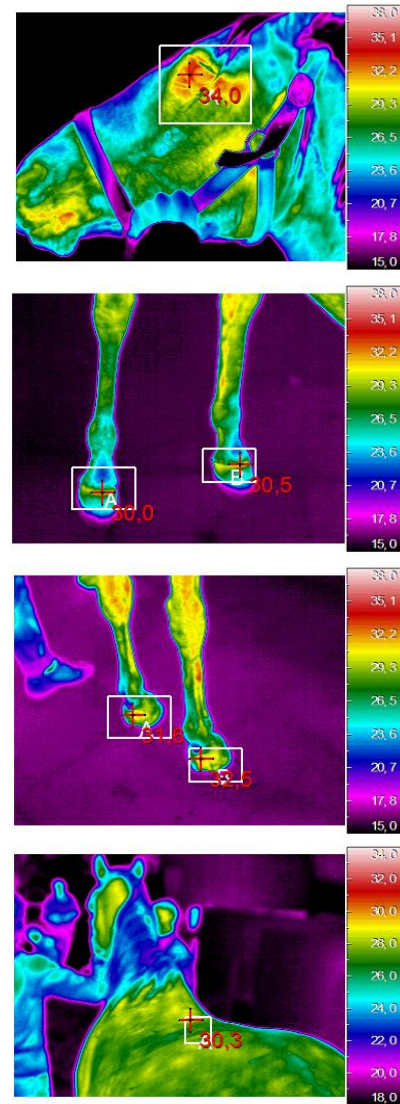


Figure 1: Points of reperere for IRT measures

Statistical analysis was performed using the statistical package SPSS (SPSS / PC statistics 21.0, SPSS Inc., Chicago, IL, USA). The data were analyzed by ANOVA (*Analysis of variance*) using a mixed model including time of measure (2 levels: before and after training), intensity of exercise (3 levels: light, medium, strong) and their interaction as fixed factors and horses as random factor. As dependent variables were considered max temperature in the lacrimal caruncle of both eyes, heart rate and cortisol level. Comparisons between least square means was performed using the Student Newman Keuls test. Interaction did not reach the level of statistical significance  $P < 0.05$  for all *dependent variables* examined and was excluded from the

model. *Correlations* between max temperature in the lacrimal caruncle, heart rate and cortisol level were also calculated. A significant difference for  $P < 0.05$  was considered.

## Results and discussion

The max temperature of lacrimal caruncle was significantly affected by the work intensity in the left eye only. The highest value was found during the light training while the lowest was recorded during the medium training (Table 2). IRT measures on the right eye followed the same trend. This finding suggested that the increase of temperature of caruncle is not related to the increase of the physical effort due to the training. As expected, heart rate significantly augmented accordingly to the increase of training intensity, while cortisol content was not affected by this factor. This could be due to a good athletic preparation, confirmed by the values obtained for the heart rates. Results obtained seem to confirm a good training program that allowed the animals to cope the maximum workload, coming back under 64 beats / minute (Regulation EIF) within 5 minutes after its end.

	Intensity of training		
	light	medium	strong
Max temperatures in lacrimal caruncle (°C):			
-left eye	34.75 <sup>a</sup>	34.12 <sup>b</sup>	34.52 <sup>ab</sup>
-right eye	34.76	34.47	34.53
Heart rate (bit/min)	44.37 <sup>a</sup>	46.33 <sup>a</sup>	55.36 <sup>b</sup>
Cortisol (ng/ml)	114.88	116.08	115.18

Table 2: Effect of different intensity of training on horses max temperature of lacrimal, hear rate and cortisol content

<sup>a,b</sup> Within a row, values without a common superscript letter differ ( $P < 0.05$ ).

	Time of measure	
	before training	after training
Max temperatures in lacrimal caruncle (°C):		
left eye	34.11 <sup>a</sup>	34,81 <sup>b</sup>
right eye	34,25 <sup>a</sup>	34,89 <sup>b</sup>
Heart rate (bit/min)	41.87 <sup>a</sup>	55,51 <sup>b</sup>
Cortisol (ng/ml)	111.78 <sup>a</sup>	118.85 <sup>b</sup>

Table 3: Effect of time of measure on horses max temperature of lacrimal, hear rate and cortisol content  
<sup>a,b</sup> Within a row, values without a common superscript letter differ ( $P < 0.05$ ).

The effect of time of measure significantly influenced all variables considered. Irrespectively of training intensity, max temperature of lacrimal caruncle of both eyes increased after physical exercise. Heart rate and cortisol content was also affected by the time of measure, due to a physiological increase in cardiac pump during the physical effort.

A significant ( $P < 0.05$ ), positive correlation was found between lacrimal caruncle temperature of both eyes and the heart rate. The r coefficient was + 0.39 for the left eye and + 0.43 for the right eye. There was not significant correlation between max temperature of caruncle and cortisol.

The absence of significant correlation between eye temperature and cortisol values may be due to the reduced variability in blood concentration due to absence of emotional stress during training. In fact, horses have been working in their familiar surroundings and with the same staff management. In literature the lacrimal caruncle seems to be the best point of *reper* for emotional stress [11]. In this study, lacrimal caruncle temperature changed after physical exercise showing the possibility to use this point of *reper* also for physical stress assesment. Nevertheless, the variation of its temperature was not related to the intensity of physical effort, suggesting that other physiological mechanisms are involved. It would be interesting to observe not only the variation before and after training

but also the trend of increase temperature in lacrimal caruncle during physical effort, in order to better evaluate the reliability of this point of reperi for stress-work related stress. Also it would be interesting to extend the trial to a larger sample of horses, in order to reduce the individual variability and the water-induced sweating, after intense work.

## References

1. E. Bartolomé, M.J. Sanchez, A. Molina, A.L. Schafer, I. Cervantes, M. Valera. Using eye temperature and heart rate for stress assessment in young horses competing in jumping competitions and its possible influence on sport performance. *Animal.*, 7, 2044-2053, 2013.
2. Hall C, Kay R, Yarnell K. Assessing ridden horse behavior: Professional judgment and physiological measures. *J. Vet. Behav.*, 9, 22-29, 2013.
3. C.H. Irvine, S.L. Alexander. Measurement of free cortisol and the capacity and association constant of cortisol-binding proteins in plasma of foals and adult horses. *J. Reprod. Fertil. Suppl.* 35: 19-24, 1987.
4. Valera M, Bartolomé E, Sanchez MJ, Molina A, Cook N, Schaefer AL.(2012) Changes in eye temperature and stress assessment in horses during show jumping competitions. *J. Equine Vet. Sci.*, 32, 827-830.
5. V. Redaelli. Utilizzo della tecnica termografica come sistema non invasivo per lo studio del benessere e dello stato sanitario nelle specie animali di interesse zootecnico e da affezione. Tesi di Dottorato di Ricerca - Università degli Studi di Milano.(2010). ([https://air.unimi.it/retrieve/handle/2434/150116/129180/PHD\\_UNIMI\\_R07755.pdf](https://air.unimi.it/retrieve/handle/2434/150116/129180/PHD_UNIMI_R07755.pdf))
6. N. Ludwig, M. Gargano, F. Luzi, M. Verga. Technical note : applicability of infrared thermography as a non invasive measurement of stress in rabbit. *Word Rabbit Sci.*, 15, 199-206, 2007.
7. D. McCafferty. The value of infrared thermography for research on mammals : previous applications and future directions. *Mammal rev.*, 37, 207-223, 2007.
8. M. Stewart, J.R. Webster, G.A. Verkerks, J.J. Colyn, K.I. Stafford. Non-invasive measurement of stress in dairy cows using infrared thermography. *Physiol. Behav.*, 92, 520-525, 2007.
9. G. Lippi, G.L. Salvagno, E. Danese, C. Tarperi, G.C. Guidi, F. Schen. Variation of Red Blood Cell Distribution Width and Mean Platelet Volume after Moderate Endurance Exercise. *Advances in Hematology Volume 2014*. Article ID 192173, 4 pages. <http://dx.doi.org/10.1155/2014/192173>.
10. Von Borell, E, Langbein, J, Després, G, Hansen, S, Lettieri, C, Marchant-Forde, J, Marchant-Forde, R, Minero, M, Mohr, E, Prunier, A, Valance, D and Veissier, I (2007) Heart rate variability as a measure of autonomic regulation of cardiac activity for assessing stress and welfare in farm animals. A review. *Physiol. Behav.* 92(3): 293-316.
11. Rusconi Clerici G., Redaelli V., Luzi F., Biganzoli E, Marano G., Bisacco F., Bergero D. (2014) La tecnica termografica nella riabilitazione equestre del soggetto autistico: risultati preliminari. *Atti del LXVIII Convegno Nazionale della SISVet, Pisa 16-18 giugno 2014*. (Pag. 6).

# MAPPING THE HEAT FLUX THROUGH AN INSULATED SMALL CONTAINER BY INFRARED THERMOGRAPHY

A. Bortolin<sup>1</sup>, P. Bison<sup>1</sup>, G. Cadelano<sup>1</sup>, G. Ferrarini<sup>1</sup>, L. Lei<sup>2</sup>, X. Maldague<sup>2</sup>

<sup>1</sup> ITC-CNR, Corso Stati Uniti n. 4, Padova I-35127, Italy, [alessandro.bortolin@itc.cnr.it](mailto:alessandro.bortolin@itc.cnr.it)

<sup>2</sup> Department of Electrical and Computer Engineering, Université Laval, 1065, av. de la Médecine, Québec City (Québec) G1V0A6, Canada,

The overall thermal transmittance of a small insulated container was measured according to the ATP (Agreement for Transport of Perishables foodstuffs) standard testing procedure. During the test a thermographic apparatus was used to map the temperature of the external walls of the container and to identify possible defects and thermal bridges. A heat flux meter was positioned on different surfaces of the container in order to assess the convective heat transfer coefficient in the different directions. The heat flux exchanged between the container and the environment calculated by IR thermography was compared with the results of the thermal transmittance value measured according to the ATP test. Finally, an IR camera was mounted on a pan-tilt head and automatically driven by a suitable software to map the temperature of the inner walls of the insulated box on a refrigerated vehicle.

## Introduction

Nowadays the correct transport of perishable foodstuffs in the refrigerated vehicles is going with the necessity of energy saving due to the ever increasing cost of energy. So it is essential that the refrigerated vehicles are equipped with a suitable thermal insulation in order to save energy, maintaining at the same time an appropriate conservation of the foodstuffs [1].

The ATP treaty (Agreement on the international carriage of perishable foodstuffs and on the special equipment to be used for such carriage [2]), is an international agreement about the means to be used for the perishable foodstuffs transport. The ATP standard test is a procedure that measures the insulating performance of containers with a global approach; however the surface temperature distribution could be uneven, because of to the presence of local defects in the structure of the equipment, such as thermal bridges, air leakages and zones of anomalous aging, that could not be detected by the ATP procedure and lead to a variation of the heat flux and temperature on the surface of the equipment. In those cases the thermographic technique, being a reliable asset in the field of non destructive tests and evaluation [3], could be

helpful. The local heat flux map of the equipment by IR thermography could give a visualization of the structure and a local evaluation of the thermal transmittance value [4, 5].

## A simplified heat transfer model

In the standard testing procedure, an air heating device is placed inside the small container. After reaching the steady state conditions, the heater delivers a power  $W$  in order to maintain a constant air temperature  $T_i$  inside the box. As the temperature outside the container is lower than the internal one, heat flows from the inside to the outside of the box where a constant air temperature  $T_e$  is maintained.

The heat transfer mechanisms are convection from the inside air to the internal wall, conduction through the wall and again convection from the outer wall to the outside air as shown in Figure 1.

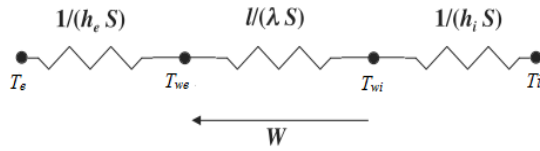


Fig. 1: One – dimensional model based on a thermal resistance network of the heat exchange through the small container.

A simplified heat transfer model based on a network of thermal resistances is then proposed for steady state conditions. The heat flux could be assumed as one–dimensional and  $h_e$  and  $h_i$  are respectively the external and internal heat exchange coefficients.  $T_{we}$  and  $T_{wi}$  are the average temperature of the internal and external walls, while  $\lambda$  is the thermal conductivity of the wall and  $l$  its thickness.

### Experimental setup

In order to verify the feasibility of the thermographic approach to the local quantitative evaluation of the heat transfer coefficient, a small insulated box (the roll container shown in Figure 2) was submitted to the standard test according to the ATP. Its walls are made of three layers: two external skins made by polyester-fiberglass and a core made by high density polyurethane foam. The idea is to measure the heat flux with a heat flux meter in a reference zone of the outside surface of the roll container. It is then possible to build a surface map of the heat flux as a linear relation of the temperature difference between the outside wall temperature and the air temperature.



Figure 2: Roll container and equipment utilized for the experimental tests: infrared camera, thermocouples, RTD, and heat flux meter.

The heat flux meter and the RTD probe are positioned:

- on the front vertical wall (in respect to the air stream);
- on the right vertical wall;
- on the back vertical wall.

The following hypotheses are assumed:

- the heat flux is one - dimensional;
- the convective coefficient values of the left and top surfaces are equal to the one calculated for the right surface.

An ATP test is performed for each position of the heat flux meter. The temperature inside the roll container is equal to 32.5°C. In order to maintain the prescribed temperature difference between interior and exterior (ATP standard requires 25±2 K), the facility is maintained at a temperature of about 7° C by the air conditioning system. Once the steady state condition is reached, several thermal images of all the roll container walls (except the bottom one) are acquired.

### Experimental results

According to the scheme described in the previous section, it was possible to calculate the convective heat transfer for each surface of the roll container  $h_e$  with the following equation:

$$h_e = \frac{q_r}{T_r - T_{out}} \quad (1)$$



where:

- $q_r$  is the heat flux through the roll container;
- $T_r$  is the surface temperature measured.

Thermographic images allow to determine the local heat flux exchanged  $q(x,y)$  between the roll container and the external environment, from the measurement of the local surface temperature  $T(x,y)$ :

$$q(x,y) = \frac{q_r}{\Delta T_r} \Delta T_{x,y} + q_r \quad (2)$$

$$= h_e \Delta T_{x,y} + q_r$$

where  $\Delta T_{x,y}=(T(x,y)-T_r)$  and  $\Delta T_r=(T_r -T_{out})$ .

As the thermographic measurement is aimed to quantify a heat flux, the geometric reconstruction of the images is of paramount importance. In this work the image processing was performed by Matlab algorithm based on homography. This technique allows to perform the image rectification and registration with the knowledge of few control points and to obtain the corrected heat flux mapping of each surfaces (Figure 3).

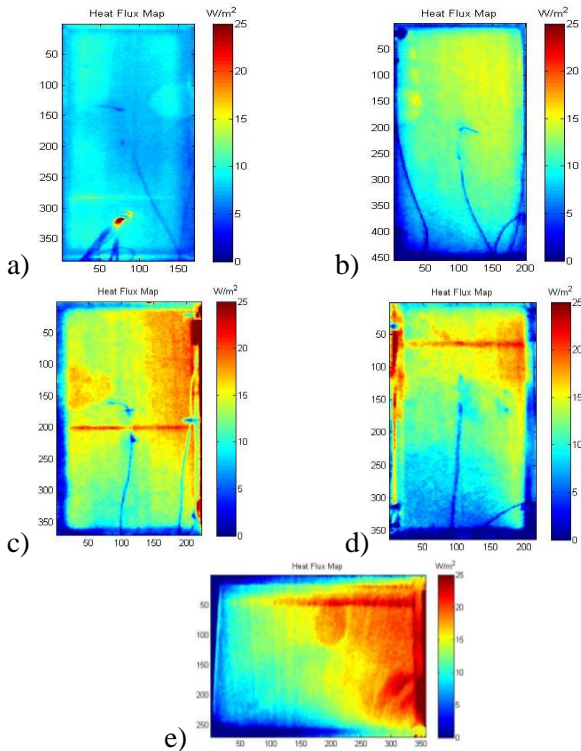


Figure 3: Heat flux map through each roll container surface (in respect to the air stream direction): a) front surface, b) back surface, c) right surface, d) left surface, e) top surface.

After the calculation of the heat flux through each surface by averaging the punctual thermal flux, the global heat flux between roll container and ambient is given by means of a weighted average of the thermal flux of each surface:

$$q_{glob} = \frac{\sum_i q_i S_i}{\sum_i S_i} \quad (3)$$

where  $q_i$  are the heat flux and  $S_i$  are the values of the area of each surface.

The average value of the heat flux of the three experimental tests is equal to  $12.7 \text{ W m}^{-2}$ , whereas a value of  $13.5 \text{ W m}^{-2}$  was obtained applying ATP standard.

### Application for an insulated vehicle

IR thermography was applied also to map the temperature of the inner walls of the insulated box on a refrigerated vehicle, similarly to what has been done for the roll-container.

An IR camera was mounted on a pan-tilt head and automatically driven by a suitable software in order to scan a wall by taking images of neighboring fields of view (Figure 4).

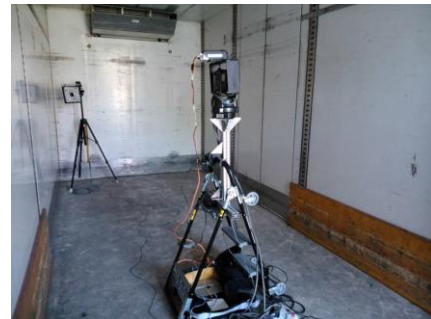


Figure 4: The inside of the truck used for the test with the experimental setup.

This equipment allows to collect several thermal images of the walls of the refrigerated vehicle. The acquisition is automatically managed by custom Labview software while the IR image processing is done in Matlab environment (Figure 5).



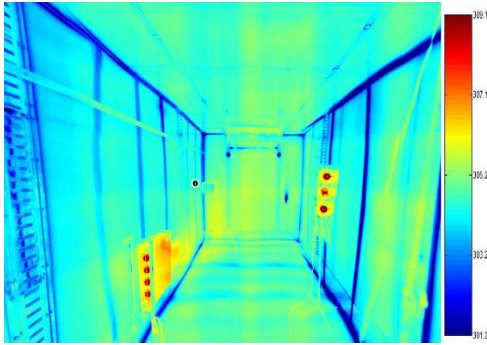


Figure 5: IR image of the internal surfaces of the refrigerated vehicle.

A thermal calibration device was utilized in order to correct the error that affects the thermal camera. The temperature target shown in Fig. 6 represented the inside temperature of the refrigerated vehicle that was measured by a RTD probe attached to the device. The difference between the temperature measured by the thermal camera and the RTD probe indicated the offset value that was applied to all the temperature values from IR camera.

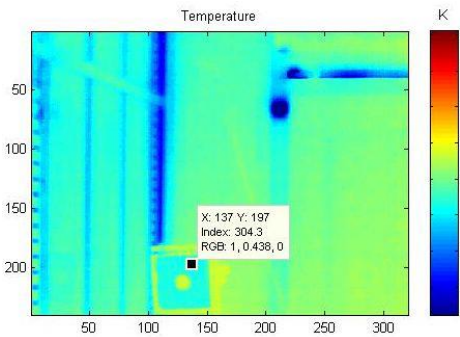


Figure 6: Target temperature from Thermography

## Conclusions

This work aims at mapping the heat flux exchanged between an insulated roll container and the external environment by means of infrared thermography. The measurement relies on a simplified thermal resistance model.

Three experimental tests according to ATP standard are performed positioning a heat flux meter and a RTD probe on three roll container surfaces that are differently impinged by the air

stream. It allows to calculate the convective heat flux coefficient for each surface that is considered in the thermal model. A strong variation of the convective heat flux coefficients is observed for the different orientations.

The raw thermographic images are processed with a dedicated algorithm in order to create geometrically corrected maps, easing the calculations and enhancing the visualization of the results.

The value of thermal transmittance obtained with the infrared thermography technique is very close to the ATP testing result. The difference between the two measurements is around 6 %.

## References

- [1] Dragano A., Rossi S., Bison P., Panozzo G. 2009, Experimental evaluation of the optical absorption coefficient of a sandwich panel for insulated vehicles. *Quantitative InfraRed Thermography Journal*, 6(2):207–223.
- [2] ATP - UN-ECE, Agreement Transport Perishables. Agreement on the international carriage of perishable foodstuffs and on the special equipment to be used for such carriage, Geneva 1970.
- [3] Maldague X. 2001, Theory and practice of infrared technology for nondestructive testing, Wiley.
- [4] Rossi S., Bison P., Cuogo G.P., Grinzato E. 2009, K-value estimation on refrigerated vehicles by thermographic analysis. *SPIE Defense, Security, and Sensing*, 72990N.
- [5] Grinzato E. and Panozzo G. Comparison of measurement of K-value by ATP internal heating method and by thermographic analysis. *International Institute of Refrigeration, Commission, D1,D2,D3:183–190.*

# EVALUATION OF INFRARED THERMOGRAPHY AS STANDALONE TECHNIQUE FOR DETECTION OF SEDIMENT-POLLUTION IN WATER

S. Lagüela<sup>1, 2</sup>, N. Caparrini<sup>2</sup>, L. López<sup>3</sup>

<sup>1</sup> Department of Cartography and Terrain Engineering, University of Salamanca. Calle Hornos Caleros, nº50, 05003 Ávila (Spain). [sulaguela@usal.es](mailto:sulaguela@usal.es)

<sup>2</sup> Applied Geotechnologies Research Group, University of Vigo, ETSE Minas, Rúa Maxwell, Campus Lagoas-Marcosende, 36310 Vigo (Spain). [susiminas@uvigo.es](mailto:susiminas@uvigo.es), [nataliac@uvigo.es](mailto:nataliac@uvigo.es)

<sup>3</sup> University of Vigo. ETSE Minas, Rúa Maxwell, Campus Lagoas-Marcosende, 36310 Vigo (Spain). [lujilo77@gmail.com](mailto:lujilo77@gmail.com)

The presence of solid elements in water provokes its invalidity for human use, both as drinking and as sanitary water. Water analysis is usually based on geochemical and geophysical analysis, implying the use of a wide variety of sensors and instruments. Infrared thermography is tested in this paper regarding its validity as standalone technique for the detection of solid pollutants in water. In order to examine the behaviour of infrared thermography for pollutant detection, the relations between solid concentration and emissivity of water are tested, so that the optimal parameters involved on the thermographic measurement are found.

## Introduction

Water pollution is an important problem worldwide, implying a continuous decrease in the volume of drinking water available, regarding both quantity and quality [1].

There are three main different sources of water pollution: microbiological, chemical, and physical- aesthetic [2]. Microbiological aspects are the most commonly analysed, and are mainly focused on faecal pollution (*Escherichia coli*) although other protozoa such as *Giardia*, and enteric viruses, are taken into account in order to determine water usability. Regarding chemical pollution, pH is the first parameter to be measured, while contaminants depend on the area and its activity [3]. For example, in rural areas analysis must be towards the determination of the concentration of phosphates and nitrates from agriculture fields, whereas in industrial areas the variety of pollutants is wider: heavy metals in the case of automotive industry, chlorides in textile industry. Last, physical

parameters focus on the appearance of water, such as turbidity, colour and odour.

The measurement of each parameter implies the use of different instruments, forcing its performance to be in the laboratory, measuring the parameters from water samples.

Multispectral satellite images are widely used for modelling Total Suspended Solids, TSS, in water, based on the modified emission of radiation of water as a function of suspended sediments [4-5]. The spectral band mostly used for this application is Near Infrared, NIR, due to the increase in emergent radiance in water provoked by the presence of sediments [6].

The thermal infrared band, TIR, has been used for the detection of oil spills in water, appealing to the difference in emissivity between clear water and the floating oil [7]. However, the thermographic technique has never been used from a quantitative approach for the analysis of water.

This paper presents an analysis of the capabilities of infrared thermography for its application to the study of sediment pollution in water. Thus, correlations between thermographic and physical-

chemical parameters of water are seek. What is more, the application of the study to different phases of a stream polluted with sediments allows the evaluation of the effectiveness of the recovery measures applied.

## Statement

Infrared thermography provides information about the temperature and the emissivity of the objects inspected. Differences in the emissivity value of different materials are usually exploited for the detection of spills on water, even when spills and water are at the same temperature. Solid pollutants do not only change water parameters, but also its appearance. Consequently, infrared thermography, in its imaging nature, seems like an adequate technique for its application to the analysis of water content.

## Approach

The capabilities of infrared thermography for the analysis of water pollution are evaluated through the study of stream Sañías, located in Cangas, NW Spain (Fig. 1). The construction of a road in the surroundings of the stream provoked the collapse of a slope and the subsequent spill of sediments to the stream.

Recovery measures are applied in order to eliminate the sedimentary material from the stream, consisting on the placement of hay packets in the stream. Hay behaves as a filter, retaining the sediments, and only allowing the circulation of clean water.

Water analysis is performed following two different approaches, the common one, and infrared thermography. This way, the results of both analysis are compared in order to identify the capabilities of the latter. Following the first approach, water samples are taken from the same position in the stream in three different occasions: just after the spill, one week after the spill and one year after the spill. Two samples of 500 mL are taken in each occasion, guaranteeing the quantity of water required for the tests as well as the possibility of repeating tests for the sake of accuracy. The first samples include the sediments from the slope; the second samples are taken after the application of the recovery measures consisting on the placement of hay packets in the stream. The third samples examine the natural state of the stream.

Regarding the new approach, thermographic images are acquired before the acquisition of the samples, of the water in the river, at the position of the acquisition of the water samples. Water temperature is measured with a contact thermometer with the aim at calculating the apparent emissivity value of water for each occasion.

Samples are examined in the laboratory, towards the determination of their physical-chemical properties. Thus, pH, electrical conductivity, TDS (Total Dissolved Solids), solved oxygen and TSS or concentration of suspended solids (fine material) are measured in each sample.

Regarding thermographic information, temperature and apparent emissivity values are defined for each sample acquisition, estimating the mean temperature value of the water area in each image (Fig. 2), and calculating the resulting apparent emissivity using as basis the temperature value measured with the thermometer and Stefan Boltzmann's law.

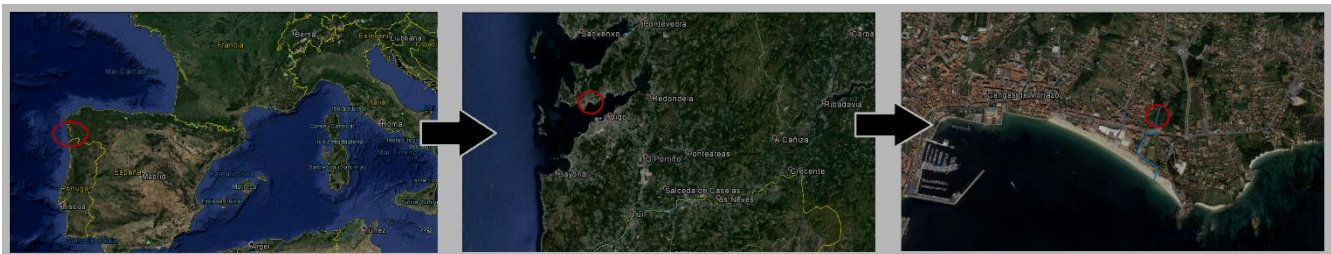


Fig. 1. Location of the stream subject of the study.

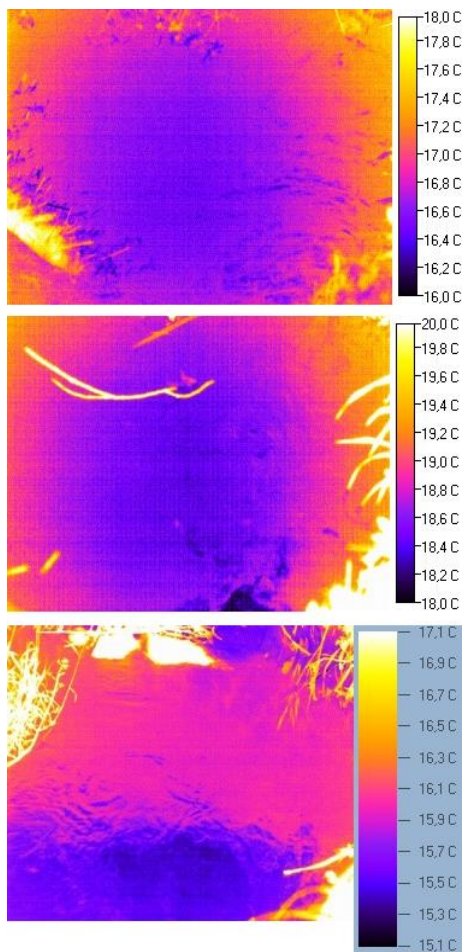


Fig. 2. From top to bottom: infrared images acquired right after, one week after, and one year after the spill of sediments.

## Results

Laboratory experiments are performed in the samples for the determination of their physical-chemical parameters: pH, TDS, conductivity, dissolved oxygen and TSS (Total Suspended Solids). Values are shown in Table 1.

	Samples no. 1	Samples no. 2	Samples no. 3
pH	6.53	6.94	7.23
TDS (mg/L)	93.13	94.58	99.55
Conductivity ( $\mu$ S)	185.28	186.45	194.24
Dissolved Oxygen (mg/L)	4.12	6.35	6.75
TSS ( $g/cm^3$ )	0.01	0.00	0.00

Table 1. Laboratory Values for physical-chemical parameters in water.

Regarding thermographic information, temperature values measured with the camera and

the contact thermometer are used in the computation of the apparent emissivity value of water in each case. Results are shown in Table 2. The low emissivity of water in the third campaign can be due to the occurrence of oil spills to the stream, which is a common operation among the surrounding industries and wine exploitations.

	Samples no. 1	Samples no. 2	Samples no. 3
Temperature Camera	16.5	18.5	14.5
Temperature Thermometer	16.3	18.0	13.7
Emissivity	0.95	0.90	0.80

Table 2. Calculation of emissivity values of water from thermographic images and thermometer values.

Apparent emissivity values show an increase in water emissivity due to the presence of suspended solids. In fact, especially for samples 1 and 2 (right after and one week after the spill), emissivity values are related to water content, since the emissivity value of earth or saturated soil is 0.95, whereas the emissivity value of hay (applied as recovery measure) is 0.85 [8]. What is more, apparent emissivity shows an opposite trend to pH, TDS, conductivity and dissolved oxygen, since all the parameters increase with the reduction in TSS except emissivity.

Correlations are searched between apparent emissivity and each physical-chemical parameter, resulting in the following equations (1 – 4):

$$\varepsilon = -0.2082 \cdot pH + 2.3197 \quad (1)$$

$$\varepsilon = -0.0224 \cdot TDS + 3.0303 \quad (2)$$

$$\varepsilon = -0.0153 \cdot \mu + 3.7756 \quad (3)$$

$$\varepsilon = -0.0452 \cdot O_2 + 1.1434 \quad (4)$$

Where  $\varepsilon$  represents apparent emissivity and  $\mu$  electrical conductivity. In all cases, R-squared is over 0.7, being 0.9189, 0.9859, 0.9559 and 0.7067 for emissivity, TDS, electrical conductivity and dissolved oxygen, respectively. Fig. 3 shows an example for emissivity.

Regarding the parameter of interest for the stream under study, TSS, correlation with emissivity is not clear, presenting an R-squared of 0.6057, as shown in Fig. 4. However, its correlation with pH



and dissolved oxygen, which are the parameters with the highest correlation with emissivity, is completely linear ( $R^2$  equal to 0.8566 and 0.9887, respectively). This way, there is an indirect manner of detecting TSS through variations in pH and dissolved oxygen in water.

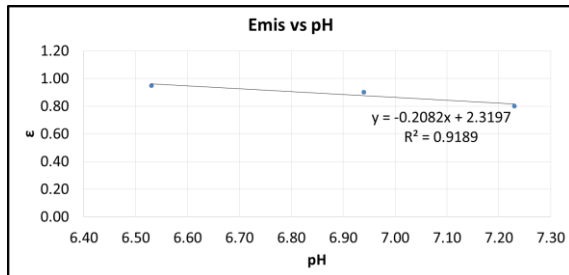


Fig. 3. Representation of pH values vs. apparent emissivity values ( $\epsilon$ ) for the three campaigns of sample acquisition.

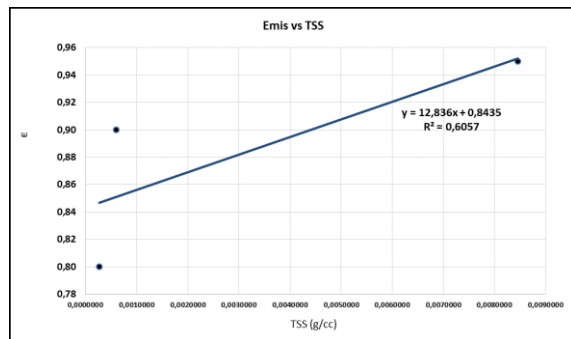


Fig. 4. Representation of TSS values with respect to apparent emissivity values ( $\epsilon$ ) for the three campaigns of sample acquisition.

## Conclusion

In this paper, infrared thermography is evaluated towards its validity for detection of suspended solids in water. A stream located in Cangas (Galicia, NW Spain) is used as case study, due to its suitability after suffering a sediment spill due to the collapse of a slope nearby.

Due to the high number of influence factors regarding temperature, focus is set on the apparent emissivity values of water, parameter that includes the external ambient conditions and angle of acquisition.

Analysis show that apparent emissivity varies with the contents of suspended solids in water, having a linear relationship with water pH,

dissolved solids and oxygen, and electrical conductivity. However, TSS does not present a linear relation with apparent emissivity. This leads to the conclusion that infrared thermography can be applied as standalone technique to the evaluation of water pollution related to suspended solids, but from an indirect approach: instead of directly deducing the presence of solids in water, it is indirectly detected through the emissivity value and its relation with pH, and dissolved oxygen.

## Acknowledgements

Authors would like to give thanks to the Ministerio de Economía y Competitividad (Spanish Government) for the financial support given through human resources grants (FPDI-2013-17516).

## References

1. Climate Hot Map. Global Warming Effects around the World. Union of Concerned Scientists. Available in: <http://www.climatehotmap.org/global-warming-effects/water-supply.html>
2. World Health Organization, Guidelines for drinking-water quality. 1997. ISBN: 9241545038
3. Ministry of Natural Environment. Handbook for spill management. 2007. ISBN: 978-84-8320-403-0.
4. E. Ayana, A. Worqlui, T. Steenhuis, Evaluation of stream water quality data generated from MODIS images in modelling total suspended solid emission, Science of the Total Environment, Vol. 523, pp. 170-177, 2015.
5. S. Chen, L. Han, X. Chen, D. Li, L. Sun, Y. Li, Estimating wide range Total Suspended Solids concentrations from MODIS 250-m imageries: An improved method, ISPRS Journal of Photogrammetry and Remote Sensing, Vol. 99, pp. 58-69, 2015..
6. J. Ritchie, P. Zimba, J. Everlitt, Remote sensing techniques to assess water quality, Photogrammetric Engineering & Remote Sensing, Vol. 69 (6), pp. 695-704, 2003.
7. M. Lega, J. Kosmatka, C. Ferrara, F. Russo, R. Napoli, G. Persechino, Using advanced aerial platforms and infrared thermography to track environmental contamination, Environmental Forensics, Vol. 13(4), pp. 332-338, 2012.
8. Thermoworks emissivity table. Available at: [http://www.thermoworks.com/emissivity\\_table.html](http://www.thermoworks.com/emissivity_table.html)

# DESIGN AND OPTIMIZATION THROUGH THERMOGRAPHY: nEMoS ARCHITECTURE

F. Salamone<sup>1\*</sup>, L. Danza<sup>1</sup>, I. Meroni<sup>1</sup>, M.C. Pollastro<sup>1</sup>

<sup>1</sup> ITC-CNR, Construction Technologies Institute- National Research Council of Italy, Lombardia Str., 49-20098 San Giuliano M.se (Italy) francesco.salamone@itc.cnr.it

The paper describes the activities involved to measure the temperature distribution in the nEMoS device in order to minimize the thermal interference of the installed sensors. nEMoS, nano Environmental Monitoring System, is an “all-in-one” device aimed at assessing the Indoor Environmental Quality (IEQ) of buildings. The two features at the basis of nEMoS are the cost-effectiveness and the consistency of the detected data. For the former of these purposes only low cost sensors and microcontrollers have been chosen while, for the latter, the detected data have been compared with those of typical commercial sensors. Through an area contactless measurement of temperature, it was possible to identify the areas that are most affected by the heating of the sensors as well as the components that manage the power supply of the microcontroller. With the help of the thermographic technique it was possible to build a new optimized case and to delete instrumental systematic errors.

## Introduction

There are three different typologies of temperature measurement techniques: invasive, semi-invasive, non-invasive [1]. The last one may be carried out by exploiting the physical principle whereby, any body at a temperature above absolute zero transmits infrared radiation corresponding to the temperature of the object. Such temperature depends on molecular motion: the greater the intensity of the movement, the greater the temperature of the object. Through thermography it is possible to measure the infrared radiation emitted by an object and its temperature distribution.

Thermography is applied in all fields where it is important to know the surface temperature of a body or parts of it. Through appropriate correlations it is possible to determine the effect associated with a particular temperature.

In this article thermography was used both to evaluate the thermal irregularities and to optimize the functional distribution of a series of sensors placed within an integrated device

for monitoring the environmental variables [2].

Local variations in temperature, in fact, may lead to an alteration of the measurement of heat-sensitive sensors and, in extreme cases, to a malfunction or breakage of the sensors. In both cases it is useful to proceed to an analysis of the temperature distribution to optimize the component layout [3]. The monitoring systems more and more are going to non-invasive technologies. The interest of the professionals to the use of shared and customizable hardware solutions is always greater. Over the past years several shared projects and low-cost alternative technologies have grown, allowing the end users to approach the electronics in a simple and fast way [4-6]. The user becomes supporter and promoter of the “maker” movement and of the *Do It Yourself* (DIY) approach, shooting down structural and technological limits [7]. The spread of this movement allowed a proliferation of devices always connected in a communicating-actuating network (i.e. objects connected to the web and interconnected to each other named Internet of Things) [8]. The revolution of DIY is the last one in chronological order. After the agricultural and the industrial revolutions, the information age, the so called Third Wave [9], draws upon the read/write

functionality of the Internet and digitally-driven design/manufacture, to enable ordinary people to invent, design, make and, sometimes, sell goods and services [10]. Anybody at any location could carry out the principles of DIY philosophy [11-13] through enabling technologies, for example Arduino [14] or Genuino [15].

The evaluation of the IEQ requires the use of tools able to detect specific environmental variables [16-17]. Following the so-called *Internet of Things* approach, that has allowed the web to evolve from the static web pages of the 90s to the web 2.0 (social networking web) of the 2000s and up to the web 3.0 (ubiquitous computing web) of the present day [18–21], a specific device has been built. ITC-CNR has developed a useful tool, called nEMoS, for assessing the Indoor Environmental Comfort (IEQ). The nEMoS device is based on the inexpensiveness and the consistency of the detected data. For the former of these purposes only low cost sensors and microcontrollers have been chosen. For the latter the detected data have been compared with those acquired by typical commercial sensors. The article describes the steps that led to the optimization of the case of this integrated device.

### Materials and methods

The case of the first prototype of nEMoS was conceived in an extremely compact way, made with 3D printing, with dimensions (L x H x W) equal to 8.5 x 6 x 7.5 cm. The case consists of 3 main parts: a base, the side structure with the housings for the various sensors and a top lid. The model, made in 3D CAD, has been printed with successive deposits of ABS, starting from the lower layer, with dimensional tolerances of the order +/- 0.5 mm along the axes x, y and z (Fig. 1). The Dimension Elite 3D printer used is based on FDM (Fused Deposition Modeling) technology.

Fig. 1 shows the monitoring station as it was implemented. All the sensors are positioned

on the top: 1. the globe thermometer, 2. the air temperature and relative humidity sensor (DHT22), 3. the anemometer (Wind sensor made by modern device), 4. the CO<sub>2</sub> concentration sensor (k-30 made by CO<sub>2</sub> meter) and 5. the LDR (that works as a luxmeter).

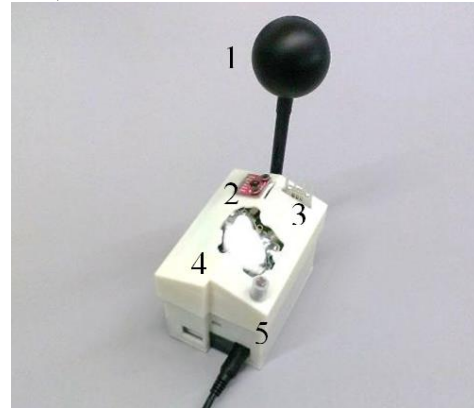


Fig. 1. First prototype of IEQ monitoring station

In order to evaluate the behaviour of the device in real working conditions and to detect instrumental systematic errors, an analysis was performed with the aid of a portable infrared camera, the Avio TVS-700, whose optical system is sensitive to infrared radiation with a wavelength in the range of 2÷14 μm, range in which the materials generally used in electronics radiate energy thus showing their thermal behaviour [22]. The analysis was carried out in three distinct phases: at the beginning of test, after 3 hours and after one day of operation.

### Thermal Analysis First Test

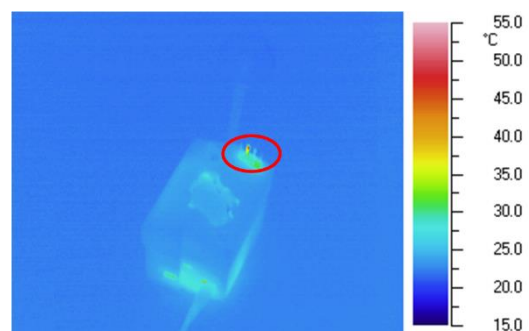


Fig. 2. 1<sup>st</sup> Case, Thermal imaging at starting time

The nEMoS device has been placed in a room with constant temperature equal to 24.5 °C throughout the whole test. At the beginning of the test (Fig. 2) it is possible to notice an almost constant



distribution of temperature along the case, slightly lower than 25 °C. A localized temperature gradient can be observed at the resistor of the anemometer, equal to about 50 °C. This sensor is based on a thermistor which is maintained at a constant temperature slightly above 50 °C (Fig. 3) and on the resulting measurement of electrical power required to maintain the temperature of the heated element according to the variation of air velocity.

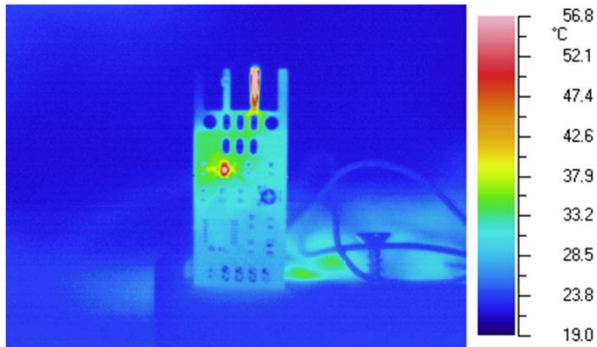


Fig. 3. Thermal imaging of the anemometer

After 3 hours of operation there is a slight variation in the distribution of the temperatures at the anemometer (Fig. 4).

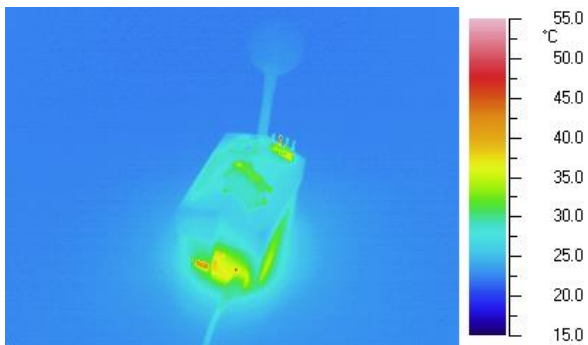


Fig. 4. 1<sup>st</sup> Case, Thermal imaging after 3 hours

A maximum temperature slightly above 50 °C can be noticed on the top of the case as well as in the lower part near the power jack, where the voltage regulator is located. However, the temperature and humidity sensor records a temperature of about 29 °C.

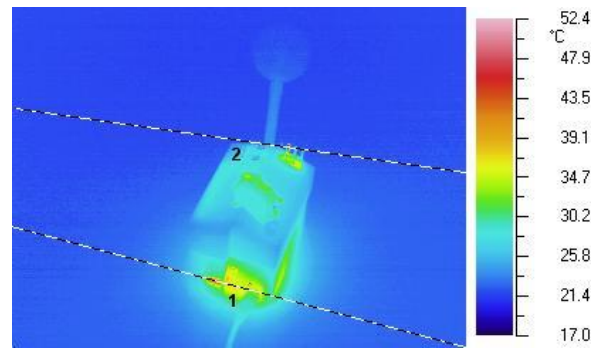


Fig. 5. 1<sup>st</sup> Case, Thermal imaging after 24 hours

After approximately 24 hours of use (Fig. 5), the situation is not changed. Profile 1 highlights the disturbance in temperature distribution due to the voltage regulator (Fig. 6).

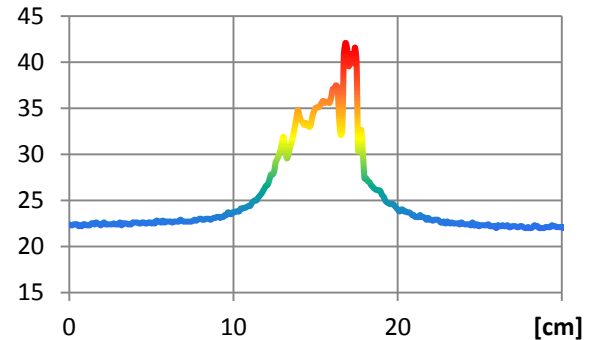


Fig. 6. Profile 1, temperature distribution

It can be observed how a disturbance of the temperature range due to the voltage regulator and to the nearby power jack extends to a diameter of about 10 cm. Profile 2 shows the field of perturbation due to the anemometer (Fig. 7).

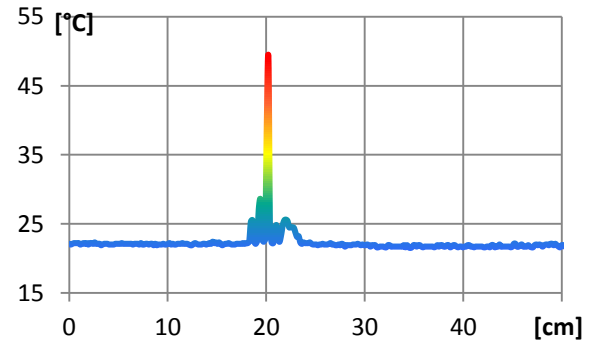


Fig. 7. Profile 2, temperature distribution

In this case the perturbation of the temperature due to the anemometer extends to a diameter of about 6 cm.

Fig. 8 describes the trend of the temperature recorded by the monitoring system.

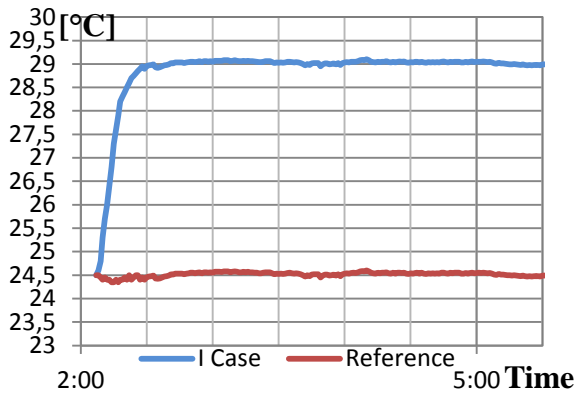


Fig. 8. 1<sup>st</sup> Case, air temperature

As it may be noticed, the first measured value, at around 2:10 pm, is that related to the beginning of data capture, when the system was "cold". The increase in temperature of the device affects the temperature measurement of the sensor. After one hour of operation the curve tends to be almost constant and equal to about 29 °C, which is a sign that it is necessary to wait about an hour to reach thermal equilibrium. Overall, with the type of case described, the system records a temperature about 4.5 °C higher than that of the surrounding air .

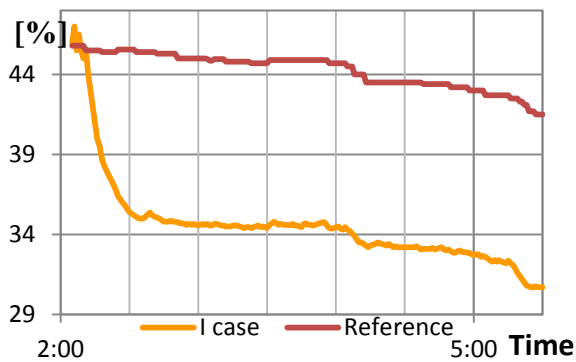


Fig. 9. 1<sup>st</sup> Case, air relative humidity

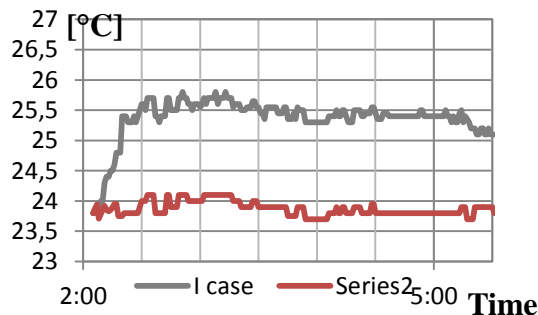


Fig. 10. 1<sup>st</sup> Case, radiant temperature

Fig. 9 and Fig. 10 show the relative humidity and the radiant temperature respectively. The aforementioned irregularity is confirmed also regarding the detection of humidity and radiant temperature due to the presence of the nearby hot wire anemometer.

## Optimization and Results

The thermographic analysis shows an interference in the measurement of the real temperature due to local overheating. To obviate the above observed drawbacks a new case was constructed.

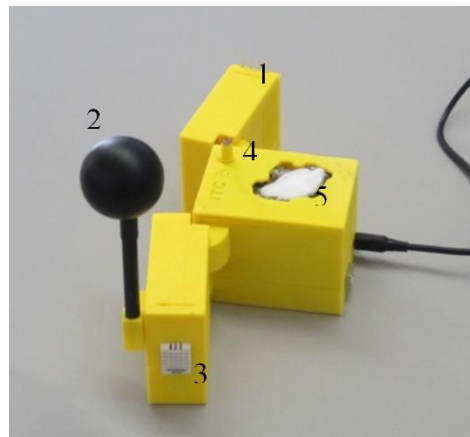


Fig. 11. Optimized case

The new case ( Fig. 11) consists of a central part and two side wings: the end of one wing provides the housing for the anemometer (1), while the globe thermometer (2) and the air temperature and relative humidity sensor (3) are housed in the end of the opposite wing . The central part contains the sensors not susceptible to temperature changes, the LDR (4) and the CO<sub>2</sub> concentration sensor (5). The auxiliary components for the data logging functions are also housed in the central part of the case.

The thermography performed after one day of operation (Fig. 12) shows no localized heating in the proximity of the globe thermometer and of the air temperature and relative humidity sensor.

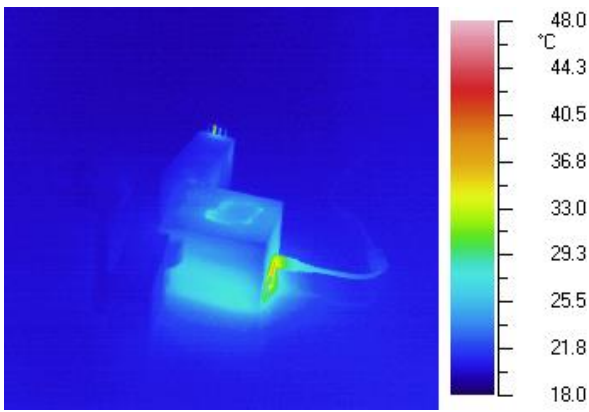


Fig. 12. nEMoS, Thermal imaging after 24 hours

At this stage the data recorded by the monitoring system as regards air temperature (Fig. 13), relative humidity (Fig. 14) and radiant temperature (Fig. 15), do not show any anomaly .

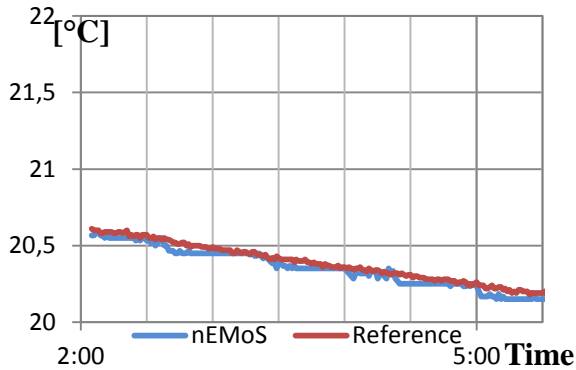


Fig. 13. nEMoS, air temperature

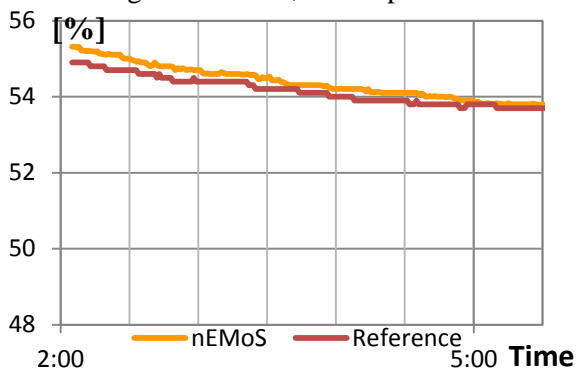


Fig. 14. nEMoS, air relative humidity

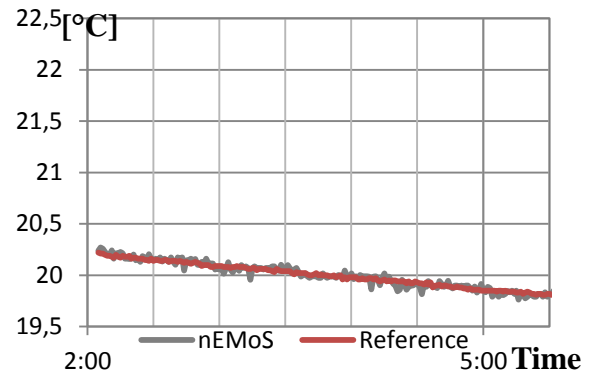


Fig. 15. nEMoS, radiant temperature

## Conclusions

The thermographic analysis allowed to identify the hottest points, establishing the scope of perturbation due to sensors and circuit elements that heat up the most and, finally, to optimize the device nEMoS for the evaluation of indoor environmental comfort.

On the one hand, the optimization of the case allowed to improve the accuracy of the instrument in terms of the difference between the experimental and the real value of the air temperature, relative humidity and radiant temperature. On the other hand, the accuracy of the data, namely the difference between the average experimental value and the actual value, is also improved.

## References

1. Childs, P. R. (2001). Practical temperature measurement. Butterworth-Heinemann.
2. F. Salamone, L. Belussi, L. Danza, M. Ghellere, I. Meroni, (2014) New scenarios of characterization of internal environmental comfort. Sustainable Housing Construction. Proceedings of the 40th IAHS World Congress on Housing, Funchal – Portugal pp.128 ISBN 9789899894907
3. Briand, D., Heimgartner, S., Grétilat, M. A., van der Schoot, B., & de Rooij, N. F. (2002). Thermal optimization of micro-hotplates that have a silicon island. Journal of Micromechanics and Microengineering, 12(6), 971.
4. Anzalone, G. C., Glover, A. G., & Pearce, J. M. Open-source colorimeter. Sensors, 2013, 13(4), 5338-5346.
5. Martínez, M. A., Andújar, J. M., & Enrique, J. M. A new and inexpensive pyranometer for the visible spectral range. Sensors, 2009, 9(6), 4615-4634.

6. Salamone, F., L. Belussi, L. Danza, M. Ghellere, I. Meroni (2015). "Design and Development of nEMoS, an All-in-One, Low-Cost, Web-Connected and 3D-Printed Device for Environmental Analysis" *Sensors*, vol 15, pp. 13012-13027, ISSN 1424-8220.
7. Fox, S. Third Wave Do-It-Yourself (DIY): Potential for prosumption, innovation, and entrepreneurship by local populations in regions without industrial manufacturing infrastructure. *Technology in Society*, 2014, 39, 18-30.
8. Gubbi, J., Buyya, R., Marusic, S., & Palaniswami, M. Internet of Things (IoT): A vision, architectural elements, and future directions. *Future Generation Computer Systems*, 2013, 29(7), 1645-1660.
9. Toffler, A. *The third wave*. New York: Bantam books, 1981, 32-33.
10. Fox, S. Paradigm shift: Do-It-Yourself (DIY) invention and production of physical goods for use or sale. *Journal of Manufacturing Technology Management*, 2013, 24(2), 218-234.
11. Anderson, C. The new industrial revolution. *Wired magazine*, 2010, 18, 2.
12. Gershenfeld, N. How to make almost anything. *Foreign Affairs*, 2012, 91(6), 43-57.
13. Hatch, M. *The maker movement manifesto*. McGraw-Hill Education 2014.
14. <http://www.arduino.org/>
15. <https://www.arduino.cc/>
16. Kolokotsa, D.; Pouliezos, A.; Stavrakakis, G.; Lazos, C. Predictive control techniques for energy and indoor environmental quality management in buildings. *Build. Environ.* 2009, 44, 1850–1863.
17. D. Kolokotsa, A. Pouliezos, G. Stavrakakis, C. Lazos, "Predictive control techniques for energy and indoor environmental quality management in buildings" *Building and Environment*, vol. 44(9), pp. 1850-1863, 2009.
18. International Telecommunication Union. *The Internet of Things*, Report 2005. Available online: <http://www.itu.int/> (accessed on 30 April 2015).
19. Gubbi, J.; Buyya, R.; Marusic, S.; Palaniswami, M. Internet of Things (IoT): A vision, architectural elements, and future directions. *Future Gener. Comput. Syst.* 2013, 29, 1645–1660.
20. Weber, R.H.; Weber, R. *Internet of Things*; Springer: New York, NY, USA, 2010.
21. Atzori, L.; Iera, A.; Morabito, G. The internet of things: A survey. *Comput. Netw.* 2010, 54, 2787–2805.
22. Lanzoni, D. (2014). *Termografia*. Maggioli Editore.

# URBAN MONITORING FROM INFRARED SATELLITE IMAGES

M. Ghellere<sup>1</sup>, A. Bellazzi<sup>2</sup>, L. Belussi<sup>3</sup>, I. Meroni<sup>4</sup>

<sup>1</sup>CNR-ITC, ghellere@itc.cnr.it

<sup>2</sup> CNR-ITC, bellazzi@itc.cnr.it

<sup>3</sup> CNR-ITC, belussi@itc.cnr.it

<sup>4</sup> CNR-ITC, meroni@itc.cnr.it

Starting from an experimental campaign in Milan, the article describes how the infrared signal recorded by Landsat 8 sensors can be used to evaluate and monitor the main urban scale environmental variables. The possibility to combine different spectral bands of infrared signal with other spectral bands is highlighted. The monitored variables have been mapped in georeferenced images using the GIS instruments. In this way, a mapping database is achieved and it can be used as a basis of information to study the urban heat islands (UHI) and the environmental changes over the years.

## Introduction

The urban climate analysis is really complex and needs a lot of data, mathematical equations, expensive and specific instruments, in addition to lengthy monitoring periods. All these factors place limitations on the systematic study of this subject.

To overcome these difficulties, new investigation techniques are based on the use of satellite images aimed at analysing the different wavelengths radiation of the earth, from the visible to infrared, with a fixed frequency.

Since 1972, LANDSAT satellites have monitored the Earth's surface and supplied useful data sets to analyse the global and local climate [1].

In this article the satellite images are functional to study the climate variables and to the energy and environmental monitoring of Milan.

## Evaluation of surface energy balance

The trend of heat and moisture in soil and atmosphere is studied in order to analyse the energy balance at urban scale. Roerink et. al [2] tested and validated the S-SEBI method (Simplified Surface Energy Balance Index): the surface energy fluxes are solved by using the remote sensing and finding a correlation with the solar radiation.

The surface energy balance is given by:

$$R_n = G_0 + H + \lambda E \quad (1)$$

Where:  $R_n$  is the net solar radiation ( $W/m^2$ ),  $G_0$  is the soil heat flux ( $W/m^2$ ),  $H$  is the sensible heat flux ( $W/m^2$ ),  $\lambda E$  is the latent heat flux ( $W/m^2$ ).

The Net Solar Radiation can be expressed as:

$$R_n = (1 - r_0)\tau K_{SUN} - L \uparrow + L \downarrow \quad (2)$$

Where:  $r_0$  is the surface albedo, calculated using the algorithm defined by Liang [3] that combined the reflectance values,  $r_i$ , corrected as a function of the solar tilt of the spectral bands 1 (blue), 3 (red), 4 (Near IR), 5 (Shortwave IR 1), 7 (Shortwave IR 2):

$$r_0 = 0.356r_1 + 0.130r_3 + 0.373r_4 + 0.085r_5 + 0.072r_7 - 0.0018 \quad (3)$$

$\tau$  is the visible transmittance in the earth's atmosphere;  $K_{SUN}$  is the extra-atmospheric solar radiation;  $L \downarrow$  and  $L \uparrow$  are the incoming and outgoing long wave radiations.

The IR radiation components are defined using the following mathematical model:

- $L \downarrow$  is calculated according to Konzelmann model [4, 5] as a function of the vapour pressure ( $e_a$ ), and temperature ( $T_a$ ) of the air

and the cloudiness ( $n$ ) of the image considered:

$$L \downarrow = \left[ \left( 0.23 + 0.483 \left( \frac{e_a}{T_a} \right)^{\frac{1}{8}} \right) \times (1 - n^3) + 0.963n^3 \right] \sigma T^4 \quad (4)$$

- $L \uparrow$  is evaluated using the approach suggested by Barsi [6, 7]. Using this methodology, at first the outgoing radiance is defined at the sensor height ( $L_{TOA,i}$ ), correcting radiation raw-data ( $L_\lambda$ ) in function of the atmospheric component (optical transmission  $\tau$ , emissivity  $\varepsilon$ , outgoing infrared radiation  $L_\mu$ , incoming infrared radiation  $L_d$ ):

$$L_{TOA,i} = \frac{L_\lambda - L_\mu - \tau(1 - \varepsilon)L_d}{\tau\varepsilon} \quad (5)$$

Where:  $L_\mu$ ,  $L_d$  and  $\tau$  are defined using the Atmospheric Correction Parameter Calculator [8] as a function of the latitude, longitude scan time of the infrared image and of available field data. Then,  $L_{TOA,i}$  is converted into surface temperature,  $T_i$ :

$$T_i = \frac{K_{2,i}}{\ln \left( \frac{K_{1,i}}{L_{TOA,i}} + 1 \right)} \quad (6)$$

In the last step the outgoing radiance  $L \uparrow$  is calculated from  $T_i$  with the Stefan-Boltzmann equation:

$$L \uparrow = \sigma T_i^4 \quad (7)$$

$G_0$  is obtained as a ratio of  $R_n$ . The algorithm of calculation is the following:

$$G_0 = \Gamma R_n \quad (8)$$

Where  $\Gamma$  is the soil heat flux to net radiation ratio, calculated in relation to  $T_i$ ,  $r_0$  and NDVI (Normalized Difference Vegetation Index) [9]. Finally,  $H$  and  $\lambda E$  are calculated as follows:

$$H = (1 - \Lambda)(R_n - G_0) \quad (9)$$

$$\lambda E = \Lambda(R_n - G_0) \quad (10)$$

Where  $\Lambda$  is the evaporative fraction derived from the correlation  $r_0$ - $T_i$  and based on the physical principle described below (see Figure 1).

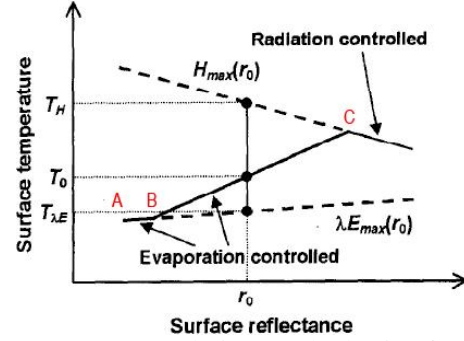


Figure 1.  $r_0/T$  correlation on the basis of S-SEBI approach

In constant atmospheric conditions, the energy fluxes are a function of the relative surface temperature so an albedo/temperature relation can be considered equivalent to an albedo/heat flux. The B and C points respectively identify the highest point of latent energy (wet surface,  $\Lambda=100\%$ ) and the highest point of sensible energy (dry surface,  $\Lambda=0\%$ ): in the middle the surface heating is due to the water evaporation. Scatterplot of  $T_i$  image on  $r_0$  image allows to defines B and C points and so the  $H_{max}(r_0)$  and  $\lambda E_{max}(r_0)$  lines.

## Experimentation data set

The experimentation was carried out using summer images of Milan territory recorded by LANDSAT 8 satellite on 01/08/2013 at 10.12 AM, path 194, row 28. The images presented both wet and dry zones and a small (5.34) percentage of cloud cover: images were suitable for the experimentation.

The following field data provided by the ARPA Lombardia weather stations [10] have been used: air temperature, relative humidity and solar radiation.



## Results

First, the  $T_i$ ,  $r_0$  and NDVI of Milan territory have been analysed.  $T_i$  varies from 30 to 59 °C, with a homogeneous distribution from the centre to the boundary of urbanized areas. In this map urban green parks emerge clearly as cold zones.

Surface albedo range is  $0.02 \div 0.4$  for most of the territory. Water bodies have a near zero albedo value and, despite their low  $T_i$  value, green and agricultural areas have albedo values near to build areas.

The NDVI range is  $-0.47 \div 0.86$ , with a mean value of 0.36. The values distribution is quite homogeneous from the city core to the suburbs. Green parks and agricultural area are more visible than in the albedo mapping despite the central area of Milan is not clearly highlighted, because of the tree lines along the road network (this cause also an increasing of mean NDVI value).

Secondly,  $r_0$ - $T_i$  correlation has been studied. Scatterplot of the  $T_i$  image on the  $r_0$  image (Figure 2) is coherent with the S-SEBI theory.

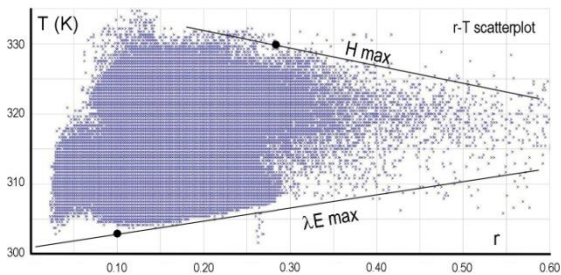


Figure 2.  $r_0 - T_i$  scatterplot of Milan images

In particular, until 0.04 albedo value,  $T_i$  does not increase proportionally. In the albedo values range between 0.10 and 0.28  $T_i$  increases linearly (evapotranspiration phase) and above the 0.28 albedo value warm pixels tend to become colder and cold pixels tend to become warmer.

On the basis of previous data, S-SEBI energy balance parameters have been determined:  $R_n$ ,  $G_0$ ,  $\lambda E$  and  $H$  (Figure 3).

The analysis underscores that higher values of  $R_n$  are recorded on the city core (fully built) and water areas. Contrariwise, green parks have low

values even if they don't emerge clearly from the urbanized areas.

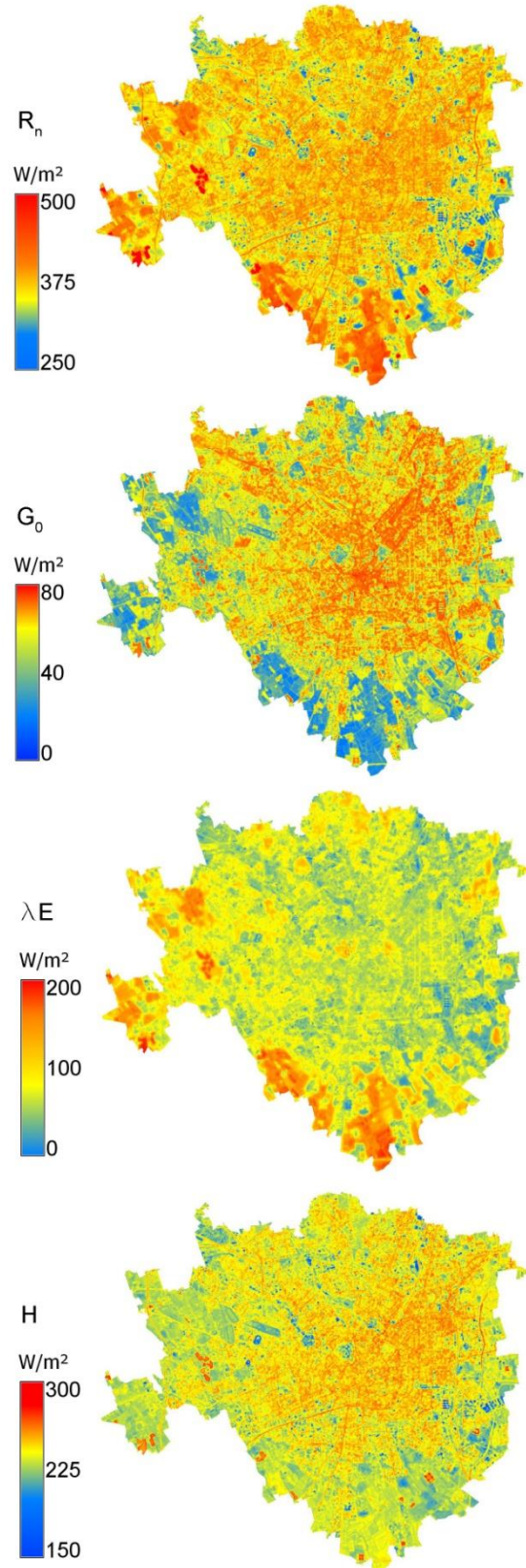


Figure 3. Mapping of S-SEBI energy balance parameters of Milan area

The  $G_0$  varies from 0 W/m<sup>2</sup> to 79 W/m<sup>2</sup>, a range of values much smaller than  $R_n$  (200÷500 W/m<sup>2</sup>). The mean value is 55 W/m<sup>2</sup>.  $G_0$  mapping highlights the land cover pattern: the centre of the city and roads has high values, while agricultural, green areas and tree-lined streets have the lowest values (especially in the southern and north-western territory of the city).  $\lambda E$  varies from 0 W/m<sup>2</sup> to 200 W/m<sup>2</sup>. The analysis shows that latent energy is low in general (mean value 74 W/m<sup>2</sup>). While the built-up part of Milan has low  $\lambda E$  values and, as a consequence, “dry” surfaces, non-built and green areas have higher energy values. However the overall distribution is more uniform than  $G_0$  with the core and the east side of Milan drier than the west side.

Lastly  $H$  varies from 100 to 284 W/m<sup>2</sup>. The values distribution is opposite with respect to latent energy  $\lambda E$ : non-built areas have no sensible energy, built areas show different colours related to the different materials/uses of the surfaces to be showed (building-red, paved-orange, asphalt-yellow). For this reason the values distribution is similar to  $G_0$ , but more uniform.

## Conclusions

Upon completion of the tests, it can be noticed that S-SEBI method with LANDSAT images is suitable monitoring and mapping of energetic and environmental aspects. All these parameters define the low cost useful base of data, regularly updated (monthly), for the analysis of the climatic effects due to urbanization processes like the creation of the UHI. In this way public administrations could use this data for important urban management actions as: analyse the urban climate trend over the time, localize the prior intervention boundaries, evaluate the impact of the adopted urban transformation strategies, define policies and prescription for future interventions (i.e. use low UHI effect materials for pavement and roofing, threshold for built ratio values, etc).

In particular, according to the experimentation, among the parameters analysed,  $T_i$ , NDVI and  $G_0$  seem to be the more useful indicators for

actuate the actions showed above.  $T_i$  allows the identification of the most critical zone by an UHI point of view. NDVI allows, by a comparison over the time, to assess the health level of green elements and optimize the maintenance interventions. Lastly  $G_0$  allows, always by a comparison over the time, to control the land cover change.

In conclusion this experimentation has demonstrated the feasibility of the use of all the kinds of IR signal (NIR, SWIR and Thermal IR) in urban monitoring as a useful tool for the management of the development of the territory.

## References

1. Roy D. P. et. al.. Landsat-8: science and product vision for terrestrial global change research. *Remote Sensing of Environment*, vol. 145, pp 154-172, 2014.
2. Roerink G. J., Su Z., Menenti M.. S-SEBI: A simple remote sensing algorithm to estimate the surface energy balance. *Physical Chemistry of the Earth, part B*, vol. 25, no. 2, pp. 147-157, 2000.
3. Liang S., Narrowband to broadband conversions of land surface albedo algorithms. *Remote Sensing of Environment*, no. 76, pp. 213- 238, 2001.
4. Konzelmann T., Roderik S.W. van de Wal, Greuell W., Bintanja R., Henneken E.A.C., Abe-Ouchi A.. Parameterization of global and longwave incoming radiation for the Greenland Ice Sheet. *Global and Planetary Change*, no. 9 pp. 143-164, 1994.
5. Flerchinger G. N., Xaio W., Marks D., Sauer T. J., Yu Q.. Comparison of algorithms for incoming atmospheric long-wave radiation. *Water Resources Research*, vol. 45, issue 3, 2009.
6. Barsi, J. A., Schott, J. R., Palluconi, F. D., & Hook, S. J.. Validation of a web-based atmospheric correction tool for single thermal band instruments. *Proceedings, SPIE*, vol. 5882. Paper 58820E. Bellingham, WA. 7 pp, 2005.
7. Yuan F., Bauer M. E.. Comparison of impervious surface area and normalized difference vegetation index as indicators of surface urban heat island effects in Landsat imagery. *Remote Sensing of Environment*, no. 106 pp. 375–386, 2007.
8. <http://atmcorr.gsfc.nasa.gov/>
9. Baastiansen W. G. M. SEBAL-based sensible and latent heat fluxes in the irrigated Gediz Basin, Turkey. *Journal of Hydrology*, vol 339, issue 1-2, pp. 87-100, 2000.
10. <http://www2.arpalombardia.it/siti/arpalombardia/meteo/osservazioniedati/datitemporeale/rilevazioni-in-tempo-reale/Pagine/Rilevazioni-in-tempo-reale.aspx>

# AUTOMATIC DETECTION OF WILDFIRE ACTIVE FRONTS FROM AERIAL THERMAL INFRARED IMAGES

M. M. Valero<sup>1</sup>, O. Rios<sup>1</sup>, E. Pastor<sup>1</sup>, E. Planas<sup>1</sup>

<sup>1</sup> Department of Chemical Engineering, Centre for Technological Risk Studies, Universitat Politècnica de Catalunya – BarcelonaTech, Av. Diagonal, 647, E-08028 Barcelona, Spain.  
*mario.miguel.valero@upc.edu*

Infrared (IR) imagery presents a great applicability in the field of wildland fires. However, most of the research conducted thus far has either focused on pre- and post- fire applications or relied on sophisticated technology. Despite the benefits it would potentially bring to operational fire management teams, real time active fire monitoring has not been achieved yet. The present article proposes a preliminary algorithm to detect and locate the fuel burning interface from thermal IR images. Since it is based on gradient instead of intensity thresholds, those images could ideally be captured with a simple low-cost camera without thermogrammetry capacities, i.e. no absolute temperature values are needed. First results are encouraging and suggest a further developed system could be deployed under operational conditions.

## Introduction

Infrared imaging applications in the field of wildland fires have been widely explored in the last years. However, the vast majority of this research has been focused on pre- and post-fire tools, namely fire risk mapping, incipient fire detection and remote measurement of burned areas (see [1]–[3] for instance). Furthermore, most of these systems have been developed for space born imagery, whose coarse spatial and temporal resolution prevents them from meeting the needs of operational wildfire monitoring [4], [5].

All in all, a lack of research has been noticed into the spatio-temporal dynamics of individual fire events [6]. Albeit some advancements can be found in [7]–[10], no autonomous system seems to have been developed so far that is capable of automatically computing the active fire front position out of thermal infrared (TIR) images. Existing solutions rely on either special working conditions (laboratory set-up [8], close views of the fire from different viewpoints [9]) or

additional support systems (visual cameras [9]). Moreover, most existing image processing algorithms apply intensity thresholding methods that can neither distinguish between flames and fire base nor detect which part of the fire contour is actually the most active. In [10] the active fire area and the active fire line are successfully extracted from multispectral images, which take advantage of the different emission profiles of active fire zones, healthy vegetation and burned areas along different spectral ranges. However, multispectral cameras are complex and expensive, which prevents them from being widely implemented at operational level for the time being. Conversely, low-cost handheld thermal imaging cameras have proved to be useful for the mapping of active fires even when viewing far off-nadir [11].

In this context, we present an algorithm that allows detecting the position of the fuel burning interface in an automatic, cost-efficient, near real-time manner. Input images may be captured by any standard low-cost TIR camera and corrections that account for bodies' emissivity or atmospheric transmissivity are not required.

Such a tool presents a great potential utility for wildfire management tasks. Current Geographic Information Systems (GIS) are powerful enough to integrate this sort of data in a decision support system suitable for operational use, where real-time accurate information is crucial.

### **Problem statement**

The problem stated here consists in automatically locating the fuel burning interface of an active wildland fire out of aerial TIR images which do not need to provide apparent or brightness temperatures. Raw signal intensities must ideally be valid inputs.

Since state of the art technology has proved to be able to ortho-normalise and geo-reference aerial images automatically and accurately [12], [13], inputs to the system are considered to be already geo-corrected frames so that the algorithm must only apply image processing techniques to obtain the boundaries of the active fire area. Outputs must then be lines defined as a series of ordered points located at the fuel burning interface.

To assess the accuracy of provided outputs, they are compared to isochrones manually defined by a trained user, understanding by isochrones the lines defining the outer position of the fire front at every time step.

### **Approach and techniques**

The main aim of the system is to locate the fuel burning interface in TIR images. This goal is achieved following two steps. Firstly, the algorithm must make use of image processing tools to successfully detect which pixels belong to the unburned-burning fuel interface. Once those pixels are selected, their coordinates must be read and the line they compose must be expressed as a sequence of ordered points.

This approach has been implemented with help of the Matlab<sup>®</sup> Image Processing Toolbox<sup>™</sup> (IPT). 3<sup>rd</sup> party functions that have been

employed are explicitly referenced in this document.

### *Detection of fire front pixels*

Active fire areas appear in IR images as most intense regions. However, the divergence in intensity is usually slight between fuel burning areas and other hot zones such as flames. This makes global thresholding methods not robust enough for this purpose. The region that is to be detected corresponds to the interface between unburned (cold) fuel and the most intensively burning (hottest) zone. For this reason, it seems a better approach to compute and threshold intensity gradients, which is the basis of a series of well-known edge detection algorithms [14].

We assessed the suitability of such techniques for this particular purpose. Both simple gradient masks and more complex edge detection algorithms were applied to a set of IR images. The studied gradient masks have been Sobel's and Prewitt's [14]–[16], whereas the Laplacian of a Gaussian (LoG) edge detector [17] and the Canny edge detector [18] have been chosen among more sophisticated algorithms.

### *Expression of the fire front as an ordered sequence of points*

Assuming input images are already ortho-normalised and geo-referenced, the task of computing the geographic coordinates of pixels is rather straight-forward. However, ordering these points requires further attention. A set of randomly distributed points must be ordered in either clockwise or counter clockwise direction. To achieve this, the line endpoints have to be previously located. Although edge detection algorithms try to maximise the connectivity of resulting edges, these are most times composed of more than one connected line. Thus, identifying the actual endpoints of the burning interface in a general case and computing them in an automatic manner may be difficult to implement.

The approach followed here relies on the assumption that the actual endpoints will generally lie the farthest from the centroid of the points set. Once one of these endpoints has been located, the curve can be read from a binary image in the right direction.

## Results and discussion

The proposed algorithms have been applied to a sequence of images captured during various field experiments conducted in Ngarkat Conservation Park, South Australia, on 3-5 March 2008 [19]. These images had previously been geo-referenced using a direct linear transformation algorithm [8]. Some illustrative results are shown in Figure

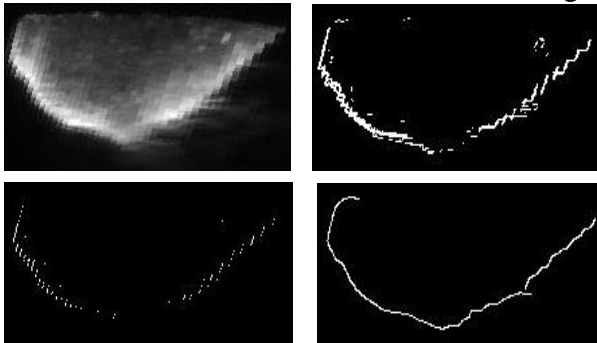


Fig. 16.

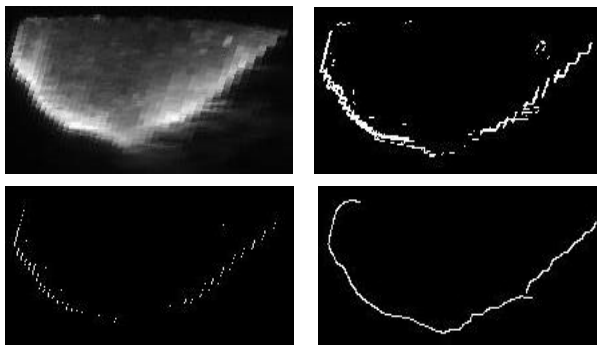


Fig. 16. Results of applying different edge detection algorithms to the same image. Up-left: original image; up-right: Sobel mask; down-left: Laplacian of a Gaussian; down-right: Canny.

The application of simple gradient masks like Sobel's and Prewitt's proved to be unsatisfactory, as did the Laplacian of a

Gaussian (LoG) detector. They were not able to detect the whole burning interface (omission errors) and they included in the output points that were obviously not part of the target boundary (commission errors). On the contrary, the Canny method returned satisfactory results. Not only did it successfully recognise the points comprising the fuel burning interface but it also omitted the flames in most cases, adjusting the output line to the fire base. Moreover, output lines are highly connected (few gaps appear).

For this reason, the Canny method was selected for the detection of the fuel burning interface. This method firstly smooths the image with a Gaussian filter and then computes the gradient magnitude, which is next double-thresholded. Final edge ridges are composed of the points above the high threshold plus those above the low threshold that are connected to the former.

In order to quantify its error, the automatically computed isochrones were compared with the isochrones manually defined by a trained user over the same set of IR images, which is considered to be the available information most similar to the ground truth (Fig. 17). This error is measured as the minimum distance from each point of each automatic isochrone to the corresponding manual isochrone. For this computation, 3<sup>rd</sup> party functions<sup>2</sup> were used.

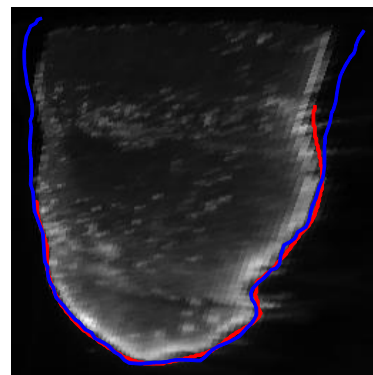


Fig. 17. Fuel burning interface defined automatically (through Canny method, red) and manually (blue) over the original image.

<sup>2</sup> <http://www.mathworks.com/matlabcentral/fileexchange/34869-distance2curve/content/distance2curve.m>

<http://www.mathworks.com/matlabcentral/fileexchange/34871-arclength/content/arclength.m>



Errors (minimum distances) averaged over each isochrone and expressed as a percentage of its total length are shown in Figure Fig. 18. For the isochrone displayed in Figure Fig. 17, which is 425 m long, the mean and maximum errors resulted 2 m and 13 m, respectively. Overall maximum detected errors stay below 10%.

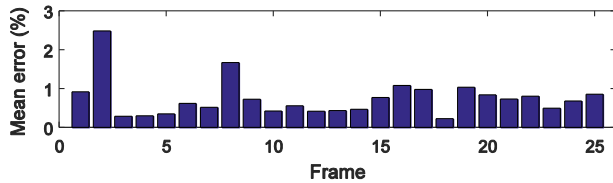


Fig. 18. Mean difference between automatically and manually computed fire fronts, as a percentage of the front length.

The algorithm proposed for extracting and ordering the points comprising every isochrone worked properly.

## Conclusion

Of the four edge detection techniques assessed, the Canny method clearly outperformed the other three when locating the fuel burning interface of an active wildfire. For the set of images that has been analysed, this interface have been successfully detected and located next to the fire base, avoiding flames in most cases. When compared to manually defined fronts, average errors fall within 2.5% of the total front length, and maximum detected errors stay below 10%. A subsequent algorithm has been developed to compute front points' coordinates and arrange these points in either clockwise or counter clockwise direction for further processing, e.g. rate of spread calculations.

Preliminary results are promising, albeit further work is needed. In order to work successfully, the Canny detector needs three parameters to be optimised, namely the standard deviation of the Gaussian filter and two gradient thresholds. So far we have tuned them manually, but they should be adjusted automatically. Also, application to a larger amount of different images captured by different cameras for

different fire behaviour regimes is needed to ensure robustness and interoperability.

## Acknowledgements

The authors thank the Spanish Ministry of Economy and Competitiveness (project CTM2014-57448-R), the Spanish Ministry of Education, Culture and Sport (FPU Programme) and the Autonomous Government of Catalonia (project no. 2014-SGR-413).

## References

- [1] L. B. Lentile, Z. A. Holden, A. M. S. Smith, M. J. Falkowski, A. T. Hudak, P. Morgan, S. A. Lewis, P. E. Gessler, and N. C. Benson, "Remote sensing techniques to assess active fire characteristics and post-fire effects," *Int. J. Wildl. Fire*, vol. 15, no. 3, p. 319, 2006.
- [2] L. Giglio, J. Descloitres, C. O. Justice, and Y. J. Kaufman, "An Enhanced Contextual Fire Detection Algorithm for MODIS," *Remote Sens. Environ.*, vol. 87, no. 2–3, pp. 273–282, Oct. 2003.
- [3] Z. A. Holden, A. M. S. Smith, P. Morgan, M. G. Rollins, and P. E. Gessler, "Evaluation of novel thermally enhanced spectral indices for mapping fire perimeters and comparisons with fire atlas data," *Int. J. Remote Sens.*, vol. 26, no. 21, pp. 4801–4808, Nov. 2005.
- [4] L. Boschetti, D. P. Roy, C. O. Justice, and L. Giglio, "Global assessment of the temporal reporting accuracy and precision of the MODIS burned area product," *Int. J. Wildl. Fire*, vol. 19, no. 6, p. 705, 2010.
- [5] S. Veraverbeke, F. Sedano, S. J. Hook, J. T. Randerson, Y. Jin, and B. M. Rogers, "Mapping the daily progression of large wildland fires using MODIS active fire data," *Int. J. Wildl. Fire*, vol. 23, no. 5, p. 655, Mar. 2014.
- [6] T. V. Loboda and I. A. Csiszar, "Reconstruction of fire spread within wildland fire events in Northern Eurasia from the MODIS active fire product," *Glob. Planet. Change*, vol. 56, no. 3–4, pp. 258–273, Apr. 2007.
- [7] J. R. Martinez-de Dios, B. C. Arrue, A. Ollero, L. Merino, and F. Gómez-Rodríguez, "Computer vision techniques for forest fire perception," *Image Vis. Comput.*, vol. 26, no. 4, pp. 550–562, Apr. 2008.
- [8] E. Pastor, A. Àgueda, J. Andrade-Cetto, M. Muñoz, Y. Pérez, and E. Planas, "Computing the rate of spread of linear flame fronts by thermal image processing," *Fire Saf. J.*, vol. 41, no. 8, pp. 569–579, Nov. 2006.



- [9] J. R. Martínez-de Dios, L. Merino, F. Caballero, and A. Ollero, "Automatic forest-fire measuring using ground stations and Unmanned Aerial Systems.," *Sensors (Basel)*, vol. 11, no. 6, pp. 6328–53, Jan. 2011.
- [10] A. Ononye, A. Vodacek, and E. Saber, "Automated extraction of fire line parameters from multispectral infrared images," *Remote Sens. Environ.*, 2007.
- [11] R. Paugam, M. J. Wooster, and G. Roberts, "Use of Handheld Thermal Imager Data for Airborne Mapping of Fire Radiative Power and Energy and Flame Front Rate of Spread," *IEEE Trans. Geosci. Remote Sens.*, vol. 51, no. 6, pp. 3385–3399, Jun. 2013.
- [12] H. Xiang and L. Tian, "Method for automatic georeferencing aerial remote sensing (RS) images from an unmanned aerial vehicle (UAV) platform," *Biosyst. Eng.*, vol. 108, no. 2, pp. 104–113, Feb. 2011.
- [13] E. M. Hemerly, "Automatic georeferencing of images acquired by UAV's," *Int. J. Autom. Comput.*, vol. 11, no. 4, pp. 347–352, Aug. 2014.
- [14] R. C. Gonzalez and R. E. Woods, *Digital Image Processing, 3rd ed.* Pearson Prentice Hall, 2008.
- [15] I. E. Sobel, "Camera Models and Machine Perception," Stanford University, 1970.
- [16] J. Prewitt, "Object enhancement and extraction," *Picture processing and Psychopictorics*, vol. 10, no. 1, pp. 15–19, 1970.
- [17] D. Marr and E. Hildreth, "Theory of Edge Detection," *Proc. R. Soc. B Biol. Sci.*, vol. 207, no. 1167, pp. 187–217, Feb. 1980.
- [18] J. Canny, "A computational approach to edge detection.," *IEEE Trans. Pattern Anal. Mach. Intell.*, vol. 8, no. 6, pp. 679–698, 1986.
- [19] Y. Pérez, E. Pastor, E. Planas, M. Plucinski, and J. Gould, "Computing forest fires aerial suppression effectiveness by IR monitoring," *Fire Saf. J.*, vol. 46, no. 1–2, pp. 2–8, Jan. 2011.

# ADVANCES IN AUTOMATED PROCESSING OF THERMAL INFRARED IMAGES FROM OSSERVATORIO VESUVIANO TIR PERMANENT SURVEILLANCE NETWORK AT CAMPI FLEGREI (POZZUOLI, ITALY)

F. Sansivero<sup>1</sup>, G. Vilardo<sup>2</sup>

<sup>1</sup> INGV Osservatorio Vesuviano, Napoli – ITALY [fabio.sansivero@ingv.it](mailto:fabio.sansivero@ingv.it)

<sup>2</sup> INGV Osservatorio Vesuviano, Napoli – ITALY [giuseppe.vilardo@ingv.it](mailto:giuseppe.vilardo@ingv.it)

The INGV Osservatorio Vesuviano permanent thermal infrared surveillance network investigates fumarole fields and diffuse degassing zones in the volcanic area of Campi Flegrei since year 2004. The automated processing system ASIRA produces daily a temperature trend representative of the surface thermal field of the investigated areas. Recently a new automated system (ASIRA 2.0) is in development to extract from IR frames more valuable evidences to characterize the surface thermal variations of studied areas. In particular the implemented co-registration of IR frames provides the opportunity to investigate the thermal evolution of the areas not only in terms of time progression but also in terms of spatial variations. Finally the plotting interface provides almost all the requested plot outputs to represent the processed data also in surveillance contexts.

## Introduction

Ground-based thermal infrared image observations are used from INGV Osservatorio Vesuviano until the year 2004 as a surveillance tool in the Campi Flegrei volcanic area (Pozzuoli, Napoli – Italy). The investigations have been focused on fumarole fields and diffuse degassing zones by using permanent stations acquiring IR frames at night-time. The IR surveillance network was developed keeping in mind two main goals: a) to produce a regularly collected dataset which can be processed to characterize the surface thermal features of the investigated volcanic areas, b) to provide a daily updated thermal trend aimed at volcanic surveillance.

An automated processing system (A.S.I.R.A. – Automated System of IR Analysis) regularly processes IR frames acquired every day. The results are displayed in the surveillance room of Osservatorio Vesuviano as they represent a useful data for volcano surveillance and hazard assessment. Recently a more advanced automated processing system (ASIRA 2.0) is in development to extract from IR frames more

valuable evidences to characterize the surface thermal variations both in time and in space. In this paper an overview of the improvements and the new methodologies which are implemented in ASIRA 2.0 will be presented.

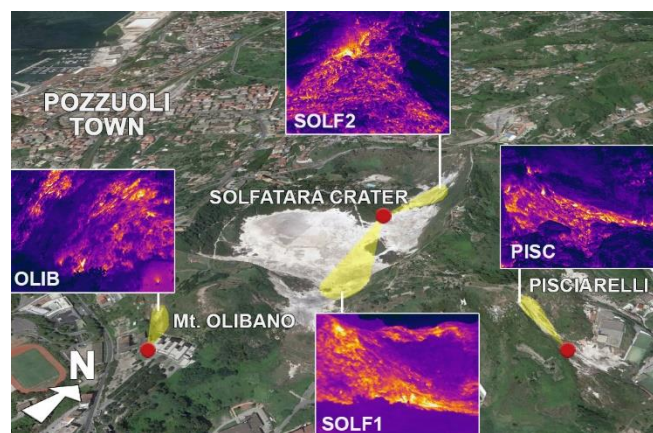


Fig. 1. The position of the permanent stations (red dots) and the investigated regions (yellow areas) of the thermal infrared network at Campi Flegrei.

## The Campi Flegrei permanent infrared network and the ASIRA automated processing system

Actually the thermal infrared network at Campi Flegrei is made of four permanent stations in the area of Solfatara at NE of Pozzuoli town (figure 1). Infrared sensors are FLIR SC645 uncooled microbolometer 640x480 pixel cameras, except for station SOLF1 (FLIR SC325) whose resolution is 320x240. All the stations acquire three IR frames every night which are corrected with air temperature and atmospheric pressure values measured before the acquisition. The IR frames are transferred through Wi-Fi or UMTS connection to the acquisition server at Osservatorio Vesuviano surveillance centre where are processed by the automated system ASIRA (figure 2).

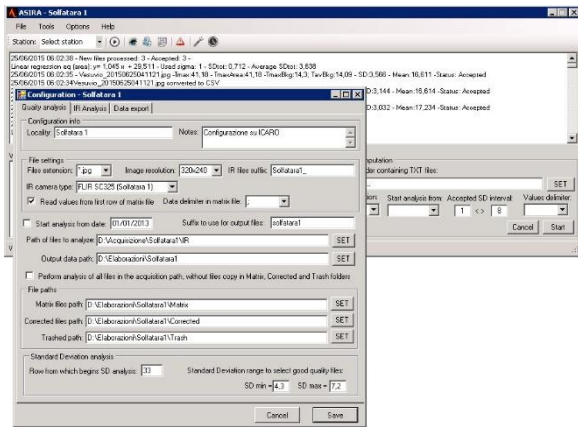


Fig. 2. A screenshot of A.S.I.R.A. (Automated System of IR Analysis)

ASIRA is a fully automated, in-house developed software which executes daily the following tasks: i) it removes low quality IR scenes from the dataset of analysis; ii) it estimates maximum temperature values in a significant area of the IR scenes; iii) it removes great part of the seasonal effects affecting the temperature values; iv) it exports the results into a database in order to be plotted and displayed at the Osservatorio Vesuviano Surveillance Room.

ASIRA produces for every IR station a time-series of residuals of maximum temperatures ( $dT(i)$ ) resulted from the removal of seasonal component by using a simple procedure of background subtraction (Sansivero et al., 2013, Vilardo et al., 2015):

$$dT(i) = T_{Max}(i) - T_{LR}(i)$$

where  $T_{Max}(i)$  is the maximum temperature of the IR image  $i$ , and  $T_{LR}(i)$  is the estimated best-fit linear regression of the background area maximum temperature *versus*  $T_{Max}(i)$ .

The system uses a very simple, but effective, theoretical approach and in some cases produced temperature trends which shown an impressive correspondence with the trends resulted from GPS and CO<sub>2</sub> data of the same area.

As the exclusive output of ASIRA are the variations of maximum temperatures residuals of investigated areas, the system does not make full use of the great potential of data from IR frames.

### The new ASIRA 2.0 automated processing system

In order to better use the potential of continuous long-term IR monitoring of high-heat flux zones, a new automated processing system (ASIRA 2.0) is in development. The main goal of this new system is a more precise removal of seasonal component from the temperature data, to produce also evidences of possible spatial changes of the ground-surface thermal features and to perform a flexible and complete data plotting. The analysis process performed by ASIRA 2.0 is based on the procedures described synthetically in the scheme of figure 3 (Vilardo et al., 2015).

Basically the analysis consists of a preliminary step which performs a quality filtering of RAW dataset based on removal of those frames that lay outside the interval of  $2 \times$  Standard Deviation of IR images. Then it follows the cross-correlation between all the frames and a reference one, in order to correct the possible loss of alignment between the sensor and target scene due to natural or technical causes. The cross-correlation is a crucial phase as it produces co-registered frames that have a precise pixel alignment and can be used for image analysis techniques requiring an accurate image placement. The co-registration is centered on a flow-based, non-rigid registration algorithm (SIFTflow - Liu Ce et al., 2011).

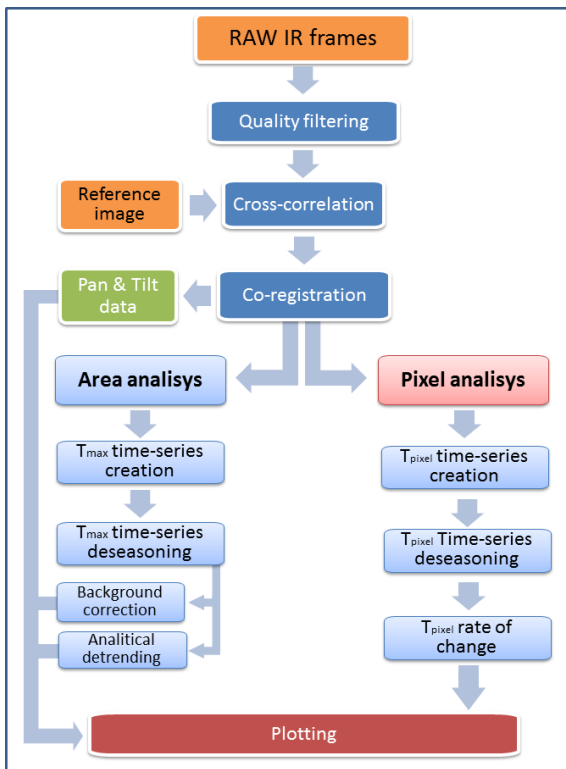


Fig. 3. Schematic diagram of procedures implemented in ASIRA 2.0.

The next step consists of the production of the time series of maximum ( $T_{max}$ ) and mean ( $T_{mean}$ ) raw temperatures for the full frame or an Area of Interest (AOI). As temperature values are strongly influenced by the seasonal variations, a seasonal correction is applied by using two different approaches: the background subtraction and the analytical removal of periodicity. The background subtraction is based on the same theoretical assumption used by ASIRA as reported before. The analytical removal of periodicity is based on a Matlab algorithm (Nowotarski et al., 2013; Weron, 2013) consisting basically of two steps: 1) signal smoothing and 2) removal of the sinusoidal long-term seasonal component using a polynomial fit function (LTFC\_SCOREF - Weron, 2013). An overview of the application of these methodologies is reported in figure 4 where a smoothed trend of temperature residuals (blue line) from Pisciarelli station is compared to GPS vertical ground displacement (black line) and  $CO_2$  (green line) trends from the same site.

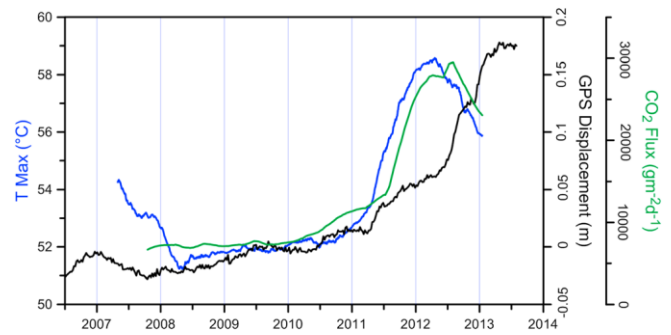


Fig. 4. Comparison between smoothed chronograms of the residuals of maximum temperatures (blue), the  $CO_2$  flux (green) and the GPS vertical ground displacement (black) at Pisciarelli (Chiodini et al., 2012; De Martino et al., 2014).

To understand the variations both in time and space of the surface temperatures field, the IR images are investigated in terms of the temperature variations of each pixel of the frame or AOI. From all the dataset a temperature time series for each pixel of the IR frame is extracted and then the seasonal component is removed by applying the analytical removal of periodicity. Then a subset of temperatures, related to a period showing a linear increase of temperature is extracted and finally the slope coefficients of the linear regression of each pixel temperature series are estimated. These slope values are used to create a map of the yearly rate of change of the  $T_{max}$  (figure 5 – Pisciarelli area) which shows the thermal behavior of every pixel in time.

The plotting features of ASIRA 2.0 are very useful both for interpretation of processed data and for the evaluation of the correct parameters to use as inputs for data processing and analysis.



Fig. 5. Map of the temperature rate of change ( $dT/yr$ ) of Pisciarelli investigated area, computed for a period of temperatures increase. The overlapping image masks the values whose  $R^2 < 0.3$  ( $R^2$  = coefficient of determination).

Main plotting features are:

- plots of single pixel time-series of both RAW



or analytically-detrended data, by selecting the pixel on the IR image or giving the coordinates;

- plots of maximum (Tmax), average (Tav) and minimum (Tmin) temperatures from all the time-series of full IR frame or of a user-defined area of interest (to set graphically);
- plot of the pixels shifts registered by the cross-correlation procedure;
- plot of the map of yearly temperatures rate of change;
- plot of Tmax and Tav from a user-selected background area;

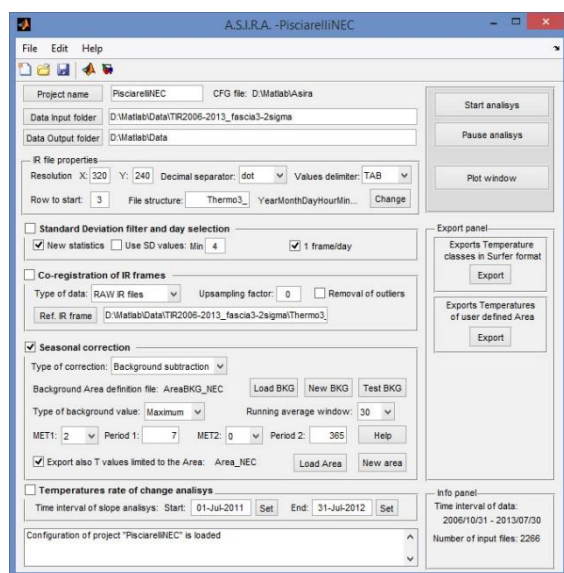


Fig. 7. ASIRA 2.0 graphical interface (Matlab 2011).

## Conclusion

For the first time a software application, developed in Matlab language, encloses several automated tools of IR image processing regarding the analysis of fumarole fields and diffuse degassing zones and eventually active volcanic areas. The automated process of analysis, starting from the RAW IR matrix files, carries to a finite product which can be used in volcanic research and surveillance, also in automated procedures.

The advances in automated processing of thermal infrared images implemented in ASIRA 2.0 are several. First of all the precise co-registration of IR frames provides the

opportunity to investigate the thermal evolution of the studied area not only in terms of time progression but also in terms of spatial variations. Furthermore, as additional output, the co-registration provides the shifts values of each IR scene in both the vertical (tilt) and horizontal (pan) directions related to a reference image. The plot of these values can give interesting information about ground slip of the site of observation due to natural events.

An interesting product of ASIRA 2.0 is the map of temperature changing rate, which provides very useful information about the migration of fumarole activity or about eruption dynamics, if observation are addressed to active volcanic vents.

Finally, the plotting interface provides almost all the requested plot outputs to represent the processed data also in surveillance contexts.

## References

1. Ce Liu, J. Yuen, A. Torralba. SIFT Flow: Dense Correspondence across Scenes and its Applications, IEEE Transactions on Pattern Analysis and Machine Intelligence, Vol. 33, No. 5, 2011.
2. Chiodini, G., S. Caliro, P. De Martino, R. Avino, and F. Gherardi, Early signals of new volcanic unrest at Campi Flegrei caldera? Insights from geochemical data and physical simulations, *Geology*, 40, 943–946, doi:10.1130/G33251.1, 2012.
3. De Martino, P., U. Tammara, and F. Obrizzo, GPS time series at Campi Flegrei caldera (2000–2013), *Ann. Geophys.*, 57(2), S0213, doi:10.4401/ag-643, 2014.
4. Sansivero, F., G. Scarpato, and G. Vilaro, The automated infrared thermal imaging system for the continuous long-term monitoring of the surface temperature of the Vesuvius crater, *Ann. Geophys.*, 56, S0454, doi:10.4401/ag-6460, 2013.
5. Vilaro, G., Sansivero F., Chiodini G., Long-term TIR imagery processing for spatiotemporal monitoring of surface thermal features in volcanic environment: A case study in the Campi Flegrei (Southern Italy). *J. Geophys. Res. Solid Earth*, 120, 812–826, doi:10.1002/2014JB011497, 2015.
6. Weron, R., DESEASONALIZE: MATLAB function to remove short and long term seasonal components (new implementation), HSC Software M013004, Hugo Steinhaus Center, Wroclaw Univ. of Technology, 2013.

# APPLICATIONS OF INFRARED SPECTROSCOPIC TECHNIQUES TO QUALITY EVALUATION IN AGRICULTURE AND FOOD PROCESS

A. Hashimoto<sup>1</sup>, K. Suehara<sup>2</sup>, T. Kameoka<sup>3</sup>

Graduate School of Bioresources, Mie University,  
1577 Kurimamachiya-cho, Tsu, Mie 514-8507, Japan,

<sup>1</sup> hasimoto@bio.mie-u.ac.jp

<sup>2</sup> suehara@bio.mie-u.ac.jp

<sup>3</sup> kameoka@mie-u.ac.jp

We focus our attention on the applications of infrared spectroscopy to the agriculture and food process sectors. This paper describe the infrared spectroscopic determination of the nitrate nitrogen content in fresh leaf for the plant vigor evaluation in the agricultural fields and infrared spectroscopic characteristics of the beverages for quality evaluation based on the fundamental subjects. As the results, infrared spectroscopy could be very effective from the foodstuff production to food process sections.

## Introduction

People are becoming more health-conscious, and therefore it is necessary to produce sustainable and high quality agricultural commodities. Food process industries are working towards securing and establishing increased food safety, food defense, and developing value-added food products and advanced/accurate post-harvest handling. To achieve a stable supply of high quality agricultural products, measurement of the nutritional state during cultivation and the optimum response to that state are very important. Therefore, quality management based on the scientific objectives during cultivation and food process are very important to produce consistently high quality products for marketing.

Plants absorb essential elements in the form of inorganic nutrients from their roots with water, and the balance of these essential elements in them plays a large role in their nutritional state. Therefore, in order to obtain the plant vigor information, understanding the kinetics of the chemical element balances

in plants at the agricultural fields is very important, and acquiring the correct information on the element balances enables control of the amount of fertilizer. We, therefore, decided to apply the X-ray fluorescent and infrared spectroscopic measurements to get the grasps chemical element balances and the plural modes of nitrogen, respectively [1, 2].

On the other hand, quality management through food supply chain is very important, and the evaluation and control of food qualities based on the objective sensing information are required in order to consistently manufacture high quality products. The quality sensing should be simple, non-destructive, simultaneous, rapid, qualitative and quantitative. In addition, the usefulness of the acquired data for software evaluations is also desired. Furthermore, through food supply chain, the qualities should be scientifically assessed using the same sensing technique. The optical spectroscopic methods could theoretically satisfy their requirements. Furthermore, the quality of foods is influenced by not only chemical components but also the interaction between the molecule and the environments.



We focus our attention on the applications of infrared spectroscopy to the agriculture and food process sectors. This paper then describes the infrared spectroscopic determination of the nitrate nitrogen content in fresh leaf for the plant vigor evaluation and infrared spectroscopic characteristics of the beverages for quality evaluation based on the fundamental subjects. These relate to the quality evaluation in the cultivation management and food process.

### Infrared Spectroscopic Measurement of Nitrate-state Nitrogen in Fresh Leaf

Valuable information on the plural modes of nitrogen contents in plant organs over the entire period of plant growth is very important. The quantitative monitoring should be carried out by a method that is a simple to use, non-destructive, simultaneous, and easy to get fast results. Incidentally, the developments of the portable spectrometers could provide substantial potential as quantitative tools in the field to analyze the plant vigor.

The amount of nitrate nitrogen in plants is one of the important nutritional state indexes, and we developed the quantitative method determining nitrate nitrogen using the spectrum of petiole juice in our previous study [3]. Measurement using juice, however, is troublesome in an actual cultivation field. A method of simply measuring the spectrum

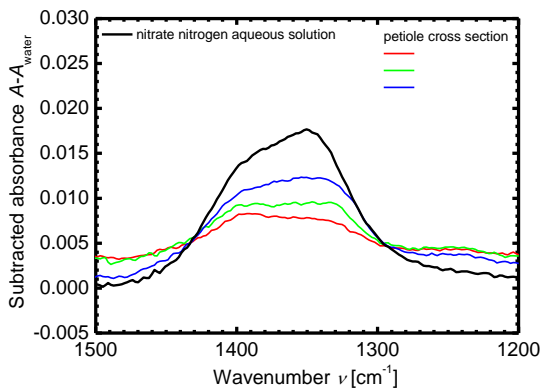


Fig. 1. Subtracted ATR spectra of nitrate nitrogen in aqueous solution and petiole cross section.

of a cut surface of a petiole [4] to acquire spectrum information equivalent to that of juice in a cultivation field is described here.

Figure 1 shows the absorbance spectra of the cut surface of the cross section of a petiole, a supply route of aqueous nitric acid and nutrients. The spectra were collected using a Fourier transform infrared (FTIR) spectrometer equipped with an attenuated total reflection (ATR) sampling accessory. The spectrum of the cross section of a petiole is quite similar to that of aqueous nitric acid in the wavenumber region from 1350 to 1400  $\text{cm}^{-1}$ . These measurement results show experimentally that infrared spectral measurement of a petiole is a simple and quick quantitative method for nitric acid. Moreover, their spectral features were also similar to those of the proteinic (casein) nitrogen in the aqueous solutions [4]. The aforementioned measuring method is considered effective for cultivation management from the viewpoint of plant physiology.

### New Developments on Quality Evaluation Based on IR Spectroscopic Analysis

#### Infrared spectroscopic characteristics of food components

Saccharides play an important role in foods, and water is a major constituent. The importance of the hydration of electrolytes, such as sodium and calcium, in foods is known as well as that of the saccharides. As shown in Figure 2, the varying patterns of the subtracted ATR spectra of glucose in the sodium chloride (NaCl) aqueous solutions were

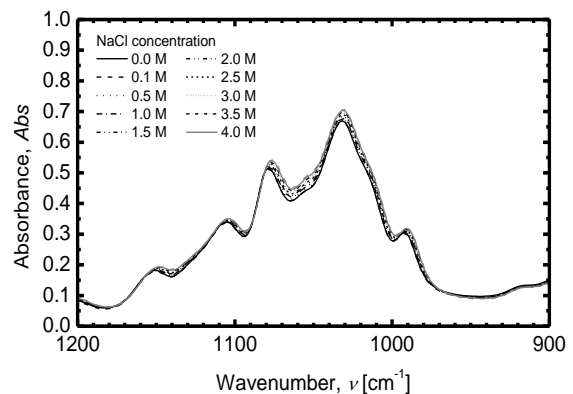


Fig. 2. Influence of NaCl concentration on absorbance spectra of 2.0 M glucose in aqueous solution with NaCl.

observed in the region from 1200 to 950  $\text{cm}^{-1}$  for each NaCl concentration [5]. It was found that the interaction between glucose and the NaCl aqueous solution depended on the concentration of NaCl, because the glucose concentration was fixed.

Additionally, the pH-dependency of the infrared absorption spectral information could be one of the most important factors for the food quality evaluation. The absorbance spectrum of the ionic dissociative material, such as organic and amino acids, in the aqueous solutions considerably changes with pH [6]. The pH-dependency of the absorbance spectrum for an ionic dissociative material in the aqueous solution could be explained by the equilibrium shift among the ionic dissociation components (ionic species). Henceforth, the spectrum of each ionic species was assumed to be not affected by the hydrogen ion concentration and to satisfy the spectral additivity.

### Coffee beverages

Here, we describe the infrared spectroscopic characteristic of brewed coffee as one of the most popular beverages. We developed an infrared spectroscopic evaluation method of brewed coffee, whose quality and taste highly depend on the chemical contents, the interactions between the components, the pH value and the temperature based on the above fundamental subjects [7].

The absorption peak shifts of the ATR spectra of brewed coffee were observed as the influences of the pH and temperatures (Figure 3). Therefore, by analyzing the spectra of the coffee components under the various pH and temperature conditions based on the ionic dissociation equilibrium theory, the spectral behavior of the brewed coffee model due to the pH and temperature changes could mainly result from those of the organic acids as the main components. Moreover, the infrared spectral information analysis could be acceptable to evaluate the profiles of the other

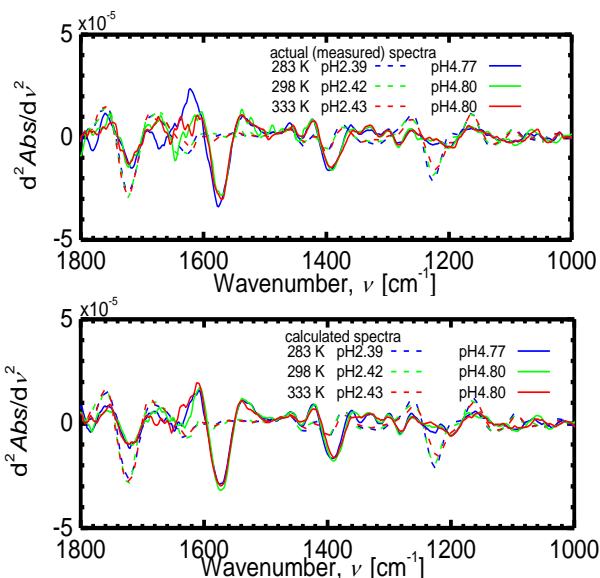


Fig. 3. pH and temperature dependencies of actual and calculated second derivative spectra of brewed coffee model..

processed foods [5] as well as that for wines [8].

The commercial canned coffee beverages containing milk and sugars were stored at 313, 333 and 353 K for several weeks. The ATR spectral feature changes during storage described the hydrolyzation of sucrose into glucose and fructose. Additionally, for the samples stored at 313 K for 4 weeks and at 333 K for 2 weeks, the intensities of the absorption peaks characterizing the sugars became weak, and the peak intensities around 2860 and 2930  $\text{cm}^{-1}$ , where the absorption bands relative to lipids, became stronger. Furthermore, by

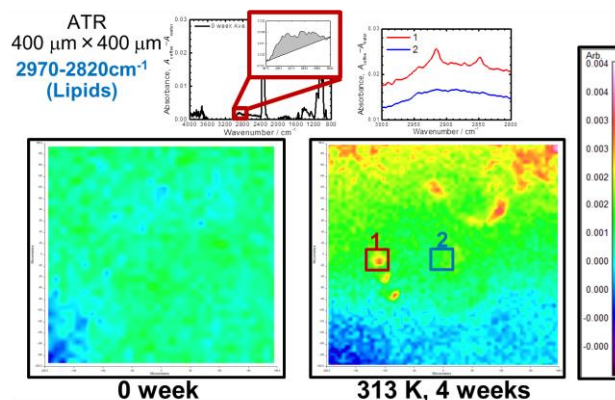


Fig. 4. Microscopic infrared images of coffee beverage before and after heating storage at 313 K.

determining the optimal measurement conditions to construct the quantitative FTIR micro-spectroscopic image, the distributions of the infrared spectral information relating to lipids were grasped. Figure 4 micro-spectroscopically represents the aggregation behavior of milk component during storage, and the images could visually indicate the quality changes of the coffee beverage.

As described above, the fundamental and canonical spectroscopic methods should be very important. Also, the combination of the macro-/micro-spectroscopic measurement could be powerful for the evaluation of the chemically and structurally complicated foods.

## Conclusion

As mentioned in this paper, infrared spectroscopy could be very effective from the foodstuff production to food process sections. For the complicated materials, we need to understand the spectral features not only for the peak analysis but also the influences of the geometric structures [9]. Additionally, the development of the flavor analysis based on the infrared spectroscopic information is desired for the quality evaluation of agricultural products and foods.

Recently, the visualization technology to decipher the complex information has been progressing. On the other hand, MEMS (microelectromechanical systems) Fourier transform infrared spectroscopy [10] is introduced as a new device that may become essential for sensing in a farm field, though they are not yet applied technologies in the field. For the further development of the infrared spectroscopic method for the quality evaluation in agriculture and food process sectors, it is important to adapt the new devices and visualization techniques for agricultural and food sciences based on the fundamental infrared spectroscopic theories.

## Acknowledgments

This work was partially supported by the Project "Integration research for agriculture and interdisciplinary fields," Ministry of Agriculture, Fisheries and Forests, Japan.

## References

1. T. Kameoka, A. Hashimoto. "A sensing approach to fruit-growing," in *Wireless Sensor Networks and Ecological Monitoring*, eds, S. C. Mukhopadhyay, J. A. Jiang, Springer-Verlag Berlin Heidelberg, pp. 217-246, 2013.
2. A. Hashimoto, T. Kameoka. Optical sensing toward quality evaluation of field crops, *Journal of the Society of Instrument and Control for Engineers*, 52, pp.702-707, 2013.
3. A. Hashimoto, N. Hayashi, K. Suehara, M. Kanou, T. Kameoka, T. Kumon, K. Hosoi, "Simple, rapid and non-destructive determination of nitrate nitrogen content using mid-infrared spectroscopic method," *Agricultural Information and IT*, pp.235-240, 2008.
4. A. Hashimoto, D. Kihara, K. Suehara, T. Kameoka, and T. Kumon. "Simple and rapid measurement of nitrate nitrogen content in plant using mid-infrared spectroscopic method," *Proc. of AFITA/WCCA 2012*, (20)-4, 2012.
5. A. Hashimoto, T. Kameoka. Applications of infrared spectroscopy to biochemical, food and agricultural process, *Applied Spectroscopy Review*, 43, pp. 389-415, 2008.
6. K. Nakanishi, A. Hashimoto, M. Kanou, T. Pan, T. Kameoka. Mid-infrared spectroscopic measurement of ionic dissociative materials in metabolic pathway, *Applied Spectroscopy*, 57, pp. 1510-1516, 2003.
7. A. Hashimoto, Y. Sugimoto, K. Suehara, T. Kameoka. Influences of pH and temperature on infrared spectroscopic features of brewed coffee, *Procedia Food Science*, 1, pp. 1132-1138, 2011.
8. A. Hashimoto, H. Mori, M. Kanou, T. Kameoka, H. Shimazu, K. Kobayashi. Mid-infrared spectroscopic characteristics of brewed coffee and simultaneous content determination of main components using an attenuated total reflection method, *Journal of Illumination Engineering Institute of Japan*, 93, pp. 501-509, 2009.
9. A. Hashimoto, T. Kameoka. Effect of infrared irradiation on drying characteristics of wet porous materials, *Drying Technology*, 17, pp. 1613-1626, 1999.
10. M. Esashi. "Revolution of sensors in micro electro mechanical systems (MEMS), *OYO BUTURI*, 80, pp.181-188, 2011.

# Thermographical monitoring of leak processes in embankments

B. Bukowska-Belniak<sup>1</sup>, A. Leśniak<sup>2</sup>, D. Kessler<sup>3</sup>

<sup>1,2</sup> AGH University of Science and Technology, al. Mickiewicza 30, 30-059 Krakow, Poland,  
<sup>1</sup>bukowska@agh.edu.pl, <sup>2</sup>lesniak@agh.edu.pl

<sup>3</sup> NeoSentio Ltd., ul. Konfederacka 23, 30-306 Krakow, Poland, dk@neosentio.pl

This paper presents the results of thermographical measurements of the experimental embankment during flooding experiments. The main goal of the measurements was to check applicability of thermography for detection and localization of leaks in soil embankment. The measurement was performed on experimental embankment, which size is in scale 1:5 comparing to Polish typical river embankments. The embankment was dry on the beginning of the experiment. Filtration of water through the embankment caused thermal changes, which were measured by thermal sensors inside the embankment. These thermal changes was also visible in infrared images. It should be noted a large impact of weather conditions on temperature measurement, in particular insolation and occurrence of clouds.

## Introduction

Thermography as a fast and remote method of thermal measurements has a wide spectrum of applications. It is often used for environmental monitoring [1,2], including observations from aircraft and drones. Infrared field measurements are difficult because of the influence of environmental conditions (season of year, time of day, weather, Sun position, rain, snow, clouds) and variability of thermal emissivity. The Earth's thermal observations are even more difficult due to the presence of vegetation and heterogeneous surface.

## Experimental embankment description

The experimental embankment was built as a part of ISMOP project [3]. It's size is in scale 1:5 comparing to Polish typical river embankments. It was constructed to investigate the effect of the method of sensors installation for the filtration process and structure stability by the NeoSentio company. The embankment consists of the following elements (cross-section in Fig.1): an

insulating layer, hydraulic trough of sheet steel, trapezoidal soil barrier, buttress filter, drainage system and piezometers system.

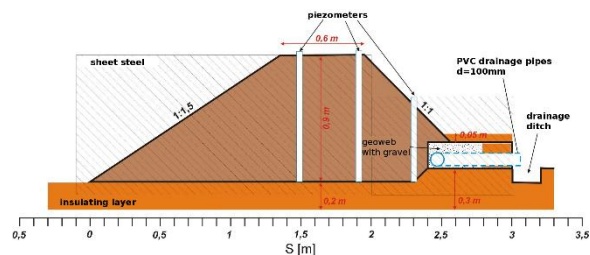


Fig. 1. Cross-section of experimental embankment.

The insulating layer is constructed of impermeable soil (filtration coefficient  $k < 1 \times 10^{-7}$  m/s). Trapezoidal soil barrier is composed of clastic native soil characterized by uneven particle size distribution indicator  $U > 6$ , where fraction  $< 0.063$  is maximum 2%. The soil was compacted in layers with a thickness of  $m = 0.1$  m, to obtain Standard Proctor Dry Density (SPDD) factor of 0.95. The buttress filter is made of a cell grid geoweb filled of soil with high permeability (filtration coefficient  $k > 1 \times 10^{-4}$  m/s). The drainage system is constructed in buttress filter area. It is divided into four sections - sectors A, B, C, D (Fig.2). The piezometers system includes 6 piezometers (B1, B2, B3, C1, C2, C3) with pressure and temperature sensors.



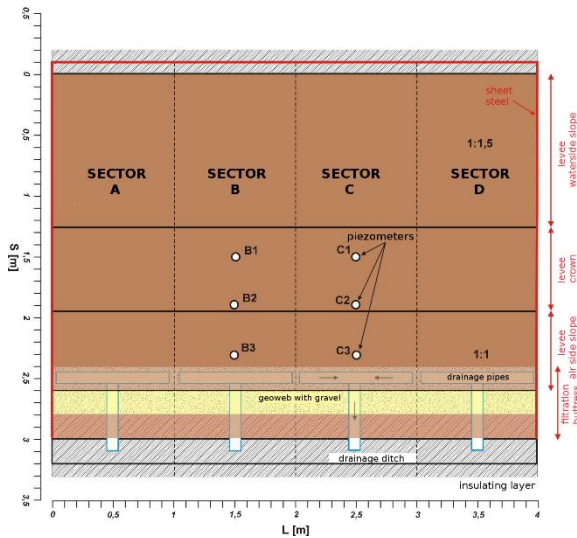


Fig. 2. Top view of experimental embankment.

Sensors: 1, 2, 3 are located in C sector's piezometers (1 in C1, 2 in C2, 3 in C3). Sensors: 4, 5, 6 are located in B sector's piezometers (4 in B1, 5 in B2, 6 in B3). Sensor 7 is located at the bottom of the tank - so it represents the level of water (pressure sensor) and temperature of water (temperature sensor).

### Experiment description

The measurement was made in mostly sunny day, air temperature was about 28-30°C, there was no rain. The embankment was located in the shade, under a tent. The soil was dry when the flooding process has begun. The flooding process started at 10:30, maximum level of water (0.8m) was at 12:30.

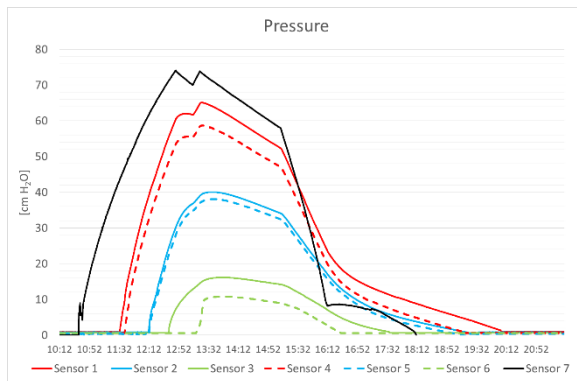


Fig. 3. Level of water in piezometers based on pressure sensors.

The results of measurements are presented in figures 3 and 4. Fig. 3 shows pressure changes in time. Black line corresponds to water level in a tank. Fig. 4 presents temperature changes.

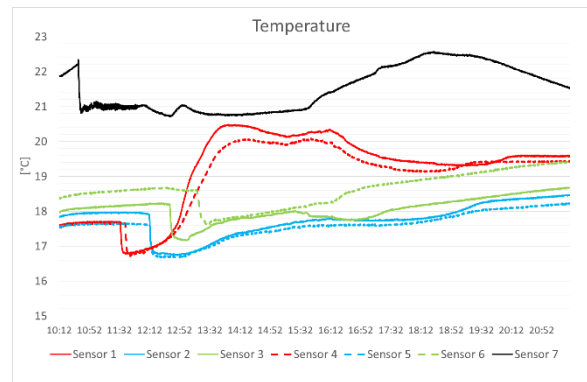


Fig. 4. Temperatures measured in piezometers.

There are visible differences between B and C sector in filtration over time. In B sector the changes are much slower in B3 and C3 piezometers level (sensors: 6, 3). There is also visible fast temperature rise in piezometers B1 and C1 (sensors: 4, 1).

### Thermographical observations

Infrared measurements was performed by FLIR T620 microbolometric camera. It's spectral resolution is equal to 620x480 pixels, thermal sensitivity NETD at 30°C is lower than 0.04°C.



Fig. 4. View of the experimental embankment in visible spectrum.

The view area of the camera covered the central part of the embankment, including B and C sectors. Image in visible spectrum of the experimental

embankment is presented in Fig.4. The protection grid against soil slide is placed on the surface of the slope.

Infrared images registered during flooding are presented in Fig. 5. Top image is registered at 13:16, middle at 14:16 and the bottom at 15:16. All images presents B and C sectors. The boundary between the sectors passes through the center of the images.

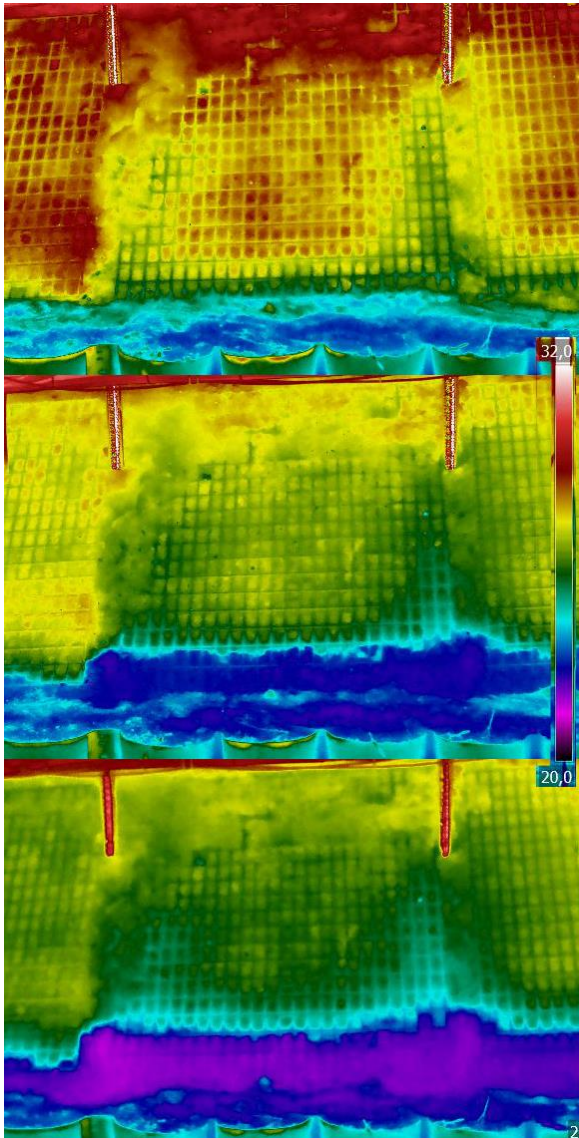


Fig. 5. Infrared images of B and C sectors of experimental embankment registered at: 13:16 (top), 14:16 (middle) and 15:16 (bottom).

In the first image there is no visible thermal changes caused by water flow – the surface of embankment is dry. Next two images presents growing water flow effect. In

saturated region the temperature is lower than in dry about 2-3°C. On the left side of the images, in sector B, the small water flow is noticeable. This indicates a hindered flow in this sector, which is also shown in piezometers readings (sensor 6).

## Conclusion

Thermography as a cheap, remote and fast method can be successfully used for environmental monitoring. Using this method allows to detect the leaks in such soil constructions as river embankments, what can help in critical leaks location.

As future work more similar experiments in different weather conditions will be performed. Also more sensors in the embankment will be installed - what can have influence for flow character inside the embankment and for the final results.

There will be more different measurements on experimental embankment in scale 1:1. Then will be checked the influence of grass, vegetation, heterogeneity in embankment's surface for thermal results.

All measurements will be validated with sensors results, weather conditions and numerical models.

*This work was financed by the National Centre of Research and Development (NCBiR), Poland, project PBS1/B9/18/2013 (no. 180535) [1].*

*This work was partly supported by the AGH University of Science and Technology, Faculty of Geology, Geophysics and Environmental Protection, as part of statutory project no. 11.11.140.613.*

## References

1. B. Bukowska-Belniak, A. Leśniak. Application of thermographic research in environmental protection. Polish Journal of Environmental Studies, Vol. 18, No. 3A, Olsztyn, pp. 38-43, 2009.
2. A. Wróbel: Zastosowania termowizji w badaniach środowiska. Pomiary termowizyjne w praktyce: praca zbiorowa pod red. H. Madury, Agenda Wydawnicza SIMP, Warszawa, 2004 (in Polish).
3. ISMOP – Computer System for Monitoring River Embankments (in Polish: Informatyczny System Monitorowania Obwałowań Przeciwpowodziowych), [www.ismop.edu.pl](http://www.ismop.edu.pl).



# A practical approach to In-situ hyperspectral imaging of wheat crop canopies

R. L. Whetton<sup>1</sup>, T. W. Waine<sup>2</sup>, A. M. Mouazen<sup>3</sup>

<sup>1,2,3</sup> Soil and AgriFood Institute, Cranfield University, Cranfield, Bedfordshire, MK43 0AL, <sup>1</sup>r.l.whetton@cranfield.ac.uk, <sup>2</sup>t.w.waine@cranfield.ac.uk, <sup>3</sup>a.m.mouazen@cranfield.ac.uk

Spectroscopic imaging technologies are established in industrial applications, but their use for in-situ (proximal) measurement of a crop canopy lacks detailed information about measurement configurations. This paper aims to identify the optimal equipment configuration of a proximal hyperspectral imager for a strong signal to noise ratio of a wheat crop canopy, considering the impact of soil moisture, total Nitrogen and NDVI.

## Introduction

Conventional farming relies upon unsustainable external inputs and high-yield varieties susceptible to disease to achieve higher yields. With the world's population estimated to reach 9 billion by 2050, sustainable approaches to increase crop yield are a necessity [1].

Hahn [2] argues that spectroscopic and imaging techniques could be integrated with agricultural vehicles; providing non-invasive and reliable systems for monitoring and mapping crop health, with further potential for both disease and early disease detection. Optical sensing provides non-destructive measurements, allowing repeated data acquisition throughout the growing season. Hyperspectral imaging (HI) takes near simultaneous spectral measurements along a series of spatial positions, providing spectral curve shape and features at higher resolutions and with improved understanding of the target than multispectral imagery [3].

Spectral reflectance in vegetation canopies is dependent on the illumination angle of the canopy architecture and plants radiative properties. Plant species, maturity, level of foliage and nutrient status are plant properties leading to radiance variability [4-5]. Crop density is of most importance when determining reflectance [6], represented by a proximal on-line normalised differential vegetation index (NDVI) scanner with nadir

viewing angle. For accurate measurement of on-line (proximal) mapping of crop health, optimising the imager's configurations is required. Spectra quality is largely affected by integration time, camera orientation, and light height and angle from the object (leaf or canopy).

## Problem statement

A need exists for automated approaches in detecting crop-disease. This should be non-destructive, rapid, and disease-specific as well as being sensitive to recognising early symptoms of disease. The use of off-line spectroscopy and imaging techniques is established in many industrial applications however their use for in-situ agricultural applications is wanting. This study aims to optimise the parameters of a proximal hyperspectral imager (spectrograph) for a strong SNR (signal to noise ratio) of a wheat crop canopy, whilst assessing the impact of variable soil Moisture, Nitrogen and crop NDVI.

## Approach and techniques

Winter wheat; *Triticum aestivum* (Solstice variety) was grown outdoors in 600 x 400 mm trays, having a depth of 120 mm with 100 seeds evenly sown in 5 parallel lines.

Camera angle	Light height m	Light distance m	Camera height m	Integration ms
0°	0.90	0.60	0.15	10
5°	1.2	0.90	0.30	20
10°		1.2	0.45	50
			0.60	1000

Table 1: Factors included in configuring hyperspectral imager (multiple configurations considered)

One tray was selected and scanned in triplicate for each configuration, and each pixel was assessed individually. The optimal configurations of the hyperspectral imager were initially assessed through factorial analysis whilst altering camera height, angle and integration time and lighting height and distance from an external halogen light source. Analysis was undertaken at growth stage 47 (Zadoks scale) whilst the head was booting (Table 1). The hyperspectral imagery [8] scanning was carried out in a 9 ha field at Duck End farm, Bedfordshire, UK 52° 5' 36.5994 W" 0° 26' 56.673 N".

Although, the hyperspectral imager captures spectra between 280 nm (ultraviolet) to 1000 nm (shortwave infrared) at 0.6 nm intervals, a good sensitivity can only be obtained in the 400 nm to 750 nm spectral range. The tractor-mounted, hyperspectral imager captures images with a pixel resolution of 1,608, over a one-second interval which is subsequently logged and geo-located using Results of the factorial analysis of the experimental setting of the hyperspectral imagery are shown in Table 2. The highest SNR of 1.688 occurs with the same configurations of 1.2 m, 1.2 m, and 10°, representing light height, light distance, and camera angle, respectively. The camera

a global positioning system. Crop NDVI measurements and edaphic properties were also established throughout the field. This system is an active sensor, illuminating the targeted plant with light of selected wavelengths of red 682–733 nm, red edge red 690 – 730 nm and NIR 760 – 850 nm.

An on-line visible and near infrared soil sensor (370-2200 nm) was used to measure Total Nitrogen (TN) and Moisture Content (MC), using the methods outlined in Mouazen *et al.* [7] using an AgroSpec Vis-NIR spectrophotometer (tec 5 Technology for Spectroscopy, Germany). Maps were created with Krigging (Fig. 2, 3, 4 and 5).

Crop spectra quality measured with the hyperspectral imager was evaluated by analysing SNR, defined here as the quality of signal and is equal to the mean divided by the standard deviation for each pixel [9]; similar to the approach of Ramamurthy *et al.* [10].

### Results

Height is negatively correlated with integration time. The integration time of 50 ms (instead of 1000 ms) was selected as the best option (although a small reduction in the SNR is expected) for the field-scale trials, enabling on-line collection of spectral data, at a shorter time.

Integration time ms	SNR	SD	Distance travelled m	Light height m	Light distance m	Camera angle °	Camera height m
1000	1.688	0.102	4	1.2	1.2	10	0.15
50	1.669	0.160	0.2	1.2	1.2	10	0.3
20	1.471	0.103	0.08	1.2	1.2	10	0.45
10	1.386	0.078	0.04	1.2	1.2	10	0.45

Table 2: Summary of the highest signal-to-noise-ratio (SNR) for each integration time and configurations used for a wheat crop canopy. Standard deviation (SD), Theoretical distance travelled (captured to a single data line).

During white card calibration, 320 marginal pixels at large light angles at either end of the line had significantly lower light absorption, which varied with height. The level of spectral absorbance varied through the integration times as expected, but the shape of the spectral signature remained the same. When height of the camera from the object was altered between 0.3 m, 0.6 m and 0.9 m, it was found that the further the camera from the object the steeper and shorter the drop in absorbance in the marginal pixels at the edge of the image.

An ANOVA was performed which showed all variables and interactions of variables had a significant influence (at 95% confidence) on SNR. Examining the principal component analysis (PCA) similarity maps, shown in Fig.1, it became apparent that the camera and light height have a strong correlation with each other but a minimal influence on SNR. The PCA similarity maps also show little correlation between TN, MC and NDVI with SNR. However, MC and TN are more closely correlated to each other. 4300 points across the field of NDVI and SNR were correlated in a scatterplot providing an  $R^2$  regression of 0.04.

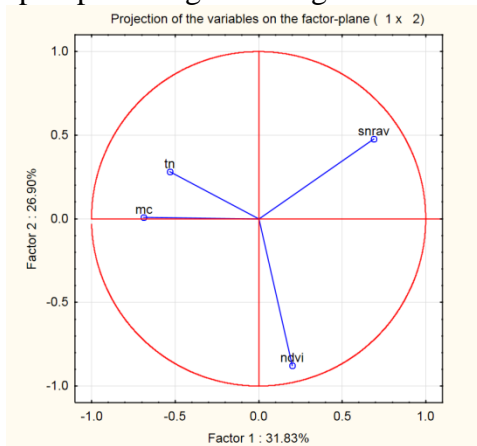


Fig. 4. PCA similarity maps developed for principal components 1 and 2, showing associations between TN, MC, average SNR and NDVI

## Example

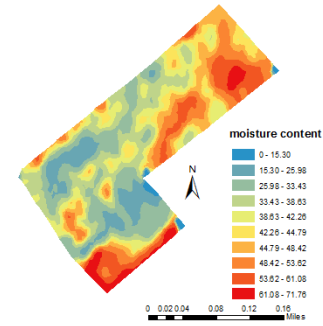


Fig. 5. Map of predicted soil moisture content

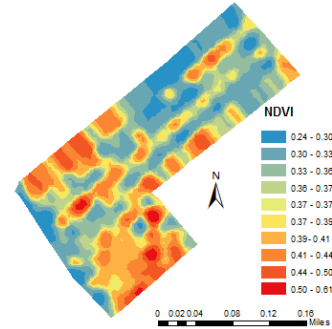


Fig. 6. Map of NDVI

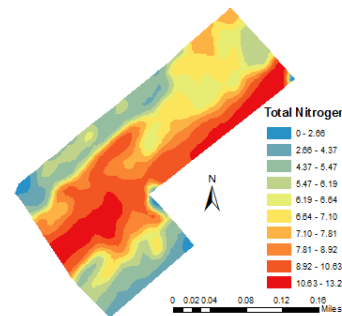


Fig. 7. Map of predicted soil total Nitrogen

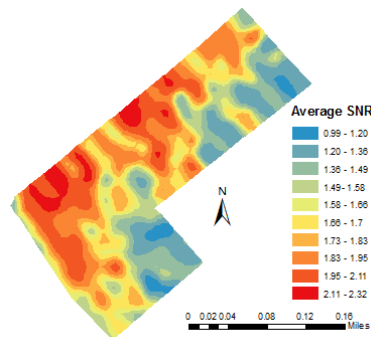


Fig. 8. Map of the average SNR per scan

## Interpretation

During field measurement with the HI, the height variability of the camera due to bounce or uneven ground was observed to be about 0.2 m of the original height of the mounting (set at 0.3 m above the crop canopy). This height variability will cause lower absorption and a lower SNR in the marginal pixels. A recommendation to overcome this correction error is to remove the first and last 320 pixels from the spectral data. Within the preliminary field scans the moisture and NDVI mapping of the field provided a visual explanation for a drop in absorbance within certain areas of the field. Comparing the MC map with the SNR map one can draw a general conclusion that areas of low MC correspond with areas of high SNR, and vice versa (areas of high MC being of low SNR). This can be explained by the fact that soil deformation in wet soils is larger than in dry soils, which increases the height variability of the camera, and thus reduces the SNR, also moister darker soils, have a reduced reflectance so less light returns to the imager. The NDVI affects the absorbance obtained by the HI, assisting to explain patterns and any areas of reduced sensitivity. If inquiring into crop disease, NDVI can also be useful as crop density affects the micro climate and thus the success of a fungal infection. Correlating the NDVI and SNR in a scatterplot provides an  $R^2$  regression of 0.04, but considering over 4300 points across the field were considered further research on the correlation between NDVI and HI is warranted and being conducted.

## Conclusions

The initial camera configurations revealed the importance of camera angle and to the sensitivity of SNR and potential future disease detection, providing optimal measurement settings. Soil

MC Influence on SNR could be visually observed in the maps, which can be attributed to soil deformation that affects original camera settings (e.g. camera height). The Results shed light on the effects of the physical soil properties and crop canopies on SNR. The 4300 points considered for the  $R^2$  value of NDVI and SNR Shows infield variation of SNR is impacted on by crop NDVI and soil and warrants further investigation.

## References

1. D.G. Hole, A.J. Perkins, J.D. Wilson, H.I. Alexander, P.V. Grice, A.D. Evans, Does organic farming benefit biodiversity?, *Biological Conservation*, 122, 113–130, 2005.
2. F. Hahn, Actual pathogen detection: Sensors and algorithms a review. *Algorithms*, 2, 301–338, 2009.
3. J.R. Gilchrist, T. Hyvärinen. Gilden Photonics Ltd and Spectral Imaging Ltd. *Hyperspectral Imaging Spectroscopy: A Look at Real-Life Applications*. Photonics.com. [Online], 2006.
4. G.P. Asner, Biophysical and biochemical sources of variability in canopy reflectance, *Remote sensing of Environment*, 64(3), 234-253, 1998.
5. N.C. Coops, M.L. Smith, M.E. Martin, & S.V. Ollinger. Prediction of eucalypt foliage nitrogen content from satellite-derived hyperspectral data, *Geoscience and Remote Sensing, IEEE Transactions on*, 41(6), 1338-1346, 2003.
6. J. Campbell & M. Norman. *An Introduction to Environmental Biophysics*. American: Springer-Verlag, 97-97, 1998.
7. A.M. Mouazen, J. De Baerdemaeker, & H. Ramon, On-line measurement of some selected soil properties using a Vis-NIR sensor. *Soil & tillage research*, 93, 13-27, 2007.
8. Gilden Photonics Ltd, 9 South Avenue, Glasgow, UK
9. S.W. Smith. *The Scientist and Engineer's Guide to Digital Signal Processing*. 2nd ed. San Diego: California Technical Publishing. p13-16, 1999.
10. R. Ramamurthy, C.F. Canning, J.P. Scheetz, & A.G. Farman. Impact of ambient lighting intensity and duration on the signal-to-noise ratio of images from photostimulable phosphor plates processed using DenOptix® and ScanX® systems, 2014.

# AIRBORNE THERMAL INFRARED HYPERSPECTRAL IMAGING FOR MINERAL MAPPING

Marc-André Gagnon, Pierre Tremblay, Simon Savary, Marc Duval, Vincent Farley, Philippe Lagueur, Éric Guyot and Martin Chamberland

Telops, 100-2600 Saint-Jean Baptiste Ave, Québec (QC), Canada, [www.telops.com](http://www.telops.com)

Minerals such as silicates (quartz), aluminosilicates (feldspar) and magnesium silicates (serpentine) are among the most commonly encountered in the environment. Airborne mineral mapping of these minerals using conventional visible-near infrared (VNIR, 0.4-1.4  $\mu\text{m}$ ) and shortwave infrared (SWIR, 1.4-3  $\mu\text{m}$ ) sensors can be very challenging since the Si-O bounds are featureless or exhibit very weak spectral features in these spectral ranges. These functional groups are turn out being very active in thermal infrared (TIR, 8-12  $\mu\text{m}$ ). In order to illustrate the benefits of TIR hyperspectral imaging (HSI) for mineral mapping, an airborne survey was carried out over an open-pit mine in Thetford Mines (Canada). Mineral mapping of lizardite, serpentinite and quartz was achieved upon linear unmixing of the spectral emissivity data illustrating the benefits of airborne TIR HSI for geological surveys.

## Introduction

The use of airborne remote sensing techniques to characterize mining environments offers many benefits as it allows coverage of large areas in a very efficient way. Both visible-near infrared (VNIR, 0.4-1.4  $\mu\text{m}$ ) and shortwave infrared (SWIR, 1.4-3.0  $\mu\text{m}$ ) are well established techniques in this field. In general, the reflectance spectral features measured in the VNIR and SWIR spectral ranges are overtones and/or combination bands from fundamental absorption bands of the longwave infrared (LWIR, 8-12  $\mu\text{m}$ ). For this reason, the reflectance features measured by VNIR and SWIR sensors are typically broad and/or suffer from strong overlapping which raises selectivity issues for mineral identification in some cases. Since the spectral features associated with fundamental vibrations are generally stronger and sharper than their overtones, using LWIR improves selectivity in certain situations. In addition, the overtone signals of many minerals such as silicate (Si-O), feldspar (Al-O-Si) and olivine ( $(\text{Mg,Fe})_2[\text{SiO}_4]$ ) are too weak to give appreciable spectral features in the VNIR and SWIR. In fact, Most silicates, aluminosilicates and magnesium silicate minerals such as quartz ( $\text{SiO}_2$ ), feldspar, serpentine (Mg-O-Si) and olivine have strong absorption bands in the LWIR spectral

range just like other commonly encountered minerals such as carbonates, phosphates and sulfates.

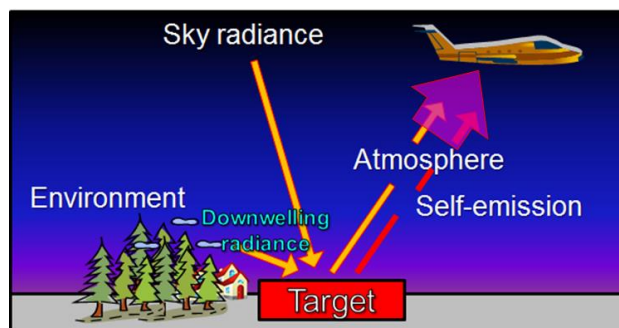


Fig.1. Schematic view of the various phenomena associated with thermal infrared airborne surveys of minerals.

The inherent self-emission associated with LWIR, also called thermal infrared (TIR), under ambient conditions allows airborne surveys in various weather and illumination conditions. However, solid targets such as minerals not only emit but also reflect thermal infrared radiation. Since the two phenomena occur simultaneously, they end-up mixed in the radiance measured at the sensor level as illustrated in Figure 1. To unveil the spectral features associated with minerals from TIR measurements, the respective contributions of self-emission and reflection in the measurement must



be «unmixed». This procedure refers to temperature-emissivity separation (TES) [1].

In order to illustrate the potential of airborne TIR hyperspectral imaging for mineral mapping, an airborne survey was carried out above an open-pit chrysotile mine using the Telops Hyper-Cam airborne system, a passive thermal infrared hyperspectral sensor based on Fourier transform spectroscopy, which provides high spectral resolution data. TES was carried out on the hyperspectral data in order to retrieve the spectral emissivity data. Spectral «unmixing» was then carried out using the spectral signatures of selected minerals which were obtained from commercial spectral libraries. Chemical maps of serpentine minerals (lizardite, serpentinite) and silicates (quartz) were obtained. The results illustrate how high resolution airborne TIR hyperspectral imaging can be successfully used to perform airborne mineral mapping of silicate minerals.

## Experimental Information

### The Telops Hyper-Cam Airborne Platform

All measurements were carried out using the Telops Hyper-Cam airborne platform. The Hyper-Cam-LW (longwave) is a lightweight and compact hyperspectral imaging instrument which uses Fourier Transfer Infrared technology. The Telops Hyper-Cam features a focal plane array detector which contains 320×256 pixels over a basic 6.4°×5.1° field of view (FOV). For the experiment, the FOV was extended to 25.6°×20.4° using a demagnifying 0.25× telescope. In its airborne configuration, the spectral resolution is user-selectable up to 1 cm<sup>-1</sup> over the 7.7 μm (1300 cm<sup>-1</sup>) to 11.7 μm (855 cm<sup>-1</sup>) spectral ranges. The Telops Hyper-Cam airborne platform is equipped with a global positioning system (GPS) and inertial motion unit (IMU) for geo-referencing and tracking of the aircraft movements in flight. An image-motion compensation (IMC) mirror uses the GPS/IMU data to compensate efficiently for the aircraft movements during data acquisition since acquiring a full datacube typically lasts about one second. The data includes all the relevant information for orthorectification and stitching. Visible image are simultaneously recorded along

with the infrared datacubes using a boresight CCD camera on the airborne platform.



Fig.2. Airborne overview of the Thetford Mines area.

### Flight Conditions

The flight was carried out above an open-pit mine in Thetford Mines (Canada) in May 2013 around 5 PM at an altitude of 3000 feet. A visible image showing different regions of the surveyed area is shown in Figure 2. The average above ground level was 800 meters leading to a ground pixel size of 1.25 m<sup>2</sup>/pixel. A spectral resolution of 6 cm<sup>-1</sup> was used which gives a total of 82 spectral bands equally spaced over the whole range covered by the FPA detector. A total of 6 parallel flight lines were required in order to survey the whole area. Ambient temperature and relative humidity at ground level were 11 °C and 26 % respectively.

### Data Processing

Temperature emissivity separation (TES) was carried out by solving Equation 1 where  $L$  is the radiance measured at the sensor level,  $\varepsilon_{\nu}$  the target spectral emissivity,  $D_{\nu}$  the effective downwelling radiance on the target,  $L_{\text{target}}$  the target's self-emission which is function of its thermodynamic temperature as described by the Planck equation,  $\tau_{\text{atm}}$  is the atmospheric transmittance, and  $L_{\text{atm}}$  the radiance associated with TIR self-emission of all atmospheric components.



$$L = [L_{target}\varepsilon_{\bar{\nu}} + Dw(1 - \varepsilon_{\bar{\nu}})]\tau_{atm} + L_{atm}(1 - \tau_{atm}) \quad (1)$$

A smoothing criterion, similar to the one described in the work of Borel [2] was used to minimize both atmospheric and downwelling radiance contributions.

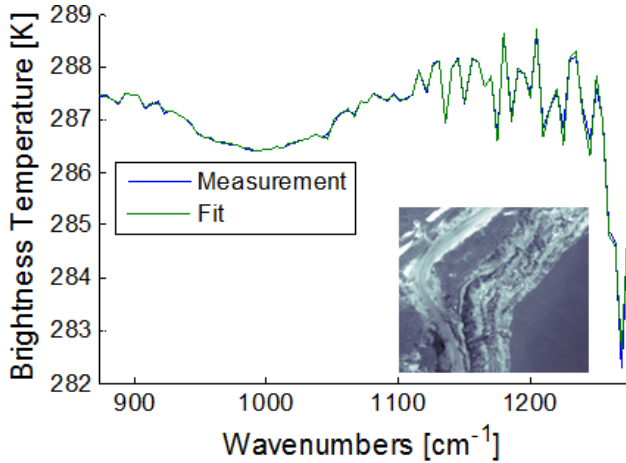


Fig.3. The infrared spectrum of a region in the mining area is presented on a brightness temperature (blue curve) scale with the best fit of Equation 1 (green curve).

## Results and Discussion

### Temperature-Emissivity Separation (TES)

In order to retrieve spectral emissivity information, Equation 1 must be solved efficiently. The infrared spectra of a region associated with the mining area is shown in Figure 3. Its geographical positions, relative to the whole survey area, is labeled in Figure 5. The broad spectral feature observed around 900-1075  $\text{cm}^{-1}$  is likely associated with serpentine minerals that are expected to be present in great proportion within this area. The sky radiance spectral features (reflection component) can be more or less observed as a function of the spectral emissivity properties of the ground material. The series of sharp peaks in the 1275-1300  $\text{cm}^{-1}$  spectral range is associated with atmospheric absorption.

In order to achieve mineral mapping, the spectral emissivity datacube must be unmixed, i.e. one must estimate the relative contributions (coefficients  $A, B \dots$ ) of the different

components ( $\varepsilon_{\bar{\nu}_n}$ ), associated with the different minerals, within the overall emissivity signal ( $\varepsilon_{\bar{\nu}_{tot}}$ ). Various strategies based on statistical, end-members, continuous wavelet analysis [4], or algebraic approaches can be used for the analysis of the emissivity data. In this case, a linear mixing approach was selected as expressed in Equation 2.

$$\varepsilon_{\bar{\nu}_{tot}} = A\varepsilon_{\bar{\nu}_1} + B\varepsilon_{\bar{\nu}_2} + C\varepsilon_{\bar{\nu}_3} + D\varepsilon_{\bar{\nu}_n} \quad (2)$$

Linear unmixing of the spectral emissivity data was carried out using reference spectra from commercial libraries such as John Hopkins University (JHU), Jet Propulsion Laboratory (JPL) and United State Geological Survey (USGS). The component list comprised quartz (sand), calcite, lizardite, serpentinite (mostly antigorite) and magnesite ( $\text{MgCO}_3$ ), granite, feldspar and dunite (mostly olivine). The spectral signature selection was carried out according to local geological information as well as recent work in a nearby area [4]. The reference spectra of a few minerals are shown in Figure 4 as well as the spectral emissivity data of two selected locations.

Reasonably good matches were obtained between the estimated spectral emissivity data and the best fit from Equation 2 as seen in Figure 4. Many factors can explain the disparities between the measurements and the fits such as the uncertainties in emissivity data retrieved from the TES algorithm or a mismatch between the encountered mineral polymorph and the one selected from the reference library. Nevertheless, a thematic mineral map, derived from the main (highest relative abundancies coefficient) component obtained for each pixel is presented in Figure 5. As expected, serpentinite and lizardite are highly located in the mining area and in the tailing pounds where the mining residues are stored. Dunite corresponds to bedrock, i.e. unaltered areas (incomplete or no serpentinization). Quartz spectral signature was exclusively detected outside of the mining area. Olivine and serpentine minerals are unlikely to be found

associated with quartz minerals because of their different crystallisation processes. Quartz is often encountered in soils, sand and urban areas as it is used in the production of many materials such as concrete and asphalt [5].

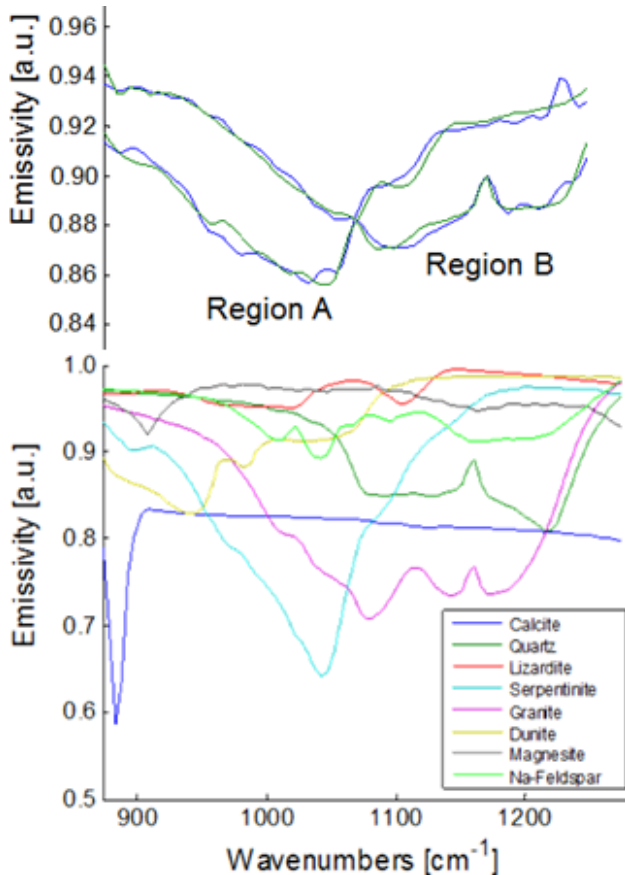


Fig.4. Spectral emissivity unmixing (top) of Region A and Region B. The blue curves correspond to the spectral emissivity curves obtained upon TES and the green curves correspond to the best fit of Equation 2. Reference spectra are shown (bottom) for comparison purposes.

### Conclusion

An airborne thermal infrared hyperspectral imaging survey was successfully carried out on an open pit mine known for containing a great variety of silicate minerals. The high spectral resolution allowed efficient temperature-emissivity separation and atmospheric compensation. The spectral emissivity data could be successfully unmixed using selected reference spectra of common geological components and a selection of mineral components likely to be found in such area. The

chemical maps derived from the emissivity data are in good agreement with the expected results illustrating the benefits of airborne thermal infrared hyperspectral imaging for mineral mapping of silicate minerals.

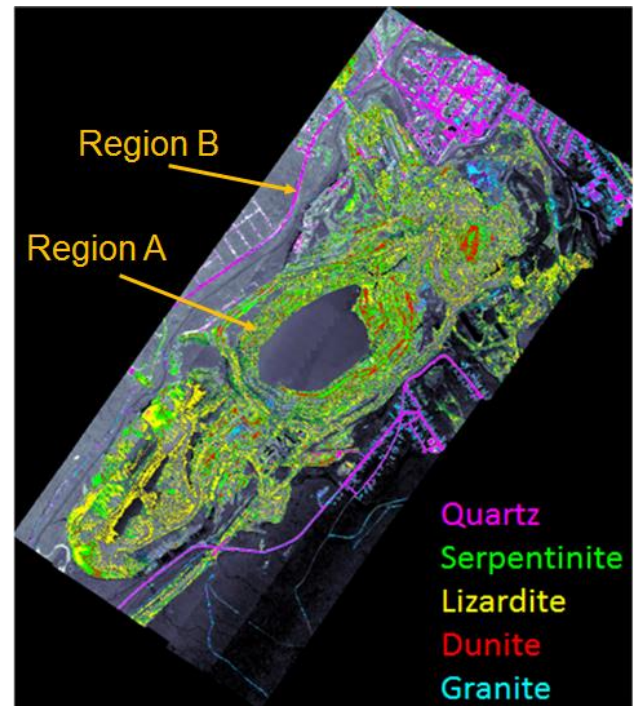


Fig.5. Thematic mineral map of the Thetford Mines area.

### References

1. A.R. Gillespie, et al., Temperature/Emissivity Separation Algorithm Theoretical Basis Document, Version 2.4, NASA, 64 p (1999).
2. C.C. Borel, ARTEMISS – an Algorithm to Retrieve Temperature and Emissivity from Hyper-Spectral Thermal Image Data, 28th Annual GOMACTech Conference., Hyperspectral Imaging Session, (2003).
3. B.J. Saikia, et al., Fourier transform infrared spectroscopic estimation of crystallinity in SiO<sub>2</sub> based rocks, Bull.Mater.Sci., 31, 775 (2008).
4. B. Rivard, et al., First geological case study of the airborne longwave hyperspectral Hyper-Cam system, Thetford Mines, Quebec, IGARSS Conference, 4025 (2014).
5. M.A. Gagnon, et al., Airborne Thermal Hyperspectral Imaging of Urban and Rural Areas, IGARSS Conference, 1369 (2014).

# HgCdTe BARRIER INFRARED DETECTORS

M. Kopytko, A. Rogalski

Institute of Applied Physics, Military University of Technology, 2 Kaliskiego Str., 00-908 Warsaw, Poland, mkopytko@wat.edu.pl

In the last decade, new strategies to achieve high-operating temperature (HOT) detectors have been proposed, including barrier structures such as nBn devices, unipolar barrier photodiodes, and multistage (cascade) infrared detectors. The ability to tune the positions of the conduction and valence band edges independently in a broken-gap type-II superlattices is especially helpful in the design of unipolar barriers. This idea has been also implemented also in HgCdTe ternary material system. In this paper we present status of HgCdTe barrier detectors grown by metal organic chemical vapor deposition (MOCVD) with emphasis on technological progress in fabrication achieved recently at the Institute of Applied Physics, Military University of Technology. Their performance is compared with other types of photodetectors.

## Introduction

Historically, the first barrier detector was proposed by A.M. White in 1983 [1] as a high impedance photoconductor. It postulates an n-type heterostructure with a narrow gap absorber region coupled to a thin wide bandgap layer, followed by a narrow bandgap contact region. The concept assumes almost zero valence band offset approximation throughout the heterostructure, what allows flow of only minority carriers in a photoconductor. Little or no valence band offset was difficult to realize using standard infrared detector materials such as InSb and HgCdTe.

The barrier detectors are designed to reduce dark current associated with Shockley-Read-Hall (SRH) processes and to decrease influence of surface leakage current without impending photocurrent (signal). In consequence, absence of a depletion region in barrier detectors offers a way to overcome the disadvantage of large depletion dark currents. So, they are typically implemented in materials with relatively poor SRH lifetimes, such as all III-V compounds. However, this reason is not important in HgCdTe devices, since influence of depletion layer dark current contribution can be omitted.

This paper attempts to provide the present status of HgCdTe barrier detectors with emphasis on technological achievements in fabrication of MOCVD-grown HgCdTe barrier detectors made recently at the Institute of Applied Physics, Military University of Technology. Their performance is compared with state-of-the-art other detectors.

## Band offsets

Contrary to the III-V semiconductor-based heterostructures, HgCdTe material does not exhibit a near zero valence band offset, which is the key item limiting the performance of nBn detectors [2-6]. Devices exhibit poor responsivity and detectivity, especially at low temperatures, where the low-energy minority carriers generated by optical absorption are not able to overcome the valence band energy barrier. Reduction of valence band offsets to a reasonably low value, by the adjustment of the Cd mole fraction in the barrier, results in a corresponding reduction of the barrier in the conduction band below a critical level, thus increasing majority carrier dark current and reducing responsivity (detectivity) at high temperatures.

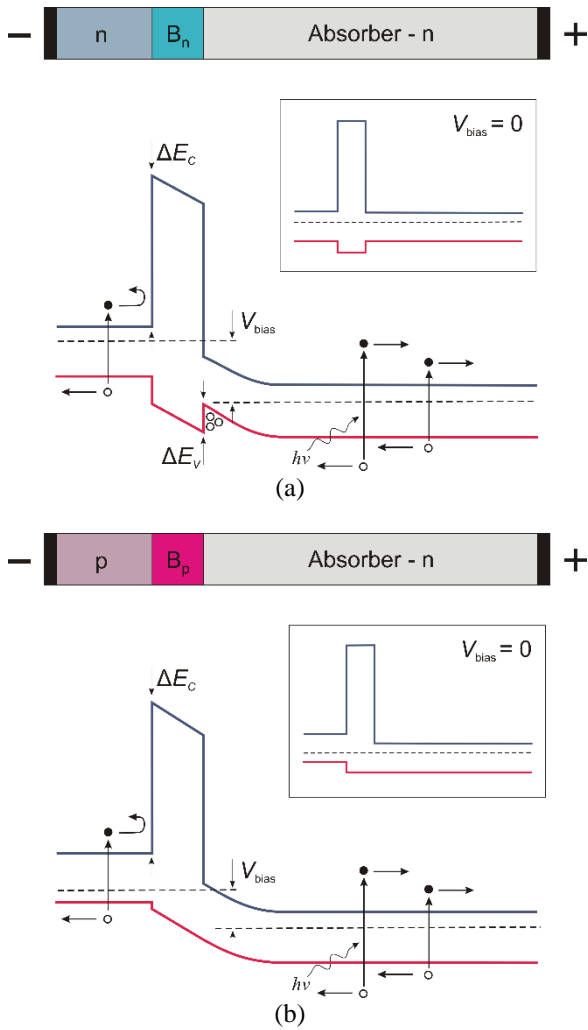


Fig. 1. Schematic band diagrams of HgCdTe barrier detectors with (a) nonzero and (b) zero valence band offset.

At low bias, the valence band barrier ( $\Delta E_v$ ) inhibits the minority carrier holes flow between the absorber and contact cap layer (Fig. 1.a). Depending on the wavelength of operation, a relatively high bias, typically greater than the bandgap energy is required to be applied to the device to collect all of the photogenerated carriers.

In HgCdTe material, proper p-type doping of the barrier reduce the valence band-offset and increase the offset in the conduction band [7]. The device with the barrier only in the conduction band is similar to that proposed in Ref. 1, in which a p-type barrier is interposed between two narrow gap n-type regions. Furthermore, due to the presence of the barrier, it is possible to replace n-type

cap contact by p-type layer (Fig. 1.b) without affecting the dark current.

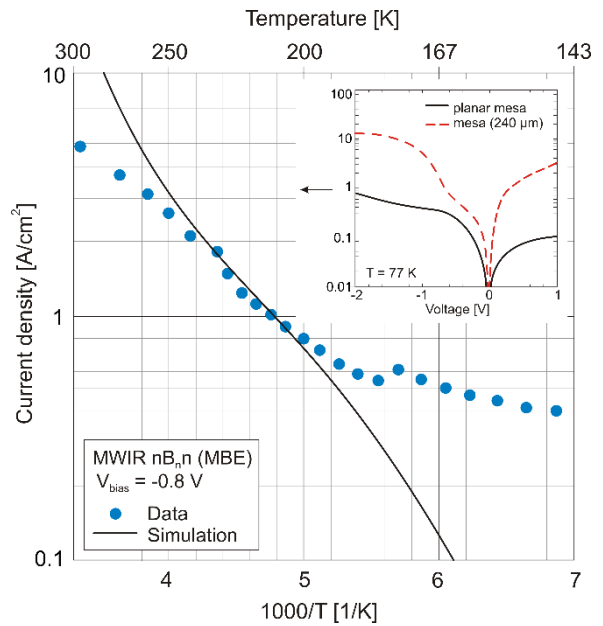


Fig. 2. Current density at 0.8 V reverse bias as a function of temperature for first-iteration MBE grown planar-mesa HgCdTe  $nB_n n$  detector. Inset: measured dark current-voltage characteristics at 77 K (after Refs. 2 and 4).

## HgCdTe barrier detectors

First MWIR HgCdTe  $nB_n n$  (n-type barrier) devices grown by molecular beam epitaxy (MBE) on a bulk CdZnTe substrate were reported by Itsuno *et al.* [2-4]. Figure 2 presents the measured and calculated current density of planar-mesa detector as a function of temperature [2]. Within the temperature range between 180 K and 250 K, the dark current increases from 1 to 3 A/cm<sup>2</sup> and corresponds to the calculated model for a diffusion limit. Below 180 K, the experimental dark current saturates due to carrier generation via surface trap states along the sidewalls in the narrow bandgap absorber induced during the mesa etching. The existence of the valence band barrier is still the main issue limiting the performance of HgCdTe  $nB_n n$  detectors. It is clearly evident in current-voltage characteristics where turn-on voltage values are in the

range of - 0.6 V to - 1.0 V. The turn-on bias range indicates the voltage required to align the valance band, enabling the collection of minority carrier holes from the absorber layer.

First HgCdTe barrier detectors with zero valence band offset were optimised at about a 3.6  $\mu\text{m}$  cut-off wavelength at 230 K. The epitaxial structures were grown in Aixtron AIX-200 MOCVD system on GaAs substrates after CdTe buffer layer [8]. The devices have  $p^+B_p$  cap-barrier structural unit, undoped (due to donor background concentration with n-type conductivity) or low p-type doped absorption layer and wide band-gap highly doped  $N^+$  bottom contact layer.

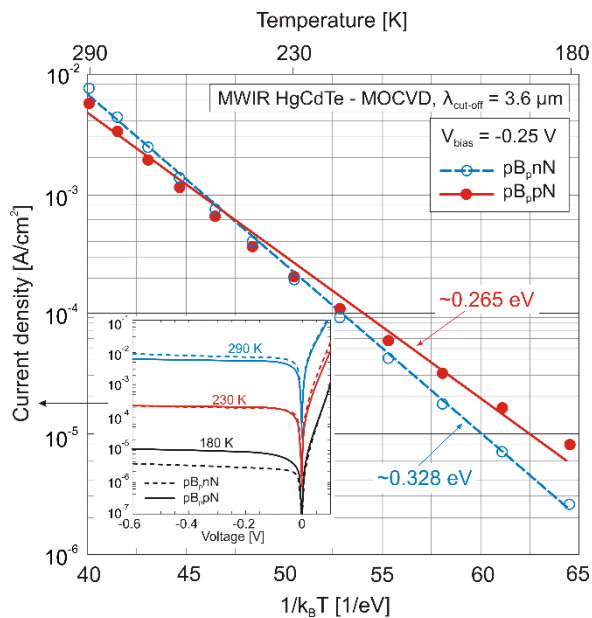


Fig. 3. Measured dark current density at 0.25 V reverse bias as a function of temperature for MOCVD grown HgCdTe  $pB_p nN$  and  $pB_p pN$  detectors with 3.6  $\mu\text{m}$  cut-off wavelength. Inset: measured dark current-voltage characteristics at different operating temperatures (after Ref. 8).

Figure 3 shows the measured dark current at 0.25 V reverse biased as a function of temperature of  $pB_p nN$  and  $pB_p pN$  detectors.<sup>27</sup> The estimated thermal activation energy of about 0.328 eV for the device with n-type absorbing layer is close to the full  $\text{Hg}_{0.64}\text{Cd}_{0.36}\text{Te}$  bandgap what indicate diffusion limited dark currents. The slope of about 0.265 eV for the device with p-type absorbing layer correspond to the

activation energies for GR behaviour (about  $0.8E_g$ ).

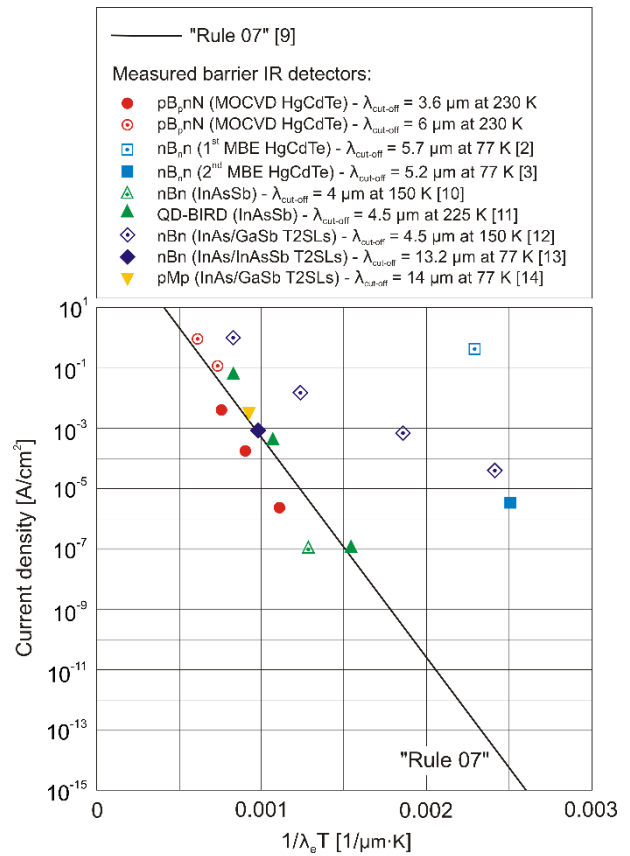


Fig. 4. Comparison of different barrier IR detectors to the “Rule 07”.

### Comparison of the detector performance

The Figure 4 compares the minimum dark current density of the analyzed structures to the values given by “Rule 07” being a simple means to compare the HgCdTe IR detectors [9]. The III-V material-based nBn performance<sup>21,28-31</sup> is also compared to the HgCdTe “Rule 07”. It is noted that the dark current density of the MBE grown nBn devices is several orders of magnitude larger than those given by “Rule 07”. Measured values of dark current density for MOCVD grown HgCdTe  $pB_p nN$  device with a 3.6  $\mu\text{m}$  cut-off wavelength are an order of magnitude lower than those determined by “Rule 07”.



## Conclusion

The idea of barrier detector has been also implemented also in HgCdTe ternary material system. However, the implementation of this detector structure in this material system is not straightforward due to the existence of a valence band discontinuity (barrier) at the absorber-barrier interface.

First MWIR HgCdTe nB<sub>n</sub> devices, with n-type barrier and poor performance, were grown by MBE. It appears however, that the proper p-type doping of the barrier reduce the valence band-offset and increase the offset in the conduction band. As a result, the performance of this type of HgCdTe barrier detector is considerable improved.

Results presented in this paper show considerable progress in fabrication of MOCVD-grown HgCdTe barrier MWIR detectors. Their performance is comparable with state-of-the-art of HgCdTe photodiodes. It is important technological advantage from the perspective of device fabrication since it requires less stringent surface passivation, and due to tolerance to threading dislocations.

## Acknowledgements

The work has been done under the financial support of the Polish National Science Centre as research Projects:  
No. DEC-2013/08/M/ST7/00913,  
No. DEC-2011/03/D/ST7/03161,  
No. DEC-2013/08/A/ST5/00773.

## References

1. A.White, "Infrared detectors," U.S. Patent 4,679,063 (22 September 1983).
2. A.M. Itsuno, J.D. Phillips, and S. Velicu, Mid-wave infrared HgCdTe nBn photodetector, *Appl. Phys. Lett.* **100**, 161102 (2012).
3. A.M. Itsuno, J.D. Phillips, and S. Velicu, Design of an Auger-suppressed unipolar HgCdTe NBnN photodetector, *J. Electron. Mater.* **41**, 2886–2892 (2012).
4. M. Kopytko, J. Wróbel, K. Jóźwikowski, A. Rogalski, J. Antoszewski, N. D. Akhavan, G. A. Umana-Membreno, L. Faraone, and C. R. Becker, Engineering the bandgap of unipolar HgCdTe-based nBn infrared photodetectors, *J. Electron. Mater.* **44**, 158-166 (2014).
5. M. Kopytko, A. Kębłowski, W. Gawron, P. Madejczyk, A. Kowalewski, and K. Jóźwikowski, High-operating temperature MWIR nBn HgCdTe detector grown by MOCVD," *Opto-Electron. Rev.* **21**, 402–405 (2013).
6. N.D. Akhavan, G. Jolley, G.A. Umma-Membreno, J. Antoszewski, and L. Faraone, Design of band engineered HgCdTe nBn detectors for MWIR and LWIR applications, *IEEE Trans. Electron Devices* **62**, 722-728 (2015).
7. M. Kopytko, "Design and modelling of high-operating temperature MWIR HgCdTe nBn detector with n- and p-type barriers," *Infrared Phys. Technol.* **64**, 47–55 (2014).
8. M. Kopytko, A. Kębłowski, W. Gawron, A. Kowalewski, and A. Rogalski, "MOCVD grown HgCdTe barrier structures for HOT conditions," *IEEE Trans. Electron Devices* **61**(11), 3803-3807 (2014).
9. W.E. Tennant, D. Lee, M. Zandian, E. PiQuette, and M. Carmody, "MBE HgCdTe technology: A very general solution to IR detection, described by „Rule 07”, a very convenient heuristic," *J. Electron. Mater.* **37**, 1406–1410 (2008).
10. P. Klipstein, O. Klin, S. Grossman, N. Snapi, B. Yaakovovitz, M. Brumer, I. Lukomsky, D. Aronov, M. Yassen, B. Yofis, A. Glozman, T. Fishman, E. Berkowicz, O. Magen, I. Shtrichman, E. Weiss, XBn barrier detectors for high operating temperatures, *Proc. SPIE* **7608**, 76081V-1–1076081V-10 (2010).
11. D.Z. Ting, A. Soibel, C.J. Hill, S.A. Keo, J.M. Mumolo, and S.D. Gunapala, "High operating temperature midwave quantum dot barrier infrared detector (QD-BIRD)," *Proc. SPIE* **8353**, 835332 (2012).
12. E. Plis, S. Myers, M.N. Kutty, J. Mailfert, E.P. Smith, S. Johnson, and S. Krishna, "Lateral diffusion of minority carriers in InAsSb-based nBn detectors," *Appl. Phys. Lett.* **97**, 123503 (2010).
13. H. S. Kim, O. O. Cellek, Zhi-Yuan Lin, Zhao-Yu He, Xin-Hao Zhao, Shi Liu, H. Li, and Y.H. Zhang "Long-wave infrared nBn photodetectors based on InAs/InAsSb type-II superlattices," *Appl. Phys. Lett.* **101**, 161114-3 (2012).
14. B.M. Nguyen, S. Bogdanov, S. Abdollahi Pour, and M. Razeghi, "Minority electron unipolar photodetectors based on type II InAs/GaSb/AlSb," *Appl. Phys. Lett.* **95**, 183502-3 (2009).



# THERMAL IMAGE ANALYSIS OF PLASTIC DEFORMATION AND FRACTURE BEHAVIOR BY THERMO-VIDEO MEASUREMENT SYSTEM

Y. Ohbuchi, N. Nagatomo, H.Sakamoto

Graduate School of Science and Technology, Kumamoto University,  
1-14-6 Kurokami Chuo-ku Kumamoto 860-8555, Japan,  
ohbuchi@mech.kumamoto-u.ac.jp

In order to evaluate the plastic deformation and fracture behavior in the structural member with some flaws, authors paid attention to surface temperature which is generated by plastic strain energy. The visualization of the plastic deformation was developed by analyzing the relation between the the extension of plastic deformation range and the surface temperature distribution which was obtained by the infrared thermo-video system.

## Introduction

In order to evaluate the plastic deformation of notched mechanical members, we paid attention to surface temperature which is generated by plastic deformation. Most of the plastic energy exhausted by plastic deforming is converted into heat. The distribution of the heat generation represents the macroscopic plastic deformed intensity.

In the present study, the tensile tests were performed on stainless steel plate with a center crack. Authors measured the distributions of specimen's surface temperature by using the thermocouple and thermography (TVS).

Furthermore FEM elasto-plastic analysis were carried out with the experiment, and the effectiveness of this non-contact measurement system of plastic deformation and fracture process by thermography system was discussed.

## Experiment

**Material and specimen.** Specimen of stainless steel, SUS304 (in the JIS standard) was used to observe the behavior of plastic deformation and the heat distribution under tensile load.

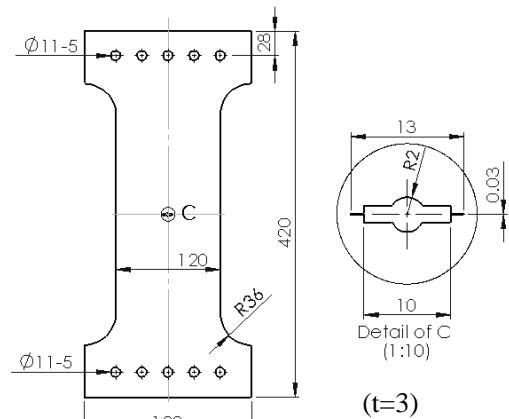


Fig. 1. The geometry and dimensions of the test specimen.

Geometry of the specimen are shown in Fig.1. The pre-crack was made by electro spark machine with 0.03 mm diameter as stress concentration parts in the center of specimen. After machining, the annealing treatment was done in these specimen. Mechanical properties of SUS304 are were calculated from stress-strain curve obtained .

**Thermal Video System.** The thermal camera which was used in this research is TVS-8500 (Thermal Video System from Nipon Avionics Co. Ltd.). The specification is shown in Table 3. Infrared thermal images and temperature data are recorded to the compact flash memory card every 0.5 second.

**Emissivity measurement.** Emissivity is one of the important factors for measuring the surface temperature by thermography method. This factor depends on the surface condition of target. The temperature measurement accuracy become high with the emissivity increasing on the surface . So, the black paint was sprayed on the specimen surface.

The appropriate emissivity was obtained by comparing thermal gradient of the specimen's surface comparing thermocouple and thermography. In this experiment, the emissivity was decided to 0.50 so that the temperature gradient obtained by the thermography and the thermocouple may become the relation of one to one.

**Experimental procedure.** First, the appearance of deformation in the vicinity of crack tip was observed by microscope camera. Simultaneously, the strain distributions near the center crack were measured by strain gauges. Next, the heat distributions on the specimen's surface were measured by using this thermo-camera under the plastic deformation and crack propagation shown in Fig.2. The experiment was executed under light shield in order to remove the reflection noises such as the inside reflection in thermo-camera and surface reflection. At the same time, temperature distribution on the specimen's surface was measured by thermocouples to verify the accuracy of temperature measurement obtained by thermography method.

The evaluation of the plastic deformation and fracture behaviors were carried out by using the universal testing machine (SHIMADZU AUTOGRAPH AG-25TB) with a constant loading speed, 25mm/min. The strain gauges pasted positions and thermocouple welded positions on the specimen's surface in both experiments.

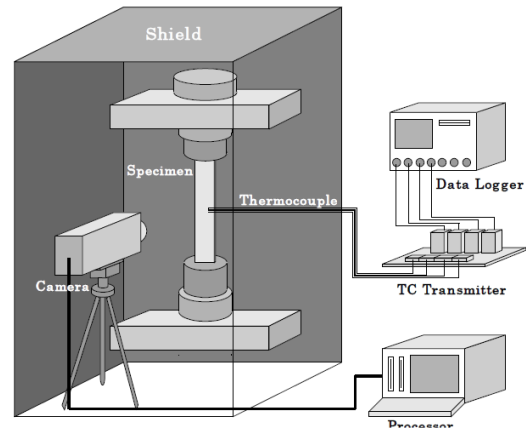


Fig. 2. Evaluation of plastic deformation test.

## Experimental results

**Fracture behaviors.** Fig.3 shows the transition of strain in the vicinity of the crack tip under constant loading. The plots pause off due to fracture of strain gauges but expansion of strain distribution around the center crack can be seen in the results. Furthermore, Crack Opening Displacement (COD) is shown in Fig.5 which was measured by images obtained by the microscope in front of the crack tip.

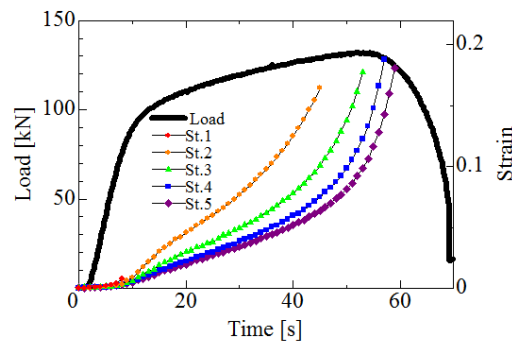


Fig. 3. Transition of strain in the vicinity of the crack tip.

**Evaluation of plastic deformation test.** The temporal response of the heat distribution of the specimen's surface under plastic deformation obtained by thermography are shown in Fig.4.

**Evaluation of plastic deformation test.** The temporal response of the heat distribution of the specimen's surface under plastic deformation obtained by thermography are shown in Fig.4. The temperature distribution per unit time was obtained as the difference thermal image of current one and

reference one (The first frame of thermal image) by the thermal image processing software.

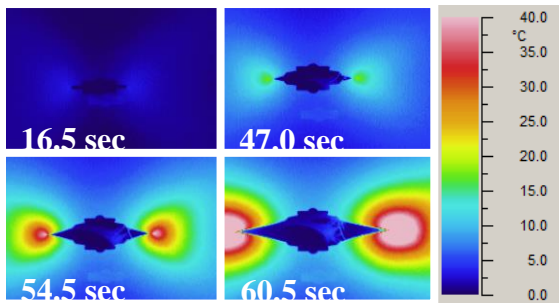


Fig. 4. Temperature distribution measured by thermography.

By using this software, the temperature rise at any point on the specimen surface can be calculated and it can be easy to compare the temperature measured by thermography with one by thermocouple. When the crack propagation starts, higher temperature rise was detected near the crack tips. Then the high temperature region extended as plastic strain region expands.

The temperature rise plots measured by thermography and thermocouples are shown in Fig.5.

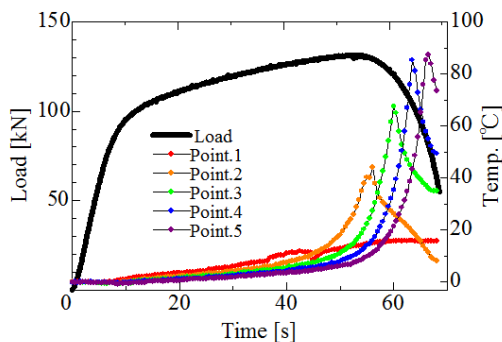


Fig. 5. Temperature rise on the specimen's surface measured by thermography.

Paying attention to the temperature change of Point1 in Fig.5, the temperature increases with the expansion of the plastic strain, though the temperature decreases just after loading due to effect of thermoelasticity.

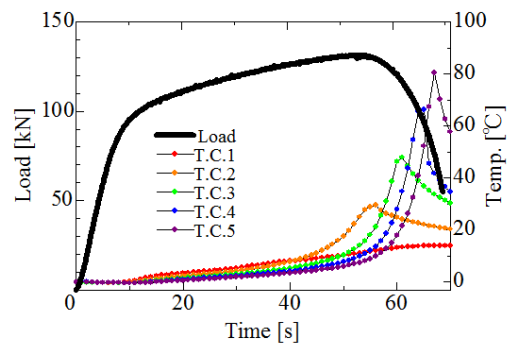


Fig. 6. Temperature rise on the specimen's surface measured by thermocouples.

Then temperature rises suddenly due to strain concentration around the crack tips just after the crack propagation start. The same behavior can be seen in T.C.1 in Fig.6. The temperature corresponding between thermography and thermocouples was almost good. However, the peaks of the temperature plots measured by thermography was little higher than that of thermocouples due to emissivity error.

### Analysis of heat generation and thermal conduction under plastic deformation

In order to study the relation between the temperature rise measured by the thermography and the plastic deformation and crack propagation, we should carry out the elasto-plastic FE analysis coupled with transient heat conduction. Figure 7 shows the calculation result to 40sec. The simulation result are good agree with the experimental one.

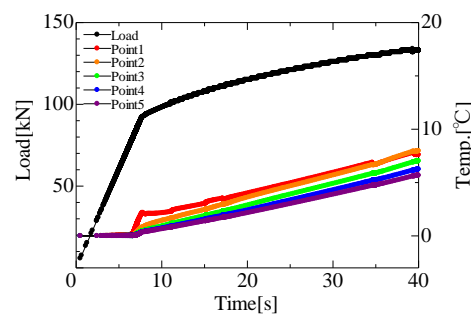


Fig. 7. The simulation of temperature rise on the specimen's surface (0<t<40sec).

## Conclusions

The experiments for the non-contact evaluation system of plastic behaviors and fracture process by using thermography had been carried out, and the propriety of the method was discussed.

The results obtained are summarized as follows:

- (1) The variation of surface temperature in metal generated by deformation can be measured by using infrared thermography in elastic region and plastic region.
- (2) The crack propagation behavior can be measured by pursuing the highest temperature points.
- (3) As the heat distribution under plastic deformation is closely related to the plastic strain distribution, the thermo-

graphy method can become an effective measurement method of the macroscopic evaluation of the plastic deformation by combined with thermal image processing.

## References

1. Hidetoshi Sakamoto, Keng Seki and Munekata Kodama, On-Line Measurement of Heat Generation by Plastic Deformation in Some Structure Members, Key Engineering Materials, Vols.177-180, pp.775-780, 2000.
2. Hidetoshi Sakamoto, Eiji Nakamachi and Lee Soo Jong, Evaluation of Plastic Behaviors in FCC Polycrystal Sheet Metal, Key Engineering Materials Vols.345-346 , pp.145-148, 2007.
3. Hidetoshi Sakamoto, Jian Shi, Yoshifumi Ohbuchi and Mitusharu Yamamoto, Evaluation of Plastic Deformation and Fracture Behaviors by Thermal Image Technique, Key Engineering Materials Vols.462-463, pp. 756-76, 2011.
4. D.J. Titman, Applications of thermo-graphy in non-destructive testing of structures, NDT&E International 34, pp.149-154, 2001.

# Micro-laser Line Thermography and High Resolution X-ray Tomography on Micro-porosities: A Comparative Study of Experiments and Simulation

H. Zhang<sup>1</sup>, L. Yu<sup>2</sup>, U. Hassler<sup>3</sup>, H. Fernandes<sup>1</sup>, W. Holub<sup>3</sup>, F. Robitaille<sup>4</sup>, S. Joncas<sup>5</sup>, M. Genest<sup>6</sup>, X. Maldague<sup>1</sup>

<sup>1</sup>Department of Electrical and Computer Engineering, Computer Vision and Systems Laboratory, Laval University, 1065 av. de la Medecine, Quebec, G1V 0A6, Canada

<sup>2</sup>Department of Physics, Physical Engineering and Optics, Center for Optics, Photonics and Lasers, Laval University, 2375 rue de la Terrasse, Quebec, G1V 0A6, Canada

<sup>3</sup>Fraunhofer Development Center X-ray Technologies (EZRT), Department of Application Specific Methods and Systems (AMS), Fraunhofer IIS, Flugplatzstrasse 75, 90768 Fuerth, Germany

<sup>4</sup>Department of Mechanical Engineering, University of Ottawa, 161 Louis Pasteur, Ottawa, K1N 6N5, Canada

<sup>5</sup>Department of Automated Manufacturing Engineering, Ecole de Technologie Superieure, 1100 rue Notre-Dame Ouest, Montreal, H3C 1K3, Canada

<sup>6</sup>Aerospace Portfolio, Structures, Materials and Manufacturing, National Research Council Canada, 1200 Montreal Road, Ottawa, K1A 0R6, Canada

Stitching is used to reduce dry-core (incomplete infusion of T-joint core) and reinforce T-joint structure. However, it might cause new types of flaws, especially micro-sized flaws. In this paper, a new micro-laser line thermography was defined. 18  $\mu\text{m}$  resolution x-ray tomography was used to validate the infrared results. A comparison of micro-laser line thermography and high-resolution x-ray tomography was performed. Then a finite element analysis was performed on infrared results. The geometrical model needed for finite element discretization was developed from measurements using 18  $\mu\text{m}$  x-ray tomography. The model was validated for the experimental results. Finally a comparison of the experiments and simulation was conducted. Finite element analysis for infrared thermography on micro-sized flaws was poorly documented. The infrared experimental phenomenon was explained on the basis of the finite element analysis.

## 1. Introduction

In this paper, a new micro-laser line thermography was used to detect a stitched 3D T-joint CFRP. 18  $\mu\text{m}$  resolution x-ray tomography was used to validate the infrared results. A comparison of micro-laser line thermography and high-resolution x-ray tomography was conducted. Then a finite element analysis was performed on the infrared results. The geometrical model needed for finite element discretization was developed from measurements using 18  $\mu\text{m}$  x-ray tomography. The model was validated for the experimental results. Finally a comparison of the experiments and simulation was conducted. Finite element analysis for infrared thermography on micro-

sized flaws was poorly documented previously. The infrared experimental phenomenon was explained on the basis of the finite element analysis.

## 2. Specimen

The complete stitched 3D T-joint CFRP is shown in Fig. 1 (a). The sample contains 6 stitching lines. The purpose of the stitching is to consolidate the T-joint structure and to reduce dry-core. The sample measures 152 mm in length, 148 mm in width, 63 mm in height, and 5 mm in thickness (excluding the T-stringer).

The front side of the sample is shown in Fig. 1 (b). A 10 mm  $\times$  152 mm zone was detected using micro-laser line thermography and high-resolution x-ray tomography.

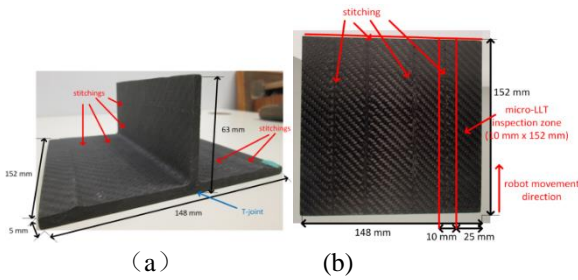


Figure 1: (a) Complete stitched 3D T-joint sample, (b) front side of the sample.

### 3. Methods and results

#### 3.1. Experiments

Figure 2 (a) shows the experimental set-up for micro-laser line thermography. In the set-up, the sample was fixed on a robot. A mid-wave infrared (MWIR) camera (FLIR Phoenix, InSb, 3-5  $\mu\text{m}$ ,  $640 \times 512$  pixels) at a frame rate of 55 Hz was used to record the temperature profile. A diode-laser was used. The laser wavelength is 805 nm. The laser beam power is 2.9 W. The heating time is 0.5 s. A convex lens was used to focalize the laser beam. A micro-lens was used to identify and characterize the micro-sized flaws. The magnification of the micro-lens is  $1\times$ . A micro-mirror was mounted between the IR camera and the sample. In Fig. 2 (b), the laser spot was converted to a laser line when the micro-mirror swung with extremely high frequency. Figure 2 (b) shows the heating source. Its length is around 10 mm and its width is around 3 mm.

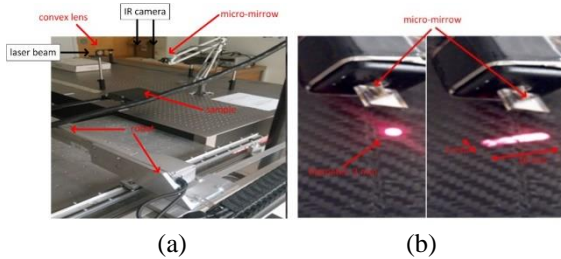


Figure 2: (a) Micro-laser line thermography experimental set-up, (b) laser spot to laser line.

Figure 1 (b) shows the detected zone. The laser line crosses a stitching line. The robot moved per 3 mm towards the direction shown in Fig. 1 (b). A total of 51 tests were performed to detect the  $10 \text{ mm} \times 152 \text{ mm}$  area

shown in Fig. 1 (b). The method is defined as micro-laser line thermography.

An X-ray micro-CT inspection was performed on the same  $10 \text{ mm} \times 152 \text{ mm}$  zone shown in Fig. 1 (b). The resolution of the inspection is  $18 \mu\text{m}$ . The purpose of the x-ray tomography inspection is to validate the micro-laser line thermography results.

Figure 3 shows the x-ray tomography results. Some specific micro-porosities are marked in the images.

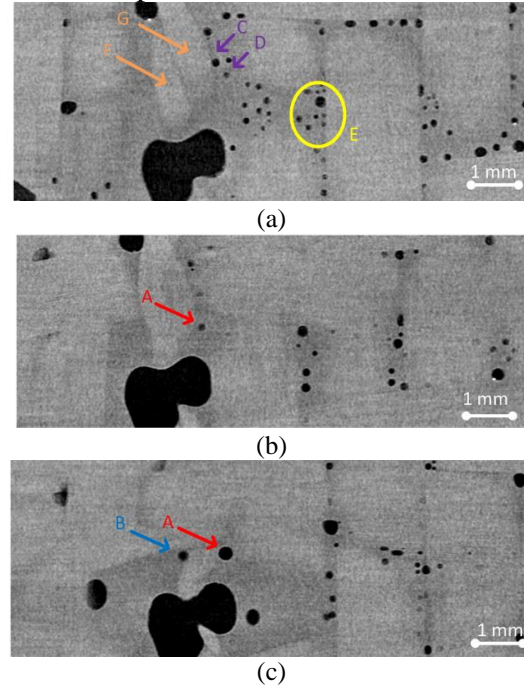


Figure 3: The x-ray tomography results (a) surface, (b) depth:  $90 \mu\text{m}$ , (c) depth:  $0.18 \text{ mm}$

Figure 3 (a) shows the surface image of a detected zone. The image was acquired using  $18 \mu\text{m}$  resolution x-ray tomography. Some micro-porosities are inspected on the surface.

Figure 4 shows the micro-laser line thermography results in the same zone.

Figure 4 (a) was acquired from preliminary image processing (cold image). In Fig. 4 (a), some micro-porosities on the surface such as 'C' and 'D' (marked in purple) are inspected. However, some other micro-porosities on the surface such as some in the zone 'E' (marked in yellow) are not inspected. The potential cause is the IR camera resolution limitation. Statistically the micro-



porosities with a diameter of less than  $54\ \mu\text{m}$  are not inspected in Fig. 4 (a).

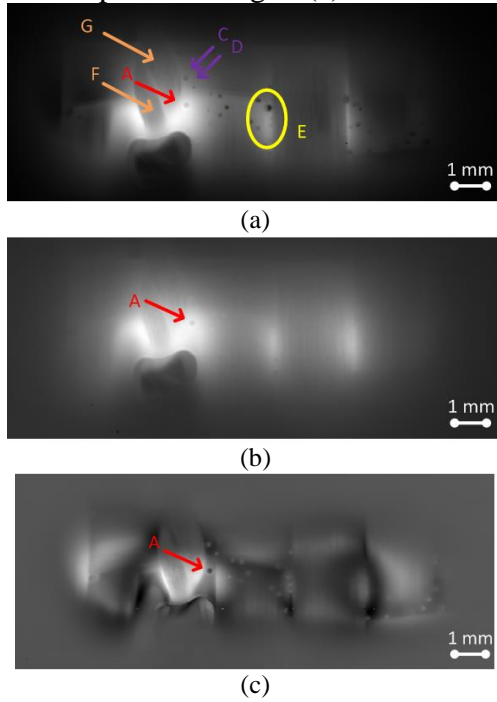


Figure 4: The micro-laser line thermography results: (a) cold image, (b) contrast rectification, (c) PCT.

In Fig. 4 (a), the micro-porosity ‘A’ (marked in red) is inspected. However, it is not inspected on the surface shown in Fig. 3 (a). It appears from the depth of  $90\ \mu\text{m}$  shown in Fig. 3 (b). Figure 3 (b) shows the x-ray tomography image from the depth of  $90\ \mu\text{m}$ . The micro-porosity ‘A’ measures a diameter of  $0.162\ \text{mm}$ . The micro-porosity ‘A’ can be inspected more clearly in the infrared image with contrast rectification shown in Fig. 4 (b). Figure 4 (c) shows the infrared image from principal component thermography (PCT). In Fig. 4 (c), the performance of the micro-porosity ‘A’ is exceptional (darker in contrast) compared to the other micro-porosities. Micro-laser line thermography can detect the micro-sized internal defects in the sample. However, the depth and the size of defects can affect the detection results.

Figure 3 (c) shows the x-ray tomography image from the depth of  $0.18\ \text{mm}$ . The micro-porosity ‘B’ (marked in blue) is inspected and has a diameter of  $0.216\ \text{mm}$  from the depth of  $0.18\ \text{mm}$ . However, the micro-porosity ‘B’

cannot be inspected in the infrared images. One potential cause is that the depth of  $0.18\ \text{mm}$  exceeds the IR camera detection limitation with the laser beam power of  $2.9\ \text{W}$ . Another potential cause is that the micro-porosity ‘B’ is below the fiber ‘F’ (marked in orange) shown in Fig. 3 (a) and Fig. 4 (a). It might reduce the heat transmission. A finite element simulation could be contributive to the analysis.

### 3.2. Finite element modeling and simulation

A finite element simulation was performed to analyze the micro-porosities ‘A’ and ‘B’. A model was implemented into COMSOL Multiphysics as a user-defined material model for predicting the non-linear behavior of heat transmission in the sample. The model was validated for the experimental results. Finally a comparison of the experiments and simulation was conducted. The geometrical model needed for finite element discretization was developed from measurements using  $18\ \mu\text{m}$  x-ray tomography. The laser-line power is  $2.9\ \text{W}$ . The power was tested in the lab. The power density is  $2.9\ \text{W} / (3\ \text{mm} \times 10\ \text{mm})$ . The laser line covered an area of  $2.5\ \text{mm} \times 0.5\ \text{mm}$ . Therefore, the power on the model is  $2.9\ \text{W} \times (2.5\ \text{mm} \times 0.5\ \text{mm}) / (3\ \text{mm} \times 10\ \text{mm})$ . The heating time is  $0.5\ \text{s}$ .

Figure 5 (a) shows the x-ray tomography measurements. Figure 5 (b) shows the corresponding model geometrical parameters. The length of the fiber ‘F’ is  $5\ \text{mm}$ , and its width is  $0.8\ \text{mm}$ . The length of the fiber ‘G’ is  $4\ \text{mm}$ , and its width is  $0.8\ \text{mm}$ . The thickness of fiber ‘F’ and ‘G’ is  $90\ \mu\text{m}$ . In Fig. 5 (a), the micro-porosities ‘A’ and ‘B’ cannot be inspected because they are below the surface. However, their positions are indicated.

The parameters of the micro-porosities ‘A’ and ‘B’ are shown in Fig. 5 (c). The parameters are also measured using x-ray tomography. The micro-porosity ‘A’ appears from the depth of  $90\ \mu\text{m}$  to the depth of  $0.36\ \text{mm}$ . It has a diameter of  $0.162\ \text{mm}$  to  $0.306\ \text{mm}$ . The micro-porosity ‘B’ appears from the depth of  $0.18\ \text{mm}$  to the depth of  $0.504\ \text{mm}$ . It has a diameter of  $0.216\ \text{mm}$  to  $0.36\ \text{mm}$ .

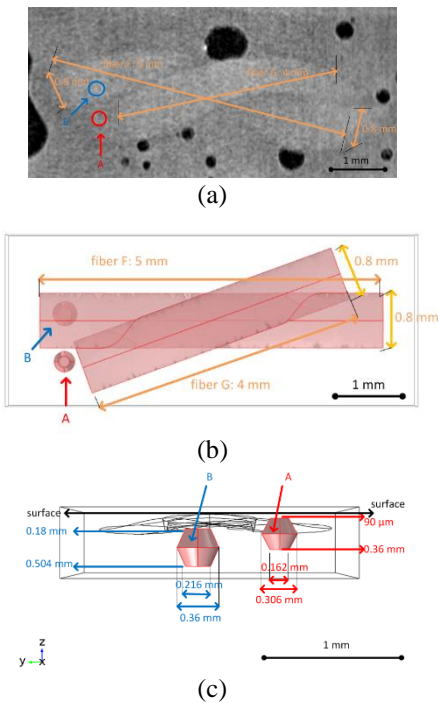


Figure 5: (a) The 18  $\mu\text{m}$  x-ray tomography measurements (surface), (b) the corresponding model geometrical parameters, (c) the geometrical parameters of the porosities ‘A’ and ‘B’.

Figure 6 (a) shows the simulation surface temperature distribution from the heating time 0.5 s. In Fig. 6 (a), the temperature on the position of the micro-porosity ‘A’ is much higher than that of the micro-porosity ‘B’.

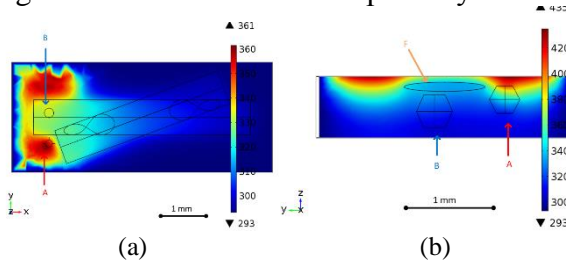


Figure 6: Slice temperature distribution when the heating time is 0.5 s: (a) x-y dimension, (b) y-z dimension.

Figure 6 (b) indicates the cause of the phenomenon inspected from the micro-laser line thermography experiments. The fiber ‘F’ reduced the heat transmission towards the micro-porosity ‘B’. It is the major reason that the micro-porosity ‘B’ was not inspected in the infrared results, but inspected in the x-ray results. A locked-in infrared inspection might be more effective to inspect micro-porosities below fiber.

## 4. Conclusion

A new micro-laser line thermography was defined. 18  $\mu\text{m}$  resolution x-ray tomography was used to validate the micro-laser line thermography results. A comparison of micro-laser line thermography and high-resolution x-ray tomography was conducted. Then a finite element analysis was performed on the micro-laser line thermography results. The geometrical model needed for finite element discretization was developed from measurements using 18  $\mu\text{m}$  x-ray tomography. The model was validated for the experimental results. Finally a comparison of the experiments and simulation was conducted. As a conclusion, micro-laser line thermography can detect the micro-sized internal defects in the sample. However, the depth and the size of defects affect the detection results. Statistically the micro-porosities with a diameter of less than 54  $\mu\text{m}$  cannot be inspected in the micro-laser line thermography results. Micro-laser line thermography can detect the micro-porosity (a diameter of 0.162 mm) from the depth of 90  $\mu\text{m}$ . However, it cannot detect the internal micro-porosity (a diameter of 0.216 mm) from the depth of 0.18 mm. The major cause is that the porosity with the diameter of 0.216 mm is below a fiber, which reduced the heat transmission.

## References

1. H. Zhang, M. Genest, F. Robitaille, X. Maldague, L. West, S. Joncas, and C. Leduc, Infrared thermography, ultrasound c-scan and microscope for non-destructive and destructive evaluation of 3d carbon fiber materials: a comparative study, in SPIE Sensing Technology+ Applications, 94850X–94850X, International Society for Optics and Photonics (2015).
2. T. Li, D. P. Almond, and D. A. S. Rees, Crack imaging by scanning laser-line thermography and laser-spot thermography, Measurement Science and Technology 22(3), (2011) 035701.

# LWIR InAs/GaSb Superlattice Photodiodes with Different Barrier Structures

J. Chen, Zh. Xu, F. Wang, Y. Zhou, J. Xu and L. He

<sup>1</sup> Shanghai Institute of Technical Physics, Chinese Academy of Sciences  
500 Yutian Road, Shanghai, 200083, China  
Email: jianxinchen@mail.sitp.ac.cn

In this paper, we will present our recent works on LWIR InAs/GaSb superlattice infrared photodetectors with different barrier structures. The photodetectors have  $pB\pi Bn$  structures with 15ML InAs/7ML GaSb as the absorption regions ( $\pi$  region), corresponding to a cutoff wavelength of about 12 $\mu\text{m}$ . 7ML InAs/7ML GaSb superlattices were employed as electron barriers while different schemes, such as InAs/AlSb and InAs/GaSb superlattices are used as hole barriers. Graded InAs/GaSb superlattice was inserted between the absorption region and the InAs/GaSb hole barrier to smooth out band transition. All the barrier structures achieved excellent electrical and optical performances at 77K temperature. The graded barrier structure has about 17% higher current response than the abrupt structure.

## Introduction

InAs/GaSb type-II superlattices have attracted significant attentions due to their excellent properties for detection of infrared radiation. These heterostructures are leading candidates for the next generation of infrared photodetectors. They theoretically have important advantages over the existing material systems, primarily HgCdTe alloys, especially at long wavelength and very long wavelength regime [1-4].

In the past few years, type-II InAs/GaSb superlattices (T2SL) infrared photodetectors have been developed rapidly [5-8]. Especially for long wavelength infrared (LWIR) photodetectors, large format 1K $\times$ 1K focal plane arrays have been realized a couple of years ago. However, despite the rapid progress, the properties of the T2SL infrared detectors reported now still has a big gap compared with the theory respect. One important issue that limits the SL detector performances is the demanding on superlattice material quality. Though they have a much longer Auger lifetime than HgCdTe materials, T2SLs have a much shorter generation-recombination lifetime than HgCdTe. The main reason comes from higher SRH recombination center densities in

T2SL structures. Therefore, in one hand it is desired to grow high quality superlattice materials with high crystal perfection for device applications. A T2SL detector usually consists of several hundred periods of alternating InAs and GaSb layers. Consequently, there exist hundreds of interfaces (IFs) in InAs/GaSb superlattices. The interface properties play an important role in determining the T2SL material quality.

On the other hand, one can take the advantages of the flexible band alignments in InAs/GaSb/AlSb heterostructure to design barrier structures to suppress the dark currents. Especially for LWIR superlattice detectors, one can employ mid wavelength infrared (MWIR) superlattice structures in LWIR P-I-N structures to form barrier heterostructures. There are different schemes for these barrier heterostructure infrared detectors. The core idea is to block the transportation of majority carriers which act as dark currents, however, not to impede the transportation the photo-generated minority carriers which act as signals. Typically MWIR InAs/GaSb superlattices are employed as electron barriers and InAs/AlSb or InAs/(GaSb/AlSb/GaSb) as hole barriers.

In this paper, we will report the design, fabrication and comparison of different barrier heterostructure LWIR superlattice photo-detectors. In particular, we will reports a double barrier heterostructure with a specially designed InAs/GaSb superlattice as the

hole barrier. In this novel superlattice detector, the whole structure is Al-free which may help to improve the materials' electrical properties.

## Experiments

The superlattice materials were grown on (100) GaSb substrates using a molecular beam epitaxy (MBE) system equipped with As and Sb valved cracker sources. Thermal effusion cells are used as Ga and In sources. Si and Be are employed as n-type and p-type dopants, respectively. Prior to the growth, the surface oxides of the GaSb substrates were thermally desorbed, which was monitored by reflection high energy electron diffraction (RHEED). The growth temperature was set at around 400°C measured by a calibrated infrared pyrometer. The growth rates were 1ML/s for GaSb and 0.75ML/s for InAs, respectively.

The lattice-mismatch of the superlattices to GaSb substrates was tuned by fine designing the interface structures and growth process, such as IF layer thickness and composition. Fig.1 shows a high resolution X-ray double crystal diffraction rocking curve, showing the full width of half maximum of its 0<sup>th</sup> order satellite peak as narrow as 19 arc sec.

The absorption region of the LWIR photo-detectors is composed of 15ML InAs/7ML GaSb superlattices. The electron barrier region consists of 7ML InAs/7ML GaSb superlattices. Different superlattice structure were employed as hole barriers. One structure is conventional 16ML InAs/4 ML AlSb superlattice, and the other is a novel 8ML InAs/4 ML GaSb superlattice. Graded superlattices with varying InAs/GaSb thickness ratio were inserted between the absorption and barrier regions to smooth out band transitions. This will help to cancel a “spike” in the abrupt heterostructure and to prevent carrier accumulation in the interfaces. The grown photodetector structures were processed into single-element devices using standard optical lithography, wet chemical etching, and E-beam evaporation of top and

bottom Ti/Pt/Au ohmic contacts. Current-voltage (I-V) and optical response measurements were performed at liquid nitrogen temperature (around 77K).

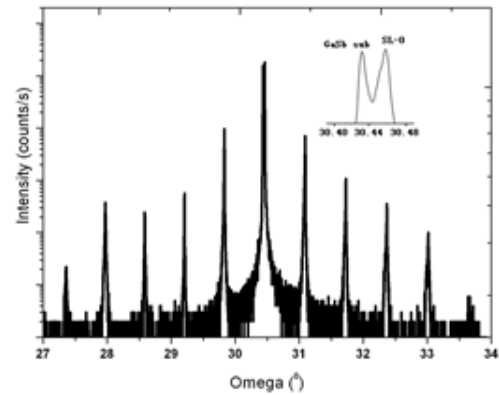


Fig.1. HRXRD curves for 200 periods of 12 ML InAs/ 12ML GaSb SL

## Results and Discussion

### pBπBn structure with InAs/AlSb hole barrier

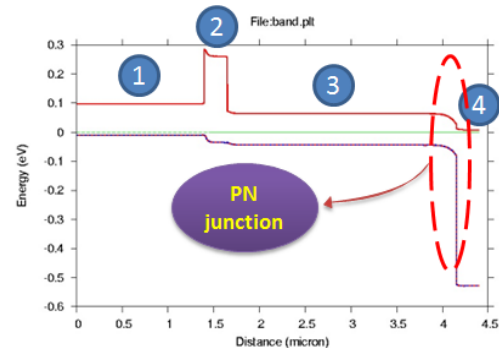


Fig.2 Potential energy curve of a pBπBn superlattice photodetector

Fig.2 shows the band diagram of a pBπBn photodetector with InAs/AlSb as the hole barrier. The detector consists of four regions. Region one is Be-doped superlattice contact layer, region two the 7ML InAs/7ML GaSb electron barrier, region three the 15ML InAs/7ML GaSb optical absorption region(π region), and region four the 16ML InAs/4 ML AlSb N-type hole barrier. The absorption region was weak P-type doped to achieve electron as minority carriers. The PN junction position was marked by a dashed “oval”.

The detector has a absorption layer thickness of 2.2 μ m. Fig. 3 shows the measured current-voltage curve of a processed photodetector. The device has

100% cutoff wavelength of  $12\ \mu\text{m}$ . The dark current density at  $-20\text{mV}$  bias was  $5.8 \times 10^{-4}\text{A/cm}^2$ . The differential resistance-area product at zero bias was  $18\ \Omega\text{cm}^2$ .

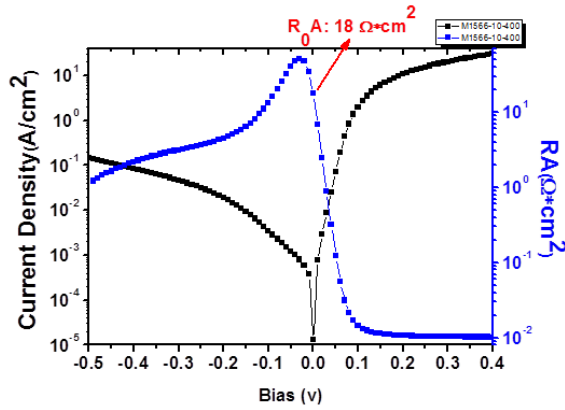
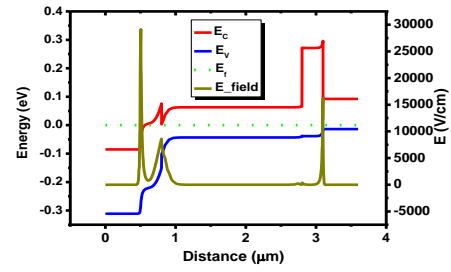


Fig.3 Current-voltage and dynamic resistance-area product of the pBπBn superlattice photodetector as a function of bias

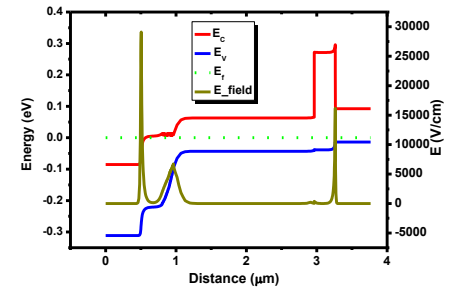
### pBπBn structure with InAs/GaSb hole barrier

Fig.4 shows the band diagrams of (a) abrupt interface and (b) graded interface pBπBn superlattice detector structures. The two structures are similar to the one shown in Fig.2 except that 8ML InAs/4ML GaSb superlattice was used as the hole barriers instead of InAs/AlSb superlattice. Though an 8ML InAs/4 ML GaSb has a smaller hole barrier height compared with the InAs/AlSb barrier, its MBE growth temperature is consistent with that of the superlattice absorption region. The InAs/GaSb superlattices are usually grown at the temperature of around  $400^\circ\text{C}$ . In contrast, Al containing materials require an elevated substrate temperature during MBE growth.

In the structure as shown in Fig.4(b), a graded superlattice layer was inserted between the absorption layer and the hole barrier layer. The graded superlattice was designed in such a way that starting from the absorption layer, we gradually decrease the InAs layer thickness from 15 ML to 7ML and GaSb layer thickness from 7ML to 4ML in each period.



(a)



(b)

Fig.4 Potential energy diagram of (a) abrupt and (b) graded pBπBn photodetector with InAs/GaSb superlattice as hole barriers

Comparing Fig. 4(a) and (b), one may observe that there is a “spike” in conduction band at the interface of the hole barrier and the absorption region in Fig. 4(a) while in Fig. 4(b) there is no such a “spike” thanks to the graded superlattice layer.

Fig. 5 shows the response spectrum of the graded pBπBn structure with a 100% cutoff wavelength of around  $12\ \mu\text{m}$ . The abrupt pBπBn has a similar shape of response spectrum except a slightly shorter cutoff wavelength of  $11.5\ \mu\text{m}$ . This difference probably comes from growth variation from run to run. Their electrical performances are also similar. The abrupt pBπBn has a dark current of  $8.8 \times 10^{-4}\text{A/cm}^2$  while the graded pBπBn has a dark current of  $3.0 \times 10^{-3}\text{A/cm}^2$ . The difference of dark current in the two structures is associated with the difference of cutoff wavelength since the dark current of an infrared detector is sensitive to its cutoff wavelength.



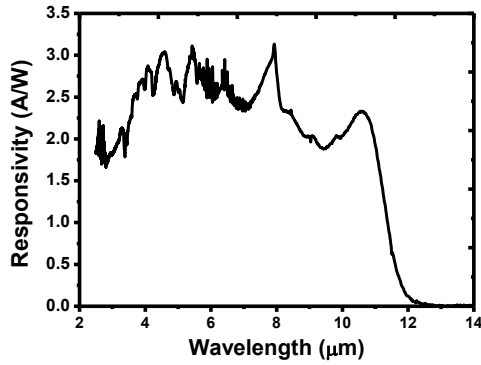


Fig.5 The response spectrum of the graded pBπBn superlattice photodetector

Fig.6 shows the measured blackbody current response of the two structures at different bias. The blackbody temperature was set at 500K for the measurement. It can be observed that the graded structure has in average 17% higher current response than the abrupt structure. We would attribute this improvement in photo-response to the conduction band grading at the interface of the hole barrier and the absorption region. The band grading gets rid of the conduction band “spike” at the interface which may impede the minority carrier transportation from the absorption region to PN junction.

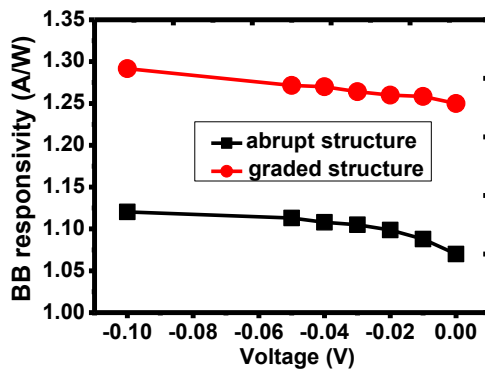


Fig. 6 Measured blackbody response of the abrupt and graded pBπBn superlattice photodetector at different bias

## Conclusion

We have designed, fabricated and measured LWIR InAs/GaSb superlattice photo-detectors with different barrier

structures. Photodetectors with either InAs/AlSb or InAs/GaSb hole barriers can achieve low dark currents. In term of MBE growth, InAs/GaSb hole barrier are consistent with the InAs/GaSb absorption region. Both abrupt and graded interface were adopted for InAs/GaSb hole barrier structure. The two structures have similar photo-response spectra and dark current characteristics. However, the graded structure photo-detector has 17% in average higher current response than the abrupt structure photodetector.

## References

1. D.L. Smith, C. Maihlot, Proposal for strained type II superlattice infrared detectors. *J. Appl. Phys.* 62 (1987) 2545.
2. E.R. Youngdale, J.R. Meyer, C.A. Hoffman and F.J. Bartoll, Auger lifetime Enhancement in In-GaInSb superlattices, *Appl. Phys. Lett.* 64 (1994) 3160-3162.
3. Rogalski, Material Considerations for Third Generation Infrared Photon Detectors. *Infrar. Phys. & Technol.* 50 (2007) 240.
4. S.D. Gunapala, D.Z. Ting, C.J. Ting, C.J. Hill, J. Nguyen, S. Soibel, S.B. Rafol, S.A. Keo, J.M. Mumolo, M.C. Lee, J.K. Liu, B. Yang and A. Liao, Demonstration of 1K x 1K Long-wave and Mid-wave Superlattice Infrared Focal Plane Arrays, *Proc. SPIE* 7808 (2010) 7808021.
5. A. Hood, A.J. Evans, A. Ikhlassi, G. Sullium, E. Piquette, D.L. Lee, W.E. Tennant, I. Vurgaftman, C.L. Canedy, E.M. Jackson, J.A. Nolde, C. Yi, E.H. Aifer, LWIR High Performance Focal Plane Arrays Based on Type II Strained Layer Superlattice Materials, *Proc. SPIE* 7660 (2010) 76601M1.
6. M. Sundaram, A. Reisinger, R. Dennis, K. Patnaude, D. Burrows, J. Bundas, K. Beech, R. Faska, D. Manidakos, 1024x1024 LWIR SLS FPAs-Status and Characterization, *Proc. SPIE* 8353 (2012) 83530W.
7. P. Manurkar, S.R. Darvish, B.M. Nguyen, M. Razeghi, J. Hubbs, High performance long wavelength infrared megapixel focal plane array based on type-II superlattices, *Appl. Phys. Lett.* 97 (2010) 193505.
8. J.B. Rodriguez, P. Christol, L. Cerutti, F. Chevrier, A. Joullié, MBE growth and characterization of type-II InAs/GaSb superlattices for mid-infrared detection, *J. Crystal Growth* 274 (2005) 6.



# NIR window and Near-Field detection of gold nanoshells

M. D'Acunto<sup>1,2</sup>, A. Cricenti<sup>2</sup>, M. Luce<sup>2</sup>, D. Moroni<sup>1</sup>, O. Salvetti<sup>1</sup>

<sup>1</sup> ISTI-CNR, via Moruzzi 1, 56124, Pisa. Italy. name.surname@isti.cnr.it

<sup>2</sup> ISM-CNR, via Fosso del Cavaliere, 100, 00133 Rome. name.surname@ism.cnr.it

The optical properties of metal nanoparticles play a fundamental role for their use in a wide range of applications. In hyperthermia treatment, for example, the nanoshells (core+metal shell) pre-embedded in a tumor cell absorb energy when exposed to the appropriate wavelengths of a laser beam and heat up thus destroying the tumor cell; nevertheless, the healthy tissues along the laser path are not affected. This is because most biological soft tissues have a relatively low light absorption coefficient in the NIR regions, characteristic known as the tissue optical window. Over such window, NIR light transmits through the tissues with the scattering-limited attenuation and minimal heating preventing the healthy tissues. In this paper, we place emphasis on the NIR response of ultrasmall metal nanoparticles and nanoshell clusters. The necessity to focus the attention on such ultra-small aggregates is based on the availability of experimental SNOM data recorded in the recent past. The optical responses of such aggregates have been analytically deduced by the reformulation of the Mie theory in evanescent wave regime. In addition, FDTD simulations were addressed to validate the numerical results. In turn, the experimental results obtained with an aperture SNOM were also enlightened.

## Introduction

The optical properties of metallic (gold, silver) nanoparticles in the visible and near-infrared (Vis-NIR) domains are governed by the collective response of conduction electrons, the so-called plasmon excitations. These form an electron gas that moves away from its equilibrium position when perturbed by an external light field inducing surface polarization charges that act as a restoring force on the electron gas. The result is a collective oscillatory motion of the electrons characterized by a dominant resonance band that, depending by the shape and size of the gold nanoparticles, falls in the Vis-NIR range [1]. Plasmons produce strong effects in both the near- and far-field response of gold nanoparticles. The far-field is fundamental for describing the macroscopic properties of absorption and scattering in colloidal dispersions and metamaterials.

The near-field properties play a key role for describing the surroundings of the particle within a distance smaller than the wavelength of

light, i.e., the optical properties between nanoparticles, and the interaction with nearby molecules and sensing powering as in the SERS techniques. Since two decades, the near-field is experimentally detected via scanning near-field optical microscopy (SNOM). It is rather surprising that near-field properties of gold nanoshells can act as nanolens with near-field enhancements that vary from 3 times for gold nanoshells with outer radii of 12-15nm, until an enhancement factor of ~450 for assemblies of gold nanospheres that can be thought of rows of nanolenses [1].

As a consequence the optical properties of nanoshell clusters play a fundamental role for their use in a wide range of applications. For example, in hyperthermia treatment, the nanoshells pre-embedded in a tumor absorb energy when exposed to the appropriate wavelengths of a laser beam and heat up thus destroying the tumor; nevertheless, the healthy tissues along the laser path are not affected [2]. This is because most biological soft tissues have a relatively low light absorption coefficient in

the Vis and NIR regions, characteristic known as the tissue optical window. Over such window, NIR light transmits through the tissues with the scattering-limited attenuation and minimal heating preventing the healthy tissues.

In this paper, we place emphasis on the NIR response of ultra-small nanoshell clusters, aggregates from 2 to 3 nanoshells or  $3 \times 3$  clusters. The necessity to focus the attention on such ultra-small aggregates is based on the availability of experimental SNOM data recorded in the recent past. The optical responses of such aggregates have been analytically deduced by the reformulation of the Mie theory in evanescent wave regime. In addition, FDTD simulations were addressed to validate the numerical results. In turn, the convolution effect of the SNOM probe tip with the nanoshell clusters was also enlightened.

### Optical response from single to randomly distributed clusters of gold shell nanoparticles: numerical and simulated results

Absorption and scattering of light by an arbitrary  $N$ -spherical nanoshell cluster depend on the sizes of the primary nanoshell, the size and topology of the cluster, the particles materials and the polarization and propagation direction of the incident wave. The simplest aggregate is a pair of nanoshells. In this case, two principal excitation modes of the aggregate are obtained: the longitudinal mode, when the electric field vector of the incident wave is along with the axis of the pair, and transverse mode with the electric field being perpendicular to this axis. In the general case of arbitrary incidence of the plane wave both modes contributes to a certain amount to the absorption and scattering by the pair. In the case of a three nanoshell cluster (triplet aggregates), the situation is very close to pair particles when the three particles are located along a line (linear triplet cluster), like in figure 1. In the case of triplet aggregates, plane waves  $p$ -polarized, characterized by the transversal oscillation of the electric field, produce the most relevant plasmon oscillation between the nanoshells, with the appearance of supplemental

modes due to the geometry of the cluster. For higher and complex clusters, extinction and scattering responses become more complicate, so we will focus the attention on the difference between a single nanoshell and a linear triplet cluster.

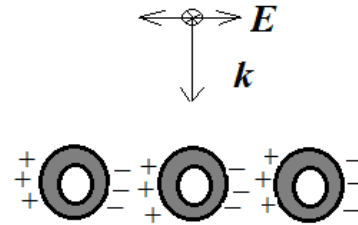


Fig. 1. A linear triplet cluster of nanoshells perpendicular to wave vector with  $p$ -polarized and  $s$ -polarized electric field vector (perpendicular to the plane wave and denoted by the cross symbol). Since the  $p$ -polarization presents an electric field oscillating along the axis of the cluster (longitudinal mode), the plasmonic effect is amplified and supplemental modes due to the interaction between subsequent nanoshells can be observed.

The optical properties of nanoshell clusters, obtained using the extended Mie theory in near-field conditions, can be described in terms of normalized efficiencies for the extinction, scattering and absorption cross sections divided by the geometrical cross section of the clusters. The incident radiation can be  $p$ -polarized or  $s$ -polarized and its wave vector is directed perpendicularly to the nanoparticle array plane as in figure 1. The absorption efficiency of the numerical integration of Mie equations for a single nanoshell and a triplet or a  $3 \times 3$  nanoshell clusters using the generalized multiparticle Mie approach in evanescent wave conditions are summarized in figure 2. Absorption efficiency is also the prevalent optical mechanism for particle with a varying gold layer in the range 0-100nm, with a  $\text{BaTiO}_3$  core dimension fixed of 100nm [3].

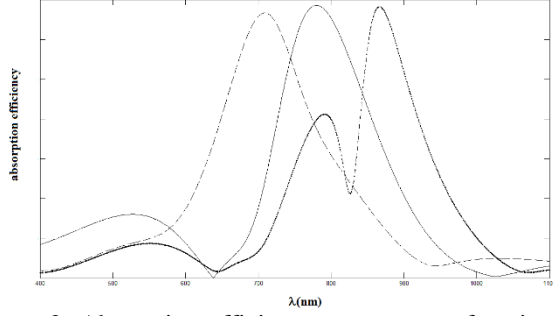


Figure 2. Absorption efficiency spectra as a function of external e.m. wavelength for, respectively, an isolated BaTiO<sub>3</sub>-gold (80nm-40nm) nanoshell, dashed line, for a triplet aggregate for the same nanoshell composition, continuous line, and 3×3 nanoshell cluster, dot-dashed line.

A FDTD simulation model is applied to analyze the near-field properties around the irradiated nanoparticles. This computational technique is commonly recognized to give an adequate picture of the electromagnetic field distribution in the near and far-fields around structures with arbitrary shapes. The main signal observed in the FDTD simulation is the Poynting vector of the evanescent wave. Since the Poynting vector is also the collected signal by the SNOM, the FDTD simulation gives a results that can be immediately compared with the experimental results. However, the observed intensity collected by the SNOM aperture tip needs a comment. As  $I_{inc}$  we choose the incident intensity, averaged over the cross-sectional area of the SNOM aperture tip perpendicular to the Poynting vector ( $\mathbf{S}=\mathbf{E}\times\mathbf{H}$ ) of the evanescent wave, then we have

$$I = \frac{1}{\pi a^2} \iint \langle S_{inc} \rangle n dA = I_{inc} \exp(-2\kappa d) \frac{I_1(2\kappa a)}{\kappa a} \frac{n_s}{n_M} \sin \theta_i \quad (1)$$

where  $I_1(2\kappa a)$  is the modified Bessel function of first order with argument  $2ka$ , and the normalization factor

$$\eta = \frac{I_1(2\kappa a)}{\kappa a} \frac{n_s}{n_M} \sin \theta_i \quad (2)$$

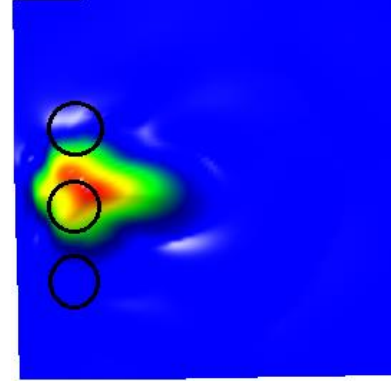


Figure 3. FDTD plot of the scattered intensity (Poynting vector) from a triplet cluster for a wavelength of  $\lambda=795\text{nm}$ , as observed at  $z=20\text{nm}$  from the particle surface.

In Eq. (1),  $d$  is the  $z$ -height of the evanescent wave before the complete extinction, in the FDTD simulation we tested the Poynting vector for a  $z=10\text{-}30\text{nm}$  range, figure 3.

To exhibit the relative absorption and scattering ability of the nanoshells, the cross sections for absorption and scattering can be defined as  $\sigma_{abs} = W_{abs}/I_{inc}$  and  $\sigma_{scat} = W_{scat}/I_{inc}$  respectively, while the efficiencies are defined as  $Q_{abs} = \sigma_{abs}/A$  and  $Q_{scat} = \sigma_{scat}/A$ , for the absorption and the scattering processes, respectively. Here, the  $I_{inc}=(1/2)\epsilon_0 c E^2$  represents the intensity of the incident wave,  $A=\pi r^2$  is the particle cross-section projected onto a plane perpendicular to the incident wave, and  $r$  is the total radius on the nanosphere. Finally, the absorption and scattering energy  $W_{abs/scat}$  are defined respectively as

$$W_{abs} = \frac{1}{2} \text{Re} \left[ \iint (\mathbf{E}_{tot} \times \mathbf{H}_{tot}^*) \cdot \mathbf{n} ds \right] \quad \text{and} \\ W_{scat} = \frac{1}{2} \text{Re} \left[ \iint (\mathbf{E}_{scat} \times \mathbf{H}_{scat}^*) \cdot \mathbf{n} ds \right] \quad (3)$$

In far field, we can insert the components fields inside the eqs (3), and integrating on all a solid angle; on the contrary, in near field, if we consider a finite dimension of tip aperture, we have that the scattered and absorbed intensity are proportional to the solid angle.

In addition, if we consider a near field solution of electric and magnetic fields and the field enhancement in  $z$ -direction in proximity of the SNOM probe tip, under some specific conditions we can observe intense enhanced absorption. Since the  $E_z$  components under the SNOM tip is about 10 times larger compared to the in-plane components, it is reasonable to suppose that when the probe signal displays a point-like absorption peaks, this can be identified with a nanoshell [4]. This is because the field enhancement caused by the local surface plasmon resonance mainly focuses on the metal-dielectric interface (and decays exponentially) is not absorbed by the biological tissue due to the transparency window.

### Experimental Results

The extinction signals of cells and small clusters of nanoshells seed on  $\text{SiO}_2$  substrates in air were measured making use of a home-made SNOM operating in air in collection mode with different illumination wavelengths ranging from visible to near infrared.

The SNOM used for the reflection mode measurements is composed by two separable cylindrical supports: the lower one contains the sample holder mounted on top of a piezoelectric scanner which is embedded in a motor controlled  $x$ - $y$ - $z$  stage. A piezo-modulated stretched optical fiber with a few tens of a nanometer pinhole and a shear-force apparatus mounted inside the top cylinder allow for topographic measurements. In figure 4, a schematic sketch of the experimental setup is shown. Any additional information on the home-made SNOM can be found in [4]. Home-made procedure for tip manufacturing was based on chemical etching process producing tips with aperture of nearly 50nm diameter. After etching process, the tip are coated by a tiny metallic (evaporated aluminum) layer so as to prevent light from coupling into the fibre from anywhere other than at the aperture of the probe.

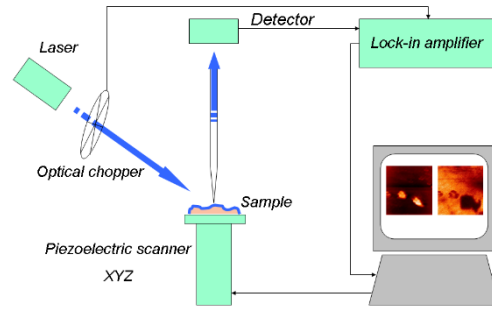


Figure 4. Schematic sketch of the experimental setup used for the SNOM acquisitions.

### Conclusions

Metal nanoshells are a type of nanoparticle composed by a dielectric core and a metallic coating. They show distinctive absorption peaks at specific wavelengths due to surface plasmon resonance with the basic advantage that the wavelengths at which resonance occurs can be tuned by changing the core radius and coating thickness. In this paper, we show the changes of optical response in visible and near infrared wavelengths from single to randomly distributed ultra-small clusters of nanoshells. The results show that the optical signal of a randomly distributed cluster of nanoshells can be supplementary tuned with respect to the case of single nanoshell depending by the geometric configuration of the clusters.

### References

1. S. Maier, Plasmonics: Fundamentals and Applications. Springer, (2007).
2. T.A. Erickson, J.W. Tunnell, in Nanomaterials for the Life Science Vol. 3: Mixed Metal Nanomaterials. Challa S.S:R. and Kumar, Wiley 2009, Year.
3. M. D'Acunto, D. Moroni, O. Salvetti, Advances in Optical Technologies, (2012)
4. A. Cricenti, M. Luce, D. Moroni, O. Salvetti, M. D'Acunto, Opto-electronics Review, 23, 39-45, 2015.

# Temperature controlled laser stimulator for pain research

K.S. Frahm, C.D. Mørch, O.K. Andersen, L. Arendt-Nielsen

Integrative Neuroscience group, SMI, Department of Health Science and Technology, Aalborg University, Denmark.

Heat stimulation of the skin is used in pain research to investigate heat pain sensitive nerve fibers. The aim of the study was to develop and validate a temperature controlled near infrared laser stimulator. A Monte Carlo model of photon absorption and a finite element model of heat transfer were established to estimate heat distribution in the skin. In a physical setup an infrared camera assessed the skin surface temperature and provided input into a PID controller adjusting the laser intensity. The model showed that the temperature at the skin surface is similar to the temperature at the dermal-epidermal junction where the pain sensitive nerve fibers terminate. In a validation study it was shown that the skin surface temperature can be controlled by the feedback controlled system, and thus showing the feasibility of using temperature controlled laser stimulator in pain research.

## Introduction

Thermal stimulation has proven a vital tool in pain research and has been used for several decades [1,2]. Often stimulation is delivered using contact heat thermodes or CO<sub>2</sub> lasers. CO<sub>2</sub> lasers emit light in the far infrared spectrum, meaning the energy is absorbed in the most superficial layers of the stratum corneum (~20µm). Previously, we have shown that the highest abundance of heat sensitive nociceptors (pain sensing nerve fibers) is located close to the dermoepidermal junction (DEJ) [3]. There are no nerve fibers present within stratum corneum [4] (M). Therefore, the thermal energy of CO<sub>2</sub> laser and thermodes are not delivered at the location of the heat-receptive nociceptive nerve endings and will have to be conducted through the skin to reach the heat-sensitive nociceptors. Near-infrared photons will penetrate deeper into the skin and thus the energy is delivered closer to the heat sensitive nociceptors.

Previous studies have indicated different heat sensitive nociceptors innervating the hairy and glabrous skin [5]. But this study applied a CO<sub>2</sub> laser setup. Moreover, the thicker epidermis in glabrous skin [2,3] may insulate the nociceptors from the thermal energy. Therefore, this study will investigate these differences

using a novel temperature controlled laser stimulator, using a near-infrared laser to heat the skin.

Thus, the aim of this study was first to ensure that the temperature at the skin surface was similar to the temperature at the nociceptor level when stimulating with a near-infrared laser and then compare it to CO<sub>2</sub> laser and contact thermode stimulation. Secondly to develop a temperature controlled laser stimulation system and use it to investigate the nociceptive system of healthy subjects, especially differences between hairy and glabrous skin.

## Materials & Methods

### *Part I. Model*

#### *Modeling the heat stimulation*

To simulate the heating of the tissue, a model was generated. The model was established as a 2D axial symmetric model (Fig. 1). The model comprises three layers, the epidermis, dermis and subcutaneous fat. The thickness of the epidermis was 50µm in hairy skin and 133µm in glabrous skin.

The thickness of the dermis was 1.3mm. The subcutaneous fat had a thickness of 4mm.

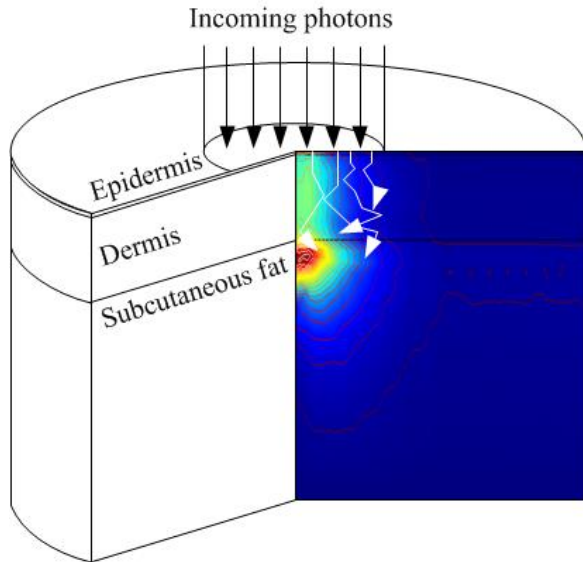


Fig. 9. Overview of the concept of the combined Monte Carlo photon simulation model and the finite element heat transfer model. The model comprised 2D axial symmetry. The black arrows indicate photons from the laser before entering the tissue and white arrows indicates the photons being scattered and absorbed inside the tissue. The colouring scheme indicates the temperature distribution in the tissue.

The first part of the model simulated the absorption of photons using the Monte Carlo (MC) technique [6]. The optical properties are seen in table 1.

Coefficients	Epidermis	Dermis	Fat
Absorption coef., $\mu_a$ [ $m^{-1}$ ]	100	100	120
Scattering coef., $\mu_s$ [ $m^{-1}$ ]	15068	15068	16000
Refractive index, $n$	1.34	1.41	1.46
Anisotropy factor, $g$	0.9	0.9	0.9

Table 1. Optical properties of the MC model

The second part of the model simulated the heat transfer and distribution in the tissue using the finite element method (COMSOL Multiphysics, Sweden). See [3] for further details regarding the finite

element model, the thermal properties are listed in Table 2.

Coefficients	Epidermis	Dermis	Fat
Thermal conductivity, $k$ [ $W/(m \cdot K)$ ]	0.21	0.58	0.16
Density, $\rho$ [ $kg/m^3$ ]	1200	1200	850
Specific heat capacity, $c$ [ $J/(kg \cdot K)$ ]	3600	3800	2300

Table 2. Thermal properties of the finite element model

A model was also created to investigate the temperature profiles in the skin using CO<sub>2</sub> laser and thermode stimulation. CO<sub>2</sub> laser stimulation and thermode stimulation were modeled as in [3].

## Part II. Experimental validation

### Subjects

12 healthy subjects (2 women, age: 22-29 years) participated in the validation study. All subjects gave written consent before starting the experiments. The subjects and investigator all wore protective goggles for the duration of the experiment. The experiments were performed in a temperature controlled room (22°C). All experiments were performed in accordance with the Declaration of Helsinki and were approved by the local ethics committee (ref. no N-20080026).

### Laser stimulation

Thermal stimulation was applied using a 20W near-infrared laser with a wavelength of 970nm (DL-20, IPG, Germany). The laser light was directed through an optical fiber and delivered perpendicular to the skin surface. The laser beam had a diameter of 8mm ( $1/e^2$ ). During laser stimulation the subject was instructed to rate the pain intensity continuously on a Visual Analog Scale (VAS), anchored as 0 – no pain and 10 – maximum imaginable pain.

### Temperature control

An infrared camera (FLiR A40, Sweden) was used to measure the temperature of the irradiated skin. The maximum skin temperature was measured and input into a PID controller



(PID controller toolbox, Labview, National Instruments, USA). Based on the measured temperature, the laser intensity was adjusted to reach the target temperature. The maximum skin temperature was sampled at 10Hz and the laser intensity was adjusted at the same rate.

### Experimental protocol

To investigate differences between skin types, stimulations were delivered both in the hairy skin at the volar forearm and the glabrous skin of the palm. The laser was moved slightly between each stimulation to avoid stimulating the same skin site repetitively.

Two types of staircase stimulations were used; one staircase increased from 35°C to 45°C and one decreased from 45°C to 35°C, both in steps of 1°C. Each temperature plateau lasted 15s.

## Results

### Model

The model showed that the temperature profiles at the surface and DEJ were similar in both glabrous and hairy skin when near-infrared diode laser stimulation was applied (Fig. 2 & 3). In contrast CO<sub>2</sub> laser stimulations (Fig. 4) and thermodes (Fig. 5) showed significant differences between the surface temperature and the temperature at the DEJ.

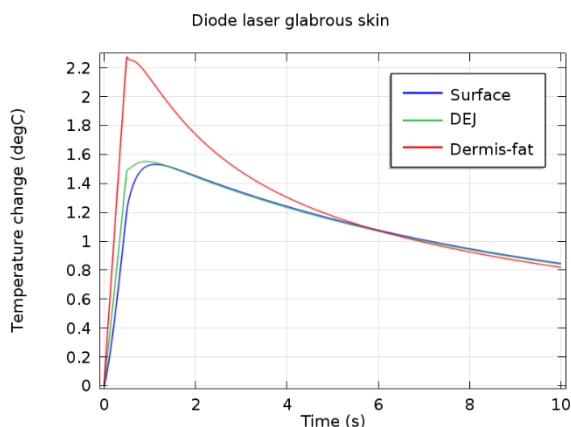


Fig. 10. Simulation of the temporal temperature profiles in glabrous skin using a 970 nm diode laser. The temperature profile at the surface (blue) and dermoepidermal junction (DEJ) were similar. The temperature was highest at the dermis-fat junction, due to insulation of the fat layer. Stimulation intensity was 1W for 0.5s.

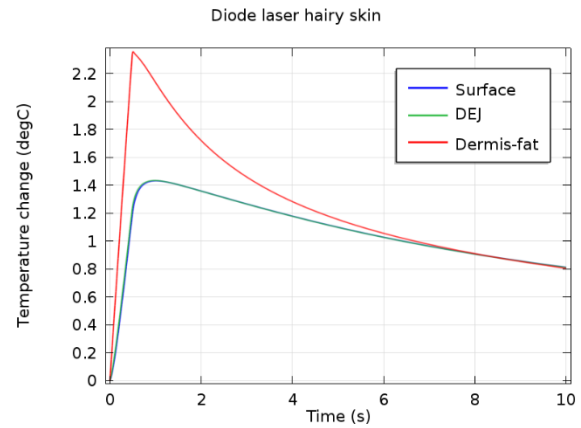


Fig. 11. Simulation of the temporal temperature profiles in hairy skin using a 970 nm diode laser. The temperature profile at the surface (blue) and dermoepidermal junction (DEJ) were similar. The temperature was highest at the dermis-fat border, due to insulation of the fat layer. Stimulation intensity was 1W for 0.5s.

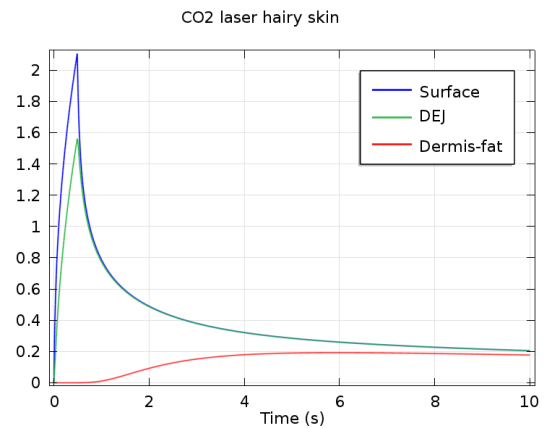


Fig. 12. An example of the temporal temperature profile during a CO<sub>2</sub> laser in hairy skin. Due to the high absorption the surface temperature is more than 25% higher than at the DEJ. Stimulation intensity was 0.2W for 0.5s.

The model also showed that when using a near-infrared laser, the highest temperature increase was likely to be found inside the fat layer rather than in the skin layers (Fig. 1, 2 and 3). This was not because more photons were absorbed in this layer, but more due to the thermal properties of the fat layer (which insulated the heat inside the fat layer) (Table 2).

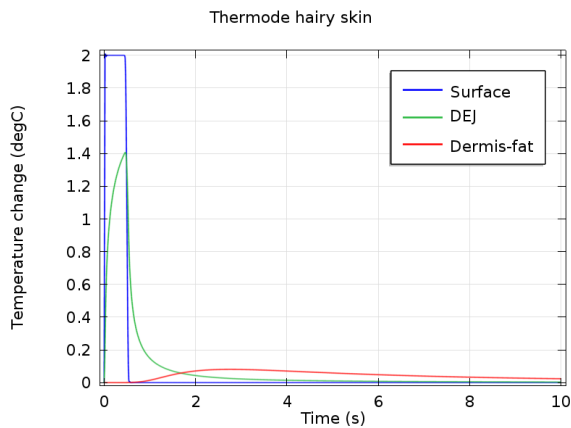


Fig. 13. An example of the temporal temperature profile during a thermode stimulation (contact heat) in hairy skin. The stimulation temperature is set to 2°C above the skin temperature. It can be seen how the temperatures are lower in the deeper layers of the skin.

### Experimental validation

The experiments showed that stimulations for similar surface temperatures were rated more painful in glabrous skin compared to hairy skin (t-test,  $p < 0.01$ ).

Comparing the VAS ratings at different temperature levels showed no significant differences between temperatures below 40 °C. However, for higher temperatures (above 40 °C) most temperatures plateaued gave VAS ratings which were significantly different from all other temperatures, except those immediately adjacent, e.g. 45°C was significantly different to 43, 42, 41°C etc. (t-test,  $p < 0.01$ ). Higher stimulus temperature was fundamentally associated with higher VAS ratings.

### Conclusions

The model showed that using a near-infrared laser the temperature profile at the skin surface and DEJ are very similar, and thus controlling the surface temperature would in essence mean controlling the temperature close to the nociceptor endings. However, an even greater temperature increase may be found inside the fat layer (Fig. 2 and 3), due to the insulating nature of this tissue.

It was shown that the developed system could accurately control the surface temperature;

consequently it can also control the temperature at the depth of the nociceptor endings.

The experimental results indicated that similar stimulations with the near-infrared laser system were perceived more painful in glabrous skin than in hairy skin. This is in contrast to stimulations using CO<sub>2</sub> lasers where the stimulations in hairy skin is rated more painful than glabrous skin [3,5]. This is most likely reflecting that the thermal energy must be conducted through the epidermal layer, whereas in this study the energy is absorbed close to the nociceptor endings when employing a near-infrared laser stimulator.

### References

1. L. Arendt-Nielsen, A. C. Chen. Lasers and other thermal stimulators for activation of skin nociceptors in humans, *Neurophysiol. Clin.*, Vol. 33, pp. 259-268, 2003.
2. E. Marchandise, A. Mouraux, L. Plaghki, F. Henrotte. Finite element analysis of thermal laser skin stimulation for a finer characterization of the nociceptive system. *Journal of Neuroscience Methods*. Vol. 223, pp- 1– 10. 2014
3. K. S. Frahm, O. K. Andersen, L. Arendt-Nielsen, C. D. Mørch. Spatial temperature distribution in human hairy and glabrous skin after infrared CO<sub>2</sub> laser radiation, *Biomed. Eng Online.*, Vol. 9, 69, 2010.
4. M. Hilliges, L. Wang, O. Johansson. Ultrastructural evidence for nerve fibers within all vital layers of the human epidermis, *J. Invest Dermatol.*, Vol. 104, pp. 134-137, 1995.
5. R. D. Treede, R. A. Meyer, S. N. Raja, J. N. Campbell. Evidence for two different heat transduction mechanisms in nociceptive primary afferents innervating monkey skin, *J. Physiol*, Vol. 483 ( Pt 3) pp. 747-758, 1995.
6. S. A. Prahl, M. Keijzer, S. L. Jacques, A. J. Welch. A Monte Carlo Model of Light Propagation in Tissue. *Dosimetry of Laser Radiation in Medicine and Biology*. Vol. 5, pp. 102-111. 1989.

# SKIN TEMPERATURE DYNAMICS DURING AN INCREMENTAL MAXIMAL TEST IN ELITE MALE CYCLISTS

Marco Gargano<sup>1</sup>, Nicola Ludwig<sup>1</sup>, Athos Trecroci<sup>2</sup>, Damiano Formenti<sup>2</sup>, Andrea Bosio<sup>3</sup>, Ermanno Rampinini<sup>3</sup>, Giampietro Alberti<sup>2</sup>

<sup>1</sup> Department of Physics, Università degli Studi di Milano, Italy, marco.gargano@unimi.it

<sup>2</sup> Department of Biomedical Sciences for Health, Università degli Studi di Milano, Italy, athos.trecroci@unimi.it

<sup>3</sup> Human Performance Laboratory, MAPEI Sport Research Centre, Olgiate Olona (Varese), Italy, physiolab@mapesport.it

Monitoring dynamics skin temperature during a prolonged physical exercise is central to assess the athletes' ability to dissipate heat from the skin surface to the environment. In the present study, seven elite cyclists were instructed to complete an incremental maximal cycling test to evaluate their skin temperature response under controlled-environment conditions. Data from thermal images revealed a clear and progressive reduction in skin temperature showing a notable ability by highly-trained cyclists to dissipate heat from the skin surface during an incremental muscular effort.

## Introduction

Infrared thermography (IRT) is an increasing popular method for skin temperature evaluation in athletic activities with a non-contact approach.

IRT has also been widely used in biomedical studies to evaluate human thermoregulation and skin temperature.

During a continued physical activity, muscular exercise causes an excessive metabolic production of heat that the body has to remove avoiding an overly increase of the internal temperature. Through an activation of vasoconstriction and vasodilatation mechanisms, blood flow is drained from core districts to the superficial layers (i.e. skin) to transfer heat for thermal dissipation by sweating [1]. Hence, the ability to dissipate heat, related to the skin temperature, is crucial

to sustain muscular efforts until the end of the exercise.

The aim of this study was to evaluate the skin temperature response during a maximal incremental exercise in elite cyclists under controlled-environment conditions.

## Methods

Seven male elite cyclists participated voluntarily in the study. The mean and standard-deviation values for age, body mass, height, body fat percentage, and oxygen uptake (VO<sub>2</sub> max) of the subjects were: 20.29±1.80 yrs, 70.14±6.00 kg, 1.77±0.03 m, 8.64±2.25 %, 66.89±4.55 ml/kg/min. All subjects were selected for similar anthropometric characteristics as showed in table 1.

Subject	Age (years)	Height (m)	Body mass (kg)	Body fat (%)	VO <sub>2</sub> max (ml/kg/min)
1	21	1.78	74.00	7.70	69.90
2	23	1.81	71.00	4.60	66.70
3	19	1.81	79.00	7.80	65.30
4	20	1.73	66.00	9.00	75.50
5	22	1.80	74.00	11.20	64.50
6	18	1.71	62.50	9.20	64.70
7	19	1.79	64.50	11.00	61.60

Table 3. Subjects' anthropometric and physiological characteristics

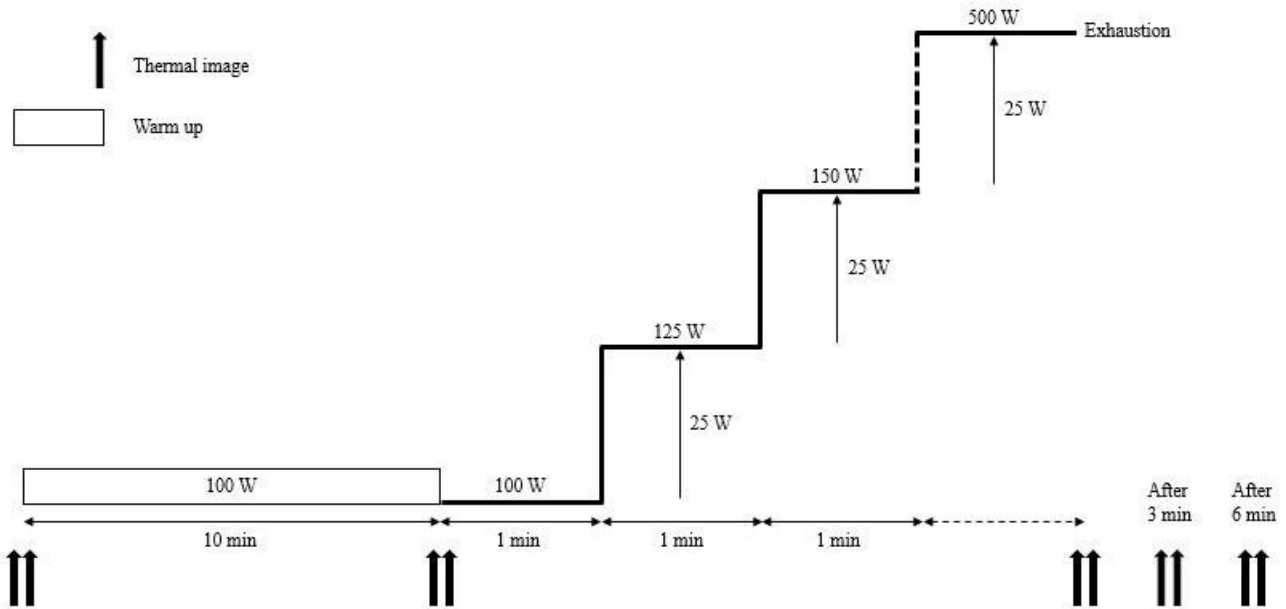


Fig. 1. Protocol of the incremental maximal test on cycle ergometer

According to the declaration of Helsinki, the study was approved by the Ethical Committee of the Università degli Studi di Milano. Subjects were deeply informed of the procedures before their participation, and a written informed consent was signed by them. They were also instructed to avoid high-intensity or strenuous physical activity 24-h prior to testing.

The protocol of the study is shown in Figure 1. After 10 min of warm up performed with a constant load of 100 W, subjects completed an incremental maximal cycling test assessing maximal oxygen uptake and maximal power output. Each participant started at a workload of 100 W with an increase of 25 W every minute until exhaustion. Pedaling cadence was kept constant throughout the test in a range between 80 and 90 rpm. Time to exhaustion point corresponded with the cyclist's

incapacity to maintain a cadence above 80 rpm. Whereas, maximal power output coincided with the workload at the same time.

Two thermal images (AVIO TVS700 micro bolometer uncooled detector) from the front surface of the cyclist's thighs were recorded interspersed by 10 s for each specific time points: pre-exercise (post-warm up) and post-exercise (exhaustion, 3 min and 6 min after the exhaustion). Before the incremental cycling test, subjects rested for 10 min in order to acclimatize the body skin with the temperature of the room. During thermal image acquisitions, subjects were asked to stay upright with leg extended toward the floor in a sitting position on the cycle ergometer (Fig. 2). All of thermal images were analyzed using Tmax method, which was recently proposed [2]. The methods consists in an assessment of temperature value of a specific area based on maximal temperature detection in a defined region of interest. Tmax methods in

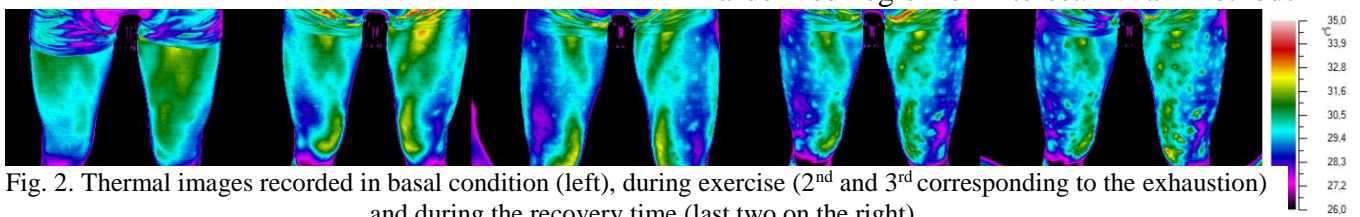


Fig. 2. Thermal images recorded in basal condition (left), during exercise (2<sup>nd</sup> and 3<sup>rd</sup> corresponding to the exhaustion) and during the recovery time (last two on the right).

this specific case permitted to obtain a value of temperature representative of muscles heating over the whole skin area of the thigh allowing to follow the temperature-time evolution of the muscular districts actually involved in the work.

Data normal distribution was verified by Shapiro Wilk's test and all data (mean  $\pm$  SD) met the assumption of normality. A One-way analysis of variance (ANOVA) for repeated measures was used to compare skin temperature dynamic among time points. Partial eta squared (Part  $\eta^2$ ) was used to estimate the magnitude of the difference within each group and the thresholds for small, moderate and large effects were defined as 0.01, 0.06, and 0.14, respectively. Overall analysis were performed using the IBM SPSS Statistics (v. 21, New York, United States) and an alpha threshold of  $P < 0.05$  was set to identify a statistical significance.

## Results and Discussion

Average time course of skin temperature is shown in Figure 3. During incremental exercise skin temperature decreased substantially from  $32.50 \pm 0.67$  °C to  $30.87 \pm 0.73$  °C ( $P = 0.002$ ; Part  $\eta^2 = 0.937$ ) between baseline and exhaustion time points. In the recovery time, after 3 min, skin temperature increased significantly ( $P < 0.01$ ) from the exhaustion time point returning similar to basal values remaining constant after 6 min from the end of the exercise. This clear up-and-down-behaviour of skin temperature was also observed by other authors [3, 4, 5]. However, to date, this is the first study that has investigated the skin temperature dynamics using the T max method during an incremental exercise. With regards to the literature, our findings showed a greater efficiency of vasoconstriction and vasodilation processes in removing heat from the core to the skin layers of highly-trained subjects.

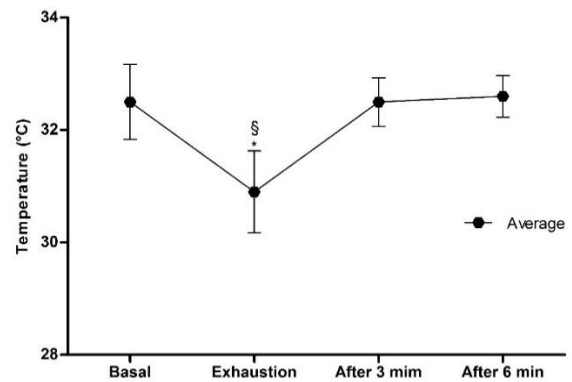


Fig. 3. Skin temperature (Average) dynamics among different time points  
\* $P < 0.05$  Exhaustion vs. Basal  
§ $P < 0.01$  Exhaustion vs. After 3 min and After 6 min.

## Conclusion

Skin temperature dynamic of muscle quadriceps showed an explicit decrease during an incremental maximal exercise and a subsequent rapid recovery immediately after. This behaviour reflects a remarkable ability to dissipate metabolic heat through the cutaneous surface by highly-trained cyclists.

## References

1. M. Torii, M. Yamasaki, T. Sasaki, H. Nakayama. Fall in skin temperature of exercising man. *Br J Sports Med.* 26(1), 29–32, 1992.
2. N. Ludwig, D. Formenti, M. Gargano, G. Alberti. Skin temperature evaluation by infrared thermography: Comparison of image analysis methods. *Infrared Phys Technol.*, 62, 1–6, 2014
3. W. Bertucci, A. Arfaoui, L. Janson, G. Polidori, Relationship between the gross efficiency and muscular skin temperature of lower limb in cycling: a preliminary study. *Computer methods in biomechanics and biomedical engineering*, 16, 114–115, 2013.
4. A. Merla, P.A. Mattei, L. Di Donato, G.L. Romani. Thermal Imaging of Cutaneous Temperature Modifications in Runners During Graded Exercise. *Ann Biomed Eng.*, 38, 158–63, 2014
5. A. Arfaoui, W. Bertucci, T. Letellier, G. Polidori, Thermoregulation during incremental exercise in masters cycling. *Journal Of Science And Cycling*, 3(1), 33–41, 2014.

## **Graphene-based devices for Terahertz photonics**

**Alessandro Tredicucci**  
**Università di Pisa, Pisa, Italy**  
**alessandro.tredicucci@unipi.it**

Graphene, a single-layer of carbon atoms arranged in a two-dimensional honeycomb lattice is nowadays attracting considerable attention for a variety of photonic applications, including fast photodetectors, transparent electrodes in displays and photovoltaic modules, and saturable absorbers. I will illustrate the realization of THz detectors based on antenna-coupled graphene field-effect transistors (FETs), and discuss the development and applications of electrically switchable metamaterial devices.



# INFRARED THERMOGRAPHY ANALYSIS OF THERMOMECHANICAL SHAPE MEMORY POLYMER BEHAVIOR – INITIAL LOADING STAGE

M. Staszczak<sup>1</sup>, E.A. Pieczyska<sup>1</sup>, M. Maj<sup>3</sup>, K. Kowalczyk-Gajewska<sup>1</sup>, D. Kukla<sup>1</sup>, H. Tobushi<sup>2</sup> and S. Hayashi<sup>3</sup>

<sup>1</sup>Institute of Fundamental Technological Research PAS, Warsaw, Poland, mstasz@ippt.pan.pl, epiecz@ippt.pan.pl; mimaj@ippt.pan.pl; kkowalcz@ippt.pan.pl

<sup>2</sup>AICHI Institute of Technology, Toyota, Japan, tobushi@aitech.ac.jp

<sup>3</sup>SMP Technologies Inc., Tokyo, Japan, hayashi@smptechno.com

Experimental results of effects of thermomechanical couplings occurring in polyurethane shape memory polymer (PU-SMP) subjected to cyclic loading at various strain rates are presented. Stress-strain characteristics were recorded by the testing machine, whereas the specimen temperature changes were measured by a fast and sensitive infrared camera. The influence of strain rate on the polymer thermomechanical behaviour was studied. It was found that the SMP is very sensitive to the strain rate. The higher the strain rate, the higher the values of the stress and temperature changes were obtained. In the initial stage of deformation a drop in temperature called thermoelastic effect, determining a limit of the material reversible deformation, was investigated.

## Introduction; material and specimens

Dynamic development of technology, increasing demand for materials as well as awareness of the environment protection cause that recently an increasing interest is observed in multifunctional smart materials, in particular in shape memory materials. The materials are able to combine the sensing and actuator functions which enable both innovative application and decrease of the device mass and sizes. One of these materials is shape memory polymer (SMP). The mechanism of exhibiting shape memory property in polymer is definitely different than the one observed in shape memory alloys, because the crystallographic phase transition does not occur in polymers. Whereas, the functional characteristics of SMP, e.g. the rigidity, elastic modulus, coefficient of thermal expansion, etc., change above and below its glass transition temperature  $T_g$ , since molecular motion of the polymer chains differs drastically below and above the  $T_g$  [1, 2]. Among various kinds of shape memory polymers the polyurethane (PU-SMP) can be distinguished due to its

good mechanical and shape memory properties, as well as low cost in comparison to Ti-based shape memory alloys. These properties allow using PU-SMP in different fields, e.g. biomedical, protection of food, textile, housing and aviation industries. The material used in the experiment was the polyurethane shape memory polymer, characterized by  $T_g \approx 45^\circ\text{C}$  and the degree of crystallinity of  $\approx 5\%$ . Results obtained from dynamic mechanical analysis suggest that it fulfills preliminary demands to function as shape memory polymer. Namely, a high glass elastic modulus  $E_g'$  (1250 MPa), a proper value of rubber modulus  $E_r'$  (12.1 MPa) and a high ratio of  $E_g'/E_r'$  (103) were obtained.

## PU-SMP subjected to loading - mechanical characteristics and temperature changes

PU-SMP specimens of a gauge length of 15 mm were subjected to tension tests performed on MTS 858 testing machine at room temperature with various strain rates:  $10^{-2}\text{s}^{-1}$ ,  $10^{-1}\text{s}^{-1}$  and  $10^0\text{s}^{-1}$ . A fast and sensitive ThermaCam<sup>TM</sup> Phoenix infrared camera (IR) was employed in order to measure in

contactless manner the temperature changes accompanying the polymer deformation and to analyze effects of thermomechanical couplings [2-4]. The maximal frequency of the IR camera is 538 Hz, window size 160 x 256 pixels, a wavelength range 3-5  $\mu\text{m}$ , thermal sensitivity 0.02 K. The camera enables obtaining the temperature distributions on the specimen surface, i.e. thermograms, which can monitor nucleation and development of the strain localization phenomena during the deformation (Fig. 1). Moreover, the IR system allows to determine a change of the SMP average temperature which is presented in the diagrams (Figs 1-5).

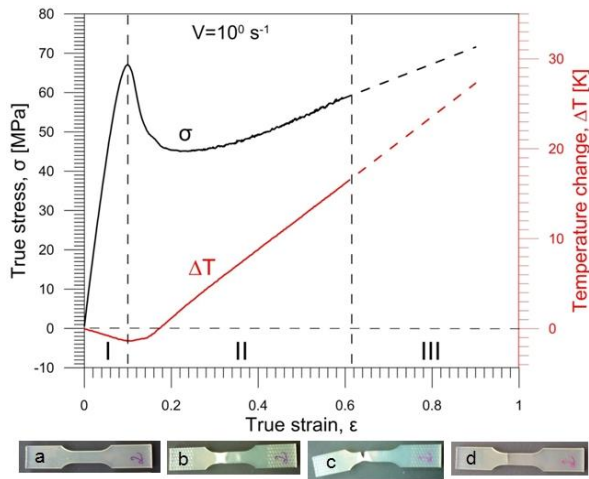


Fig.1. Stress  $\sigma$  and temperature change  $\Delta T$  vs. strain  $\epsilon$  and photos of various stages of the SMP tension.

The temperature changes of the SMP linked to the stress-strain curve enable distinguishing various stages of the SMP deformation process (Fig. 1). The first (I) is the reversible elastic stage of the deformations, described by theory of elasticity. In the case of tension, a small drop in temperature is observed, the strain is low and the SMP shape does not change significantly (Fig. 1a). The second (II) is the plastic stage, associated with change of the material structure, namely the polymer chains straightening. Moreover, strong localization effects can be observed (Fig. 1b). Like in metals, this deformation stage is characterized by a dissipative character [5], which in polymers can be related to strengthening of the chains. The polymers are very sensitive to the

strain rate and their deformation is accompanied by significant temperature changes. The higher the strain rate the more dynamic run of the deformation mechanisms and the larger temperature are observed. The stage III is related to the damage mechanisms. In this stage a breaking of the polymer chains occurs, leading to the specimen rupture (Fig. 1c) and huge increase of its temperature, especially locally, in the rupture area [2]. The SMP specimen after loading, taking off the grips of testing machine and subsequent heating at  $T_g+20^\circ\text{C}$ , is shown in Fig. 1d.

### Investigation of a limit of SMP reversible deformation - thermoelastic effect

Empirical identification of the boundary between the elastic and the plastic regimes of deformation is really complex, especially for materials without pronounced yield point, like most of polymers. In this case, the methods based on the measurement of the specimen temperature under mechanical loading are usually very efficient. In the initial, elastic loading stage the temperature changes due to thermoelastic couplings are negative in tension, while positive during the subsequent plastic deformation. The temperature change of the specimen subjected to adiabatic uniaxial elastic deformation is called a thermoelastic effect and can be described by Kelvin formula (1):

$$\Delta T_{el} = - \frac{\alpha T \Delta \sigma_s}{c_p \rho} \quad (1)$$

where  $\alpha$  denotes the coefficient of linear thermal expansion,  $T$  – the sample absolute initial temperature,  $\Delta \sigma_s$  – the isentropic change of stress,  $c_p$  – the specific heat at constant pressure,  $\rho$  – the material density.

So, the value of maximal drops in the material temperature can be used for evaluating a limit of the reversible material deformation. An example of the stress and the related temperature change vs. strain obtained for the PU-SMP subjected to tension with strain rate  $10^{-1}\text{s}^{-1}$  (strain range 8%) is shown in Fig. 2.

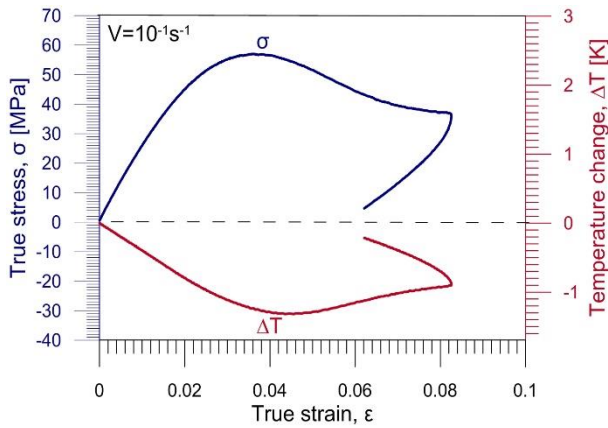
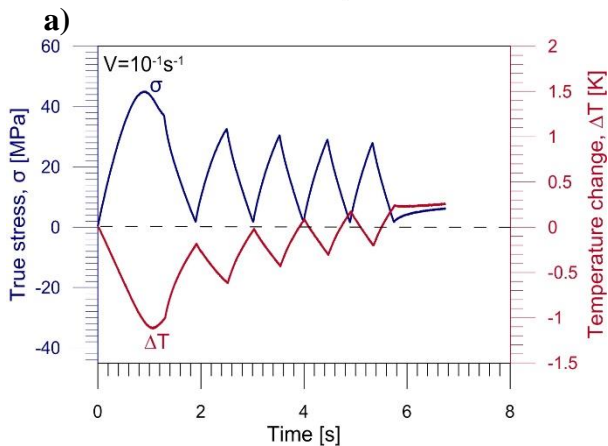
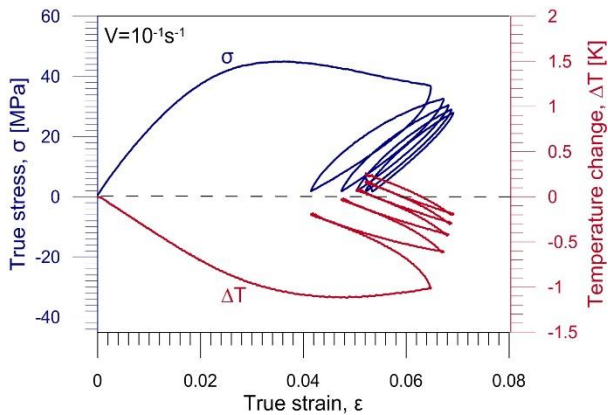


Fig. 2. Stress  $\sigma$  (blue line) and temperature change  $\Delta T$  (red line) vs. strain  $\epsilon$  for SMP tension with  $10^{-1}\text{s}^{-1}$ .

After obtaining the maximal value (59 MPa) the stress decreases due to the structure changes and the localization phenomena. The initial loading was accompanied by a drop in temperature  $\approx -1.3$  K, followed by a smooth temperature increase caused by the dissipative

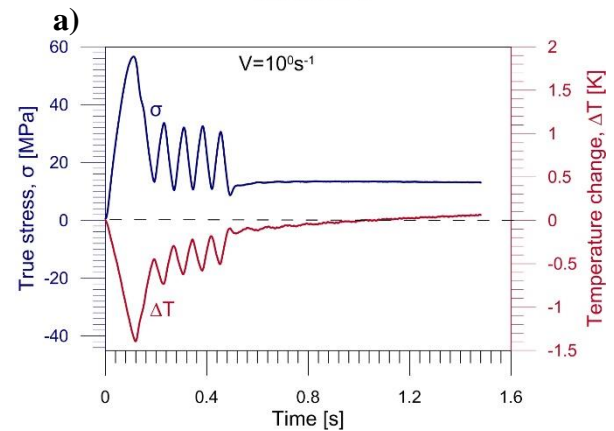
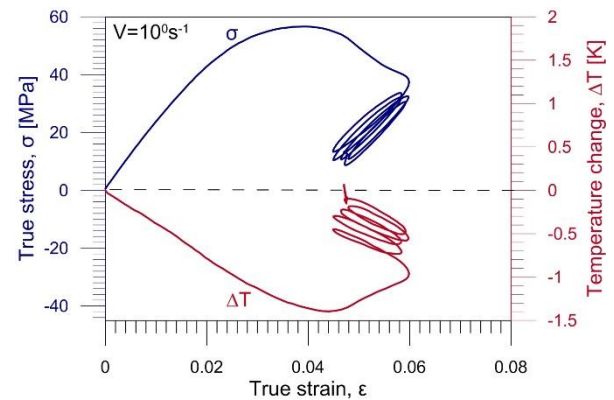


**b)** Fig. 3. Stress  $\sigma$  and temperature change  $\Delta T$  for strain rate  $10^{-1}\text{s}^{-1}$ : a) vs. strain  $\epsilon$ ; b) vs. time.

mechanisms. During unloading, the specimen temperature increases significantly which is probably caused by superposition of the positive thermoelastic effect and exothermic effects of the SMP relaxation processes.

Next figures present the stresses and their related temperature changes, obtained for the PU-SMP tension cyclic loading within strain range approximately 6% carried out with various strain rates. The stress and the temperature change vs. strain for the strain rate  $10^{-1}\text{s}^{-1}$  are shown in Fig. 3a, vs. time in Fig. 3b, respectively.

In order to estimate the influence of the strain rate, the test was also conducted for the 10 times higher strain rate  $10^0\text{s}^{-1}$  (Fig. 4). The higher strain rate, the higher stress values and the higher temperature changes were obtained. For each strain cycle, a decrease in the specimen temperature during the initial (elastic) loading and the temperature increase during the unloading proces was observed.



**b)** Fig. 4. Stress  $\sigma$  and temperature change  $\Delta T$  for strain rate  $10^0\text{s}^{-1}$ : a) vs. strain  $\epsilon$ ; b) vs. time.

Looking at the results obtained for various strain rates presented in Figs 3-4 it can be noticed that at the higher strain rate not only the higher stresses and temperature changes have been obtained, but also the difference between the first and the subsequent cycles of the loading are significantly larger. This is caused by a huge impact of the initial thermodynamic state of the SMP specimen. At the higher strain rate the test conditions are closer to adiabatic which significantly influence both the SMP structure as well as its thermomechanical behaviour in subsequent loading-unloading cycles. A comparison of the results presented above, namely the stress and temperature changes vs. strain for cyclic loading carried out with various strain rates  $10^{-2}\text{s}^{-1}$ ,  $10^{-1}\text{s}^{-1}$  and  $10^0\text{s}^{-1}$  are shown in Fig. 5.

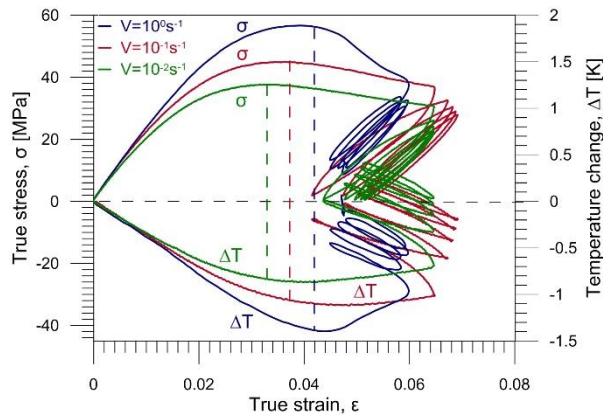


Fig. 5. Stress  $\sigma$  and temperature change  $\Delta T$  vs. strain  $\epsilon$  for SMP tension with strain rates:  $10^{-2}\text{s}^{-1}$ ,  $10^{-1}\text{s}^{-1}$  and  $10^0\text{s}^{-1}$ .

In the initial stage of strain a decrease of the specimen temperature is observed, while at higher strain the temperature increases due to initiation and evolution of the dissipative mechanisms of the deformation. Basing on the change in the character of the specimen temperature during its loading a limit between the elastic and the plastic regimes was determined. It was observed that at the higher strain rates higher temperature drops and larger yield points were obtained (Fig. 5). Using the values of maximal drops in temperature, limits of the reversible deformation were estimated (Table 1).

Strain rate	$10^{-2}\text{s}^{-1}$	$10^{-1}\text{s}^{-1}$	$10^0\text{s}^{-1}$
$\Delta T_{\max}$ [K]	- 0.86	- 1.11	- 1.39
$\sigma_{\text{rev}}$ [MPa]	38	45	56

Table 1. Yield points estimated for PU-SMP

## Conclusions

Effects of thermomechanical couplings during cycling tension in new multifunctional material PU-SMP were studied. It was found that the SMP is characterized by good mechanical and shape memory properties, as well as high sensitivity to the strain rate, manifested by both mechanical and thermal results. Limits of the SMP reversible deformation were evaluated with a high accuracy due to advanced infrared technique. At the higher strain rate higher values of the yield points were obtained. The significant difference between the first and the subsequent loading cycles was caused by a great influence of thermodynamic state the initial SMP. The experimental results will be compared with the predictions obtained using the recently developed model [2].

## Acknowledgments:

The research has been carried out with support of the Polish NCN - Grant 2011/01/M/ST8/07754. Authors are grateful to L. Urbański for remarks and support.

## References

1. H. Tobushi, R. Matsui, K. Takeda, E.A. Pieczyska. Mechanical Properties of Shape Memory Materials, Nova Sc. Publishers, New York, 2013.
2. E.A. Pieczyska, M. Maj, K. Kowalczyk-Gajewska, M. Staszczak, A. Gradys, M. Majewski, M. Cristea, H. Tobushi, S. Hayashi. Thermomechanical properties of polyurethane shape memory polymer - experiment and modelling, Smart Materials and Structures, Vol. 24, pp. 045043-1-16, 2015.
3. E.A. Pieczyska, S.P. Gadaj, W.K. Nowacki. Thermoelastic and thermoplastic effects investigated in steel, polyamide and shape memory alloys, Proceedings of SPIE, Thermosense XXIV, USA, 4710, pp. 479-497, 2002.
4. E.A. Pieczyska, S.P. Gadaj, W.K. Nowacki. Temperature changes in polyamide subjected to tensile deformation, Infrared Physics and Technology, Vol. 43/3-5, pp. 183-186, 2002.
5. A. Chrysochoos. Infrared thermography applied to the analysis of material behaviour: a brief overview, QIRT Journal, Vol. 9, N. 2, pp. 193-208, 2012.

# INFRARED THERMOGRAPHY APPLIED TO SOLID OXIDE FUEL CELLS AT OPERATING TEMPERATURES

A. Amato<sup>1</sup>, A.S. Aricò<sup>2</sup>, M. Lo Faro<sup>2</sup>, R. Montanini<sup>1</sup>, S.A. Piccolo<sup>1</sup>, A. Quattrocchi<sup>1</sup>, G. Squadrito<sup>2</sup>, S. Trocino<sup>2</sup>, S.C. Zignani<sup>2</sup>

<sup>1</sup> Department of Engineering, University of Messina, Messina, Italy  
{rmontanini, aquattrocchi, amato}@unime.it, seanpiccolo@gmail.it

<sup>2</sup> CNR-ITAE (Istituto di Tecnologie Avanzate per l'Energia "Nicola Giordano"), Messina, Italy  
{gsquadrito, arico, lofaro, trocino, zignani}@itae.cnr.it

Mechanical failure, or cathode delamination, induces performance degradation in solid oxide fuel cells (SOFCs). Thermal imaging may provide a powerful tool for monitoring SOFC electrode processes, but, due to the typical design of pellet-type cells, a direct optical access to the electrode surface is usually prevented. In this paper, a specially designed SOFC is introduced, that allows temperature distribution to be measured while still preserving electrochemical performance. A case study is also presented, highlighting the effectiveness of infrared thermal imaging in detecting the onset of cell failure during normal operation.

## Introduction

Solid oxide fuel cells (SOFCs) are a frontier technology for the conversion of chemical energy contained in hydrocarbons (fossil and renewable) into electricity and heat [1,2]. Although their electrochemical performance and materials issues have been intensely investigated in recent years, there are very few experimental studies dealing with the problem of measuring the temperature distribution of the electrode surfaces of SOFCs at working temperatures (typically 600-1000 °C).

Adžić et al. [3] proposed a dedicated instrumentation based on a custom designed flat type thermocouple which was mounted on a precision traversing mechanism to scan the target surface. The sensing probe needed to be placed in close proximity (but not in contact) with the electrode surface thus affecting measurement uncertainty; in addition, temperature values are actually not recorded simultaneously. Guo et al. [4] developed an experimental technique based on Sagnac interferometry and single-point infrared sensing for in situ surface deformation and temperature measurements of a solid oxide anode under

operating condition. In this way, the anode structural degradation could be assessed.

Infrared thermography may provide definite advantages with respect to scanning single-point measurements, allowing the aforementioned limitations to be overcome. Brett et al. [5] exploited infrared imaging to assess the temperature increase accompanying polarization of heavily loaded gadolinium doped ceria pellet cells. A similar approach has been used by Ju et al. [6], who investigated, both numerically and experimentally, the performance of a planar-type SOFC and the relationship between current and temperature distribution. More recently, Pomfret et al [7] demonstrated the ability to spatially and temporally map SOFC anode temperatures in operating cells using a Si-CCD camera based NIR imaging system on fragments of Ni/YSZ cermet anodes. A specific calibration was necessary in this case in order to infer temperatures values from the intensity reading of the camera.

A common restriction associated with the measurement of the temperature distribution on SOFC electrodes derives from the presence of electrical contacts required for drawing the



current from the fuel cell. These are usually made of a highly conductive metal, typically platinum or gold, which has a very low emissivity and partially covers the electrode surface, thus preventing full thermal imaging of cathode or anode processes.

In this paper, we faced this problem by developing a specially designed SOFC with outer collector that allows temperature distribution to be measured more accurately while still preserving electrochemical performance. A case study is also presented, highlighting the effectiveness of infrared thermal imaging in detecting the onset of cell failure during normal operation.

### Customized SOFC configuration

Thermal imaging of SOFC electrode surface has already been reported in literature [5-7] by employing standard cell configurations in which platinum or gold gauzes are used as electric contacts (Fig. 1a).

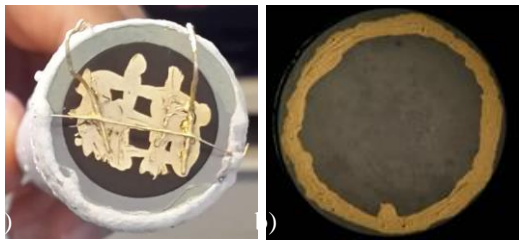


Fig. 1. Pellet-type SOFC: a) standard cell layout; b) customized cell layout with gold ring.

Usually these gauzes have a mesh of  $0.25 \times 0.25 \text{ mm}^2$  and grant good electric contact and effective reactant and product diffusion to and from the electrodes. Nevertheless, this layout tends to hide the underneath area, thus hindering thermal imaging of the electrochemical processes taking place at the cathode/anode surfaces. Moreover, infrared measurements may be inaccurate, because of the high thermal conductivity and low emissivity of gold.

To overcome this problem, a special cell has been realized, which consists of a gold ring located outside the active cathode area (Fig. 1b),

while for the anode the standard configuration was kept. Preliminary tests proved that this custom design results in similar electrochemical performance ( $\pm 1\%$ ) with respect to the standard one. The active area has a diameter of about 2 cm.

### Testing procedures

Fig. 2 shows a scheme of the experimental set up.

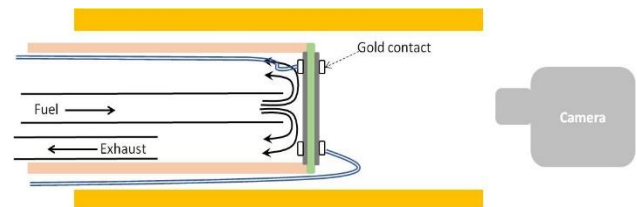


Fig. 2. Scheme of the experimental set-up, not in scale.

The tube supporting the customized cell was equipped with fuel inlet, exhaust outlet, and two small alumina tubes for electrically insulating the two gold contacts. The supporting tube was then inserted centered into a cylindrical oven. The IR camera was placed in front of the cell cathode that is directly exposed to the air entering the open side of the oven. Tests were performed in steady-state conditions at about  $750 \text{ }^\circ\text{C}$ . Both voltage/current and electrochemical impedance spectroscopy (EIS) characterizations have been carried out too. A pre-treatment of 20 h in the presence of  $\text{H}_2$  at  $800 \text{ }^\circ\text{C}$  was adopted in order to allow for a complete reduction of the anode [8]. The experiments were conducted by feeding dry fuels to the anode compartment, whereas the cathode compartment was exposed to static air.

### IR measurements

Infrared thermography tests were carried out by means of an indium antimonide (InSb) focal plane array cooled infrared camera (FLIR mod. SC 7200) working in the mid-IR spectral range



(3.6 – 5.1  $\mu\text{m}$ ), with 320×256 spatial resolution. The IR camera was equipped with a 50 mm lens, having an instantaneous field of view (IFOV) of 11°×8.8°. Absolute measurement accuracy stated by the manufacturer is  $\pm 1^\circ\text{C}$  or 1%, while temperature differences as small as 20 mK can typically be detected. The cathode surface was preliminary characterized to assess its emissivity at 750 °C. An average value of 0.98 was obtained; this value was then used to correct apparent temperatures measured by the IR camera.

### IR images processing

Thermal images were analyzed using a dedicated image processing software originally developed in Matlab™. The software is able to process several images in batch for each cell: it extracts the region of interest (ROI) from each thermal image, performs temperature correction for emissivity, producing a false color image and a histogram of the temperature; the software can also fit a theoretical statistical distribution to the histogram by means of the Maximum Likelihood Estimation method. The false color image of the ROI is useful to visually evaluate possible hotspots, temperature variations and structural defects while the histogram against the theoretical distribution is useful to perform a quantitative evaluation of the temperature distribution. To perform image segmentation, a semi-supervised approach based on Canny edge detection algorithm was adopted after an image enhancing by histogram equalization and edge sharpening; once a mask of the ROI had been obtained, it was used to process all the images relative to a specific button cell.

### Results

In Fig. 3 basic results concerning thermal imaging of a customized SOFC are reported. As the cell is working regularly without cracks or electrochemical problems, the cathode surface

showed a rather uniform temperature distribution ( $744 \pm 3^\circ\text{C}$ ) with internal pixels that are slightly cooler than the external ones (first row of Fig. 3). In the raw image, it can be observed that due to the very low emissivity of the gold ring, significant reflections are generated. In normal working conditions the polarization curve (i.e. I/V curve) is regular and also the EIS doesn't show any atypical behavior. It should be noted that the temperature histogram appears asymmetric also at steady state and open circuit, i.e. without power generation.

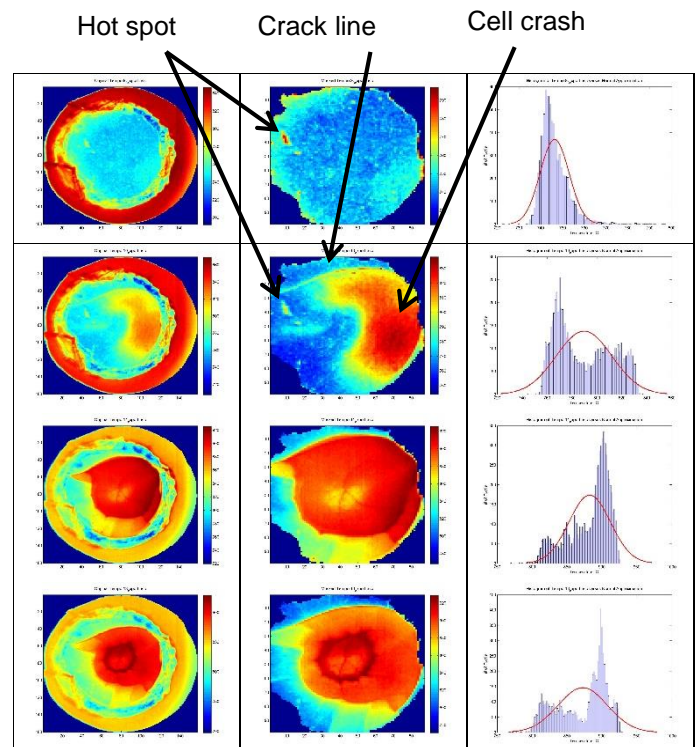


Fig. 3. Evolution of an hot spot to a crack after 46 h of test running. First column: raw thermal images; second column: post-processed thermal images; third column: temperature histograms showing bins of pixels having the same temperature. The red line overlaid to each histogram displays the Gaussian approximation fit.

As can be clearly observed by the thermal images, the cell presented an hot-spot in the left region of the investigated active area, which is most likely associated with a pre-existent defect on the porous cathode surface. This hot-spot behaved as a precursor for cell failure, with formation of a macroscopic crack line that eventually produces the complete cell crash. The direct mixing of hydrogen and oxygen generates

a local sharp rise in temperature that creates the conditions for creep propagation. This resulted in a sharp fall out in cell power generation.

Assessment of hot-spots on the active surfaces is very important for diagnostic purposes, attending that reliability and long-term operation of SOFCs are still open issues that need to be addressed before their commercialization. These hot-spots seem to be correlated to the structural integrity of the cathode surface and should be optically visible at microscopic level, but are difficult to be correlated to the electrochemical behavior. Actually, electrochemical measurements do not allow to observe anomalies until the cell crashes. Thermal images instead, when properly post-processed, can provide earlier evidence of local failure.

## Conclusion

Infrared thermography can be a powerful tool for the diagnostic of solid oxide fuel cells but its application can be complicated because of the intrinsic construction of pellet-type SOFCs. When looking to other studies already reported in literature [5-7], it can be observed that thermal mapping of SOFC electrode surfaces is always partially masked because of the metal gauze used for electric connection. This gauze also creates problems in IR measurements due to the very low emissivity of Pt or Au.

In this work, we developed a customized configuration of a pellet-type SOFC which allows these limitations to be overcome while keeping equivalent electrochemical performance. The practical application to a defected cell was also addressed in this study.

The obtained results, although preliminary, are encouraging about the possibility to use IR thermography for studying the link between cell fabrication defects and cell failure.

Future work is aimed at developing an effective non-destructive low temperature technique for quality assurance of SOFC cells. If developed, this technique will allow to reduce significantly

SOFC stack failures and endurance and, consequently, SOFC production costs.

## Acknowledgements

This work was supported by the research project TESEO “High Efficiency Technologies for On-board Energetic and Environmental Sustainability” (PON02\_00153\_2939517).

## References

1. G. Squadrito, L. Andoloro, M. Ferraro and V. Antonucci. Hydrogen fuel cells technology, Chapter 16 in A. Basile and A. Iulianelli (eds), “Advances in Hydrogen Production, Storage and Distribution”, Woodhead Publishing Limited, Cambridge, UK, 2014.
2. S.C. Singhal, K. Kendall. High-temperature Solid Oxide Fuel Cells: Fundamentals, Design and Applications, 1st ed., Elsevier, Oxford, 2003.
3. M. Adžić, M.V. Heitor, D. Santos. Design of dedicated instrumentation for temperature distribution measurements in solid oxide fuel cells, *Journal of Applied Electrochemistry*, Vol. 27, pp. 1355-1361, 1997.
4. H. Guo, G. Iqbal, B. S. Kang. Development of an in situ surface deformation and temperature measurement technique for a solid oxide fuel cell button cell, *International Journal of Applied Ceramic Technology*, Vol. 7 (1), pp. 55-62, 2010.
5. D.J.L. Brett, P. Aguiar, R. Clague, A.J. Marquis, S. Schottl, R. Simpson, N.P. Brandon. Application of infrared thermal imaging to the study of pellet solid oxide fuel cells, *Journal of Power Sources*, Vol. 166 (1), pp. 112-119, 2007.
6. G. Ju, K. Reifsnider, X. Huang. Infrared Thermography and Thermoelectrical Study of a Solid Oxide Fuel Cell, *Journal of Fuel Cell Science and Technology*, Vol. 5, pp. 03100- 1/6, 2008.
7. M.B. Pomfret, D.A. Steinhurst, D.A. Kidwell, J.C. Owrutsky. Thermal imaging of solid oxide fuel cell anode processes, *Journal of Power Sources*, Vol. 195, pp. 257-262, 2010.
8. M. Lo Faro, R. M. Reis, G. G. A. Saglietti, S. C. Zignani, S. Trocino, P. Frontera, P. L. Antonucci, A. Ticianelli, A. S. Aricò. Investigation of Ni-based alloy/CGO electro-catalysts as protective layer for a solid oxide fuel cell anode fed with ethanol, *J. Appl. Electrochem.*, Vol. 45, pp. 647-656, 2015.

# ELECTRICAL PERFORMANCE OF N-STRUCTURE T2SL PHOTODETECTORS

M. Hostut<sup>1</sup>, T. Tansel<sup>2</sup>, S. Elagoz<sup>3</sup>, A. Kilic<sup>4</sup>, Y. Ergun<sup>4</sup> and A. Aydinli<sup>5</sup>

<sup>1</sup> Div. of Physics Education, Faculty of Education, Akdeniz University, mhostut@akdeniz.edu.tr

<sup>2</sup> Institute of Nuclear Science, Hacettepe University, tunaytansel@hacettepe.edu.tr

<sup>3</sup> Department of Nanotechnology Eng., Cumhuriyet University, elagoz@cumhuriyet.edu.tr

<sup>4</sup> Department of Physics, Anadolu University, yergun@anadolu.edu.tr, abkilic@anadolu.edu.tr

<sup>5</sup> Department of Physics, Bilkent University, aydinli@fen.bilkent.edu.tr

Temperature dependent of dark current measurement is an efficient way to verify the quality of an infrared detector. Low dark current density values are needed for high performance detector applications. Identification of dominant current mechanism in each operating temperature with extracted their minority carrier lifetimes are highly important for understanding of carrier transport and improve the detector performance. InAs/AlSb/GaSb based T2SL N-structure with AlSb unipolar barriers is aimed to design having with low dark current but high resistance and detectivity. Here we present electrical and optical performance of N-structure photodetectors.

## Introduction

InAs/AlSb/GaSb based superlattice (SL) material system known as 6.1A material family is highly desirable for designing new high performance photodetectors operating in the mid wavelength infrared range (MWIR). Depending on the doping concentrations and configuration of the constituent alloys of InAs, AlSb and GaSb in the superlattice period, superlattice band structure may be adjusted in order to improve electrical and optical performance of photodetectors. There have been new high performance type-II SL detector architectures reported up to date. These include nBn, pBp, XBn, CBIRD, pBIBn, W and M structures. The details of the detector structures are reviewed by Martyniuk *et al.* [1]. Recently, we proposed new detector architecture called N structure. N-structure is a pin photodiode with a unipolar electron barrier which aims to improve electron and hole wave functions overlap. The layer configurations and energy band alignment of the structure are shown in Fig. 1 (a) and (b) respectively. In the detector structure, thin AlSb layers are placed in between InAs and GaSb layers. Under reverse bias AlSb barriers push the carriers towards GaSb/InAs interfaces to increase electron

and hole wave functions overlap enhancing type-II optical transition (Fig. 2). Comparing to standard InAs/GaSb superlattice detectors, the overlap of carrier wave functions is increased by about 25% with N-structure design [2]. The specific detectivity was measured as  $3 \times 10^{12}$  Jones with cut-off wavelengths of 4.3  $\mu\text{m}$  at 79 K reaching to  $2 \times 10^9$  Jones and 4.5  $\mu\text{m}$  at 255 K [3]. In this study, we report current density-voltage (J-V) characteristics of InAs/AlSb/GaSb based type-II SL N-structure photodiodes as a function of temperature (87-271K). We then fit dark current densities by using Shockley Formula to extract minority carrier lifetimes at different temperatures.

## Experimental Results

The superlattice photodiode was grown by commercially (IQE Inc. USA) with molecular beam epitaxy. First a 100 nm GaSb buffer layer is deposited on unintentionally p-type doped (100) GaSb substrate followed by a 20 nm lattice matched  $\text{Al}_{0.4}\text{Ga}_{0.6}\text{As}_{0.04}\text{Sb}_{0.96}$  buffer layer. 1000 nm thick p-type GaSb:Be ( $p=1 \times 10^{17} \text{ cm}^{-3}$ ) bottom contact is grown on the buffer layer. The p-i-n detector structure consists of 9/2/8.5 MLs) of InAs/AlSb/GaSb SL layers as 90 periods of p-

region with GaSb:Be ( $p=1.5 \times 10^{17} \text{ cm}^{-3}$ ), 60 period of i-intrinsic region and 40 periods of n-region with InAs:Te ( $n=5 \times 10^{17} \text{ cm}^{-3}$ ). The device is terminated by 20 nm InAs: Te n-contact ( $n=5 \times 10^{17} \text{ cm}^{-3}$ ). Standard lithography was used to define square mesas with different dimensions. The fabrication details are given by elsewhere [4]. The J-V curves are fitted by using Shockley Formula in order to identify the dominant dark current mechanism in each operating temperature range. We then extracted minority carrier lifetimes of the MWIR SL photodiode quantitatively [5]. We are measured responsivity spectra of the detector at various temperatures. Fig. 3 shows the responsivity spectrum of the structure at 79K. The device gives 50% cut-off wavelengths at  $4.2 \mu\text{m}$ .

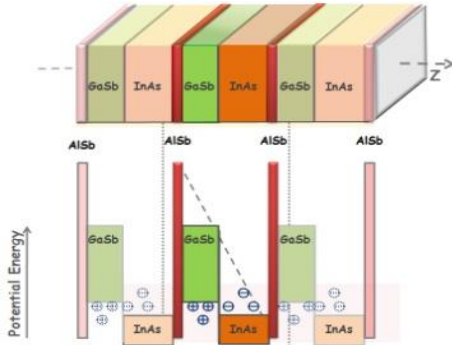


Fig.1. (a) Layer sequence in growth direction, (b) conduction and valence band profiles for asymmetric InAs/AsSb/GaSb based T2SL N-structure [3].

In this design, we use the detector structure with short period of absorption layer in order to measure minority carrier lifetimes. For this structure, the peak responsivity of  $0.35 \text{ A/W}$  at  $3 \mu\text{m}$  can be seen low but, if the absorption layer is increased four times; the responsivity value will be reached to  $1.4 \text{ A/W}$  value with a basic calculation of linear extrapolation.

Temperature dependence of the band gap energy  $E_g(T)$  of the SL structure is extracted from responsivity spectra with fitting curve (solid line) by using Varshni's equation shown in inset of Fig.3.

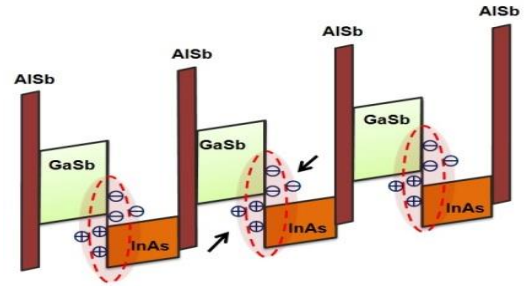


Fig. 2. Conduction and valence band profiles for N-structure with electron and hole confinement under reverse bias [3].

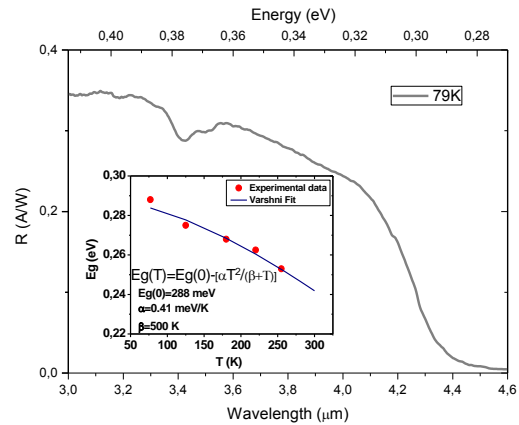


Fig. 3. Responsivity spectrum of N-Structure at 79K. Inset shows Varshni fit for band gap energy extracted from optical response spectra for different temperatures.

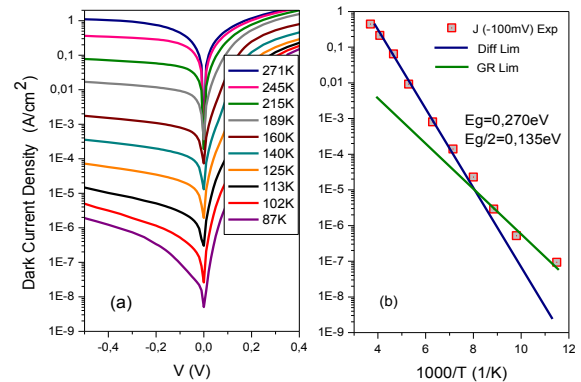


Fig. 4. (a) Temperature dependence of dark current density, (b) Arrhenius plot of dark current density vs inverse temperature ( $1000/T$ ).

Dark current density-voltage measurements are carried out under dark conditions for different operating temperatures ranging from 87K to 271K by using HP41420A source measure unit. Figure 4 (a) shows the dark current density-voltage

characteristics of  $500 \times 500 \mu\text{m}^2$  diodes under applied bias voltage range  $[-0.5\text{V}, 0.5\text{V}]$ . At 87K and under  $-0.1\text{V}$  bias voltage, the dark current density is measured as  $9.29 \times 10^{-8} \text{A/cm}^2$  and corresponding dynamic resistance area product (RA) is determined as  $6.43 \times 10^5 \Omega\text{cm}^2$ . Extracted from Fig. 4 (a), the inverse temperature ( $1000/T$ ) dependence of dark current density under  $-100 \text{mV}$  bias is shown in Fig.4 (b). In the temperature range 271–125 K, the dark current density reveals diffusion-limited behavior (Arrhenius type) with associated activation energy of 270 meV which is close to the band gap energy. In the lower temperature range (100–80 K), the dominant mechanism starts to become generation recombination (GR) which mostly depends on the deep trap levels inside the band gap ( $E_g/2$ ). To illustrate the bias dependent dominant dark current components of diffusion ( $J_{\text{DIFF}}$ ) and GR ( $J_{\text{GR}}$ ) current, we use the model given by elsewhere [6]. We then fit the dark current densities to determine the minority carriers of diffusion and GR time constants. The experimental data and modeled data for dark current density components at 160K are shown in Fig.5 with fitting parameters of minority carrier lifetimes. We have also calculated minority lifetimes at various temperatures given by Fig. 6. While diffusion lifetimes are increased with increasing temperature ranging from 1 to 120ns, GR lifetimes mostly behave regardless of temperature.

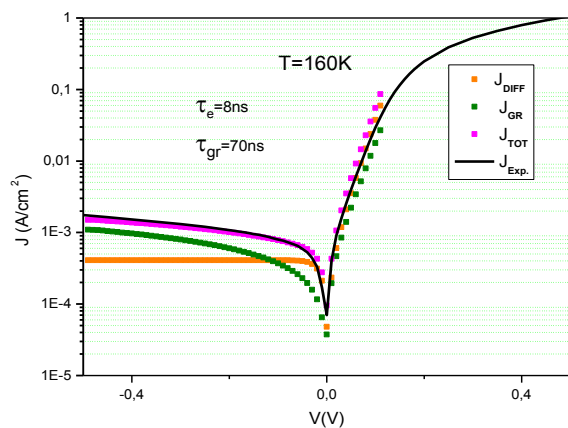


Fig. 5. Experimental  $J_{\text{Exp}}$ . (solid line) and modeled  $J_{\text{DIFF}}$  (yellow dot),  $J_{\text{GR}}$  (green dot) and  $J_{\text{TOT}}$  total dark current densities versus voltage of N-structure SL photodiode at  $T = 160 \text{K}$ .

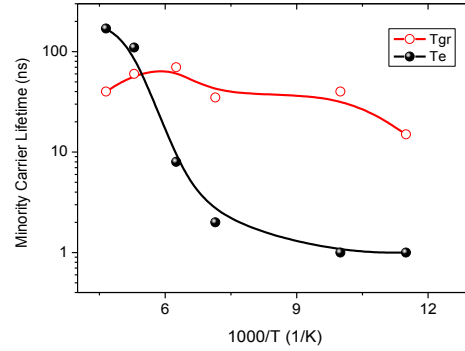


Fig. 6. Calculated diffusion ( $\tau_e$ ) and GR ( $\tau_{\text{GR}}$ ) lifetimes at various temperatures.

## Conclusion

Temperature dependence of J–V characteristics is analysed in InAs/AlSb/GaSb based T2SL N-structure. Deduced from J–V curve-fitting, minority carrier lifetimes have been estimated in the temperature range 87–215 K. At 87K and under  $-0.1\text{V}$  bias voltage, the dark current density is measured as  $9.29 \times 10^{-8} \text{A/cm}^2$  and corresponding dynamic resistance area product (RA) is determined as  $6.43 \times 10^5 \Omega\text{cm}^2$ . In the temperature range 271–125 K, the dark current density reveals diffusion-limited behaviour (Arrhenius type) with electron lifetime values between 1ns and 120ns. In the lower temperature range (125–87 K), the dominant mechanism starts to become generation recombination (GR) with GR lifetimes varies between 15-70ns.

## References

1. P. Martyniuk, M. Kopytko, and A. Rogalski, *Opto-Electron. Rev.*, 22 127-146 (2014)
2. O. Salihoglu, I. A. Muti, K. Kutluer, T. Tansel, R. Turan, Y. Ergun, and A. Aydinli *Appl. Phys. Lett.* 101, 073505 (2012)
3. M. Hostut, M. Alyoruk, T. Tansel, A. Kilic, R. Turan, A. Aydinli, Y. Ergun, “N-structure based on InAs/AlSb/GaSb superlattice photodetectors” *Superlat. & Microst.* **79** (2015) 116-122.
4. O. Salihoglu, A. Muti, K. Kutluer, T. Tansel, R. Turan and A. Aydinli, *J. Appl. Phys.* 111 (2012) 074509.
5. C. Cerveva, I. Ribet-Mohamed, R. Taalat, J.P. Perez, P. Christol and J.B. Rodriguez, *J of Electronic Materials*, 41 (2012) 2714-2718.

6. C. Cervera, J.B. Rodriguez, R. Chaghi, H. Ait-Kaci, J.B. Rodriguez, and P. Christol, J. Appl. Phys. 106, 024501 (2009).

**Acknowledgement:** Y.Ergun and A. Kilic acknowledges the supports of Anadolu University (BAP Grant: 13005F108). Author T. Tansel also thanks to Prof.Dr. R. Turan for using experimental set up for his experiments.



# INFRARED SCANNING NEAR-FIELD OPTICAL MICROSCOPY IN MATERIAL SCIENCE AND BIOLOGY

A. Cricenti, M. Luce

Istituto di Stuttura della Materia, via Fosso del Cavaliere 100, 00133 Roma, Italy

We will give an overview of our activity in the field of Infrared Scanning Near-Field Optical Microscopy (SNOM): several applications in Material Science and Biology will be presented as well some recent developments in instrumentation. In particular, by using SNOM we could observe differences in the chemical distribution of the different bonds in biological cells: in fact by coupling a SNOM with a tunable infrared source (FEL) it is possible to perform a spectroscopic study on the spatial distribution of chemical species and on other laterally-fluctuating properties. This approach has also the potential to provide early diagnostics for oesophageal cancer.

## Introduction

The advent of Scanning Near-Field Optical Microscopy (SNOM) [1-8] has augmented at a microscopic level the usefulness of IR-spectroscopy. Two-dimensional imaging of chemical constituents makes this a very attractive and powerful new approach. An important first step in the evaluation of biological structures is the IR characterization of the biological growth medium. The growth medium is composed of several products [9], primarily Sulphur and Nitrogen-Oxide compounds, whose vibrational stretch mode absorption bands occur in the infrared around  $7\ \mu\text{m}$  [10]. SNOM images were taken by tuning the Free electron laser (FEL) to  $\lambda=6.95\ \mu\text{m}$ , i.e., at such absorption band, and at  $6.6\ \mu\text{m}$ , i.e., outside the absorption band, in order to estimate the noise-background contributions. A major requirement is a suitable IR photon source: which is both intense and tunable. Tunability is required to cover the relevant absorption bands. Intensity is a critical point because of the inefficient light transmission of the narrow fiber tip. FEL sources are ideal for this problem because of their unique combination of extreme intensity and broad tunability. The FEL photons are sent to the sample surface, and detected after reflection

by the narrow-point optical fiber tip mounted on our SNOM module.

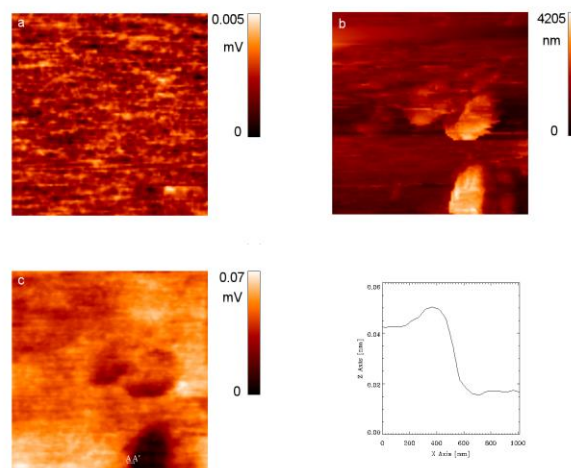


Fig. 1.  $20 \times 20\ \mu\text{m}^2$  SNOM reflection images obtained with  $\lambda=6.95\ \mu\text{m}$  photons (image c) and with  $\lambda=6.6\ \mu\text{m}$  (image a). Corresponding topographical image (b) and line profile A-A taken from (c).

Fig.1 (left-hand side) shows two  $20 \times 20\ \mu\text{m}^2$  SNOM reflection images obtained with  $\lambda=6.95\ \mu\text{m}$  photons (image c) and with the adjacent wavelength,  $\lambda=6.6\ \mu\text{m}$  (image a). In the reflection images darker areas correspond to stronger absorption. The contrast between the

featureless image off-absorption and the microstructures of the on-absorption image is striking. Are these microstructures really related to the growth medium constituents or are they just artifacts? To answer this question we compare the corresponding shear-force (topological) image of Fig. 1b. First of all the same topological image is observed at the two different wavelengths (image b). The topological images show the presence of several biological growth medium grains with width and height of few micrometers. Furthermore, if we are dealing with artifacts, we would expect a similar optical image when collecting data at 6.6  $\mu\text{m}$  (image c) and 6.95  $\mu\text{m}$  (image a): absolutely no one-to-one correlation is observed between the two SNOM images, ruling out artifacts. This proves, in fact, that the dark regions in the on-absorption SNOM image of Fig. 1c correspond to regions with strong growth medium component concentrations related absorption.

It is quite instructive to analyze the lateral resolution of the topographic and spectroscopic-SNOM images obtained in this work. For the topographic images, line scans yield a lateral resolution of between 50 and 80 nm, demonstrating the high quality of the fiber tips. On the other hand, similar line scans for the spectroscopic SNOM images (see the slope in the profile A-A' taken from (c)) demonstrate a lateral resolution of 200 nm, which is well below the classical-microscopy limit ( $\lambda/2$ ). A lateral resolution value better than  $\lambda/30$  was obtained at 6.95  $\mu\text{m}$ .

## Conclusion

In summary, we have performed IR wavelength-selective high resolution near-field measurements of a growth medium film that can be used to grow biofilm. This successful test of spectroscopic SNOM is intrinsically interesting, since it lends credibility to the frequently proposed biological applications of SNOM. But its impact is much more general: it is clear that spectroscopic SNOM can be applied, for example, to a wide variety of biological,

polymer and semiconductor systems. In all cases, FEL-based SNOM techniques can reveal two-dimensional chemical structures, thus making it a uniquely complete probe on a sub-micron scale. Future work will include not only the characterization of cellular and sub-cellular structures but also the in-vivo monitoring of up-taken external agents. This approach has also the potential to provide early diagnostics for oesophageal cancer.

## References

1. E. Betzig and J.K. Trautman, *Science* 257, 189 (1992).
2. E. Betzig, P.L. Finn, J.S. Wiener, *Appl. Phys. Lett.* 60, 2484 (1994).
3. H. Heinzelmann and D.W. Pohl, *Appl. Phys. A* 59, 89 (1994).
4. NATO ASI Series "Near Field Optics", eds. D.W. Pohl and D. Courjon, Kluwer Academic Press (1992) vol. 262.
5. J. Almeida, T. dell'Orto, C. Coluzza, G. Margaritondo, O. Bergossi, M. Spajer, D. Courjon, *Appl. Phys. Lett.* 69, 2361 (1996).
6. A. Cricenti, R. Generosi, P. Perfetti, J. M Gilligan, N. H. Tolk, C. Coluzza, G. Margaritondo *Appl. Phys. Lett.* 73, 151 (1998).
7. A. Piednoir, C. Licoppe, F. Creuzet, *Opt. Commun.* 129, 414 (1996).
8. B. Knoll, F. Keilmann, *Nature* 399, 134 (1999).
9. D.de Beer, P.Stoodley, F. Roe, Z. Lewandowski, *Biotechnology and Bioengineering* 43, 1131 (1994).
10. J.H. van der Maas, *Basic Infrared Spectroscopy* 2nd ed., pag. 88-89, Heyden & Son LTD, London 1972.
11. A.D. Smith, M.R.F. Siggel-King, G. Holder, A. Cricenti, M. Luce, P. Harrison, D.S. Martin, M. Surman, T. Craig, S.D. Barrett, A. Wolski, D. Dunning, N.R. Thompson, D.M. Pritchard, A. Varro, S. Chattopadhyay, P. Weightman, *App. Phys. Lett.*, 102, 053701 (2013).

# The focus on engineering steps for high temperature HgCdTe photodiodes optimization.

P. Madejczyk<sup>1</sup>, W. Gawron<sup>1</sup>, P. Martyniuk<sup>1</sup>, A. Kęblowski<sup>2</sup>, W. Pusz<sup>2</sup>, J. Pawluczyk<sup>2</sup>, M. Kopytko<sup>1</sup>, J. Rutkowski<sup>1</sup>, A. Rogalski<sup>1</sup>, J. Piotrowski<sup>2</sup>

<sup>1</sup> Institute of Applied Physics, Military University of Technology, Kaliskiego 2, 00-908 Warsaw, Poland

<sup>2</sup> Vigo System S.A., 129/133 Poznanska Str., 05-850 Ozarow Mazowiecki, Poland

The authors report on energy gap engineering solutions to improve the high-temperature performance of HgCdTe photodiodes. MOCVD technology with a wide range of composition and donor/acceptor doping and without post grown annealing seems to be an excellent tool for HgCdTe heterostructure epitaxial growth structure. The  $N^+/G/\pi/G/P^+/G/n^+$  (where G denotes graded interface region) HgCdTe photovoltaic device concept of a specific barrier bandgap architecture integrated with Auger-suppression is a good solution for high operating temperature (HOT) infrared detectors. The thickness, the composition and the doping level of each subsequent layer were optimized with respect to photoelectrical parameters like dark current, the responsivity and the response time. In this paper we focus on single exemplary step in the progressive optimization process.

## Introduction

The dark current in HgCdTe photodiodes is usually determined by Auger generation processes at elevated temperatures, because the low-doped absorber layer becomes intrinsic and the carrier concentration is higher than the doping level [1]. The device structures with a combination of exclusion and extraction junctions in  $N^+/\pi/P^+$  configurations have demonstrated suppression of Auger mechanisms by reducing the absorber carrier density below thermal equilibrium in a reverse bias condition [2]. Presently, obtaining the structure type  $P^+/\pi/N^+$  with abrupt interfaces is difficult or even impossible for technological reasons. Because of interdiffusion processes in HgCdTe material during the growth processes in both molecular beam epitaxy (MBE) or MOCVD techniques the designed  $N^+/\pi/P^+$  structure takes the form of  $N^+/G/\pi/G/P^+$  structure where G denotes graded interface region. The graded interface regions G are more extended in structures deposited by MOCVD technique than G regions in structures deposited by MBE technique because of the differences in the growth temperatures. Typically the substrates are kept at temperatures

180-200°C in MBE and 350-360°C in MOCVD technologies, respectively. In order to improve electrical contact properties of metallization to  $P^+$  layer the structure was upgraded with  $p^+/n^+$  tunnelling junction on the top. Thus, ultimate architecture of developed devices take form of  $N^+/G/\pi/G/P^+/G/n^+$ . More detailed study of this architecture was described in ref [3]. In order to facilitate shaping the graded interface regions designed structure destined directly for the deposition takes a form of  $N^+/N/P1/\pi/P2/P^+/p^+/n^+$  structure.

## Device Structure

Previously reported  $N^+/N/P1/\pi/P2/P^+/p^+/n^+$  structure [3] was modified in such way that P2 layer was divided onto P2 and P3 sublayers (Fig.1). Such modification was designed in order to facilitate band gap grading and doping level controlling at interface regions. The interdiffusion of elements: Hg, Cd, Te (including As and I as dopant elements) in HgCdTe heterostructure during the growth process at 350°C contributes to interface abruptness decreasing which deteriorates photoelectrical properties of constructed devices. In this paper

we focus on single exemplary step in the progressive optimization process. The composition of inserted P3 sublayer was modified in consecutive deposited structures described as: #A6 and #A9. In presented experiment the composition  $x$  of P3  $\text{Hg}_{1-x}\text{Cd}_x\text{Te}$  sublayer in #A6 structure is 0.27 while in #A9 was changed to 0.33. The parameters of the other layers remain unchanged.

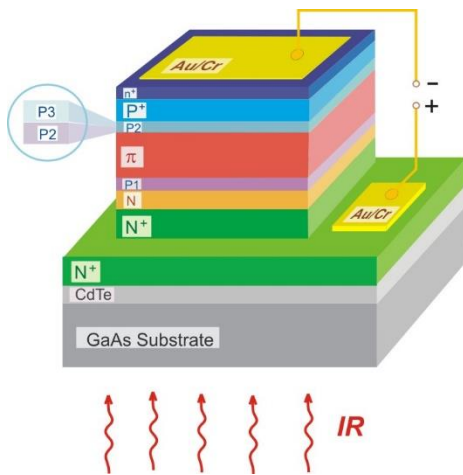


Fig. 1. Schematic structure of modified  $\text{N}^+/\text{N}/\text{P1}/\pi/\text{P2}/\text{P}^+/\text{p}^+/\text{n}^+$  with additional P3 sublayer.

## Results

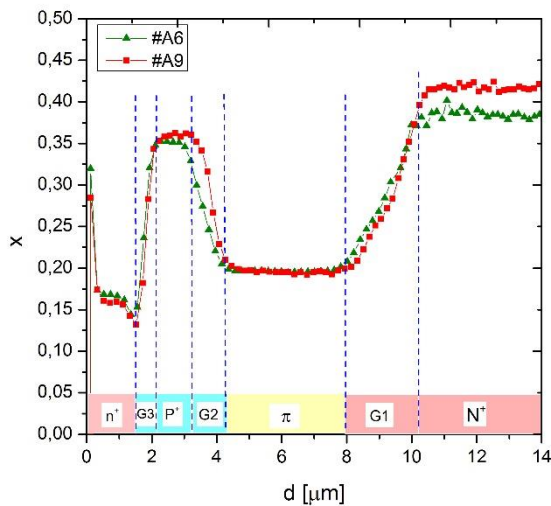


Fig. 2. Composition  $x$  profiles of analysed  $\text{Hg}_{1-x}\text{Cd}_x\text{Te}$  structures acquired from SIMS measurements.

Figure 2 shows  $x$ -composition profiles of analysed #A6 and #A9  $\text{Hg}_{1-x}\text{Cd}_x\text{Te}$  structures acquired from SIMS measurements performed

on CAMECA IMS 6F setup. The  $x$ -composition has been calculated by taking into account the measured counts for Cd, Hg and Te elements. Designed P2 and P3 sublayers seen in Fig.1 create G2 graded gap region in the real structure located between absorber  $\pi$  and  $\text{P}^+$  exclusion layer. The shift in  $x$ -composition of P3 designed sublayer from  $x=0.27$  for #A6 sample to  $x=0.33$  for #A9 sample inhibits the interdiffusion rate in G2 region increasing its sharpness. Such abrupt G2 shape of #A9 sample comply more suitable with the requirements of nonequilibrium operation mode by enhanced electron exclusion from the absorber region. Shaping of G1 interface layer formed from designed N and P1 sublayers is much difficult question because it remains about one hour longer at the growth temperature than the G2 region. Extended interdiffusion processes in G1 interface contribute to substantial reduction in the steepness of its profile.

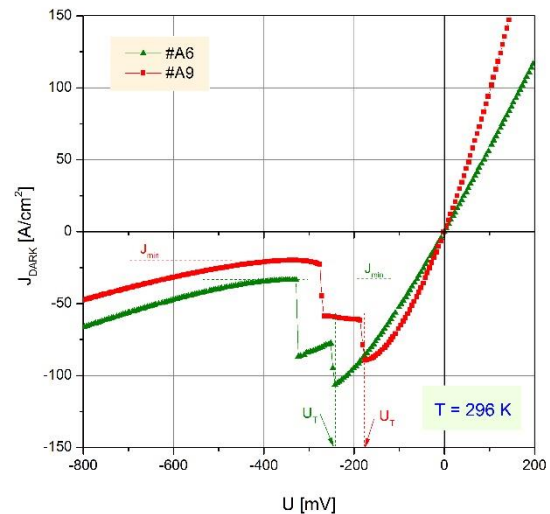


Fig. 3. The dark current density versus bias voltage for #A6 and #A9  $\text{HgCdTe}$  photodiodes measured at room temperature.

The current-voltage characteristics comparison of #A6 and #A9  $\text{HgCdTe}$  structures measured at room temperature are presented in Fig. 3. The current-voltage characteristics have been measured using the Keithley 2400 sourcemeter. The electrical area of devices is  $17.7 \cdot 10^{-9} \text{ m}^2$ . The negative differential resistance is seen for both presented characteristics and evidences the

suppression of Auger processes due to exclusion and extraction phenomena. The threshold voltage  $U_T$  where Auger-suppression commences is about 175 mV for #A9 and about -250mV for #A6 structure. The value of the threshold voltage depends usually on the series resistance and the operating temperature. The minimal current value -  $J_{\min}$  is about 23 A/cm<sup>2</sup> for #A9 structure and about 33 A/cm<sup>2</sup> for #A6 structure. Lower values of  $J_{\min}$  current are more favorable because it contributes to lower noises and higher detectivities of the photodetectors. Corrected abruptness of G2 region in #A9 structure caused Auger suppression more effective and gives lower  $J_{\min}$  current value.

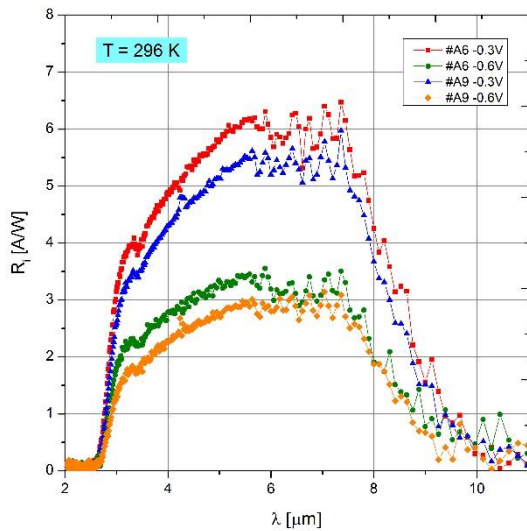


Fig.4. The current responsivity versus wavelength for #A6 and #A9 HgCdTe structures measured at room temperature for different reverse voltage.

Figure 4 presents the comparison of the current responsivity versus wavelength for #A6 and #A9 HgCdTe structures measured at room temperature. The spectral characteristics have been measured at different reverse voltage using the Perkin Elmer FT-IR Spectrometer type Spectrum 2000. The values of the reverse biases were usually selected considering current-voltage analysis and are typically beyond the threshold voltage  $U_T$  (marked in Fig. 3). For both applied reverse voltages: -0.3V and -0.6V the current responsivity is slightly higher for #A6 structure. However this difference is vague and

be close to measurement uncertainty attributed most probably to non-uniformities in the device processing.

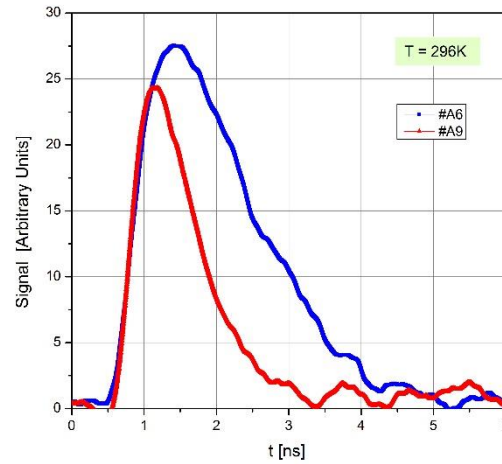


Fig. 5. The response time of #A6 and #A9 structures measured at different temperatures.

The response time is an important parameter of infrared detectors especially used in telecommunication applications. The response time has been measured using the Laser PL2210A and Optical Parametric Generator PG711/DFG with pulse width < 25ps both Ekspla products and DSO 90804A 8 GHz Agilent Oscilloscope. The response time of #A6 and #A9 structures measured at 296K are presented on Fig. 5. The response time of #A6 structure is about 1.9ns while the response time of #A9 structure is about 1.2ns at 296K. The response time is shorter for #A9 structure than for #A6 structure. Corrected abruptness of G2 region in #A9 structure caused Auger suppression more effective and gives response time shorter. Each of the presented characteristics form Fig. 5 was measured under reverse bias -0.6V.

## Conclusion

In this paper we focus on single exemplary step in the progressive optimization process. Corrected abruptness of G2 region contributed to reduce the response time from 1.9ns to 1.2 ns at room temperature.

## References

1. A. Rogalski, Infrared Detectors, second edition, CRC Press, Boca Raton, 2011.
2. T. Ashley, C.T. Elliott, "Nonequilibrium devices for infra-red detection", *Electron. Lett.* **21**(10), 451–452 (1985).
3. P. Martyniuk, W. Gawron, P. Madejczyk, A. Rogalski, J. Piotrowski, "Modeling of HgCdTe LWIR detector for high operations temperature conditions", *Metrol. Meas.Syst.*, Vol. XX, No.2, pp. 159-170, 2013.



# The Automated Marker-Free Longitudinal IR Breast Image Registration Algorithm

Chi-En Lee<sup>1</sup>, Chung-Ming Chen<sup>2</sup>

<sup>1</sup> Institute of Biomedical Engineering, National Taiwan University  
No1, Sec. 1, Jen - Ai Rd., Taipei 100, Taiwan

E-mail: d00548004@ntu.edu.tw Tel: +886-978-617776

<sup>2</sup> Institute of Biomedical Engineering, National Taiwan University  
No1, Sec. 1, Jen - Ai Rd., Taipei 100, Taiwan

E-mail: chung@ntu.edu.tw Tel: +886-2-3366-5273

Longitudinal IR image registration is an essential step toward the quantitative analysis of the heat energy and pattern change in a time course study. Longitudinal IR image registration is a very difficult task in general because it is impractical and unlikely to keep markers attached on a body surface of a subject for weeks or even longer. Moreover, no anatomic fiducial markers may be found on a body surface. The new longitudinal IR image registration algorithm, i.e., the GPC longitudinal IR image registration algorithm, is the genetic particle competition (GPC) mechanism to select the corresponding points of two IR images fully automatically and may be easily extended to other parts of the human body. The performance assessment shows that the mean registration error is about 0.74 pixels, which is reasonable for longitudinal IR image registration.

## 1. Introduction

The Infrared (IR) image has the advantages of noninvasion, no risks, and low-cost to reveal the heat distribution on the surface of human body. It has been long-time considered as a potential medical imaging modality for diagnosis of various diseases. Example for the breast cancer detection, the metabolic activity and vascular circulation of tumor tissues would be exuberant to make higher temperature areas than surrounding normal tissues while the tumor grows [1,2]. Therefore, tumor may be detected by observing the variation of high-temperature areas or heat patterns [3-5]. But the determination of the breast cancer by using only one-time point infrared image is too arbitrary, so the longitudinal approaches based on the variation of heat pattern over several time points are more reliable for

determining the breast tissues with or without cancerous tissues.

If the longitudinal IR images taken at different time are aligned in the spatiotemporal domain well, the pixel-wise tissues on the breast surface can be analyzed via the change of heat areas [6]. However, the longitudinal IR image registration is generally a hard and unresolved problem in the past, because it is impractical and unlikely to keep markers attached on a body surface of a subject for weeks or even longer, and it is not like X-ray mammograms, MRI images and ultrasound images to find anatomic fiducial markers as feature points to build relationships for transformation models easily [7-9]. To overcome this problem, a marker-free longitudinal IR image registration algorithm was developed to build two novel types of fiducial points and manual determination of corresponding pairs of fiducial points between two images [10]. Nevertheless, manual determination of corresponding pairs is not only labor-intensive and time-consuming, but likely leading to inter-observer's difference. To remedy the deficiencies caused by human intervention, a fully automatically

longitudinal IR image registration algorithm, called genetic particle competition (GPC) registration algorithm, has been developed for efficiently pairing up corresponding points. Moreover, GPC may be easily extended to other parts of the human body.

## 2. Material and Method

### 2.1 Image Acquisition

One IR cameras are employed to measure middle-wavelength IR (MIR) radiation in the 3–5 $\mu\text{m}$  wavelength bands with high temperature sensitivity and spatial resolution. The MIR camera are made by FLIR System with  $320 \times 256$  pixel, 0.02  $^{\circ}\text{C}$  temperature sensitivity and 0.6mm spatial resolution at 1m. There is a chair in front of the MIR camera. The room temperature was approximately 25 degrees Celsius during the photogram.

### 2.2 Algorithm

As sketched in Fig. 1, the flowchart of the new longitudinal IR image registration algorithm includes four stages: (1) initial registration between two IR images, (2) generation of the feature points on the breast surface, (3) establishment of the correspondence between feature points, (4) deformation of the IR images.

The Scale-Invariant Feature Transform (SIFT) is a popular algorithm to detect and describe local features in image [11]. It is used to find the initial corresponding points between the 1<sup>st</sup> IR image and the n<sup>th</sup> IR image. The nonlinear spatial transformation, called Thin Plate Splines (TPS) model [12], refers to the corresponding points found by SIFT to attain a rough registration of the nth IR image to the 1st IR image. The GPC algorithm is based on two novel types of fiducial points. One is the corner points of heat patterns generated by Harris corner detector [13], and the other is the branch points of the skeletons of heat patterns generated by eigenvalues of Hessian matrix for each pixel.

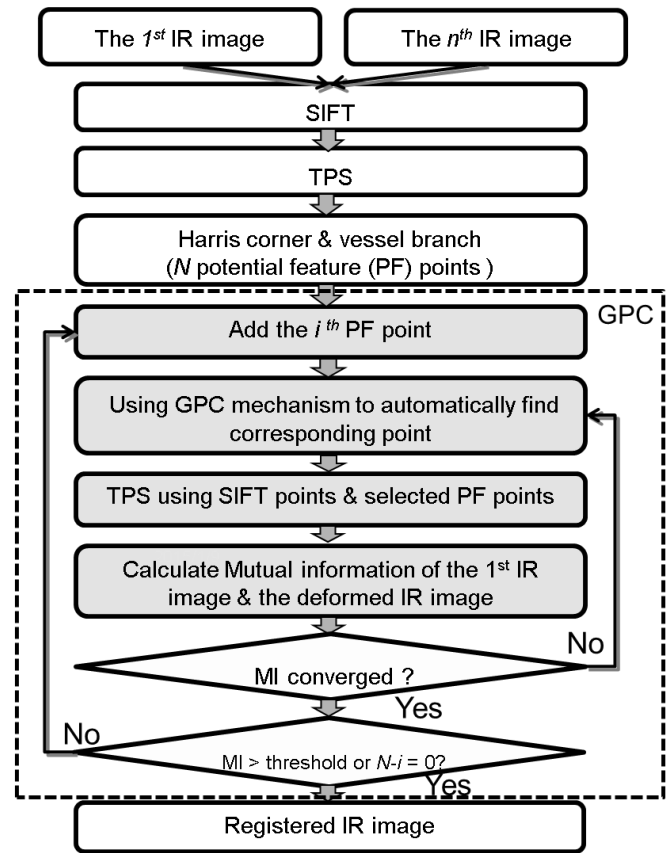


Figure 1. The flowchart of the GPC longitudinal IR image registration algorithm.

#### 2.2.1 Corner points and branch points of the skeletons of heat patterns

*Harris corner detector:* It is used to determine feature points on the corner of heat pattern. The basic idea is the local auto-correlation function of a signal which measures the local changes of the signal with patches shifted by a small amount in different directions.

*Hessian matrix :* The skeleton of heat patterns is generated by evaluating the eigenvalues of the Hessian matrix for each pixel. It can provide the morphological information of heat patterns.

The corner points and the branch points of the skeletons of heat patterns are derived, as shown in Fig. 2(a) and 2(b) for the 1<sup>st</sup> IR image and the deformed n<sup>th</sup> IR image, respectively. These fiducial points are defined as the potential feature (PF) points.

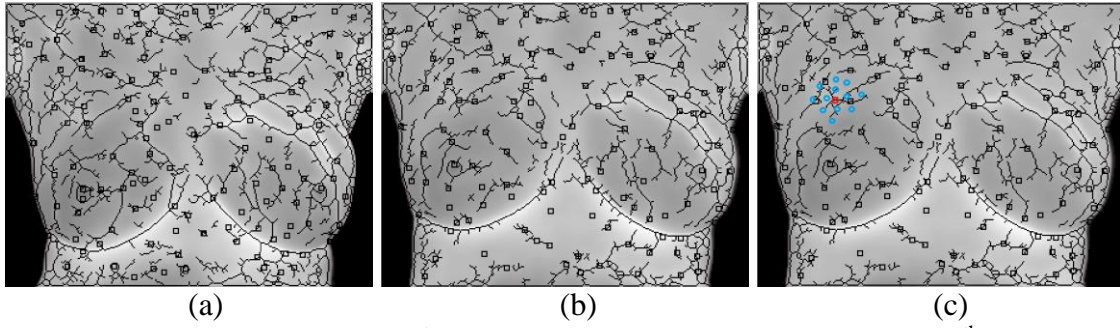


Figure 2. (a) the feature points on the 1<sup>st</sup> IR image, (b) the feature points on the n<sup>th</sup> IR image, (c) for a feature point on the n<sup>th</sup> IR image, the red dot indicating the initial corresponding point and the blue dots indicating those randomly generated candidate points.

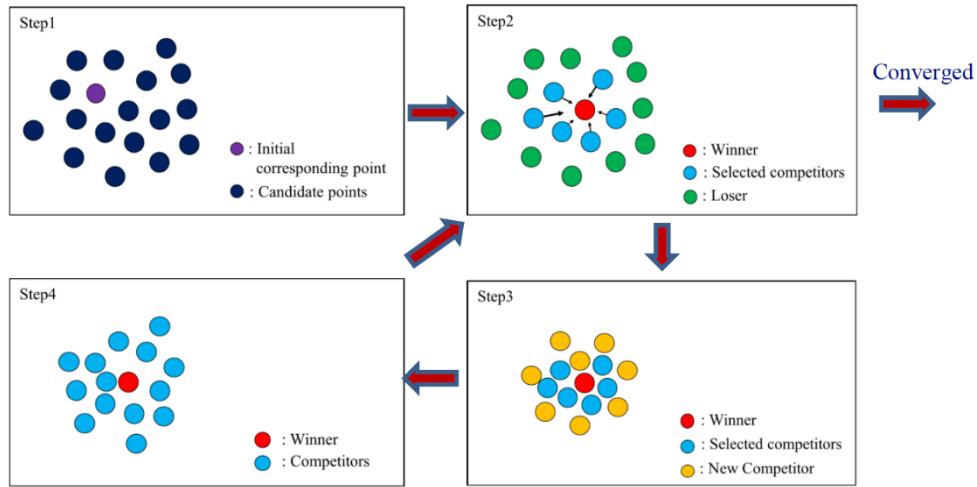


Figure 3. Illustration of the GPC mechanism.

### 2.2.2 The GPC registration algorithm

The basic idea of the GPC registration algorithm is to incorporate genetic evolution, particle searching, and competition mechanism into the optimization process of finding the corresponding pairs of fiducial points between two images. It picks one PF point on the 1<sup>st</sup> IR image and finds the nearest feature point on the deformed n<sup>th</sup> IR image as the initial corresponding point (e.g., the red dot on Fig. 2(c)). The GPC mechanism is carried out to find the corresponding point as follows: (Fig. 3)

**Step1.** Randomly generate a set of candidate points around the initial corresponding point, which form the competitors.

**Step2.** For each of the competitors, (a) perform TPS together with all SIFT-points and all selected PF-points on the deformed n<sup>th</sup> IR image, resulting in a candidate deformed n<sup>th</sup> IR image, (b) calculate the mutual

information (MI) between the 1<sup>st</sup> IR image and the candidate deformed n<sup>th</sup> IR image. Rank the competitors according to their associated MI values. Define the competitor with the maximal MI as winner, those ranked the top 50% of MIs as the selected competitors, and the rest as the losers. These selected competitors will move toward the winner, and each moving distant of the selected competitor is due to the difference of the MI with winner. If the MI of the winner converges, define the winner as a new selected PF-point and go to Step 5. Otherwise, go to Step 3.

**Step3.** Replace the losers by new randomly generated competitors.

**Step4.** Re-define the selected and the new competitors as competitors. Go to Step 2.

**Step5.** If the MI converges and exceeds the threshold or every PF-points have been evaluated, the registration process for the n<sup>th</sup> IR image is end. Otherwise, go to Step 1.

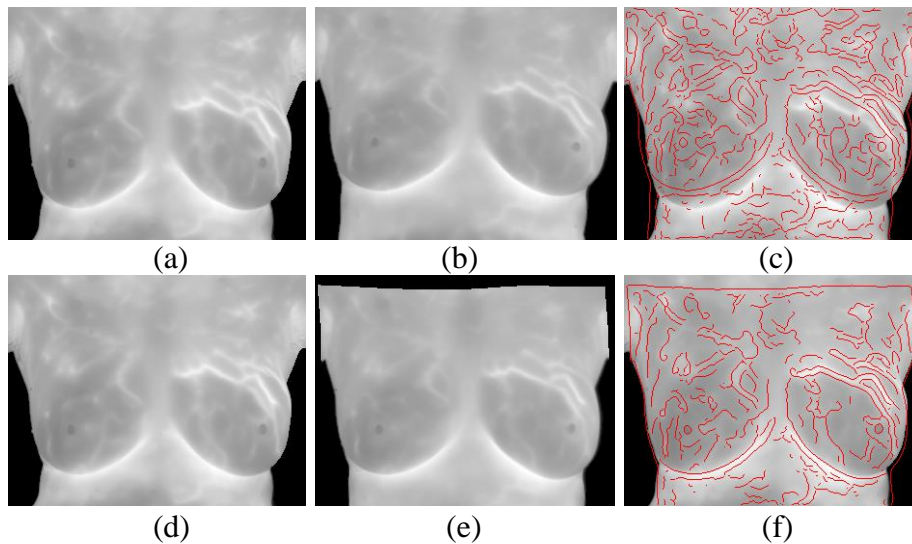


Figure 4. (a) the 1<sup>st</sup> IR image, (b) the n<sup>th</sup> IR image, (c) Canny edges of the n<sup>th</sup> IR image superimposed onto the 1<sup>st</sup> IR image; Registration results by using the GPC registration algorithm, (d) the 1<sup>st</sup> IR image, (e) the deformed n<sup>th</sup> IR image, (f) the superimposed image combining the Canny edges of Fig. 4(e) and the IR image of Fig. 4(d).

### 3. Result and Discussion

In Fig. 4(a) and 4(b), two IR images are labelled as the 1<sup>st</sup> IR image and the n<sup>th</sup> IR image. To demonstrate the spatial deviation of the n<sup>th</sup> IR image from the 1<sup>st</sup> IR image, the Canny edges of the n<sup>th</sup> IR image is superimposed onto the 1<sup>st</sup> IR image in Fig. 4(c). It can be found out that there are much spatial deviation of them. After using the fully automated GPC longitudinal IR image registration algorithm, Fig. 4(d) and 4(e) show the registration results for the Fig. 4(a) and 4(b). Fig. 4(b) was deformed into Fig. 4(e), which was well registered to Fig. 4(d) as demonstrated by the superimposed image, i.e., Fig. 4(f), combining the Canny edges of Fig. 4(e) and the IR image of Fig. 4(d).

To quantify the quality of the registration results, a subject was kept 15 markers (e.g., the black dot) on the breasts as shown in Fig. 5 and taken six-times IR photograms. These markers are selected to calculate the mean distance between the true marker positions and the marker positions on the deformed images. To emphasize that the rest of markers in Fig. 5 are not used for GPC longitudinal registration. The mean distance among 6 registration results is 0.74

pixels and the maximum distance among all markers is 1.63 pixels.

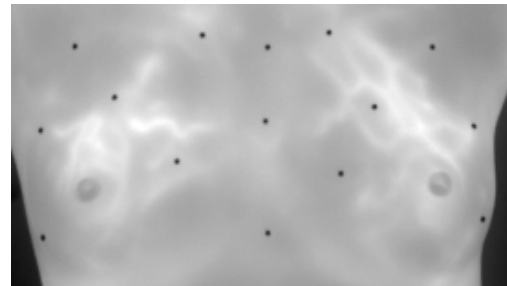


Figure 5. 15 markers for performance assessment of the proposed algorithm on the subject.

### 4. Conclusion

An automated marker-free longitudinal IR image registration algorithm is proposed in this paper to remedy the deficiencies caused by human intervention. It achieved well registration results that mean error is 0.74 pixels and maximum error is 1.63 pixels. The proposed algorithm may serve as a tool for longitudinal registration to analyze the heat energy and pattern change during a time course, and it may be easily extended to other parts of the human body.

## References

1. Zhixiong, G., and Kan-Wan, S., "Simulated parametric studies in optical imaging of tumors through temporal log-slope difference mapping," *Med. Eng. Phys.*, 2007, 9:1142–1148.
2. Tan, J. M. Y., Ng, E. Y. K., Acharya, R., et al., "Comparative study on the use of analytical software to identify the different stages of breast cancer using discrete temperature data," *J. Med. Syst.*, 2009, 33:141–153.
3. Barnes R. B., "Thermography of the Human Body," *Science*. 1963; 140: 870.
4. A. M. Stark and S. Way, "The use of thermovision in the detection of early breast cancer," *Cancer*, vol. 33, no. 6, pp. 1664–1670, 1974.
5. Luciano Boquete, Sergio Ortega, Juan Manuel Miguel-Jiménez, José Manuel Rodríguez-Ascariz, and Román Blanco, "Automated Detection of Breast Cancer in Thermal Infrared Images, Based on Independent Component Analysis," *Journal of Medical Systems*, vol. 36, Issue 1, pp. 103-111, February 2012.
6. B. Zylberberg, J. Salat-Baroux, J. H. Ravina et al., "Initial chemoimmunotherapy in inflammatory carcinoma of the breast," *Cancer*, vol. 49, no. 8, pp. 1537–1543, 1982.
7. W.R. Crum, T. Hartkens, and D. L.G. Hill, "Non-rigid image registration: theory and practice," *British Journal of Radiology*, vol. 77, no. 2, pp. S140–S153, 2004.
8. C.R. Meyer, J.L. Boes, B. Kim et al., "Demonstration of accuracy and clinical versatility of mutual information for automatic multimodality image fusion using affine and thin-plate spline warped geometric deformations," *Medical Image Analysis*, vol. 1, no. 3, pp. 195–206, 1997.
9. P. J. Kostelec, J. B. Weaver, and D. M. Healy Jr., "Multiresolution elastic image registration," *Medical Physics*, vol. 25, no. 9, pp. 1593–1604, 1998.
10. C.Y. Lee, Z.W. Chang, W.J. Lee, C.Y. Lee, S.C. Lee, C.S. Huang, Y.C. Chang, C.M. Chen, "Longitudinal registration for breast IR image without markers," in *Proceedings of the 11<sup>th</sup> International Conference on Quantitative InfraRed Thermography*, pp. 397, 2012.
11. David G. Lowe, "Object recognition from local scale-invariant features," *Proceedings of the International Conference on Computer Vision 2*, pp. 1150–1157, 1999.
12. J. Duchon, "Splines minimizing rotation-invariant semi-norms in Sobolev spaces," *Constructive Theory of Functions of Several Variables Lecture Notes in Mathematics*, vol. 571, pp. 85-100, 1977.
13. C. Harris, and M. Stephens, "A combined corner and edge detector," *Proceedings of the 4<sup>th</sup> Alvey Vision Conference*, pp. 147–151, 1988.

# DEGRADATION OF SOME EXPERIMENTAL DENTAL COMPOSITE MATERIALS

S. Boboia (Cuc)<sup>1</sup>, D. Prodan<sup>1</sup>, L.Silaghi-Dumitrescu<sup>1</sup>, C. Saroși<sup>1</sup>, V.Prejmorean<sup>2</sup>, A. Saplonțai<sup>3</sup>, M. Moldovan<sup>1</sup>

<sup>1</sup>"Babes Bolyai" University - "Raluca Ripan" Chemistry Research Institute, Fântânele 30,  
Cod 400294, Cluj-Napoca, Romania,  
stancabobo@yahoo.com

<sup>2</sup>"Babes Bolyai" University - Faculty of Mathematics and Computer Science, M Kogălniceanu 1,  
Cod 400084, Cluj-Napoca, Romania,

<sup>3</sup>"Iuliu Hațieganu" University of Medicine and Pharmacy of Cluj-Napoca, Babeș 8,  
Cod 400012, Cluj-Napoca, Romania

The purpose of this study is to evaluate the degradation in time of some experimental dental composite. Thirteen Bis-GMA/TEGDMA-based experimental dental composites consisting of 6 different ratios of fillers in relation to the inorganic phase and each of this samples have 2 ratios of initiation system. The degradation behavior of experimental composite biomaterials polymerized and immersed in two different environments (water and alcoholic solution) was followed by IR spectroscopy, RAMAN spectroscopy and scanning electron microscopy SEM. The composites containing the largest quantity of particle exhibited minimum degradation. SEM analysis showed that only the samples immersed in alcoholic solution and with a small amount of filler present some fractures at the surface of the dental composites.

## Introduction

Because the dental composites preparation consists in incorporating an inorganic phase (filler) into a cross-linked polymer matrix with three-dimensional structure, it is deduced that the polymerization process, which is photochemically or chemical activated, the polymerization result of each individual system is dependent on its composition, namely on the concentration and chemical structure of dimethacrylate monomer diluents, initiators and inhibitors [1].

Several studies carried out that the polymers from the matrix showed that may be subject to a myriad of degradation processes in the oral cavity [2]. Polymer degradation does not occur as a result of isolated processes, but due to several factors as: saliva, chewing, thermal and chemical dietary changes [3,4].

The resulting polymer network and its properties are influenced by the degree of polymerization, the binding between the strands, the length of the chain, the residual monomers, the gaps and the heterogeneity from the network.

The filler - organic matrix connection is the most important for a proper composite properties, and from this point of view is easy to justify why a filler-matrix bond selling could be the first destruct mechanism. Water may cause a rupture at the silane-resin interface and the appearance of the powder at the composite surface. In addition the water molecules can diffuse into the polymer matrix and can attack glass particles, silicon dioxide, causing the separation of particles which having the effect on the drastic reduction in the mechanical strength [5-7].

The degradation of some experimental dental composite biomaterials developed and immersed in two different environments (water and alcoholic solution) was followed by IR, Raman and scanning electron microscopy (SEM).



Table 1. Composition of dental biomaterials

% Samples	Organic Phase		Inorganic Phase					Chemical Initiation System	
	Bis-GMA	TEGDMA	Quartz	Glass with Sr	FAP	TCP	SiO <sub>2</sub>	DHEPT (% from Paste A)	BPO (% from Paste B)
S1a	24.5	10.5	26	23	6.5	6.5	3	1	2
S1b	24.5	10.5	26	23	6.5	6.5	3	0.7	1.2
S2a	31.5	13.5	22	19	5.5	5.5	3	1	2
S2b	31.5	13.5	22	19	5.5	5.5	3	0.7	1.2
S3a	26	9	26	23	6.5	6.5	3	1	2
S3b	26	9	26	23	6.5	6.5	3	0.7	1.2
S4a	34	11	22	19	5.5	5.5	3	1	2
S4b	34	11	22	19	5.5	5.5	3	0.7	1.2
S5a	19	16	26	23	6.5	6.5	3	1	2
S5b	19	16	26	23	6.5	6.5	3	0.7	1.2
S6a	25	20	22	19	5.5	5.5	3	1	2
S6b	25	20	22	19	5.5	5.5	3	0.7	1.2
SP*	34	11	22	19	5.5	5.5	3	CQ: 0.5	DMAEM: 1

\* Photochemical Initiation System

**Bis-GMA:** 2,2-bis[4-(2-hydroxy-3-methacryloyloxypropoxy) phenyl]propane (synthesized in Department of Polymer Composites laboratory); **TEGDMA:** Triethyleneglycol dimethacrylate (Aldrich, Germany); **FAP:** Fluoridated hydroxylapatite (synthesized in Department of Polymer Composites laboratory); **SiO<sub>2</sub>:** Colloidal silica (Romania); **BPO:** Benzoyl peroxide (Merck, Germany); **CQ:** camphorquinone (Aldrich, Germany); **DMAEM:** dimethylaminomethylmetacrylate (Aldrich, Germany); **DHPET:** N,N-dihydroxyethyl-p-toluidine (Aldrich, Germany); **TCP:** Ca<sub>3</sub>(PO<sub>4</sub>)<sub>2</sub>; Tricalciumphosphate (synthesized in Department of Polymer Composites laboratory).

## Approach and techniques

For this study were performed 13 dental composite samples, the difference between them being 6 different ratios of fillers in relation to the inorganic phase and each of this samples have 2 ratios of initiation system. The percentage composition of samples is shown in Table 1.

For degradation analyze the composite samples are polymerized in a teflon mold with a diameter of 5 mm and 0.5 mm thickness.

## Infrared Spectroscopy (IR)

Polymerized samples were studied using JASCO FT-IR 610 at the "Raluca Ripan" Institute of Chemistry Research, Cluj-Napoca. The samples were examined immediately after polymerization reaction (reference value) and after 8 and 14 days of samples immersion in water/alcohol solution.

## RAMAN Spectroscopy (RAMAN)

Preparations were studied using a Bruker IFS 120HR with full mode Raman FRA 106 and a resolution of 2 cm<sup>-1</sup>. For excitation of the samples was used Nd-YAG laser radiation of 770 nm. The study was conducted at the

National Institute of Research and Development of Isotopic and Molecular Technologies Cluj-Napoca. The samples were examined immediately after the polymerization and after 7 days of immersion in water /alcoholic solution.

## Scanning electron microscopy (SEM)

The sample surface investigation was performed with an electronic microscope QUANTA 133 from FEI company. The samples were analyzed immediately after polymerization reaction and after 14 days of immersion.

## Results and discussion

### Infrared Spectroscopy (IR)

IR spectra highlights the characteristic bond bands of Si-O-Si at ~ 1059 cm<sup>-1</sup> and probably Si-O-CH<sub>2</sub> because the band is broader and covers the 1190 to 1140 cm<sup>-1</sup> area corresponding to the Si-O-CH<sub>2</sub> bond.

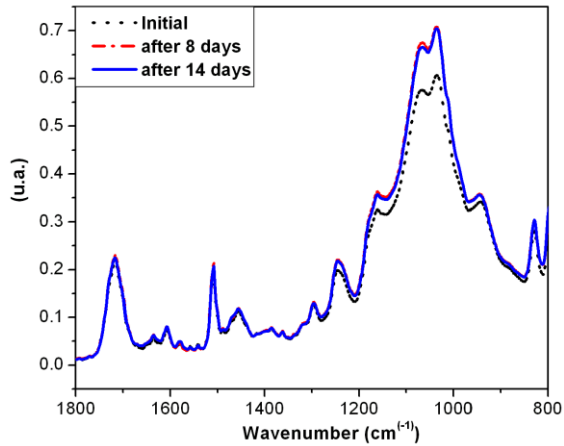


Figure 1. IR spectra of composites SP investigated after immersion in water

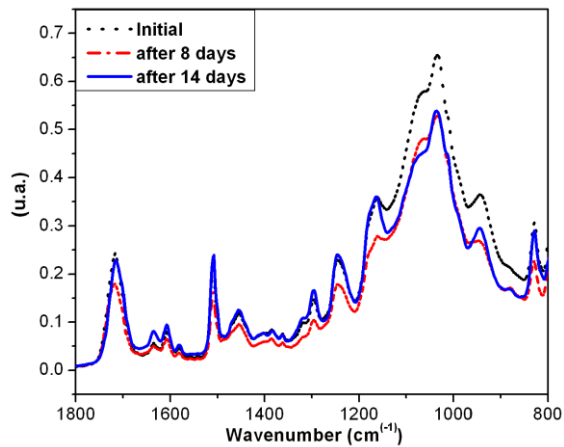


Figure 2. IR spectra of composites SP investigated after immersion in alcoholic solution

IR spectra recorded on the same samples composition but immersed in water or alcohol solutions, have highlighted the intensity reduced of the characteristic peaks of Si-O-Si bond (Figure 1, 2). In all samples is observed that the decreased intensity peaks at  $\sim 1059 \text{ cm}^{-1}$  is more pronounced in alcoholic solution for samples 3b and 4b [8]. Reducing the peak intensity at  $\sim 1059 \text{ cm}^{-1}$  can be explained by the breakage of the Si-O-Si bond. Breaking the Si-O-Si bond and not the Si-C bond it can be justified by comparing the binding energies of Si-O and Si-C in dry environment. Thus in the dry Si-O bond energy is  $89.3 \text{ kcal/mol}$  and Si-C bond is  $57.6 \text{ kcal/mol}$ .

## RAMAN Spectroscopy

It can observe a reduction in intensity of the ester peak at  $1720 \text{ cm}^{-1}$ , due to partial ionization of the carboxyl groups. There were no differences in the intensity at  $1638 \text{ cm}^{-1}$  for C-C group of methacrylate fragments which are linked to radical polymerization with the existent residual monomer. It is also observed, for all samples (stored in water and alcohol solution), the absence of specific methacrylate band C=C assigned wavelength from  $1297 \text{ cm}^{-1}$ , due to the lost risk of releasing residual monomers [9]. Raman spectra (Figure 3, 4) recorded for the same samples revealed no significant changes regarding the effect of alcoholic solution or water on the organic components of experimental composite systems studied.

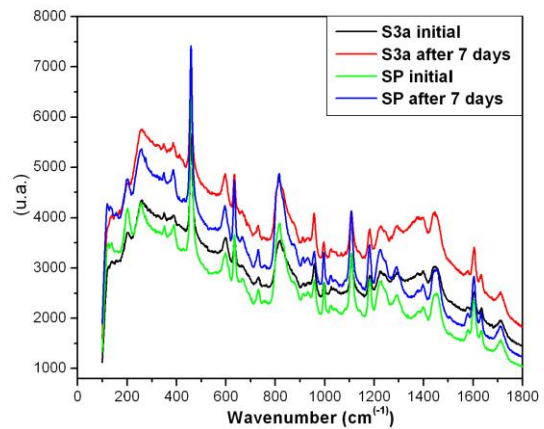


Figure 3. RAMAN spectra of composites investigated after immersion in water

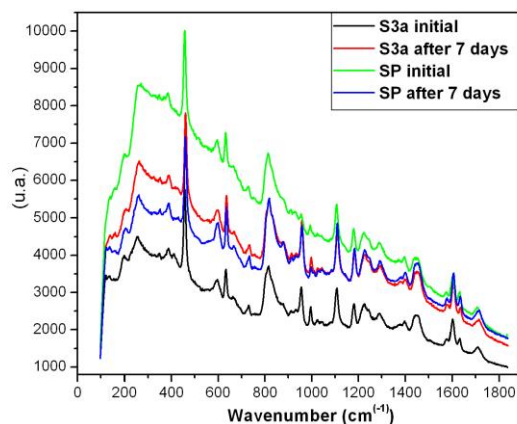


Figure 4. RAMAN spectra of composites investigated after immersion in alcoholic solution

## Scanning electron microscopy (SEM)

SEM recorded images show that immersion of the composite material in distilled water (Figure 11), does not induce a greater release of the filler to the similar composite materials stored in alcoholic solution (Figure 12) [10,11].

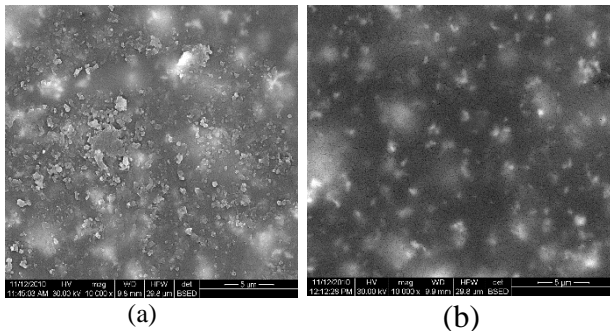


Figure 11. SEM images of SP composite obtained before(a) and after (b) immersion in distilled water. Magnification X 5 $\mu$ m

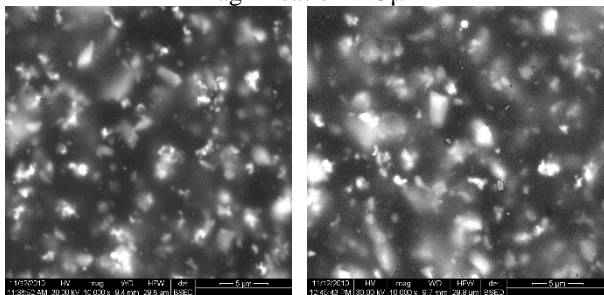


Figure 12. SEM images of SP composite obtained before(a) and after (b) immersion in alcoholic solution. Magnification X 5 $\mu$ m

## Conclusion

Most fractures in the surface of the composites was observed in the samples immersed in an alcoholic solution. The tendency to introduce more filler in the dental biomaterial composition, in desire to increase the modulus of elasticity, wear resistance, compressive strength and to reduce thermal expansion and contraction of water absorption polymerization of the composite can present a danger. If the debonding occurs in a composite rich in filler, the above mentioned properties will deteriorate more than in the case of composites with less fillers.

## Acknowledgements

This work was funded by: the Romanian Ministry of Education and Research, national project PNII no: 127/2014, 191/2014.

## References

1. M. E. Schrader, A. Block, Tracer study of kinetics and mechanism of hydrolytically induced interfacial failure, J Polym Sci Part C, Vol.34, pp.281-291, 1971.
2. J. L. Ferracane, Hygroscopic and hydrolytic effects in dental polymer networks, Dent Mater, Vol.22, pp.211–22, 2006.
3. J. P. Santerre, L. Shajii, B. W. Leung, Relation of dental composite formulations to their degradation and the release of hydrolyzed polymeric-resin-derived products, Crit Rev Oral Biol Med, Vol.12, pp.136–51, 2001.
4. L. Holland, The properties of glass surface, Interscience Publ., J. Wiley, New York, 1964.
5. N. K. Sarkar, A. Karmaker, A. Prasad, F. Shih, Simulation of in vivo degradation of dental composites, J. of Mat. Sci. Lett., Vol.18, pp.17-49, 1999.
6. S. El-Safy, N. Silikas, D. C. Watts, Creep deformation of restorative resin-composites intended for bulk-fill placement, Dent Mater, Vol.28, no.8, pp.928–935, 2012.
7. C. P. Turssi, J. L. Ferracane, K. Vogal, Filler Features and their effects on wear and degree of conversion of particulate dental resin composites, Biomaterials, Vol.26, pp.4932-4937, 2005.
8. D. Fried, N. Ashouri, T. M. Breunig, R. K. Shori, Mechanism of water augmentation during IR laser irradiation of dental enamel, Lasers Surg Med, Vol.31, pp.186-193, 2002.
9. R. J. Scougall-Vilchis, Y. Hotta, M. Hotta, T. Idono, K. Yamamoto, Examination of composite resins with electron microscopy, microhardness tester and energy dispersive X-ray microanalyzer, Dent Mater J, Vol.28, pp.102–112, 2009.
10. L. Han, H. Ishizaki, M. Fukushima, T. Okiji, Morphological analysis of flowable resins after long-term storage or surface polishing with a mini-brush, Dent Mater J, Vol.28, pp.277–284, 2009.
11. M. Toledano, R. Osorio, E. Osorio, Sorption and solubility of resin-based restorative dental materials, J Dent, Vol.31, No.1, pp.43-50, 2003.

# ADHESION STUDIES OF DENTAL SEALANTS TO ENAMEL BY USING OPTICAL MICROSCOPY AND LOCK-IN INFRARED THERMOGRAPHY

M. Streza<sup>1\*</sup>, D. Dadarlat<sup>1</sup>, D. Prodan<sup>2</sup>, I. Hodisan<sup>3</sup>, S. Boboia<sup>2</sup>, C. Prejmerean<sup>2</sup>

<sup>1</sup> NIR&DIMIT, 67-103 Donat Street, 400293 Cluj-Napoca, Romania, streza.mihaela@gmail.com

<sup>2</sup> Babes-Bolyai University, Raluca Ripan Chemistry Research Institute, Fantanele Street, 400294 Cluj-Napoca, Romania, cristina.prejmerean@gmail.com

<sup>3</sup> Iuliu Hațieganu University of Medicine and Pharmacy, Emil Isac Street, 400023 Cluj-Napoca, Romania, ioanahodisan@yahoo.com

The aim of this study was to investigate the sealant/enamel interface by lock-in thermography technique and optical microscopy. In this regard 10 non-carious human teeth were sealed with experimental and commercial sealants and then longitudinally sectioned in slices that were then examined. Lock-in thermography showed its capacity to detect the presence of possible microgaps along the whole interface. No difference between the adhesion capacity of sealants to dental enamel was observed.

## Introduction

Dental caries are one of the most common diseases in both children and adults, but are largely preventable. In order to prevent or stop the dental caries process before it reaches the ends stage of the disease, fissure sealants can be applied to the top face of teeth. The sealant forms a protective layer that keeps food and bacteria away from the pits and fissures of the teeth. Dental sealants are a safe and cost-efficient dental procedure for patients prone to cavities, such as children and teenagers. The lack of adaptation between a dental filling and tooth structure has for many years been a major problem in dentistry. In order to obtain a good dental adhesion, a perfect adaptation of the sealant to the tooth surface is required. This is why the evaluation of a dental restoration in a non-invasive way is of special importance in clinical practice. In dentistry there are only two investigation techniques currently used for the evaluation of marginal adaptation of different

composites to primary teeth cavities: (1) dye penetration scoring system and (2) scanning electron microscopy (SEM).

Thermography is a method widely used in internal medicine, but too little in dentistry, in spite of its non-invasive character. In dentistry IR thermography is mainly used for temperature monitoring of dental stuffs during the curing process. Two recent publications dealing with the evaluation of a dental restoration by lock-in thermography technique (LiT) showed the capability of the method for gap detection.

The diagnosis of incipient and moderate dental lesions is currently made by X-ray radiography which is invasive and has a poor sensitivity. Polarized Raman spectroscopy is another emerging technology in the field of dental diagnosis which uses the degree of polarization in the backscattered light to differentiate between intact and carious enamel **Error! Reference source not found.** Mandelis et al.

**Error! Reference source not found.** was the first to apply photothermal radiometry (PTR) and laser luminescence to detect fissures and early demineralization in human teeth.

The aim of this study is to analyze the sealant/enamel interface by lock-in thermography technique, based on the idea that the presence of an interface gap will bear information carried out by a perturbation of the amplitude or phase of the thermal wave (compared to sound enamel). In order to check the capabilities of this method, complementary investigations were carried out by optical microscopy.

### Materials and experimental setup

Two experimental light-curing giomers (G1 and G2) were prepared as monopastes by mixing the resins with the hybrid filler in a weight ratio of 1:1. The resin of G1 giomer was formulated using 2,2-bis[4-(2-hydroxy-3-methacryloxypropoxy)phenyl] propane (Bis-GMA) and the resin of G2 giomer contained an urethane tetramethacrylate Bis-GMA analogue as base monomer. Triethyleneglycoldimethacrylate was used as diluting monomer. Base monomer: diluting monomer ratio in the resins was 1:1 (wt). For the obtaining of the hybrid filler, pre-reacted glass filler (PRG), fluorohydroxy-apatite and a silanized barium fluoro-alumino-boro-silicate glass powder were mixed and then sifted together (1:1:3 wt ratio). The PRG was synthesized using the copolymer obtained from the acrylic acid, itaconic acid and N-acryloyl leucine (4:1:0.5 molar ratio) grafted with N-methacryloyloxyethylcarbamoyl-N'-6-hydroxy-hexylamine [6]. Silanation was carried out with A-174 silane. The commercial pit and fissure sealant Fissurit F, Vocco GmbH (FS) was used as control.

10 recently extracted non-carious human teeth were sealed with each material (G1, G2, FS), were embedded in polymethyl methacrylate (PMMA) and then were sectioned longitudinally in slices of 2 mm thickness using a diamond saw (Isomet 1000, Buehler, USA) as is shown in Fig. 1.

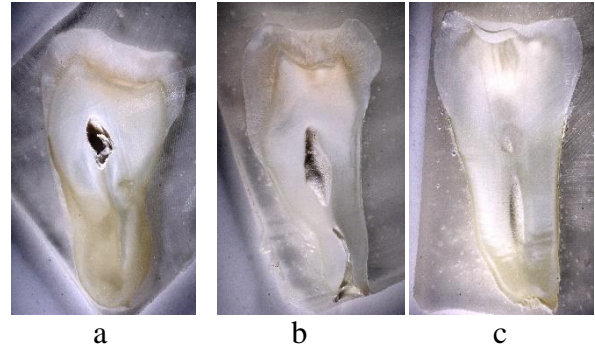


Fig. 1. Slices of teeth sealed with G1 (a), G2 (b) and Fissurit FS (c) and embedded in PMMA.

### Approach and image analysis procedure

The tooth is a multilayered structure where each layer has its own thermal/optical properties and inhomogeneities. The heat generation and transfer in such turbid media are thereby very complicated and are governed by scattering of light and photon diffusion.

In the 400-700 nm wavelength range, both enamel and dentine strongly scatter the light, with coefficients of the order of  $\mu_{\text{scat, enamel, vis}} = 60 \text{ cm}^{-1}$ . In the meantime, they have relatively low absorption,  $\mu_{\text{abs, enamel, vis}} = 1 \text{ cm}^{-1}$  and  $\mu_{\text{abs, dentine, vis}} = 4 \text{ cm}^{-1}$ . The photons are scattered in the materials along complex trajectories before an absorption event occurs. Taking into account a homogeneous half-space with absorption and scattering coefficients  $\mu_{\text{abs}}$  and  $\mu_{\text{scat}}$ , illuminated by an intensity  $I_0$  in a point-like region, one can define an effective coefficient

$$\mu_{\text{eff}} = \sqrt{3\mu_{\text{scat}} \cdot (\mu_{\text{scat}} + \mu_{\text{abs}})}$$

The optical intensity at a distance  $r$  from the source follows a radial repartition law of the form

$$I(r) = I_0 \cdot (1/r) \cdot e^{-\mu_{\text{eff}} \cdot r}$$

Knowing the optical properties of enamel,  $\mu_{\text{abs, enamel, vis}}$  and  $\mu_{\text{scat, enamel, vis}}$ , we obtain  $\mu_{\text{eff}} = 53 \text{ cm}^{-1}$ , and we get the (1/e) radius of the region where heat is deposited around:  $r_{1/e, \text{vis}} = 700 \mu\text{m}$ . As a result, a point-like laser spot in the visible will heat a relatively large and diffuse half-sphere-shaped region having a radius  $r_{1/e, \text{vis}}$  (which is smaller than the size of tooth having several mm).

The thermal wave perturbations related to the presence of cracks are very weak compared to the excitation background. The image processing algorithm based on the second spatial



derivative of the amplitude will improve the quality of the resulted images by enhancing the signature of defective zones. Our proposed workflow of image processing includes the following steps: (1) introducing a threshold factor ( $a$ ) that creates a mask for the amplitude image; (2) applying the second derivative of the amplitude in order to emphasize local contrasts containing the useful signal.; (3) filtering out the spatial heat source fluctuations; (4) binarization of the resulted image and filtering out the noise.

## Results and Discussion

Three preparations were selected from each group and each slice has been analyzed by optical microscopy and LIT.

Fig. 2 shows the optical image of the slice FS. It can be clearly seen the sealant/enamel interface which shows no defects in the sealant region. The position indicated by the circle in fig. 2 shows the laser spot located near the interface.

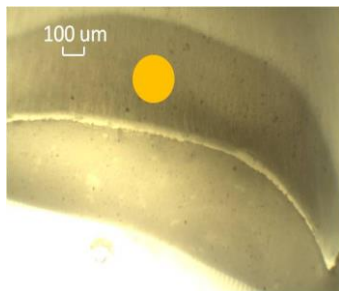


Fig. 2. Optical image of specimen FS.

Fig. 3 ((a)-(b)) represents the DC image and the profile along the marked lines for FS, which are strongly disturbed. This image is very difficult to analyze.

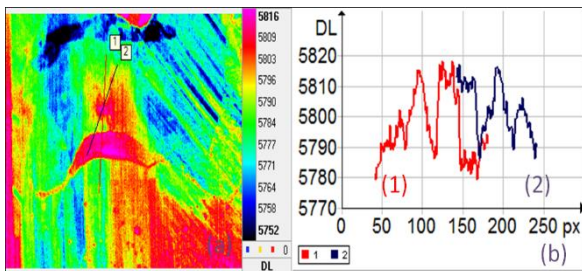


Fig. 3. DC image (a) and corresponding profiles (b).

Fig. 4a shows the amplitude image at the excitation frequency  $f_0$  after applying the lock-in

detection procedure. This image has a better contrast. No perturbation in the temperature profile is detected (fig. 4b), meaning that the heat flow at sealant/enamel interface is not disturbed. This means that no discontinuities are detected at the investigated interface.

Another optical image of the specimen G1 is shown in fig. 5. The presence of a gap at the sealant/enamel interface can be observed. The same lock-in procedure was applied to this specimen (the heat source is drawn in fig. 5 by the spot located close to the interface under investigation).

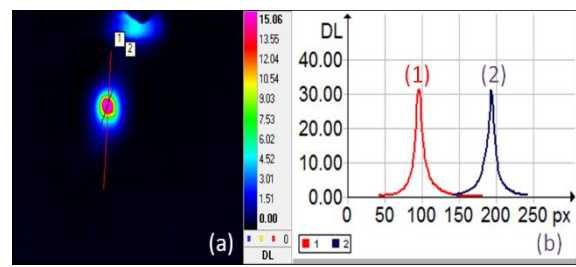


Fig. 4. Amplitude image (a) and corresponding profiles (b).

In this case the heat flow is disturbed at sealant/enamel interface, as can be clearly seen in amplitude and phase images (see fig. 6- 7).

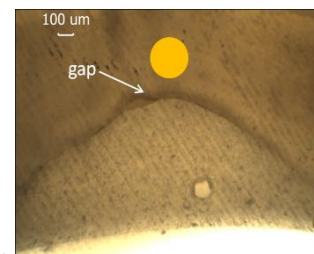


Fig. 5. Optical image of specimen G1.

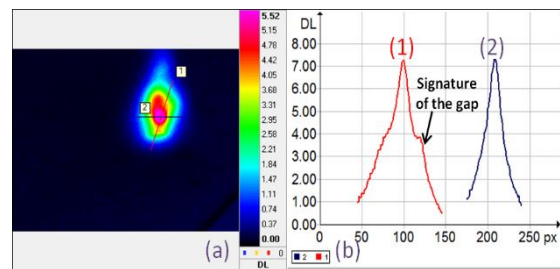


Fig. 6. Amplitude image (a) and corresponding profiles (b).



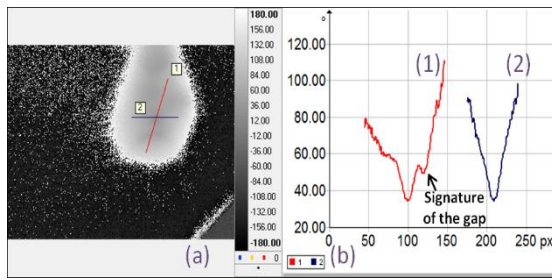


Fig. 7. Phase image (a) and corresponding profiles (b).

Both amplitude and phase images provide information about the fissure localization on the surface. The thermal wave disturbance above the flaw shows a propagation delay as compared to a reference signal (see Fig. 7b) or a small perturbation of the amplitude above the defective zone as compared to sound enamel (see Fig. 6b).

The gap acts as a thermal barrier disrupting the heat diffusion. To be detected, the gap must be located within the diffusion region of the heat. In order to highlight the small temperature variations surrounding the flow, the second spatial derivative of the amplitude image is applied. In doing so, the contrast given by the presence of a gap at interface is enhanced and more features become visible. The irrelevant fluctuations from the laser area were filtered out, by using a mask. The contour of the gap is slightly visible (Fig. 8).

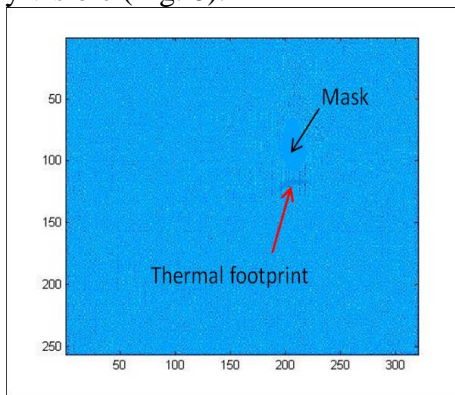


Fig. 8. Enhanced amplitude image.

The binary image after applying the image processing algorithm previously described is shown in Fig 9. This image reveals the presence of a discontinuity at the sealant/enamel interface.

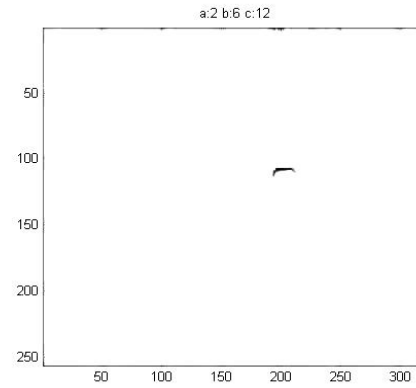


Fig. 9. Resulting binary image.

## Conclusion

In this paper, the adaptation of two experimental giomer sealants (G1 and G2) and one commercial composite sealant (FS) to the tooth has been analyzed by optical microscopy and lock-in thermography. Concerning the materials there were no significant differences in the behavior of the three dental sealants. The experimental giomer G2 which contains the urethane Bis-GMA could be a good candidate in dental applications as pit and fissure sealant taking into account its capacity of adhesion to dental enamel. Lock-in thermography showed its capacity to detect defects located at dental interfaces. Nevertheless, for a proper interpretation of infrared thermograms, a correct excitation frequency must be selected. Both scattering and absorption of light in teeth must be taken into account as well.

## Acknowledgements

The study was supported by the Ministry of Education Research and Youth of Romania, through the National Research Program PN-II-PT-PCCA-2011-3.2-1419.

## References

1. Gu,Ja-Uk, Choi,Nak-Sam; : NDE of the Internal hole defect of dental composite restoration using infared lock-in thermography, *Journal of the Korean Society for Nondestructive Testing*, vol. 33, pp 40-45, 2013.
2. Gu,Ja-Uk, Choi,Nak-Sam: Evaluation of Delamination of Dental Composite Restoration using Infrared Lock-in

- Thermography, *Composite Research*, vol. 25, pp. 236-240, 2012.
3. A. C.T. Ko et al : Detection of early dental caries using polarized Raman spectroscopy, *Optics Express*, vol. 14, no. 1, pp. 203-215, 2006.
  4. A. Mandelis &al. : Novel dental depth profilometric imaging using simultaneous frequency-domain infrared photothermal radiometry and laser luminescence, *Proceeding of SPIE*, vol. 3916, pp.130, 2000.
  5. N. Tabatabaei, A. Mandelis, M. Dehghany, K. H. Michaelian, and B. T. Amaechi, "On the sensitivity of Thermophotonic Lock-In Imaging and Polarized Raman Spectroscopy to early dental caries diagnosis," *Journal of Biomedical Optics* **17**, p. 02502, 2012.
  6. T. Buruiana et al. Synthesis of poly(alkenoic acid) with L-leucine residue and methacrylate photopolymerizable groups useful in formulating dental restorative materials *J. Biomater. Sci. Polym. Ed.* 25, 749-765, 2014

# INFLUENCE OF COMPOSITION AND LIGHT CURING MODES UPON THE DEGREE OF CONVERSION OF DENTAL GIOMERS EVALUATED BY FTIR SPECTROSCOPY

C. Prejmerean<sup>1</sup>, D. Prodan<sup>1</sup>, M. Vlassa<sup>1</sup>, T. Buruiana<sup>2</sup>, L. Colceriu<sup>3</sup>, M. Moldovan<sup>1</sup>

<sup>1</sup>Babes Bolyai University - Raluca Ripan Chemistry Research Institute, Fantanele Street, Nr. 30, 400294, Cluj-Napoca, Romania, cristina.prejmerean@gmail.com, doina\_prodan@yahoo.com, mihaela\_cecilia@yahoo.com, mmarioara2004@yahoo.com

<sup>2</sup>Petru Poni Institute of Macromolecular Chemistry, Aleea Grigore Ghica Voda, nr. 41A 700487 Iasi, Romania, tbur@icmpp.ro

<sup>3</sup>Iuliu Hațieganu University of Medicine and Pharmacy, Louis Pasteur Street, Nr 4, 400349 Cluj-Napoca, Romania, loredana\_cc@yahoo.fr

The aim of the present study was to evaluate the influence of the resin composition and of the photo-polymerization modes upon the degree of conversion of dental resins and of the corresponding giomers. In this purpose a series of new experimental resins and the corresponding new giomers were investigated. A halogen lamp and a diode-blue LED lamp were used for the curing of materials. The results showed that the composition of the resins greatly influenced the conversion. ATR-FTIR was found to be a suitable technique for the evaluation of conversion in giomer-type dental structures.

## 1. Introduction

Longevity, fluoride release and recharge abilities are crucial for the clinical performances of aesthetic dental restorative materials. Considering these requirements, during the last decade, a new class of hybrid materials which combine the chemistry of diacrylic resin composites with the one of the glass ionomer cements were introduced on the market by Shofu (Kyoto, Japan), and its were named giomers. In the formulation of giomers, the superficially active glass is pre-reacted with a polyacid and then blended with the resin to form a composite-type structure [1]. The glass core is thus protected from moisture, conferring these materials long-term aesthetics and durability as well as controllable ion release and recharge properties [2, 3].

The giomers harden by the radical polymerization of the monomers from the resin matrix. A crosslinked three-dimensional polymer network is formed in which the filler particles are dispersed. Because of the gel effect up to 50% methacrylate groups remain unreacted in the form of residual double bonds (RDB). Most of the RDB are pendant methacrylate groups attached to the polymer network and a small proportion of them represent the free residual monomer (about 10%). The presence of the RDB has a plasticizing effect on the polymer, greatly influencing the properties of the composite material (mechanical strengths, discoloration, wear, etc.).

The aim of the present work was to study the influence of the resin composition and of the photo-polymerization modes upon the degree of conversion of dental copolymers and of the corresponding giomers using the FTIR technique.

## 2. Materials and methods

### 2.1. Preparation of dental copolymers

Disk copolymers of 5 mm diameter and 0.5 mm thickness were obtained in Teflon molds by exposing the dental resins for 40 sec to OPTILUX 501 halogen lamp (Demetron, Kerr Co., wavelength 400nm-505nm, intensity 100mW/cm<sup>2</sup>-1999mW/cm<sup>2</sup>), and respectively for 20 sec to diode-blue LED E lamp (Guilin Woodpecker Medical Instruments Co. wavelength 420 nm-480 nm, intensity 850mW/cm<sup>2</sup>-1000mW/cm<sup>2</sup>). The distance of the material to the light sources was 1 mm. The resins consisted of 2,2-bis[4-(2-hydroxy-3-methacryloxypropoxy-phenyl)propane (Bis-GMAcom) or a original synthesized urethane tetra-methacrylate Bis-GMA analogue obtained by the addition of methacryloyloxyethyl-2-bromoethylurethane to the Bis-GMA glycidyl hydroxyl groups (Bis-GMAexp) and triethyleneglycol dimethacrylate (TEGDMA). In the resins 0.5% (by weight) camphorquinone and 1% (by weight) dimethylaminoethyl-methacrylate was dissolved.

Table 1 presents the composition and the modes of photopolymerization of the investigated resins.

Resin/Copolymer Code	Bis-GMA com %	Bis-GMA exp %	TEG-DMA %	Halo gen lamp	LED E lamp
R1/C1	70	-	30	√	-
R2/C2	70	-	30	-	√
R3/C3	-	70	30	√	-
R4/C4	-	70	30	-	√

**Table 1. The composition and the modes of photopolymerization of the experimental resins**

### 2.2. Preparation of experimental giomers

The giomers were prepared by mixing the resins described at previous paragraph with the experimental hybrid fillers. For the obtaining of the hybrid fillers, a new pre-reacted glass filler (PRG), fluorohydroxy-apatite (FAp) and a silanized barium fluoro-alumino-boro-silicate

glass powder were mixed and then sifted together.

The PRG was synthesized using the 50% aqueous solution of the polyalkenoic acid obtained from the acrylic acid, itaconic acid and N-acryloyl leucine (4:1:0.5 molar ratio) grafted with *N*-methacryloyloxyethylcarbamoyl-*N'*-6-hydroxy-hexylamine [4] and a active glass powder belonging to the oxidic system SiO<sub>2</sub>, Al<sub>2</sub>O<sub>3</sub>, CaF<sub>2</sub>. Silanation was carried out with A-174 silane.

Disk samples of giomers of 5 mm diameter and 0.5 mm thickness were prepared in Teflon molds by exposing the giomer pastes for 20 sec to diode-blue LED E lamp The giomer composition is shown in Table 2.

Giomers code	Copolymer Matrix		Hybrid Filler		
			PRG %	FAp %	Glass %
G1	C2		50		50
G2	C2		35	15	50
G3		C4	50		50
G4		C4	35	15	50

**Table 2. The composition of the experimental giomers**

### 2.3. Determination of conversion

The conversion of the monomer mixtures (resins) was assessed by determination of the residual double bonds (RDB) using the infrared spectroscopy method. The amount of the RDB was determined as percentage of the amount of the originally methacrylic groups present in the monomer mixtures. The decrease of the absorbance intensity of the methacrylate group C = C absorbance ( $A_{meth}$ ) from 1635 - 1640 cm<sup>-1</sup> was monitored. The absorption band of the phenyl group ( $A_{arom}$ ) from 1605 - 1610 cm<sup>-1</sup> was used as internal standard [5]. The degree of conversion was calculated using the formulas:

$$RDB\% = (A_{meth}/A_{arom})_F / (A_{meth}/A_{arom})_I \times 100 \quad (1)$$

where F means the final state (after curing) and I means the initial state of the material (before curing).

$$DC\% = 100\% - RDB\% \quad (2)$$

The FTIR spectra of the liquid monomer mixtures (resins) prepared as liquid thin films between KBr plates and the solid corresponding copolymers prepared as KBr pellets were recorded on a JASCO 610 FTIR Spectrophotometer.

ATR-FTIR spectra of giomers (pastes and solids) were recorded on FTIR spectrophotometer (Jasco FTIR-610) equipped with an ATR (attenuated total reflectance) attachment with a horizontal ZnSe crystal (Jasco PRO400S). The resolution of the spectra was  $4\text{ cm}^{-1}$ , and scans were repeated 100 times. The appropriate amount of the samples were placed on the ZnSe crystal, and then the FTIR spectrum was measured.

### 3. Results and discussion

#### 3.1. Conversion of dental resins

Table 3 shows the degree of conversion (%) of the investigated copolymers at 1, 2, 3 and 7 days after the initial polymerization of the appropriate resins using the two dental lamps.

Copolymer samples	DC (%)			
	C1	C2	C3	C4
after 1 day	45.9	49.0	72.8	78.6
after 2 days	50.2	49.6	77.0	80.6
after 3 days	51.	53.8	78.4	82.0
after 7 days	52.2	56.2	79.4	82.5

**Table 3. Degree of conversion obtained for the experimental copolymers**

As one can see from the data of Table 3 the conversion increases in time between the first and the seventh day after the initial polymerization. If one compares the copolymers polymerized using the Optilux 501 halogen lamp with the copolymers cured with LED E lamp (C1 versus C2 and C3 versus C4), it can be observed that those obtained with the LED E lamp presents higher conversions than those

polymerized with the halogen lamp. This behaviour can be explained by the higher photopolymerization efficiency of the LED lamp obtained because of the narrow spectrum of light (around 470 nm, the maximum absorption band of CQ) and because of the good conversion of the electrical power into a visible light.

The results presented in Table 3 point out that there is a significant difference (around 30%) between the RDB recorded in the case of copolymers which contain commercial Bis-GMAcom which is used in most current commercial composites (C1 and C2) and the copolymers based on the original Bis-GMA urethane analogue (Bis-GMAexp). Bis-GMAexp characterized by a lower viscosity than Bis-GMAcom and consequently by a longer gel time led to the obtaining of much higher degree of vinyl conversions of the corresponding copolymers [6]. As examples, in figures 1 and 2 are presented the FTIR spectra of R4 resin and C4 copolymer, respectively at 7 days after polymerization.

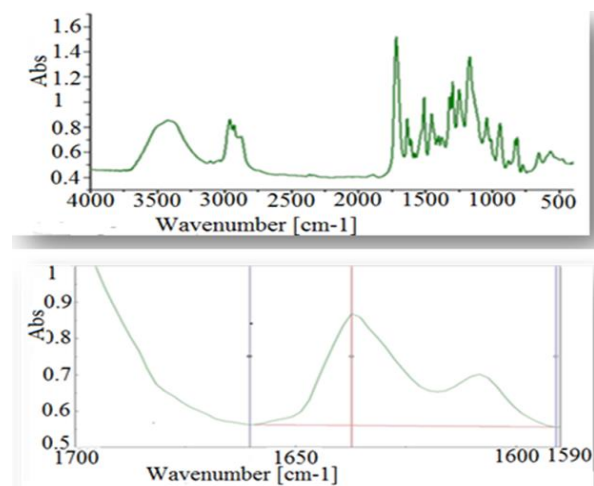


**Fig. 1. FTIR Spectra of R4 resin (before curing) at 4000-400  $\text{cm}^{-1}$  (a) and 1700-1590  $\text{cm}^{-1}$  (b)**

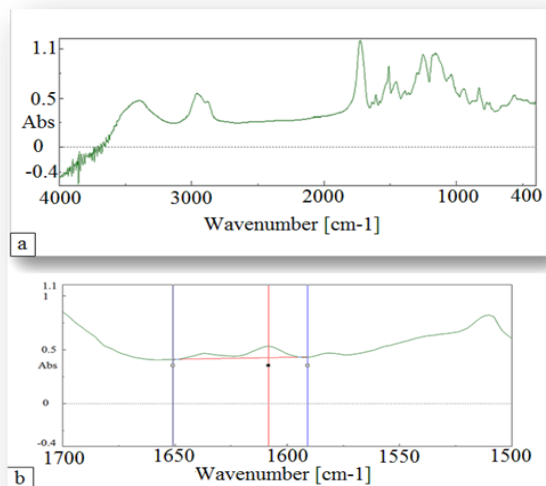


Fig 2. FTIR Spectra of the C4 copolymer after 7 days from light-curing, at 4000-400  $\text{cm}^{-1}$  (a) and 1700-1500  $\text{cm}^{-1}$  (b)

### 3.2. Conversion of dental giomers

As in the case of copolymers the data presented in Table 4 show significant differences between the conversion obtained for the giomers based on commercial Bis-GMA and the giomers based of original Bis-GMA urethane derivative after 24 hours. When comparing the giomers with the same copolymer matrix but different fillers, slightly higher conversions in the case of nano-FAP containing materials were obtained.

Giomer Code	G1	G2	G3	G4
DC%	45.3	50.2	72.1	78.9

**Table 4. Degree of conversion recorded for the experimental giomers**

The conversion values obtained for the investigated giomers are very closed to those obtained for the originating copolymers. This shows that there was a proper curing in the new experimental giomers, and that ATR-FTIR method is an appropriate method for determining the conversion in giomer-type structures. As example, figure 3 shows the spectra of G4 giomer before and after 24 hours from the light-curing.

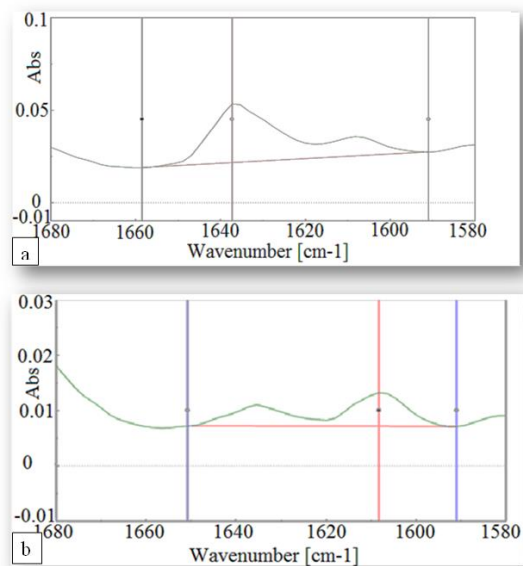


Figure 3. The ATR-FTIR Spectra of Giomer 4 at 1680 -1580  $\text{cm}^{-1}$  (a) paste before curing (b) solid after 1 day from light-curing

### Conclusions

IR spectroscopy is currently the most common technique used to determine the conversion of dental resins. ATR-FTIR was found to be a suitable technique for the evaluation of conversion of giomers (the latest generation of composites).

High conversions of resins in dental composite-type materials significantly influence their performances. The experimental giomers containing the original Bis-GMA urethane analogue could be good candidates for dental restorative applications.

### Acknowledgements

This work was supported by the Romanian National Authority for Scientific Research, CNDI-UEFISCDI, PNII Projects no: 189/2012 (GIODENT) and no: 165/2012 (COSMETIC-DENT).

### References

- M.C. Sunico, K. Shinkai, Y. Katoh, Two-year clinical performance of occlusal and cervical giomer



- restorations, *Operative Dentistry-University Of Washington*, Vol. 30, 3, pp. 282-289, 2005.
15. J. D. Griffin, Unique Characteristics of the Giomer Restorative System, *Inside Dentistry*, Vol. 10, 3, pp. 84-86, 2014.
16. T. Itota, T.E. Carrick, M. Yoshiyama, J.F. McCabe, Fluoride release and recharge in giomer, compomer and resin composite, *Dental Material*, Vol. 20, 9, pp. 789-795, 2004.
17. T. Buruiana, M. Nechifor, V. Melinte, V. Podasca, E. C. Buruiana, Synthesis of poly (alkenoic acid) with L-leucine residue and methacrylate photopolymerizable groups useful in formulating dental restorative materials, *Journal of Biomaterials Science, Polymer Edition*, Vol. 25, 8, pp. 749-765, 2014.
18. I.E. Ruyter, P.P. Györoösi, An infrared spectroscopic study of sealants, *Scandinavian Journal of Dental Research*, Vol. 84, pp. 396-400, 1976.
19. J. G. Leprince, W. M. Palin, M. A. Hadis, J. Devaux, G. Leloup. Progress in dimethacrylate-based dental composite technology and curing efficiency, *Dental Materials*, Vol. 29, 2, pp. 139-156, 2013.

# Unsupervised Automatic tracking of Thermal changes in Human Body

**Bardia Yousefi<sup>1</sup>, Julien Fleuret<sup>1</sup>, Seyed Alireza Ghaffari<sup>1</sup>, Simon Fréchet<sup>1</sup>, Félix Labrie Larrivée<sup>1</sup>,  
Marcelo Sung Ma Jo<sup>1</sup>  
Matthieu Klein<sup>3</sup>, Xavier Maldague<sup>1</sup>, Raymon Watts<sup>2</sup>**

<sup>1</sup>Department of Electrical and Computer Engineering, Laval University, Québec, QC G1V 0A6, Canada

<sup>2</sup>RT thermal Inc., 7167 Elkhorn Dr., West Palm Beach, FL. 33411 USA

<sup>3</sup>Visioimage Inc., 2560, Rue Lapointe, Sainte-Foy, G1W 1A8, Quebec City, Canada

An automated system for detecting and tracking of the thermal fluctuation in human body is addressed in this paper. It applies HSV based k-means clustering which initialized and controlled the points which lie on the ROI boundary. Afterward a particle filter tracked the targeted ROI in the thermal video stream. There were six subjects have voluntarily participated on these experiments. For simulating the hot spots occur during the some medical tests a controllable heater utilized close to the subjects body. The results indicated promising accuracy of the proposed approach for tracking the hot spots. However, there were some approximations (e.g. the transmittance of the atmosphere and emissivity of the fabric) which can be neglected because of independency of the proposed approach for these parameters. The approach can track the heating spots efficiently considering the movement in the subjects which provided a confidence of considerable robustness against motion-artifact usually occurs in the medical tests.

## I. Introduction

The medical applications of thermography have expanded more than a decade[1] in the very broad categories and involve various fields of medicine such as breast cancer [2,3], dermatology [4,5], avian flu [6,7], dentistry [8,9], psychology[10], prevention. Measuring the body temperature through non-invasive method is a challenging task which involves many researchers in the field of thermography to itself. Utilization of the thermal instruments provides a powerful tool for avoiding the invasive operations which give inconvenient circumstances for the human subject. In some cases, it is not possible to use some other methods like thermometers, particularly under the radiological exposure that any external tools might give some artifacts or possible issues. Here, a thermal image processing techniques for finding and tracking the thermal spots within the increasing at the temperature. It involves the authors to voluntarily participant as human subject experiment for thermal spot tracking.

## II. Proposed method for automatic tracking the hot spots

Having the knowledge of overheating gives the possibility to imply thermographic devises and consequently create a system for automatic detection

and tracking the heating spots seems needed using thermal image/video analysis. Here, the approach presents a system which automatically detects and tracks the hot spots within the thermal video sequence. There is an initialization and control possible points which have heated and lie on the boundary of a region of interest (ROI) in every frame of thermal video stream. The ROI initialization is needed for detecting the overheating spots and initiates an automatic particle filter tracking process.

### A. Unsupervised Clustering in HSV

For clustering of the thermal image obtained from the experiments. The main and first question which might be asked is why to use of Hue Saturation Value (HSV) for unsupervised clustering of thermal image. The simple answer can be due to separation of luma, whose contains intensity information of the image, from chroma which has color information. It is more unlikely for the RGB color system which is normally using for the purposes of clustering. It is due to the reason that it gives the robustness to removing shadows or lighting variations. In the RGB color system, the implementation details regarding the color display are concerned however in the HSV there is the actual color components are in target. It

means the RGB is more a computer treated way of the color to be shown and HSV is more look-like the capture of the components in the way of humans perceives the color. Response (or resonation) of the human eye is only limited to three main light frequencies not to red, green and blue surprisingly which is not linear and provides pure color distinguish response of the retina combining three color component responses.

Besides, the separation of luma and chroma provides a histogram construction or thresholding rules using only saturation and hue. This works regardless of lighting changes in the value channel and practical clustering gives reasonable efficiency. The unsupervised clustering method uses for the purpose of the project is K-means clustering. It efficiently provides the ROI cluster from the thermal image which initials the particle filter for tracking these regions in order to automatically detect and monitor the hot spots.

### B. Particle filter

Finding the hotspot looks easier as compare with updating the thermal increases and thermal region expansion within the time. There is a necessity for tracking the hot spots on the surface of body and having confident outcome regarding not losing the ROI location. Moreover, tracking algorithm must have reasonable robustness against uniform surfaces. This approach uses a particle filter tracker [11, 13] to track and adapt on the tracking problem. It provides suitable condition to change the ROI during the video sequences. The particle filter has been used in many tracking purposes in the object recognition and similar applications on video processing [11-13].

There are some assumptions consider for the tracking algorithm as follows:

- The analysis of the thermal tracking takes place in the false colored images from having intensity of 0 to 255 corresponding for each color(however clustering is done in HSV color system);
- The ROI is always in the field of view (FOV) of thermal camera;
- Temperature of the ROI (subject) is higher than the surrounding environment (similar with real condition);
- The temporarily ROI is not in particular shape and must be adjusted through the algorithm; however the thermal increases (level of intensity) is an unpredictable contour shape having upward trend. The shape comprises the temporarily occlusion and

other unwilling external factors influence the frame images e.g. motion artifact (the system is robust against motion artifacts);

- The ROI updates throughout the time of the experiment and temperature updates by upward trend to find the hot spots in the subject.

Using the proposed method as a tracking algorithm, particle filter works in the time  $t$  and approximates the tracking recursively target by a finite set of posterior distribution weighted samples.

In general, particle filters are the simulation class filters for approximation of random variables recursively. Let  $\alpha_t | Y_t = (y_1, y_2, \dots, y_t)'$  are the random variables and  $\alpha^1_t, \dots, \alpha^M_t$  are particles having the discrete probability mass of  $\pi^1_t, \dots, \pi^M_t$ .

Discrete points approximation of the variables shown by  $f(\alpha_t | Y_t)$  and for  $\pi^j_t$  are assumed to be equal  $1/M$  which desired amount of  $M$  for the particles to approximate the density of  $\alpha_t | Y_t$ . It is noticeable that the particles are locates in the ROI which is previously defined and incrementally updates throughout the thermal experiment. It gives an approximation for density prediction by particle support and empirical prediction

$$\hat{f}(\alpha_{t+1} | Y_t) = \sum_{j=1}^M \hat{f}(\alpha_{t+1} | \alpha^j_t) \pi^j_t$$

A mixture of echoes while the filtering work and densities till producing up to proportionality,

$$\hat{f}(\alpha_{t+1} | Y_{t+1}) \propto \hat{f}(y_{t+1} | \alpha_{t+1}) \sum_{j=1}^M f(\alpha_{t+1} | \alpha^j_t) \pi^j_t$$

This is an approximation to the true density filtering. New particles produced  $\alpha^1_{t+1}, \dots, \alpha^M_{t+1}$  with weights  $\pi^1_{t+1}, \dots, \pi^M_{t+1}$  and this iterates through the data. This includes the online tracking problems and estimation of the one-step-ahead density  $f(y_{t+1} | Y_t)$  which here is very much relevant to update in the ROI and the spreading the hot spots within test [11-13].

### III. Experimental and Simulation Results

This approach applied followed by the proposing a method for heating spots detection in the infrared video stream. The main part of the approach is related to computer programming modification and simulation on image analysis. The results of the proposed approach are revealed by the analysis in the model situation for benchmarking. The experimental results extensively reveal the

effectiveness of the proposed method and robustness against any possible movements.

### A. Experiment on the hot spots tracking

The mentioned analyses for finding the suitable fabric which has reasonable thermal properties is done to find appropriated gown for the patients. The fabric can be offered to be used as gown for some medical applications. It provides more reliable thermal and machine vision situation to observe the hot spots for prevention of the possible burning during the exposure. For this aim, an experiment has been conducted by the authors. The procedure of the experiment looks similar the position of the patients. The experiment is done by six participants. The experiment has done in the room temperature due to have more thermal similarity with actual situation. Each participant just wore the gown which made by the selected fabric and lied down on

thermal variations. For simulating the hot spots in the surface of human body, a controllable heating element has been used. However for simplicity of the implementation and simulation the feeling heat temperature has been chosen around 55°C. The blackbody also has been utilized as a reference and has been set for the temperature of the human body in the normal situation (around 37°C). The blackbody located next to the subject bed and in front of the IR camera. The controllable heater took several minutes to reach the certain temperature and during this time all the thermal variations have been recorded accordingly. The heater is located closed to the subject gave more similarity to the real condition.

### B. Results of the tracking

In this section, the result of the proposed approach

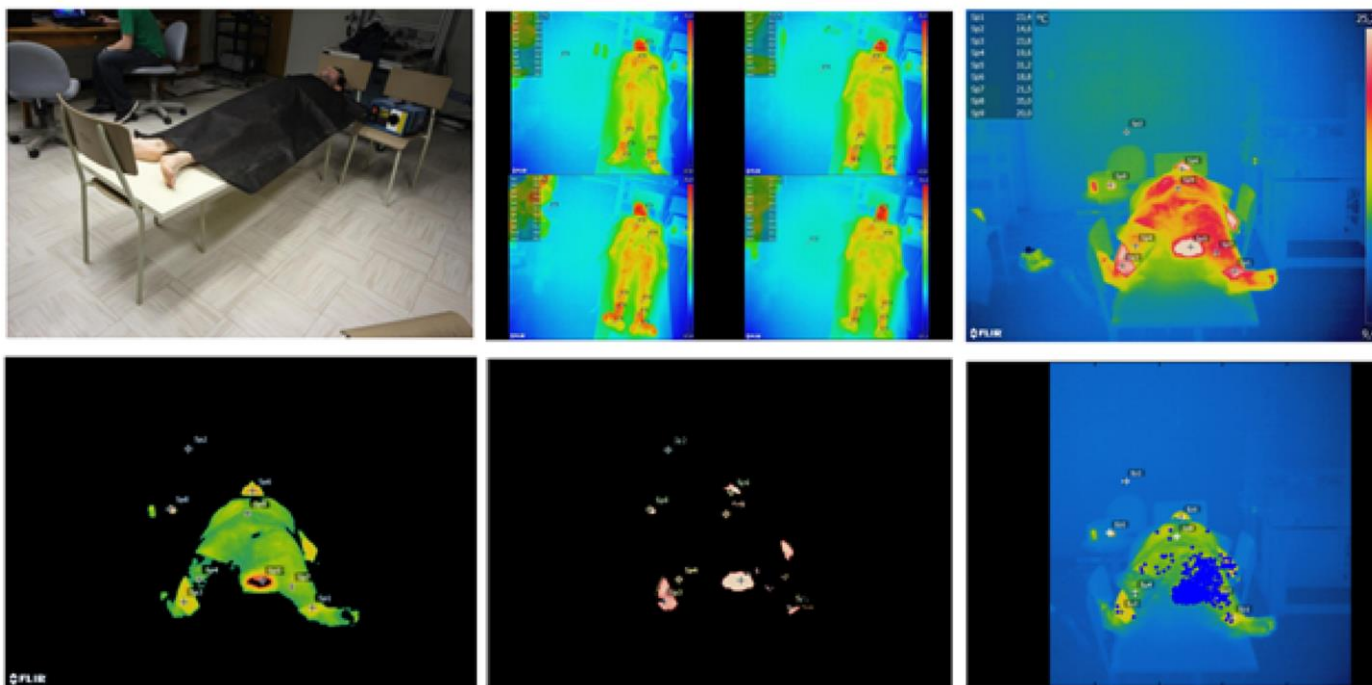


**Figure 1.** The figure presents the results of the segmentation for different clusters. The image at upper-left side reveals the visible image of a participant; upper-middle and upper-right images show the original IR images taken with FLIR (A65). The lower-left and lower-middle images are shown the different clusters. The lower-right image demonstrates the particle tracking results for heating tracking in the video stream. The selection of the human body in the IR-image using some other methods like active-contours involve the system into several unnecessary morphological operations but it is a suitable technique for tracking as well. However, implying the k-means clustering is seemingly faster as compare and reasonably accurate.

the bed made for the experiment. The IR-camera is located in front of the bed and the distance of the camera and its angle was similar to the actual situation. Every experiment longing around 11 minutes and JENOPTIK and FLIR recorded the

presents for tracking hot spots in video stream. But the approach divided into several sections and each section has its own task. The k-means cluster has used to find the ROI which contains human body region having thermally higher intensity as

foreground and compare with background where lower temperature (background) has. As k-means clustering is an unsupervised learning procedure so there was no training set has been used for the approach. The thermal video sequence was 30 frames per seconds which is high for the actual purpose of the approach. It is because of slowly changing process in the thermal variations. Due to the mentioned fact and having low computational complexity, the system considered one thermal frame processed per second. The sampling could be even lesser but applying particle filter required stepwise variations to have efficient tracking. The size of the thermal images for every frame was included 560\*640 pixels and it has false color to have better visual discrimination of the heat. The clustering gave the ROI that includes human subject region in thermal image. It gave hot spots which are the targets for being tracked throughout the test. Particle filter provided a very good tracking outcome within the video. The particles created for tracking the hot spots are very much spread throughout the human subject which gave possible point of heats where were not feasible to be visually found but in numeric and quantitative analyses these point have hot spot temperatures. They gave the reason for been found by the particles. Therefore, the particles concentration has higher and more stable heating temperature that were constantly tracked by the particles and provided the accurate detection within the thermal images sequence. The unstable heating points were not continuously track by the particles and just temporarily detection which vanished over the sequences. The figure 1 reveals two images taken during the particle tracking in the IR images. The approach had reasonably responded on the all the subjects tried for hot spot tracking. The hot spots have been tracked during the whole thermal video sequences which represented efficiency of the approach in tracking the thermal changes within the actual situation. It is noticeable that the subjects were having slight movements in the streams and particles could track them. These results indicate the robustness of the approach against any movement and particularly motion artifact which is common problem in the medical tests.

#### IV. Conclusion

The presented approach addressed an automatic system for detect and track the thermal fluctuation that can be occurred in the medical examinations. It applied HSV based k-means clustering which

initialized and controlled the points which lie on the ROI boundary. Afterward a particle filter tracked the targeted ROI during the video sequence. The proposed approach has been tested during some experiments and under almost similar circumstance. There were six subjects have voluntarily participated on these experiments. For simulating the hot spots occur, a controllable heater utilized near to the subject bodies. The results indicated promising accuracy for the proposed approach in tracking the hot spots. However, there was some approximation done regarding the transmittance of the atmosphere and emissivity of the fabric which can be neglected because of independency of the proposed approach for these parameters. The approach can track the heating spots efficiently however it can be done for the moving subjects as well which provide considerable robustness related of the motion artifact occurs during the medical test. As the future work it can be more scrutinized and even possibly more experiments can provides more concrete outcome gives confident regarding the method. The internal heating and its external effects needs further attention for future work of this research.

#### Acknowledgment

This research project is done under Chaire de recherche du Canada en vision infrarouge multipolaire (MIVIM).

#### References

- [1] Jones, B.: A reappraisal of the use of infrared thermal image analysis in medicine. *Medical Imaging, IEEE Transactions on* 17(6), 1019–1027 (1998)
- [2] Amalu, W.: Nondestructive testing of the human breast: the validity of dynamic stress testing in medical infrared breast imaging. In: *Engineering in Medicine and Biology Society, 2004. IEMBS '04. 26<sup>th</sup> Annual International Conference of the IEEE*, vol. 2, pp. 1174–1177 (2004)
- [3] Ng, E.K., Fok, S., Peh, Y., Ng, F., Sim, L.: Computerized detection of breast cancer with artificial intelligence and thermograms. *Journal of Medical Engineering and Technology* 26(4), 152–157 (2002)
- [4] Parsi, K., Kossard, F.: Thermosensitive lichen amyloidosis. *International Journal of Dermatology* 43(12), 925–928 (2004)
- [5] McDougali, A., Salter, D.: Thermography of the nose and ear in relation to the skin lesions of lepromatous leprosy, tuberculosis, leishmaniasis, and lupus pernio. *Journal of Investigative Dermatology* (68),16–22 (1977)
- [6] Camenzind, M., Weder, M., Rossi, R., Kowtsch, C.: Remote sensing infrared thermography for massscreening at airports and public events: Study to evaluate the mobile use of infrared cameras to identify persons with elevated body temperature and their use for mass screening. *Tech. Rep.* 204991, EMPA Materials Science and Technology (2006)

- [7] Chiang, M., Lin, P., Lin, L., Chiou, H., Chien, C., Chu, S., Chiu, W.: Mass screening of suspected febrile patients with remote-sensing infrared thermography: Alarm temperature and optimal distance. *Journal of the Formosan Medical Association* 107(12), 937–944 (2008)
- [8] Tabatabaei, N., A. Mandelis, et al. (2011). "Thermophotonic lock-in imaging of early demineralized and carious lesions in human teeth." *Journal of biomedical optics* 16(7): 071402-071402-071410.
- [9] Zhang, L., A. S. Kim, et al. (2013). "Trimodal detection of early childhood caries using laser light scanning and fluorescence spectroscopy: clinical prototype." *Journal of biomedical optics* 18(11): 111412-111412.
- [10] Shastri, D., Merla, A., Tsiamyrtzis, P., Pavlidis, I.: Imaging facial signs of neurophysiological responses. *Biomedical Engineering, IEEE Transactions on* 56(2), 477–484 (2009)
- [11] Isard, M., Blake, A.: Condensation – conditional density propagation for visual tracking. *International Journal of Computer Vision* 29(1), 5–28 (1998)
- [12] Pitt, M. K., & Shephard, N. (1999). Filtering via simulation: Auxiliary particle filters. *Journal of the American statistical association*, 94(446), 590-599.
- [13] Bilodeau, G. A., Torabi, A., Lévesque, M., Ouellet, C., Langlois, J. P., Lema, P., & Carmant, L. (2012). Body temperature estimation of a moving subject from thermographic images. *Machine Vision and Applications*, 23(2), 299-311.



# PROPAGATION OF THERMAL PULSE IN TISSUE

G. Paez<sup>1,3</sup>, M. Strojnik<sup>2</sup>, and M. K. Scholl<sup>3</sup>

<sup>1,2</sup>Centro de Investigaciones en Optica, A. P. 1-948, C.P. 37000, Leon, Gto., Mexico

<sup>3</sup>Alenka Associates, P. O. Box 27488, Tempe, AZ 85285, USA

<sup>1</sup>gpaez@cio.mx, <sup>2</sup>mstrojnikp@aol.com, <sup>3</sup>michelle.scholl@gmail.com

We examine the mechanisms of pulse propagation inside tissue to assess the wavelengths where the pulse might propagate to an occlusion and reflect from its boundary. We develop the wave equation for pulse, and deduce the propagation parameters inside tissue.

## 1. Introduction

The detection of tumors, that may or may not be malignant, is currently accomplished with positron emission tomography (PET), CT (computed tomography) scans, and x-ray transillumination. They are all considered highly damaging to the living tissue, to the point of provoking their own class of cancers.

The possibility of using the infrared (IR) radiation to detect occlusions a few cm within a surface layer would be very welcome by the population as a screening method. It would replace x-ray imaging, often under somewhat uncomfortable conditions and of still-debated credibility as a diagnostic tool. The other optical technique that has been studied recently includes transillumination in visible-near infrared region, often referred to as therapeutic region. Currently, the best approach in this spectral region recommends supplementing imaging with the established magnetic resonance imaging (MRI).

The IR cameras for laboratory use were engineered in early seventies. Just about the same time, the “war on cancer” was declared. Researchers started pointing IR cameras at woman’s breast to discover subsurface tumors and at feet of diabetics to understand diverse manifestations of neural damage to the feet, referred to as neuropathy.

Both of these lines of research are currently pursued, because the development of IR detector materials, number of pixels in the focal plane arrays, and their sensitivity continues to improve on a yearly basis. Sophisticated experimental setups continue to be conceived to extract the relevant information from the specimen.

One such technique includes the sample irradiation with pulses of thermal energy, as illustrated in Fig. 1.[1,2] A technique must be refined to allow the identification of tumor tissue within abundant and varying IR signal from other tissues, vascular and oxygen transport system.

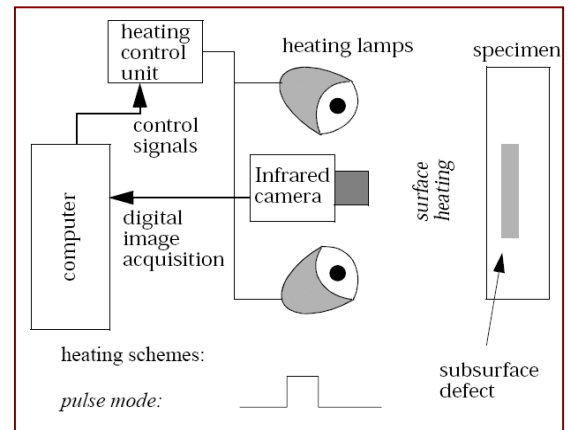


Fig. 1. In pulse tomography, an infrared (heat) pulse propagates inside material. An occlusion interferes with its free propagation, causing heat accumulation in the region between the input surface and the occlusion. This results in an increase in surface temperature, that may be detected by an IR camera.

## 2. Theory: heat transfer equation

Heat transfer equation is a 2<sup>nd</sup> order (in space) inhomogeneous, partial differential equation (with heat sources).

$$\nabla^2 T(x, y, z, t) - \left( \frac{cd}{k} \right) \frac{\partial T(x, y, z, t)}{\partial t} = p(x, y, z, t) \quad (1)$$

$T(x, y, z, t)$  = temperature distribution inside the

irradiated sample, in [K];  
d = density, [kg/m<sup>3</sup>];  
c = specific heat capacity, in [(W sec)/(kg K)];  
t = time, in [s];  
k = the heat conductivity vector, in [W/(mK)];  
p(x,y,z,t) = time- and position-dependent power per unit volume, in [W/m<sup>3</sup>];  
α = k/(dc), thermal diffusivity, [m<sup>2</sup>/s].

Note that d, c, k, and α are piecewise continuous functions of z. They have discontinuity at boundaries with other layers, surfaces, and inclusion boundaries.

We assume that the irradiated area is large compared to propagation distance of laser pulse inside the sample. The dependence on transverse coordinates may be neglected. The heat equation in surface layer of thickness h includes the heat generation term due to absorption of irradiated power inside it.

$$\frac{\partial^2 T(x,y,z,t)}{\partial z^2} - \left(\frac{cd}{k}\right) \frac{\partial T(x,y,z,t)}{\partial t} = p(x,y,0,t) \quad (2)$$

This equation is, in general, difficult to solve, requiring numerical solutions. It may be solved for some specific forms of irradiation.

### 2.1 Homogeneous equation

No heat generation sources exist outside thin surface layer of thickness h where the radiation is absorbed.

$$\frac{\partial^2 T(x,y,z,t)}{\partial z^2} - \frac{cd}{k} \frac{\partial T(x,y,z,t)}{\partial t} = 0 \quad (3)$$

This homogeneous equation may be solved analytically. We assume that the solution to this equation is separable in spatial and temporal coordinates.

$$T(x,y,z,t) = f(x,y,z)g(t) \quad (4)$$

We substitute Eq. 4 into Eq. 3. Upon some manipulation, we find.

$$\frac{\partial g(t)}{\partial t} + \left(\frac{k}{dc}\right) \left[ \frac{\frac{\partial^2 f(x,y,z)}{\partial z^2}}{f(x,y,z)} \right] g(t) = 0 \quad (5)$$

From Eq. (5), we can read the time constant. It depends on the spatial distribution of temperature, and material constants of the absorbing material.

$$\tau(x,y,z) = \left(\frac{dc}{k}\right) \left[ \frac{f(x,y,z)}{\frac{\partial^2 f(x,y,z)}{\partial z^2}} \right] \quad (6)$$

Then we obtain the time-dependent part for the wave equation.

$$g(t) = g(t_0) \exp\left(-\frac{t}{\tau}\right) \quad (7)$$

Temperature increase due to pulse irradiation must remain low (~5 K) in biological applications, in order to maintain low power levels of irradiation, and total irradiation energy. Both cause damage.

### 2.2 Solution to wave equation

We substitute Eq. (7) into wave equation (3) to see whether we can consider thermal wave propagation between the heated surface layer and the in-homogeneity, or a change in material boundary.

$$\frac{df^2(x,y,z)}{dz^2} + \left(\frac{cd}{k\tau}\right) f(x,y,z) = 0 \quad (8)$$

The positive sign in both terms in Eq. (8) implies that waves are decaying. The solution to the wave equation consists of two waves, one propagating in positive z-direction and the other one propagating in the negative. Their physical interpretation is that the first wave is the incoming pulse, while the second one is the pulse reflected at inhomogeneity or change in material properties.

$$f(x,y,z) = f_{0+/-}(x,y) \exp(-/+ \beta z) \quad (9)$$

Functions  $f_{0+/-}(x,y)$  are the 2-D distributions at

the boundaries.

$$\beta = \sqrt{\frac{cd}{k\tau}} = (\alpha\tau)^{-1/2} \quad (10)$$

The variable  $\beta$  denotes the rate of dissipation of the thermal wave upon propagation.

### 3. Propagation of thermal pulse

We substitute Eqs. (9) and (7) into Eq. (4). We consider the wave propagating toward the positive z-axis and negative z-axis after the reflection.

$$\Delta T(x, y, z, t) = \Delta T_{0\pm}(x, y) \exp\left(\pm\beta z - \frac{t}{\tau}\right) \quad (11)$$

Here we combined the constant terms, and ignored the DC value of temperature, considering that it remains constant on the average.

$$\Delta T_{0\pm}(x, y) = f_{0\pm}(x, y)g(t_0) \quad (12)$$

At the occlusion boundary at  $z_B$ , the temperature pulse achieves the following value after propagation time  $t_B$ . We evaluate expression (11) at a boundary of the occlusion,  $z = z_B$ ,  $t = t_B$ .

$$\begin{aligned} \Delta T(x, y, z_B, t_B) &= \Delta T_B(x_B, y_B, z_B, t_B) \\ &= \Delta T_B(x, y) \exp(-\beta z_B) \exp\left(-\frac{t_B}{\tau}\right) \end{aligned} \quad (13)$$

At  $(x_B, y_B, z_B)$ , the wave is reflected with reflection coefficient  $R$ , which could depend on transverse coordinates when occlusion is not planar. This would be the case for biological occlusions. The wave amplitude is then reduced.

$$\begin{aligned} \Delta T_B(x_B, y_B, z_B, t_B) &= R(x_B, y_B, z_B) \quad (14) \\ &x \Delta T_{0+}(x, y) \exp(-\beta z_B) \exp\left(-\frac{t_B}{\tau}\right) \end{aligned}$$

This is the amplitude of the wave that propagates from the occlusion to left (toward negative z-axis), starting at time  $t = t_B$  and from the coordinate origin at  $z = z_B$ .

$$\begin{aligned} \Delta T(x, y, z, t) &= \Delta T_B(x_B, y_B, z_B) \quad (15) \\ &x \exp[-\beta(z_B - z)] \exp\left[-\frac{(t - t_B)}{\tau}\right] \end{aligned}$$

We may substitute Eq. (14) into Eq. (15).

$$\begin{aligned} \Delta T(x, y, z, t) &= R(x_B, y_B, z_B) \Delta T_{0+}(x, y) \quad (16) \\ &x \exp[-\beta(2z_B - z)] \exp\left(-\frac{t}{\tau}\right) \end{aligned}$$

We evaluate this expression for  $z = 0$ . There the camera records surface temperature distributions.

$$\begin{aligned} \Delta T(x, y, 0, 2t_B) &= R(x_B, y_B, z_B) \Delta T_{0+}(x, y) \quad (17) \\ &x \exp(-2\beta z_B) \exp\left(-\frac{2t_B}{\tau}\right) \end{aligned}$$

Thermal wave, reflected off the inclusion is incident on the front surface at  $t = 2t_B$ . We use the following variables.

$$\alpha = \frac{k}{cd} \quad (18)$$

$$\tau = \frac{1}{\alpha} \frac{f(z)}{\left[\frac{d^2 f(z)}{dz^2}\right]} = (\alpha\beta^2)^{-1} \quad (19)$$

The time when the reflected thermal wave returns is a measurable quantity, and is therefore considered known. We can calculate the speed of pulse propagation (group velocity, or rate of energy transport) from Eq. (11a) as follows.

$$v = \frac{\Delta z}{\Delta t} = (\beta\tau)^{-1} = \sqrt{\frac{\alpha}{\tau}} \quad (20)$$

The occlusion is located at depth  $z_B$ .

$$z_B = \frac{t_B}{\beta\tau} = t_B \sqrt{\frac{\alpha}{\tau}} \quad (21)$$

Thus, the depth of occlusion may be determined upon measuring the time that the input temperature distribution is reflected at the

occlusion and returned back on the front surface. Constants  $\alpha$  and  $\tau$  are calculated from the properties of material. They may also be calibrated for specific materials, especially in the case of the biological samples.

#### 4. Biological parameters

Diffusivity of biological tissues, including tumors and cancerous growth, may be calculated from their thermo-mechanical parameters. We assume density of water, and specific heat capacity:  $\rho_{H_2O} = 1.05 \times 10^3 \text{ kg/m}^3$  and  $c_{H_2O} = 4.190 \times 10^3 \text{ J/(kg K)}$ . The specific heat capacity  $c$  is calculated according to the water content formula of the tissue. [4]

$$c_{H_2O}^{\%} = c_{H_2O} \left\{ \left( \frac{\%}{H_2O} \right) + 0.4 \left[ 100 - \left( \frac{\%}{H_2O} \right) \right] \right\} \quad (22)$$

Diffusivity may be calculated from published thermo-mechanical tissue parameters. Calculated diffusivity for tissues of interest in breast cancer investigation, including fat and (cancerous) tumors, is presented in Table 1.

Table 1. Diffusivity from published thermo-mechanical tissue parameters.

Tissue	k[W/mK]	H <sub>2</sub> O [%]	c[J/(kg K)]	10 <sup>8</sup> a [m <sup>2</sup> /s]
fat H <sup>1</sup>	0.209 [4]	60 [4]	3184 [4]	6.25
skin dermis H	0.308 [4]	70 [4]	3436 [4]	8.54
H skin epidermis	0.209 [4]	60 [4]	3184 [4]	6.25
tumor periphery	0.511 [5]	80 [5]	3687 [5]	13.2
tumor core	0.561 [5]	90 [5]	3940 [5]	13.6
colon cancer H	0.545 [6]	90 [6]	3939 [6]	13.2
Pure water	0.627 [3]	100 [3]	4190 [3]	14.3

<sup>1</sup>H refers to human

#### 5. Conclusion

Several laser types are available around 1  $\mu\text{m}$ . At this wavelength, the absorption coefficient of thermal pulse in tissue is about  $10^3 \text{ m}^{-1}$ . Table 2

presents time constant and speed of thermal pulse propagation in representative tissues calculated from their thermo-mechanical parameters. The pulses slowly propagate to the occlusion and back. When the temporal separation between their creation on the front surface and their return on the front surface, upon reflection at the occlusion, is equal to  $2t_B$ , they provide depth of occlusion,  $z_B$ .

NIR/SWIR cameras (InGaAs sensitive pixels) may be employed for image detection. Even better, individual sensing elements may be interwoven with pulsed laser diode sources for an emitter-detector system operating at 1  $\mu\text{m}$ . A flexible cloth may be assembled to drape a convex sensing surface around tissue for occlusion search.

Table 2. Time constant and speed of pulse propagation from thermo-mechanical parameters.

Tissue	$\lambda$ [m]	t [s]	v [mm/s]
fat H	930	16	0.0625
dermis H	930	11.5	0.085
epidermis H	930	16	0.0625
tumor periphery	930	6.6	0.15
tumor core	930	7.5	0.13
colon cancer H	930	6.6	0.15
pure H <sub>2</sub> O	930	7	0.14

<sup>1</sup>H refers to human

#### References

1. J. C. Ramirez-Granados, G. Paez, and M. Strojnik, "Three-dimensional reconstruction of subsurface defects by using pulsed thermography video," *Appl. Opt.* 51(16), 1153-1161 (2012).
2. J. C. Ramirez-Granados, G. Paez, and M. Strojnik, "Reconstruction and analysis of pulsed thermographic sequences for nondestructive testing of layered materials," *Appl. Opt.* 49(9), 1494-1502 (2010).
3. M. Strojnik, G. Paez, "Spectral dependence of absorption sensitivity on concentration of oxygenated hemoglobin: pulse oximetry implications," *J. Biomed. Opt.* 18 (10), Paper 108001 (2013).
4. T. E. Cooper and G. J. Trezek, "Correlation of thermal properties of some human tissue with water content," *Aerospace Med.* 42, 24-27 (1971).

5. M. L. Cohen, "Measurement of the thermal properties of human skin. A review," *J. Invest. Dermatol.* 69, 333-338 (1977).
6. K. R. Holmes and M. M. Chen, "Local thermal conductivity of Para-7 fibrosarcoma in hamster," *1979 Advances in Bioengineering*, ASME, New York, NY, 147-149 (1979).
7. J. W. Valvano, J. R. Cochran, and K. R. Diller, "Thermal conductivity and diffusivity of biomaterials measured with self-heated thermistors," *Int. J. Thermophys.* 6, 301-311 (1985).

# NEW THERMAL METHOD TO ASSESS ENDURANCE LIMIT OF STAINLESS STEELS

R. De Finis, D. Palumbo, F. Ancona, U. Galietti

Politecnico di Bari, [rosa.definis@poliba.it](mailto:rosa.definis@poliba.it)  
[davide.palumbo@poliba.it](mailto:davide.palumbo@poliba.it)  
[francesco.ancona@poliba.it](mailto:francesco.ancona@poliba.it)  
[umberto.galietti@poliba.it](mailto:umberto.galietti@poliba.it)

The development of a product requires a good agreement in time management between the period of design and marketing, to meet the customer's demands. In design environment, the mechanical strength characterization represents a critical activity because of long lasting tests to assess endurance limit of materials. Indeed, Standard method "Staircase" requires to test at least 15 samples and thus it results in a very time consuming test. The fatigue tests can be quickly carried out with a new thermal method involving in the Infrared Thermography. The aim of this paper is firstly to show a thermal technique for an early assessment of the damage phenomena during a fatigue test, and secondly to illustrate the strong points of a new method based on infrared measurements for assessing endurance limit for both austenitic and martensitic stainless steels. Moreover, a comparison with Standard Test Method "Dixon" is shown.

## . Introduction and problem statement

Infrared thermography has been successfully used as an experimental, non-destructive, real-time and non-contact technique to observe physical processes of: damage, fatigue, and failure on specimens both metallic and composites [1]. The material intrinsic dissipation indeed, is related to the damage phenomena, and can be evaluated with specimen surface temperature monitoring [1]. In particular the thermal sources can be used to assess the fatigue limit. In literature, different approaches have been performed to study the fatigue damage with thermography based on: the monitoring of the surface temperature [2][3], the evaluation of "dissipative" thermal heat sources, the evaluation of the phase variation in thermographic signal. Nonetheless, the temperature is a very sensitive parameter to the environmental temperature and loading machine heating and then, all the heat sources influencing the results have to be considered in the analysis. [2] De Finis et All propose a robust technique to thermal data analysis in

order to filter out all the noisy sources and for early detecting the dissipation process. However, temperature measurements are also affected by thermal properties of the material such as thermal conductivity: high conductivity (e.g. aluminium alloys or welded joints) involves in the low temperature reached during the test. Another problem related to the use of temperature is represented by the lattice microstructures which cause extremely low temperature increments [2],[4]. To avoid these 'external' influences another approach based on the study of evolution of signal phase variation, has been set up. [4],[5] The method concerns the use of the thermoelastic signal despite of the loss of adiabatic conditions. By demodulating thermal signal the harmonic analysis allows to obtain 1° phase and 2° amplitude components and thus the external heat source influence can be eliminated. This procedure provides two significant parameters for assessing fatigue behaviour of material [6]. In particular the phase shift of first component synchronous at the mechanical frequency is related to the appearance of plastic zones or cracks in the material and so it is strictly related to damage [4]. Moreover, if thermal phenomena are present a double mechanical load



frequency component arises related to dissipative heat sources in the material and thus it is associated to the temperature [6]. In this paper the phase shift and double frequency harmonic amplitude are jointly used to carry out a fatigue damage study for assessing endurance limit of material.

### Approach and techniques

The thermoelastic stress analysis is a full-field, well-established and non-contacting technique for evaluating surface stress map by measuring small temperature increments if adiabatic condition are present [4], [7],[8]. For a linear elastic, isotropic and homogeneous material the temperature change occurs isoentropically and hence the classical thermoelastic equation (1) states:

$$\Delta T = -T_0 K \Delta \sigma_I \quad (1)$$

Where K is the thermoelastic constant,  $\Delta \sigma_I$  is the change in the stress invariant and  $T_0$  is the specimen environmental temperature. The reversible conversion between mechanical and thermal energy is possible only if adiabatic condition are achieved. [7],[8]. If the intrinsic stress level in the material exceed yield strength high stress gradients and local plasticity appear caused by dissipative heat sources. In these conditions the classical thermoelastic equation (1) lose validity and TSA cannot be used for assessing surface Fig. 19.

stress field of material. Nevertheless, the phase of thermoelastic signal still represents an important parameter to evaluate fatigue behavior of material. Considering a reference signal issued by load cell of loading machine, the thermoelastic signal and reference signal are considered as two vectors rotating at the same speed (the same mechanical frequency). Time after time the shift in phase values is constant and it varies only in case of loss of adiabatic condition.

The reference signal is used to filter out the thermoelastic signal by means of a lock-in amplifier. Hence, for studying the fatigue behavior the thermoelastic signal can be represented by its phase shift with respect reference signal and its amplitude [4]. Obviously, a suitable signal demodulation must be realized. To do this, the adopted mathematics model to describe temperature change during the test, is [6],[9]:

$$T_m(t) = a + bt + \Delta T_1 \sin(\omega t + \varphi_1) + \Delta T_2 \sin(2\omega t + \varphi_2) \quad (2)$$

Where “a” coefficient is proportional to the environmental temperature, “b” coefficient depends on mechanical load frequency and time, “f” is the mechanical load frequency,  $T_{1,2}$  and  $\varphi_{1,2}$  are respectively amplitude and phase shift of first and second harmonic component of Fourier Fast Transform[5],[6]. In this paper the assessment of fatigue behavior of martensitic and austenitic stainless steel is shown by evaluating  $\varphi_1$  and  $T_2$  parameters of thermal signal demodulation.

A typical setup for assessing signal is drawn in and

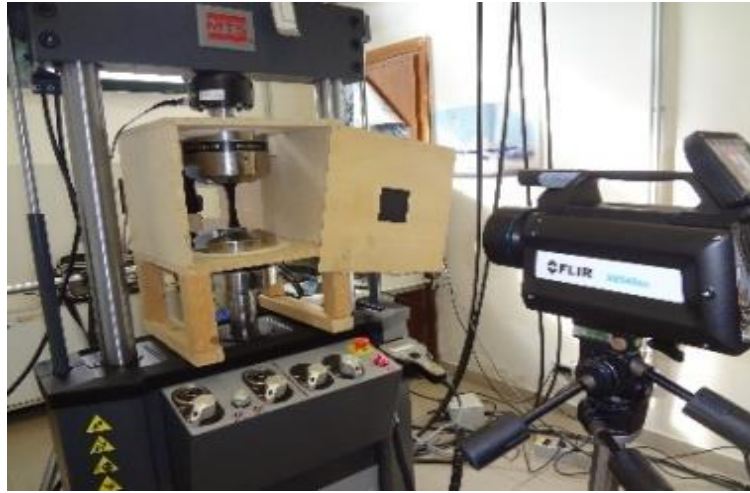


Fig. 19 Loading Machine and IR detector

The tested materials are the austenitic AISI 316 and martensitic X4 Cr Ni 16-4 stainless steels. Martensitic stainless steels have a higher mechanical strength obtained by a quenching heat treatment but limited corrosion resistance. The AISI 316 material is a well-known austenitic stainless steel while X4 Cr Ni Mo 16-4 deal with the addition of Chromium in the lattice (11–16% in weight) that allows for [10]:

- improvement of corrosion resistance through the formation of oxides,
- avoidance of the depleting of Chromium from lattice .

During the fatigue tests the load is stepped and incremental. Three specimen for both material have been tried.

The ‘dog-bone’ shaped, smoothed specimens are sprayed with matt black for increasing emissivity. An insulated chamber covers the clamping area in order to minimize environmental heat change.

The procedure for processing phase data does not consider any external heat influences and consists in applying a Gaussian filter to all data matrix for each loading step. In the data matrix the pixel is a single value of phase shift or  $2^\circ$  order amplitude component, all the pixels refers to the gauge length of specimen. Moreover, a reference data matrix has been subtracted from the leftovers to eliminate the noise of early load steps (Fig. 20). For specimen 1 of AISI 316 the reference load step has been fixed to 35 MPa while for X4 Cr Ni 16,4 material the subtracted

image refers to 167,50 MPa. For the  $T_2$  parameter during the data processing any subtraction has been made. In the next paragraph are shown the results for both materials.

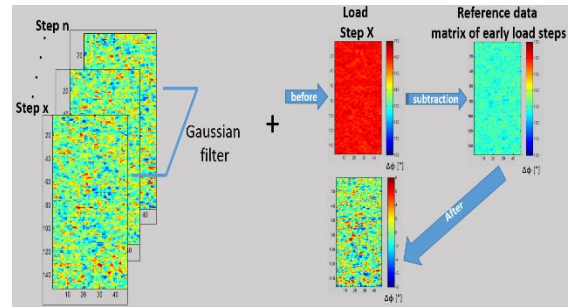


Fig. 20. Smoothing procedure for phase data matrix.

## Results and Interpretation

In this paper a comparison between phase,  $T_2$  data and the Dixon method results is done.

The phase trends refers to the difference between  $98^\circ$  and  $2^\circ$  percentile calculated for each data matrix of the test. The endurance limit assessed for the three specimens refers the load step before the maximum phase increase (Fig. 21a,b). Referring the  $T_2$  parameter, the fatigue limit found for each specimen has been evaluated by a data regression analysis (Fig. 21a,b). The analysis consists in interpolating early five data and subtracting both the slope and offset of this straight line to the others. A threshold value equal to the data standard deviation is set up to discriminate the value at which damage occurs.

As drawn in Fig. 21a,b for AISI 316 material, the damage is rather widespread in the gauge length of specimen. The threshold value depends on the crystal lattice and thus different microstructures behave differently. In this case, for austenitic stainless steels the high yield strength allows to a global plastic work affecting homogeneously the whole material (as shown in phase and T2 matrix images Fig. 21a,b).

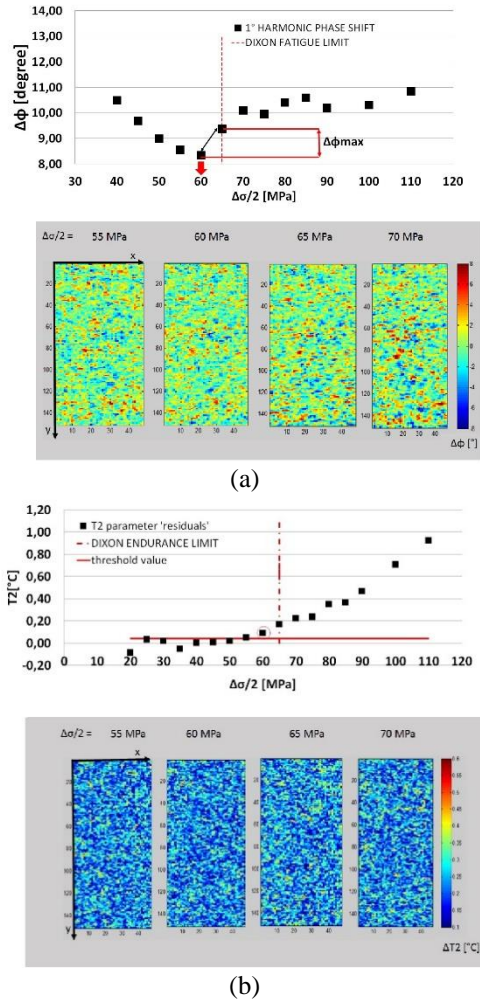


Fig. 21 AISI 316 analysis: phase shift(a) and T<sub>2</sub> parameters(b).

In martensitic tested specimen, a fatigue crack is instead developed during the test. The analysis allow to monitor the fatigue crack growing in the material by studying two different parameter and their trends. The threshold value for X4 Cr Ni 16,4 is different from AISI 316 threshold, and in regression analysis it has to be 6 times incremented (with respect previous austenitic

material case) because of the different crystal lattice.

Table 5 and Table 6 shows that, for both materials, the average value of phase results are higher than T2 average value, and thus, for AISI 316 the fatigue limit found by phase is very close to Dixon endurance limit. This phenomenon can be explained by considering the intrinsic difference in meaning between phase and second order amplitude components: the first is a manifestation of occurring damage while the second represents the dissipative heat sources due to a localized stress concentration in the material. The obtained T2 value could be lower than phase mean value because the dissipative heat sources appear before any material failure.

AISI 316	phase analysis results [MPa]	2° harmonic amplitude analysis [MPa]
AVERAGE	<b>63,33</b>	<b>60,00</b>
STD. DEV.	2,89	5,00
		ENDURANCE LIMIT 'DIXON' METHOD [MPa]
		<b>64,58</b> (3,51 MPa standard deviation)

Table 5. AISI 316 Endurance limit results: different methods.

X4 Cr Ni 16,4	phase analysis results [MPa]	2° harmonic amplitude analysis [MPa]
AVERAGE	<b>197,50</b>	<b>184,17</b>
STD. DEV	0,00	2,89

Table 6. X4 Cr Ni 16,4 Endurance limit results: different methods.

## Conclusion

In this paper two different fatigue behaviors have been analyzed referring to martensitic and austenitic stainless steels. The analysis concerns the evaluation of two parameters related to thermoelastic signal: phase shift and second

order harmonic amplitude that allow to study the damage.

Referring to the tested materials it is possible to observe the great dependence from the lattice: the austenitic microstructure dissipates energy by affecting all the surrounding lattice planes, while the martensitic microstructure leads to a stress concentration only in localized zones that may become fatigue cracks. As shown by analysis, the phase shift  $\Delta\phi$  parameter is capable to detect the plasticity zone and the  $\Delta T_2$  analysis involves in an assessment of dissipative heat sources not-necessarily close to damage (a dissipative heat sources can be localized inside the material but these one could not cause a failure). Moreover, for assessing the fatigue limits of both materials by using these parameters a post-processing method has been applied. The showed method to post-process the data allows to obtain results in good agreement with theoretical assumptions and they are also very close to Dixon endurance fatigue limit evaluation. Then, the thermoelastic signal provides different parameters that can globally describe the fatigue behavior of material by representing different phenomena.

## References

1. M.P. Luong. Infrared Thermographic Scanning of Fatigue in Metals, Nuclear Engineering and Design, 158, pp. 363-376, 1995.
2. R. De Finis, D. Palumbo, F. Ancona, U. Galietti. Fatigue Limit Evaluation of Various Martensitic Stainless Steels with New Robust Thermographic Data Analysis, International Journal of Fatigue, 74, pp. 88-96, 2015.
3. G. La Rosa, A. Risitano. Thermographic Methodology for Rapid Determination of the Fatigue Limit of Materials and Mechanical Components, International Journal of Fatigue, 22, pp. 65-73, 2000.
4. D. Palumbo, U. Galietti. Characterization of Steel Welded Joints by Infrared Thermographic Methods, Quantitative Infrared Thermography Journal, 11, N. 1, pp. 29-42, 2014.
5. U. Galietti, D. Palumbo, R. De Finis, F. Ancona. Fatigue Damage Evaluation with New Thermal Methods. 3<sup>th</sup> International Workshop On Advanced Infrared Technology And

- Applications, September 11-14, Tourin (Italy), 2013.
6. J.C. Krapez, D. Pacou, G. Gardette. Lock-in thermography and fatigue limit of metals. Quantitative Infrared Thermography Conference QUIRT 2000. July 18-21, Reims (France), 2000.
7. W.J. Wang, J.M. Dulieu-Barton, Q. Li. Assessment of Non-Adiabatic behaviour in Thermoelastic Stress Analysis of Small Scale Components, Experimental Mechanics, 50, pp. 449-461, 2010.
8. P.Stanley. Beginnings and Early Development of Thermoelastic Stress Analysis, Strain, 44, pp. 285-287, 2008.
9. U. Galietti, D. Palumbo, R. De Finis, F. Ancona. Fatigue Limit Evaluation of Martensitic Steels with Thermal Methods, Quantitative Infrared Thermography 12<sup>th</sup> International QIRT Conference, July 7-11, Bordeaux (France), 2014.
10. MF. McGuire. Martensitic Stainless Steels. Stainless Steels for Design Engineers. Asm International, pp. 123-35, 2008.

# BARRIER LAYER INDUCED CHANNELING EFFECT OF AS ION-IMPLANTATION IN HgCdTe AND ITS INFLUENCES ON ELECTRICAL PROPERTIES OF P-N JUNCTIONS

C. -Z. Shi<sup>1</sup>, C. Lin<sup>2</sup>, Y. -F. Wei<sup>3</sup>, L. Chen<sup>4</sup>, M. -X. Zhu<sup>5</sup>, R. -J. Ding<sup>6</sup>

Research Center for Advanced Materials and Devices, Shanghai Institute of Technical Physics,  
Chinese Academy of Sciences, 500 Yutian Road, Shanghai, 200083, China,

<sup>1</sup> shichangzhi@mail.sitp.ac.cn

<sup>3</sup> yfwei@mail.sitp.ac.cn

<sup>5</sup> zhmx@mail.sitp.ac.cn

<sup>2</sup> chun\_lin@mail.sitp.ac.cn

<sup>4</sup> chenlu@mail.sitp.ac.cn

<sup>6</sup> dingrj@mail.sitp.ac.cn

The HgCdTe layers ( $x_{\text{Cd}} \sim 0.285$  and  $0.225$ ) were grown by MBE and LPE, respectively, followed by the deposition of CdTe and ZnS films as barrier layers by thermal evaporation. Then, the p-on-n photodiodes were fabricated by arsenic ion implantation, Hg overpressure annealing, passivation and metallization. The SIMS and TEM results indicate that the evaporated CdTe layer with column structure induces the channeling effect of arsenic ion implantation causing the device performance degradation. This effect could be suppressed by depositing CdTe film with layered structure through E-beam evaporation. Finally, the I-V and C-V characteristics of these p-n junctions were estimated and analyzed.

## Introduction

With the advantage of the tunable forbidden gap corresponding to the response cutoff-wavelength range covering the entire IR spectrum[1], HgCdTe has always been the preferred material applied for the IR photo-voltaic detectors. In order to achieve the diode structure, the impurities, such as B, As, should be incorporated into the material during film growth or by ion-implantation. Compared to the in-situ doping, the ion-implantation process provides a more unsophisticated solution for doping. Recently, in the research work on the ion-implantation of HgCdTe, the implanted boron ions with light mass are considered to exist in the form of B hexagonal interstitials (donor dopants) in the p-type HgCdTe epilayer[2], forming the n-on-p type structure. Although the n-on-p boron implantation process has already become the standard technology for the HgCdTe IR detectors[3], the p-on-n device, especially based on As ion implantation, has been persistently researched as a candidate. The p-on-n device has the advantages of low dark current, low series resistance and high operating temperature[4]. However, it is quite difficult to implant As ions into HgCdTe since the As ion is much heavier. So, for the fabrication of the p-on-n device, the

im-plant energy of As ions into HgCdTe is usually so high ( $\sim 360\text{keV}$ [3,5,6]) that large numbers of implant damages are generated in the surface layer. The barrier layer deposited on the HgCdTe is used to protect the vulnerable surface of HgCdTe and absorb parts of implant damages[7,8]. Accordingly, the micro-structure of the barrier layer could have a significant impact on the distribution of implant damages and As ions in HgCdTe, which has not been reported in the literatures. In this paper, the As-implanted p-on-n HgCdTe photodiodes were fabricated based on different barrier layers, and the influences of the implantation channeling effect induced by barrier layers on the distributions of As ions and implant damages were studied. Finally, the electrical properties of these p-n junctions were measured and analyzed.

## Experimental

The HgCdTe epilayers (MW:  $x_{\text{Cd}} \sim 0.285$  and LW:  $x_{\text{Cd}} \sim 0.225$ ) were grown by MBE (on the Si substrate) and LPE (on the CdZnTe substrate), respectively. Then, for the sample A, the CdTe barrier layer was deposited by thermal evaporation on the CdZnTe-based HgCdTe, called TE CdTe; for the sample B, the ZnS film was thermally evaporated on the CdZnTe-based

HgCdTe, called TE ZnS; for the sample C and D, the CdTe layers were deposited by E-beam evaporation, called EB CdTe, on the CdZnTe-based and Si-based HgCdTe layers, respectively. All the above samples were implanted by As ions at 360keV with the dose of  $2 \times 10^{14} \text{cm}^{-2}$  and then subjected to the Hg overpressure annealing in two temperature steps of 410°C and 240°C. Particularly, the sample A, C and D were implanted selectively with the mask, and then the planar p-on-n photodiodes were fabricated by Hg-rich annealing activation, passivation, metallization, indium-bump deposition, etc.

The As profiles of the unannealed and annealed samples were measured by SIMS. Meanwhile, the microstructure of the three barrier layers and the implant damages in the surface layer were characterized by STEM. Finally, the I-V and C-V characteristics of the p-on-n photodiodes were measured and analyzed.

## Results and discussions

Firstly, the microstructure of the three barrier layers was observed by TEM as shown in Fig.1. It can be seen that the TE CdTe film has column structure, while the EB CdTe film shows layered structure. And the ZnS film seems to be polycrystalline. The different microstructures of these three barrier layers give rise to the distinctness in the distributions of As dopants and implant damages before and after annealing.

Fig.2 provides the TEM cross-section images of the damage layers in sample A, B and C. As seen in Fig.2, the thicknesses of the implant damage layers for sample A, B and C are around 340nm, 210nm and 270nm, respectively. Due to the column structure of the TE CdTe layer, the sample A has the deepest damage layer, and the thickness of the amorphous layer in the surface region is near 170nm, close to the sample C. Similar to silicon[9], the implant induced amorphous layer is formed so rapidly that it could block the subsequent ion implantation. Thus, the formation of defects beneath the amorphous layer could not be later than the

amorphization of the surface material. It implies that the As ions go into the HgCdTe more rapidly and deeply for the sample A. By contrast, the thicknesses of the amorphous layer and the damage layer for sample B are smaller, so it can be considered that the compact polycrystalline ZnS possesses better barrier effect for As ions than CdTe.

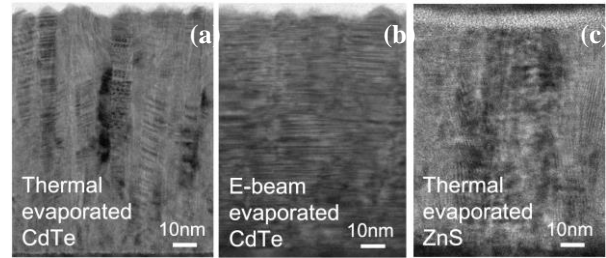


Fig.1. TEM images of cross sections of (a) TE CdTe, (b) EB CdTe and (c) TE ZnS barrier layers.

Subsequently, the As ion profiles of sample A, B and C before and after annealing were characterized by SIMS as illustrated in Fig.3. As shown in Fig.3(a), the depths of the end-of-range (EOR) for As ions in sample A, B and C are 0.86, 0.64 and 0.7 $\mu\text{m}$ , respectively. Although the sample A has the deepest EOR, its lattice damage and surface amorphization are most serious. It is noteworthy that the distribution of the As ions in the annealed sample A presents the channeling effect as shown in Fig.3(b), and the phenomenon can be called barrier layer induced channeling effect (BLICE). According to the above TEM observation, this effect is most likely due to the ballistic implantation of As ions through the cribrate TE CdTe layer rather than the implantation extended defects[10], resulting in the linearly graded distribution of As ions. However, the BLICE effect is undesirable for device performance. It could introduce a certain amount of point defects deeper in HgCdTe by the rapid diffusion of As ions under the BLICE effect, similar to the rapid diffusion of dopants and the formation of point defects under the dose effect[6,9]. In order to suppress this effect, the EB CdTe layer with the layered structure was deposited instead of the TE CdTe layer. On the other hand, although the diffusion depth of As ions in the annealed sample B (TE ZnS) is a little larger than the sample C as shown in Fig.3(b),



the effective dose and the peak concentration of the former are an order of magnitude lower than the latter, due to the stronger barrier effect of ZnS. In summary, the EB CdTe barrier layer could avoid the BLICE effect under the guarantee of effective dose and peak concentration.

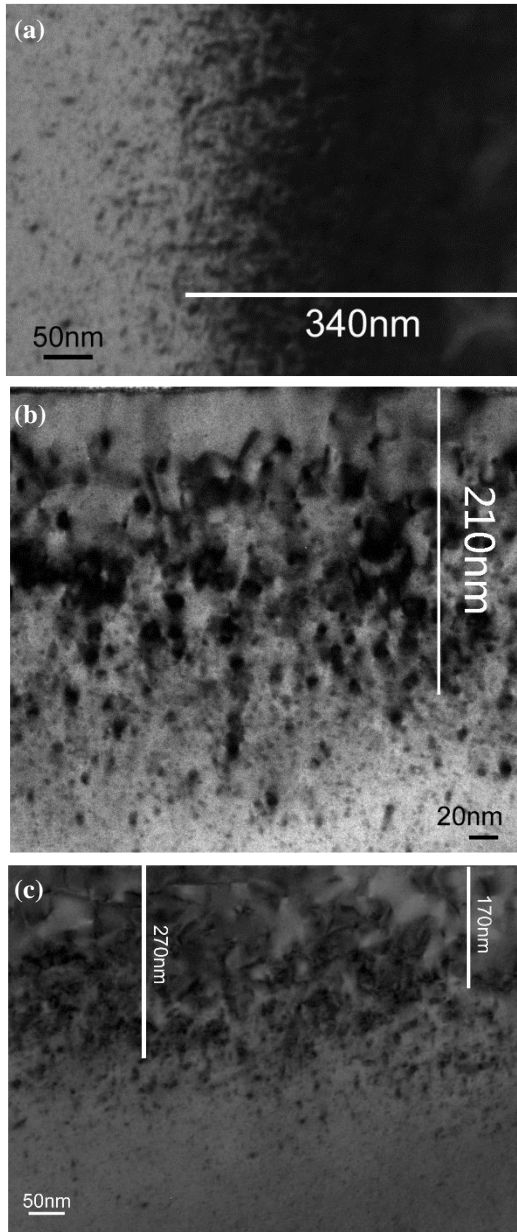


Fig.2. TEM images of implant induced damages in surface layers of HgCdTe samples with (a) TE CdTe, (b) TE ZnS, (c) EB CdTe as barrier layers.

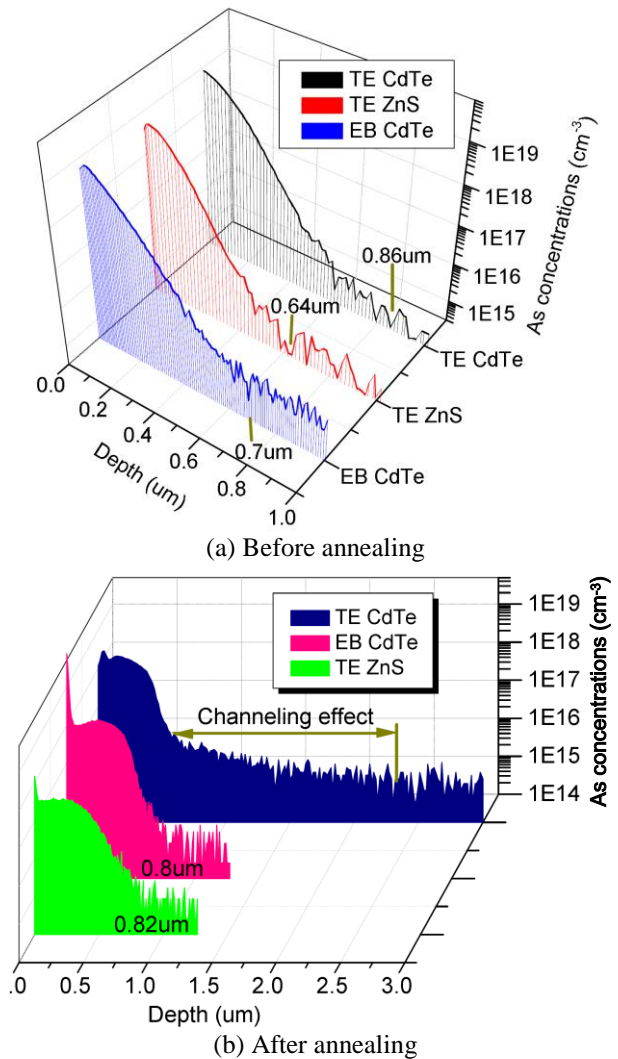


Fig.3. SIMS profiles of As concentrations in HgCdTe with TE CdTe, TE ZnS and EB CdTe as barrier layers before and after Hg overpressure annealing.

Finally, the IV characteristics of the p-on-n photo-diodes based on the sample A and C were measured by the cold probe at 100K with Keithley 4200-SCS. The I-V and R-V characteristic curves in Fig.4 indicate that the BLICE effect could aggravatingly degrade the device performance, which is likely due to the introduction of defect levels deeper in HgCdTe epilayer by the BLICE effect. Additionally, because the LW HgCdTe material is not suitable for the C-V measurement[11], only the C-V curve of the p-on-n photo-diode based on the sample D was measured by Keithley 590 C-V Analyzer and plotted in Fig.5. By curve fitting, it indicates that the capacitance  $C^{-3}$  of the p-n junction is proportional to the voltage V, so it

can be considered that the p-n junction is the diffused junction.

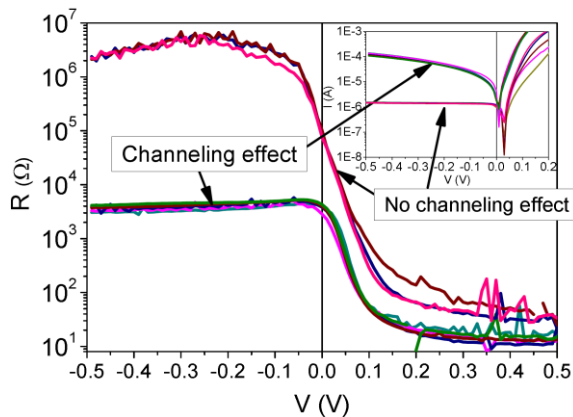


Fig.4. I-V and R-V curves of photodiodes with and without channeling effect.

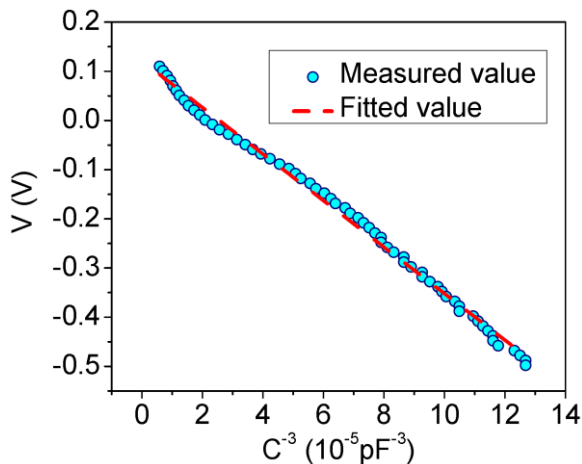


Fig.5.  $C^{-3}$ -V curve of the p-on-n photodiode

## Conclusion

The three barrier layers (TE CdTe, Te ZnS and EB CdTe) were deposited on the MW and LW HgCdTe epilayers to investigate the influence of the film microstructure on the distributions of the implanted As ions and implant damages in this paper. By SIMS characterization and TEM observation, the BLICE effect was discovered in the sample with TE CdTe as a barrier layer. The conclusion indicates that the BLICE effect is attributed to the ballistic implantation of As ions through the TE CdTe layer with column structure. This effect can introduce point defects deeper in HgCdTe layer by the rapid diffusion of As ions, thereby degrading the device performance. Moreover, the experiment results

show that the EB CdTe barrier layer with layered structure can avoid this effect. Although the BLICE effect also does not occur to the sample with ZnS barrier layer, the effective dose and peak concentration of the implanted As ions in HgCdTe are lowered by an order of magnitude approximately. Finally, the I-V characteristic curves testify the influence of the BLICE effect, and the C-V measurement shows that the prepared p-n junction is a diffused junction.

## References

1. H. Figgemeier, J. Wenisch, D. Eich, et al. MCT by MBE on GaAs at AIM: State of the Art and Roadmap, Proc. of SPIE, Vol. 9451, pp. 945127-1-10, 2015.
2. Tang Dong-Hua, Xue Lin, Sun Li-Zhong, et al. Doping effect of boron in Hg<sub>0.75</sub>Cd<sub>0.25</sub>Te: first-principles study, Acta Physica Sinica, Vol. 61, No. 2, pp. 027102-1-10, 2012.
3. L. Mollard, G. Destefanis, G. Bourgeois, et al. Status of p-on-n Arsenic-Implanted HgCdTe Technologies, Journal of Electronic Materials, Vol. 40, No. 8, pp. 1830-1839, 2011.
4. L. Mollard, G. Bourgeois, C. Lobre, et al. p-on-n HgCdTe Infrared Focal-Plane Arrays: From Short-Wave to Very-Long-Wave Infrared, Journal of Electronic Materials, Vol. 43, pp. 802-807, 2014.
5. L. Mollard, G. Destefanis, N. Baier, et al. Planar p-on-n HgCdTe FPAs by Arsenic Ion Implantation, Journal of Electronic Materials, Vol.38, No.8, pp. 1805-1813, 2009.
6. C. Lobre, D. Jalabert, I. Vickridge, et al. Quantitative damage depth profiles in arsenic implanted HgCdTe, Nuclear Instruments and Methods in Physics Research B, Vol. 313, pp. 76-80, 2013.
7. Z. H. Ye, J. Huang, W. T. Yin, et al. HgCdTe Photodiode Arrays Passivated by MBE In-situ Grown CdTe Film, J. Infrared Millim. Waves, Vol. 30, No. 6, pp. 495-498, 2011.
8. Z. H. Ye, J. Huang, W. T. Yin, et al. HgCdTe Mid-wavelength Infrared Detector with Interface Passivated by Hydrogen Implantation, J. Infrared Millim. Waves, Vol. 30, No. 3, pp. 260-262, 2011.
9. S. Tian, S.-H. Yang, S. Morris, et al. The effect of dose rate on ion implanted impurity profiles in silicon, Nuclear Instruments and Methods in Physics Research B, Vol. 112, pp. 144-147, 1996.
10. L.O. Bubulac, D. S. Lo, W. E. Tennant, et al. p on n ion-implanted junctions in liquid phase epitaxy HgCdTe layers on CdTe substrates, Appl. Phys. Lett., Vol. 50, pp. 1586-1588, 1987.
11. H. Q. Lu, J. Zhao, X. Y. Li, et al. Study of Electrical Characteristics of HgCdTe pn Junction Formed by Low Energy Ion Beam Milling, J. Infrared Millim. Waves, Vol. 17, pp. 21-24, 1998.

# ANALYSIS OF TEMPERATURE-CURRENT RISE IN MODERN PCB TRACES BY MEANS OF THERMOGRAPHY

K. Petrosyants<sup>1,2</sup>, I. Kharitonov<sup>1</sup>, A.A. Popov<sup>1</sup>

<sup>1</sup> **Moscow Institute of Electronics and Mathematics of National Research University  
“Higher School of Economics”, eande@miem.edu.ru**

<sup>2</sup> **Institute for Design Problems in Microelectronics, Russian Academy of Sciences**

Higher functionality of today's electronic products demands high density integration of electronic components. In this field, printed-circuit-board (PCB) are the perspective technology to build a variety of electronic systems for different applications. Two types of boards were investigated: high current for power applications and high density boards for modern electronic equipment. The set of IR images and temperature-current diagrams for different substrate materials were investigated. Current and temperature limits for all test boards were defined to provide high level of board reliability.

## Introduction

The global trend in the electronic industry driven by automotive, aerospace, computer, telecommunication, hand held equipment and other products is showing up in improved performance and better human interface. So the electronic equipment is demanding miniaturization and function integration. In this field, printed-circuit-board (PCB) embedding technology has the potential to play the important role with the possibility to build a variety of electronic modules and systems for different applications. However, miniaturization and function integration increase the equipment power density and as a result - increase the operating temperatures of electronic components and current carrying traces. These factors decrease the reliability and life time of electronic equipment. So the very important problem of PCB design is the thermal analysis to provide the optimal technology solution.

The thermal effects in active and passive electronic components were completely investigated and analyzed [1,2]. But the physical and technological limitations in modern PCB copper traces in the context of their thermal stability are still under consideration. A few works where thermographic technique was used for control

and monitoring of PCB systems were published [3,4]. The purpose of this work was investigation and analysis of modern PCB current carrying capacity of traces (CCCT) in dependence of board materials and trace sizes (thickness, width, length) to provide high levels of electro-thermal stability and operating reliability of electronic systems realized on new boards.

## Test boards for thermographic analysis of temperature-current rise in traces

Two types of test boards [5,6] have been fabricated and investigated:

1) Test board for high current application (power supply units, electromechanical, automotive and other power equipment). The boards (Fig. 1) were manufactured using FR-4 substrate (of 1.5mm thickness) with dimensions 100x200 mm<sup>2</sup>. The board was manufactured in two versions: with nominal copper layer thicknesses of 18 and 35 μm and traces with the different shapes, widths and lengths.

2) High density boards for modern equipment (Fig. 2). The boards were manufactured using perspective substrates: Al<sub>2</sub>O<sub>3</sub> ceramic substrate (of 500 μm thickness) and aluminium/polymide (240 μm / 4,0 μm) substrate with dimensions 60x48 mm<sup>2</sup>. Trace parameters: material Ti-Cu-Ni-Au (0,05-2-0.3-0.2 μm), length L = 1,5 – 28 mm, widths W = 150 - 530 μm.

## Thermographic analysis of temperature-current rise in test PCB traces

Thermographic analysis of temperature-current rise in PCB traces was conducted using Flir A40 IR camera with macro (17  $\mu\text{m}$  resolution) lens, precise micro positioning system and specially developed software tool (IRDataProc) for object emissivity coefficients map generation and object temperatures correction [7,8].

Thermal images of all conducting traces of test boards were investigated in dependence of electric current. Maximal temperatures of the traces were defined and plotted as a function of electric current.

### Results for high current test board.

The measured I-T characteristics and IR images of traces with different shapes, widths and lengths (see Fig. 1) and Cu layer thickness of 18 and 35  $\mu\text{m}$  values are presented in Fig. 3 – Fig. 4 .

It is seen from Fig. 4 that (for the same current values) trace “G” has much more higher temperature values in comparison with the other traces.

### Results for high density test boards (Fig.2).

The measured I-T characteristics and IR images are presented for different trace widths (Fig. 5), ceramic and aluminium/polymide substrates (Fig. 6), trace lengths (Fig. 7).

It is seen from Fig. 6 that ceramic substrate provides much more better heat removing for traces in comparison with aluminium/polyimide substrate.

Analyzing the temperature measurement results for traces with different lengths in Fig. 7 it is seen that the maximal length 27.5 mm is limited by the temperature value of 122.4°C.

## Conclusion

Temperature- current characteristics of PCB conducting traces were measured and analyzed by means of thermography techniques for two types of boards: high current for power applications and high density for modern electronic equipment.

- Current and temperature limits for traces with different layer thickness, substrate materials, trace widths and lengths were defined based on board reliability.

- The results allowed to provide recommendations on design of reliable boards for modern electronic equipment. These results were used by PCB designers in their projects.

This work was carried out within the framework of the National Research University Higher School of Economics’ Academic Fund Program under grant 15-01-0165 and the Russian Foundation for Basic Research under grant 14-29-09145.

## References

1. D. Wolpert, P. Ampadu. Managing temperature effects in nanoscale adaptive systems, Springer Science+Business Media ,2012.
2. A. D. Kraus, A. Bar-Cohen. Thermal Analysis and Control of Electronic Equipment, Hemisphere Publishing Corporation, 1983.
3. F. Lehtiniemi, A. Hynninen. Applications of infrared thermography in electronics research, Nokia Research Center, 2000.
4. C. R. Wagh, V. B. Baru. Detection of Faulty Region on Printed Circuit Board With IR Thermography, International Journal of Scientific & Engineering Research, Vol. 4, Issue 11, pp. 1-4, 2013.
5. Dr. Johannes Adam, ADAM Research. Thermal Management of Boards and Current Carrying Capacity of Trac, Bodo’s Power Systems. Germany, 2011, <http://www.bodospower.com/>
6. A. Lese, U. Scheuermann. High Load Current on FR-4 Printed Circuit Board – Design Considerations and Limits, Proceedings of PCIM 2004, pp. 42-47, 2004.
7. K. O. Petrosyants, I. A. Kharitonov, P. A. Kozyanko A.A. Popov. Electronic components thermal regimes investigation by IR thermography, Proceedings of the 12-the International Workshop on Advanced Infrared Technology and Applications. Torino : Politecnico di Torino, pp. 185-189, 2013.
8. K. O. Petrosyants, I. A. Kharitonov, P. A. Kozyanko, N. I. Rjabov. The Multilevel System for Thermal Control of Electronic Components, Proceedings of the International Conference on Advances in Computer Science and Electronics Engineering (CSEE 2014), 08-09 March, 2014, Kuala Lumpur, Malaysia. Institute of Research engineers and Doctors, pp. 150-155, 2014.

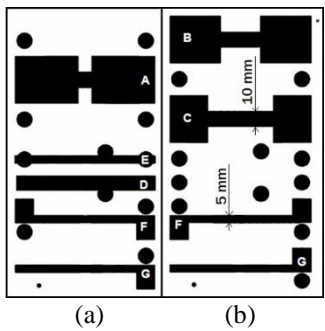


Fig. 1 Layouts of high current test board [6] with different trace structures: top layer (a), bottom layer (b).

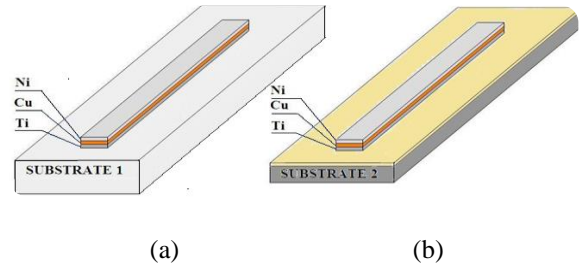


Fig. 2 Structures of modern high density test board: with ceramic  $\text{Al}_2\text{O}_3$  ( $500 \mu\text{m}$ ) substrate (a), with aluminium / polyimide ( $240 / 4,0 \mu\text{m}$ ) substrate (b).

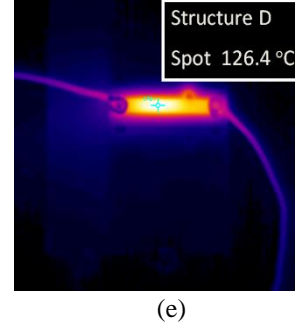
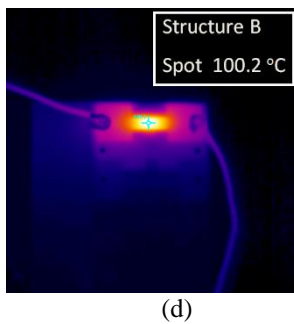
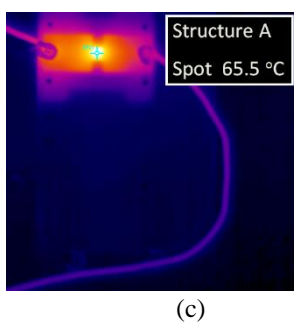
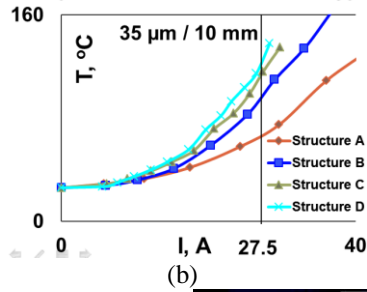
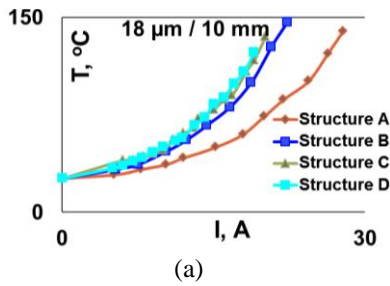


Fig. 3. I-T characteristics for traces A-D (Fig. 1) with  $18 \mu\text{m}$  (a),  $35 \mu\text{m}$  (b) layer thickness. IR images of the mentioned traces for 7.5A current and  $18 \mu\text{m}$  thickness (c) –(e).

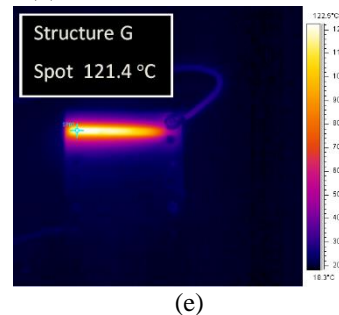
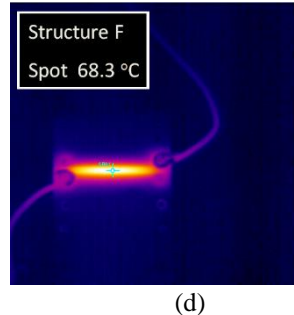
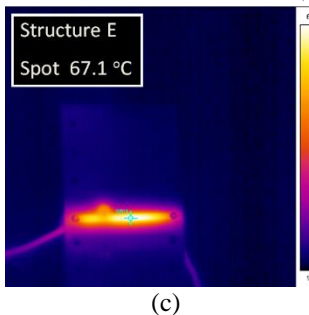
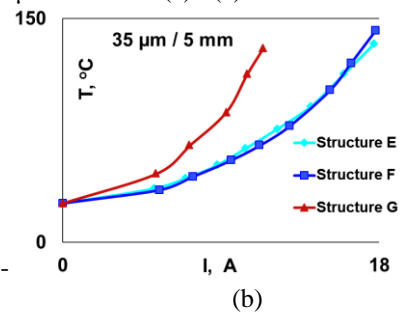
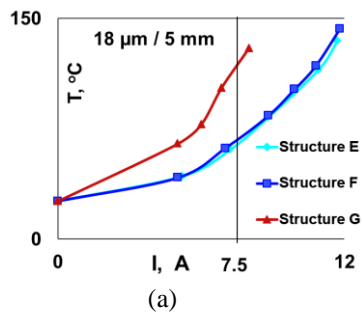


Fig. 4. I-T characteristics for traces E- G (Fig. 1) with  $18 \mu\text{m}$  (a),  $35 \mu\text{m}$  (b) layer thickness ; IR images of traces with the mentioned structures for 7.5A current and  $18 \mu\text{m}$  thickness (c) –(e).



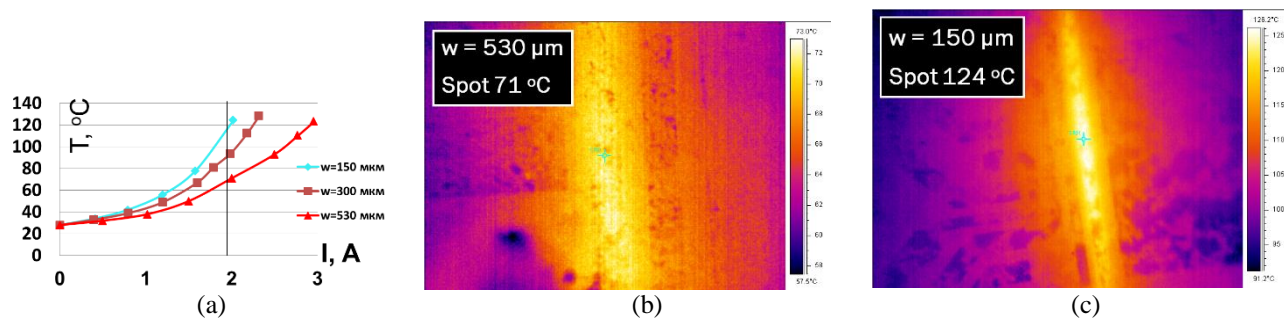


Fig. 5. I-T characteristics (a) for high density traces (see Fig 2) with different widths and IR images (for 2A current) for trace placed on a polyimide board for the different trace widths of traces (b) – (c).

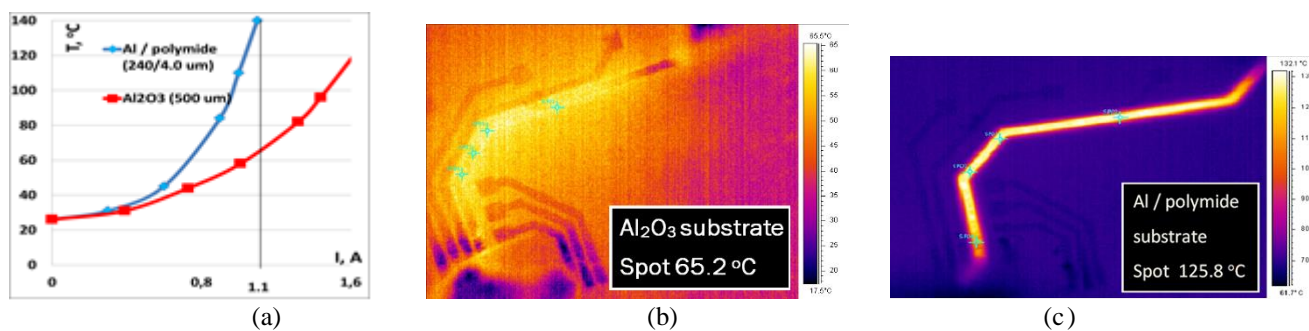


Fig.6. I-T characteristics (a) for high density traces (Fig 2) for different substrates; IR trace images (for current of 1.1A) for trace placed on a ceramic (b) and Al/polyimide (c) substrates .

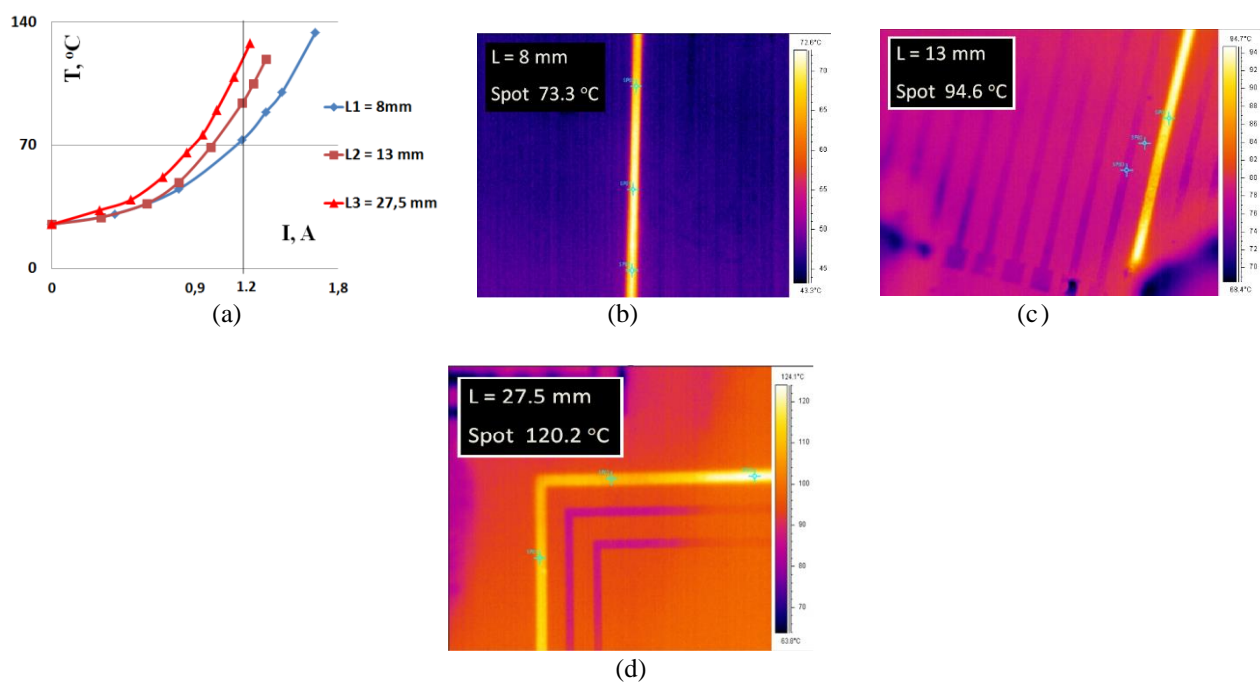


Fig. 7. I-T characteristics (a) for high density traces (Fig 2) with different lengths; IR images (for current of 1.2 A) for trace placed on Al/polyimide substrate for different trace lengths (c)-(d).



## Method of 3D Solar Energy conversion.

Valeri I. Kotelnikov, Elena A. Ryazanova.

Tuvinian Research Institute SB RAS, International st., 117 A, Kyzyl, Tuva, Russia, 667007  
e-mail: tikopr@mail.ru

We have studied experimentally the problem of collecting solar energy and make their efficiency higher. It was discovered that a three-dimensional photovoltaic 3DPV structures can generate measured energy densities higher by a factor of 2–20 than stationary flat PV panels. We have found that the same structures work better not only because it made in 3D. We have found PV panels have not linear dependency from geometry. It seems that the conversion efficiency depends on the process of absorption of the solar energy too or in other words on the E. Yablonoich limit. Our findings suggest that quantity of material of solar panels may be decreased for generation same electricity.

### Introduction

The Sun is the ultimate source of energy that sustains all life. The Sun exposes the Earth with enough solar energy in one hour to power the entire world for one year. If we can capture a small portion of this energy and cost-effectively convert it into useful electricity, then we can inhabit the Earth for as long as the Sun exists without worrying about a shortage of energy. This single fact has propelled the solar industry on a path of exponential growth.

Converting the solar flow into affordable electricity is an enormous challenge. The main barriers to widespread adoption of PV technology include system costs (3–5 \$/Watt-peak) of which ~60% is due to installation costs, the limited number of peak insolation hours available in most locations.

The main approach applied so far to alleviate these problems has been to search for lower-cost active layers with higher power conversion efficiencies. However, efficiency improvements can only partially reduce the installation costs and cannot change the pattern of solar energy generation, since these aspects are related to the PV system design.

Marco Bernardi et al [1] formulate, solve computationally and study experimentally the problem of collecting solar energy in three dimensions.

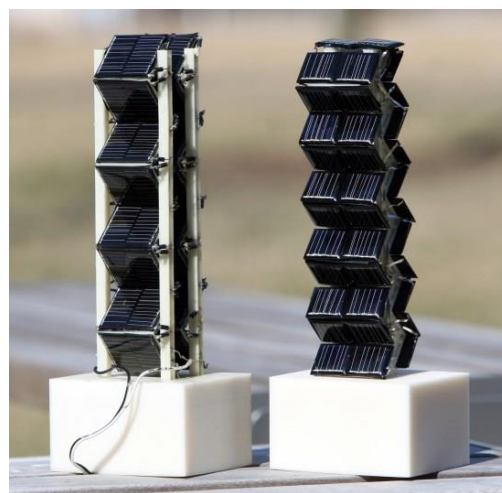


Fig. 1. Three-dimensional photovoltaic structure.

They demonstrate that absorbers and reflectors can be combined in the absence of sun tracking to build three-dimensional photovoltaic (3DPV) structures that can generate measured energy densities (energy per base area, kWh/m<sup>2</sup>) higher by a factor of 2–20 than stationary flat PV panels. For the structures considered there, they compared to an increase by a factor of 1.3–1.8 for a flat panel with dual-axis sun tracking. The increased energy density is countered by a larger solar cell area per generated energy for 3DPV compared to flat panels (by a factor of 1.5–4 in our conditions), but accompanied by a vast range of improvements. Authors wrote 3DPV can double the number of peak power generation hours and dramatically reduce the seasonal, latitude and weather variations of solar energy generation compared to a flat panel design.



Fig.2. Dielectric core-shell optical antennas.

Yiling U et al [2] demonstrate a new light trapping technique that exploits dielectric core-shell optical antennas to strongly enhance solar absorption. This approach can allow the thickness of active materials in solar cells lowered by almost 1 order of magnitude without sacrificing solar absorption capability. They investigate the fundamental mechanism for this enhancement multiplication and demonstrate that the size ratio of the semiconductor and the dielectric parts in the core-shell structure is key for optimizing the enhancement.

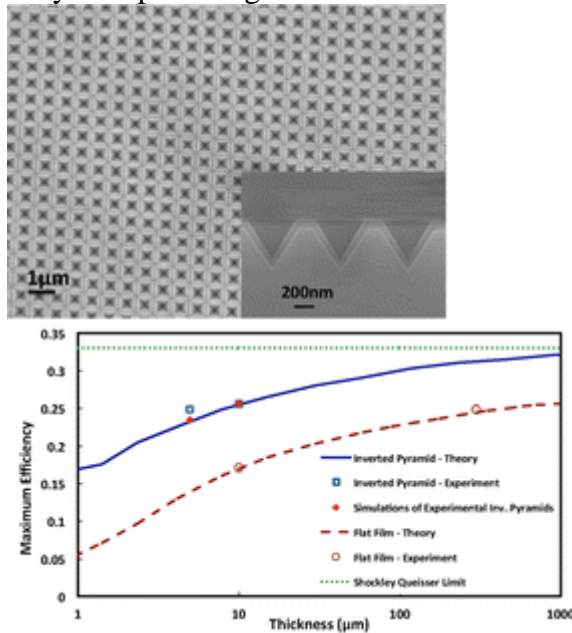


Fig.3. Inverted nanopyramid light-trapping scheme for c-Si thin films

Anastassios Mavrokefalos et al [3] approve thin-film crystalline silicon (c-Si) solar cells with light-trapping structures can enhance light absorption within the semiconductor absorber layer and reduce material usage. They demonstrated that an inverted nanopyramid light-trapping scheme for c-Si thin films, fabricated at wafer scale via a low-cost wet etching process, significantly enhances absorption within the c-Si layer. A broadband enhancement in absorbance that approaches the

Yablonovitch limit [4] is achieved with minimal angle dependence.

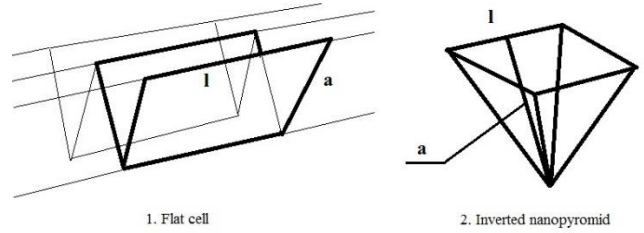


Fig.4. 1. Flat cell texture and 2. Inverted nanopyramid.

We have calculated that the surface of nanopyramid ( $S_p$ ) and surface of a part of hatching ( $S_l$ ) with same linear dimensions are equal.

$$S_p = p \cdot a / 2 \quad (1)$$

where:

p - perimeter.  
a - apothem.

$$S_l = 2 \cdot a \cdot l \quad (2)$$

where:

a - apothem.  
l - length.

$l = p/4$  and we may replace l and p/4, so:

$$S_l = 2 \cdot a \cdot p/4 = p \cdot a/2 = S_p \quad (3)$$

As we can see  $S_p$  and  $S_l$  is equal. Fabricating of the nanopyramids on the solar cell surface is complex and expensive process. We may simply manufactured scratched solar cells with higher efficiency.

So, in summary of sentences above we have guessed a way of improving solar cell's efficiency. It seems to be better to use a ratio of visible and whole square of solar cell to make it better. In accordance to this idea, we build a new angular PV converter.

It is a device with at least two solar cells placed opposite and oriented of wide end to a sun. It is two couples of solar cells one (external) is horizontally oriented and another (internal) is set with angle between cells each of it connected sequential. Results of testing of the experimental device presented in the Tab.1. Solar cell dimensions: length - 150 mm, width - 80 mm.

Tab.1.

Geometry	Power Watts
Horizontally oriented	0.19
Angle between cells	0.40

We have tested the dependence of power of solar cell and its geometry (Fig.6.). An analysis of it show non-linear dependence of absorption of photons.

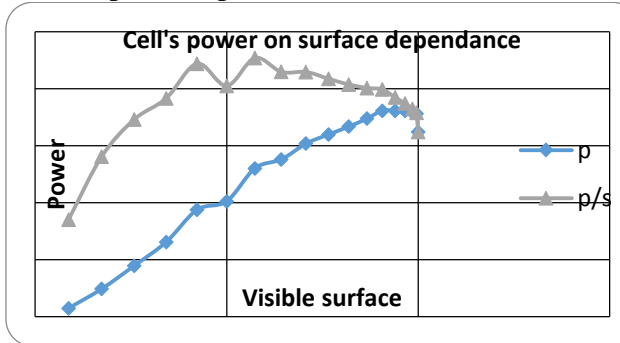


Fig.6. Power productivity of solar cell.  
 p - power of cell, p/s - power per area of lighting.

### Conclusion

We increased power of solar cell twice. It can generally apply to a wide range of inorganic and organic active materials. 3D solar cells that capture nearly all of the light that strikes them and could boost the efficiency of photovoltaic systems while reducing their size, weight and mechanical complexity.

Conclusions:

We guess that the efficiency of PV conversion depend on the ratio of visible and whole square of solar cell. Here we demonstrate that a focline is better than an inverted nanopyramid light trapping. The focline can be fabricate at the any process, enhances absorption within the any type of solar cell. The way we tested is a cheapest way to improve the solar cell's technology.

Where we can use it? In the PV industry, of course. We could use it in another way. We may convert heat radiation (infrared) from fuel combustion directly to electricity. It is estimated that somewhere between 20 to 50% of industrial energy input is lost as waste heat in the form of hot exhaust gases, cooling water, and heat lost from hot

equipment surfaces and heated products. Typically, the process converts the latent energy in a fuel stock (coal, gas, uranium) into mechanical energy in a generator and ultimately electrical energy. In all of these cases, though, some of the input energy is lost in the process.

The efficiency of generation varies widely with the technology used. In a traditional coal plant, for example, only about 30-35% of the energy in the coal ends up as electricity on the other end of the generator. There is, therefore, tremendous economic and ecological incentive to improve the efficiency of power generation so that more of the energy content of the input fuel is carried through to the output electricity.

The transmission and distribution system, then, includes everything between a generation plant and an end-use site. Along the way, some of the energy supplied by the generator is lost due to the resistance of the wires and equipment that the electricity passes through. Most of this energy is converted to heat. Just how much energy is taken up as losses in the system depends greatly on the physical characteristics of the system in question as well as how it is operated. It is considered, that losses between 6% and 8% are normal, but it seems to us it is about 15-20% in the local grids.

So, what we have defined?

Process	Amount	Energy
Waste heat	20-50%	50-80% Energy persist
Generation	30-35%	15- 28% Energy persist
Transmission	6-8%	13- 25% Energy income to the user

As we can see only 13-25% of energy of a fuel may be used on the user's side. We need to improve our technologies of energy conversion. It is because we study follows energy system – burn device, concentrating unit, optical fiber, photovoltaic device. We should select semiconductor with long infrared area of radiation. This way will allow us to increase an efficiency of energetic system at least on 15-18%.

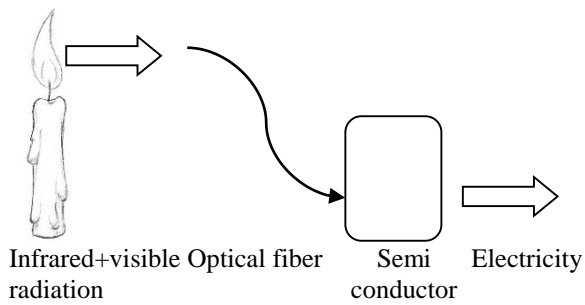


Fig. 7. Heat radiation conversion.

**References:**

1. Marco Bernardi, Nicola Ferralis, Jin H.Wan, Rachelle Villalon and Jeffrey C. Grossman. Solar energy generation in three dimensions. *Energy Environ. Sci.*, 2012, 5, 6880-6884
2. Yiling Yu, Vivian E. Ferry, A. Paul Alivisatos, and Linyou Cao. Dielectric

- Core-Shell Optical Antennas for Strong Solar Absorption Enhancement. *Nano Lett.*, 2012, 12 (7), pp 3674–3681
3. Anastassios Mavrokefalos, Sang Eon Han, Selcuk Yerci, Matthew S. Branham, and Gang Chen. Efficient Light Trapping in Inverted Nanopyramid Thin Crystalline Silicon Membranes for Solar Cell Applications. *Nano Lett.*, 2012, 12 (6), pp 2792–2796
4. Yablonovitch, E. J. *Opt. Soc. Am.* 1987, 72, 899–907
5. Mallarie McCune, Wei Zhang, and Yulin Deng. High Efficiency Dye-Sensitized Solar Cells Based on Three-Dimensional Multilayered ZnO Nanowire Arrays with “Caterpillar-like” Structure. *Nano Lett.*, 2012, 12 (7), pp 3656–3662

# INFLUENCES OF ION BEAM CURRENT ON DOPANT PROFILES AND BARRIER LAYER INDUCED CHANNELING EFFECT IN ARSENIC IMPLANTED HgCdTe EPILAYER

C.Z. Shi<sup>1</sup>, C. Lin<sup>2</sup>, Y.F. Wei<sup>3</sup>, L. Chen<sup>4</sup>, M.X. Zhu<sup>5</sup>, Q.Z. Sun<sup>6</sup>, R.J. Ding<sup>7</sup>

Research Center for Advanced Materials and Devices, Shanghai Institute of Technical Physics,  
Chinese Academy of Sciences, 500 Yutian Road, Shanghai, 200083, China,

<sup>1</sup> shichangzhi@mail.sitp.ac.cn

<sup>4</sup> chenlu@mail.sitp.ac.cn

<sup>7</sup> dingrj@mail.sitp.ac.cn

<sup>2</sup> chun\_lin@mail.sitp.ac.cn

<sup>5</sup> zhmx@mail.sitp.ac.cn

<sup>3</sup> yfwei@mail.sitp.ac.cn

<sup>6</sup> qzsun@mail.sitp.ac.cn

The influences of the beam current on the dopant profiles and barrier layer induced channeling effect (BLICE) in As implanted LPE HgCdTe ( $x_{\text{Cd}} \sim 0.238$ ) epilayers covered by different barrier layers (ZnS and CdTe) before and after annealing were studied. The results indicate that the increase in the depth of the sufficiently thick damage layer caused by raising beam current could hinder the indiffusion of As ions and suppress the BLICE. And by improving the structure of the barrier layer, the BLICE phenomenon could be avoided.

## Introduction

Arsenic has become the preferred acceptor doping material for the p-on-n HgCdTe IR detectors based on ion implantation, due to its high solubility, low diffusivity and wide doping levels[1]. To achieve the p-on-n structure, As should be incorporated by ion implantation and then electrically activated by annealing. So far, many studies have been reported on the influences of technological parameters (such as energy, dose[2], sub-strate temperature[3], Hg vapour pressure, annealing temperature and time[4]) on dopant profiles and device performance. But little research work has been devoted to the beam current effects. Here, the influences of beam current on the dopant profiles and the BLICE of As implanted HgCdTe were studied. Moreover, the implant induced damages under different beam currents were characterized to analyze the defect formation and the amorphization of surface region.

## Materials and Methods

The HgCdTe epilayers ( $x_{\text{Cd}} \sim 0.238$ ) were grown on CdZnTe substrates by liquid phase epitaxy (LPE). The CdTe and ZnS barrier layers were deposited as barrier layers on HgCdTe by thermal

evaporation, respectively. Then, the samples were implanted using As ions at 360keV with the dose of  $2 \times 10^{14} \text{cm}^{-2}$ . For the low ion beam current ( $< 100 \mu\text{A}$ ), the beam currents were in the range of 0.2~1.2uA and 0.2~1.5uA (the dose rates, i.e., beam current densities, were estimated to be  $0.008 \sim 0.048 \mu\text{A}/\text{cm}^2$  and  $0.008 \sim 0.06 \mu\text{A}/\text{cm}^2$ ) for the thermal evaporated (TE) CdTe and ZnS samples, respectively. In contrast, the TE CdTe sample was implanted with As ions in a high beam current of 100uA (dose rate  $\sim 2.2 \mu\text{A}/\text{cm}^2$ ) at the same energy and dose. In addition, the HgCdTe sample covered by the E-beam evaporated (EBE) CdTe layer was implanted in an As<sup>+</sup> beam current of 0.2uA to study the effect of film microstructure on the BLICE. Finally, the As profiles in HgCdTe were measured by SIMS, and the implant induced damages were characterized by TEM, as well as the microstructure of barrier layers.

## Experimental Results

Fig.1 and Fig.2 show the As SIMS profiles of as-implanted and annealed HgCdTe samples covered by ZnS and TE CdTe barrier layers implanted at different beam currents, respectively. It can be seen from Fig.1(a)-1(d) that the depth of the end-of-range (EOR) for As decreases with increasing



beam current. However, the beam current has no significant effect on the As profiles of the annealed samples (Fig.1(e)). By contrast, the effect of the beam current on the As profiles of as-implanted samples covered by TE CdTe layers is so small that it can be neglected, as shown in Fig.2(a). In Fig.2(b)-2(d), it should be noted that the increase of beam current can suppress the BLICE. The differences of the beam current effect between the samples with ZnS and TE CdTe barrier layers may be attributed to the implant induced damages and surface amorphization, which will be discussed later.

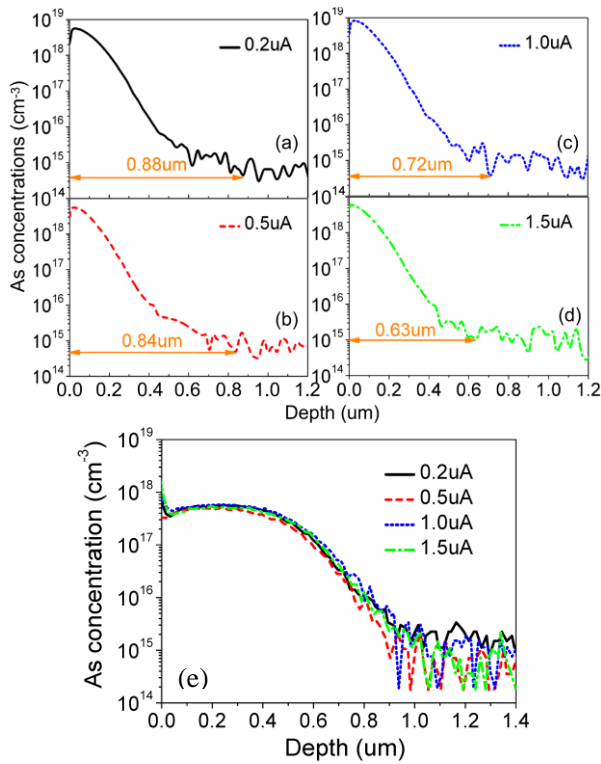


Fig. 1. As SIMS profiles of samples with ZnS barrier layers implanted at different beam currents (a)-(d) before and (e) after annealing.

In order to analyze the microstructure of as-implanted samples and barrier layers, the TEM cross-section images were acquired. As shown in Fig.3, the TE CdTe layer has column structure, whereas the ZnS film appears to be polycrystalline. According to the SIMS results provided in Fig.1 and Fig.2, the BLICE phenomenon only occurs to the TE CdTe samples rather than ZnS samples. Thus, it can be considered that the column structured CdTe layer gives rise to the ballistic

implantation of As ions resulting in the BLICE, rather than the implantation extended defects [3].

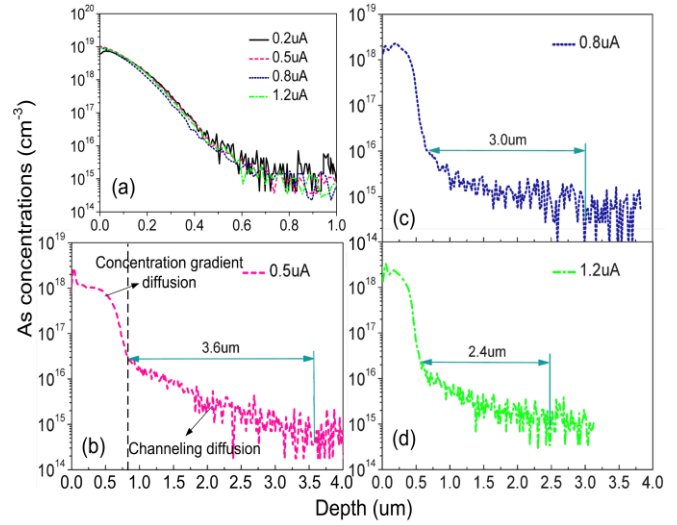


Fig. 2. As SIMS profiles of samples with TE CdTe barrier layers implanted at different beam currents (a) before and (b)-(d) after annealing.

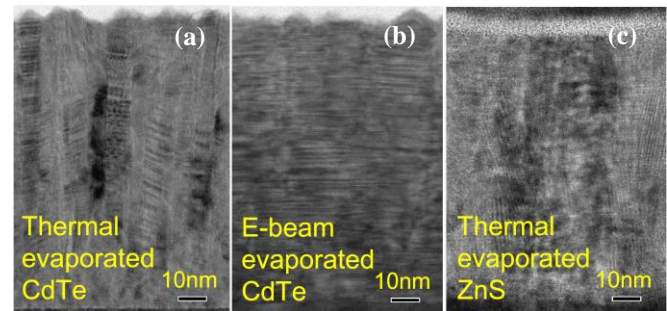


Fig. 3. TEM images of microstructure of three barrier layers. (a) TE CdTe, (b) EBE CdTe, (c) TE ZnS.

## Discussions

The TEM images of damages in HgCdTe samples (the beam currents are 0.5 and 1.5 $\mu$ A, respectively) with ZnS barrier layers are provided in Fig.4. Although the depths of damage layers are approximately identical, the damage density of the latter is higher than that of the former according to the gray scale, indicating that the increase of beam current can only aggravate the damage to the lattice but not effect the depth of damage layer obviously under low beam current. Additionally, the amorphization of surface layer occurs to the as-implanted HgCdTe material. As shown in Fig 4(a) and 4(b), the thickness ( $\sim$ 100nm) of the amorphous region in the higher beam current



sample is more than that ( $\sim 70\text{nm}$ ) in the lower beam current sample.

Accordingly, for the higher beam current, the higher density of defects and the thicker amorphous layer are generated, and they can prevent the subsequent dopant ions from being implanted into deeper regions. More-over, the defects and the amorphous layer are formed quite rapidly during implantation, similar to Si[5]. Thus, the higher the beam current is, the more difficult the As ions are implanted into HgCdTe deeply, which causes the decrease in the EOR depth of ZnS samples with increasing beam current. On the other hand, the elimination of implant induced defects and amorphous region could be finished in a short time [6,7] and the diffusion coefficient ( $\sim 420^\circ\text{C}$ ) of As in HgCdTe is very low under a concentration gradient[4], so the effects of damages and amorphous regions on the indiffusion of As ions are not significant for the ZnS samples.

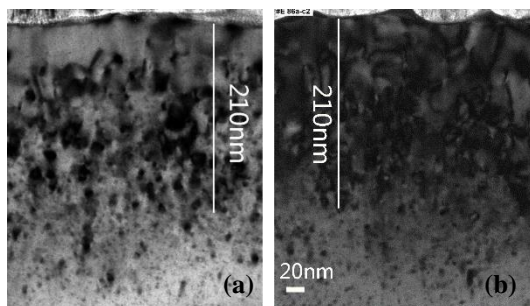


Fig. 4. TEM images of implanted induced damages in HgCdTe samples with ZnS barrier layers implanted at the beam currents of (a)  $0.5\mu\text{A}$  and (b)  $1.5\mu\text{A}$ .

However, due to the column structure of TE CdTe layer as shown in Fig.3(a), a ballistic implantation occurs to a small part of As ions (not observed from the SIMS profiles) and many channels could be generated in the lattice. As shown in Fig.2(a), the insensitivity of the As profiles in as-implanted TE CdTe samples to beam current is likely due to that the higher densities of damages and thicker amorphous regions are formed in TE CdTe samples (the thicknesses of damage layer and amorphous region are  $\sim 280\text{nm}$  and  $\sim 180\text{nm}$ , respectively, as shown in Fig.5(b)) than the ZnS samples. Although the ballistic implantation of As ions creates many deep channels into the lattice

at the beginning of implantation, the thick damage layer in the surface region is generated so rapidly that the near-surface portions of these channels are blocked completely before the total dose of As ions is implanted into the lattice. Therefore, the EOR depths of the As profiles in the as-implanted TE CdTe samples have a slight decreasing trend with improving beam current.

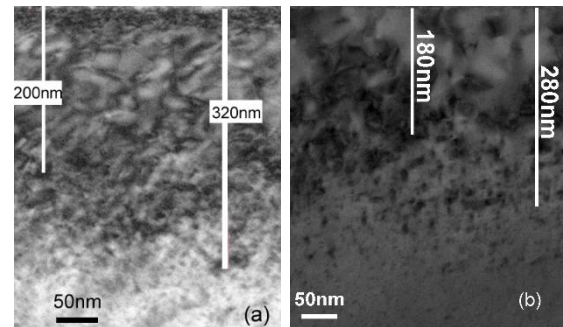


Fig.5. TEM images of implanted induced damages in HgCdTe samples with TE CdTe layers implanted at the beam currents of (a)  $100\mu\text{A}$  and (b)  $0.2\mu\text{A}$ .

Notably, both the depths of the concentration gradient diffusion zone and the channeling diffusion zone decrease with increasing beam current as shown in Fig.2(b)-(d). Because the depths of the damage layer and the amorphous layer in TE CdTe samples are much larger than that of ZnS samples, the drag of trapping As ions by the defects in the amorphous region and damage layer could hinder the indiffusion of As ions more remarkably before these defects are eliminated by annealing. It implies that the elimination or recrystallization of the damage layer takes place layer by layer starting from the interface between the damage layer and the crystal, similar to the recrystallization of grain boundary in polysilicon [8]. This deduction could be supported by the fact that a long dislocation defect band exists in the surface layer of the HgCdTe sample implanted with a high dose after Hg overpressure annealing [7]. So, it can be concluded that the increase in the depths of the damage layer and the amorphous layer caused by heightening beam current could impede the concentration gradient diffusion and channeling diffusion when the depth of the damage layer exceeds a certain depth.

For comparison, the TEM images of the samples covered by TE CdTe barrier layers for different beam currents (100 $\mu$ A and 0.2 $\mu$ A) are provided in Fig.5. It can be seen that the further increase in the beam current could enlarge the depths of the damage layer and the amorphous layer. However, the As profiles are almost not affected (not provided here), indicating that the sufficiently thick damage layer, especially the amorphous layer, in the surface layer are generated rapidly at the beginning of implantation, so the As profiles become insensitive to the variation of beam current. But the BLICE effect after annealing was further suppressed by the higher beam current.

Additionally, the EBE CdTe barrier layer, which has a layered structure as shown in Fig.3(b), was deposited to avoid the BLICE. The As profile of the as-implanted EBE CdTe sample has no significant difference with the TE CdTe sample, while the BLICE effect does not occur to the annealed sample as shown in Fig.6. It indicates that the BLICE effect could be avoided by improving the film micro-structure of the barrier layer.

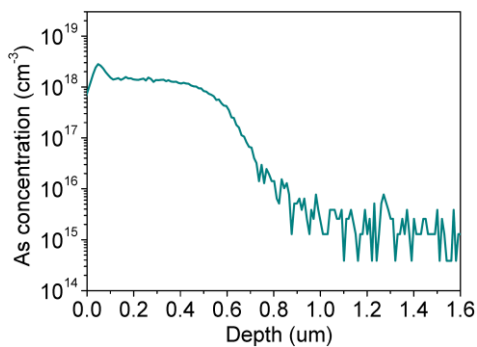


Fig.6. As SIMS profile of the annealed sample with EBE CdTe as the barrier layer.

## Conclusion

In this paper, the influences of the beam current on the induced damages and dopant profiles of As implanted HgCdTe samples with different barrier layers were investigated. When the depth of the damage layer is not too large, the increase in the defect density of the damage layer produces a significant drag to the As ion implantation in HgCdTe, and the rapid elimination of the damage layer during annealing makes the indiffusion of As

ions insensitive to the beam current; when the depth of the damage layer, especially the amorphous layer, is large sufficiently, the amorphous region formed at the beginning of implantation could block the implant induced channels thereby hindering the subsequent As ion implantation, however, during the elimination or recrystallization of the amorphous damage layer, the trapping of the defects to As ions also could hinder the concentration gradient and channeling diffusion of As ions, thereby suppressing the BLICE effect. Finally, the BLICE effect can be avoided by improving the microstructure of the CdTe film through the proper deposition method.

## References

1. F. Gemain, I. C. Robin, S. Brochen, et al. Arsenic Complexes Optical Signatures in As-doped HgCdTe, *Appl. Phys. Lett.*, Vol.102, pp.142104, 2013.
2. L. Mollard, G. Destefanis, G. Bourgeois, et al. Status of p-on-n Arsenic-Implanted HgCdTe Technologies, *J Electron. Mater.*, Vol.40, No.8, pp. 1830-1839, 2011.
3. L.O. Bubulac, D. S. Lo, W. E. Tennant, et al. P on n Ion-implanted Junctions in Liquid Phase Epitaxy HgCdTe Layers on CdTe Substrates, *Appl. Phys. Lett.*, Vol.50, No.22, pp. 1586-1588, 1987.
4. L. Mollard, G. Destefanis, N. Baier, et al. Planar p-on-n HgCdTe FPAs by Arsenic Ion Implantation, *J Electron. Mater.*, Vol.38, No.8, pp. 1805-1813, 2009.
5. S. Tian, S.-H. Yang, S. Morris, et al. The effect of dose rate on ion implanted impurity profiles in silicon, *Nuclear Instruments and Methods in Physics Research B*, Vol. 112, pp. 144-147, 1996.
6. D. Shaw, P. Capper. Activation kinetics of the As acceptor in HgCdTe, *J Mater Sci: Mater Electron*, Vol.19, pp. 67-73, 2008.
7. L.O. Bubulac, J. Bajaj, W.E. Tennant, et al. Characteristics and Uniformity of Group V Implanted and Annealed HgCdTe Heterostructure. *J Electron. Mater.*, Vol.25, No.8, pp. 1312-1317, 1996.
8. C.-Z. Shi, X.-W. Liu, R.-Y. Chuai. Current-induced recrystallization of polycrystalline silicon nano thin films deposited at different temperatures and its influences on piezoresistive sensitivity and temperature coefficients, *Sens. Actuat. A*, Vol.162, pp. 284-290, 2010.

# Detection of abnormalities under skin tissue by thermography

H. Trabelsi<sup>1,2</sup>, N. Kadri<sup>1</sup>, N. Slokom and E. Sediki<sup>2</sup>

<sup>1</sup>Université de Tunis El Manar, Laboratoire de Biophysique et technologies médicales, Institut Supérieur des Technologies Médicales de Tunis, 9 RUE Z. Essafi, 1006 Tunis, Tunisia

<sup>2</sup>Université de Tunis El Manar, Unité de Rayonnement Thermique, Faculté des Sciences de Tunis, 2092 El Manar I, Tunis, Tunisia

**Abstract:** This is a simulation study focusing on the effect of the temperature response of a biological tissue due to the existence of abnormal inclusions under skin or abnormal functionality. The Pennes bioheat transfer equation is used as a biophysical model to describe heat loss and circulatory system contribution to heat transfer in a tissue under skin. The objective of this study is to obtain the temperature mapping on the skin, in view of the existence of a tumor, and later, see the influence of different parameters such as location, size, conductivity, metabolic generation heat and blood perfusion on the temperature mapping. After the introduction of the mathematical model of bioheat transfer in the skin tissue, we present the discrete grid of the medium and boundary conditions including radiation. Finally, we give numerical results concerning tumor detection under skin tissue. We try to extend the obtained model to handle clinical observations concerning evaluation of patients at high risk for lower extremity peripheral arterial disease.

## Introduction

The single-point temperature is used as an indicator for health in medical routine. However, it is possible that temperature maps at multiple points or thermograms can provide diagnostic information about anatomy and functionality of explored organs or tissues [1]. In fact, it is established that abnormalities affecting blood circulation, local metabolism, inflammation can affect skin temperature mapping. As a theoretical investigation, temperature mapping can be derived from a balance of heat transfer by conduction through the tissue, the metabolic heat production of tissue and the rate of volumetric blood. We can suppose that perfusion is proportional to the gradient between arterial blood temperature and the temperature of the local tissue, where the blood temperature approached core temperature of the body. At the skin surface, the temperature is also affected by convection and radiation heat transfer with ambient air.

The main objective of this work is to show the possibility of temperature mapping to predict location and size of imbedded abnormal inclusions into normal tissue. First, we analyze

the Pennes model proposed to simulate the heat transfer in a human body. Second, we give a numerical implementation of the model in a bidimensional case. In particular we analyze the linearization of radiative boundary conditions. Finally, we present some results about detection of tumor under skin tissue by thermography. We try to extend the obtained model to evaluate blood circulation in diabetic patients.

## Numerical simulation of tumor detection

Bioheat transfer developed here is based on the Pennes equation [2]. This model supposes that the biological material is homogeneous and has isotropic thermal properties. The blood vessels are assumed to be isotropic. It suits for heat transfer in living tissue. It takes into account only metabolic heat generation and convective heat transfer due to the circulation of blood. In two-dimensional case, we consider a region formed of two sub-domains as shown in Figure 1. Sub-domain 1 is a rectangular Layer under the skin; it is formed by healthy tissue. The second sub-domain is a circular tumor formed by affected tissue. The corresponding mathematical expression of steady-state bio-heat balance is given through the following equation:

$$\lambda_i \left( \frac{\partial^2 T_i}{\partial x^2} + \frac{\partial^2 T_i}{\partial y^2} \right) + W_b C_b (T_b - T_i(x, y)) + Q_{m_i} = 0 \quad (1)$$

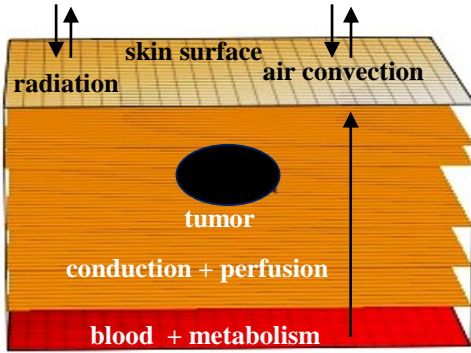


Fig1. Geometry of the studied medium with boundary conditions

where  $i = 1, 2$ , is a number which is relative to healthy tissue and affected tissue (tumor) respectively,  $T(x, y)$  is the tissue temperature,  $\lambda$  is the tissue thermal conductivity,  $W_b$  is the blood perfusion rate,  $C_b$  is the blood specific heat,  $T_b$  is the blood temperature, and  $Q_m$  is the tissue metabolic heat generation rate.

Results of numerical simulation allow to obtain the temperature mapping on the skin, in view of the existence of a tumor, and to see the influence of different parameters such as location, size, conductivity, metabolic generation heat and blood perfusion.

For the heat transfer at skin surface (top

boundary) a convection and a radiation

condition is imposed:

$$-\lambda_1 \frac{\partial T_1}{\partial n}(x, L_y) = h(T_{air} - T(x, L_y)) + \varepsilon \sigma (T_{air}^4 - T^4(x, L_y))$$

Where  $h$  is a convective heat transfer coefficient and  $T_{air}$  is the ambient air temperature. It is possible,  $\varepsilon$  is a matched air-skin emissivity, it is supposed to be the same for both and  $\sigma$  is the Stefan Boltzmann coefficient. The other boundary conditions are

$$-\lambda_1 \frac{\partial T_1}{\partial n}(0, y) = -\lambda_1 \frac{\partial T_1}{\partial n}(L_x, y) = 0 \text{ and } T(x, 0) = T_c$$

Where  $T_c$  is the core temperature in the body, we make use of the assumption

$$T_c = T_b = 37^\circ C$$

## Discretization

To solve this system, we use finite difference method. We consider a uniform grid:

$$\Delta x = \Delta y = \tau$$

we approximated the Laplacian term by a second order difference scheme:

$$\left( \frac{\partial^2 T}{\partial x^2} + \frac{\partial^2 T}{\partial y^2} \right) \Big|_{i,j} = \frac{T_{i+1,j} - 2T_{i,j} + T_{i-1,j}}{\tau^2} + \frac{T_{i,j+1} - 2T_{i,j} + T_{i,j-1}}{\tau^2}$$

So, one obtains:

$$\lambda_{i,j} \left( \frac{T_{i+1,j} - 2T_{i,j} + T_{i-1,j}}{\tau^2} + \frac{T_{i,j+1} - 2T_{i,j} + T_{i,j-1}}{\tau^2} \right) + (W_b C_b)_{i,j} (T_b - T_{i,j}) + (Q_m)_{i,j} = 0$$

So into the medium, the discrete temperature is

given as :

$$T_{i,j} = \frac{\lambda_{i,j}}{\beta_{i,j}} (T_{i+1,j} + T_{i-1,j} + T_{i,j+1} + T_{i,j-1}) + \frac{\tau^2}{\beta_{i,j}} ((W_b C_b)_{i,j} T_c + (Q_m)_{i,j})$$

where:  $\beta_{i,j} = 4\lambda_{i,j} + \tau^2 \lambda_{i,j}$

At the left boundary, temperature is obtained through:

$$\frac{\partial T}{\partial x} \Big|_{i,j} = \frac{T_{2,j} - T_{0,j}}{2\tau} = 0 \text{ so } T_{2,j} = T_{0,j}, \quad j = 2, \dots, N_y - 1$$

## Results

### Effect of the tumor size

The extent of the tumor affects the temperature distribution on the skin or above the tumor. even an increase in radius of 10% gives detectable increase of skin surface temperature above the tumor. As the radius increases, active tumor area increases and temperature on the skin surface becomes more important

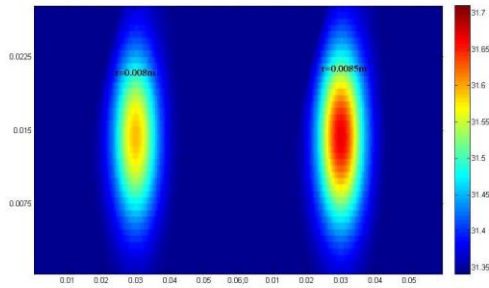


Fig2. Effects of tumor size on temperature mapping at skin surface

### Effect of the tumor conductivity

The effect of the conductivity is inverse to the temperature: increase in the tumor conductivity gives lower temperature on the skin above tumor. This leads to the conclusion that a less conductive tumor is easier to locate provided it has larger conductivity than normal tissue.

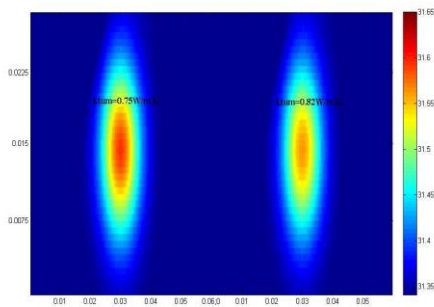


Fig3. Effects of tumor conductivity on temperature mapping at skin surface

We tried to extend the obtained model to handle the possibility of early detection of peripheral vascular disease essentially for the patients with diabetes [3,4]. We compare numerical temperature mapping obtained by numerical simulation with thermograms of confirmed patients. This could evaluate blood circulation for high risk patients.

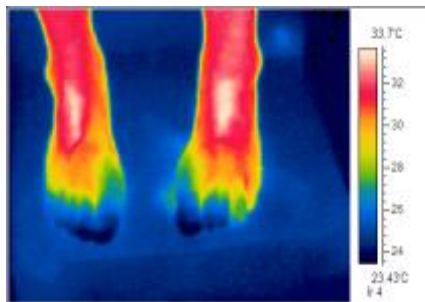


Fig 4. Infrared thermal image of the feet of a patient with diabetes exposed to peripheral disease

### Conclusion

Numerical simulation of bioheat transfer confirm the possibility to detect a tumor under skin and other abnormalities by infrared thermography. The effect of different parameters on the temperature mapping of skin give the limitations of this technique and the possibilities to improve it.

### References

1. D. Pascoe, J.B Mercer, and De Weerd, L., Physiology of iHandbook, 3rd. edition; Medical Devices and Systems, CRC press, New York chapter 21, pp 1-20, 2006
2. J. P. Agnelli, A. Barrea, C. V. Turner. Tumor location and parameter estimation by thermography, Mathematical and Computer Modelling Volume 53, pp 1527-1534, 2011
3. CL Huang, YW Wu, CL Hwang, YS Jong, CL Chao, WJ Chen, YT Wu, WS Yang. The application of infrared thermography in evaluation of patients at high risk for lower extremity peripheral arterial disease, J Vasc Surg. 54(4), pp1074-80, 2011
- 4.
5. M. Bharara, J. E. Cobb, and D. J. Claremont, MSc, DPhil, FIPEM. Thermography and Thermometry in the Assessment of Diabetic Neuropathic Foot: A Case for Furthering the Role of thermal Techniques. Lower extremity wounds, vol.5(1), pp : 250-260, 2006



# A COMPARATIVE STUDY BETWEEN VISUAL, NEAR INFRARED AND INFRARED IMAGES FOR THE DETECTION OF VEINS FOR INTRAVENOUS CANNULATION

M. Asrar<sup>1</sup>, A. Al-Habaibeh<sup>2</sup> and M R Houda<sup>3</sup>

<sup>1,2</sup> Product Design, Nottingham Trent University, Nottingham, NG1 4BU, UK

<sup>1</sup>maryam.asrar2013@my.ntu.ac.uk; <sup>2</sup>Amin.Al-Habaibeh@ntu.ac.uk

<sup>3</sup>Consultant Obstetrician and Gynaecologist, Airedale General Hospital, Steeton, West Yorkshire, UK.  
mhouda@nhs.net

The process of identification and locating of veins plays an important role to reduce health care cost and suffering of patients during intravenous cannulation. This paper compares between three technologies to assess their suitability and capability for the detection of veins. Three types of cameras are used in this study, a visual camera, an infrared camera and a near infrared camera. The collected data has then been subjected to analysis and comparison using different image processing techniques, namely grayscale, invert grayscale, histogram equalisation, edge detection (difference of Gaussians) and unsharp mask enhancement to improve the visualisation of veins. In this study, the near infrared images supported by suitable LED illumination has been found to be the most effective technology and the most cost effective for the visualisation of veins.

**Keywords** - Vein locating systems; intravenous access; infrared thermography; vein detection; visualisation enhancement.

## Introduction

Peripheral intravenous cannulation is the procedure of inserting a cannula into the peripheral veins, in most cases the veins of the hand or forearm. It is used for many medical procedures such as maintaining hydration, administering blood or blood components and administering drugs such as antibiotics [1]. Numerous studies have identified the difficulties faced by clinical staff to perform intravenous cannulation [2]. For example, in the USA it is estimated that more than 400 million intravenous (I.V.) catheters are used daily to deliver medicine in the USA with success rate of about 72.5% in the first attempt [3].

The use of several attempts for intravenous cannulation increases the suffering of patients, and could cause damage to veins and neighboring tissues. Therefore, it is vital to setup the route of the peripheral vein effectively on the first attempt. Astonishingly, there is presently limited literature regarding the visibility of veins in patients or the patient characteristics associated with difficult IV

access. Earlier studies reported a range of aspects that influence vein visibility needed for vein cannulation [4, 5, 6, 7]. Patients who have difficult venous access are a major challenge for modern medical care. A patient's level of hydration influence the ability to identify their veins. If the patient is obese, normal cues are typically absent making venous access enormously complex. Pediatric patients bring their own challenges with smaller vessels.

## Problem statement

- The major problem faced by the doctors today is the difficulty in accessing veins for intravenous drug delivery. With improper detection of veins, several problems such as bruises, rashes, blood clot etc. could occur.
- Subcutaneous fat or dark skin color reduces the visualization of blood vessels underneath the skin.
- Gaining intravenous access in children can be difficult.

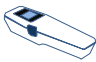






This paper is aiming to compare between visual, infrared and near infrared images for the detection of veins and to establish an easy,



compact, safe and reliable visualization device with minimal interference in the usual routine of vessel puncturing.

### Vein Locator Systems

Many vein locator systems are currently available in research and industry to improve vascular access. The current vein locating systems available for this purpose in the market have some limitations, drawbacks and are somehow costly. There are various challenges to be found throughout the design and implementation of a device such as the lighting system, the image processing algorithms, the physical design and the cost. Although, a few devices based on the infrared technique have been implemented, there still exists a strong need to develop such medical devices. Table 1 presents a summary of the most common vein locator systems available in industry.

Vein Locator Systems	Company	Working Method	Schematic Presentation
AccuVein AV300 Vein Viewing System	AccuVein®	Near-infrared is used to locate peripheral veins beneath the surface of the skin.	
Vein locator BS2000+	Wuxi Belson Medical System Co.,LTD	Vein locator BS2000+ uses near-infrared light and LED as light source.	
Veinlite®	Warrior Edge, LLC	It works by illuminating the de-oxygenated blood in veins.	
Economical Dualhead Vein locator BM1000	Wuxi Belson Medical System Co.,LTD	It uses near-infrared light source.	
VascuLuminator	DKMP by	It works with the help of near-infrared light source.	
Luminetx VeinViewer	Luminetx	A near-infrared LED source differentiates red blood cells of subcutaneous veins from surrounding tissues and arteries.	
Veinsite hands-free system	VueTek Scientific	It uses near-infrared light to image superficial veins to a depth of 7mm.	

**Table 1. Vein locators with their working methods and schematic diagrams [8, 9, 10, 11, 12, 13, 14]**

To visualise the veins accurately there are limitations in relation to capabilities of different vein locating systems presently available in the market. The main focus of this study is on the detection of veins and the enhancement of

visualisation using different camera technologies and image processing.

### Methodology

Schematic diagram of the methodology is shown in Fig.1. The visual, near infrared and infrared images are captured and processed by different image processing techniques to enhance the visualisation of veins. Regions of interest are selected in all images, processed by image processing techniques presented in Fig.1 and prepared for a comparison process.

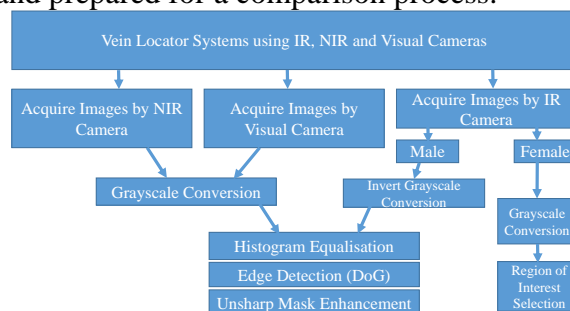


**Fig. 1. The research methodology.**

### Experimental work

A vein locator system is designed to take images of veins in hands/forearms using all infrared, near infrared and visual cameras at a time. The vein locator system is connected to a laptop in which three software are used to capture or analyse data in the form of images which are AMCap for visual camera by Wintec, Quickcam for near infrared camera by Logitech and FLIR report 2.2 for high resolution infrared camera FLIR E25. Vein finding system consists of a camera holder/fixture with rigid support to rest the subject's hand, several types of cameras and an electronic circuit to control the intensity of LED lights for visual and near infrared data.

### Results

Tables 2 to 4 present the main results of the study. Images are taken at different distances from cameras and with all possible combinations of intensities of LED lights. All obtained images are of same subject (female) except infrared images which are also captured of a male subject for making a comparison between male and female infrared images before and after cold stimulation.

Distance of arm from Wintec visual camera (low resolution)	Intensity of light	Intensity of infrared light	Obtained image
Zoom out	High	Low	
Zoom out	High	High	
Zoom out	Low	Low	
Zoom in	Low	No effects	
Medium	Low	No effects	

**Table 2. Visual images data**

Male			Female		
Time	IR Images by FLIR E25	Grayscale Images after Temperature Adjustments	Time	IR Images by FLIR E25	Grayscale Images after Temperature Adjustments
Before cold stimulation			Just after cold stimulation (Arm)		
Just after cold stimulation			27 seconds after cold stimulation (Arm)		
32 seconds after cold stimulation			Just after cold stimulation (Wrist)		
Hand image after cold stimulation			15 seconds after cold stimulation (Wrist)		

**Table 3. Infrared images before and after cold stimulation**

### Discussion

Images in Tables 2 to 4 are processed by different image processing techniques and presented in Table 5. Firstly regions of interest are selected for all images. Secondly all NIR and visual images are converted to grayscale. Thirdly color levels are adjusted using histogram equalisation technique when black point is set at a value of 50 whereas white point at 200. Fourthly edge detection (difference of Gaussians) is applied selecting smoothing parameters such as radius 1 = 250 and radius 2 = 8.0. Finally unsharp mask enhancement is done on all NIR and visual images with these parameters such as radius = 380, amount = 4.7 and threshold = 38. IR male images after selecting ROI are converted to invert grayscale.

Then same image processing techniques are applied as above with only difference of unsharp mask enhancement parameters which are; radius = 40, amount = 5 and threshold = 40. Female IR images are not affected much by above image processing techniques so they are just converted to grayscale after selecting ROI. NIR, visual and IR images are arranged in Table 5 after image processing for comparison of three technologies to assess their suitability for the detection of veins.

Intensity of light	Intensity of infrared light	Obtained image
Low	Low	
High	Low	
Moderate	Low	
Low	Moderate	
High	Moderate	
Moderate	Moderate	
Low	High	
High	High	
Moderate	High	

**Table 4. Near Infrared data**

Qualitatively it is resulted that veins in NIR images of Table 4 can be seen clearly when compared to veins in visual and IR images of Tables 2 and 3 respectively. Obviously best results for the detection of veins are obtained by near infrared camera at several combinations of intensities of light and IR light as shown in Table 4 and Table 5.

Processed Near Infrared Images			Processed Low and High Resolution Visual Images	Processed Infrared Images	
Intensity Combinations		Processed Near Infrared Images		Male	Female
Light Intensity	IR Intensity				
Low	Low				
High	Low				
Moderate	Low				
Low	Moderate				
High	Moderate				
Moderate	Moderate				
Low	High				
High	High				
Moderate	High				

**Table 5. Processed near infrared, visual and infrared images.**

## Conclusions

This study has compared between visual, infrared and near infrared technologies for the detection of veins. It has been found that using grayscale image processing combined with histogram equalisation, edge detection (difference of Gaussians) and enhancement (unsharp mask) make the near infrared technology with suitable LEDs lighting intensities, the most efficient technology to be used. The results also show that using a cold press (cold stimulation) for IR images helps to enhance the visualisation of veins. Further work will be needed to compare the three technologies for a wide ranges of image processing techniques.

## References

1. [http://www.ruh.nhs.uk/training/prospectus/clinical\\_skills/documents/cannulation\\_and\\_venepuncture\\_workbook.doc](http://www.ruh.nhs.uk/training/prospectus/clinical_skills/documents/cannulation_and_venepuncture_workbook.doc), accessed on 25 August 2015
2. Doniger, J. Stephanie, et al. "Randomized controlled trial of ultrasound-guided peripheral intravenous catheter placement versus traditional techniques in difficult-access pediatric patients." *Pediatric emergency care* 25.3: 154-159 (2009).
3. [http://www.terumo-europe.com/Relevant%20Product%20Info/Surflash\\_%20First%20Puncture%20Success%20Study.pdf](http://www.terumo-europe.com/Relevant%20Product%20Info/Surflash_%20First%20Puncture%20Success%20Study.pdf), accessed on 25 August 2015.
4. Costantino, G. Thomas, et al. "Ultrasonography-guided peripheral intravenous access versus traditional approaches in patients with difficult intravenous access." *Annals of emergency medicine* 46.5: 456-461. (2005).
5. Dargin, M. James, et al. "Ultrasonography-guided peripheral intravenous catheter survival in ED patients with difficult access." *The American journal of emergency medicine* 28.1: 1-7 (2010).
6. Aponte, J. John, et al. "Age interactions in the development of naturally acquired immunity to Plasmodium falciparum and its clinical presentation." *PLoS med* 4: e242 (2007).
7. Mbamalu, David, and A. Banerjee. "Methods of obtaining peripheral venous access in difficult situations." *Postgraduate medical journal* 75.886: 459-462 (1999).
8. <http://www.accuvein.com/products/catalog/av300-vein-viewing-syste>, accessed on 6 July 2014.
9. <http://www.aliexpress.com>, accessed on 7 July 2015.
10. <http://www.veinlite.com>, accessed on 8 July 2015
11. <http://www.portable-ultrasound-scanner.com>, accessed on 27 August 2015.
12. [http://www.yueshenyl.cn/product/1896497141-221137422/hot\\_sale\\_portable\\_vasculuminator\\_device.html](http://www.yueshenyl.cn/product/1896497141-221137422/hot_sale_portable_vasculuminator_device.html), accessed on 8 July 2014.
13. <http://www.techeblog.com/index.php/tech-gadget/25000-vein-viewer-by-luminetx>, accessed on 5 July 2014.
14. <http://www.vision-systems.com>, accessed on 5 July 2014.

# **SENSOMOTOR WAISTCOAT – A HELPFUL TOOL FOR BLIND PEOPLE AND CHILDREN WITH CEREBRAL PALSY TO SUPPORT SPACE PERCEPTION AND IMPROVE BODY SCHEME**

**R. Lampe<sup>1</sup>, T. Blumenstein<sup>2</sup>, V. Turova<sup>3</sup>, A. Alves-Pinto<sup>4</sup>**

<sup>1</sup> Markus Würth Stiftungsprofessur für Cerebralpareesen und Kinderneuroorthopädie, Forschungseinheit Buhl-Stromaier Stiftung, Orthopedic Department, clinic “rechts der Isar” of the Technical University of Munich, Ismaninger str. 22, 81675, Munich, Germany  
renee.lampe@tum.de

<sup>2</sup> Forschungseinheit Buhl-Stromaier Stiftung, Orthopedic Department, clinic “rechts der Isar” of the Technical University of Munich, Ismaninger str. 22, 81675, Munich, Germany  
t.blumenstein@tum.de

<sup>3</sup> Forschungseinheit Buhl-Stromaier Stiftung, Orthopedic Department, clinic “rechts der Isar” of the Technical University of Munich, Ismaninger str. 22, 81675, Munich, Germany  
v.turova@tum.de

<sup>4</sup> Forschungseinheit Buhl-Stromaier Stiftung, Orthopedic Department, clinic “rechts der Isar” of the Technical University of Munich, Ismaninger str. 22, 81675, Munich, Germany  
ana.alves-pinto@tum.de

A sensomotor waistcoat for better space orientation is developed. The waistcoat is equipped with ultrasonic sensors that measure distances to obstacles. The information on distances is given back to the person through vibrations produced by vibration motors incorporated into the sensomotor waistcoat. A study with blind persons showed very promising results.

## **Introduction**

In a study we examined in a group of children with cerebral palsy and a group of youths and adults with blindness whether we can improve space orientation and body scheme with a self-created sensomotor waistcoat.

Cerebral palsy is a damage of the developing brain that is caused by pre-, peri- or postnatal injury and according to extent and localization of the damage, it involves different symptoms. The most obvious symptom is a movement disorder with a spastic muscle tone. Often cerebral palsy is also accompanied by problems with space orientation and deficiency of body scheme, cognitive and behavior problems, seizure, dysarthria and visual problems [1].

Vibration therapy i.e. vibration of the whole body or the planta of the foot to improve balance and posture is applied in rehabilitation of patients with cerebral palsy [2,3] Various haptic devices for virtual representation of objects and environments are used in sensorimotor rehabilitation of patients with central nervous system disorders [4]. Also playing the piano and auditory feedback is discussed in [5] as possible methods of improving the hand motor function. However, there is a lack of aids in spatial orientation for patients with cerebral palsy.

Blind people are affected since birth or have an acquired visual lost. Normally they had a well-developed perception for space orientation and hearing so they are able to detect the environment. Therefore, delivering appropriate spatial information may facilitate to enhance their spatial performance [6].

With our self-developed sensomotor waistcoat we want to reduce problems like space orientation and perception in children with cerebral palsy and also we want to support blind people in receiving an additional better representation of their space surrounding with the intention to help them to move safely.

## Method

In a self-developed sensomotor waistcoat (Fig. 1) we integrated 10 ultrasonic sensors which are placed in front, back and on both sides of the body, so it can scan a 360 degree environment. Also we have integrated 10 small vibration motors in the garment. Sensors measure the distance to nearby obstacles: This information about distances and directionality is given back to the person through different intensity of vibrations depending on the distance to the obstacle. The ultrasonic sensors and the vibration motors are controlled by a microcontroller board (Fig. 2). Data are recorded in a SD-card and wireless via Bluetooth. In our study 13 blind people were instructed to walk through a parkour (Fig. 3) as close to the middle as possible with the blind cane, with the waistcoat or with both tools. The parkour was 150 cm wide and 15 m long. All the participants were able to sense vibration. The threshold for starting vibration was tuned individually depending on the distance ( $d$ ) between the left and right upper arms of the person. The vibration started as the distance to the wall of the parkour became smaller than or equal to  $(150-(d+20))/2$  cm. The parkour was changed for every running to prevent memorizing the way. The same experimental procedure was used for healthy controls.

In the second part of the study we used the sensomotor waistcoat also with 9 children with cerebral palsy. The experimental procedure for this group was different from that one for blind people because our objective was to prove if training with the waistcoat can improve perception for environment distance. The task was to walk without waistcoat around a row of

two carton boxes according to a predetermined way. This task was fulfilled before and after



Fig. 1. Sensomotor waist.

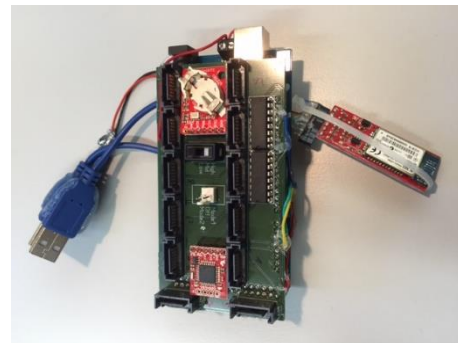


Fig. 2. Microcontroller board.



Fig. 3. Running through the parkour.



training. Walking training consisted of several exercises. The children had to walk through the parkour with and without the waistcoat keeping the 30 cm distance from the left/right wall. For the opposite side, the threshold for starting vibration was  $(150-30-2 \times 7.5-d)$  cm. Then the exercise was repeated with the decreased required distance of 10 cm. Also the perception was verified with the exercise, in which the children should recognize the place and the order of three subsequent vibrations produced using direct control of the vibration motors in the waistcoat.

## Results

Data collected with blind participants showed that they were capable, already in the first passage with the sensomotor waistcoat, to avoid colliding with the walls and keeping a relatively straight trajectory. Figure 4 demonstrates experimental results for a blind and healthy participant.

The occurrence of distances to the obstacle on the right and on the left side is shown using, respectively, white and red columns. One can see that sensomotor waistcoat provides better overlapping of white and red columns than the cane, which means more regular walking through the parkour.

In a questionnaire filled out after the experiments participants found the waistcoat very helpful.

The second study related to children with cerebral palsy has also shown promising results. An example of measurement, for a participant with  $d=50$  cm is presented in Fig. 5. One can see that the sum of all areas below the threshold value of 30 cm is smaller in the case of usage of the sensomotor waistcoat, which means the improvement of the outcome.

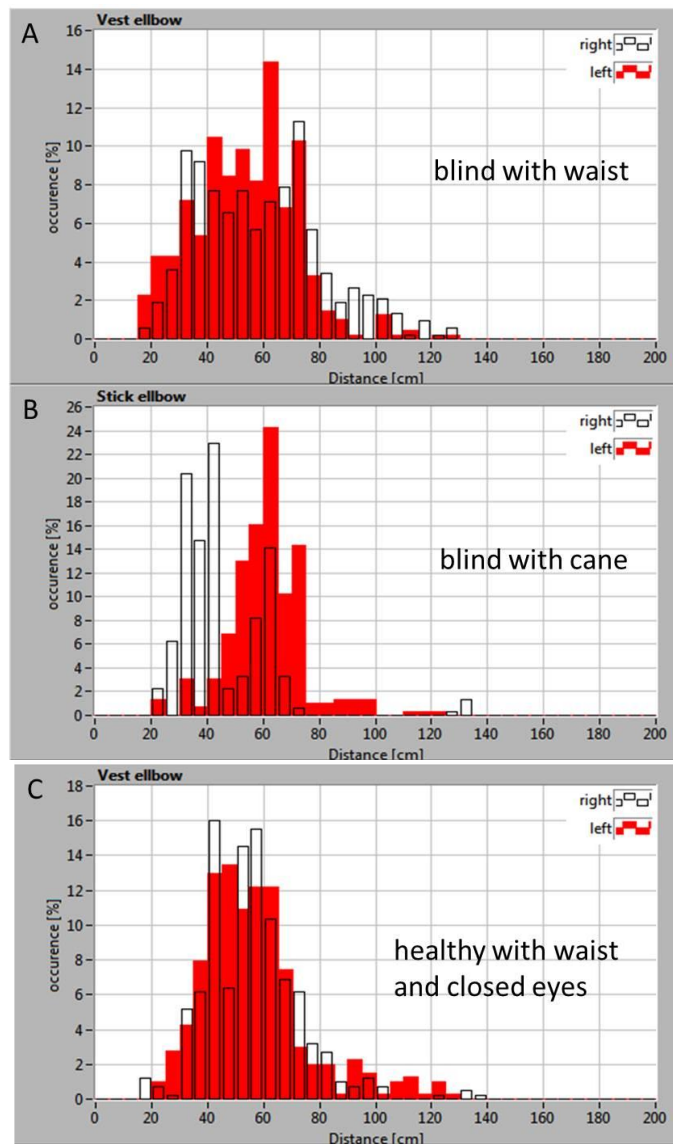


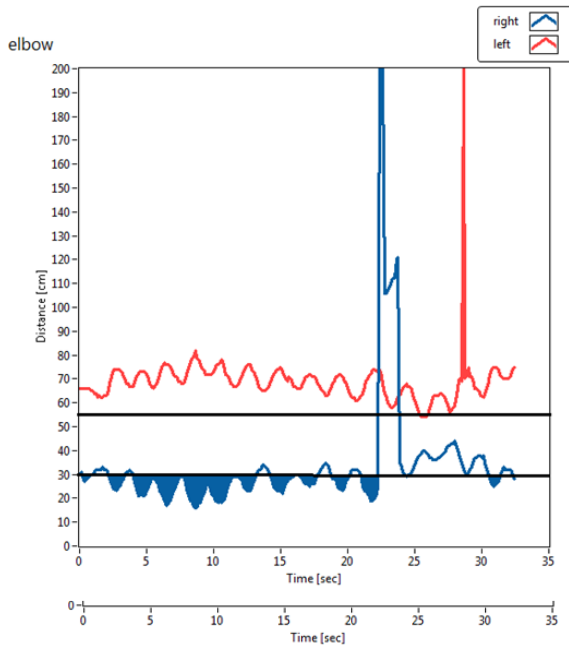
Fig. 4. Occurrence of distances to the obstacle on the right (white columns) and on the left (red columns) in experiment: (A) blind participant wearing sensomotor waistcoat, (B) blind participant walking with a cane, (C) healthy participant walking with closed eyes and wearing sensomotor waistcoat.

$K = \frac{\sum A_i}{t_0}$  To evaluate the quality of completing the task in several training runs the following value was computed:

Here,  $A_i$  is the area laying under the threshold for the run  $i$  (filled with the blue color in Fig. 5),  $t_0$  is the time needed for completing the task.



A



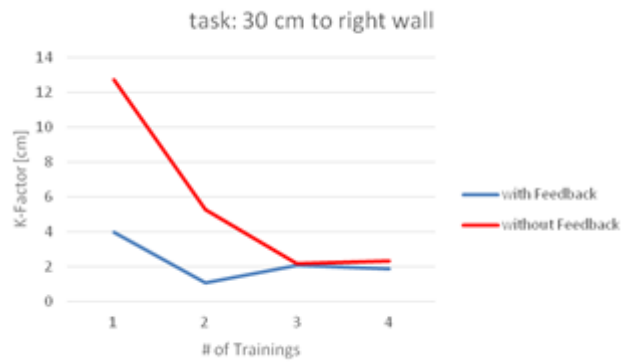
B

Fig. 5. Measurement results for a participant with cerebral palsy, having the distance between the left and right upper arms of 50 cm: Without the sensomotor waistcoat (A); with the sensomotor waistcoat (B).

Figure 6 shows the value of  $K$  versus the training day. The red curve corresponds to the experiments without the sensomotor waistcoat, the blue one stands for training with the sensomotor waistcoat. Lower values of  $K$  under usage of the waistcoat approve the benefit of feedback. Clear reduction of  $K$  with the training day both with and without

Fig. 6. Measurement results for a participant with cerebral palsy, having the distance between the left and right upper arms of 50 cm: Value  $K$  versus training day.

feedback shows the importance of training for the improvement of spatial orientation and evaluation of distances.



## Conclusion

The sensomotor waistcoat was very positively received both by blind participants and patients with cerebral palsy. It has the potential to bring more autonomy in daily life and to improve the perception of one's own body.

## References

1. S. Stotz. Treatment of Cerebral Palsy. München: Pflaum Verlag, 2000.
2. G. Schlee, D. Reckmann, T. L. Milani. Whole body vibration training reduces plantar foot sensitivity but improves balance control of healthy subjects, *Neurosci Lett*, Vol. 506(1), pp. 70-73, 2012.
3. C. M. Williams, J. Michalitsis, A. Murphy, B. Rawicki, T. P. Haines. Do external stimuli impact the gait of children with idiopathic toe walking? A study protocol for a within-subject randomised control trial, *BMJ open*, Vol. 3(3), 2013.
4. S. Demain, C. D. Metcalf, G. V. Merrett, D. Zheng, S. Cunningham. A narrative review on haptic devices: relating the physiology and psychophysical properties of the hand to devices for rehabilitation in central nervous system disorders. *Disability and Rehabilitation: Assistive Technology*, Vol. 8(3), pp. 181-189, 2013.
5. R. Lampe, A. Alves-Pinto, T. Blumenstein, V. Turova. Brain plasticity related piano training in youths with neurodevelopmental disorders. *Brain Stimulation*, Vol. 8(2), 2015.
6. O. Lahav. Using Virtual Environment to Improve Spatial Perception by People Who are Blind, *Cyberpsychol Behav*, Vol. 9(2), pp. 174-177, 2006.

# DETECTION AND QUANTIFICATION OF MACULAR EDEMA FROM OPTICAL COHERENCE TOMOGRAPHY IMAGES

## Detection and Quantification of Macular Edema from Optical Coherence Tomography Images

N. Slokom<sup>1</sup>, I. Zghal<sup>2</sup>, H. Trabelsi<sup>1,3</sup> and E. Sediki<sup>3</sup>

<sup>1</sup>Université de Tunis El Manar, Laboratoire de Biophysique et Technologies Médicales, Institut Supérieur des Technologies Médicales de Tunis, 9 RUE Z. Essafi, 1006 Tunis, Tunisia

<sup>2</sup> Institut Hedi Raies d'ophtalmologie de Tunis ,Boulevard 9 Avril 1938, 1006 Tunis

<sup>3</sup>Université de Tunis El Manar, Unité de Rayonnement Thermique, Faculté des Sciences de Tunis, 2092 El Manar I, Tunis, Tunisia

Optical coherence tomography (OCT) using near infrared light is becoming one of the most important modalities for the noninvasive assessment of retinal eye diseases. In many cases, processing OCT image is important for local retinal abnormalities detection. In this paper, we propose a method to identify and quantify fluid filled regions in SD-OCT of the macula. First, we expose the general principle of the OCT and the general scheme of an OCT device based on the Michelson Interferometer. Next, we present equations for each of the two modes used in OCT: Time-domain (TD-OCT) and spectral-domain (SD-Domain). Then we do a comparison of the two modes. Finally, we propose a segmentation algorithm of SD-OCT to detect cystoids within retina. Once the contours of the lesions are outlined, quantitative analysis of the surface area of the lesions is performed.

### Introduction

Optical coherence tomography (OCT) is a non invasive imaging technique that can generate high-resolution and high-contrast cross-sectional images using interference of light. Since time-domain OCT (TD-OCT) was introduced in the early 1990s [1], OCT is ideally suited for ophthalmology because the eye is directly optically accessible [1]. Actually spectral-domain OCT (SD-OCT), allows a fast scanning of retinal volumetric data with micrometer axial resolution. It is useful in diagnosing and management of a variety of ocular diseases such as macular edema [2]. Macular edema is characterized on OCT by retinal thickening and intra-retinal areas of decreased reflectivity secondary to fluid accumulation may be present. Frequently, intra-

retinal edema is contained in fluid-filled region (cystoid) and is named Cystoid macular edema (CME) which is classified by round, optically clear regions within the neurosensory retina [3].

In order to detect cystoids and quantify the liquid they contain, image processing is performed. It will help ophthalmologists, guide their diagnosis and OCT images will be more easily interpreted in case of macular edema.

### General principle of the OCT

OCT is an extension of optical coherence domain reflectometry to imaging in two or three dimensions [4]. This imaging technique generates a cross-sectional image by recording

axial reflectance profiles while the transverse position of the optical beam on the sample is scanned. Thus, the longitudinal location of tissue structures are determined by measuring the time-of-flight delays of light backscattered from these structures.

OCT is an interferometric technique, relying on interference between a split and later re-combined broadband optical field. A typical OCT schematic is shown in (Fig.1) [5]. The split field travels in a reference path, reflecting from a reference mirror, and also in a sample path where it is reflected from multiple layers within a sample. Due to the broadband nature of the light, interference between the optical fields is only observed when the reference and sample arm optical path lengths are matched to within the coherence length of the light. Therefore, the depth (axial) resolution of an OCT system is determined by the temporal coherence of the light source. Sharp refractive index variations between layers in the sample medium manifest themselves as corresponding intensity peaks in the interference pattern [5].

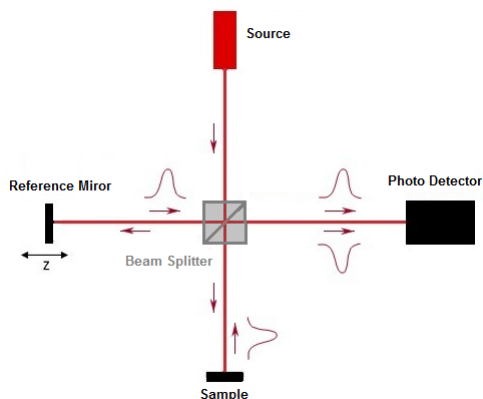


Fig. 1. Basic OCT system, based on a Michelson interferometer.[5]

### Time domain OCT (TD-OCT)

The system described above, where a reference mirror is scanned to match the optical path from reflections within the sample, is called time-domain OCT (TD-OCT). The first commercial OCT instruments have been developed for ophthalmology was based on the TD-OCT configuration [6].

In TD-OCT the low-coherence source used is broadband, the reference arm delay is repetitively scanned in length, a single-channel photoreceiver is employed, and the required signal processing consists of detecting the envelope of the detected fringe burst pattern corresponding to interference between the reference arm light and each successive scattering site in the sample[5].

The study focused on light in the detector arm composed from components from the sample  $E_S(\omega)$  and reference  $E_R(\omega)$ . The irradiance in the detector arm is therefore proportional to the product of these two components and is also proportional to the power spectrum of the source  $\{G(\omega)\}$ . It is given by equation (1) [6] :

$$I_D \propto \text{Re} \left\{ \int_{-\infty}^{\infty} \langle E_S(\omega) \cdot E_R^*(\omega) \rangle d\omega \right\} \quad (1)$$

$$\propto \text{Re} \left\{ \int_{-\infty}^{\infty} G(\omega) \exp(-i\Delta\phi(\omega)) d\omega \right\}$$

$$\text{Where } \phi(\omega) = 2k_s(\omega)l_s - 2k_r(\omega)l_r. \quad (2)$$

If the source used is in gaussian spectrum, the irradiance will be as follows :

$$I_D \propto \text{Re} \left\{ \exp[-i\omega_0\Delta\tau_p] \exp\left[-\frac{\sigma_\omega^2 \Delta\tau_g^2}{2}\right] \right\}$$

(3)

Where  $\sigma_\omega$  is the standard deviation of the angular frequency spectrum and  $\Delta\tau_p$  and  $\Delta\tau_g$  are respectively the phase delay and group delay. This represents the autocorrelation term for a Gaussian source. The equation (3) contains two oscillatory terms. The first oscillatory term is a rapid oscillatory term or the phase modulation. The second oscillatory term is much slower, is Gaussian in shape, and is the envelope of the autocorrelation function. It is this second term that primarily carries ranging information. The autocorrelation function is the inverse Fourier transform of the source power spectrum as per the Wiener-Khinchine theorem [7]. The axial resolution is given by the equation (4):

$$\Delta l = \frac{2Ln2}{\pi} \frac{\lambda_0^2}{\Delta_\lambda} \quad (4)$$

## Spectral domain OCT (SD-OCT)

Most of the components are identical to the setup of the Time-Domain technology. The key difference is that in an SD-OCT system the reference arm length is fixed. Instead of obtaining the depth information of the sample by scanning the reference arm length, the output light of the interferometer is analyzed with a spectrometer (hence the term Spectral-Domain). The measured spectrum of the interferometer output contains the same information as an axial scan of the reference arm. The map of optical reflectivity versus depth is obtained from the interferometer output spectrum via a Fourier Transform. The total interference signal is given by [7] :

$$I(k) = G(k) \left( 1 + 2 \int_{z_0}^{\infty} a(z) \cos\{2knz\} dz \right) + G(k) \left( \int_{z_0}^{\infty} \int_{z_0}^{\infty} a(z') a(z) \exp\{i2kn(z-z')\} dz dz' \right) \quad (5)$$

Where  $G(k)$  is the spectral intensity distribution of the light source,  $a(z)$  is the backscattering coefficient of the object signal, with regard to the offset  $z_0$ ,  $n$  is the refractive index,  $z_0$  is the offset of the reference plane and object surface,  $2r$  is the pathlength in the reference arm,  $2(r+z)$  is the pathlength in the object arm, and  $2z$  is the difference in pathlength between the sample and reference arm. The first term is a DC term  $\{G(k)\}$ . The second term encodes the depth information of the object. The backreflection intensity is found in  $a(z)$  while the corresponding optical pathlength difference is found in the argument of the cosine term. The third term describes the mutual interference of all elementary waves. In terms of the Fourier transform (F) of the equation (5):

$$I(k) = G(k) \left( 1 + \frac{1}{2} F\{A(z)\} + \frac{1}{8} F\{AC[A(z)]\} \right) \quad (6)$$

Taking the inverse Fourier transform of equation (6), we obtain:

$$F^{-1}[I(k)] = F^{-1}\{G(k)\} \otimes \left( \delta(z) + \frac{1}{2} A(z) + \frac{1}{8} AC[A(z)] \right) \quad (7)$$

$$F^{-1}[I(k)] = A \otimes (B + C + D)$$

The OCT information is contained within the convolution product  $A \otimes C$  while the other two convolution products  $A \otimes B$  and  $A \otimes D$  are

respectively the DC signal component and the mutual interference among scatters in the sample arm.

## Comparison SD-OCT and TD-OCT

The major advantage of SD-OCT is the substantial improvement in the quality of cross-sectional images as shown in (Fig.2). The improvement of imaging quality is mainly caused by the shortening of measurement time, which as a consequence also enables one to acquire an increased amount of data during the examination [8]. In addition, artifacts from the movement of the eye are reduced. The second factor determining quality improvement is a substantial increase of axial resolution obtained due to the use of a spectrally broadband light source (femtosecond laser), which is the result of a lack of a fundamental relationship between imaging sensitivity and axial resolution in the case of SD-OCT.

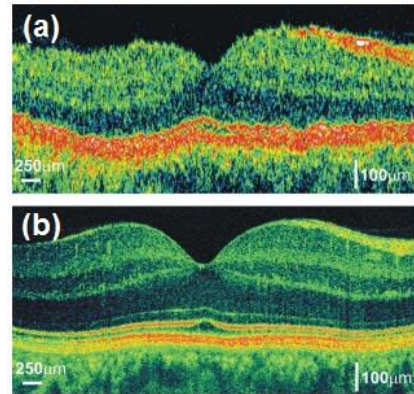


Fig 2. A comparison of in vivo cross-sectional images of the human retina in the macular region obtained by TD-OCT (a) versus SD-OCT (b) [8].

In addition, the SD-OCT gives a true measure of retinal thickness (retinal thickness from RPE to ILM) while OCT - TD presents measures under estimated (retinal thickness from IS/OS to ILM) as presented in (Fig.3). Therefore, the SD-OCT allows a best diagnostics of the retinal thickness and the study of nerve fiber layer of retina[9].

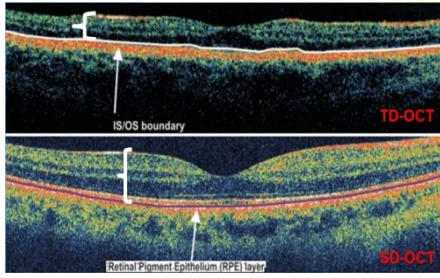


Fig.3. Comparison of retinal thickness between retinal images obtained with a TD-OCT and SD-OCT [9].

## Detection and quantification of fluid-filled region in retina

The OCT systems allow a fast scanning of retinal volumetric data with micrometer axial resolution, which is useful in diagnosing and management of a variety of ocular diseases such as glaucoma [10], macular hole, age related macular degeneration, diabetic retinopathy, and macular edema [2]. Macular edema is characterized on OCT by retinal thickening and intra-retinal areas of decreased reflectivity secondary to fluid accumulation may be present. Frequently, intra-retinal edema is contained in fluid-filled region (cystoid) and is named Cystoid macular edema (CME) which is classified by round, optically clear regions within the neurosensory retina [3].

Calculation of retinal thickness and volume by the current OCT system includes fluid-filled regions along with actual retinal tissue. In order to quantify these fluid-filled regions independently from the retinal tissue, they must be outlined. We evaluated the ability of a deformable model to yield accurate shape descriptions of cystoids macular edema. Since the number and size of cystoids indicate the progression and severity of the disease in the patient, lesion detection may significantly aid in analysis of treatments and diagnosis[11]. With such quantification, the OCT will allow improved monitoring of patients, earlier detection of pathology, and more-precise treatment protocols.

- *Methods*

In order to detect cystoids, we applied the distribution metric for image segmentation

proposed by S. Romeil and al. at [12] which arises as a result in prediction theory. Forming a natural geodesic, the metric quantifies “distance” for two density functionals as the standard deviation of the difference between logarithms of those distributions. Using level set methods, an energy model based on the metric into the Geometric Active Contour (GAC) framework was incorporated. The efficiency of this technique was proved in various imaging modalities such as segmentation of a heart [12] and brain [13] from MRI images and lesions detection in breast ultrasound images [14].

Formally, a contour  $C$  is the zero-level set of a signed distance function  $\phi: \mathbb{R}^2 \rightarrow \mathbb{R}$  such that  $\phi < 0$  represents the inside of  $C$  (the lesion) and  $\phi > 0$  represents the outside of  $C$ . By modeling each pixel as a random variable  $z$ , we evaluate the probability density functions (PDF)  $p_{in}(z, \phi)$  and  $p_{out}(z, \phi)$  for the pixels inside and outside  $C$ . The *distance* between pixels inside and outside  $C$  is the standard deviation of the difference between the logarithms of  $p_{in}(z, \phi)$  and  $p_{out}(z, \phi)$ . We maximize this distance by maximizing the energy functional [10]: (8)

$$E(z, \phi) = \sqrt{\varepsilon \left[ \left( \log \frac{p_{in}(z, \phi)}{p_{out}(z, \phi)} \right)^2 \right]} - \varepsilon \left[ \log \frac{p_{in}(z, \phi)}{p_{out}(z, \phi)} \right] \quad (8)$$

Where  $\varepsilon[f(z)]$  denotes the expected value of  $f(z)$ .  $\phi$  (and thus  $C$ ) evolves according to the equation :

$$\frac{\partial \phi}{\partial t} = \nabla_{\phi} E(z, \phi) \quad (9)$$

Evolution stops when convergence has been achieved or after a maximum number of iterations.

Fig.4-(b) show GAC results for an OCT image obtained from a patient having multiple lesions in the central part of the retina.



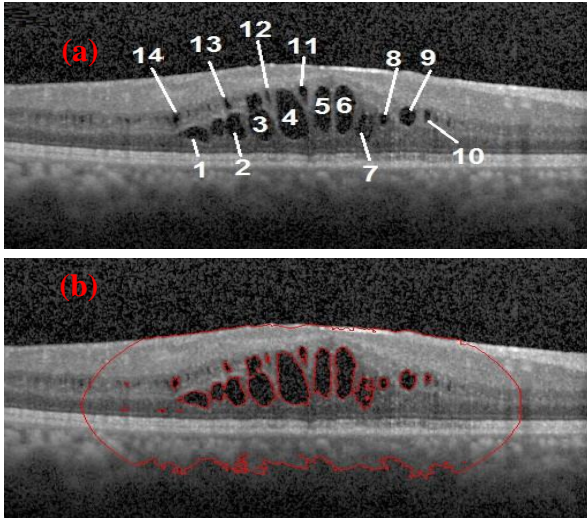


Fig. 4 : (a) Original OCT image displaying multiple fluid-filled regions in the central part of the retina.(the numbers marks the fluid-filled regions for using above) and (b) GAC results (solid curves plotted in red).

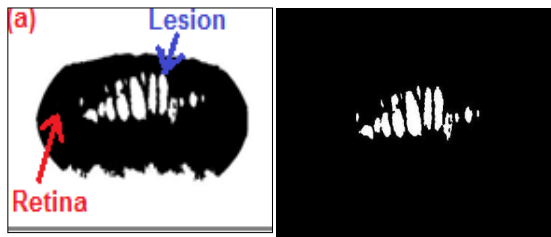


Fig. 5 (a) Binary image of detected contour and (b) Result of the merger of the retina with its surroundings.

Once the contours of the lesions are outlined, result is converted to binary as shown in the Fig.5-(a). The resulting image is composed of three parts: the area surrounding the retina with white, the detected portion of the retina in black and the fluid-filled regions present in the retina in white. In order to keep only the fluid filled regions corresponding to the accumulated cystoids liquid, the first two above mentioned portions are merged. The result is shown in Fig.5-(b).

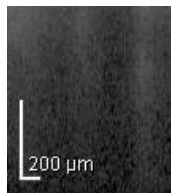


Fig.6 The defined scale of the conversion of the pixels to the mm<sup>2</sup>

Finally, we calculate the surface of fluid-filled regions using counting the digital pixels. In this

work, obtained results are converted in (mm<sup>2</sup>) unit. As illustrated by Fig. 6, an image region of 0.04 mm<sup>2</sup> contains a set of (16 × 52) pixels.

- *Evaluation of the segmentation accuracy*

For evaluating the performance of the segmentation technique several benchmarks are proposed by the researchers. Recall and precision measure [15] are used to quantify detection method performance [16].

$$precision = \frac{TP}{TP + FP} \quad (10)$$

$$recall = \frac{TP}{TP + FN} \quad (11)$$

Where  $TP$  represents the number of fluid-filled pixels that correctly detected,  $FP$  represents the number of pixels that are missed, and  $FN$  represents the number of pixels that falsely detected [17]. The detection method considered efficient if high recall and precision scores are achieved [16].

In addition, the semi-automatic segmentation process for the OCT retinal lesions was compared to the manual segmentation as a preliminary estimate of global accuracy. The performance of GAC algorithm was evaluated both qualitatively and quantitatively. First, a clinical expert (i.e., an ophthalmologist) was asked to manually outline the lesion contours on each experimental data set using a computer mouse. Manual tracing was carried out using a software tool that allowed tracing and extracting the fluid-filled regions from retina. Second, the lesions were segmented using the GAC algorithm by the author, and these results were finally compared against the manual extraction procedure performed by the ophthalmologist. The clinical expert was also asked to indicate those contours as visually correct where the contours from the GAC algorithm could be accepted as is with no additional user intervention.

- *Results*

Fig.7 compares the GAC snake's extracted contours with the clinician's hand drawn



contours for the patient analyzed. A visual comparison shows generally good agreement between the two interpretations. Table I provides some details of the qualitatively and quantitatively tests performed using the lesion's contours extracted from the subject analyzed. A total of 14 lesions were considered in the analysis.

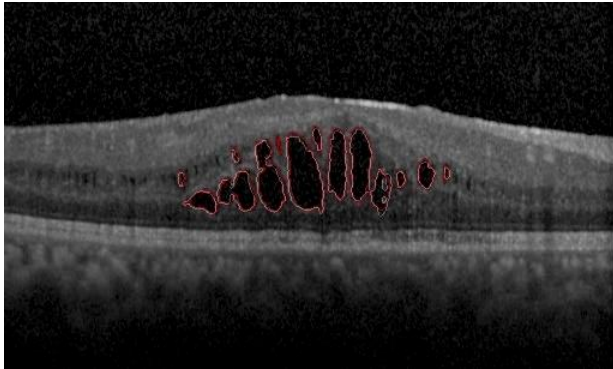


Fig 7. Comparison between fluid-filled regions contours extracted by GAC algorithm (white curves) and contours hand drawn by a clinical expert (red curves).

The qualitative evaluation led to 95% visually acceptable contours that were classified as good and fair extraction cases by the ophthalmologist (see Table I). Many of the discrepancies between the clinical expert's interpretation and the GAC algorithm's contours seemed to be attributable to poor contrast at the lesion's contours

Lesion	Recall (%)	Precision (%)	Expert's Comments
1	92,68	99,35	Good extraction
2	87,35	96,71	Good extraction
3	92,10	98,81	Good extraction
4	91,40	98,74	Good extraction
5	85,77	98,64	Good extraction
6	84,94	98,44	Good extraction
7	78,80	87,50	Fair extraction
8	78,82	98,53	Good extraction
9	80,00	100	Good extraction
10	63,46	100	Fair extraction
11	60,47	100	Fair extraction
12	33,33	78,57	Fair-Poor extraction
13	59,57	96,55	Fair extraction
14	71,70	84,44	Fair extraction

Table I. Comparison of qualitative and quantitative measures from GAC snake's extracted and expert's contours.

For quantitative evaluation, we also compared the area of the lesions calculated from the

clinical experts and GAC snake algorithm extracted contours (see Fig. 7). Lesion's area values have been plotted following the same lesion's order per subject on table I (see Fig 8).

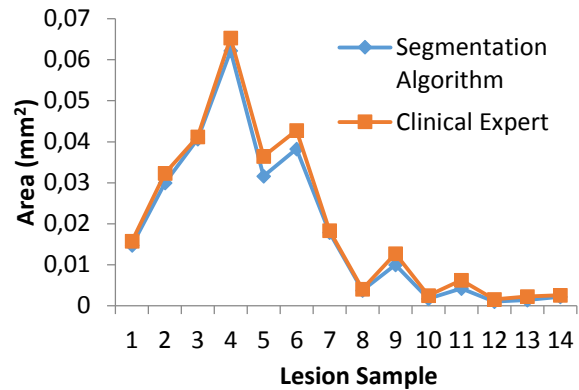


Fig.8 A comparison between the calculated area of the lesions from the clinical expert's and GAC algorithm extracted contours.

As can be seen, lesion's extracted contours classified as a fair extraction result by the clinical expert show discrepancies between the manual and GAC snake segmentation. Note that the area calculated using the GAC is smaller than those from the expert and the difference in area between all extracted contours using the snake algorithm and the expert's contours is of the order of  $10^{-3} \text{ mm}^2$ .

## Conclusion

In this work, a segmentation algorithm of SD-OCT images to detect cystoids within retina is developed. Once the contours of the lesions are outlined, quantitative analysis of the surface area of the lesions is performed. Results show a good agreement between automated quantitative evaluation and qualitative evaluation done by an ophthalmologist.

## Reference

1. D. Huang, E. A. Swanson, C. P. Lin, J. Schuman, W. G. Stinson, W. Chang, M. R. Hee, T. Flotte, K. Gregory, C. A. Puliafito. Optical coherence tomography, Science 254 (5035), 1178-1181, 1991.
2. H. W. Van Dijk, F. D. Verbraak, P. H. B. Kok, M. K. Garvin, M. Sonka, K. Lee, J. H. DeVries, R. P. Michels, M. E. J. van Velthoven, R. O. Schlingemann, and M. D. Abr`amoff. Decreased retinal ganglion cell layer thickness in type 1 diabetic patients, Investigative

- Ophthalmology & Visual Science 51(7), 3660–3665, 2010.
3. E. Bouma, G. J. Tearney, «Handbook of optical coherence tomography», New York, Basel: Marcel Dekker Inc., 2002
  4. M. E. Brezinski, G. J. Tearney, B. E. Bouma, J. A. Izatt, M. R. Hee, E. A. Swanson, J. F. Southern and J. G. Fujimoto. Optical Coherence Tomography for Optical Biopsy Properties and Demonstration of Vascular Pathology, *Circulation*, Vol 93, 1206–1213, 1996.
  5. A F Fercher, W Drexler, C K Hitzenberger and T Lasser. Optical coherence tomography—principles and applications, *Rep. Prog. Phys.*, Vol 66, 239–303, 2003.
  6. M. Brezinski, *Optical Coherence Tomography : Principales and Applications*, USA, 2006.
  7. M. Born and E. Wolf. *Principles of Optics*, Sixth edition (Oxford: Pergamon) (1980), pp 494-499
  8. M. Wojtkowski. High-speed optical coherence tomography: basics and applications, *Applied Optics* Vol. 49, pp. D30-D61, 2010.
  9. Z. Yaqoob, Wu. Jigang and Y. Changhuei. Spectral domain optical coherence tomography: a better OCT imaging strategy, *BioTechniques*, vol 39, S6-S13, December 2005.
  10. D. C. Hood, S. C. Anderson, M. Wall and R. H. Kardon. Structure versus function in glaucoma: An application of a linear model, *Investigative Ophthalmology & Visual Science*, 48(8), 3662–3668, 2007.
  11. R. S. Breiman, J. W. Beck, M. Korobkin, R. Glenn, O. E. Akwari, D. K. Heaston, A. V. Moore, and P. C. Ram, “Volume determinations using computed tomography,” *AJR*, vol. 138, pp. 329–333, 1982.
  12. S. Romeil, G. Tryphon and T. Allen. A New Distribution Metric for Image Segmentation, *SPIE*, Vol. 6914, 691404\_1-9, 2008
  13. Y. Li and M. Mandal. Fully Automated Segmentation of Corpus Callosum in Midsagittal Brain MRIs, 35th Annual International Conference of the IEEE EMBS, Osaka, Japan, 3 - 7 July, 2013
  14. K. D. Marcomini, H. Schiabel, A. Adilton and O. Carneiro. Quantitative evaluation of automatic methods for lesions detection in breast ultrasound images, *SPIE* Vol. 8670, 867027\_1-7, 2013.
  15. N.T Nguyen, T. D. Bui. Automated Posture Segmentation In Continuous Finger Spelling Recognition, *IEEE 3rd International Conference on Human-Centric Computing, HumanCom 2010*.
  16. F. Gasparini, R. Schettini, Skin Segmentation Using Multiple Thresholding, In *Internet imaging VII, IS and T/SPIE, SPIE*, pp. 60610F-1-8, 2006.
  17. Q. Dong, Y. Wu and Z. Hu, Gesture Segmentation from a Video Sequence Using Greedy Similarity Measure, *IEEE 18th International Conference on Pattern Recognition (ICPR 2006)*. pp. 331 – 334, September 2006.

# INFRARED IMAGING TO STUDY HAND SKIN MICROCIRCULATION IN HEALTHY AND SYSTEMIC SCLEROSIS VOLUNTEER

B. Jalil<sup>a</sup>, O. Salvetti<sup>a</sup>, V. Hartwig<sup>c</sup>, L. Potì<sup>b</sup> and A. L'Abbate<sup>c,d</sup>

<sup>a</sup>Istituto di Scienza e Tecnologie dell'Informazione "Alessandro Faedo" CNR, Pisa, Italy

<sup>b</sup>Consorzio Nazionale Interuniversitario per le Telecomunicazioni, CNR, Pisa, Italy

<sup>c</sup>Istituto di Fisiologia Clinica, CNR, Pisa, Italy

<sup>d</sup>Istituto di Scienze della Vita, Scuola Superiore Sant'Anna, Pisa, Italy

In this paper, we have presented our study on microcirculation spatial heterogeneity. We processed Near-Infrared Spectroscopic (NIRS) 2D images of haemoglobin O<sub>2</sub> saturation in the hand skin of a normal volunteer and the one affected by systemic sclerosis (SSc). The images were acquired during baseline, ischemia and reperfusion. We used an NIR spectroscopic camera (Kent camera, Kent Imaging, Calgary, Canada) to acquire oxygen-saturation 2D maps of the whole-hand palmar surface. Background and noise limiting the segmentation process were removed by edge detection. Segmentation of test areas in each condition was obtained by means of thresholding based region growing. Results highlight differences in microcirculation in hand skin of normal and pathological subject.

## 1. Introduction

The mapping of hemoglobin (Hb) O<sub>2</sub> saturation in the hand skin during baseline, ischemia and reperfusion is the object of the present work. Assessment of Oxygen Saturation (StO<sub>2</sub>) is important to study clinical condition and in monitoring several pathological changes, especially in critically ill patients. The microcirculation including oxygenation and its consumption are often disturbed in such patients. Systemic sclerosis (SSc) is one of such dysfunction. SSc is a complex multi organ disease characterized by widespread fibrosis, vascular alterations, particularly of small vessels, and auto-antibodies against various cellular antigens. The aim of this work is to study the feasibility of NIR spectroscopic 2D palmar whole-hand imaging in the evaluation of micro vascular dysfunction in SSc. For this purpose, an SSc patient was studied for comparison with a healthy control at rest and during ischemia reperfusion by rapid sequential imaging of the hand. Recently Hartwig et al, have presented their work on SSc patient in [1]. In [2], we had used multiscale analysis based NIRS imaging to study oxygen saturation. Lipcsey et al. reviewed the application of NIRS in anaesthesia and

intensive care [3]. In another study, they had estimated the forearm blood flow using NIRS [4]. Gruartmoner et al. have used near-infrared spectroscopy to study whether thenar tissue StO<sub>2</sub> and its changes derived from an ischemic challenge are associated to weaning off mechanical pulmonary ventilation [5]. Also, Gerovasili et al. used near infrared spectroscopy to study vascular occlusions in order to estimate different parameters [6]. They had provided the review of NIRS in clinical application specifically during vascular occlusion. A similar study is provided by Mayeur et al. They have presented their results performing vascular occlusion tests using NIRS in [7].

In this work, we used NIRS 2D imaging of palmar hand to study microcirculatory features in different hemodynamic conditions. Near infrared light penetrates into tissue: it is partially absorbed by tissue chromophores such as Hb + myoglobin (Mb) in their oxy- and deoxy-forms and partially scattered. The difference in absorptions is used by a NIRS-sensitive camera system to calculate the oxygen saturation level (stO<sub>2</sub>).

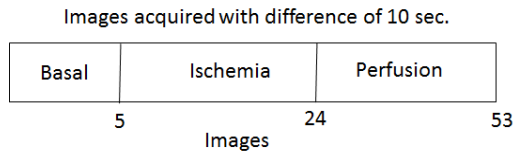


Figure 14. Experimental protocol.

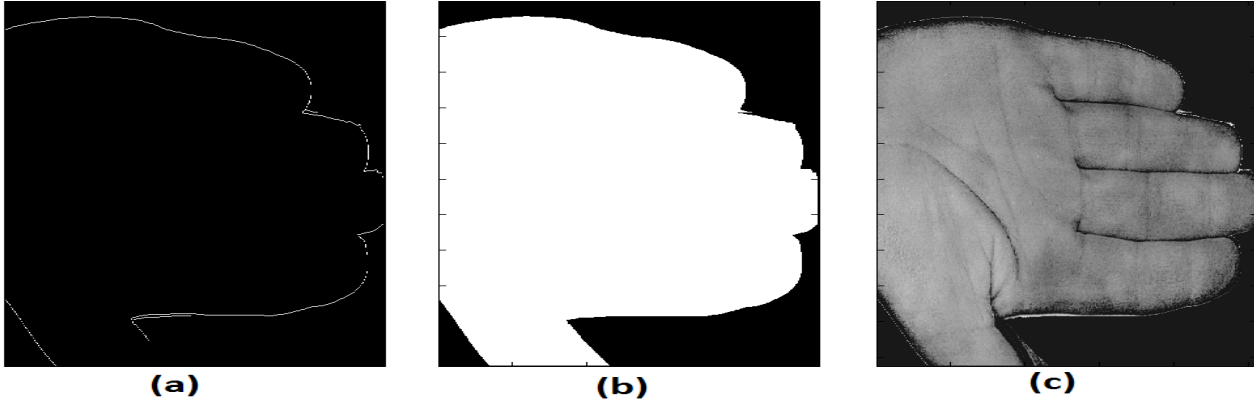


Figure 15. Results of the background removal procedure on a hand image of the SSc patient. a) The obtained edges with canny edge detector, b) Filling inside the edges area to make mask, c) NIRS image of the hand after removing background.

## Hardware and Data Set

The Kent imaging camera is a non-invasive tissue oxygenation measurement system based on near infrared light. The camera reports and approximates value of  $stO_2$  in superficial tissue (2-3 mm depth). Total of 53 images are acquired in each case. The first 4 images correspond to basal condition. The 5<sup>th</sup> image is the first one in ischemia condition (cuff occlusion of brachial artery) and the 24<sup>th</sup> image is the first one of the reperfusion condition.

We worked on a semi-automatic segmentation technique to highlight areas of oxygenated blood in hand skin using NIRS images. Two sets of NIRS images are obtained from healthy and patients suffering from systemic sclerosis (SSc).

## 2. Background Removal

Edges are significant local changes of intensity in an image and occur on the boundary between two different regions. We had applied canny edge detection to remove background from the hand surface [8]. The algorithm runs in 5 separate steps:

- **Smoothing:** Blurring of the image to remove noise.
- **Finding gradients:** The edges should be marked where the gradients of the image has large magnitudes.
- **Non-maximum suppression:** Only

local maxima should be marked as edges.

- **Double thresholding:** Potential edges are determined by thresholding.
- **Edge tracking by hysteresis:** Final edges are determined by suppressing all edges that are not connected to a very certain (strong) edge.

The obtained results are shown in Figure 2. We had initially detected the edges and the by filling the area inside, the global mask was obtained. All infrared images were then applied mask to remove unwanted background.

## 3. Feature Extraction

Texture analysis can base on repeated occurrence of some gray-level configurations. This configuration varies rapidly in fine textures, more slowly in coarse textures. However occurrence of gray-level configuration may be described by matrices of relative frequencies, called co-occurrence matrices. Similarly application of energy masks boosts up some of the lower intensity texture within the image.

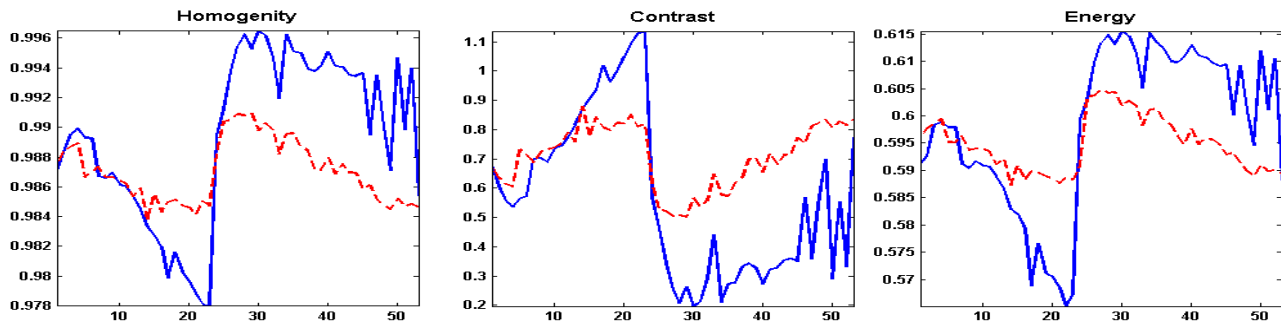


Figure 3. Homogeneity, contrast and energy of all the images during the test protocol. Blue: SSc patient, dotted red: healthy subject.

In this work, we had estimated these statistical properties (contrast, homogeneity and energy) of near infrared images to examine the different statistical parameters in healthy and SSc patients.

#### 4. Results

Figure 3 shows the results relative to homogeneity, contrast and energy of all the images during the test protocol, both for SSc patient (blue line) and healthy subject (red line). In spite of the parameters' values in the baseline condition are similar for both subjects, their variations during the study protocol are wider for the SSc patient. Moreover, for the SSc patient the extreme value of the parameters (minimum and maximum) occurs for different image respect to the healthy subject: this means that in the patient the microcirculation has a different dynamic behavior due to the microvascular abnormalities.

Figure 4 shows the histogram of some selected NIRS images acquired during the study protocol for both patient and healthy subject. Image 1 is relative to the baseline condition: the histograms denote differences in the basal oxygen saturation level between the two subjects. Image 23 is relative to the end of ischemia phase. Image 24 is the first image acquired after the cuff release: in this case the histograms of SSc patient image has a tail at lowest intensity value that denotes a singular heterogeneity in the distribution of the oxygen. This heterogeneity is still present one minute after the cuff release (Image 29) and also weakly two minutes after the cuff release (Image 35). In the final image (Image 52), that

is the last acquired at the end of the study protocol, the two histograms are quite similar to

indicate a temporary recovering in microvascular function for the SSc patient after the ischemia-reperfusion stimuli.

#### 5. Discussion and Conclusion

Image analysis performed in this work reveals some differences in the oxygen saturation levels between SSc patient and healthy subject during the study protocol. In particular, in SSc a higher spatial heterogeneity of StO<sub>2</sub> were observed in the basal condition as well as during ischemia and reperfusion.

In addition, the results revealed striking differences in the dynamic micro vascular response to the ischemic insult. From the images histogram in Figure 4, it is possible to note that in the healthy volunteer, the oxygen saturation level has a rapid and homogeneous recovery starting from the first image after the cuff deflation, while the SSc patient had a much slower increase in some areas. Moreover, this recovery of basal StO<sub>2</sub> is markedly inhomogeneous in the SSc patient as compared with the control. These findings underline two important hallmarks of 2D NIR spectroscopy technology: the ability to explore large portions of tissue, rather than just small samples, with a high spatial resolution and, thanks to the very short acquisition time, the ability to follow a dynamic phenomenon with a sufficiently high time resolution. From the study results, although limited to one patient and one control, we can conclude that NIR spectroscopy 2D mapping of oxygen saturation using multiple

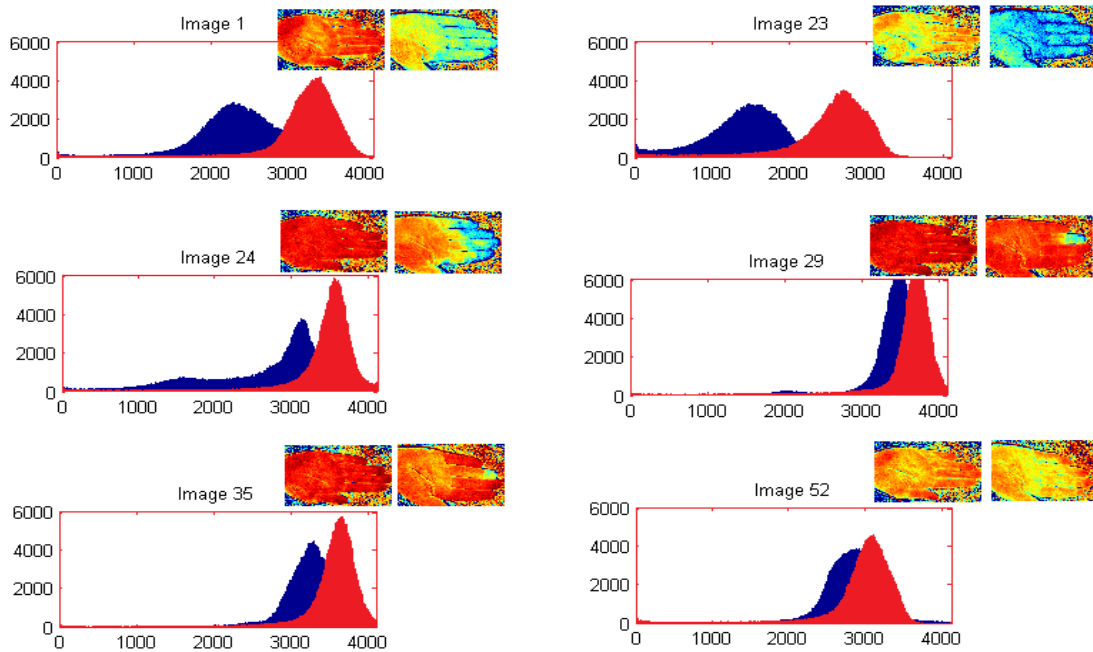


Figure 4. Histogram of some selected NIRS images of SSc patient (blue) and healthy control (red). On the top right corner of each graph, the relative NIRS images are reported (left: healthy subject, right: SSc patient)

sequential images allow the microcirculatory spatial heterogeneity to be visualized and quantified both in SSc patients and in healthy volunteers. Such spatial information is impossible to obtain with commonly used techniques which explore few tissue samples (generally the thenar eminence only). The image processing presented here considered the oxygen saturation level in the entire hand allowing to get a comprehensive view of the state of the microcirculation. With this kind of analysis it is possible to extract some clinical information complementary to that obtained with the analysis limited to some individual regions of interest [1].

### Acknowledgement

This work has been supported by 'Regione Toscana, Direzione Generale Competitività e Sviluppo Competenze, Area di Coordinamento della Ricerca'.

### References

1. V. Hartwig et al., Title?? J. Near Infrared Spectrosc. 23, 59–66 (2015).
2. Jalil B., Salvetti O., Poti L., L'Abbate A., Marinelli M., Hartwig V. Heterogeneity of hand skin microcirculation assessed by near infrared 2D imaging. In: AITA 2013 - 12th International Workshop on Advanced Infrared Technology and Applications (Torino, Italy, 10-13 September 2013). Proceedings, pp. 141 - 145. Fondazione 'Giorgio Ronchi', 2013
3. Miklos Lipcsey, Nicholas CZ Woinarski and Rinaldo Bellomo, Near infrared spectroscopy (NIRS) of the thenar eminence in anesthesia and intensive care, Annals of Intensive Care, (2012)2-11.
4. Woinarski NC, Suzuki S, Lipcsey M, Lumsden N, Chin-Dusting J, Schneider AG, Bailey M, Bellomo R., Near-infrared spectroscopy of the thenar eminence to estimate forearm blood flow, Critical Care and Resuscitation, 15 (2013) 323-6.
5. Guartmoner G<sup>1</sup>, Mesquida J, Masip J, Martínez ML, Villagra A, Baigorri F, Pinsky MR, Artigas A. Thenar oxygen saturation during weaning from mechanical



- ventilation: an observational study. *European Respiratory Journal*, 43 (2014) 213-220.
6. Vasiliki Gerovasili, Stavros Dimopoulos, Georgios Tzanis, Maria Anastasiou-Nana, Serafeim Nanas. Utilizing the vascular occlusion technique with NIRS technology. *International Journal of Industrial Ergonomics*, 40 (2010) 218-222.
  7. Mayeur C, Campard S, Richard C, Teboul JL, Comparison of four different vascular occlusion tests for assessing reactive hyperaemia using near-infrared spectroscopy. *Critical Care Medicine*. 39 (2011) 695-70.
  8. J Canny, A computational approach to edge detection, *Pattern Analysis and Machine Intelligence*, IEEE, 1986.

# MEASUREMENTS WITH A QWIP INFRARED CAMERA: SIGNAL TREATMENT AND NOISE CORRECTION

S. Boccardi, G.M. Carlomagno, C. Meola

Department of Industrial Engineering/Aerospace Division - University of Naples Federico II  
Via Claudio 21, 80125 Napoli, Italy, [simone.boccardi@unina.it](mailto:simone.boccardi@unina.it), [carmagno@unina.it](mailto:carmagno@unina.it),  
[carmeola@unina.it](mailto:carmeola@unina.it)

The present work is concerned with the use of an infrared imaging device to measure very small temperature variations, which are related to thermo-elastic effects developing on composite materials, under relatively low loads. As it comes out from previous work, such temperature variations are difficult to measure being at the edge of the IR camera resolution and/or affected by the instrument noise. Conversely, they may be valuable to get either information about the material characteristics and its behavior under load, or to assess the delamination overall extension. An image post-processing procedure is herein described which, with the help of a reference signal, allows for suppression of the instrument noise and better discrimination of thermal signatures induced by the load.

## Introduction

Infrared thermography (IRT) is gaining ever more interest for both the academic and the industrial fields. This is supported from being this the topic of four International Symposia [1-4] which continue to be held from many years. Its success is due to its non-contact and remote working way and to its multifarious exploitations; practically, every application which is temperature dependent may benefit from the use of an infrared imaging device.

IRT has proved helpfulness in many industrial and research fields. Amongst its many applications, an infrared imaging device is helpful for thermo-elastic stress analysis (TSA) purposes [5-6] and to monitor the surface temperature change (thermoelastic effect) which is experienced by a body when subjected to volume variations under load [7].

Two tasks are herein addressed:

- cyclic bending tests;
- impact tests.

The first one is intended to get information on the material characterization due to the already found good agreement with the bending moment trend [8,9].

The second one supplies information useful for the comprehension of the material impact damaging mechanisms [10,11]. In particular, it has been shown as the use of an infrared imaging device for monitoring the impact event is advantageous when the investigation regards the material performance for design purposes [12]. Furthermore the presence of undisclosed delamination is crucial, especially in composites used for the construction of aircraft, since it may led to catastrophic consequences.

Both tasks are involved with measurements of very small temperature variations linked to thermoelastic/thermoplastic effects on composite materials. Of course, the measurement accuracy depends strongly on the magnitude of temperature differences while some limitations may arise when attempting to measure temperature variations which are very small and at the edge of the instrument resolution. In this regard, a difficult task is to perceive the temperature variations which develop under relatively low loads and/or are associated with very light delamination. The purpose of this work is to show that, by proper signal treatment and correction of the instrument noise with the use of a reference signal taken in an unsolicited zone, it is possible to get reliable measurements of very small temperature variations.

## Testing apparatus and procedure

Two types of tests are carried out: impact tests and cyclic bending tests. Impact tests are performed with a modified Charpy pendulum which allows enough room for positioning of the infrared camera to view the surface opposite to the impact (Fig.1).

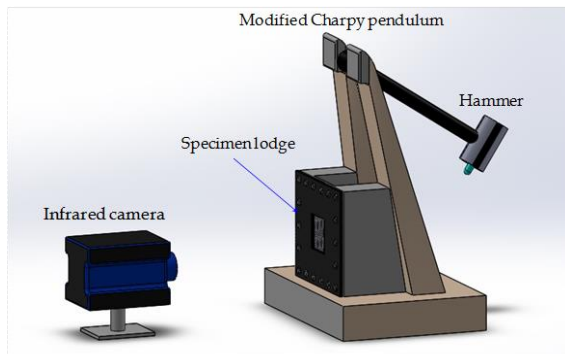


Fig. 1. Sketch of impact tests setup.

For bending tests a cantilever beam specimen is clamped on its bottom side (fixture) and is free to bend under the cyclic harmonic force applied at the opposite upper end (Fig.2). The bending is operated with a machine which allows changing of both bending frequency and specimen deflection.

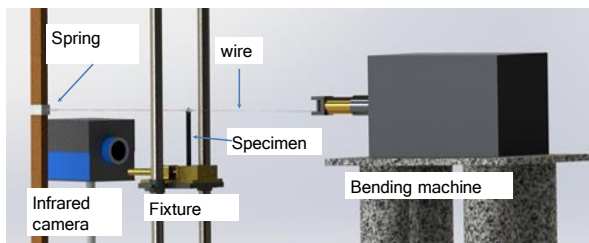


Fig. 2. Sketch of cyclic bending tests setup.

In both types of testing, the SC6000 LW (Flir systems) is used to visualize temperature variations occurring over the specimen surface. Sequences of thermal images are acquired at 60 Hz during cyclic bending and at 84 Hz during impact tests. These two frame rate values are found to be the most appropriate for the specific objectives.

## Image post-processing and data analysis

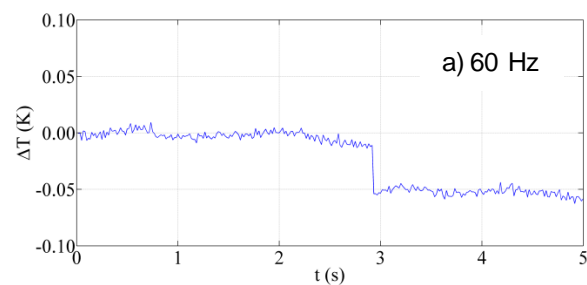
The sequences of thermal images are post-processed to extract  $\Delta T$  images according to:

$$\Delta T(i, j, t) = T(i, j, t) - T(i, j, 0) \quad (1)$$

$i$  and  $j$  representing lines and columns of the surface temperature array,  $t$  the time instant at which one image is recorded; more specifically,  $t = 0$  indicates the first image of the sequence, before loading, for which the specimen surface is at ambient temperature.

A different data analysis is performed owing to the specific loading mode. In fact, for cyclic bending the interest is towards the variation of  $\Delta T$  by moving away from the fixture in analogy with the bending moment diagram. Conversely, in the case of impact tests, the assessment of the delamination extension is of great concern. Whatever the type of analysis, a drawback is the instrument noise which may affect small  $\Delta T$  values.

Fig.3 shows  $\Delta T$  plots taken at the two frame rates of 60 Hz (Fig.3a) and 84 Hz (Fig.3b) which are used to respectively collect sequences of images during bending and impact tests. It is worth noting that, to visualize the instrument noise, the  $\Delta T$  plots of Fig.3 are taken by viewing a blackbody at steady state conditions. It is possible to see that both signals are affected by a random jumping trend. However, it can be observed that the  $\Delta T$  jumps amplitude is quite small reaching in the worst case about 0.1 K, which does not affect the measurement of enough large temperature variations. Indeed, in most of the infrared thermography applications, this condition is fulfilled. Instead, problems may arise when attempting to use the infrared camera in extreme conditions such as in the measurement of temperature variations induced by thermo-elastic effects, which are very small and below 0.1 K.



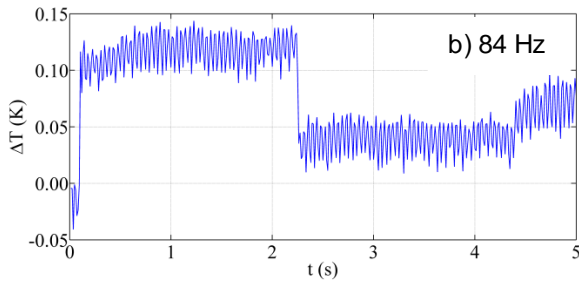


Fig. 3.  $\Delta T$  distribution with time for 60 and 84 Hz.

### Cyclic bending tests

Four measurement positions (PM) are chosen along the specimen length  $L$ , starting about 10 mm far from the fixture ( $x = 0$ ) and moving towards the forced side (Fig.4). In each PM, a data plot in time is extracted and subjected to noise correction owing to an unsolicited reference area [9].

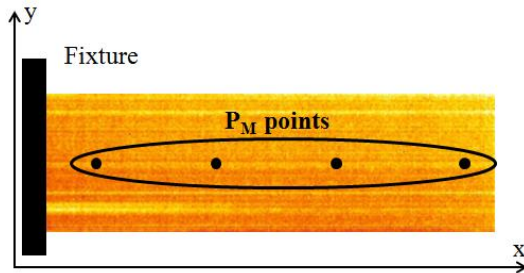


Fig. 4. Measurement points over the specimen surface.

More specifically, raw data plots extracted in the four points along the specimen length are shown in Fig.5. As can be seen the raw signal is affected by random abrupt jumps like those already displayed in Fig.3. By subtracting the noisy signal, which is recorded in an unsolicited reference area, the corrected signal reported in Fig.6 is obtained. From Fig.6 two observations can be made. The first one regards the effectiveness of the reference-area based correction method. It is worth noting that the alternate jump effect, due to its random nature, has to be accounted for during the sequence acquisition. The second observation from Fig.6 regards the variation of the  $\Delta T$  amplitude which decreases with increasing  $x/L$  (i.e. moving away from the fixture).

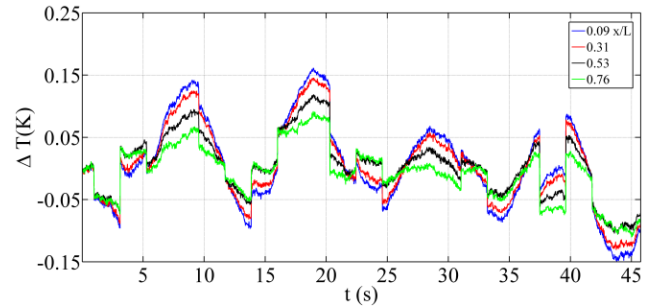


Fig. 5. Raw signal in four points along  $x$ .

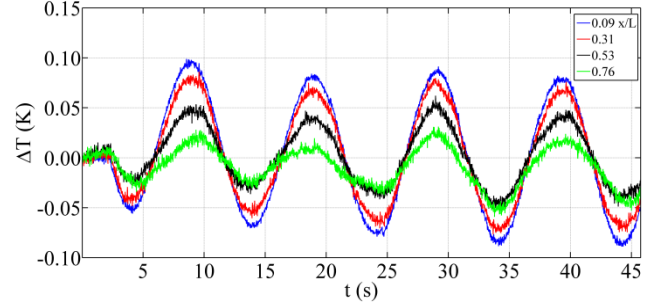


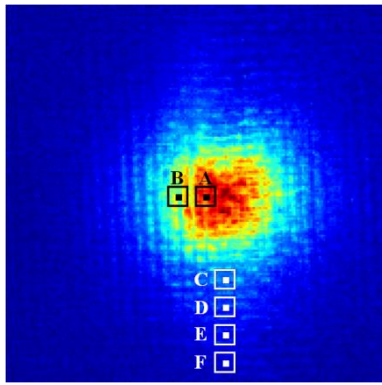
Fig. 6. Corrected signal in the four points as in Fig.5.

### Impact tests

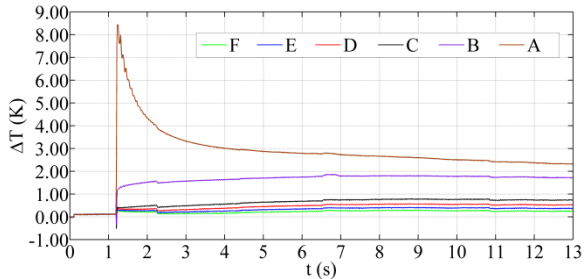
A  $\Delta T$  image taken on the specimen side opposite to impact is shown in Fig.7a. The maximum  $\Delta T$  value is attained in the red central zone, where the impact damage is more important, and decreases moving away towards the specimen periphery, where delamination becomes ever more lighter vanishing in the sound material.

The  $\Delta T$  distribution with time in the A-F points is shown in Fig.7b. In more details, each plot refers to the average amongst a 100 pixels area. To better display the slighter  $\Delta T$  distributions, the C-F plots are replicated in Fig.7c with a smaller scale. As can be seen the raw signal is again affected by the random abrupt jumps; this effect is more pronounced for small  $\Delta T$  variations while it becomes irrelevant as  $\Delta T$  increases.

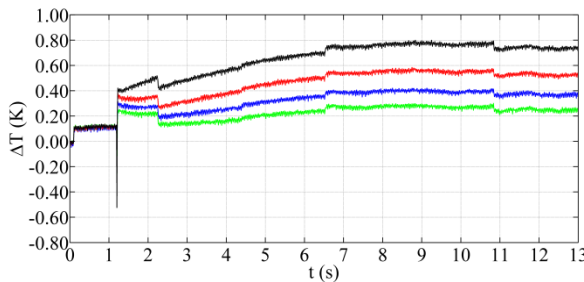
In a similar way as already done for cyclic bending tests, each data plot is corrected owing to a reference sound area. The corrected signals are shown in Fig.7d. Again, all the random jumps are eliminated and the restored signals allow for assessing the extension of the impact damage.



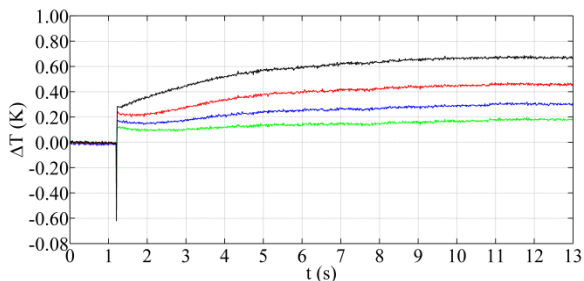
a)  $\Delta T$  image



b) raw  $\Delta T$  plots



c) raw  $\Delta T$  plots in points C-F



d) corrected  $\Delta T$  plots in points C-F

Fig. 7. Corrected signal in the four points as in Fig.5.

## Conclusion

The LWIR QWIP SC6000 camera was used to measure the small temperature variations, which are related to thermo-elastic effects developing under either cyclic bending, or impact, tests of composite materials. It has been shown that in both cases the measurement of

small temperature variations is difficult due the noisy signal. As demonstrated, it is possible to account and eliminate the noise in a simple and effective way with the use of a reference area. Of course, once the noise is removed, the temperature variations linked to thermo-elastic effects can be measured and exploited for materials characterization.

## References

1. Proc. Annual SPIE Thermosense Conferences, Bellingham, WA 1978-.
2. Proc. Advanced Infrared Technology & Applications (AITA) 1991-.
3. Proc. Biennial Quantitative Infrared Thermography (QIRT) Conferences, 1992-.
4. Proc. InfraMation, 2000-.
5. J.M. Dulieu-Barton, T.R. Emery, S. Quinn, P.R. Cunningham. A temperature correction methodology for quantitative thermoelastic stress analysis and damage assessment Measurements Science and Technology, Vol. 17, pp. 1627-1637, 2006.
6. U. Galietti, D. Modugno, L. Spagnolo. A novel signal processing method for TSA applications Measurements Science and Technology, Vol. 16, pp. 2251- 2260, 2005 .
7. C. Meola, G.M: Carlomagno. Infrared thermography to impact-driven thermal effects Applied Physics A, Vol. 96, pp. 759-762, 2009.
8. C. Meola, G.M. Carlomagno, C. Bonavolontà, M. Valentino, Monitoring composites under bending tests with infrared thermography, Advances in Optical Technologies, Vol 2012, 7 pages, 2012.
9. S. Boccardi, G.M. Carlomagno, C. Bonavolontà, M. Valentino, C. Meola, Infrared thermography to monitor Glare® under cyclic bending tests with correction of camera noise Proc. QIRT 2014, Bordeaux, France, 7-11 July 2014.
10. C. Meola, G.M. Carlomagno, Infrared thermography to evaluate impact damage in glass/epoxy with manufacturing defects, International Journal of Impact Engineering, Vol 67, pp 1-11, 2014.
11. C. Meola, S. Boccardi, N.D. Boffa, F. Ricci, G.M. Carlomagno Infrared thermography to evaluate impact damaging of composites, Proc. of ECCM16 Seville (Spain) 22-26 June 2014, Paper 0318, Program book: ISBN-10: 84-616-9798-7
12. C. Meola, S. Boccardi, N.D. Boffa, M. Di Palma, L. Maio, G.M. Carlomagno, Impact Damaging of Carbon Fibre-reinforced Composites: a Comparison between Infrared Thermography and Ultrasonics, Proc. 11th ECNDT, Prague, Czech Republic, 6-10 October 2014, ISBN 978-80-214-5018-9.

# IR3D Analysis - three-dimensional imaging in active thermography and non-destructive testing

P. Hellstein<sup>1</sup>, M. Szwedo<sup>2</sup>

<sup>1</sup> AGH University of Science and Technology, Mickiewicza 30 Ave., 30-059 Krakow, Poland, hell@agh.edu.pl

<sup>2</sup> MONIT SHM LLC, Lublańska 34, 31-476 Kraków, Poland, mszwedo@monitshm.pl

A novel 3D temperature mapping method is presented, which is especially designed for non-destructive testing methods such as active thermography. For the first time the results may be observed and rendered in real-time and are available directly after the analysis is finished. The system allows to project not only raw temperature data, but also processed images, which allow for precise localisation of defects after thermographic inspection.

## Introduction

With the lowering size and cost of 3D scanners it has been become increasingly popular to use them in variety of measurement systems. Three-dimensional scanners are mainly used as an extension to existing diagnostic systems, by including information about the dimensions and size of the object. 3D scanners have already been introduced to thremography analyses, they are mainly used in medical fields, building inspections and energy auditing [1]. The combination of infrared data with geometrical information allows for better visualisation of registered thermogram and its precise localisation on inspected object.

Several infrared systems have been presented in the past few years, which allowed to perform mapping of thermal information on 3D model. Unfortunately they suffered from constraints regarding the size of inspected object and were not very flexible. Furthermore the measurement system had to be stationary during the whole analysis. The first mobile system was introduced by Stephan Vidas [2]. It was designed for energy auditing and required long post-processing to perform the 3D temperature mapping. Just recently the system has been upgraded [3] to allow for real-time visualisation of results during the measurement. This does not

change the fact, that HeatWave, as well as all other existing systems, can only be used for passive thermography analyses, with temperatures that are time-independent.

This paper introduces a novel approach to 3D thermal mapping, which for the first time uses it for for active thermography measurements. The difficulty of such application comes from the fact that such analyses register thermograms, which vary in time. This required a new thermal mapping method, which maps temperatures using ray-tracing GPU rendering algorithms. The mapping is being performed in real-time during image viewing. This allows the user to perform different kinds of processing algorithms on analysed image and observe a live update on 3D model of the inspected structure.

The proposed IR3D Analysis system uses classical pulse-thermography and enhances it with advanced visualisation methods. The presented solution is not limited to analysis of small areas. It has been designed especially for non-destructive diagnostics of large, industrial structures such as boats, planes and wind-turbine blades.

## System overview

The designed system is used for inspection with the use of pulse-thermography. Pulsed thermography is an active thermography technique with external thermal excitation. The excitation is applied to the



sample's surface by means of heat irradiation generated by halogen lamps. Thermal energy propagates through the sample and when they come across a discontinuity, the propagation path is altered, which can be observed as changes on the surface temperature distribution.



Fig. 22 IR3D Analysis system

The IR3D Analysis hardware consists of an infrared camera with two halogen lamps that heat the inspected structure (Fig. 22). The lamps are fully programmable via a controller, which can modify their heating power and modulation frequency. A 3D scanner is attached directly to the infrared camera with a specially manufactured frame. All hardware is closed in a metal casing and can be mounted on a camera tripod.

A FLIR A300 infrared camera has been used, with 320x280 pixel resolution and 3 Hz maximum acquisition rate. Because the system is intended to be used in inspection of large constructions, the camera has been equipped with a 4 mm fish-eye lens, which increases its field of view from  $25^\circ \times 18.8^\circ$  to  $90^\circ \times 73^\circ$ . This results in fewer images that need to be registered to cover the whole inspected object, but also introduces large distortions. For accurate temperature mapping, it is necessary to reduce all distortions with proper geometrical calibration of lens system. This has been performed with a Peltier unit matrix calibration board, introduced previously by the authors [3], which uses thermoelectric

coolers to increase the contrast and efficiency of calibration images.

The 3D scanner is a Structure IO Sensor, that is designed for mobile applications. The scanner is powered from USB port, it is very light (95 grams) and has small dimensions (119.2mm x 27.9mm x 29mm), which makes it ideal for mobile diagnostic purposes. Many available scanners cannot be placed closer than 80 cm from the structure. In active thermography it is desirable to place the system close to the structure, to increase the heating efficiency. The Structure IO minimum registration distance is 40 cm, which allows to place the system in finest distance from the inspected object.

Additionally to geometrical calibration of the camera, the relative calibration between the scanner and the infrared is necessary to perform the temperature mapping. It is also important to register the data from both the infrared camera and the 3D scanner with timestamps that can be related to each other with millisecond precision.

The designed system is very mobile and versatile. It can be mounted differently depending on the requirements (Fig. 23). The system can operate wirelessly, streaming the necessary data to the computer performing measurement.



Fig. 23 IR3D Analysis system mounted on robot, performing an automatic inspection of a part of wind-turbine blade from both sides

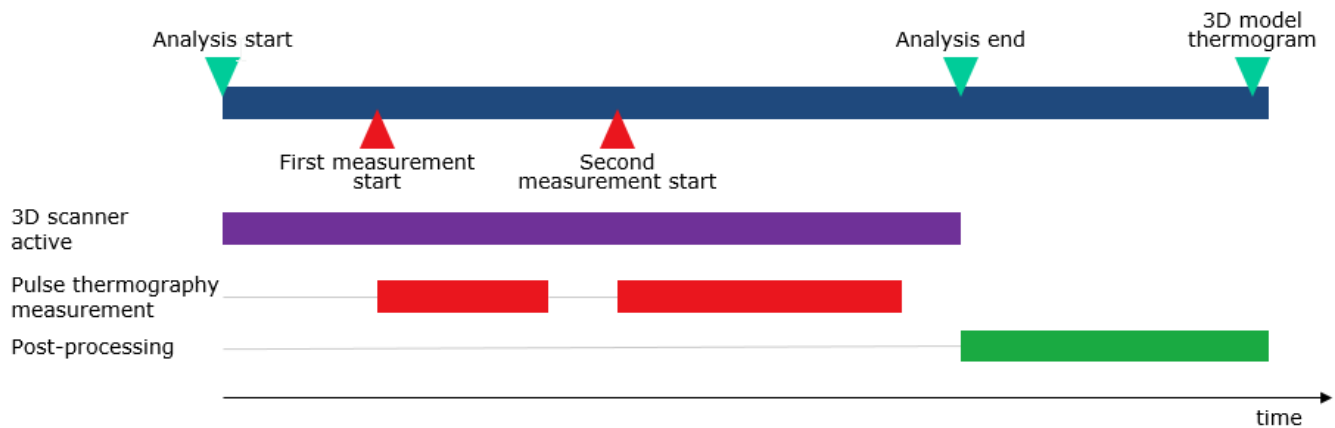


Fig. 24 Measurement procedure of IR3D Analysis with active thermography

## Measurement procedure

When performing a diagnostic of large composite structures, it is often necessary to perform extensive amount of pulse-thermography measurements. Single measurement consists of two phases – heating and cooling. In order to obtain a 3D representation of a measured object, the 3D scanner has to be active through whole analysis (Fig. 24), even between single thermography measurements. After whole object has been inspected, the results consists of both thermograms and depth files, with corresponding related timestamps.

After analysis it is necessary to generate a 3D model, with camera positions and orientations for every registered timestamp. This can be achieved with a cloud fusion algorithm called Kinect Fusion [4], or its open-source equivalent Kinfu. It is an Iterative Closest Point algorithm that looks for transformation between two consecutive point clouds, which share a common group of points. It has been shown that cloud fusion using Kinfu algorithm can operate in real-time during the acquisition of depth files, but in order to minimise the hardware requirements for the measurement system this step is performed in post-processing.

Original Kinfu algorithm has limitations regarding the volume within which the cloud fusion can be performed, which is around

3x3x3 meters, depending on the required resolution. To overcome this, an alternative algorithm called KinfuLargeScale has been used, which does not restrict the user to specific registration volume. This allows to measure much larger constructions which are typically diagnosed with active thermography, such as boats or planes. The accuracy of 3D reconstruction for typical scene size is around 10 mm [5].

## Data visualisation

The results of IR3D Analysis are viewed in a special real-time GPU renderer created as a module to ThermoAnalysis software [6]. The ray-tracing rendering engine is based on SmallLuxGPU, which is a part of LuxRender open source physically based renderer. The temperature mapping is done by a newly designed type of lighting called CameraLight, which imitates the behaviour of a normal projector. It has been modified to take into consideration the camera distortions, that have to be removed, before mapping the temperatures on fused 3D model.

When results are viewed, it is possible to move to any desirable time during the whole analysis and observe the position of the measurement system. The real-time renderer is deeply integrated with the rest of the software, which means all typical processing methods are available to the user. In active thermography an unprocessed image often does not reveal any information about the defects that may be present in the structure. It is often required to use advanced processing methods such as TSR. The proposed real-time rendering system

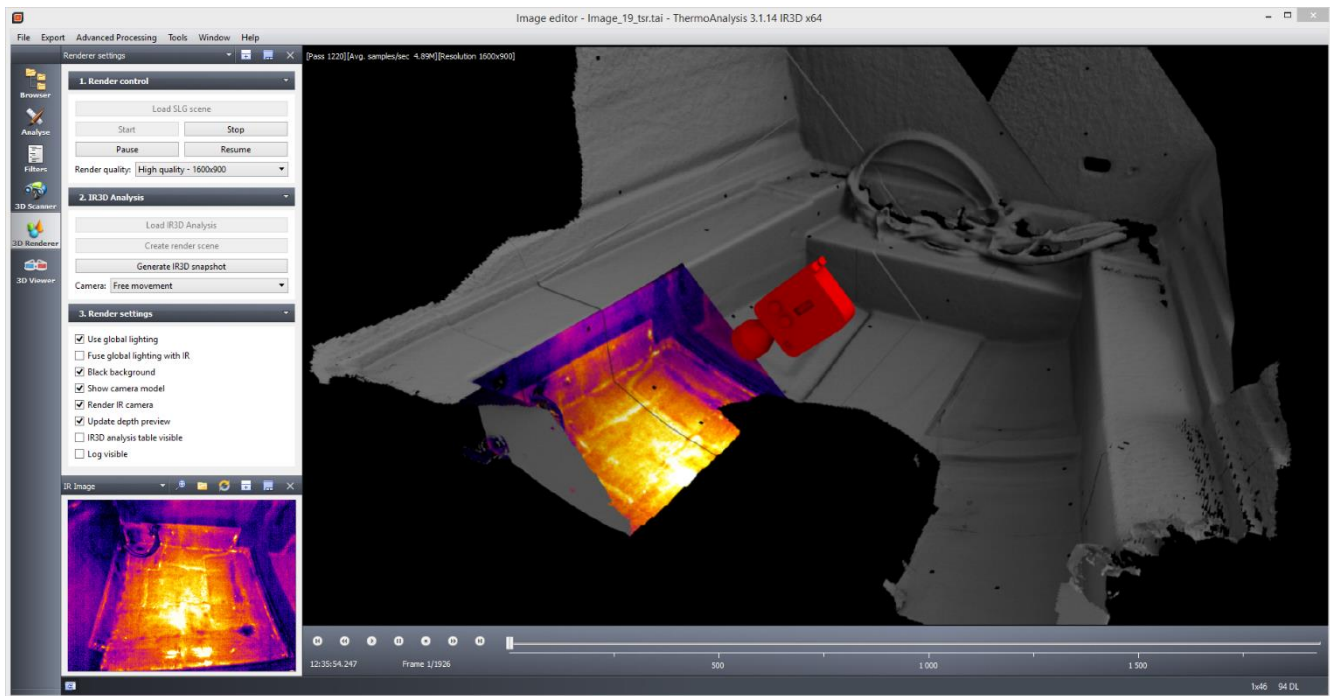


Fig. 25 Visualisation of the results after IR3D Analysis of boats hull

allows to immediately see the updated infrared image on the geometrical representation of the object.

## Results

Several measurements were performed on different types of structures. Fig. 25 shows the results from a part of a boats hull. It has been inspected with pulsed-thermography to diagnose possible delaminations and voids in composite material. An unprocessed image did not reveal any defects. After processing has been applied a large, vertical delamination has appeared. The final infrared image can be observed in the lower left corner of the application. By looking at the 3D render, it is possible to observe the surroundings, in which the measurement was taken and precisely diagnose the location of the delamination, which is an important information that minimises the time required to repair the inspected object.

## Conclusion

The authors presented a novel approach to 3D temperature mapping, which allows it

become a valuable tool in visualisation and localisation of defects in non-destructive testing methods, such as active thermography.

## References

1. D. Borrmann, A. Nuchter, M. Dakulovic, I. Maurovic, I. Petrovic, D. Osmanovic, and J. Velagic, "The Project ThermalMapper – Thermal 3D mapping of indoor environments for saving energy," *Proceedings of the 10th International IFAC Symposium on Robot Control (SYROCO)*, vol. 10, 2012.
2. S. Vidas and P. Moghadam, "HeatWave: A handheld 3D thermography system for energy auditing," *Energy and Buildings*, vol. 66, pp. 445–460.
3. Vidas, S., Moghadam, P., & Sridharan, S. (2014). Realtime mobile 3D temperature mapping. *IEEE sensors journal*, 15(2), 1145-1152.
4. M. Szwedo, P. Hellstein, "Qualitative diagnostics of wind-turbine blades inspection using active thermography", *QIRT 2014, Bordeaux, France*.
5. S. Izadi, R. A. Newcombe, D. Kim, O. Hilliges, D. Molyneaux, S. Hodges, P. Kohli, J. Shotton, A. J. Davison, and A. Fitzgibbon, "KinectFusion : Real-Time Dynamic 3D Surface Reconstruction and Interaction," *ACM SIGGRAPH*, 2011.
6. S. Meister, S. Izadi, P. Kohli, M. Hammerle, C. Rother, and D. Kondermann, "When Can We Use KinectFusion for Ground Truth Acquisition?", *Workshop on Color-Depth Camera Fusion in Robotics, IROS*, 2012.
7. MONIT SHM, "ThermoAnalysis", accessed May 2015, <http://www.monitshm.pl/thermoanalysis>.

# MONITORING OF THE CROSS WEDGE ROLLING PROCESS BY THERMOGRAPHY

G. Traxler<sup>1</sup>, A. Baghbanpourasl<sup>2</sup>

<sup>1</sup> Profactor GmbH, 1150 Vienna, Graumannsgasse 7 C3, gerhard.traxler@profactor.at

<sup>2</sup> Profactor GmbH, 4407 Steyr-Gleink, Im Stadtgut A2, amirreza.baghbanpourasl@profactor.at

The cross wedge rolling process is monitored by a thermographic camera to gain information about the stability of the process and the quality of the product. One of the thermographic results is the part's temperature, which should stay inside a small range for good product quality. In addition, the time evolution of temperature profiles, which are assumed to be a consequence of the production condition, have to be the same whenever a new part is processed. To verify the accuracy of the temperature measurements, the surface temperature is compared with calculations using Finite Difference Method (FDM), and a machine learning method by observing the time evolution of temperature profiles using template matching and principal component analysis (PCA), delivers a measure for deviation of the process from its normal behavior. The results show the successful application of the method. This monitoring technique can be used for various thermal processes with a minimum adaptation effort.

## Introduction

In the project CoVaForm [1] valuable materials, like bainitic grade steel [2] and titanium shall be saved by use and development of the cross wedge rolling (CWR) process, which is a fleshless forming operation [3]. To produce parts like turbine blades or hip implants, more forging steps are needed to form the complex shape. CWR is used to produce the preforms, and achieves material utilizations up to 100%.

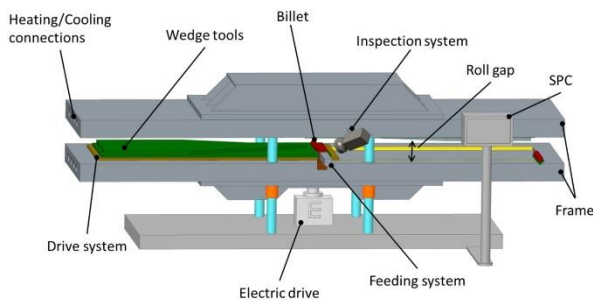


Fig. 1. CWR-machine with inspection system

The CWR-machine has a top and a bottom pressing plate (wedge tool, Fig. 1). Once pressed onto the billet, the plates move horizontally in

opposite directions, forming the billet according to the geometry of the wedge tool (e.g. Fig. 2, right). The billet is visible through the roll gap only and while it is revolving, the position of the axis remains fixed. First experiments were done with billets with a length of 100mm and a diameter of 20mm.

The main idea of this work is to perform an automatic quality control. The part is hot processed; therefore, we can use thermography to gain direct information about the surface of the part by observing the surface of the part through the rolling gap. The thermal information is then analysed to detect possible problems in the product quality. Evaluation of quality shall be done by observation of the working-piece while rolling and forming is taking place. Machine learning techniques are needed to automatically observe the thermal images, detect the repetitive signature of a normal production process, and to alarm when an anomaly occurs.



Beforehand, for proper interpretation of the thermal images the accuracy of the measured temperature values has to be verified.

Knowing the initial temperature of the working-pieces, the surface temperature can be calculated at any time using governing heat equations. By comparing the calculations with readings of the camera, validity of the readings can be verified.

## Approach

To verify the readings of the camera, the temperature at two points of time are considered: First, the initial temperature right after taking out the piece from furnace and second, after handling the part to the starting position of the CWR machine. The initial temperature is known and is in the range from 1000°C to 1250°C. It takes about 10s to move the part to the starting position. A simple finite difference method (FDM) is utilized to calculate the temperature (1).

$$\rho c_p \frac{\Delta T}{\Delta t} = \lambda \left( \frac{\Delta^2 T}{\Delta x^2} + \frac{\Delta^2 T}{\Delta y^2} + \frac{\Delta^2 T}{\Delta z^2} \right) \quad (1)$$

The boundary conditions were set to convective (2) and radiative (3) heat transfer at the entire surface.

$$\Delta T_{x_1 \leftarrow \text{air}}^{t+\Delta t} = \frac{\alpha (T_{\text{air}} - T_{x_1}^t) \Delta t}{\rho c_p \Delta x} \quad (2)$$

$$\Delta T_{x_1 \leftarrow \text{air}}^{t+\Delta t} = \frac{\varepsilon \sigma (T_{\text{Umg}}^4 - T_{x_1}^4) \Delta t}{\rho c_p \Delta x} \quad (3)$$

The calculation is done with thermal conductivity (at 950°C)  $\lambda = 19 \text{Wm}^{-1}\text{K}^{-1}$ , density (at 950°C)  $\rho = 4280 \text{kgm}^{-3}$ , specific heat capacity (at 950°C)  $c_p = 635 \text{Jkg}^{-1}\text{K}^{-1}$  and thermal transfer coefficient (steel to air, natural convection)  $\alpha = 45 \text{Wm}^{-2}\text{K}^{-1}$ . It is shown by Traxler et al. [4] that the emissivity value of the hot material after a rolling process is close to 1, therefore in this simulation we set  $\varepsilon = 1$ . This assumption is further verified by using relevant experimental methods, namely by taking

temperature values from a location, at which an emissivity close to 1 can be expected due to its geometry, as shown in Fig. 2.

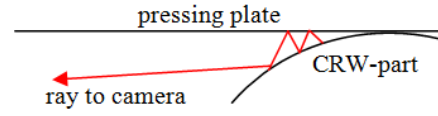


Fig. 2. Multiple reflections in the CRW-machine.

An emitted ray of infrared radiation (Fig. 2) is reflected by the pressing-plate, which acts much like a mirror. When the reflected beam hits the CRW-part again, the fraction that reflects will be increased by the emitted radiation. Due to such multiple reflections, sometimes referred as cavity-effect, the effective emissivity gets close to 1.

Thermal images are captured by camera during CWR-process with a sampling period of 100 ms (Fig. 3).

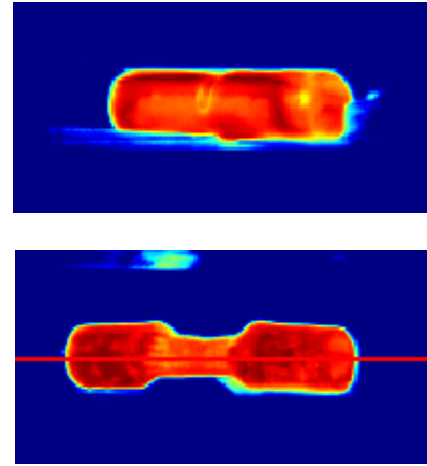


Fig. 3. (Up) thermal image of the part before and (down) after (down) process. Time evolution of the profile along the red horizontal line is used to produce the signature of the production process.

For monitoring the process and controlling the quality of the products, thermal profiles along the axis of the piece are collected and assembled into an image, as it typically is done with line scan cameras.

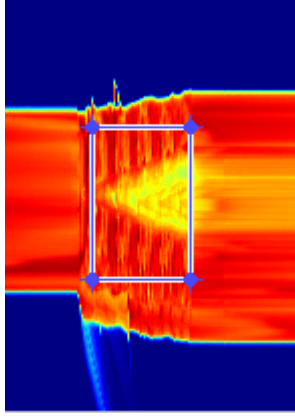


Fig. 4. Evolution of the temperature profile (time advances from left to right). The rectangle shows the area of interest (signature)

Figure 4 shows the time evolution of the profile measured along the red line shown in Fig. 3 (down). The rectangle in Fig. 4 is the area of interest, which contains the temporal window, in which the CWR-process is in progress. This region represents a unique signature that is always observable in normal operation. The signature is used to train a machine-learning algorithm for detecting abnormal behaviour or product during and after the process.

To detect the signature in time evolution of the profile of each sample a template matching technique is used. For this reason, this region is selected manually from one of the sample profiles and used as a template for further template matching operation. Normalized cross correlation is applied for template matching operation as implemented in Matlab® software package [5, 6].

The signatures are further processed to reduce the dimensionality of the data. Principal component analysis can be used to reduce effectively the dimension of the space of the representation of data and to represent them with a more meaningful set of parameters. We will keep the first  $n$  most important components resulting from PCA to feed to the further anomaly detection algorithm. Practically  $n$  can be much smaller than the total number of components. The coefficients of the components of the samples along each PC create a distribution with a specific mean value and

variance. These parameters are used to approximate the distribution with a Gaussian. After the training stage, each new sample will be compared with the calculated distribution: if the sample resides far from the centre of the Gaussian, given a user-defined threshold, or in other terms if the value of the distribution function fall below a specific threshold for the sample, it will be considered as an anomaly [7]. The distribution has the following form:

$$f(\bar{x}) = e^{-\frac{x_1^2}{\sigma_1^2}} e^{-\frac{x_2^2}{\sigma_2^2}} \dots e^{-\frac{x_n^2}{\sigma_n^2}} \quad (4)$$

Where  $\sigma$ 's are standard deviation for the coefficients of each PC.

In practice, to prevent numerical underflow, logarithm of the distribution function is used. Therefore we define the following quantity that measures deviation from normality:

$$d(\bar{x}) = \frac{x_1^2}{\sigma_1^2} + \frac{x_2^2}{\sigma_2^2} + \dots + \frac{x_n^2}{\sigma_n^2} \quad (5)$$

## Results and discussion

For verification of the emissivity, temperature values at the scan-position were compared to the values taken from the gap between billet and pressing plate. The value, taken from the gap is assumed to show the correct value, since emissivity is close to 1 in the gap due to geometrical considerations. Because of nearly equal temperature values at the gap and at the scan-line, differing just for 10K, the emissivity must be close to 1 at the scan-line too.

Fig. 5 shows the result of the FDM calculation for the cooling down progress. The mean value of 10 measurements, taken from the thermal sequences when the rolling process starts, is 800°C (calculated by camera-software with an emissivity set to 1). This value is quite close to the calculated temperature of 820°C. Adjusting the emissivity to 0.965 in the camera-software displays 820°C, which means, that the real value of the emissivity is 0.965. Due to uncertainty in



duration for transfer of the billet from the furnace to the initial rolling position, and limited accuracy in temperature measurement, this result is believed to be reliable enough for further evaluation.

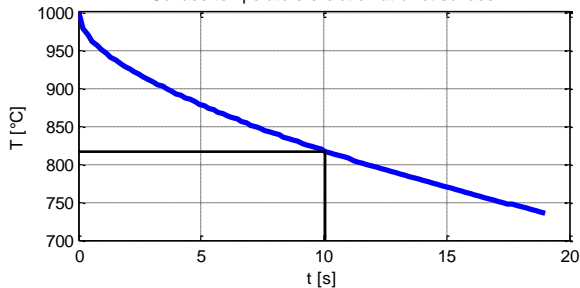


Fig. 5. Cooling down of Ti6AlV4 working-sample; temperature at surface of billet-barrel at middle height

In addition it was found, that there is a lower surface temperature at two positions at the circumflex of the piece. It is caused by the contact of the working piece with the top and bottom rolling plates and consequently heat transfer to these colder objects. This is the explanation for the periodic pattern in the thermal sequences of the revolving part. In each revolution, two colder stripes are observed, as shown in all the time evolution of profiles (e.g. Fig. 4).

After validation/Calibration of the camera readings, several cross wedge rolling process are recorded in action for the purpose of training procedure. Template matching using normalized cross correlation is applied for finding the signatures in the time evolution of the profiles of the recorded videos. Fig. 6 shows the template and the automatically detected signatures of two other samples. Finding the match does not guaranty the existence of a normal signature in the profile.

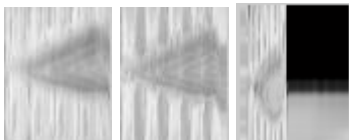


Fig. 6. (Left) Template and the matched signatures for (middle) a normal and (right) an unusual process

For example the matched signature in Fig. 6 (right), that is related to a rolling process with a

much faster rolling speed than the two other signatures, clearly shows a deviation from what it has been seen before.

Therefore, the match has to be further analyzed for anomaly detection. Since the signature is repetitive among different samples, dimensionality reduction techniques can reduce the number of parameters that are needed to represent the signature from thousands (that is the number of the pixels to represent each signature) to a small quantity of numbers. In this work, principal component analysis is performed for reducing the dimensionality of the samples.

Since the number of training profiles is limited, it is needed to produce more training examples from existing videos. This is achieved in two steps: 1- shifting the profile line (Fig. 3) off axis, 2- shifting the signature in time, i.e. shifting the area of interest in Fig. 4 to right and/or left. This way, about 120 signatures are created from each video resulting in about 1600 total training signatures each consisted of 3600 pixels. Producing these extra samples by such shifts is reasonable, since they can be physically observed due to fluctuations in measurement or the process. Fig. 7 shows first, second, and 50<sup>th</sup> PC. As it is clear from the figure, the first components can capture the main features of the signatures; while higher order components contain more noise like features that are of less importance.

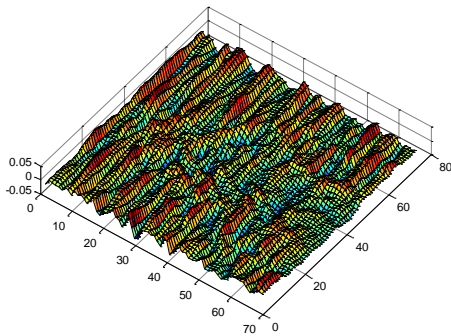
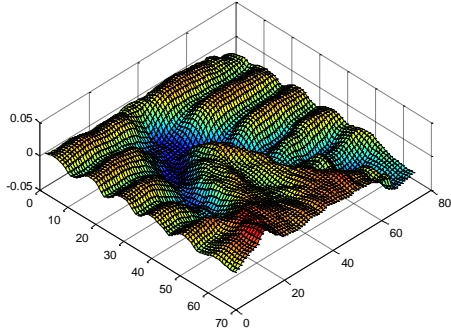
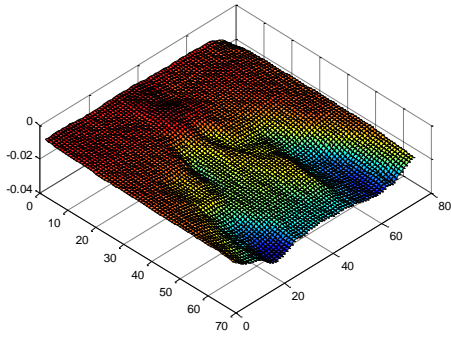


Fig. 7. First, second and 50<sup>th</sup> PC of the training signatures

After training and during the production process, any time a part is produced the video segment containing the rolling process is evaluated for detecting anomaly. The operations in this stage are performed using the results of the principal component analysis. The evaluation profile (presented initially as a vector of pixel values) is projected along the vectors of PCs and the resulting coefficients ( $x_i$ ) are used to calculate deviation (eq. 5). The variance of the training data set along the  $n$ th PC as  $n$  increases monotonically decreases (Fig. 8).

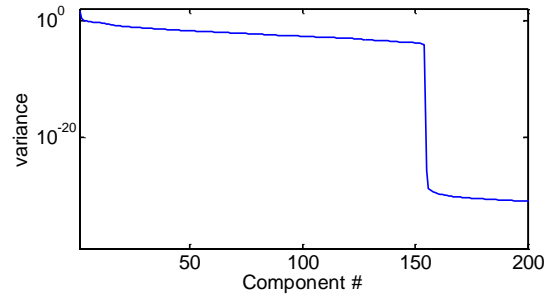


Fig. 8. Variance of the first 200 PCs

In order to avoid numerical errors due to division to very small numbers in eq. 5, deviation will be calculated using the first 150 PCs. Based on the deviation values calculated for the samples that are known to be good samples, a threshold is defined. The samples with a deviation above the threshold will be flagged as abnormal.

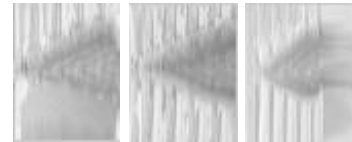
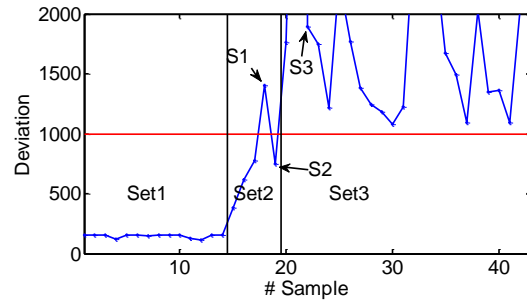


Fig. 9. (Up) the value of deviation measure calculated for 3 sets of data. Set1, set2, and set3 correspond to training set, evaluation set produced with the same rolling parameters, and the evaluation set produced with a different (abnormal) rolling parameter (that is faster rolling speed). The threshold is plotted in red. (Down) from left to right are the samples labeled in the plot as S1, S2, and S3. High deviation values are correctly calculated for S1 and S3

Figure 9 shows the result of the calculations on three different sets. Set 1, contains the training data (without previously mentioned shifts in space and time), set 2 is an evaluation set produced with the same rolling condition as for the training set, and set 3 is a set of samples produced with an abnormal rolling speed. As it is clear from the results all the samples that are

produced by an abnormal parameter, have a deviation value higher than normal samples, except the sample labeled as S1, that as it is clear from the image contains abnormalities in the signature. Based on this plot a threshold value of 1000 seems to be a reasonable value for threshold (Fig. 9, red line).

## Conclusion

Finite difference simulations and a machine learning method were used to set up an automated quality control system for cross wedge rolling process. Machine learning algorithm utilizes template matching, PCA and anomaly detection methods. Principal components analysis effectively reduced the number of presentation parameters to a small and more meaningful set of coefficients. In evaluation stage, a sample is flagged as abnormal if the projection of it on PCs results in coefficients that are unexpected compared to the distribution of the coefficients of the training set. The analysis could robustly distinguish between normal and abnormal samples.

The use of general tools such as thermography and mathematical models like template matching and PCA makes this method easily

adoptable for various production processes that consist of a repetitive task producing a thermal signature

## References

1. CaForm is a project funded in the European Union's Seventh Framework Program (2007-2013), [www.covaform.eu](http://www.covaform.eu).
2. Physical properties of 34Cr4: density=7850kg/m<sup>3</sup>, thermal conductivity=43, 1W/m/K, heat capacity=460J/kg/K, <http://www.metalravne.com/steelselector/steels/VC130.html>
3. T. Blohm, M. Stonis, B. –A. Behrens: Flat cross-wedge rolling for preforming reduced-flash forgings. In: FORGING magazine, Penton Publication, vol. 24 (2014), no. 4, pp. 16-18.
4. G.Traxler, J.Klärner, G.Huelble-Koenigsberger, „Broken Roll detection, application, algorithm and its basic principles of sensing”, Electronic Imaging 16-20 Jan. 2005, San Jose CA-USA, SPIE Vol. 5679-17
5. J.P. Lewis, Fast Template Matching, Vision Interface 95, Canadian Image Processing and Pattern Recognition Society, Quebec City, Canada, May 15-19, 1995, p. 120-123.
6. Haralick, Robert M., and Linda G. Shapiro, Computer and Robot Vision, Volume II, Addison-Wesley, 1992, pp. 316-317.
7. V. Barnett, T. Lewis, Outliers in statistical data. 3rd ed, Wiley, 1994.

# Infrared and Vibration Based Bearing Fault Detection Using Neural Networks

O. Janssens<sup>1</sup>, L. Verledens, R. Schulz<sup>2</sup>, V. Ongenaes<sup>3</sup>,  
K. Stockman<sup>2</sup>, M. Loccufier<sup>2</sup>, R. Van de Walle<sup>1</sup>, S. Van Hoecke<sup>1</sup>

<sup>1</sup> MMLab, Department of Electronics and Information Systems, Ghent University-iMinds

<sup>2</sup> SYSTeMS, Department of Electrical Energy, Systems and Automation, Ghent University

<sup>3</sup> IBCN, INTEC, Ghent University-iMinds

In this paper, a fault detection system is proposed which uses thermal imaging, additional to vibration analysis, for bearing fault detection. Eight conditions/faults are tested, and for each one of them, several recordings are made using different bearings to ensure generalization of the fault-detection system. Features are extracted from the vibration signals and used as input for a random forest classifier and a support vector machine. To deal with infrared images, the system uses neural networks to learn from the raw pixel values. At last, the different classifiers are combined, resulting in a system that is able to detect the different conditions with an accuracy of 97.5 %.

## Introduction

To avoid costs, machines generally operate non-stop. Therefore, if a non-disruptive fault occurs, repairs are not always directly performed. By not knowing the details of the damage, such as affected components and severity, efficient counter-measures can not be taken. Consequently, future corrective maintenance can be more expensive as the costs for repairing/replacing broken components, as well as the cost due to down time, may escalate. As a result, failure prevention has become critical regarding maintenance decisions. To reduce costs and downtime, predictive maintenance can be used which employs condition monitoring (CM) to detect faults and predict failures.

CM is done by monitoring signals, generated by a machine, using a combination of sensors. By monitoring these signals, different conditions can be identified, such as bearing damage, weight imbalance, misalignment and lubricant contamination. For example by using vibration analysis, several types of bearing faults and machine conditions can be detected, such as raceway faults, rolling-element faults and cage-faults. However,

smearing faults are much harder to detect as they do not result in a new cyclic frequency, opposed to the aforementioned bearing faults [1]. To improve automated CM, additional signals need to be considered such as temperature. As thermographic patterns differ depending on the machine's condition, infrared (IR) imaging is a suitable candidate sensor.

This research focuses on automated bearing fault detection using IR imaging in combination with vibration analysis. Next, related literature is discussed which highlights IR based fault detection for rotating machinery. Afterwards, our fault detection system is discussed. Finally, the results are presented together with the conclusions.

## Related literature

Previous work on automatic IR based CM focuses on the detection of shaft misalignment, bearing looseness, rotor imbalance and general bearing faults. To detect these conditions, image processing and machine learning algorithms are used after one another. Often, a first step of the image processing pipeline will consist of extracting a region of interest (ROI). This can be done manually or via an algorithm such as Otsu thresholding [2] or watershed-based algorithms [3]. When the ROI is segmented, the image can be enhanced to reveal

interesting features [4]. From this (enhanced) ROI, features are extracted such as the standard deviation, mean, skewness, kurtosis, variance, entropy, energy, central moments, maximum and minimum [2]. It is also possible to extract features from the histogram [4, 5] or from the discrete wavelet decomposition of the thermal image [7, 8]. It is also common to either remove or fuse indiscriminating features to create better features using principle component analysis [3], independent component analysis [5], discriminant analysis [4] or relief algorithm [7, 8]. The resulting features are used to classify the condition of the rotating machine. Used classification algorithms are: support vector machine [5, 6], relevance vector machine [4], self-organizing map [2] or linear discriminant analysis [7, 8]. Most of these previous approaches will result in a system that can detect the machine's condition with an accuracy of 74 % up to 100 % [2] - [8]. Nevertheless, the methods have often been trained and tested on IR images of the same bearing, therefore not ensuring generalization of the system. Furthermore, the faulty and healthy conditions researched up until now are also easily detectable using vibration analysis, resulting in no added value of using an IR imaging sensor.

Within our approach, five different bearings were tested for every condition, and new types of faults have been classified.

### Test-setup

The dataset created for the experiments is generated using the set-up depicted in Fig 1. With this setup eight conditions are created. The first condition consists of a healthy bearing using the required amount of lubricant and a grease reservoir. The second condition consists of a healthy bearing where the lubricant is diluted and for which no grease reservoir is present. The third condition is similar to the second condition, but the lubricant is further diluted. The fourth condition is the same as the first condition, but an outer-raceway fault is mechanically

introduced by adding three thin shallow grooves to the raceway. The last four conditions are the same as the first four, but imbalance is created by adding a 13 gram bolt to the outer disk at a radius of 5.4 cm. Note that only the condition of the right bearing is modified.

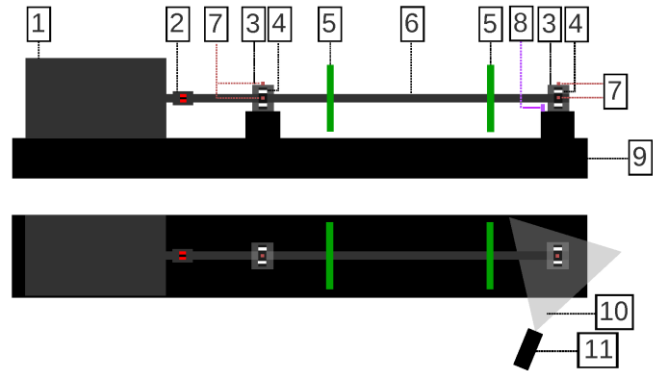


Fig. 16. Side-view and top-view of the set-up. Labels: 1. servo-motor; 2. coupling; 3. bearing housing; 4. bearing; 5. disk; 6. shaft; 7. accelerometer; 8. thermocouple; 9. metal plate; 10. field of view; 11. camera

For every condition five bearings were tested during one hour, while the thermal camera was capturing. An example of a thermal image can be seen in Fig. 2. Also, accelerometers were used to capture the first and last 10 minutes of the vibration signals. More information about the setup and dataset can be found in [11].



Fig. 17. Example of a thermal image of the bearing housing

## Feature extraction

Neural networks are used to learn new, good features for the IR recordings. For the vibration signals, hand-crafted, state-of-the-art features are created.

**IR:** To classify the IR records, per recording 500 samples are extracted. Each sample contains three time series, and every time series has 225 time steps. This results in a design matrix per recording with the following dimensions: [500 x 675]. Each time serie is in fact a single pixel which is tracked throughout the video. The relevant pixels to track are those contained in two ROIs extracted by Gaussian mixture-based background/foreground segmentation [12]. An example of the segmentation results can be seen in Fig. 3. As can be seen, the seal and the top of the housing are segmented. Since there are 500 samples, and per sample there are 3 pixels being tracked for 225 time steps, there are in fact 1500 pixels tracked in a single recording.

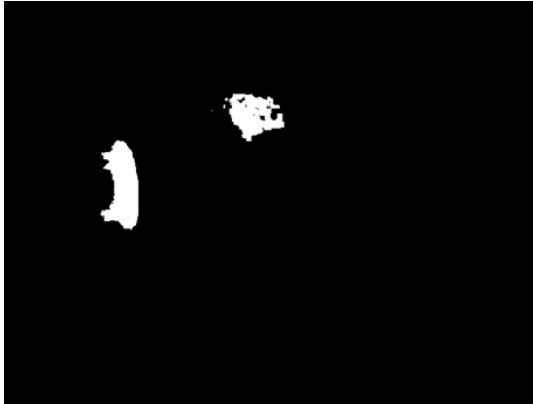


Fig. 18. Segmented seal and housing top

**Vibration:** From the vibration measurements, the amplitude at the rotation frequency (25 Hz) is extracted as it is indicative of imbalance [9]. This amplitude is extracted from the frequency spectrum after applying a moving average filter using a 10 second window with 50% overlap. Furthermore, the kurtosis and peak values are also extracted as they are indicative of bearing damage [10].

## Classification

Both IR and vibration features are used in the classification system shown in Fig. 4. In this architecture, conditions are isolated one at a time. E.g. in step 1, a classification system is trained to distinguish between MILB (-IM) and the other conditions. Afterwards the samples are accordingly separated.

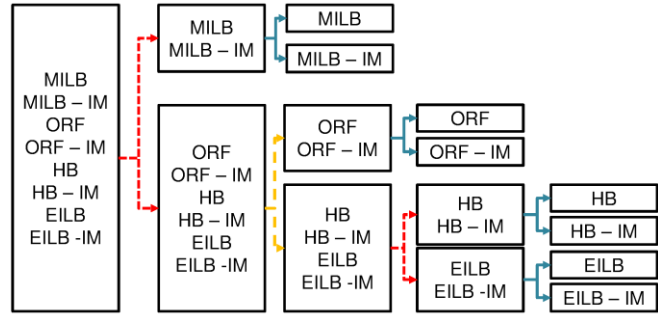


Fig. 19. Architecture of the classification system

In the proposed system three classification techniques are used. The first one is a neural network (NN) classifier (represented as a red dashed line in Fig 4.). This NN uses the infrared data described above. The neural network has 675 input neurons which are connected to a hidden layer consisting of 325 neurons. This hidden layer is connected to another hidden layer which has 40 neurons. Finally, the last hidden layer is connected to an output layer which contains 2 neurons.

The neurons in the output layer use the softmax activation function as it outputs the class probability, and the remaining neurons use rectified linear activation functions (ReLU). The use of ReLus reduces the training time and allows for deeper networks to be used, enabling more abstract representations of the data to be learned [13]. Additionally, drop-out is also used during training to reduce overfitting. The training itself is done using stochastic gradient descent with momentum in combination with simulated annealing. As the neural network uses raw pixel values, which span the entire video sequence, the neural network learns features from spatio-temporal information.

The second classifier is a random forest (represented as a yellow dashed line in Fig. 4). The random forest consists of 10 decision trees and uses the kurtosis and peak features extracted from the



vibration data. The third classifier is a support vector machine which uses a third degree polynomial kernel (represented as a blue line in Fig 4.). This classifier uses the amplitude at the rotation frequency to distinguish between the balance and imbalance conditions. The presented architecture and classification algorithms were experimentally determined to be optimal.

### Validation procedure

In order to validate the system, hold-one-bearing-out cross-validation is used. This means that the system is trained on the data gathered from four bearings, and afterwards tested on the unseen data from one bearing. This is done five times so that every bearing is tested once.

### Results

To quantify the results, the accuracy, recall, precision and f1-score are calculated. These metrics are shown in Table 1.

Accuracy	Precision	Recall	F1-score
97.5 % ( $\sigma = 5.6\%$ )	96.3 % ( $\sigma = 8.4\%$ )	97.5 % ( $\sigma = 5.6\%$ )	96.8 % ( $\sigma = 7.5\%$ )

Table 7: Classification results

From this table it can be concluded that the system can classify the condition of the unseen bearings almost perfectly. The system is only mistaken regarding one bearing condition, which can possibly be attributed to the recording procedure.

### Conclusion

In this paper an infrared and vibration based fault detection system is proposed. By combining neural networks on infrared images with vibration analysis, it is shown that several types of bearing faults/conditions can be detected.

### References

1. P. Boškosi, J. Petrovčič, B. Musizza and Đ Juričić, Detection of lubrication starved bearings in electrical motors by means of vibration analysis, *Tribology International*, Vol. 43, N. 9, pp. 1683 – 1692, 2010
2. A. Widodo, D. Satrijo, T. Prahasto, Toni, G. Lim, B-K, Choi, Confirmation of Thermal Images and Vibration Signals for Intelligent Machine Fault Diagnostics, *International Journal of Rotating Machinery*, pp. 1-10, 2012
3. H. Fandino-Toro, O. Cardona-Morales, and J. Garcia - Alvarez, G. Castellanos-Dominguez, Bearing Fault Identification using Watershed-Based Thresholding Method, *Advances in Condition Monitoring of Machinery in Non-Stationary Operations*, pp. 137-147, 2014.
4. V. T. Tran, B. Yang, F. Gu, A. Ball, Thermal image enhancement using bi-dimensional empirical mode decomposition in combination with relevance vector machine for rotating machinery fault diagnosis, *Mechanical Systems and Signal Processing*, Vol. 38, N. 2, pp. 601-614, 2013
5. G. Lim, Y. Ali, and B. Yang, The Fault Diagnosis and Monitoring of Rotating Machines by Thermography, *Engineering Asset Management and Infrastructure Sustainability*, pp. 557-565, 2012
6. G. Lim, D. Bae, J. Kim, Fault diagnosis of rotating machine by thermography method on support vector machine, *Journal of Mechanical Science and Technology*, Vol. 28, N. 8, pp. 2948–2952, 2014
7. A. Younus, B. Yang, Wavelet co-efficient of thermal image analysis for machine fault diagnosis, *International Conference on Mechanical Engineering*, pp. 1–7, 2009
8. A. Younus, B. Yang, Intelligent fault diagnosis of rotating machinery using infrared thermal image, *Expert Systems with Applications*, Vol. 39, pp. 2082–209, 2012
9. M. Monte, F. Verbelen, B. Vervisch, The use of orbitals and full spectra to identify misalignment, *IMAC XXXII*, Springer International Publishing, pp. 215–222, 2014
10. R.B.W Heng and M.J.M. Nor, Statistical analysis of sound and vibration signals for monitoring rolling element bearing condition, *Applied Acoustics*, vol. 53, N. 3, pp 211 – 226, 1998
11. O. Janssens, R. Schulz, V. Slavkovikj, K. Stockman, M. Loccufier, R. Van de Walle, S. Van Hoecke, Thermal Image based Fault Diagnosis for Rotating Machinery, submitted to *Infrared Physics & Technology*, 2015
12. Z. Zivkovic. Improved adaptive gaussian mixture model for background subtraction, *ICPR 2004*, vol. 2, pp. 28–31, 2004.
13. G.E. Dahl, T.N. Sainath, and G.E. Hinton. Improving deep neural networks for lvcsr using rectified linear units and dropout, *Acoustics, International Conference on Speech and Signal Processing* pp. 8609–8613, 2013

# CHARACTERIZATION OF TERAHERTZ PENETRATION AND APPLICATIONS FOR COMPOSITE MATERIALS

K.H. Im<sup>1</sup>, J.W. Park<sup>2</sup>, I. Y. Yang<sup>3</sup>, S.K. Kim<sup>4</sup>, J. A. Jung<sup>5</sup>, D.K. Hsu<sup>6</sup>

<sup>1</sup>Department of Automotive Eng., Woosuk University, 490 Hujung-ri, Samrae-up, Wanju-kun, Jeonbuk, Korea, 565-701 and khim@woosuk.ac.kr

<sup>2</sup>Dept. of Naval Architecture and Ocean Eng., Chosun University, Gwangju 501-759, Korea and jwpark@chosun.ac.kr

<sup>3</sup>Dept. of Mechanical Design Eng., Chosun University, Gwangju, Korea, 501-759, mailing and iyyang@chosun.ac.kr

<sup>4</sup>Division of Mech. System Eng., Chonbuk Natl. University, Jeonju, Jeonbuk, 561-756, Korea sunkkim@chonbuk.ac.kr

<sup>5</sup>Dept. of Mechanical and Auto. Engineering, Songwon University, Gwangju 501-210, Korea and jungja@songwon.ac.kr

<sup>6</sup>Center for Nondestructive Evaluation, Iowa State University, Ames, Iowa 50011, USA and dkhsu@iastate.edu

Terahertz waves (T-ray) for the nondestructive evaluation was investigated on composite materials. The T-ray signals in the Terahertz time domain spectroscopy(TDS) mode is similar to that of ultrasonics; however, unlike the conventional ultrasound, the T-ray pulse can detect impact damages on the composites. In carbon composites the penetration of T-ray waves was investigated in order to measure the painting thickness, which are strongly affected by the angle between the electric field vector of the terahertz waves and the intervening fiber directions. Intensive characterization of T-ray for the for nondestructive evaluation (NDE) of carbon composite reinforced plastics (CFRP) composites is being discussed on E-field influence with a couple of cured and uncured CFRP plies.

## Introduction

Terahertz time domain spectroscopy (TDz-TDS) is an important noninvasive and accurate detection of defects and impact damages in composites. The TDS is based on the generation of a few cycle terahertz pulses using a femtosecond laser that excites a photoconductive antenna. Sub-picosecond bursts of THz radiation are generated and can be subsequently detected with high signal to noise ratio. With the emitted power distributed over several T-rays, a very broad bandwidth is spanned [1-5].

Due to a wide range of applications and the simplicity of the technique, THz-TDS has the potential to be the first T-ray imaging system which is portable, compact, and reliable enough for practical application. These advances have led to the development of the commercial T-ray imaging spectrometers [2].

Despite the promise of T-rays for nondestructive evaluation (NDE) of materials, there have not been too many reports on their use in materials evaluation and structural testing. T-rays can readily penetrate considerable thickness of dielectric materials and hence; non-conducting polymer composites can be inspected using T-ray. In this work, the use of T-rays has been

investigated as an NDE tool for detecting and characterizing flaws and damage in non-conducting composites. The degree of penetration of T-rays in carbon reinforced resin composites is a function of fiber orientation, and the relationship is studied quantitatively. The degree of penetration is defined based on the angle of function between the carbon fiber direction and the E-field direction of T-ray. In order to define the characterization of E-field direction, intensive experimentations were performed using a couple of cured and uncured CFRP plies with 0 and 90 degrees.

For a convenient and reliable techniques needed for the measurement of paint thickness on composites, it is important to control the paint thickness because of the large surface area, and hence the substantial weight, of the paint on an airplane. The painting thickness on the composites were measured by the T-ray techniques.

### Measuring refractive index

Fig. 1 shows a diagram showing the geometry of the reflection mode and the propagation direction of terahertz wave signal. This method is inducing the refractive index by transmission mode at time domain of terahertz wave through media of test specimen and air. In this setup, by obtaining respective TOF through measurement of the time required for T-ray to reach pulse receiver from the pulse emitter without test specimen and the time when refracted by test specimen of certain thickness, the refractive index can be obtained [4].

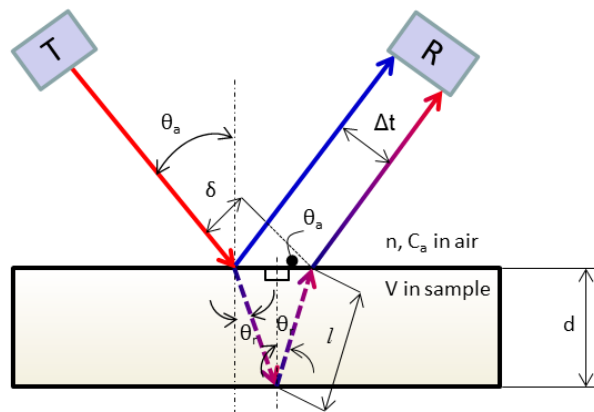


Fig. 1 Diagram showing the geometry of the reflection mode

Resonance frequency,  $\Delta f$  is obtained based on considering geometry time delay and oblique T-ray trace length below;

$$\Delta f = 1/\Delta t \quad (1)$$

### T-ray system

A schematic of terahertz time-domain spectroscopy system (THz-TDS) was being utilized for the nondestructive test system. The terahertz instrumentation systems used in this research were provided by TeraView Limited. The instrumentation includes a time domain spectroscopy (TDS) pulsed system and a frequency domain continuous wave (CW) system.

The TDS system has a frequency range of 50GHz – 4 THz and a fast delay line up to 300ps. The beam is focused to focal lengths of 50 mm and 150 mm and the full width at half maximum (FWHM) beam widths are 0.8mm and 2.5mm respectively.

### Evaluation of E-field directions

Terahertz wave has certain limitation in its transmissivity in electrically conductive materials unlike non-conductive materials. Experimentally, we have measured the angular dependence of the power transmission through a 3-ply laminate of cured/uncured unidirectional carbon composite laminate using the CW terahertz system. The angular dependence of the transmitted power at 0.1 THz is shown in Fig. 2. Therefore, we had to study comparatively whether it may be applicable for carbon fiber and glass fiber as well. Particularly, the carbon fiber reinforced plastics (CFRP) is composed of electrically conductive carbon fiber and non-conductive matrix. According to the existing references, it is said that the electrical conductivity in radial direction of the carbon

fiber is approximately 3 times bigger than that in axial direction. CFRP composites is composed of uni-directional fibers and its lamination is made in many different methods, which affects the electrical conductivity. Particularly, the lateral (vertical to fiber axis) generation mechanism of the conductivity depends on the fiber contacts between contiguous fibers. Therefore, the experiment was conducted in terahertz transmission mode as shown in Fig.2. In Fig.2 (a) and (b), it was studied about the transmission in E-fields  $90^\circ$  and  $0^\circ$  to the fiber direction of CFRP composite laminates. Because of the highly anisotropic electrical conductivity ( $\sigma_l \gg \sigma_t$ ), the penetration of terahertz waves through a unidirectional carbon composite depends on the relative angle between the electrical field vector and the fiber axis [4]. Where the directions of E-field and fiber coincides (case of (b)  $0^\circ$ ), the receiving signal of terahertz wave could not be seen since the fiber hinders the terahertz wave travel as shown in the cases of cured and uncured samples.

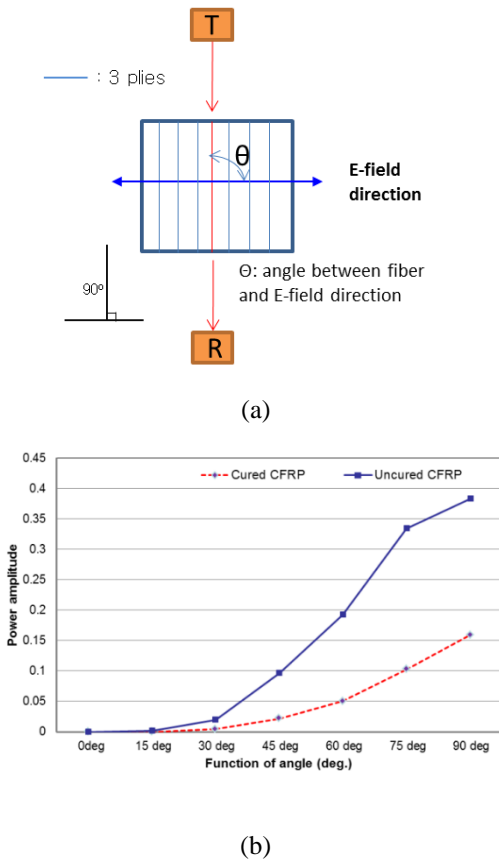


Fig.2 Angular dependence of transmitted power of THz terahertz waves through (a) setup for T-ray testing and (b) a 3-ply

laminates of cured/uncured unidirectional carbon composite laminate

### Painting thickness

The simplest thickness measurement using T-ray is a reflection mode time-of-flight measurement. A CFRP plate for a use of airplane was scanned using T-ray system as shown in Fig. 3. Also, Fig. 3 shows a A-scan and FFT images respectively. Notice that a T-ray time domain data in Fig. 3(a) seemed to show peaks with a regular spacing (see a  $\Delta t$ ). We estimated in the lab and found that the value of delta-t ( $\Delta t = 2\text{ps}$ ) seemed to be consistent with a ply thickness as shown in Fig. 3. One thing was done for a FFT on the data and resonance frequency ( $\Delta f = 0.5\text{THz}$ ) was obtained as shown in Fig.3 (b), which was obvious with the close relation between TOF and FFT. This does prove that there are reflections or echoes at the ply interfaces in the CFRP plate due to the regularly spaced peaks.

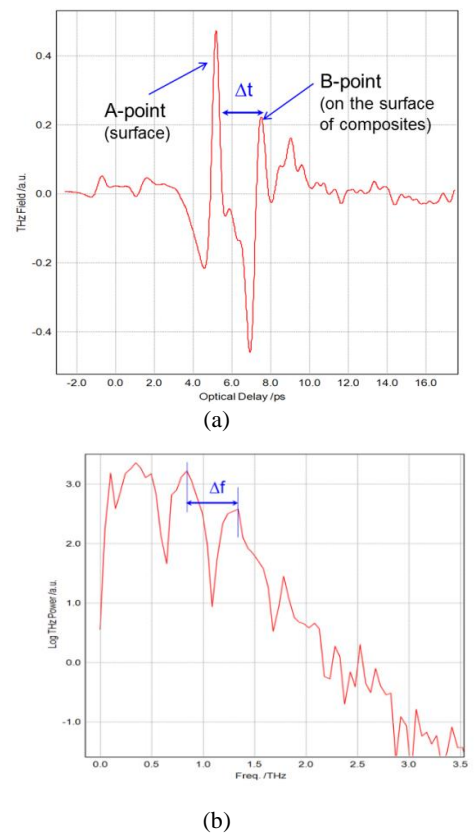


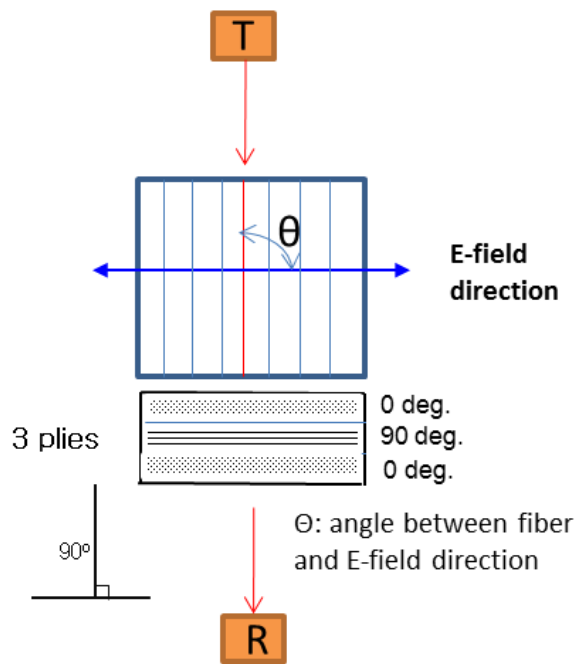
Fig.3 Measurement method of painting thickness based on (a) time-of-flight and (b) resonance frequency methods

## Penetration of orthotropic carbon composite

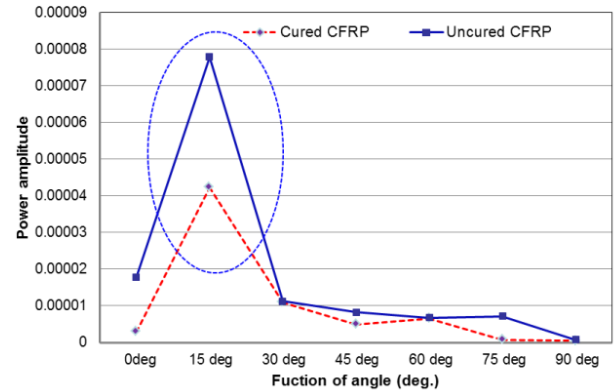
Based on the electrical conductivity in carbon composites, the penetration ability of orthotropic configuration in a carbon composite laminate was investigated. The layup configuration is [0/90/0].

Fig.4 shows T-ray set up testing (a) and angular dependence (b) of transmitted power of THz terahertz waves through a 3-ply laminate [0/90/90] in cured/uncured unidirectional carbon composite laminate.

The fiber orientations in the first ply of the laminate was  $0^\circ$ . Using TDS terahertz waves in the through-transmission mode, the power amplitude was obtained. It was found that only higher power amplitude generated at around  $15^\circ$  as shown in Fig.4(b) because the T-ray could penetrate the CFRP sample based on best combination for scan testing.



(a)



(b)

Fig.4 T-ray Testing configuration (a) and angular dependence (b) of transmitted power of THz terahertz waves through a 3-ply

## Conclusions

It was found that the degree of penetration depended on the orientation of the electric field vector with respect to the carbon fiber axis. Examination of T-ray power amplitude in the T-ray could be predicted based on combined conductivity of the two plies for qualitative agreement with the experimental results. Also, a convenient and reliable technique is needed for the measurement of paint thickness on composites.

## Acknowledgment

This research was supported by Basic Science Research Program through the National Research Foundation of Korea (NRF) funded by the Ministry of Education, Science and Technology (No. 2015R1D1A3A01016775)

## References

1. B. Christian , G. Mac B. A. Peter, B. Thomas , H. Per and C. Kasper, "Wind tunnel test on airfoil Risø-B1-18 with an Active Trailing Edge Flap," Wind Energy, Vol. 13, pp.207-210, 2010.
2. J. V. Rudd, and D. M. Mittleman, "Influence of Substrate-Lens Design in Terahertz Time-Domain

- Spectroscopy," J. Opt. Soc. Amer. B, Vol. 19, No. 2, pp. 319-329, 2000.
3. I. S. Gregory, C. Baker, W. R. Tribe, I. V. Bradley, M. J. Evans, E. H. Linfield, A. G. Davies, and M. Missous, "Optimization of Photomixers and Antennas for Continuous-Wave Terahertz Emission," IEEE Journal of Quantum Electronics, Vol. 41, No. 5, pp. 717-728, 2005.
  4. K. H Im, K.S. Lee, I. Y. Yang, Y. J. Yang, Y. H. Seo and D. K. Hsu, " Advanced T-ray Nondestructive Evaluation of Defects in FRP Solid Composites", International Journal of Precision Engineering and Manufacturing, Vol. 14, No. 6, pp. 1093-1098, 2013
  5. R. Huber, A. Brodschelm, A. Tauser and A. Leitenstorfer, A., "Generation and Field-Resolved Detection of Femtosecond Electromagnetic Pulses Tunable up to 41 THz," Appl. Phys. Lett., Vol. 76, pp. 3191-3199, 2000.



# NONDESTRUCTIVE DETECTION OF CORROSION DAMAGE UNDER CORROSION PROTECTION COATING USING INFRARED THERMOGRAPHY AND TERAHERTZ IMAGING

T. Sakagami<sup>1</sup>, D. Shiozawa<sup>2</sup>, Y. Tamaki<sup>2</sup>, H. Ito<sup>2</sup>, A. Moriguchi<sup>2</sup>, T. Iwama<sup>2</sup>  
K. Sekine<sup>3</sup>, T. Shiomi<sup>4</sup>

<sup>1</sup> Dept. of Mechanical Engineering, Kobe University,  
1-1 Rokkodai, Nada, Kobe 657-8501 Japan  
sakagami@mech.kobe-u.ac.jp

<sup>2</sup> Dept. of Mechanical Engineering, Kobe University

<sup>3</sup> High Pressure Institute of Japan

<sup>4</sup> Japan Oil, Gas and Metals National Corporation

Nondestructive testing (NDT) techniques using pulse heating infrared thermography and terahertz (THz) imaging were developed for detecting deterioration of oil tank floor, such as blister and delamination of corrosion protection coating, or corrosion of the bottom steel plate under coating. Experimental studies were conducted to demonstrate the practicability of developed techniques. It was found that the pulse heating infrared thermography was utilized for effective screening inspection and THz-TDS imaging technique performed well for the detailed inspection of coating deterioration and steel corrosion.

## Introduction

Large-scale 110,000kl class oil storage tanks have been using for crude oil stockpiling. For the maintenance of crude oil storage tanks, integrity evaluation against corrosion in the bottom steel plate is one of the very important issues. Surface of the bottom steel plate is protected by corrosion protection paint coating. However, due to the deterioration of corrosion protection paint by water soaking in long- standing use, steel plates have corrosion problems. Large-scale oil tanks must be inspected every 10 years under the fire laws in Japan. During shut-down maintenance program, deterioration condition of bottom steel plate and corrosion protection paint is inspected by visual testing technique. Visible blisters in paint coating due to the corrosion of bottom steel plate or cohesive failure of paint coating are detected by the skillful inspectors, and the condition of the bottom steel plate is evaluated by paint removing destructive test. However this inspection process requires much time, cost and labor. In addition, it is important in the high-quality integrity evaluation of tank floor to detect invisible deterioration in the coating and bottom steel plate. To solve this

problem, development of effective and reliable NDT techniques is essential.

In this study, NDT techniques using pulse heating infrared thermography and terahertz time-domain spectroscopy (THz-TDS) imaging were developed for detecting and evaluating deterioration damages of oil tank floor, such as blister and delamination of corrosion protection coating, or corrosion of the tank floor steel plate under corrosion protection coating.

## Pulse heating thermography

NDT techniques based on pulse heating thermography have been developed by many researchers, and they have been applied for many kinds of materials and structures [1]. When pulse heat flux is applied to the test sample with defects, defects can be identified from localized high temperature regions appearing on the objective surface just above the defects. The present authors [2] investigated the feasibility of pulse heating thermography for detecting invisible latent corrosion damages under the paint coating.

Figure 1 shows the pulse thermography system employed for the field test in crude oil storage

tank. High-speed infrared camera with InSb array detector was employed combined with 9600J high-power xenon flash lamps for pulse heat application to the tank floor. Self-reference lock-in data processing [3] was employed to improve signal-to-noise ratio, followed by application of the median filter for spot noise elimination as well as the moving average image binarization for automatic defect identification.

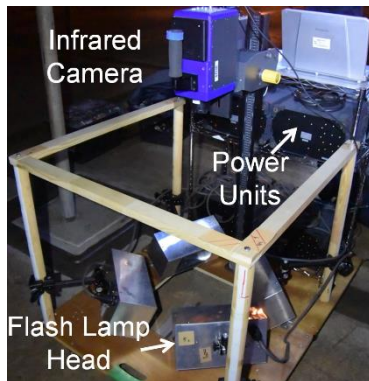


Fig. 1 Pulse thermography system

### THz-TDS imaging

In the previous paper [4], the present authors developed a nondestructive integrity evaluation technique for steel plate coated by corrosion protection paint utilizing transmission property of THz wave for the paint coating. THz wave transmittance was investigated for red rust (iron(III) oxide ( $\text{Fe}_2\text{O}_3$ )) and black rust (iron(II) iron(III) oxide ( $\text{Fe}_3\text{O}_4$ )). Transmittance of THz wave measured for  $420\mu\text{m}$  paint sheet with glass flakes for preventing water soak and  $380\mu\text{m}$  paint sheet without glass flakes is shown in Fig. 2. It is found that transmittance is almost same for both samples under  $0.5\text{THz}$ ; in contrast over  $0.5\text{THz}$ , transmittance of the coating with glass flakes is rapidly decreasing compared with that for coating without glass flakes.

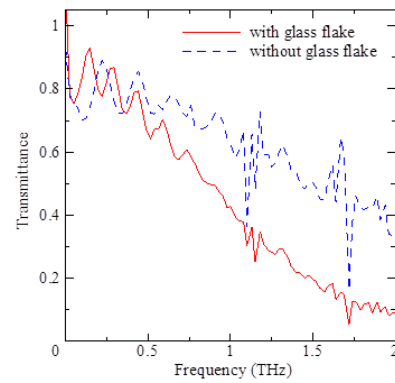


Fig. 2 THz wave transmittance for coating THz imaging of corrosion under paint coating was conducted for steel plate samples with artificial corruptions using THz-TDS system [4]. It was found that B-scope and 3-D tomographic imaging of corrosive materials under coating can be constructed based on time-domain THz wave reflection measurement data (THz pulse-echo method). Frequency-domain THz reflection data were utilized successfully for separate identification of iron(III) oxide and iron(II) iron(III) oxide under the coating based on their spectrum absorption characteristics. Feasibility of the developed NDT technique using THz-TDS was demonstrated by the laboratory test using THz-TDS imaging system installed on the optical bench.

In this study, practicability of the THz-TDS imaging for NDT of tank floor deterioration was investigated using transportable THz-TDS system developed by Pioneer Corporation. Experiment state in the oil tank under shutdown maintenance is shown in Fig. 3. THz wave emitter and receiver were installed in the small blue box mounted on the X-Y scanning stage. Specifications of the employed THz system are shown in Table 1.

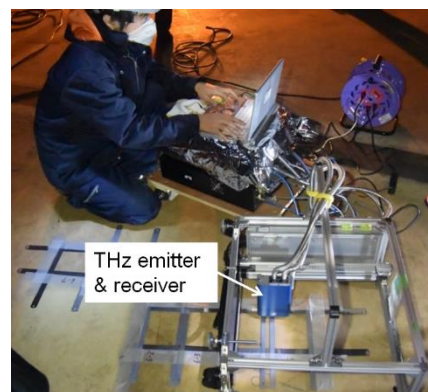


Fig. 3 THz-TDS imaging system

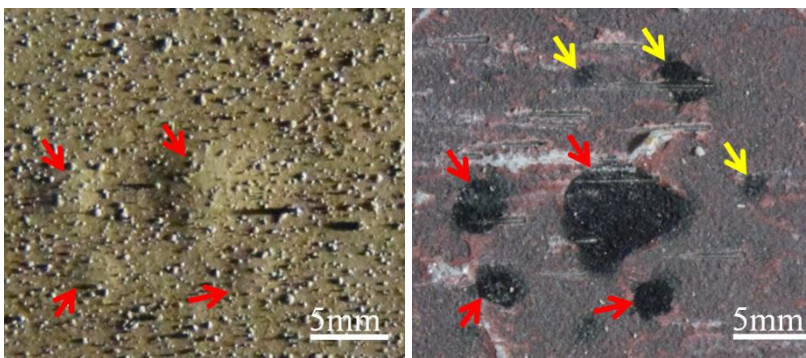
Table 1 Specifications of THz-TDS system

Spectral range	0.1 – 2.0 THz
Dynamic range	55dB
Scanning rate	10 samples/s
Power consumption	70W

### Results of field experiment

Experimental studies were conducted in the oil tank under shutdown maintenance in one of the national oil storage stations in Japan. Test areas were chosen on the tank floor where some blisters were found by visual testing. Each test area had a rectangular shape (140mm×105mm) and was marked by the stainless steel rulers as shown in Fig. 3. NDT by the pulse heating thermography was applied first, followed by data acquisition by the transportable THz-TDS imaging system. After conducting NDT by both techniques, coating was removed to evaluate corrosion condition of the bottom steel plate.

Visible images of the test area taken before and after removing paint coating are shown in Figs. 4(a) and 4(b), respectively. It is found from Fig. 4(b) that the blisters found in paint coating were caused by the occurrence of black rust. Several blisters caused by relatively large black rusts marked by red arrows can be identified visually, however small black rusts indicated by yellow arrows did not make visible blisters. This fact shows that visual testing is insufficient for the detection of early stage corrosions in the bottom steel plate.



(a) Before coating removal (b) After coating removal  
Fig. 4 Visible images of tank floor taken before and after coating removal

### Results of pulse heating thermography

Result of corrosion detection by pulse heating thermography is shown in Fig. 5. This image was generated by the moving average image binarization processing that detected localized high temperature regions in the self-reference lock-in image obtained from sequential infrared data after pulse heating. It is found that black rusts can be clearly identified including early stage corrosions without generating visible blisters on the surface.

### Results of THz-TDS imaging

In the time domain imaging, waveform of THz pulse measured by THz-TDS is utilized to obtain defect structure based on the time of flight information like ultrasonic pulse-echo method. Obtained time domain image is shown in Fig. 6. It is found that almost all black rust corrosions can be detected demonstrating the feasibility of THz-TDS imaging for corrosion detection under paint coating. Further B-scope THz pulse-echo image constructed from THz pulses obtained along the line A-A in Fig. 6 is shown in Fig. 7. Coating layer, corrosion layer and steel plate can be identified in the image. Also thickness of corrosion can be estimated based on the time-delay of THz pulse.

By utilizing frequency spectrums of THz reflection or absorption of the target materials, frequency domain imaging can be conducted for material identification. Corrosion process of

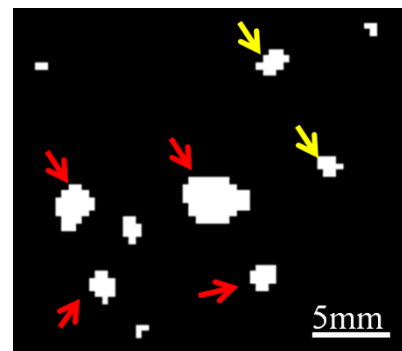
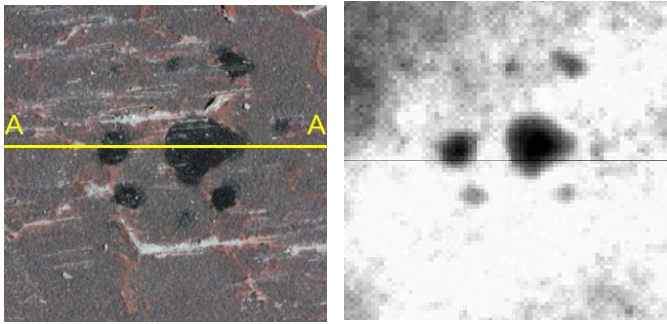


Fig. 5 Corrosion detection by pulse heating thermography



(a) Visible image (b) Time domain image  
 Fig. 6 Result of THz time domain imaging

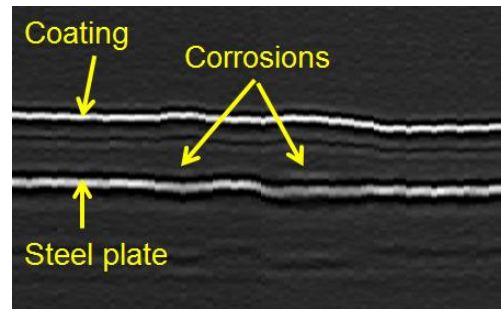


Fig. 7 B-scope THz pulse-echo image

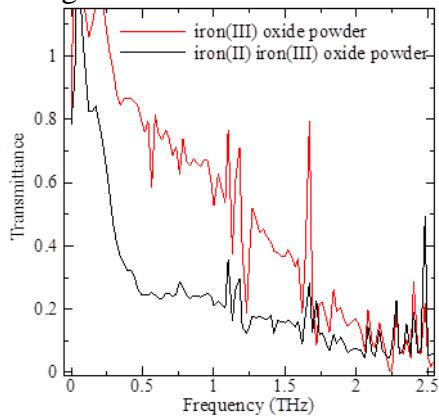
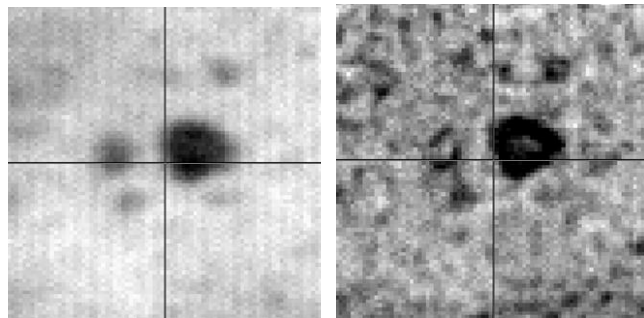


Fig. 8 Transmittance of THz wave for iron (III) oxide and iron (II) iron (III) oxide



(a) 0.33 THz (b) 0.52 THz  
 Fig. 9 Results of THz frequency domain imaging

the bottom steel plate of oil tank is reported as follows. In the begging stage, black rust (iron(II) iron(III) oxide) is formed when soaked water reaches bottom steel plate. Further deterioration of corrosion protection paint initiates paint cracking and oxide is provided into interface between paint and steel plate. Then black rust changes into red rust (iron(III) oxide) by chemical reaction with oxide, and material loss of substrate steel becomes severe. Therefore it is important to separately identify these corrosive materials under protection paint for evaluating corrosion condition of the steel plate. Figure 8 shows spectrum transmittance obtained for iron(II) iron(III) oxide and iron(III) oxide. Transmittance of THz wave for iron(III) oxide is high in low frequency range below 0.5 THz; in contrast, transmittance for iron(II) iron(III) oxide shows rapid decreasing between 0.2THz and 0.5THz. This spectrum absorption characteristic enables us to conduct separate identification of black rust and red rust.

Results of frequency domain imaging obtained at 0.33THz and 0.52THz are shown in Fig. 9. It is found that black rusts (iron (II) iron(III) oxide)

are identified clearly in the frequency domain imaging due to their THz absorption. Corrosion shape becomes sharp in higher frequency; in contrast the image becomes noisy because THz transmittance in paint coating becomes lower for higher frequency.

### Conclusions

In this study, NDT techniques using pulse heating infrared thermography and THz-TDS imaging were developed for detecting and evaluating deterioration damages of oil tank floor. It was found that both NDT techniques can be successfully applied to detect invisible corruptions under paint coating.

### Acknowledgment

The authors would like to acknowledge Mr. Takishita and Mr. Ogasawara of Pioneer Corporation for their supports in using THz-TDS imaging system.

## References

- (1) X. Maldague and S. Marinetti: Pulse phase thermography, *J. Appl. Physics*, Vol. 79, pp.2694-2698, 1996.
- (2) T. Sakagami, S. Kubo, K. Sekine, M. Yamada, K. Nakata, H. Maruyama: Development of a thermographic NDT technique for detection of latent blister in corrosion protective coating on oil storage tank under pulse heating, *SPIE Proceedings* 4360, pp.554-559, 2001.
- (3) T. Sakagami, T. Nishimura and S. Kubo: Development of a self-reference lock-in thermography and its application to crack monitoring. *SPIE Proceedings* 5782, pp.379–387, 2005.
- (4) A. Moriguchi, T. Tanaka, T. Sakagami, M. Hangyo: Nondestructive evaluation of steel plate coated with corrosion protection paint utilizing transmission property of THz wave, *Proc. 13th International Symposium on Nondestructive Characterization of Materials (NDCM-XIII)*, The Open Access NDT Database: [www.ndt.net /id=15538](http://www.ndt.net/id=15538)



# CARBON FIBER COMPOSITES INSPECTION AND DEFECT CHARACTERIZATION USING ACTIVE INFRARED THERMOGRAPHY

H. Fernandes<sup>1</sup>, C. Ibarra-Castanedo<sup>1</sup>, Hai Zhang<sup>1</sup> and X. Maldague<sup>1</sup>

<sup>1</sup>Computer Vision and Systems Laboratory, Laval University, Quebec City (Quebec) G1K 7P4, Canada. E-mail: henrique-coelho.fernandes.1@ulaval.ca

Composite materials are widely used in the industry. One of the reasons is because they have strength and stiffness comparable to metals with the added advantage of significant weight reduction. Infrared thermography (IT) is a safe non-destructive testing (NDT) technique that has a fast inspection rate. In active IT an external heat source is used to stimulate the material being inspected in order to generate a thermal contrast between the feature of interest and the background. In this paper carbon fiber-reinforced polymers (CFRP) are inspected using IT. More specifically, carbon/PEEK (*Polyether ether ketone*) laminates with square *Kapton*<sup>®</sup> inserts of different sizes and at different depths are tested with three different IT techniques: pulsed thermography, vibrothermography and line scan thermography.

## Introduction

The use of composite materials, or composites, in the aeronautic industry has grown in recent years. Manufacturers have expanded the use of composites to the fuselage and wings because composites are typically lighter and more resistant to corrosion than are the metallic materials that have traditionally been used in airplanes. An example of the use of composites in commercial aircrafts is the Boeing 787 whose material mass percentage is composed of more than 50% composites (excluding the engines). This increasing demand motivates the industry to not only develop better and more cost efficient techniques to manufacture these materials but also to develop techniques to inspect and assure the quality of these materials during their lifetime.

In this paper, infrared thermography (IT) is used to detect delaminations (artificial inserts) placed on different layers of a carbon fiber-reinforced polymer (CFRP) flat laminate prior to moulding. The laminate layup is [0<sub>2</sub>/90<sub>2</sub>]<sub>6</sub>, i.e. it has 24 layers where the first two layers have 0° oriented fibers and the third and fourth layers have 90° oriented fibers. A prepreg prior to mould is 0.16 mm

thick and after moulding about 0.13 mm thick. Inserts are made of *Kapton*<sup>®</sup> tape (0.06 mm thick) and have three different sizes: 4 x 4 mm, 3 x 3 mm and 2 x 2 mm. Their positions prior to moulding can be seen in Figure 1.

## Active Thermography

In active thermography an external heat source is required to stimulate the material for inspection generating a thermal contrast between the feature of interest and the background. The active approach is adopted in many cases given that the inspected parts are usually in equilibrium with the surroundings [1].

Three different active IT techniques are used. The first two approaches use optical sources with different scanning modes. The first active approach tested is a static surface scanning inspection in reflection mode: the classical pulsed thermography configuration (PT). The second one is a dynamic line scanning technique where the energy source and camera are in movement with regards to the test sample (LST). The last active IT approach tested uses a mechanical source (ultrasound excitation) to generate heat in the sample being inspected. This last approach is commonly called vibrothermography (VT). Results obtained are quantified and compared. Next we briefly describe



the infrared thermography technique applied in this paper and later present some results.

### **Pulsed thermography (PT)**

In pulsed thermography (PT), the specimen surface is submitted to a heat pulse using a high power source such as photographic flashes. Figure 2 shows a schematic set-up of a PT inspection. A heat pulse can be seen as a combination of several periodic waves at different frequencies and amplitudes. After the thermal front comes into contact with the specimen's surface, heat travels from the surface through the interior of the specimen by conduction. As time elapses, the surface temperature will decrease uniformly for a sound area. On the other hand, subsurface flaws (e.g. cracks, delaminations, porosity, disbonds, inclusions, etc.) can be considered as barriers to heat flow, which produce abnormal temperature patterns on the surface of the sample. This abnormal temperature distribution can be detected with an infrared camera.

### **Line scanning thermography (LST)**

Line scan thermography (LST) is a dynamic active thermography technique, which can be employed for the inspection of materials by heating a component, line-by-line, while acquiring a series of thermograms with an infrared camera. This can be done in two ways, either the thermographic head, consisting of an infrared camera and an energy source, moves along the surface while the part is motionless [2], or it may be the component that is in motion while the thermographic head stands still [3]. In both cases, the thermal history for every pixel or line of pixels can be precisely tracked by controlling the heating source speed and the rate of data acquisition. In the original acquisition sequence the inspected sample appears to be moving so the sequence must be reconstructed in order to have the variation on time and not on space. The reconstructed matrix is obtained by following the temporal

evolution of every pixel line independently, in such a way that, a given pixel line of the original sequence is recovered frame by frame (through time) and reallocated into a new sequence of images. Figure 3 shows a possible set-up for a LST inspection. In Figure 3 the thermographic head is composed of an infrared camera and a heat source. The thermographic head moves in one sense (top to bottom) covering the entire surface of the sample to be inspected while the latter remains motionless.

### **Vibrothermography (VT)**

Vibrothermography (VT), also known as ultrasound thermography, utilizes mechanical waves to directly stimulate internal defects, contrary to optical methods (e.g. PT an LST), which heat the surface of the material. Figure 4 shows a schematic set-up of a VT inspection. The mechanical waves injected into the specimen travel through the material and dissipate their energy mostly at the defects' interface, thus heat is locally released [4]. Heating is generated via three mechanisms: frictional rubbing, plastic deformations and viscoelastic losses. The thermal waves then travel by conduction to the surface where they can be detected with an IR camera.

VT is extremely fast, although it is necessary to relocate the transducer (and to immobilize the specimen again) to cover a large area for inspection. Hence, VT is more suitable for relatively small objects. It is the most appropriate technique to inspect some types of defects, e.g. micro cracks. On the contrary, it does not perform very well in some other cases in which application of optical techniques are straightforward, e.g. water detection. Nonetheless, probably the most inconvenient aspect of VT is the need of holding the specimen. On the other hand, there is only minimal heating of the inspected specimen since energy is usually dissipated mostly at the defective areas, although there is some localized heating at the coupling and clamping points.

## Infrared Image Processing

### Principal Component Thermography (PCT)

In principal component thermography (PCT) [5], the data sequence is decomposed into a set of orthogonal statistical modes (known as Empirical Orthogonal Functions or EOFs) obtained through Singular Value Decomposition (SVD). The most meaningful information is placed in the firsts EOF images.

The SVD of a  $M \times N$  matrix  $A$ , where  $M > N$ , can be calculated as follows:

$$A = URV^T \quad (1)$$

where  $U$  is a  $M \times N$  orthogonal matrix,  $R$  being a diagonal  $N \times N$  matrix (with singular values of  $A$  present in the diagonal),  $V^T$  is the transpose of a  $N \times N$  orthogonal matrix (characteristic time) as proposed by Rajic in [5].

Hence, in order to apply the SVD to thermographic data, the 3D thermogram matrix representing time and spatial variations has to be reorganised as a 2D  $M \times N$  matrix  $A$ . This can be done by rearranging the thermograms for every time as columns in  $A$ , in such a way that time variations will occur column-wise while spatial variations will occur row-wise. Under this configuration, the columns of  $U$  represent a set of orthogonal statistical modes known as empirical orthogonal functions (EOF) that describe the data spatial variations. On the other hand, the principal components (PCs), which represent time variations, are arranged row-wise in matrix  $V^T$ . The first EOF will represent the most characteristic variability of the data; the second EOF will contain the second most important variability, and so on. Usually, original data can be adequately represented with only a few EOFs. Typically, an infrared sequence of 1000 images can be replaced by 10 or less EOFs.

### Pulsed Phase Thermography (PPT)

In pulsed phase thermography (PPT), originally proposed by Maldague and Marinetti in [6] and recently reviewed by Ibarra-Castanedo and Maldague in [7], data is transformed from the time domain to the frequency spectra using the 1D discrete Fourier transform (DFT):

$$F_n = \Delta t \sum_{k=0}^{N-1} T(k\Delta T) \exp(-j2\pi nk/N) = Re_n + Im_n \quad (2)$$

where  $j$  is the imaginary number,  $n$  designates the frequency increment ( $n=0,1,\dots,N$ ),  $\Delta t$  is the sampling increment, and  $Re$  and  $Im$  are the real and imaginary parts of the transform respectively. In this case, real and imaginary parts of the complex transform are used to estimate the amplitude and the phase as described in [8]:

$$A_n = \sqrt{Re_n^2 + Im_n^2} \quad (3)$$

$$\phi_n = \tan^{-1} \left( \frac{Im_n}{Re_n} \right) \quad (4)$$

DFT can be applied to any waveform. The phase, Equation (4), is of particular interest in NDT given that it is less affected than raw thermal data by environmental reflections, emissivity variations, non-uniform heating, and surface geometry and orientation. These phase characteristics are very attractive not only for qualitative inspections but also for quantitative characterization of materials as will be pointed out later.

A linear relationship exists between defect depth  $z$  and the inverse square root of the blind frequency (which can be observed from experimental data). According to [9], blind frequency  $f_b$  is the frequency at which the phase contrast is enough for a defect to be visible (at frequencies higher than  $f_b$ , it is not possible to detect it). The thermal diffusion length ( $\mu$ ), described in [10], can be used to fit experimental data and estimate the depth ( $z$ ) as proposed by [11]:

$$z = C_1 \sqrt{\frac{\alpha}{\pi f_b}} = C_1 \mu \quad (5)$$

where the thermal diffusion length is  $\mu = 2\alpha/\omega$  [m],  $\omega$  [rad/s] is the angular frequency,  $\alpha$  is the thermal diffusivity of the material,  $f_b$  [Hz] is the blind frequency and  $C_1$  is an empirical constant where it has been observed that  $1.5 < C_1 < 2$  when

working with the phase, with  $C_1=1.82$  typically adopted in several works such as in [12, 13].

## Experiments

Figure 5 shows the experimental setups used to inspect the part. For all inspections a mid-wave infrared (MWIR) camera (FLIR Phoenix, InSb, 3-5  $\mu\text{m}$ , 640x512 pixels windowed to 320x256 pixels in some cases) at a frame rate of 55 Hz (for PT and VT experiments) and 220 Hz (for LST experiments) was used to record the temperature profiles. In the pulsed thermography inspection case, two photographic flashes (with pulse duration of 5 ms and producing 6.4 kJ per flash) were used to heat the sample. Images were recorded in reflection mode. In the second case, the line scan inspection, a thermographic head was used consisting of the same MWIR camera used for the PT inspection and an electrical actuator with a quartz infrared lamp (1600 W). Samples were kept motionless while the thermographic head moved at a constant speed of 50 and 100 mm/s. In the vibrothermography case, the transducer horn was pressed against the sample and a burst of ultrasound waves (15 - 25 kHz, 2200 W) at a modulation frequency of 0.5 Hz and with amplitude modulated between 10-60% of maximum power was delivered to the sample for each inspection. The plate was inspected twice due to the position of the inclusions on the sample and the transducer horn contact spot. In the VT experiments, the sample was rotated 180° clockwise thus in the first VT experiment the row of largest inserts appears on the image and in the second VT experiment the row of smallest inserts appears while the middle row is repeated in both experiments. However, the second VT image result is presented rotated in this paper. Thus, the row with the smallest inserts appears on the bottom of the image result.

## Qualitative results

The sequences acquired in each experiment were then processed using PCT. Figure 6 shows the second EOF images of the inspections using the three different techniques. For the LST inspection, an additional step was performed to rearrange the data into a new pseudo-static sequence where changes occur in time and not in space (the plate appears to be motionless like in a PT inspection). A procedure to obtain this pseudo-static sequence is described in [14]. As it can be seen in Figure 6, the three techniques successfully detect all delaminations.

## Quantitative results

For the PT inspections, quantitative results were also calculated. For the 3 x 3 mm delaminations, i.e. inserts in the second row, the estimated depth of each insert was calculated based on the phase images obtained with PPT. Equation 5 was used for this purpose.

PPT was applied on the raw sequence and blind frequencies ( $f_b$ ) of each defect were calculated. The respective blind frequencies, calculated based on the phase profiles, for the defects #1 (insert on the 2<sup>nd</sup> layer at depth ~0.13 mm), #2 (insert on the 3<sup>rd</sup> layer at depth ~0.26 mm), and #3 (insert on the 4<sup>th</sup> layer at depth ~0.39 mm), are  $f_{b1} = 19$  Hz,  $f_{b2} = 7$  Hz, and  $f_{b3} = 2.6$  Hz, which give, by applying Equation 5 with  $\alpha_{CFRP} = 4.2 \times 10^{-7} \text{ m}^2/\text{s}$  and  $C_2 = 1.82$ , estimated depths of 0.151 mm, 0.2488 mm and 0.4082 mm, respectively. Based on the specifications provided in Figure 1, the estimated depths are close to the reported nominal depths. Figure 7 shows the phase profiles of each one of the three 3 x 3 mm inserts with a respective sound area defined just next to the insert. The crossing of the insert phase profile with the sound area phase profile indicates the blind frequency of the insert which was used to estimate its depth.

## Conclusions

In this paper three active IT techniques were used to inspect a CFRP laminate with artificial inserts. Inserts of different sizes and on different layers (depths) were detected by all techniques. Results

were quantified and compared for the PT inspection. The depths of inserts located at 0.13, 0.26 and 0.39 mm from the surface were successfully estimated using phase profiles obtained with PPT. On the qualitative side, PT and VT showed an increased defect contrast with respect to LST. Nevertheless, the presented LST results suggest that, for cases where the use of PT is restricted, e.g. when one is inspecting complex shaped parts, the use of LST is a viable solution. In this case the thermographic head would move in a controlled fashion (being able to move in all dimensions), for instance using a robot [14], in order to follow the shape of the sample.

## References

1. Maldague, X., 'Theory and Practice of Infrared Technology for Nondestructive Testing', John Wiley & Sons, New York, 2001.
2. Woolard, D. F. and Cramer, K. E. Cramer, 'Line Scan Versus Flash Thermography: Comparative Study on Reinforced Carbon-Carbon', Proc. SPIE, Thermosense XXVII, G. Raymond Peacock, Douglas D. Burleigh and Jonathan J. Miles (eds.), Vol 5782, pp 315-323, 2005.
3. Oswald-Tranta, B. and Shepard, S., 'Comparison of Pulse Phase and Thermographic Signal Reconstruction Processing Methods' Proc. SPIE, Thermosense XXXV, Gregory R. Stockton, Fred P. Colbert, (eds.), Vol 8705, pp 87050S1-9, 2013.
4. Pieczonka, L. and Szwedo, M., 'Vibrothermography', in T. Stepinski, T. Uhl, W.J. Staszewski, (Eds.), *Advanced Structural Damage Detection: From Theory to Engineering Applications*. Wiley, 2013, pp. 233–261.
5. Rajic, N., 'Principal component thermography for flaw contrast enhancement and flaw depth characterisation in composite structures', *Composite Structures*, Vol 58, No 4, pp 521-528, 2002.
6. Maldague, X. and Marinetti, S., 'Pulse phase thermography'. *Journal of Applied Physics*, Vol 79, No 5, pp 2694-2698, 1996.
7. Ibarra-Castanedo, C. and Maldague, X., 'Review of pulse phase thermography'. *Proc. SPIE - Thermosense: Thermal Infrared Applications XXXVII*. Vol 9485, pp 94850T-94850T-10, 2015.
8. Ibarra-Castanedo, C. and Maldague, X., 'Pulsed phase thermography reviewed'. *Quantitative InfraRed Thermography Journal*, Vol 1, No 1, pp 47-70, 2004.
9. Bai, W. and Wong, B.S., 'Evaluation of defects in composite plates under convective environments using lock-in thermography'. *Measurement Science and Technology*, Vol 12, No 2, pp 142-150, 2001.
10. Busse, G. and Rosencwaig, A., 'Subsurface imaging with photoacoustics'. *Applied Physics Letters*, Vol 36, No 10, pp 815-816, 1980.
11. Ibarra-Castanedo, C., 'Quantitative subsurface defect evaluation by pulsed phase thermography: depth retrieval with the phase'. Ph.D. thesis, Université Laval, Canada, 2005.
12. Meola, C., Carlomagno, G.M. and Giorleo, L., 'The use of infrared thermography for materials characterization'. *Journal of materials processing Technology*, Vol 155, pp 1132-1137, 2004.
13. Meola, C. and Carlomagno, G.M., 'Recent advances in the use of infrared thermography'. *Journal of Applied Physics*, Vol 79, No 5, pp 2694-2698, 2004.
14. Ibarra-Castanedo, C., Servais, P., Ziadi, A., Klein, M. and Maldague, X., 'RITA - Robotized Inspection by Thermography and Advanced processing for the inspection of aeronautical components', *Proc. QIRT 12 – Quantitative Infrared Thermography*, Bordeaux, France, July 7-11, 2014, available online: QIRT-2014-164.



Figure 1 – Position of the artificial inserts on the layers of the laminate

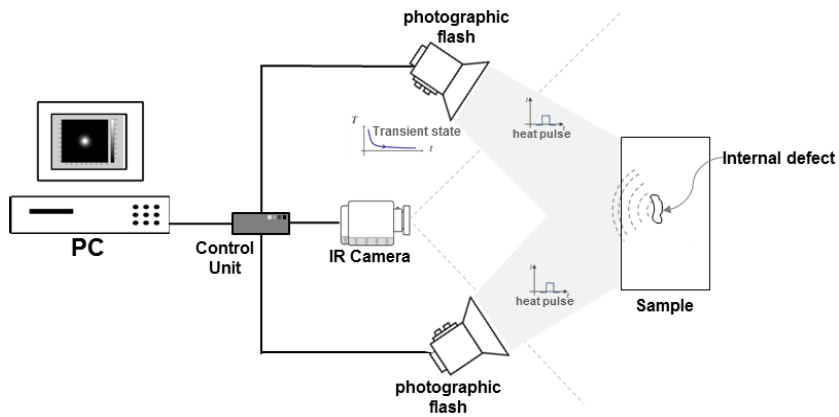


Figure 2 – PT schematic set-up

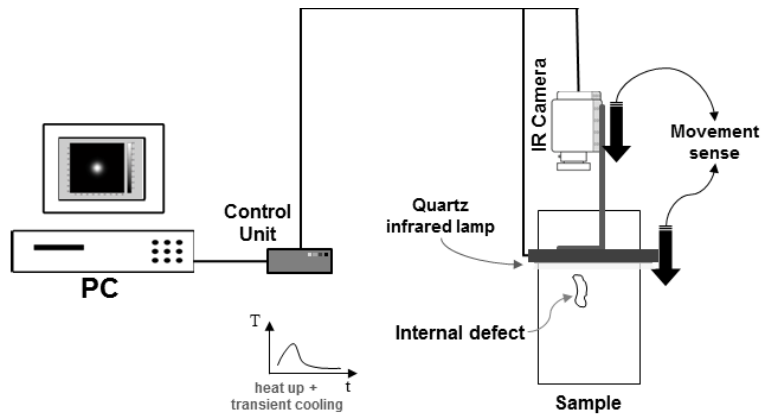


Figure 3 – LST schematic set-up

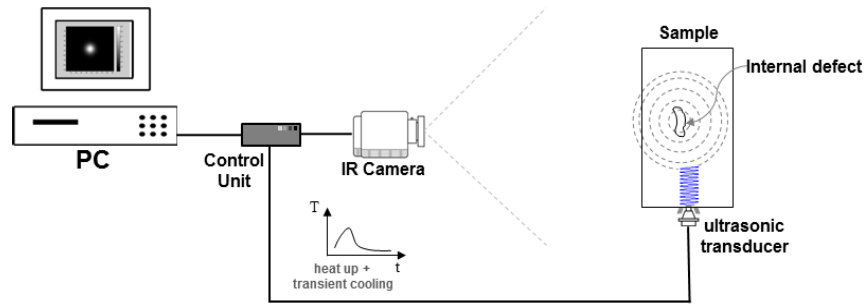


Figure 4 – VT schematic set-up

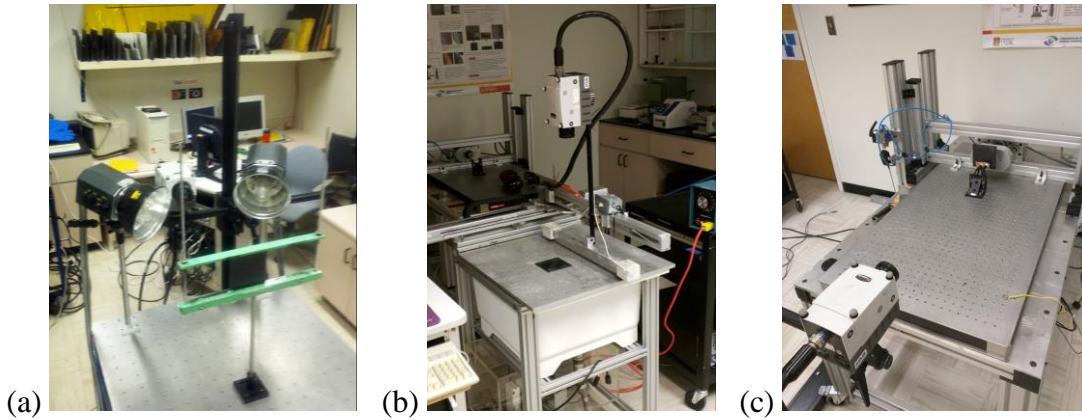


Figure 5 – Laboratory setups – (a) PT, (b) LST and (c) VT

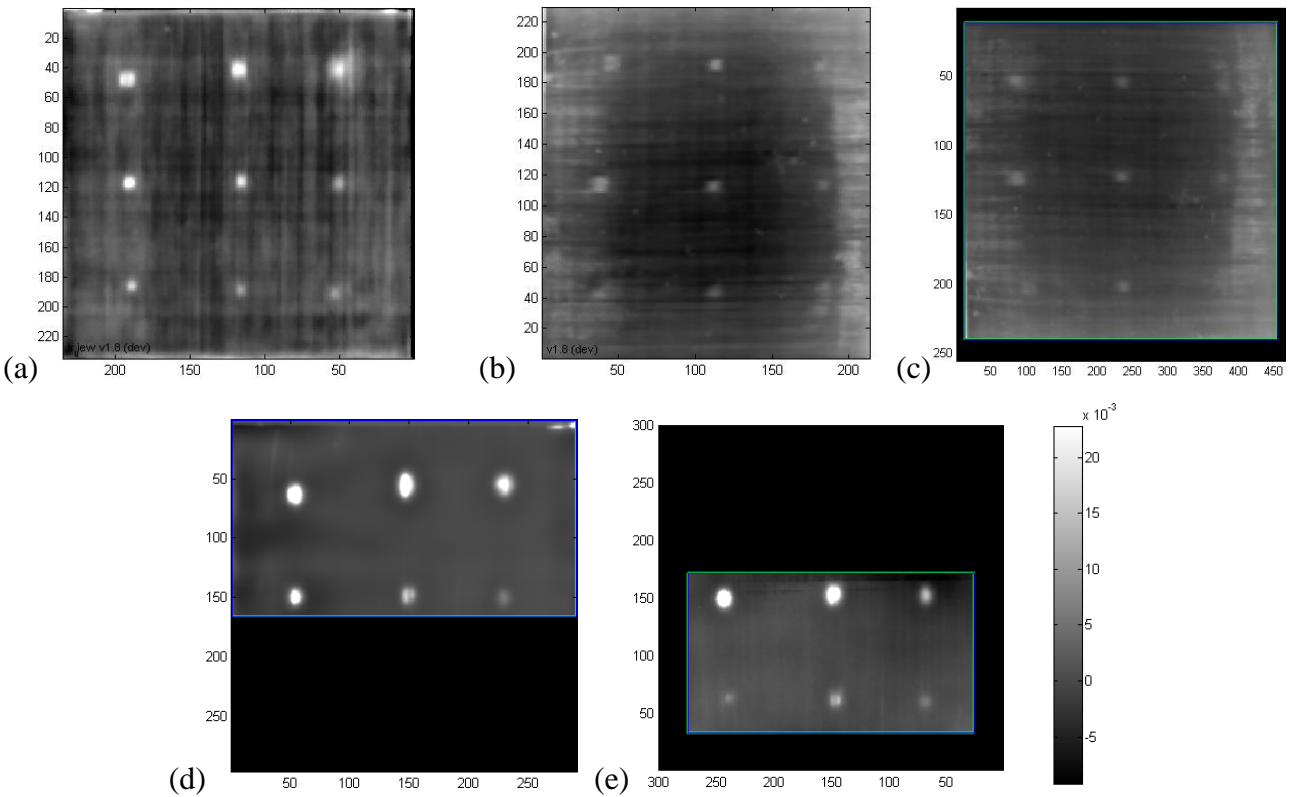
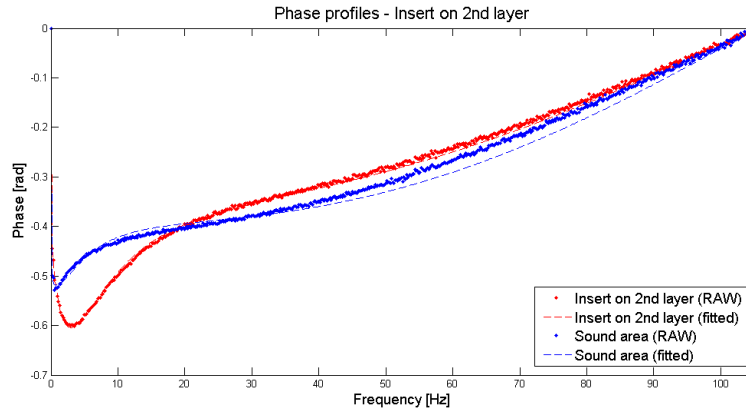
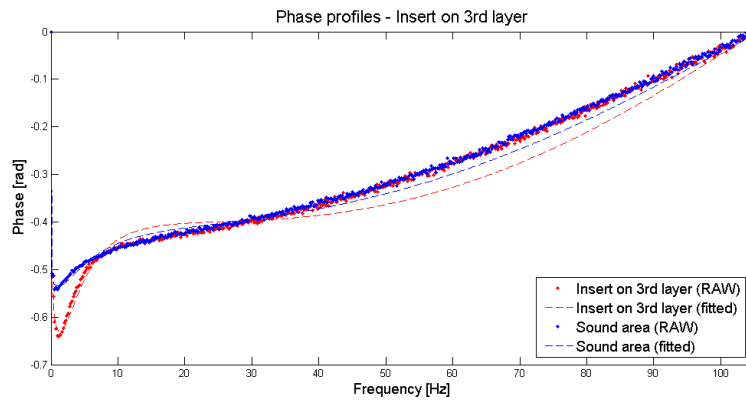


Figure 6 – Results obtained with PCT – (a) PT, (b) LST thermographic head moving at 100 mm/s, (c) LST thermographic head moving at 50 mm/s, (d) VT showing the biggest inserts and (e) VT showing the smallest inserts

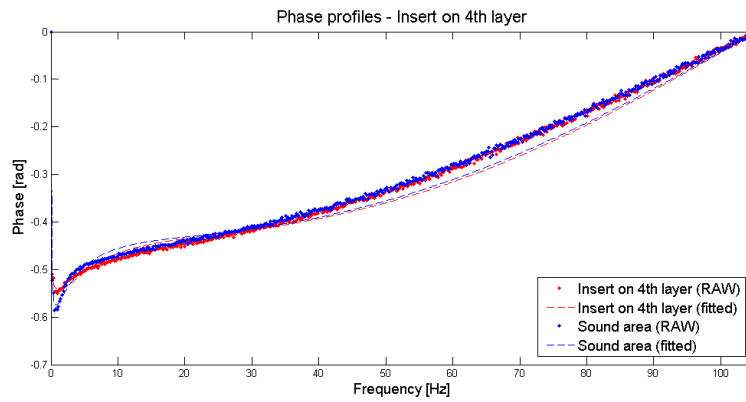




(a)



(b)



(c)

Figure 7 – Phase profiles obtained with PPT for the three 3x3 mm delaminations. (a) Insert on 2<sup>nd</sup> layer – approximately at 0.13 mm ( $f_{b1} = 19$  Hz), (b) insert on 3<sup>rd</sup> layer – approximately at 0.26 mm ( $f_{b2} = 7$  Hz), and (c) insert on 4<sup>th</sup> layer – approximately at 0.39 mm. ( $f_{b3} = 2.6$  Hz)

# Measurement of materials emissivity – Influence of the procedure

E. Barreira<sup>1</sup>, E. Bauer<sup>2</sup>, N. Mustelier<sup>3</sup>, V.P. Freitas<sup>4</sup>

<sup>1</sup> CONSTRUCT-LFC, University of Porto, Faculty of Engineering, Civil Engineering Department, Porto, Portugal, barreira@fe.up.pt

<sup>2</sup> University of Brasilia, Faculty of Technology, Civil and Environmental Engineering Department, Brasilia, Brazil, elbauerlem@gmail.com

<sup>3</sup> Civil Engineer, Porto, Portugal, niubis@yahoo.com

<sup>4</sup> CONSTRUCT-LFC, University of Porto, Faculty of Engineering, Civil Engineering Department, Porto, Portugal, vpfreita@fe.up.pt

Emissivity is one of the parameters that most influence measurements by infrared thermography, as it rules the effective radiation emitted by the surface, regarding the black body. For in situ measurements, the surface emissivity is defined using black tape with known emissivity. The tape is glued over a portion of the surface under study and its temperature is measured considering the tape emissivity. The surface emissivity is adjusted by equating the temperatures of the tape and of the surface near it. In this work the accuracy of this method was evaluated, by comparison with measurements made with an emissometer. The emissivity of ten different materials commonly used in buildings was assessed, considering a black tape of well-known emissivity.

## Introduction

Infrared thermography is a non-contact and non-destructive testing technology that has been applied to buildings for a couple of decades, to evaluate its performance. It has been used to detect insulation defects, air leaks [1], moisture problems [2-6], thermal bridges [7], to inspect HVAC systems [8] and construction details [9-10], and to evaluate defects in façades [9-11].

Emissivity is a highly material-dependent surface property, which defines the material's capacity to emit energy [12]. The literature provides emissivity values for different materials in accordance with the surface characteristics, temperature and wavelength of the measurement. Most common building materials, with the exception of metals, have emissivity values over 0.8. If a quantitative analysis is required, the material emissivity should ideally be assessed. The emissivity setting inputted into the camera, as it is related to the amount of radiation emitted by the surface, will give rise to great errors if there are significant deviations between the emissivity

specified for measurement and the real emissivity of the target [13].

Therefore, evaluating practical procedures performed in situ to determine the surfaces emissivity is very important. One of the most current procedures consists in using black tape with known emissivity [12]. In this work the accuracy of this method was evaluated, by comparison with measurements made with an emissometer. The emissivity of ten different materials commonly used in buildings was assessed.

## Testing procedures

### *Materials under study*

The black tape used as reference was the Scotch® 3M +33 Super. Its emissivity was assessed using the emissometer and it was obtained a value of 0.90. Several samples were used to assess emissivity: autoclaved aerated concrete (AAC), stainless steel, gypsum, mortar,

ceramic tile, pine wood, limestone, granite, solid brick and cork.

*Emissivity using infrared thermography (IRT)*

The test procedure consisted of heating the samples in an oven at 70° C for 24 hours. Before the measurement, all the calibration procedures were carried out. Each sample was removed from the oven and placed inside a cardboard box to minimize the reflection effect (Fig.1). To define the emissivity of each sample, the emissivity of the reference black tape was used ( $\epsilon = 0.90$ ). It was also considered an emissivity value from the literature ( $\epsilon = 0.95$ ), in order to evaluate the influence of the adopted emissivity for the reference black tape. The tape was glued over a portion of the surface under study and thermal images were taken. Using the camera software, the tape temperature was measured considering its emissivity. The temperature value was an average of the tape temperatures inside a defined area. The surface emissivity was adjusted by equating the average temperature of the tape and the average temperature of the surface near it, considering a similar area. This procedure is well described in [12]. The basic properties of the IR camera are shown in Table 1.

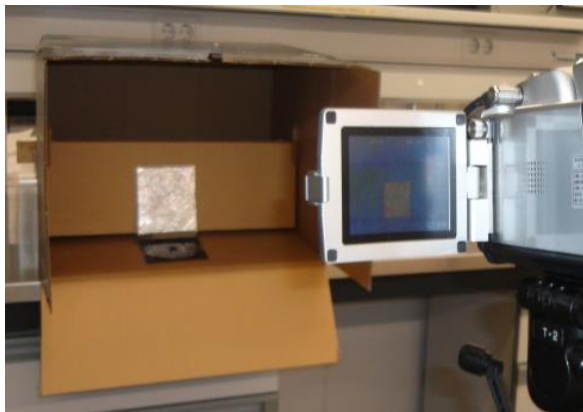


Fig. 1. IRT – Test set up.

<b>Infrared camera</b>	<b>FLIR T 400</b>
Measuring range (°C)	-20 to 120
Accuracy (°C; %)	±2
Resolution (°C)	0.05 at 30° C

Spectral range (µm)	7.5 to 13.0
Thermal image (pixels)	320 (H) x 240(V)
Field of view (°)	25(H) x 19(V)
I.F.O.V (mrad)	1.36

Table 1. Technical characteristics of the IR camera.

*Emissivity using the emissometer*

Measurements made using the emissometer are in accordance with the standard ASTM C1371 – 04a (2010) [14]. This test method consists of employing a differential thermopile emissometer, which comprises one thermopile that is covered with a black coating and one that is covered with a reflective coating, for total hemispherical emittance measurements. The detector thermopiles are heated in order to provide the necessary temperature difference between the detector and the surface. The equipment is calibrated using two standards, one with a high emittance and the other with a low emittance, which are placed on the heat sink. Each specimen was placed on a flat surface and, after the thermal equilibrium was achieved, its emittance was quantified by comparison to the emittances of the standards (Fig. 2). The accuracy of the measured values according to the maker is +/-0.02 [15].

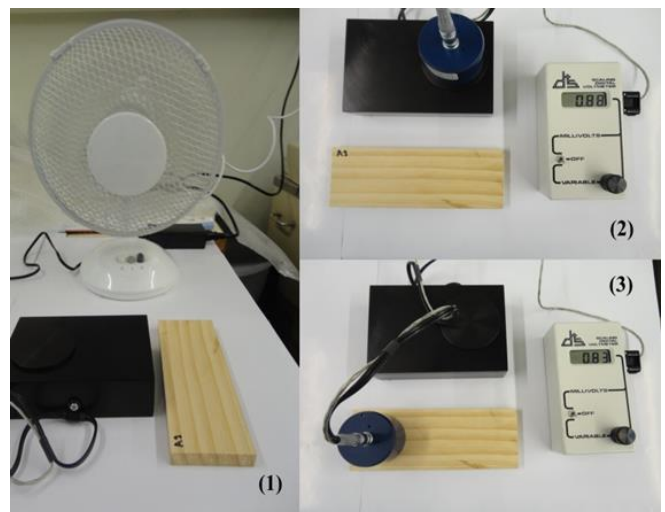


Fig. 2. Emissometer – Test set up: (1) Period to achieve thermal equilibrium; (2) Calibration procedure; (3) Measurement

## Results

Fig. 3 shows the thermal images obtained during the test and Table 2 displays the values obtained with the emissometer and the IR camera, considering the black tape emissivity of 0.90 (real value) and 0.95 (value from the literature).

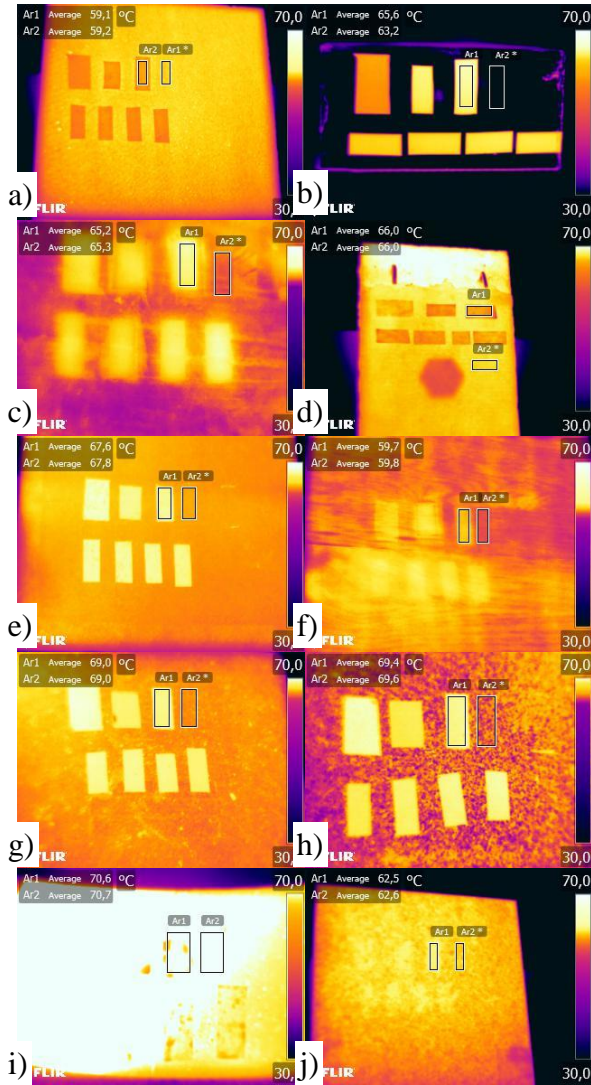


Fig. 3. Thermal images: a) ACC, b) stainless steel, c) gypsum, d) mortar, e) ceramic tile, f) pine wood, g) limestone, h) granite, i) solid brick, j) cork limestone.

It is possible to see that values obtained using IRT ( $\epsilon = 0.9$ ) are quite similar to the ones measured with the emissometer. The only exception is the stainless steel. That may be related with the low emissivity and high reflectivity of the material, which may affect IRT measurements.

If the tape emissivity is assumed to be 0.95, the differences regarding the emissometer values increase. That was expected as the real emissivity value of the tape is smaller. The only exceptions are the ceramic tile and the granite. That may be related with the fact that these materials have a heterogeneous color pattern, varying from white to black, and are glazed, which may affect the measurements.

Material	IRT	IRT	Emis.
	$\epsilon = 0.90$	$\epsilon = 0.95$	
AAC	0.93	0.98	0.9
stainless steel	0.07	0.07	0.16
gypsum	0.84	0.89	0.79
mortar	0.94	0.99	0.93
ceramic tile	0.83	0.88	0.88
pine wood	0.87	0.92	0.86
limestone	0.85	0.90	0.87
granite	0.82	0.87	0.87
solid brick	0.9	0.95	0.91
cork	0.87	0.92	0.84

Table 2. Emissivity values obtained with IRT ( $\epsilon = 0.90$  and  $\epsilon = 0.95$ ) and the emissometer.

Table 3 shows the differences between the values obtained with IRT (considering emissivity 0.90 and 0.95) and the emissometer. Differences are on average 8.7% for IRT  $\epsilon = 0.90$  and 10.7% for IRT  $\epsilon = 0.95$ , if the difference for stainless steel is considered. If that material is excluded, then the averages are 3.4% and 5.8%, respectively.

Material	Emis. vs IRT	Emis. vs IRT
	$\epsilon = 0.90$	$\epsilon = 0.95$
AAC	3.3%	8.9%
stainless steel	56.3%	55.0%
gypsum	6.3%	12.7%
mortar	1.1%	6.5%
ceramic tile	5.7%	0.0%
pine wood	1.2%	6.9%
limestone	2.3%	3.0%
granite	5.7%	0.0%
solid brick	1.1%	4.4%
cork	3.6%	9.8%

Table 3. Differences between emissivity values using IRT

( $\epsilon = 0.90$  and  $\epsilon = 0.95$ ) and the emissometer.

Considering the sum of the differences, if the stainless steel is taken into account, the obtained values are 86.5% for IRT  $\epsilon = 0.90$  and 107.0% for IRT  $\epsilon = 0.95$ . However, the value is quite lower if the stainless steel is not considered (30.3% for IRT  $\epsilon = 0.90$  and 52.0% for IRT  $\epsilon = 0.95$ ).

Using emissivity values in Table 2, without considering the stainless steel, a statistical analysis was performed using the software SPSS-V23. Two nonparametric tests were performed to compare paired samples (Emis. vs IRT  $\epsilon = 0.90$  and Emis. vs IRT  $\epsilon = 0.95$ ), for a level of significance of 5% (Sign Test and Wilcoxon Signed-Rank Test) [16]. The p-values obtained are presented in Table 4. The results show that statistically the values obtained with IRT  $\epsilon = 0.90$  and with the emissometer are identical, with a very good level of significance. On the contrary, the pairs of values IRT  $\epsilon = 0.95$  / emissometer are not statistically identical.

Test	Emis. vs IRT $\epsilon = 0.90$	Emis. vs IRT $\epsilon = 0.95$
Sign	1.000	0.016
Wilcoxon Signed-Rank	0.952	0.018

Table 4. p-values for nonparametric tests to compare paired samples.

### Conclusion

This test allowed verifying that the assessment of emissivity by IRT using the black tape method is feasible as the obtained values are quite similar to the ones given by an emissometer. The only exception is when assessing the emissivity of metallic materials, with high reflection. It was also possible to see that it is essential to use the correct emissivity value of the reference black tape, otherwise the materials emissivity obtained with IRT are quite different from the real ones.

### References

1. S. Ocaña, I. Guerrero, I. Requena. Thermographic survey of two rural buildings in Spain, *Energy and Buildings*, Vol. 36 (6), pp. 515-523, 2004.
2. C. Balaras, A. Argiriou. Infrared thermography for building diagnostics, *Energy and Buildings*, Vol. 34 (2), pp. 171-183, 2002.
3. N. Avdelidis, A. Moropoulou, P. Theoulakis. Detection of water deposits and movement in porous materials by infrared imaging, *Infrared Physics & Technology*, Vol. 44 (3), pp. 183-190, 2003.
4. E. Grinzato, G. Cadelano, P. Bison. Moisture map by IR thermography, *Journal of Modern Optics*, Vol. 57 (18), pp. 1770-1778, 2010.
5. J. Lerma, M. Cabrelles, C. Portalés. Multitemporal thermal analysis to detect moisture on a building façade, *Construction and Building Materials*, Vol. 25 (5), pp. 2190-2197, 2011.
6. E. Edis, I. Flores-Colen, J. Brito. Passive thermographic detection of moisture problems in façades with adhered ceramic cladding, *Construction and Building Materials*, Vol. 51, pp. 187-197, 2014.
7. F. Asdrubali, G. Baldinelli, F. Bianchi. A quantitative methodology to evaluate thermal bridges in buildings, *Applied Energy*, Vol. 97, pp. 365-373, 2012.
8. E. Grinzato. State of the art and perspective of infrared thermography applied to building science, In: Meola C, editor. *Infrared thermography recent advances and future trends*, Bentham Books, 2012.
9. M. Chew. Assessing building façades using infra-red thermography, *Structural Survey*, Vol. 16 (2), pp. 81-86, 1998.
10. F. Cerdeira, M.E. Vázquez, J Collazo, E. Granada. Applicability of infrared thermography to the study of the behavior of stone panel as building envelopes. *Energy and Buildings*, Vol. 43, pp.1845-1851, 2011.
11. S.S. Freitas, V.P. Freitas, E. Barreira. Detection of façade plaster detachments using infrared thermography – A nondestructive technique. *Construction and Building Materials*, Vol. 70, pp. 80-87, 2014.
12. N. Avdelidis, A. Moropoulou. Emissivity considerations in building thermography, *Energy and Buildings*, Vol. 35 (7), pp. 663-667, 2003.
13. E. Bauer, V.P. Freitas, N. Mustelie, E. Barreira, S.S. Freitas. Infrared thermography – Evaluation of the results reproducibility, *Structural Survey*, Vol. 33 (1), pp. 20-35, 2015.
14. ASTM, C1371 – 04a Standard Test Method for Determination of Emittance of Materials Near Room Temperature Using Portable Emissometers, ASTM, 2010.
15. Devices & Services Company, AE1 Model – Operating Instructions, Dallas, Texas, nd.
16. D. Montgomery, G. Runger. *Applied Statistics and Probability for Engineers*, John Wiley & Sons, Inc., New York, USA, 2003.

## **Infrared Thermography and NDT: 2050 Horizon**

**Fariba Khodayar, Saeed Sojasi, Xavier Maldague**

**Computer Vision and Systems Laboratory, Laval University, Quebec, QC, Canada;  
{fariba.khodayar.1, saeed.sojasi.1, maldagx}@gel.ulaval.ca**

Society is changing fast, new technologies and materials are coming in which requires new inspection approaches. Infrared Thermography (IRT) has emerged in the recent years has an attractive and reliable technique to address complex Non-destructive (NDT) problems. Companies are now providing turnkey IRT-NDT systems, but the big question we ask now is what is next? What will be IR - NDT in 2050? This is obviously a very complex question and nobody can answer it since the future is elusive, no gurus could tell us now with certainty what the world will look like 35 years from now!

Nevertheless, we can think about the future of IR NDT. Our analysis shows that new developments will happen in various directions such as acquisition, stimulation, processing and obviously an always-enlarging range of applications with new materials, which will have particular inspection requirements.

In this paper, we will present our vision of IRT of the future starting from the current situation and extrapolating future trends. This is a perilous exercise but let's try!



# STRESS BASED NDE USING INFRARED THERMOGRAPHY

R.C. Tighe<sup>1</sup>, J.M. Dulieu-Barton<sup>2</sup>, S. Quinn<sup>3</sup>

<sup>1,2</sup> University of Southampton, UK. <sup>1</sup>rcw1n09@soton.ac.uk, <sup>2</sup>janice@soton.ac.uk

<sup>3</sup> Research Institute for Industry, University of Southampton, UK. s.quinn@soton.ac.uk

An initial study is presented where a series of composite plates containing simulated defects such as ply cuts are inspected. The simulated damage was identified using an infra-red technique known as thermoelastic stress analysis (TSA) which enables a map of surface stresses to be generated based on the measured temperature field. The strain change required for the TSA is induced by using a small permanent magnetic shaker that imposes an excitation at the plate resonant frequency. The work forms the basis for using TSA as an on-site NDE tool, with a view to new inspection approach for pipework found in a coal fired power station. Novel remote loading approaches are considered for TSA including a pneumatically powered shaker. For demonstration purposes a laboratory trial of the pneumatic system is being undertaken, which is also discussed.

## Introduction

Thermoelastic stress analysis (TSA) is an active thermographic approach during which a cyclic load is applied to the component of interest within the material elastic range. An infrared (IR) detector is used to monitor the small surface temperature changes of the component, which are directly related to the principal stress changes (i.e. the thermoelastic effect). Lock in processing is employed to obtain the thermoelastic temperature change from the thermal response obtained from the IR detector. Stress information about the component is established using

$$\frac{\Delta T}{T} = K(\sigma_1 + \sigma_2) \quad (1)$$

where  $\Delta T$  is the thermoelastic temperature change,  $T$  is the absolute temperature of the component and  $\sigma_1$  and  $\sigma_2$  are changes in the principal stresses.  $K$  is the thermoelastic constant equal to  $\alpha / \rho C_p$ , where  $\alpha$  is the coefficient of thermal expansion,  $\rho$  is density and  $C_p$  specific heat at constant pressure.

TSA is typically a laboratory based technique as usually it relies upon the cyclic load being applied by a servo-hydraulic test machine. Previous work [1] has shown that resonant

excitation can provide sufficient load for feature identification using TSA, see fig 1. TSA  $\Delta T/T$  data for forced and resonant loading of a panel is shown in fig 1a and b. The thermoelastic signal collected using resonant excitation is generally significantly lower magnitude than forced loading although the stress map acquired highlights the same features as forced loading, see fig.1c. Without the requirement of a test machine TSA is then able to be a mobile NDE technique suitable for onsite assessments.

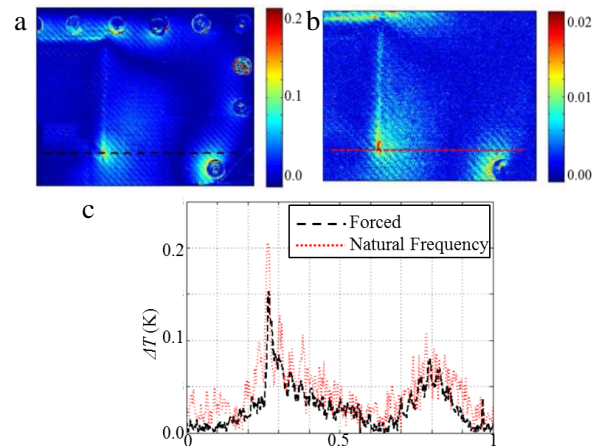


Fig.1. TSA data of a) forced [2] and b) resonant excitation c) profile plots through a and b (resonant excitation is scaled by 10 for comparison) [1].

It is currently practice in the energy sector to shut down units within power stations for a period for maintenance, repair or replacement dependent largely on a pre-defined time-based approach. A non-destructive evaluation approach able to assess the integrity of the components and welds would enable selective replacement and allow a picture of system health to be obtained. The overall goal is to use TSA as a stress based NDE tool that can be used on site as a health monitoring tool.

Initial work has focused on the detection of features in aluminium and glass fibre reinforced plastic (GFRP) plates. The next step is to undertake laboratory based studies on a representative pipe section prior to applying the technique on site to inspect pipe components such as those shown in fig.2.



Fig.2. Example survey sites for inspection.

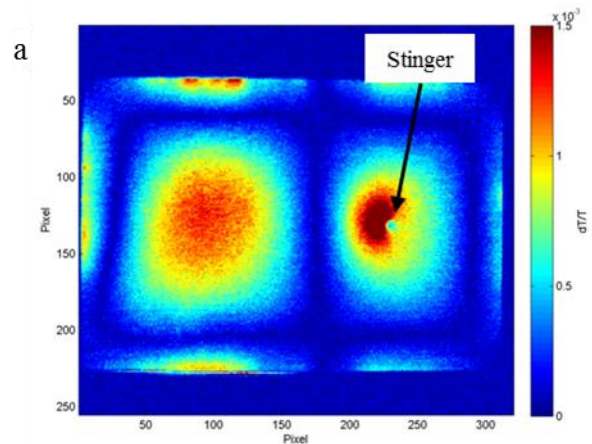
### Clamped plate studies

Interrogation of rectangular plate samples clamped on four sides using resonant excitation was undertaken. The internal clamp dimensions were 330 x 203 mm. Four plates were inspected; an undamaged aluminium 6061 plate of 0.9 mm thick and three GFRP/epoxy panels with layup [0, 90, 0] giving a thickness of 0.9 mm were used. The aluminium plate was used as a control sample to ensure the detection of the stresses induced by the modal excitation was possible using the current experimental set up. One GFRP panel was undamaged; the second ‘ply cut’ panel contained two ply cuts in the central ply transverse to the fibres; and finally a ‘box cut’

panel contained a larger section of the central ply removed to create a thinner section of panel.

The plates were excited using a LDS V201 permanent magnetic shaker from Brüel and Kjær controlled using a signal generator and amplifier. The shaker was connected to the plate using a rigid stinger which was attached using beeswax enabling its position to be adjusted. The reference signal for the lock in algorithm was collected using a force transducer positioned between the shaker and the plate. The IR detector was a FLIR SC5000 with a frame rate of 383 Hz; an integration time of 700  $\mu$ s was used to avoid blurring. The data was processed using the manufacturer’s software Altair and Altair LI.

The results for the aluminium plate excited at its second mode at 144 Hz are given in fig.3 [3]. The second mode is expected to generate two equal and peaks. The bias introduced by the stinger is apparent both in the TSA  $\Delta T/T$  data in fig.3a and the profile plot in fig.3b where the rigid stinger causes a stress concentration due to the local reinforcement the rigid stinger provides.



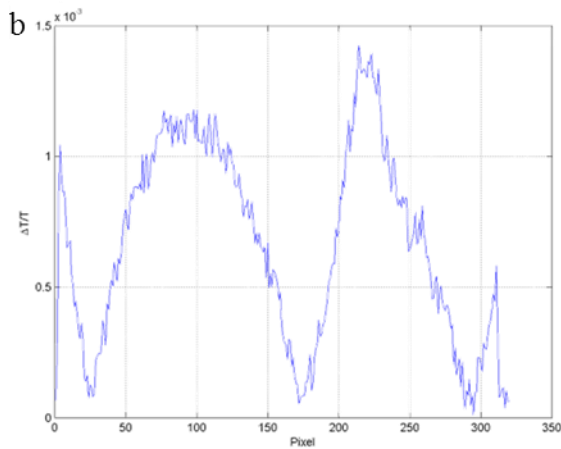


Fig.3. a)TSA  $\Delta T/T$  data and b) profile data taken horizontally across the undamaged aluminium plate in second mode excitation.

The GFRP panels were all excited at 110 Hz. The TSA  $\Delta T/T$  data for the control panel is presented in fig.4a. The data is less well defined than the aluminium panel due to the anisotropy of the material. Again the effect of the stinger is evident and the mode shape is identified. The damaged panels were excited at the same frequency as the control panel in this case as it was envisaged that an expected excitation frequency of a component would be known so damage could be identified by any deviations from the expected mode shape. The  $\Delta T/T$  data for the GFRP panel with ply cuts is shown in fig.4b. A ply cut is highlighted at the anti-node where a stress concentration is created. A second cut is present in this plate however it is coincident with the central node in the second mode, i.e. along the centre of the plate, and so is not identified in this mode. It is important to note when using natural frequency excitation regions of zero stress will exist at the nodes and so any features found in these regions will not be identified. Tests should be repeated at a different mode which would shift the zero stress region(s) to enable different defects to be identified. The final GFRP plate with box cut is shown in fig.4c. The region where the material is removed is highlighted. The modal frequency for this plate is significantly different to the control due to the change in thickness of the panel in this region. Using the 'expected' frequency it is possible to identify the extent of the removed region of material.

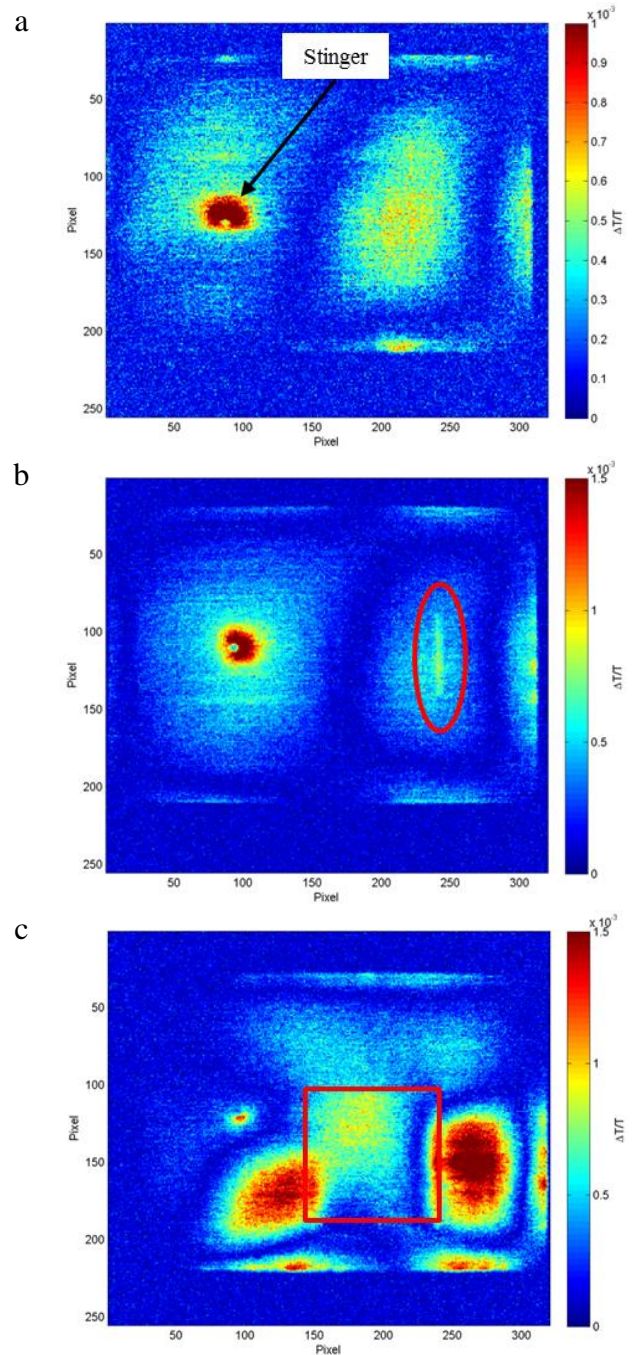


Fig.4. TSA  $\Delta T/T$  data for a) undamaged, b) ply cut and c) box cut GFRP panels.

### Towards onsite pipe inspections

The first challenge of natural frequency excitation of the pipe systems is to identify a loading device capable of providing appropriate force and frequency excitation. In the case of inspecting pipes in the power station it is important that the shaker must be as versatile as possible allowing a range of pipe diameters to be



excited. Typical pipes found in the power stations vary in length between half a metre and 10s of metres. There are also variations in the outer diameter (OD) between 40 – 48 mm and wall thickness of the pipes, typically between 6-10 mm. All these variations in parameters result in required loading frequencies between a few Hz and a few hundred Hz.

A pneumatically driven shaker may be suitable for this application. Pneumatic shakers work by using the flow of compressed air to turn an eccentrically weighted turbine wheel which then creates a vibration excitation. Varying the air flow rate varies the frequency and force of the vibration. The pneumatic shaker selected was a GT36 from Vibratechniques Ltd. It was necessary to design and manufacture a specialist clamping system to attach the shaker to the pipes allowing for variation in ODs.

The setup for laboratory TSA application of the sample pipe is given in fig.5. The reference signal for the lock-in is provided using an accelerometer. The natural frequencies of pipes are checked using instrumented hammer tests where the frequency response function is analysed to find the excitation frequency. A sample pipe of 1.5 m long was provided. Two end plates were TIG welded to the pipe based on the welding procedure found in power stations. The pipe ends in the vicinity of the welds are the focus of inspection in the trails.

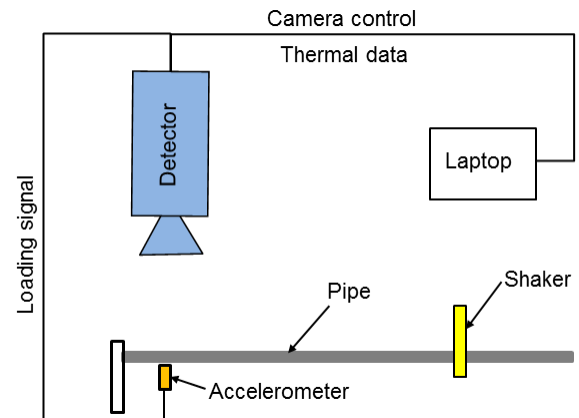


Fig.5. Schematic for TSA pipe inspection for laboratory inspection.

## Conclusion

The use of natural frequency excitation for the inspection of components and identification of damage using TSA has been validated using panel components. A loading system for onsite inspection of pipes has been developed and initial laboratory trials are underway. An initial site inspection trial is scheduled for August 2016.

## References

1. J.M. Dulieu-Barton, R.K. Fruehmann, and S. Quinn. A full-field stress based damage assessment approach for in-situ inspection of composite structures, *Key Engineering Materials*, vol. 569, pp. 3-10, 2013.
2. D.A. Crump, J.M. Dulieu-Barton, J. Savage. Design and commission of an experimental test rig to apply a full-scale pressure load on composite sandwich panels representative of an aircraft secondary structure, *Measurement Science and Technology*, vol. 21, pp. 1-16, 2010.
3. R.K. Fruehmann, R.C. Waugh, and J.M. Dulieu-Barton. A fresh look at assessing structural performance using imaging techniques. *SPIE Newsroom*. DOI: 10.1117/2.1201506.005788, 2015.

# STUDY ON HEAT GENERATION BEHAVIORS IN SONIC-IR METHOD

H. Tanabe<sup>1</sup>, Y. Izumi<sup>2</sup>, T. Hibino<sup>3</sup>, T. Takamatsu<sup>4</sup>, T. Sakagami<sup>5</sup>

<sup>1</sup> The University of Shiga Prefecture, Hassaka 2500, Hikone, Shiga 522-8533, Japan,  
tanabe@mech.usp.ac.jp

<sup>2</sup> The University of Shiga Prefecture, Hassaka 2500, Hikone, Shiga 522-8533, Japan,  
izumi.yu@mech.usp.ac.jp

<sup>3</sup> The University of Shiga Prefecture, Hassaka 2500, Hikone, Shiga 522-8533, Japan,  
katakiyu1025@gmail.com

<sup>4</sup> The University of Shiga Prefecture, Hassaka 2500, Hikone, Shiga 522-8533, Japan,  
takamat@mech.usp.ac.jp

<sup>5</sup> Kobe University, Rokkodai 1-1, Nada, Kobe 657-8501, Japan,  
sakagami@mech.kobe-u.ac.jp

In the present study, we experimentally investigate the fundamental physics of heat generation at defects while using the Sonic-IR method. A contact point between a half-column specimen and a long beam specimen was observed, and the relationship between the temperature change at the contact point and the excitation distance during Sonic-IR testing was investigated. The relationship between the temperature change and the excitation distance exhibited an almost symmetrical distribution about the midpoint of the long beam specimen. The heat generation near the contact point would be strongly affected by the natural vibration of the long beam specimen. The relationship between the temperature change and the contact load was also investigated. The variation of the heat generation for the contact load can be explained by changes in the friction force and the relative sliding between the contact surfaces.

## Introduction

Sonic-IR (vibrothermography) is a non-destructive testing method for finding cracks, delaminations, or other defects [1]-[7]. In this method, defects in an object are detected through infrared imaging of frictional heating at the defects caused by high-frequency ultrasonic waves. Although a number of studies have examined this method, explaining the heat generation behavior quantitatively remains difficult.

In the present study, in order to further clarify the fundamental physics of the heat generation at fatigue cracks that occurs when using the Sonic-IR method, and to discuss the detectability of cracks when using this method, the effects of the distance from the excitation position to the crack

and the contact load acting between two crack faces (which corresponds to residual stress) on the heat generation were investigated.

## Experimental method

In order to investigate the effects of the distance from the excitation position to the crack on the heat generation, the direct and simplest method would be to introduce cracks at various positions on a specimen and to compare the heat generation for each crack. However, the introduction of identical cracks (having the same crack length, crack opening displacement, roughness of crack faces, residual stress, and so on) at various positions on a specimen is very difficult. Therefore, in the present study, the contact surfaces between

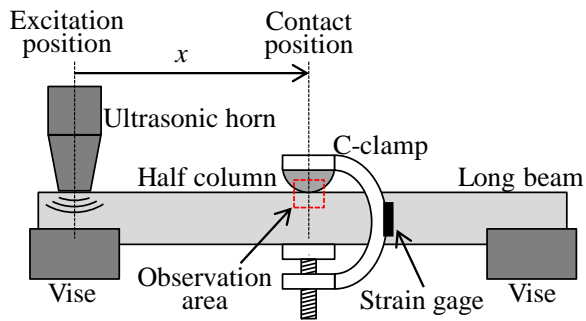


Fig. 1 Schematic diagram of the experimental setup used to investigate the effects of excitation distance.

a half-column specimen and a long beam specimen, as shown in Fig. 1, were investigated rather than crack faces. The relationship between the excitation distance and the heat generation was investigated by changing the distance between the excitation position and the half-column specimen (the excitation distance,  $x$ ).

The material used for the specimens in the present study was rolled steel for general structures, JIS SS400. The dimensions of the long beam specimen were 1400 mm  $\times$  25 mm  $\times$  25 mm. The radius of the half-column specimen was 25 mm, and its length was 50 mm. The half-column specimen was pressed against the long beam specimen by a c-clamp, as shown in Fig. 1. The excitation distance  $x$  was varied from 300 mm to 1100 mm in 50 mm intervals. A strain gauge was attached to the c-clamp in order to measure the contact load, and the contact load was set to 250 N at each position.

An ultrasonic plastic welder (UPW1521G6, Ultrasonic Engineering Co., Ltd. Japan) was used for the ultrasonic wave source. The excitation frequency of the welder was 21 kHz, and the excitation time was set to 1.325 s.

The temperature distribution near the contact point was continuously measured at a frame rate of 113 Hz using an infrared thermograph (Phoenix, Indigo Systems (FLIR Systems)). The temperature resolution of the thermograph was 0.025 K.

The effects of the contact load on the heat generation were also investigated. Figure 2

shows the experimental setup used for this investigation. The half-column specimen described earlier was also used for this experiment. The half-column specimen was clamped in a vise, and the ultrasonic wave was input from the vise by the ultrasonic plastic welder UPW1521G6. The contact load between the half-column specimen and the vise was varied, and the temperature distribution near the contact point was continuously measured at 113 Hz using the infrared thermograph. The contact load was measured by a strain gauge attached to the vise. The excitation time was set to 0.325 s.

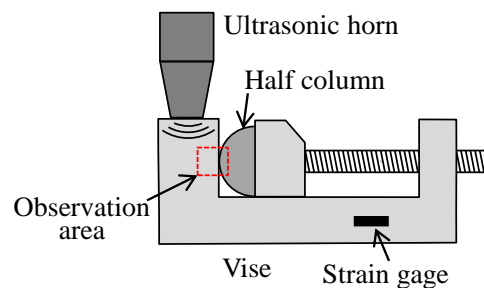


Fig. 2 Schematic diagram of the experimental setup used to investigate the effects of the contact load.

## Experimental results and discussion

The heat generation behavior in the observation area near the contact surfaces was investigated by infrared thermography, while changing the excitation distance,  $x$ . As examples of the observation results, the time variation of the temperature images obtained at  $x = 300$  mm is shown in Fig. 3. The heat generation near the contact point was detected and the temperature increased with increasing excitation time.

In order to discuss the relationship between the change of the heat generation and the excitation distance quantitatively, the temperature change,  $\Delta T$ , generated during the excitation time at a square area of 1 mm  $\times$  1 mm including the contact point was obtained from the infrared image for each excitation distance. Figure 4 shows the



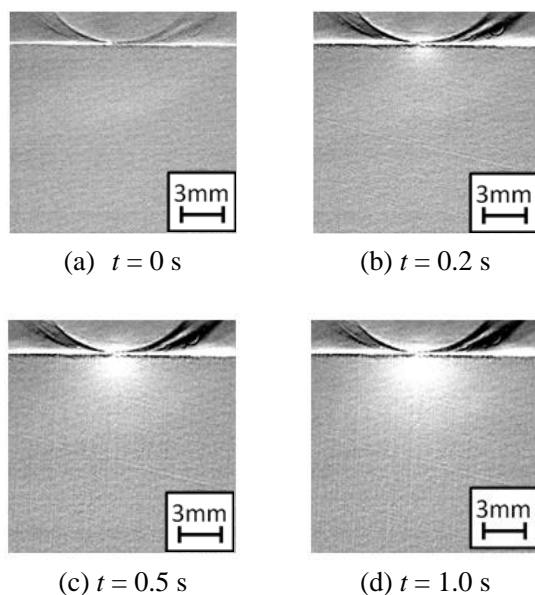


Fig. 3 Time variation of the temperature image obtained by the Sonic-IR method at  $x = 300$  mm.

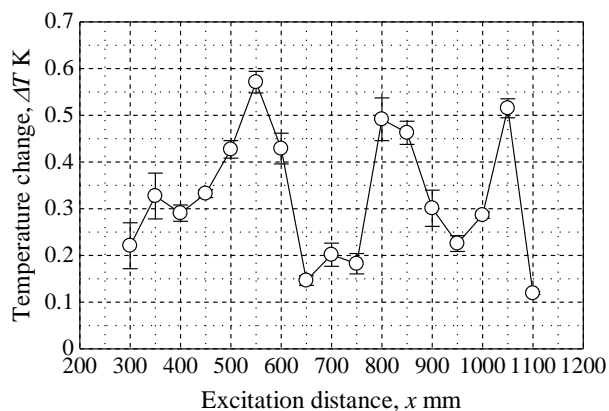


Fig. 4 Relationship between the temperature change near the contact point and the excitation distance.

relationship between the temperature change,  $\Delta T$ , near the contact point and the excitation distance,  $x$ . The temperature change could be detected at each  $x$  from 300 mm to 1100 mm, and an approximately symmetrical distribution about the point at  $x = 700$  mm was obtained. The point  $x = 700$  mm is the midpoint of the long beam specimen. The monotonous decrease of the temperature change with increasing the excitation distance  $x$  was not recognized in Fig.3. Based on these results, the heat generation in this experiment is considered to be strongly affected not by the progressive wave propagated from the

excitation point but rather by the characteristic vibration of the long beam specimen.

Next, the investigation results related to the effects of the contact load on the heat generation are described. The half-column specimen was clamped in a vise (Fig. 2) under the various load conditions, and the temperature distribution near the contact point was measured at each contact load. As an example, Fig. 5 shows an infrared image obtained at a contact load of 174 N and an excitation time of 0.325 s.

The temperature change,  $\Delta T$ , generated during the excitation time at a square region of  $2 \text{ mm} \times 2 \text{ mm}$  near the contact point was calculated from the infrared images. Figure 6 shows the relationship between the temperature change,  $\Delta T$ , and the contact load,  $W$ . When the contact load is less than 600 N, the temperature change,  $\Delta T$ , increases with the contact load. However, when the contact load increases further, the temperature change,  $\Delta T$ , decreases with the increase in the contact load.

The friction force increases with the contact load. Therefore, the increase in the magnitude of the temperature change under a small contact load can be explained by the increase in the friction force. However, when the friction force increases further, sticking may occur between the contact surfaces, which would decrease the relative slip between the contact surfaces. Therefore, it is expected that the heat generation caused by the friction cannot

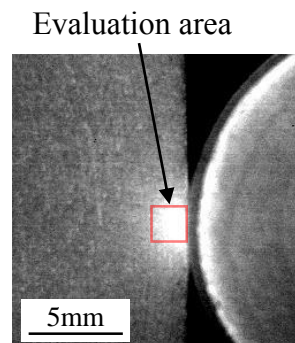


Fig. 5 Infrared image obtained under a contact load of  $W = 174$  N and an excitation time of  $t = 0.325$  s.

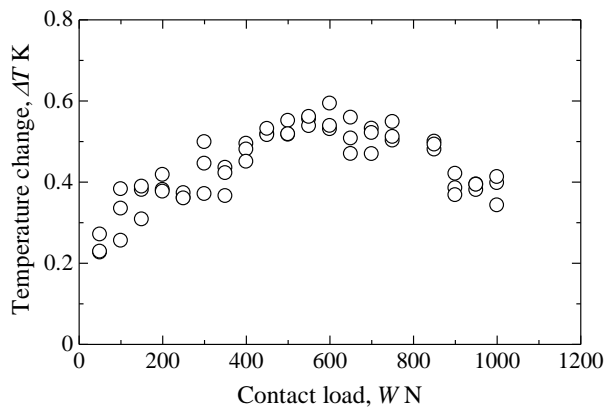


Fig. 6 Relationship between the contact load and the temperature change.

increase even if the contact load increases. The reason for the tendency for the magnitude of the temperature change to decrease, observed under higher contact loads, can be explained by sticking between the contact surfaces.

## Conclusions

1. The relationship between the temperature change during the excitation time near the contact point and the excitation distance was investigated. The temperature change for the excitation distance exhibited an approximately symmetrical distribution about the midpoint of the specimen.
2. The heat generation near the contact point is strongly affected by the characteristic vibration of the long beam specimen.
3. The relationship between the magnitude of the temperature change and the contact load was

investigated. When the contact load is comparatively small, the temperature change increases with the contact load. However, when the contact load increases further, the temperature change decreases with the increase of the contact load.

4. The variation of the heat generation for the contact load can be explained by the change in the friction force and sticking between the contact surfaces.

## References

1. E. G. Henneke II, K. L. Reifsnider, and W. W. Stinchcomb, Thermography - An NDI Method for Damage Detection, *J. Metals*, Vol. 31, pp. 11-15, 1979.
2. L. D. Favro, X. Han, Z. Ouyang, G. Sun, H. Sui, and R. L. Thomas, Infrared imaging of defects heated by a sonic pulse, *Rev. of Sci. Instrum.*, Vol. 71, pp. 2418-2421, 2000.
3. S. D. Holland, First measurements from a new broadband vibrothermography measurement system, *Review of quantitative nondestructive evaluation*, Vol. 26, pp. 478-483, 2007.
4. T. Sakagami, R. Katsumata, K. Kuroki, Y. Harada, and S. Kubo, Detection of Stress Corrosion Cracking by Sonic-IR Technique, *Proc. of the 7th International Conf. on NDE in Relation to Structural Integrity for Nuclear and Pressurized Components*, pp. 1087-1093.
5. S. D. Holland, et al., Quantifying the vibrothermographic effect, *NDT & E International*, Vol. 44, pp. 775-782, 2011.
6. F. Mabrouki, M. Thomas, M. Genest, and A. Fahr, Frictional heating model for efficient use of vibrothermography, *NDT&E International*, Vol. 42, pp. 345-352, 2009.
7. J. Renshaw, J. C. Chen, S. D. Holland, and R. B. Thompson, The sources of heat generation in vibrothermography, *NDT & E International*, Vol. 44, pp. 736-739, 2011.

# THERMAL RESPONSE MEASUREMENT OF BUILDING INSULATING MATERIALS BY INFRARED THERMOGRAPHY

G. Ferrarini<sup>2</sup>, P. Bison<sup>1</sup>, A. Bortolin<sup>1</sup>, G. Cadelano<sup>1</sup>

<sup>1</sup> Dipartimento di Ingegneria Industriale, UNIPD, Padova, Italy

<sup>2</sup> Consiglio Nazionale delle Ricerche, ITC, Padova, Italy

paolo.bison@itc.cnr.it

The most common building retrofit measure involves the installation of a new insulating layer. During the European Project ECOSHOPPING, several insulating materials were screened and tested to select the most appropriate for the retrofit of a commercial building. To investigate the dynamic behavior of the wall, several wall samples were tested in laboratory with an experimental layout that resembled an outdoor installation, where a sinusoidal thermal stimulus was imposed on the back of the specimen. The surface temperature evolution over time was recorded with an infrared camera both on the front and on the back surfaces of the specimen, in order to measure the time shift. The results were compared with a mathematical model.

## Introduction

The impact of energy saving that could be obtained with the retrofit of existing building is underlined by technical standards and laws at a national and European level. The European Union promotes and funds different project about sustainability and energy efficiency of buildings; amongst them the European FP 7<sup>th</sup> Project ECOSHOPPING [1] is aimed at reducing the energy impact of a commercial building located in Hungary. One of the main energy saving measures available for the retrofit of this building is the installation or the replacement of the insulating layer.

The main benefit of insulation is achieved in steady-state conditions, typical of the winter season. A better insulating performance means a decrease of heating demand, as the latter is directly related to the thermal transmittance (U-value) of the wall. However the insulating layer has a role also in periodic thermal conditions, typical of the summer season. The type and the position of the insulating material inside the wall stratigraphy can improve both energy efficiency [2] and thermal comfort [3].

Infrared thermography is a valid technique for the evaluation of building elements and it showed interesting results also in transient regime and in long data acquisition studies [4]. The dynamic thermal behavior of walls could be influenced by the water content [5] but in this work the materials are in dry conditions.

## Mathematical Model

A wall is usually stimulated by a periodic sinusoidal heat source (the sun) with a period equal to 24 hours (Fig.1). The temperature variation on the stimulated (outer) side of the wall is transferred through the wall to the internal surface, that shows a periodic temperature oscillation that is time shifted and attenuated with respect to the original signal. This behavior can be modeled with the heat equation.

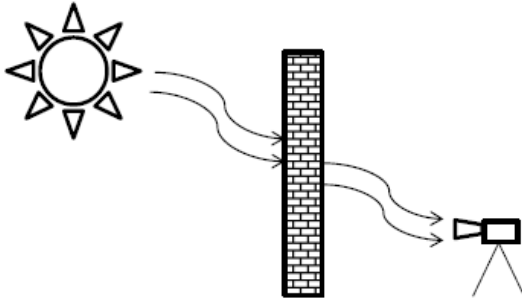


Figure 1. The periodic thermal stimulus of the sun on the outer surface of the wall is visible, with a time shift and an attenuation, as a periodic temperature variation on the inner side of the wall.

This problem is usually modeled with a one-dimensional equation [6, 7]:

$$\frac{\partial^2 T(x,t)}{\partial x^2} = \frac{1}{\alpha} \frac{\partial T(x,t)}{\partial t}$$

where  $T$  = the temperature at position  $x$   
 $t$  = time

$\alpha$  = the thermal diffusivity  $\frac{k}{\rho C_p}$

$k$  = thermal conductivity (W / m °K)

$\rho$  = density ( kg / m<sup>3</sup>) and

$C_p$  = specific heat ( J / kg °K)

The heat flux at any position  $x$  and time  $t$  is given by:

$$q(x,t) = -k \frac{\partial T(x,t)}{\partial x} \quad (2)$$

In both equations,  $k$ ,  $\rho$ , and  $C_p$  are assumed to be constant. This equation could be solved using the Laplace transform, that changes this partial differential equation into an ordinary differential equation.

Considering only the temperature and heat flux at the surfaces of the wall of thickness  $\ell$ , it is possible to rewrite the boundary terms.  $T_1(s)$  and  $T_2(s)$  are equal to  $T(0,s)$  and  $T(\ell, s)$ , which are the transform of the temperature at the inner and outer surfaces respectively.  $q_1(s)$  and  $q_2(s)$  are equal to  $q(0,s)$  and  $q(\ell, s)$ , which are the transform of the heat flux at the inner and outer surfaces respectively.

The values of  $T_1(s)$  and  $q_1(s)$  are the following:

$$T_1(s) = \left( \cosh(\ell\sqrt{s/\alpha}) \right) T_2(s) + \dots + \left( \frac{1}{k\sqrt{s/\alpha}} \sinh(\ell\sqrt{s/\alpha}) \right) q_2(s) \quad (3)$$

$$q_1(s) = \left( k\sqrt{s/\alpha} \sinh(\ell\sqrt{s/\alpha}) \right) T_2(s) + \dots + \left( \cosh(\ell\sqrt{s/\alpha}) \right) q_2(s) \quad (4)$$

For notational convenience, we may now define new variables as follows:

$$A(s) = \cosh(\ell\sqrt{s/\alpha})$$

$$B(s) = \frac{1}{k\sqrt{s/\alpha}} \sinh(\ell\sqrt{s/\alpha}) \quad (5)$$

$$C(s) = k\sqrt{s/\alpha} \sinh(\ell\sqrt{s/\alpha})$$

$$D(s) = \cosh(\ell\sqrt{s/\alpha})$$

With these new variables, Eq. 3 and 4 become:

$$T_1(s) = A(s) T_2(s) + B(s) q_2(s), \quad B(s) \neq 0 \quad (6)$$

$$q_1(s) = C(s) T_2(s) + D(s) q_2(s) \quad (7)$$

We can rewrite these equations in matrix form as:

$$\begin{bmatrix} T_1(s) \\ q_1(s) \end{bmatrix} = \begin{bmatrix} A(s) & B(s) \\ C(s) & D(s) \end{bmatrix} \begin{bmatrix} T_2(s) \\ q_2(s) \end{bmatrix} = [Z] * [T, q] \quad (8)$$

where  $Z$  is the transfer matrix of the single layer. For a multilayer building component, the overall transfer matrix is the product of each layer matrix as in:

$$Z = Z_N \cdot Z_{N-1} \dots Z_3 \cdot Z_2 \cdot Z_1 \quad (9)$$

where  $Z_1, Z_2, Z_i, \dots, Z_N$ , are the transfer matrices of the different layers, beginning from layer 1. Layer 1 is conventionally the internal layer.

The transfer matrix from environment to environment through the building component is:  $Z_{tot} = Z_{b2} \cdot Z \cdot Z_{b1}$  (10)

where  $Z_{b1}$  and  $Z_{b2}$  are the transfer matrices of the boundary layers, given by:

$$Z_b = \begin{bmatrix} 1 & -R_s \\ 0 & 1 \end{bmatrix} \quad (11)$$

where  $R_s$  is the surface resistance [ $m^2 K W^{-1}$ ] of the boundary layer, that includes both convection and radiation. Values of this parameter are available in [8].

Each element of the  $Z$  matrix is therefore a complex number that could indicate the effect of a temperature or flow heat variation on a surface cause by the stimulation of the opposite surface or the time delay between cause and effect. The time delay between the maximum of an effect and its corresponding cause is calculated from the phase shift of the transfer matrix element  $Z_{ij}$

$$\Delta t_{ij} = \frac{T}{2\pi} \varphi_{ij} = \frac{T}{2\pi} \arg(Z_{ij}) \quad (12)$$

## Experimental setup

The measured samples are sandwiches made by three layers: two outer plasterboard slabs and one internal insulating layer. The thickness and thermal properties of the different materials were measured in laboratory and are reported in table 1.

Material	Thermal conductivity [ $W m^{-1} K^{-1}$ ]	Specific heat [ $J kg^{-1} K^{-1}$ ]	Volumic mass [ $kg m^{-3}$ ]	Thickness [m]
Plasterboard	0.227 $\pm 0.007$	1000 $\pm 50$	820 $\pm 20$	0.0125 $\pm 0.0001$
Aerogel	0.0187 $\pm 0.0006$	1200 $\pm 70$	175 $\pm 5$	0.005 $\pm 0.0001$
EPS	0.040 $\pm 0.0016$	1140 $\pm 70$	17 $\pm 1$	0.06 $\pm 0.0001$

Polyuret hane	0.0259 $\pm 0.0005$	1530 $\pm 45$	44 $\pm 2$	0.05 $\pm 0.0001$
---------------	------------------------	------------------	---------------	----------------------

Table 1. Thermal properties of the tested materials

The active source of the experimental setup is a 1 kW lamp that is controlled with a customized software. The lamps delivers a sinusoidal heating on the back surface of the sample with an amplitude equal to the 60% of the lamp power and a period equal to 2 hours. A FLIR SC660 thermal camera (spectral response  $7,5\mu m - 13,5\mu m$ , NETD  $<30 mK$ ,  $640 \times 480$  pixel) is placed towards the front size of the sample, looking also at a thermally reflective mirror (aluminum foil) that is placed in a direction that optimizes the reflected temperature of the back surface of the specimen (Fig,2). A brick is placed in the field of view of the camera in order to have a stationary thermal reference.

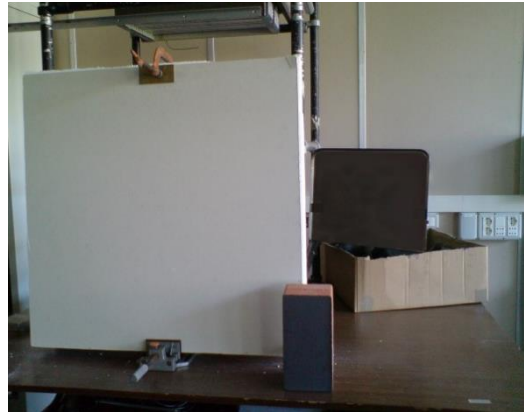


Figure 2. Experimental setup as seen by the thermal camera: the white sample is heated by a modulated lamp placed behind it, a reflective element (on the right) captures the oscillation of the back temperature over time.

The data acquisition begins with some images before the thermal stimulation (cold images) where two markers are placed on the surfaces in order to verify the camera alignment and focus. Then the lamp is turned on and the data are acquired for at least three entire periods.

## Results

Four experimental tests were performed on different materials and layer configurations. The temperature profile of the central area on front and back layer are extracted from the thermal

sequence. The data are centered, scaled and fitted with a sinusoidal model. The time shift is calculated on the last period as the time difference between the maximum value recorded on the front and on the back surface of the sample (eq. 13).

$$\Delta t_{meas} = t(T_{max,front}) - t(T_{max,back}) \quad (13)$$

A first experiment was performed with a stimulation period equal to 10 minutes on a plasterboard slab and compared to the calculated time shift, as shown in table 2.

Sample	Measured timeshift [min]	Calculated timeshift [min]
Plasterboard	1.72	1.83

Table 2. Measured time shift values on a plasterboard slab with a stimulation period equal to 10 minutes.

The other three experiments were performed on sandwiches with two external plasterboard slabs and one internal insulating layer. The results obtained with a stimulation period equal to 2 hours are reported in Table 3.

Sample	Measured timeshift [h]
Plasterboard +Aerogel +Plasterboard	0.359
Plasterboard +EPS +Plasterboard	0.438
Plasterboard +Polyurethane +Plasterboard	0.630

Table 3. Measured time shift values on different samples with a stimulation period equal to 2 hours.

The results show that the trend of the measured values is consistent with the modeled one, as the

time shift is increasing as indicated by the measured thermal properties of the material.

## Conclusion

A new methodology, based on infrared thermography, is proposed for the measurement of thermal response of building elements. The laboratory testing on several samples and the comparison with the mathematical model verified the feasibility of this method. Further studies will try to extend this method to an on-site survey of buildings, taking advantage of the periodic sun radiation.

## References

1. ECOSHOPPING, European FP7<sup>th</sup> Project. [www.ecoshopping-project.eu](http://www.ecoshopping-project.eu). Accessed 04/04/2015
2. E. Kossecka, J. Kosny, Influence of insulation configuration on heating and cooling loads in a continuously used building, *Energy and Buildings*, Vol. 34, Issue 4, pp. 321-331, 2012
3. C. Di Perna, F. Stazi, A. Ursini Casalena, M. D’Orazio, Influence of the internal inertia of the building envelope on summertime comfort in buildings with high internal heat loads, *Energy and Buildings*, Vol. 43, Issue 1, Pages 200-206, 2011
4. Bortolin, A., Cadelano, G., Ferrarini, G., Bison, P., Peron, F., Maldague, X., High resolution survey of buildings by lock-in IR thermography, *Proceedings of SPIE - The International Society for Optical Engineering*, 8705, art. no. 870503, 2013
5. G. Cadelano, P. Bison, A. Bortolin, G. Ferrarini, F. Peron, M. Giroto, M. Volinia, Monitoring of historical frescoes by timed infrared imaging analysis, *Opto-Electronics Review*, Vol. 23, Issue 1, 2015
6. D. C. Hittle, R. Bishop, An improved root-finding procedure for use in calculating transient heat flow through multilayered slabs, *International Journal of Heat and Mass Transfer*, Vol. 26, Issue 11, pp 1685-1693, 1983
7. ISO 13786:2006 Thermal performance of buildings components – Dynamic thermal characteristics – Calculation methods
8. UNI EN ISO 6946:2008 Building components and building elements – Thermal resistance and thermal transmittance – Calculation method



# SOLAR LOADING THERMOGRAPHY FOR ARCHITECTURAL HERITAGE SURVEYS: PLUMB THE DEPTH BY LOOKING AT THE FAÇADE

S. Sfarra<sup>1</sup>, P. Bison<sup>2</sup>, A. Bortolin<sup>2</sup>, G. Cadelano<sup>2</sup>, G. Ferrarini<sup>2</sup>, D. Paoletti<sup>1</sup>, C. Ibarra-Castanedo<sup>3</sup>, X. Maldague<sup>3</sup>, F. Peron<sup>4</sup>

<sup>1</sup> Las.E.R. Laboratory, Department of Industrial and Information Engineering and Economics (DIIE), University of L'Aquila, Piazzale E. Pontieri no. 1, Loc. Monteluco di Roio, L'Aquila I-67100, Italy, stefano.sfarra@univaq.it

<sup>2</sup> ITC-CNR, Corso Stati Uniti no. 4, Padua I-35127, Italy, paolo.bison@itc.cnr.it

<sup>3</sup> Computer Vision and Systems Laboratory (CVSL), Department of Electrical and Computer Engineering, Université Laval, 1065, av. de la Médecine, Québec City (Québec) G1V0A6, Canada, IbarraC@gel.ulaval.ca

<sup>4</sup> Università IUAV di Venezia, Santa Croce 191 Tolentini, Venice I-30135, Italy, fabio.peron@iuav.it

The paper is centered on two case-studies in which the role of the sun as thermal stimulus is discussed working with the infrared thermography (IRT) technique. The first case-study is based on *Santa Maria di Collemaggio* Church in L'Aquila (Italy), initially built in the second half of the XIII century. The second case-study talks about a masterpiece of Venetian Gothic, *i.e.*, *Palazzo Ducale* in Venice (Italy). In both cases, the striking jewel-box effect of the facades is due to a pattern of blocks of alternating pink and white stones. The facades and one lateral side of the Church constructed by using the masonry local system named, "*apparecchio aquilano*" have been inspected. Sub-superficial anomalies such as cracks, buried structures, humidity and metal reinforcements can be visualized exploiting the solar cycle.

## Introduction

Contrary to the passive approach, the active approach requires an unnatural external heat source to stimulate the materials under inspection; in addition, the time  $t$  of the thermographic experiment is a fundamental and indispensable variable to be considered.

Above all in the conservation field, the distinction among passive and active approach is not as clear as it seems. For example, it is interesting to note that, in the past, moisture evaluation of building envelope has been attributed into the passive approach.

In such cases, the passive label is debatable since the solar loading is a natural form of external thermal stimulation [1]. A debatable solution for this controversy could be to consider as passive all thermography approaches in which the user has little or no control over the source of energy.

Although the use of advanced processing algorithms [2] is not a *condicio sine qua non* in order to obtain interesting results into the architectural heritage field if a time-lapse approach is used [3], in the present case, the analysis of the thermograms by using the principal component thermography (PCT) technique appears a smart choice.

This is due to the fact that both the heating and cooling phases can be concurrently processed, or a selection of thermograms coming from the total sequence acquired in order to limit the influence of unwanted external conditions on the structure to be inspected, such as shadows or pouring rain.

The results presented herein complement previous works performed on the same buildings [4–5], by providing further and interesting results to be discussed.

## Specific remarks of the inspected facades

The rebuild of the façade of the *Collemaggio* Church carried out as a result of the 1915 earthquake follows the approved design of 1919 [6]. The external stones were numbered and positioned again in the same positions, following one condition: the solid bricks were placed up to + 17 m, while the hollow bricks from + 17 m to the top of the roof in order to lighten the upper part vulnerable to vibrations. The connection to the wall was realized by means of horizontal and vertical anchor bolts applied on the internal structure in reinforced concrete. The rebuilding of the dichromate stone cladding was performed simultaneously with the wall. The ashlar of the cladding were blocked by iron clamps placed inside the masonry.

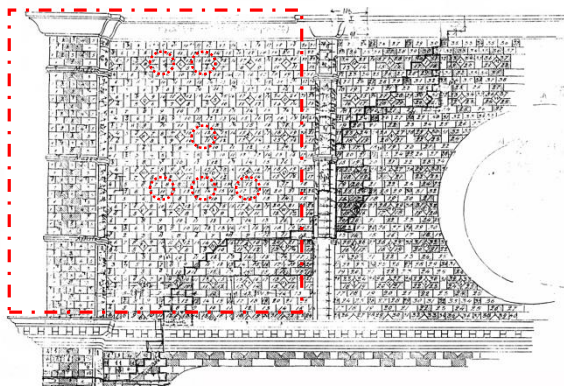


Fig. 1. Drawing of a part of *Collemaggio* façade [7]

Fig. 1 shows the positions of some of the iron clamps, indicated by dotted circles, and the location and extend of the demolished part in addition to the previous collapsed part, taking into account the environmental effect on the masonry that remained uncovered for different time. The inspected part is surrounded by a dotted rectangle.

Additionally, the lateral façade of the same Church, was completed by using a particular constructive technique based on stones (Fig. 2) and named “*apparecchio aquilano*” [6]. This technique is characterized by the presence of stony ashlar placed in staggered horizontal courses.



Fig. 2. Thermographic inspection of the lateral *Collemaggio* façade showing from top to bottom: the position of the infrared camera, the inspected part linked, and the satellite view of the Church showing the sun path during the day of acquisition (June 07<sup>th</sup> 2013, image from [www.sunearthtools.com](http://www.sunearthtools.com)).

The façade of Palazzo Ducale in Venice was constructed using Istria’s stones. This type of limestone shows important characteristics of resistance and durability to the saline action. It should be noted that in Venice stone façades do not generally have a structural function like a weight-bearing wall. The latter is carried out by the underlying solid brick masonry, more plastically deformable, even where the ashlar of the external coating exhibit a remarkable thickness. However, it appears very important the self-supporting function of the facades, often built by blocks of great thickness, held on the rear structure just by using mortars. In the past, many constructions built in this area do not employed iron clamps. For example, the external layer of the upper wall of Palazzo Ducale (Fig. 3), showing designs thanks to polychrome lozenges, is realized using stone blocks of variable thickness (between 100 and 250 mm, approximately) perfectly corresponding on the external side, without any sub-superficial reinforcement in metal. Indeed, the latter, as discussed in the case of *Collemaggio* Church, usually connect the layers across the stones [8].

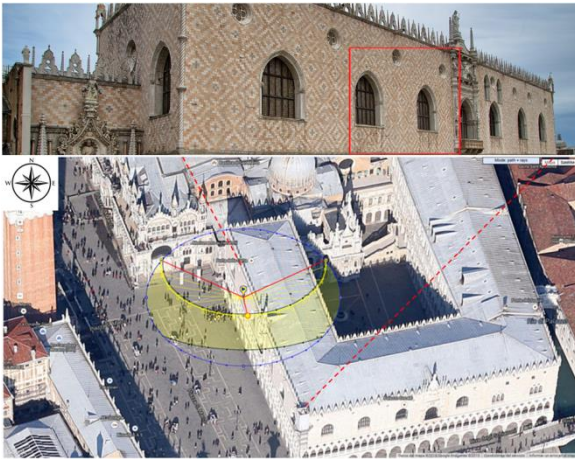


Fig. 3. Thermographic inspection of the Palazzo Ducale façade: the inspected part linked to (top), and the satellite view (bottom) of the Church showing the sun path during one of the fourteen days of acquisition (July 2<sup>nd</sup> 2011, image from www.sunearthtools.com).

### Data acquisition and image processing

The Sun is a periodic heat source with period equal to 24 hours. During the day-time the Sun works as a source producing a positive heat flux, while during the night-time the earth irradiate towards the sky that can be viewed as a sink producing a negative heat flux. It is expected that the amplitude of the temperature oscillation decreases going deeper and deeper into the solid, and the phase of the periodic thermal wave is delayed [5]. In the first case scenario, a FLIR S65 HS (320 x 240, 7.5 – 13  $\mu\text{m}$ ) thermal camera has been used, while in the second case scenario, a FLIR SC660 (640 x 480, 7.5 – 13  $\mu\text{m}$ ) thermal camera has been employed. In the inspection of the *Collemaggio* Church, the frame rate was set at 1 image every 60 seconds, while during the image acquisition of *Palazzo Ducale*, the same parameter was set at 1 image every 180 seconds. In both case scenarios, thermograms were analyzed using PCT technique, which reorganizes data into new components that take into account the main spatiotemporal variances of the sequence.

### Experimental results and discussion

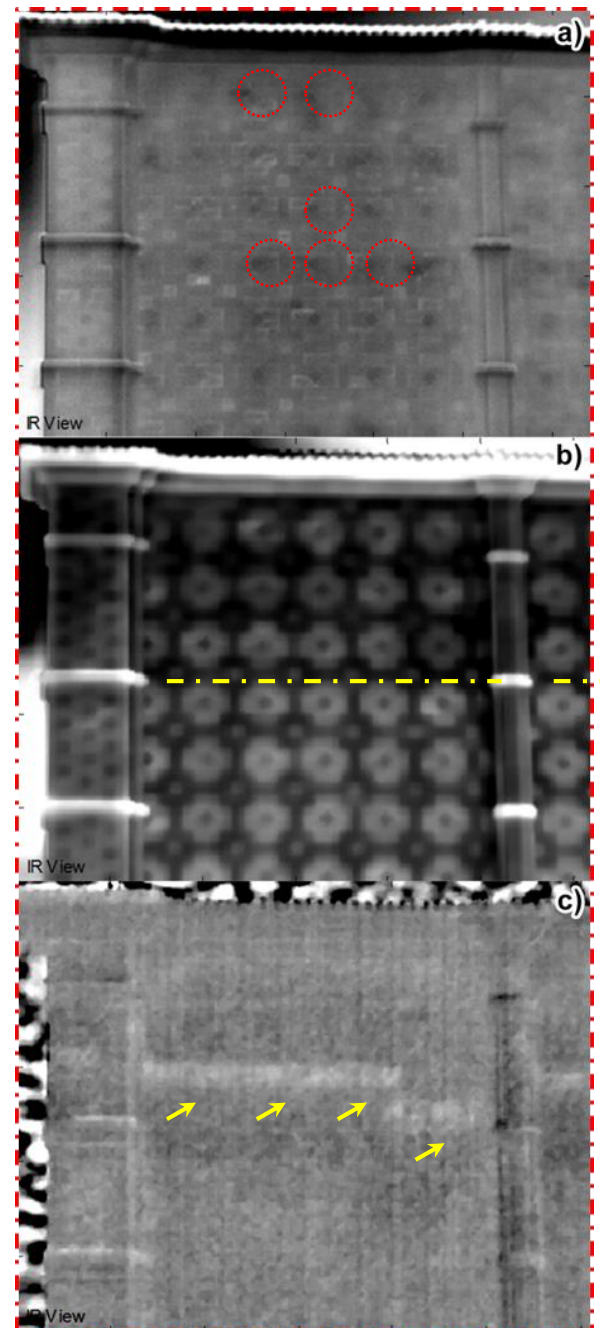


Fig. 4. Façade of *Collemaggio* Church. PCT results from 848 thermograms (1 day): a) EOF<sub>1</sub>, b) EOF<sub>4</sub>, and c) EOF<sub>103</sub>

Figure 4 and Figure 5 present some processed results from the *Collemaggio* Church. In Fig. 4a, iron clamps (Fig. 1) have been detected in the lateral wall of the Church, while in Fig. 4b and 4c the border area between the solid and hollow bricks and two sub-superficial horizontal reinforcing structures have been indicated, respectively.



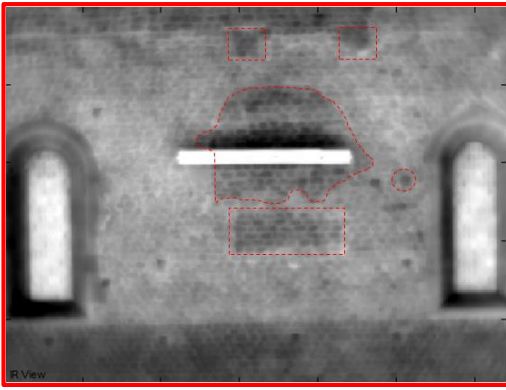


Fig. 5. Lateral façade of *Collemaggio* Church. PCT result from 453 thermograms (1 day): EOF<sub>1</sub>

In Fig. 5, some sub-superficial buried structures are signaled by red dotted lines. The most important features are surrounded by dotted squares, because both their shapes and position in height are very close to those detected on the main façade in [9], by using the ground penetrating radar (GPR) technique. In addition, it is very interesting to note the difference among the shape of the thermal imprint of the walled window positioned between the current windows, and its shape visible to the naked eye (Fig. 2).

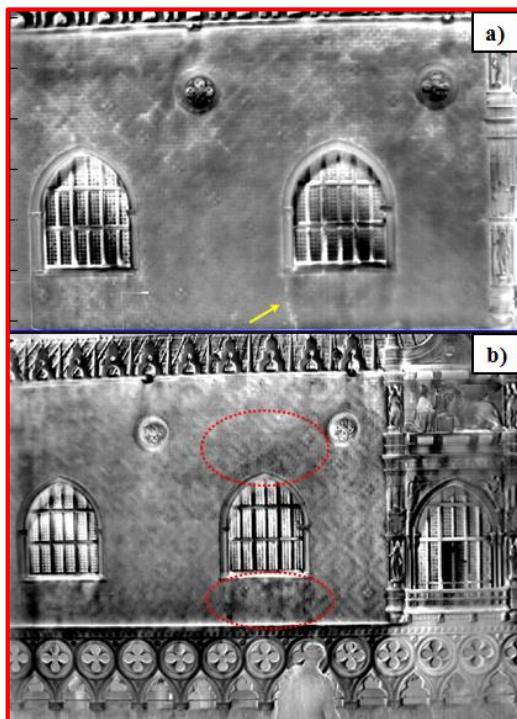


Fig. 6. Façade of *Palazzo Ducale* turned towards the small square. PCT results from 706 thermograms (14 days): a) EOF<sub>13</sub> (cropped image), and b) EOF<sub>23</sub>

Figure 6 shows two results from the *Palazzo Ducale* façade. In Fig. 6a a crack is apparently seen below one of the window, while some off-centered tiles (see the two regions in Fig. 6b, above and below the same window) also appear in correspondence to wet surfaces detectable in additional results not herein reported. Additional results will be presented during the Conference.

## Conclusions

The solar loading approach reveals its ability to detect sub-superficial features, working from one to several days. The frame rate between each thermogram must be relatively short and, in general, it is dependent to the weather condition and thermal excursion into the period of acquisition. It is evident that an historical research is always needed in the cultural heritage field.

## References

1. X.P.V. Maldague. Theory and practice of infrared technology for nondestructive testing. New York: John Wiley & Sons; 2001.
2. C. Ibarra-Castanedo, M. Genest, N. Avdelidis, C.-H. Jen, J.M. Piau, S. Guilbert, X. Maldague, A. Bendada. Comparative study of active thermography techniques for the nondestructive evaluation of honeycomb structures, *Res. Nondestruct. Eval.*, 20(1), pp. 1-31, 2009.
3. M. Fox, D. Coley, S. Goodhew, P. De Wilde. Time-lapse thermography for building defect detection, *Energ. Buildings*, 92, pp. 95-106, 2015.
4. S. Sfarra, A. Bendada, C. Ibarra-Castanedo, D. Ambrosini, D. Paoletti, X. Maldague. Santa Maria di Collemaggio Church (L'Aquila, Italy): historical reconstruction by non-destructive testing techniques, *Int. J. Archit. Herit.*, 9(4), pp. 367-90, 2015.
5. A. Bortolin, G. Cadelano, G. Ferrarini, P. Bison, F. Peron, X. Maldague. High-resolution survey of buildings by lock-in IR thermography, *Thermosense: Thermal Infrared Applications XXXV*, Proc. SPIE 8705, Orlando (USA), 2013.
6. C. Bartolomucci. Santa Maria di Collemaggio. Interpretazione critica e problemi di conservazione. Roma: Palombi Ed.; 2004.
7. Picture from Archivio Centrale dello Stato Italiano.
8. A.C. Dell'Acqua, V. Degli Esposti, A. Ferrane, G. Mochi. Tradizioni del costruire nel territorio nazionale. Città di Castello (PG): Alinea Ed.; 2011.
9. D. Ranalli, M. Scozzafava, M. Tallini. Ground penetrating radar investigations for the restoration of historic buildings: the case study of the Collemaggio Basilica (L'Aquila, Italy), *J. Cult. Herit.*, 5(1), pp. 91-9, 2004.

# COMPLEMENTARITY OF TERRESTRIAL LASER SCANNING AND IR THERMOGRAPHY FOR THE DIAGNOSIS OF CULTURAL HERITAGE: THE CASE OF PACENTRO CASTLE

I. Nardi<sup>1</sup>, S. Sfarra<sup>1</sup>, D. Ambrosini<sup>1</sup>, D. Dominici<sup>2</sup>, E. Rosciano<sup>3</sup>

<sup>1</sup>University of L'Aquila – DIIE Dept. – I 67100 Monteluco di Roio (L'Aquila)  
iole.nardi@graduate.univaq.it; {stefano.sfarra, dario.ambrosini}@univaq.it

<sup>2</sup>University of L'Aquila – DICEAA Dept. – I 67100 Monteluco di Roio (L'Aquila)  
donatella.dominici@univaq.it

<sup>3</sup>A.S.I. – Italian Space Agency – 75100 Contrada Terlecchia (Matera)  
elisa.rosciano@est.asi.it

This work deals with the combining of Terrestrial Laser Scanning (TLS) and the IR Thermography (IRT) techniques that are based on different principles, although information gathered from surveys can be merged for a wider knowledge on the health state of a building or a structure. The structure on which the measurement campaign has been performed is the Pacentro Castle, located in the Abruzzo Region (Italy). The two techniques let to identify critical and weak points of the structure, for possible future maintenance intervention.

## Introduction

The need of conservation of the cultural heritage lead to the development of new techniques, models or post-processing methods [1]. With increasing frequency, well-established methods and techniques are mixed to achieve a detailed knowledge of a phenomena, or to better understand the causes of damages, whether they are visible or not.

In the field of the architectural heritage, in the last few years several studies aimed to mix, combine and integrate different techniques. A particular interest is addressed to the integration of Terrestrial Laser Scanning (TLS) and IR Thermography (IRT) techniques that provide complementary information.

The TLS retrieves the 3D shape of an object through the triangulation of a laser light, providing clouds of thousands or millions of points which measure the distance between the laser source and the object.

The IRT provides the thermal digital image of an object by converting the measure of the heat energy to an electrical signal using a microprocessor.

The recent literature in the field [2-5] witnesses that metric information gathered through a laser scanner can refine the thermal study of the structure available through an IR camera. Furthermore, a method that matches and rectifies an IRT image stack has been recently proposed [6]: using a set of targets it is possible to monitor indoor microclimatic conditions [7]; in addition, through the photogrammetric technique and the information gathered from sensors, it is possible to reconstruct a 2D or 3D model.

These works, however, usually aim to *texture* the information obtained by IRT and TLS techniques, by using specific post-processing tools and software.

In this paper, these techniques are used but information on the conservation of the Castle are gathered simply by comparing the 3D map obtained by TLS and the thermal field recorded by the IR camera, showing that for diagnostic purposes, in specific cases, it is not necessary a complex post-processing phase of data or images.

## A case study: the Pacentro Castle (Italy)

The structure on which the measurement campaign has been performed is the Pacentro Castle, located in Abruzzo Region, at 718 m a.s.l (Fig.1). The Castle was probably built in the 11<sup>th</sup> century for defense purposes, since the neighborhood was continuously besieged. Later, it was used as prison, and subsequently as abode of the local feudatory. After the XV Century, the Castle was progressively dismissed, and then it went through a consequent decay, until the reinforcement interventions, which occurred during the end of the '70s.

The configuration of the Castle, that includes three square-based towers, three fortified cylindrical towers, and a surrounding wall (all of them made of rough-cut stones), suggests the strategic and architectural importance of the manor, that took its configuration between the Middle Ages and the Renaissance.



Fig. 1. The Pacentro Castle: (a) East view (b) North view and (c) captured in a historical photograph.

The North-West tower (23 m high), which has a blunted corner, has been built in different ages, as precise hints suggest that levels have been added. Furthermore, a series of big aligned holes on the south façade, repeated at different heights, suggest the presence of wooded floors hold by wood beams, in order to obtain three further floors, adjacent to the ones in the tower.

The North-East tower (24 m high) is distinguished by the elegance and beauty of decoration and machicolations, while the South-

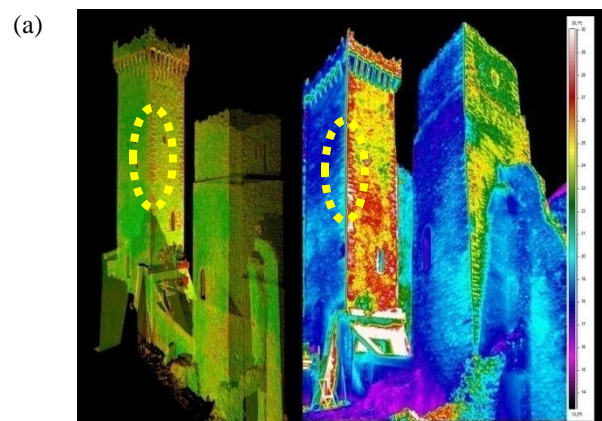
East tower is different from the others, since it is tapered from the second offset, probably because of the height of the construction, that nowadays, although partially destroyed, is 23 m high.

## Measurement campaign

The campaign took place on June 16<sup>th</sup>, 2011.

The equipment used for this work was a thermographic camera FLIR ThermaCAM<sup>®</sup> S65 HS, whose detector is an uncooled microbolometric focal plane array, size 320 x 240 pixels.

For the Terrestrial Laser Scanner survey, a phase based laser scanner Leica HDS 6200 has been used. Among the huge panorama of laser scanners, phase-based scanners are the most accurate and guarantee very high acquisition rates [8]. They have the capability to cover a maximum range of 80 m. In this survey campaign, the maximum resolution (super high mode) has been used to guarantee the highest accuracy. A point spacing of less than 4 mm has been used. Three laser scanner point clouds containing more than one million of points have been acquired. Several thermal images have been acquired too. A 3D model of the Castle has finally been developed. A comparison between the results is shown in Fig. 2.





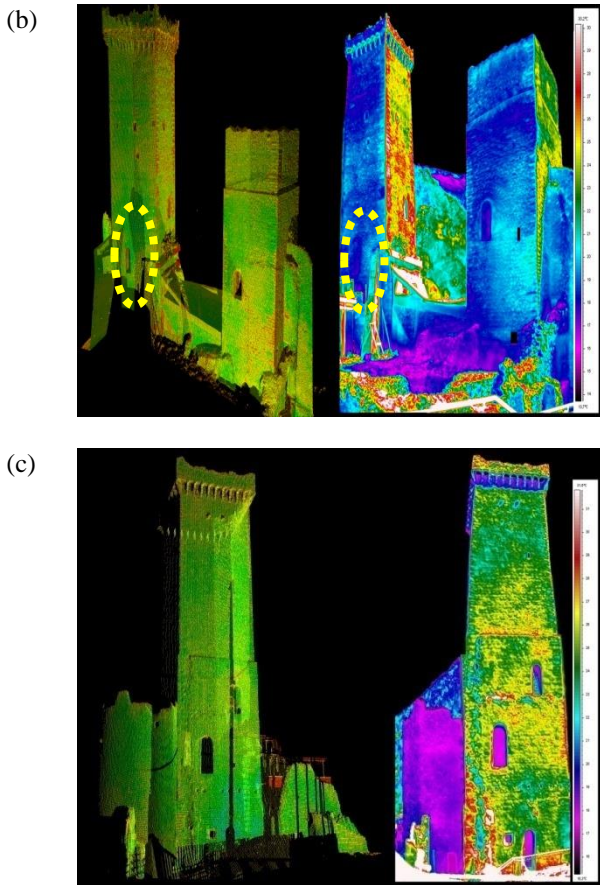


Fig. 2. Tridimensional models (on the left) and IR images (on the right) of the Pacentro Castle: (a) South-West view; (b) West view; (c) South view of the North-West tower.

To create the metric 3D model some magnetic and printed in common sheet points (targets) have been placed around the area to scan. At the end of every laser scanner station they have been used as referencing marker to reattach the point clouds. The post processing operations have been performed using the software Cyclone 8.1. At first every point cloud has been manually filtered to delete the noisy data. The second step has been the automatic alignment of the point clouds using the targets [9]. The entire model has been referenced in a local reference system (a point cloud has been taken as master coordinate system). The final rms on the three point clouds has been less than 6 mm.

The two products (the final 3D model and the IR images) have not been referenced together. The IR images clearly outline the use of different materials in the structure, since they release in different ways the heat of the sun stored during

the day. Such kinds of anomalies are detectable to a trained eye even in the TLS scan, by observing the colorful render of the corner (Fig. 2 (a)).

The use of different materials is probably due to maintenance interventions during the years. It is also possible that the edges of the tower suffered for ageing process due to weathering, and the needed consolidation has probably been performed by inserting bricks in the pre-existent ashlar.

A singularity of the Castle is hidden in the South-East tower, where thanks only to the IR images it is possible to sketch, near the west window, a series of ashlar circle arranged (Fig. 3(a)). This peculiarity suggests that, in ancient times, the opening was wider, and then it has been resized probably for safety requirements.

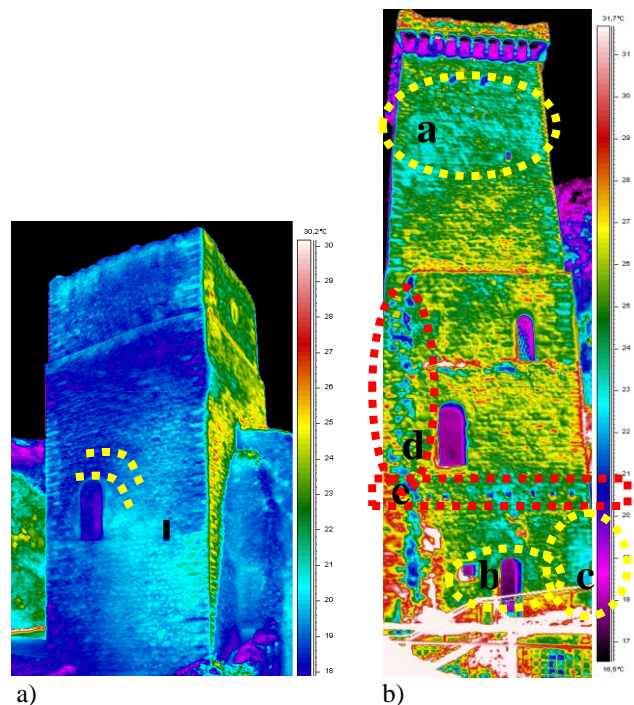


Fig. 3. Detail of the IR images of: a) the South-East tower, West side; b) of the North-West tower, south side, with marks on the main thermal irregularities.

A remarkable difference between TLS and IRT stands in the perspective perception: the first technique renders openings' depth, while the second one, based on superficial information, flattens the image render. This confirms the need to use together the two techniques in order to have a complete description of a structure: zones

with non-uniform temperature distribution might be openings not visible at LWIR spectrum (see Fig. 2(b)).

A detailed IR images of the south side of the North-West tower allows to detect thermal irregularities due to damages (Fig. 3(b)).

In particular, defects *a*, *b*, and *c* (yellow dotted areas) are probably due to water seepage, while defect *d* (red dotted area) shows past restorations realized with materials different from the originals [10]. The irregularity *e* highlights holes in the structure needed to hold several wood beams; the latter support the floor.

As perspective of the present work, the water seepage damage will be better visualized by using a long acquisition, *i.e.*, working under the solar conditions [11].

## Conclusion

This work is focused on the complementarity of two techniques commonly used in artwork diagnostic: TLS and IRT. Although based on different operating principles, these techniques allow to provide useful information on the health state of a masonry or a structure. Despite the current practice, the analyses have been performed by comparing the information and images provided by the techniques, showing that is not always necessary, for diagnostic purposes, a complex texture of the information.

Indeed, an appropriate IR survey, performed after setting the parameter relating to thermal image (emissivity, temperature of background, etc.) can make easier the interpretation of a TL scan without any reference point or texture of the image. This offers the great opportunity to quickly investigate lots of ancient buildings, without further processing steps, that would require expert users.

## References

1. F. Mercuri, U. Zammit, N. Orazi, S. Paoloni, M. Marinelli, F. Scudieri, Active infrared thermography applied to the investigation of art and historic artefacts, *Journal of Thermal Analysis and Calorimetry* 104, pp. 475-485, 2011.
2. S. Lagüela, J. Martinez, J. Armesto, P. Arias. Energy efficiency studies through 3D laser scanning and thermographic technologies, *Energy and Buildings* 43, pp.1216-1221, 2011.
3. M.I. Alba, L. Barazzetti, M. Scaioni, E. Rosina, M. Previtali, Mapping Infrared Data on Terrestrial Laser Scanning 3D Models of buildings, *Remote Sensing* 3, pp. 1847-1870, 2011.
4. C. Maierhofer, R. Krankenhagen, M. Röllig, J. Schlichting, M. Schiller, T. Seidl, R. Mecke, U. Kalisch, C. Hennen, J. Meinhardt, Investigating historic masonry structures with a combination of active thermography and 3D laser scanner, *QIRT Journal*, vol 8, pp 115-118, 2011.
5. A. Costanzo, M. Minasi, G. Casula, M. Musacchio, M.F. Buongiorno, Combined use of Terrestrial Laser Scanning and IR Thermography applied to a historical building, *Sensors* 15, pp. 194-213, 2015.
6. C. Frazen, C. Frazen, G. Siedler, S. Vetter, Orthogonal IRT Imaging, *Digital Heritage International Congress, IEEE Publisher*, vol 1, pp. 633-636, 2013.
7. FB. Djupkep, X. Maldague, A. Bendada, P. Bison, Analysis of a new method of measurement and visualization of indoor conditions by infrared thermography, *Review of Scientific Instruments* 84(8): 084906, 2013.
8. J.I. San José, J. Martínez Rubio, J.J. Fernández Martín, J. García Fernández, Comparing time-of-flight and phase-shift. the survey of the royal pantheon in the basilica of san Isidoro (León), *International Archives of the photogrammetry, Remote Sensing and Spatial Information Sciences*, Volume XXXVIII-5/W16, 2011.
9. D. Dominici, E. Rosciano, M. Alicandro, M. Elaiopoulos, S. Trigliozi, V. Massimi, Cultural Heritage documentation using geomatic techniques; case study: San Basilio's monastery-L'Aquila. *Digital Heritage-International Congress 2013-28 oct-1 Nov, Marseille; France\_ ISBN 978-1-4799-3169-9*, pp. 211-217.
10. D. Paoletti, D. Ambrosini, S. Sfarra, F. Bisegna, Preventive thermographic diagnosis of historical buildings for consolidation, *Journal of Cultural Heritage* 14, pp. 116-121, 2013.
11. E. Edis, I. Flores-Colen, J. de Brito, Quasi-quantitative infrared thermographic detection of moisture variation in facades with adhered ceramic cladding using principal component analysis, *Building and Environment* 94, pp. 97-108, 2015.

# Thermography for depth profiling in cultural heritage

P. Bison<sup>1</sup>, F. Clarelli<sup>2</sup>, G. Inglese<sup>3</sup>

<sup>1</sup> Istituto per le Tecnologie della Costruzione (ITC) CNR, Corso Stati Uniti 4, 35127 Padova, Italy. Email: paolo.bison@itc.cnr.it

<sup>2</sup> Istituto per le Applicazioni del Calcolo (IAC) CNR, Via Madonna del Piano 10, 50019 Sesto Fiorentino (FI) Italy. Email: f.clarelli@iac.cnr.it

<sup>3</sup> Istituto per le Applicazioni del Calcolo (IAC) CNR, Via Madonna del Piano 10, 50019 Sesto Fiorentino (FI) Italy. Email: gabriele@fi.iac.cnr.it

Deterioration of monuments is a very crucial problem for people working in the field of cultural heritage. A key point is to obtain information regarding the damage in a totally non-invasive way. By this work, we propose a new non-invasive tool that permits to evaluate the thickness of gypsum layer grew by sulfation on marble stones, using a mathematical model on data detected by pulsed infrared thermography.

## Introduction

Air pollution is one of the most serious factors of degradation of carbonate stones, which compose some of the most important monuments and artifacts in the world. Pollutants such as sulfur dioxide ( $SO_2$ ) and nitrogen oxides ( $NO_x$ ) play an important role in the monuments degradation. In particular, the  $SO_2$  is the most important factor in the deterioration of calcareous stones. Indeed  $SO_2$  can react with calcium carbonate ( $CaCO_3$ ), producing an external layer of gypsum. This process greatly depends on the structure of the stone and on the presence of moisture [1]. A sharp gypsum-marble interface has been used in a mathematical model able to describe the evolution of calcium carbonate stones under the attack of atmospheric  $SO_2$ , taking into account both swelling of the external gypsum layer and the influence of humidity [2].

For the sake of historical importance of monuments, we propose a new method that permits us to estimate the thickness of the gypsum layer formed on the marble surface, heating the surface area where is located the gypsum layer, while an infrared (IR) camera monitors changes in the surface temperature. This method is non-invasive and non-contact

technique. It is based on both pulsed infrared thermography and a mathematical model to reconstruct the profile of the effusivity and the thickness of the gypsum.

In this way, we can exploit this method in-situ, because of the possibility to achieve fast experiments and data analysis.

## Experimental apparatus

We adopted a marble sample with a thin layer of gypsum. The formation of the gypsum layer on marble sample was investigated by X-ray diffraction (XRD), the experiment is deeply described in the paper [3]. SEM analysis of the marble sample is in figure 1.



Figure 1. SEM image of marble-gypsum sample.

Here, we estimate an average value  $L_g \sim 80 \mu\text{m}$  of the gypsum layer thickness.

### Approach and techniques

In this section, two procedures are described aiming at analyzing the same set of data coming from the pulsed infrared thermography experiment. In the first, by assuming a sharp transition between the superficial layer of gypsum and the substrate of marble, a well known exact solution of the heat conduction is adopted. In the second, a depth profiling inversion procedure is used, that can be adopted also in case of non-sharp (smooth) change of in-depth thermal properties. We assume to have a gypsum thin layer over a semi-infinite marble sample and a heat pulse is delivered on the surface. The exchange of the environment is considered negligible.

The relevant thermal properties are the conductivity ( $k$ ), the mass density ( $\rho$ ) and the specific heat ( $c$ ), that are homogeneous in the gypsum layer and different from those of marble. The temperature ( $T$ ) has to satisfy:

$$\frac{\partial T}{\partial t} = \frac{\partial}{\partial z} \left( D_g \frac{\partial T}{\partial z} \right); 0 \leq z \leq L_g; t \geq 0; \quad (1)$$

$$\frac{\partial T}{\partial t} = \frac{\partial}{\partial z} \left( D_m \frac{\partial T}{\partial z} \right); L_g \leq z \leq \infty; t \geq 0; \quad (2)$$

$$T(t=0) = 0; \quad (3)$$

$$-k_g \frac{\partial T}{\partial t} = Q \cdot \delta(t); z = 0; \quad (4)$$

We assume the continuity of temperature and fluxes on the boundary between gypsum and marble.

The exact solution of the external boundary temperature ( $z=0$ ) is

$$T_0(t) = \frac{Q}{b_g \sqrt{\pi}} \left( 1 + 2 \sum_{n=1}^{\infty} \Gamma^n e^{-\frac{n^2 L_g^2}{D_g t}} \right); \quad (5)$$

where  $\Gamma = \frac{b_g - b_m}{b_g + b_m}$ ,  $b_g$  is the gypsum effusivity,

$b_m$  is the marble effusivity,  $Q$  is the absorbed energy,  $D_g$  is the gypsum diffusivity,  $D_m$  is the marble diffusivity and  $M_g$  is the gypsum thickness.

Experimental surface temperature detected by IR camera can be approximated by eq. (5). To do that, we calibrate the analytical solution's parameters with experimental data.

By least squares method, we find out the temperature behavior in a logarithmic plot in figure 2.

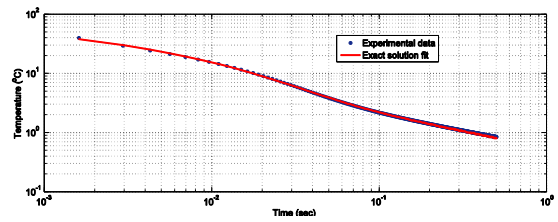


Figure 2. Log-plot of experimental data (dotted blue line) and exact solution (red line) which fits experimental data.

By minimum square method, we estimated the following parameters:

$$\beta_1 = \frac{Q}{b_g \sqrt{\pi}} = 1.49$$

$$\beta_2 = \frac{D_g}{L_g^2} = 29.499$$

$$\beta_3 = \frac{b_g - b_m}{b_g + b_m} = -0.451$$

Assuming to know the properties of marble and gypsum, in particular the gypsum diffusivity  $D_g = 1.1 \cdot 10^{-7}$  ( $\text{m}^2/\text{sec}$ ), we obtain  $L_g \approx 61$  ( $\mu\text{m}$ ).

### Depth profiling -Krapez Method

In-depth variations of the thermal properties, in case of non-sharp transition, can be associated to the concept of apparent effusivity [4]. Starting from the temperature solution for the semi-infinite solid, the apparent effusivity describes the in-depth variation of the thermal properties



as a time dependence of effusivity according to the following eq. (6).

$$b_{app}(t) = \frac{Q}{T(t)\sqrt{\pi t}} \quad (6)$$

At this point, we go one step further, i.e. we want to adopt a method which allows us to obtain an effusivity profile depending on the in-depth variable instead of the time one.

The profile reconstruction in space can be obtained by a method described by Krapez in the paper [5]. This method for effusivity profile retrieval, requires a Laplace inversion. The adopted method for inversion is the Stehfest algorithm implemented for this purpose.

We choose the particular case of a Dirac pulse of energy density  $Q$ , so the effusivity profile is in eq.(7)

$$b(\xi) = Q \cdot \text{Exp}\left(-LT^{-1}\left[\frac{1}{s} \log(s\hat{T}_0(s^2))\right]\right) \quad (7)$$

Where  $\hat{F} = LT[f]$  is the Laplace transform of  $f$ . The effusivity profile in eq. (7) can be obtained using the Stehfest method, which gives:

$$F(\xi) = (LT^{-1})\left[\frac{1}{s} \log(s\hat{T}_0(s^2))\right] \quad (8)$$

Where  $s = \sqrt{p}$ , and  $\xi = 2\sqrt{t}$ . Thus

$$F(\xi) = \frac{\log(2)}{\xi} \sum_{m=1}^M \left( V_m \frac{1}{s} \log(s\hat{T}_0(s^2)) \right). \quad (9)$$

We used the number of Stehfest coefficients  $N$  as regularizing parameter, and the optimum value obtained is  $N=8$ . The effusivity profile obtained by Krapez method is in figure 3, it starts from about 918 and ends close to 2450. We choose the half max point  $\xi_h \approx 0.42$ .

Following [5], we get

$$z = \frac{1}{2\rho_g c_g} \int_0^{\xi_h} b(\xi) d\xi \approx 73(\mu m).$$

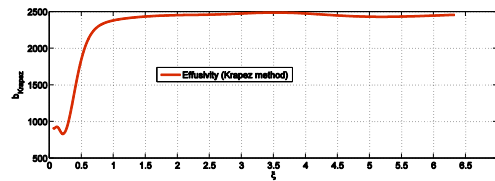


Figure 3. Effusivity profile obtained by Krapez method with  $n=8$ .

## Conclusion

This technique gives us a good approximation of the gypsum thickness, with 61 ( $\mu m$ ) in the first case, and 73 ( $\mu m$ ) with the Krapez method. These results seems to be a good approximations of the value obtained by SEM, that is  $L_g = 80$ . This method permits us to detect gypsum thickness in a non-invasive way.

## References

1. E.A. Charola; Acidic deposition on stone; US/ICOMOS Scientific Journal 3, p. 19-58, (2001).
2. F. Clarelli, A. Fasano, R. Natalini; Mathematics and monument conservation: free boundary models of marble sulfation; SIAM Journal On Applied Mathematics; vol. 69; p. 149- 168, ISSN: 0036-1399 (2008).
3. P. Bison, F. Clarelli, A. Vannozzi; Pulsed Thermography for Depth Profiling in Marble Sulfation; Int. J. Thermophys, 36:1123–1130, (2015).
4. D. Balageas, J.C. Krapez and P. Cielo; Pulsed photothermal modeling of layered materials; J. Appl. Phys. 59, 348 (1986).
5. J.C. Krapez; Thermal effusivity profile characterization from pulse photothermal data; J. Appl. Phys. 87, 4514 (2000).

# Lock-in thermography applied to real time crack detection in constructional steelwork

Paul D. Toasa Caiza<sup>1</sup>, Thomas Ummenhofer<sup>1</sup>

<sup>1</sup> Karlsruhe Institute of Technology. KIT Steel & Lightweight Structures. Research Center for Steel, Timber & Masonry. Otto-Ammann-Platz 1, D-76131 Karlsruhe. paul.toasa@kit.edu.

The demand of non-destructive methods to detect cracks caused by fatigue or brittle behavior in constructional steel structures has increased in the last years. Lock-in thermography is a promising method to detect cracks in weld seams and notches. This paper presents an experimental setup, which allows crack detection in real time without subsequent image analysis. The success of this configuration is based on the use of a static converter, which generates a quadratic and periodic voltage signal of high amplitude and high frequency. This voltage is supplied into a coil, and the resulting current is a triangle signal of high amplitude. The induced electromagnetic field caused by the current signal increases the density of the eddy currents which cause the temperature variation in the crack region. The temperature field is visualized and recorded with an IR camera, which shows in real time the occurrence of cracks.

## Introduction

The general principle of non-destructive testing (NDT) based on active thermography is: activate the specimen by thermal or mechanical means in order to obtain a significant temperature field which can reveal the presence of structural damages [6].

Particularly, the lock-in thermography is based on the generation of thermal waves inside a specimen while an IR camera records variations of surface temperature.

From the recorded information it is possible to observe and analyze the magnitude and the phase images of the generated thermal fields. This allows the detection of structural damages such as cracks or delaminations.

## Lock-in thermography with electro-magnetic induction

According to the Faraday's law of induction, an induced electromagnetic field (emf) can be generated by the variation of an electric field within a coil. The emf opposes the creating flux by generating the eddy currents, which flow in magnetic materials and in conductors operating

at high frequency, see [1, 5]. The resulting eddy currents cause temperature variation in discontinuities on the surface of a metallic specimen located close to the coil.

A common experimental setup to apply this phenomenon consists of a high frequency generator, a coil, an IR camera and a PC, even though, in some cases two generators and two coils have been used [3].

A high frequency sine wave voltage signal is generated and supplied into the coil, so that a cosine wave current signal is generated. The eddy currents caused by this high frequency current signal leads to temperature variation at the surface in the vicinity of cracks. The IR camera records the temperature variation during a period of few seconds. Afterwards, an image analysis of the amplitude images obtained with the IR camera is performed in order to obtain the phase images [2, 3].

This configuration has been used in order to detect small cracks in metallic samples and several investigations have been performed by applying this principle. In these cases, the variation of the electric field has been done by



the generation of sine wave current signals from 100 kHz to 550 kHz [2, 3, 7, 8, 9].

Because of the time consumption for every recording, its subsequent image analysis, the need of a cooling system, the laboratory local conditions and the comparatively small size of the tested specimens, this kind of test methodology cannot be applied to perform real time crack detection on large steel structures such as bridges, railway axles or beams.

### Experimental setup for real time crack detection on large steel structures

In order to overcome the limitations mentioned above, the frequency and the electrical power of the generated current signal in the coil is optimized by using a static converter known as power inverter. The power inverter consists of six pulse bridges made from MOSFETs<sup>1</sup> of silicon carbide, see Figure 1.

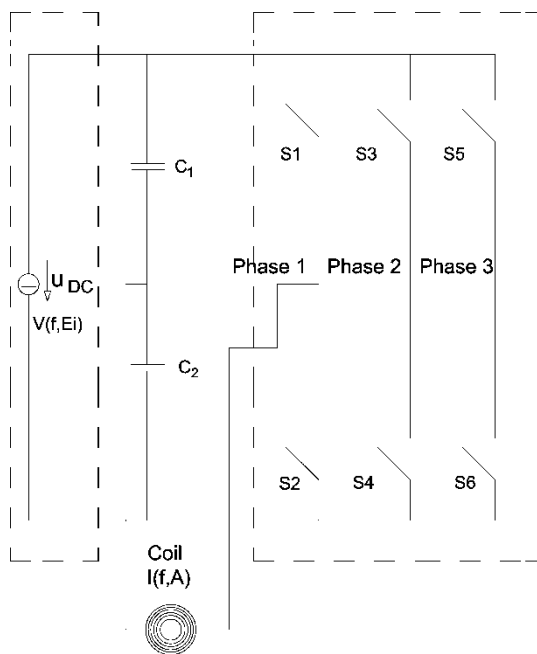


Fig. 1. Power's diagram of the static converter.

<sup>1</sup> Metal-oxide-semiconductor field-effect transistor.

The inverter generates a quadratic and periodic voltage signal of high amplitude  $E_i$  and high frequency  $f$ .

One phase of the inverter is supplied to the coil and the current intensity on the coil is a triangle

and periodic signal with the same high frequency  $f$  and high amplitude  $A$ , see Fig. 1.

This procedure allows reducing the generation time which is necessary to cause the temperature variation into the crack. This leads to a considerable reduction of the testing time.

Moreover, inducing a triangle current signal into the coil increases the AC loss, which increases the eddy currents density, see [1]. From the physical point of view, this fact helps to prevent:

- a). the slow heating and cooling down of the coil.
- b). the thermal shock of the coil, which usually demands the use of a heat exchanger [2].

In fatigue loaded steel structures it is very important to detect small cracks and defects in weld seams and geometrical notches to prevent accidents and reduce the cost of maintenance. For this reason a specimen made of steel S355J2+N was used, and its geometry is the same as the specimen used in [4], see Fig. 2. The specimen is 10mm thick and has a small fatigue crack at the notch. The crack was generated by a high cycle fatigue test, it has a length of 24mm and has a CMOD<sup>2</sup> of around 25 $\mu$ m, see Fig. 3.

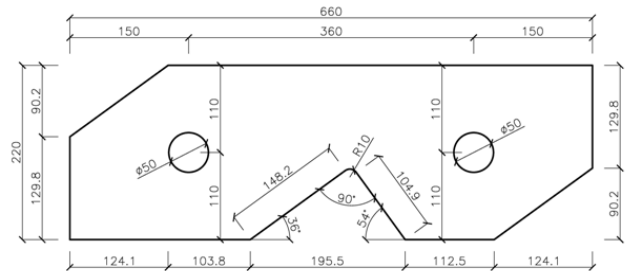


Fig. 2. Specimen made from S355J2+N steel.

<sup>2</sup> Crack Mouth Opening Displacement.

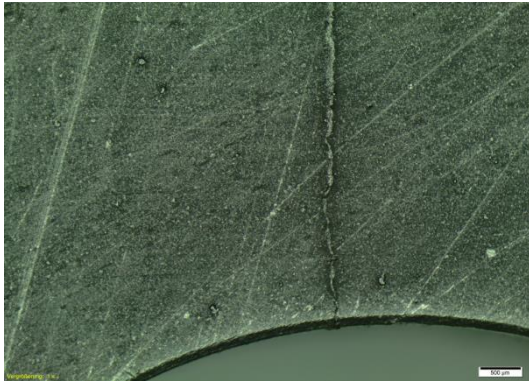


Fig. 3. Microscopic picture of the crack on the notch of the steel specimen.

The IR camera used during the experiments was a FLIR SC4000 and its recording frequency was set to 40 Hz. The Fig. 4 shows the corresponding experimental setup.

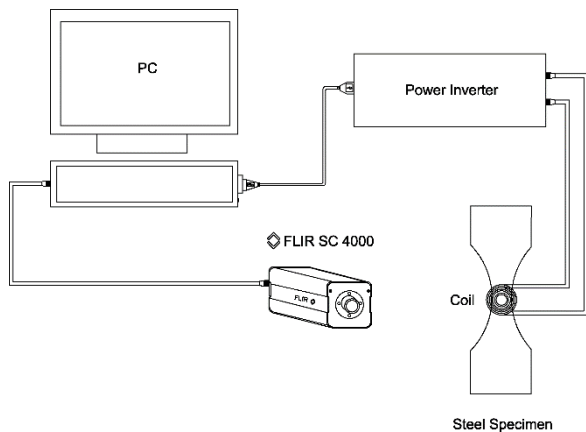


Fig. 4. Experimental setup with a power inverter

### Experimental Results

Two kinds of experiments were performed on the specimen described in the previous section. The inverter generated a voltage of 300V. The frequency of the current signal was 100 kHz and its amplitude 20A. The recording time was 10 seconds which lead to 400 thermographical images. The test setup is shown in the Fig. 5. All of the tests were performed under natural light in a laboratory room.



Fig. 5. Recording setup for the lock-in experiments

The first kind of testing was done by recording the temperature variation in the area which contains the fatigue crack without moving the coil. The generation of the current signal was manually switched on/off every second.

The visualization of the crack was possible every time when the system was switched on, see Figure 6. Moreover, the crack detection was instant and no subsequent image analysis was required, which means the testing was performed in real time.

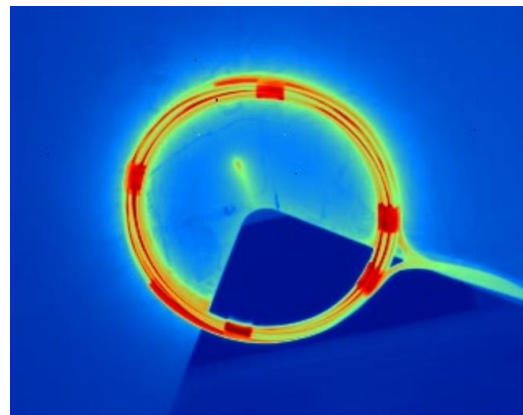


Fig. 6. Crack visualization without moving the coil

The variation of the normalized temperature in the vertex of the crack shows the switching of the system and the fast heating and cooling see Fig. 7.

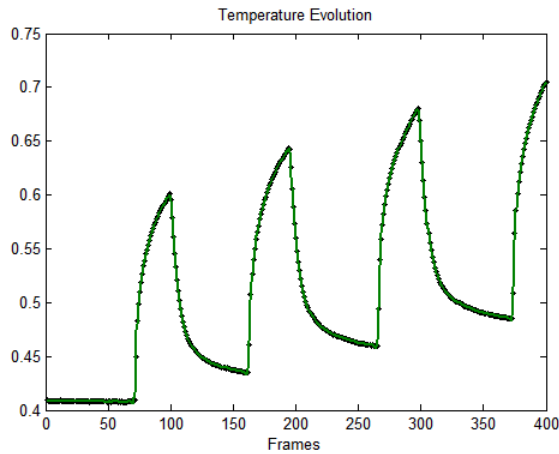


Fig. 7. Variation of the normalized temperature in the vertex of the crack

During the second experiment the coil was in motion in order to observe if a real time test of bigger areas is possible. For this reason, the generation of the current signal was always kept switched on and not stopped. In this case, the visualization of the crack was both clear and instant. Fig. 8 shows four images of the amplitude video. This fact shows the big advantage when large structures need to be tested.

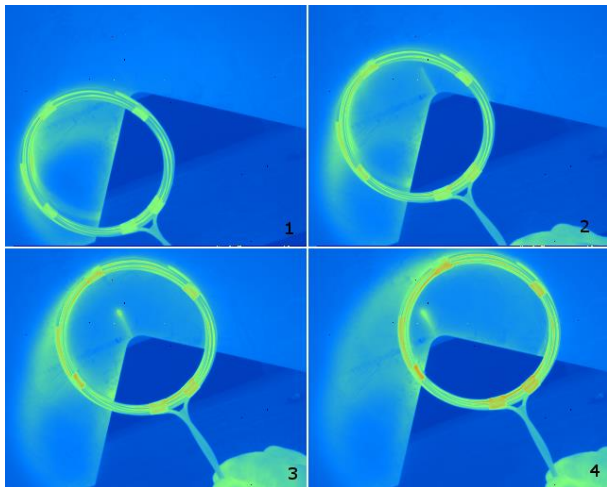


Fig. 8. Images of the crack visualization while the coil is moving

The variation of the normalized temperature in the pixel corresponding to the crack's vertex shows that its heating is higher when the center of the coil passes over it, see blue points in Fig. 9. The red points represent the pass of the coil over the crack's vertex.

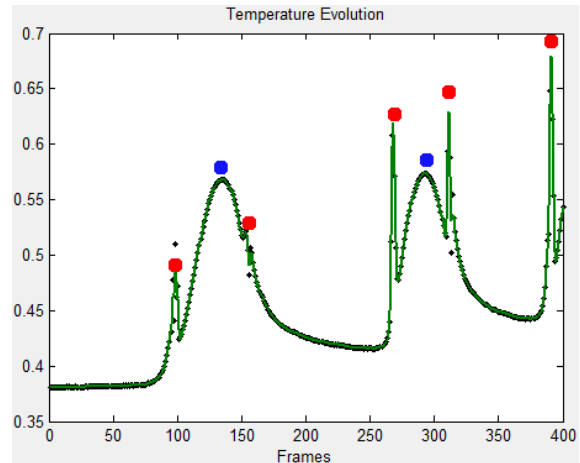


Fig. 9. Variation of the normalized temperature on the pixel which corresponds to the crack's vertex

Since in both applications the crack detection was instant and no subsequent image analysis was required, a trigger to synchronize the signal generation and the recording with the IR camera is not necessary.

## Conclusion

The method presented in this paper allows testing large steel structures on real time under normal environmental conditions.

The use of the power inverter allows optimizing the signal generation and the related eddy currents.

In our experimental setup the subsequent image analysis, the synchronization's trigger and the cooling system are not necessary, and the recording time per area is reduced. Moreover, the NDT can be performed in situ, since a dark environment is not necessary.

Because of these characteristics, the cost of performing this NDT is reduced considerably.

Considering that there exist different complex geometries in steel structures, a FEM simulation of the electromagnetic field taking into account these geometries is necessary. This simulation

will allow designing coils to be used with a wide range of geometries.

## References

1. W.G. Hurley, W.H. Wölfle. Transformers and inductors for power electronics. John Wiley & Sons Ltd. 2013.
2. G. Riegert, T. Zweschper, G. Busse. Lockin thermography with eddy current excitation, QIRT Journal, Vol. 1, N° 1/2004, pp. 21-32, 2004.
3. B. Oswald-Tranta, M. Sorger. Localizing surface cracks with inductive thermographical inspection: from measurement to image processing, QIRT Journal, Vol. 8, N° 2/2011, pp. 149-167, 2011
4. R. Plum, T. Ummenhofer. Structural-thermal finite element simulation of vibrothermography applied to cracked steel plates, QIRT Journal, Vol. 8, N° 2/2011, pp. 201-220, 2011
5. J. Vrana. Grundlagen und Anwendungen der aktiven Thermographie mit elektromagnetischer Anregung. Dissertation, Naturwissenschaftlich-Technischen Fakultät III, Universität des Saarlandes, 2008
6. X. P.V. Maldague. Theory and practice of infrared technology for nondestructive testing. John Wiley & Sons, Inc. 2001
7. U. Netzelmann, G. Walle. Induction thermography as a tool for reliable detection of surface defects in forged components. 17th World conference on nondestructive testing. Shanghai, China, 2008
8. G. Zenzinger, J. Bamberg, W. Satzger, V. Carl. Thermographic crack detection by eddy current excitation. Nondestructive Testing and Evaluation Vol. 22, Iss. 2-3, 2007
9. M. Genest, D.C. Dudzinski, S. Bulmer, R.K. Kersey. Crack detection using induction thermography for thermomechanical fatigue tests. AIP Conference Proceedings, 1335, 1727-1734, 2011
- 10.

# DEVELOPMENT OF NEW SONIC-IR METHOD USING ULTRASONIC WAVE INPUTTED THROUGH WATER

Y. Izumi<sup>1</sup>, H. Tanabe<sup>2</sup>, T. Hibino<sup>3</sup>, T. Takamatsu<sup>4</sup>, T. Sakagami<sup>5</sup>

<sup>1</sup> The University of Shiga Prefecture, Hassaka 2500, Hikone, Shiga 522-8533 Japan, izumi.yu@mech.usp.ac.jp

<sup>2</sup> The University of Shiga Prefecture, Hassaka 2500, Hikone, Shiga 522-8533 Japan, tanabe@mech.usp.ac.jp

<sup>3</sup> The University of Shiga Prefecture, Hassaka 2500, Hikone, Shiga 522-8533 Japan, katakiyu1025@gmail.com

<sup>4</sup> The University of Shiga Prefecture, Hassaka 2500, Hikone, Shiga 522-8533 Japan, takamat@mech.usp.ac.jp

<sup>5</sup> Kobe University, Rokkodai 1-1, Nada, Kobe 657-8501 Japan, sakagami@mech.kobe-u.ac.jp

Sonic-IR, which is based on the detection of the temperature rise due to frictional heating at the defect faces under ultrasonic excitation, has an advantage in the detection of closed defects. However, in conventional sonic-IR method, to directly input an acoustic energy from ultrasonic transducer to the test area via ultrasonic horn, which may give scratches and deformation in the test object. In this study, we developed a new sonic-IR method using ultrasonic wave inputted through water, and practicability of the proposed method for the detection of fatigue crack was experimentally investigated. As a result, it was found that crack detection can be conducted by proposed technique without damage or deformation to the test object.

## Introduction

Sonic-IR, which is also called vibrothermography, is one of the active thermographic NDT technique. This method, which is based on the detection of the temperature rise due to frictional heating at the defect faces under ultrasonic excitation, has an advantage in the detection of closed defects. The method was originally developed by Henneke [1] at 1979 and has been advanced and improved more recently [2-5]. However, in conventional sonic-IR method, to directly input an acoustic energy from ultrasonic transducer to the test area via ultrasonic horn as shown in Fig.1(a), which may give scratches and deformation in the test object.

In this study, we develop a new sonic-IR method using ultrasonic wave inputted through water as shown in Fig.1(b), and practicability of the proposed method for the detection of fatigue crack is experimentally investigated.

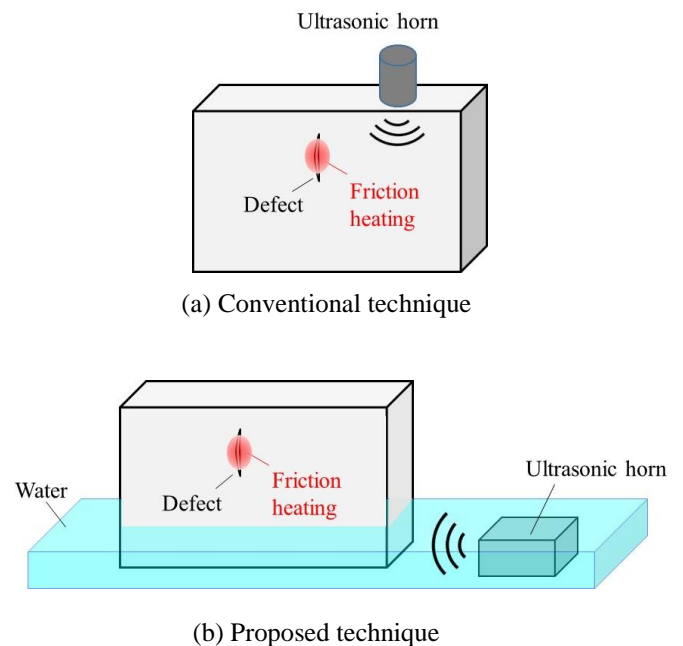


Fig. 1. Principle of defect detection by Sonic-IR technique.

## Sonic-IR method

Sonic-IR technique is also called as vibro-thermography. When an objective material with a defect such as crack and delamination is fluctuated by acoustic energy, friction between the defect surfaces generates frictional heat and localized temperature rise is observed. By measured using infrared thermography to the temperature rise, it is possible to detect the defect. This temperature rise by measuring using an infrared thermography, it is possible to detect a defect is measured by infrared thermography. In the proposed sonic-IR technique, ultrasonic wave inputted through water is employed. Therefore, the technique may be conducted without giving the scratches and deformation of the test object.

## Self-reference lock-in data processing

For S/N improvement of the infrared temperature signal, self-reference lock-in processing technique [6] was employed. In the self-reference lock-in thermography, a reference signal was constructed from the reference region arbitrarily set on the same sequential infrared images. Distribution of relative intensity values of the infrared temperature change against that in the reference region can be obtained by the following least squares approach even under the arbitrary temperature change, provided that the temperature change in the reference region has the similar and in-phase waveform as the objective area of the infrared temperature measurement.

Assume that waveform of temperature change at a reference region on the objective surface is expressed as  $f_n$ . The temperature value on an objective surface can be approximated as follows.

$$Y_n = a + bf_n \quad (1)$$

Where  $a$  is the DC offset,  $b$  is an influence coefficient of the reference,  $n$  is the frame number. To calculate the influence coefficient  $b$ , the square sum of deviations between

approximate expression  $Y_n$  and measured temperature  $y_n$  defined as follows is minimized.

$$\Delta^2 = \sum_{n=1}^N (y_n - Y_n)^2 \quad (2)$$

Where  $N$  is the total frame number. Then,  $b$  is obtained by the following equation.

$$b = \frac{\begin{vmatrix} N & \Sigma y_n \\ \Sigma f_n & \Sigma y_n f_n \end{vmatrix}}{\begin{vmatrix} N & \Sigma f_n \\ \Sigma f_n & \Sigma (f_n)^2 \end{vmatrix}} = \frac{N \Sigma y_n f_n - \Sigma y_n \Sigma f_n}{N \Sigma (f_n)^2 - (\Sigma f_n)^2} \quad (3)$$

When this calculation is performed on all the pixels, it is possible to obtain the correlation between the infrared signal in reference region and that in any region. Values of  $b$  indicate a relative intensity of infrared temperature change against that in the reference region.

This method does not require any external reference signal and can be applied even under arbitrary temperature change. Obtained values of  $b$  are effectively employed for detection of significant temperature change due to defect.

## Experimental setup

Testing was conducted for several test samples with introduced fatigue crack. The specimen material was chromium molybdenum steel, JIS SCM440, and dimensions of the specimen were 125 mm in length, 25 mm in width and 10 mm in thickness as shown in Fig.2. On one side at the center of the specimen, artificial slits of 2.0 mm length and tip radius  $\rho = 100 \mu\text{m}$  were introduced by wire electrical discharge machining (EDM). Cracks were propagated from slit tip by four point bending fatigue testing. The details of specimens and of fatigue test condition are shown in Table 1.

Sonic-IR system used in this study is shown in Fig.3. Branson ultrasound bath system, model S8500, was used to generate the acoustic energy in the samples. The maximum ultrasonic



excitation power was 500 W, and the ultrasonic frequency was set to 25 kHz, 40 kHz and 80 kHz. For thermal image measurement, the high performance infrared camera (FLIR systems, phoenix infrared camera) with InSb infrared sensors (temperature resolution: 25 mK, spectral range: 3.0 - 5.0  $\mu\text{m}$ , spatial resolution: 320 $\times$ 256 pixels) was employed. Infrared measurement frequency was set to 113 Hz.

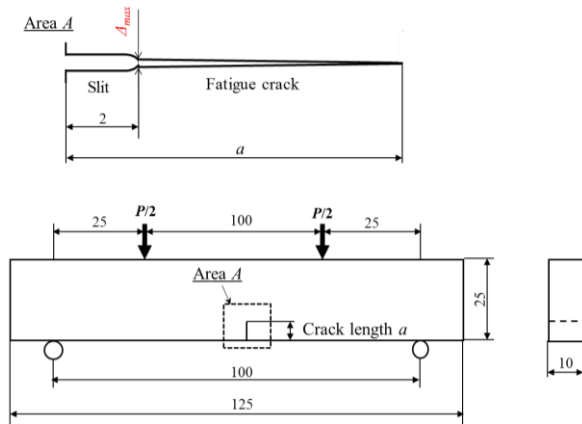


Fig. 2. Specimen shape and condition of 4 point bending fatigue testing.

Specimen No.	No.1	No.2	No.3
Crack length $a$ [mm]	9.8	8.9	8.8
Maximum crack opening width $\Delta_{\text{max}}$ [ $\mu\text{m}$ ]	37	17	9
Stress ratio $R$	0.1	0.4	0.2
Maximum loading $P_{\text{max}}$ [kN]	51.8	53.2	50.3

Table 1. Details of specimens and fatigue test condition.

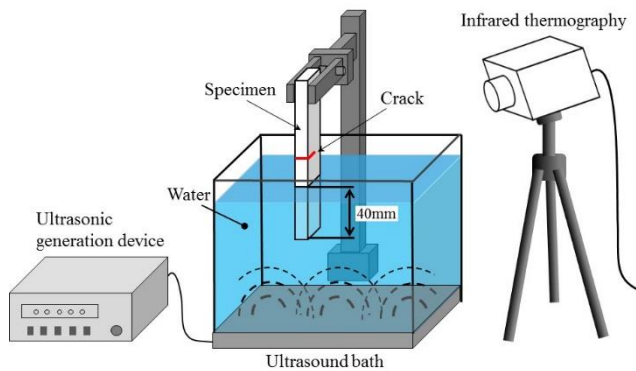
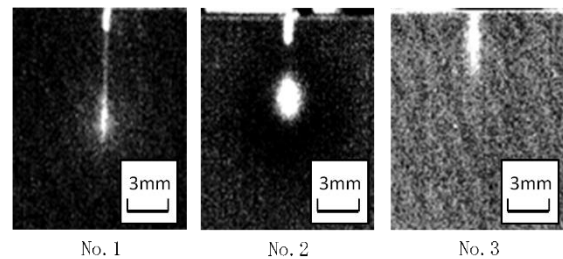


Fig. 3. Schematic illustration of the sonic-IR method using the ultrasound bath.

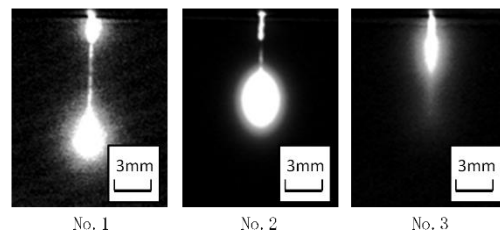
## Experimental results

Experimental results obtained for specimen No.1, No.2 and No.3 are shown in Fig.4. Fig. 4(a) show the self-reference lock-in results obtained by using ultrasonic bath at ultrasonic frequency  $f = 80$  kHz. It is found from these figures that significant temperature rises are observed at the crack under ultrasonic excitation via water. In cases where ultrasonic frequency is 25 kHz and 40 kHz, significant temperature rises are also observed.

Fig.4(b) show the self-reference results obtained by conventional sonic-IR technique using ultrasonic horn at ultrasonic frequency  $f = 21$  kHz and excitation power = 1500 W [7]. Quantitative comparison of the proposed method and the conventional method of heating value, since the ultrasonic oscillation output are significantly different, could not be conducted. Then it makes a comparison of the heat-generating position. The results is shown in Fig.5. From this figure, in this experiment using the crack specimens, a clear difference in the heating position of the proposed method and the conventional method were not found. From the above results, it was found that crack detection can be conducted by proposed technique as with conventional technique.



(a) Proposed technique ( $f = 80$  kHz)



(b) Conventional technique ( $f = 21$  kHz)

Fig. 4. Self-reference lock-in images observed by sonic-IR measurement.

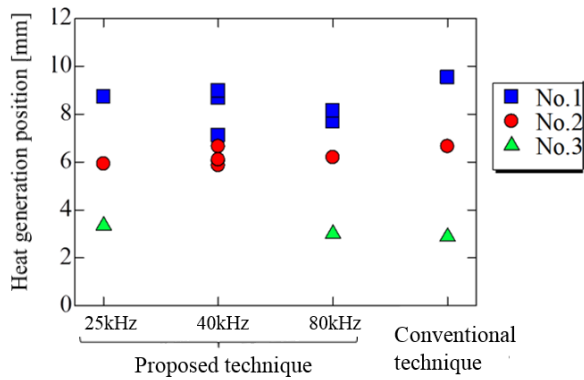


Fig. 5. Heat-generating position.

## Conclusions

In this study, we developed a new sonic-IR method using ultrasonic wave inputted through water, and practicability of the proposed method for the detection of fatigue crack was experimentally investigated. As a result, it was found that crack detection can be conducted by proposed technique without damage or deformation to the test object.

## Acknowledgements

This research was partly supported by Branson Ultrasonics, Emerson Japan, Ltd.

## References

1. E. G. Henneke II, K. L. Reifsnider & W.W. Stinchcomb: Thermography – An NDI Method

- for Damage Detection, *J.Metal*, Vol. 31(9), pp.11-15, 1979.
2. A. Gleiter, G. Riegert, Th. Zweschper, R. Degenhardt & G. Busse: Advanced Ultrasound Activated Lockin-Thermography for defect selective depth resolved imaging, *Proceedings of SPIE*, Vol. 6205, 62051F, 2006.
3. S. M. Shepard, T. Ahmed & J. R. Lhota: Experimental Considerations in Vibrothermography, *Proceedings of SPIE*, Vol. 5405, pp.332-335, 2004.
4. R. Montanini, G. L. Rossi & F. Freni: Ultrasound Lock-in Thermography as a Quantitative Technique for Quality Control Assessment of Cast Iron Turbocharger Components, *Proceedings of 10th International Conference on Quantitative Infrared Thermography*, 2010.
5. T. Sakagami, R. Katsumata, K. Kuroki, Y. Harada and S. Kubo: Detection of Stress Corrosion Cracking by Sonic-IR Technique, *Proceedings of the Seventh International Conference on NDE in Relation to Structural Integrity for Nuclear and Pressurized Components*, pp.1087-1093, 2009.
6. T. Sakagami, T. Nishimura, S. Kubo, Y. Sakino and K. Ishio, Development of a Self-reference Lock-in Thermography for Remote Nondestructive Testing of Fatigue Crack : 1st Report, *Fundamental Study Using Welded Steel Samples*, *Transactions of the Japan Society of Mechanical Engineers. A*, Vol.73, No.724, pp. 1860-1867, 2006.
7. Y. Izumi, H. Tanabe, T. Takamatsu and T. Sakagami, Applicability Evaluation of Sonic-IR Technique for Fatigue Crack Detection, *Proceedings of The 5th US-Japan NDT Symposium*, 2014.

# COMPARISON BETWEEN THERMOGRAPHIC AND HEAT FLUX METER TECHNIQUE: A CASE STUDY

P.Aversa<sup>1</sup>, U. Galietti<sup>2</sup>, V. Luprano<sup>1</sup>, D.Palumbo<sup>2</sup>, C. Racioppo<sup>2</sup>, R. Tamborrino<sup>2</sup>

<sup>1</sup> ENEA Research center of Brindisi, SS 7"Appia" Km 714, 72100, Brindisi,  
patrizia.aversa@enea.it, vincenza.luprano@enea.it

<sup>2</sup> DMMM, Politecnico of Bari, Viale Japigia, 182, 70126, Bari, umberto.galietti@poliba.it,  
davide.palumbo@poliba.it, cristina.racioppo@poliba.it, rtamborrino@libero.it

The estimation of the energy performance of existing buildings requires the knowledge of the overall heat transfer coefficient (U-value) of the walls. U-values can be calculated through a theoretical approach. The heat flow meter (HFM) method suffers from some disadvantages so, in this work, an alternative approach based on infrared thermography (IRT) has been proposed for in situ measurements. In this paper, the aim is the evaluation of the transmittance with both Thermographic and Heat Flux Meter technique: a case study is described.

## Introduction

The energy efficiency of existing buildings plays a strategic role in achieving the objectives of the latest European Directive 2012/27/UE, in fact, member States must develop a long-term strategy to promote the restructuring of the residential and commercial buildings, both public and private [1].

With the energy efficiency is intended to reduce energy consumption, reducing environmental impact, but also to decrease operating expenses; it follows of against a revaluation of the building market value.

Hence the energy audit of the buildings appears to be an effective tool in order to take action on energy renovation of existing buildings, which averagely is characterized by inefficiencies that lead to waste of energy. The diagnosis and the energy certification of existing buildings, pose to the technical, the problem of determining the value of the transmittance of opaque closures of which are not known thermophysical characteristics.

The evaluation of the transmittance of the structure is crucial and very complicated. For new buildings we have project data, as regards the existing building, but in the absence of this data, is made a stratigraphy of the materials

which however is not always possible to perform.

For this reason, the option to use non-invasive techniques such as HFM and IRT is considered, [2], [3], [4], [5].

The energy audit of the buildings, in according to the UNI EN 13187:2000 [6], the exclusive Italian reference on the execution of thermographic investigations, both the irregularities of thermal envelope and the energy upgrading of existing buildings can be evaluated. The standard is not applicable to the determination of the level of thermal insulation of opaque walls or the air tightness of the housing for which you need additional methods including HFM in situ in accordance with ISO 9869[7].

A real case study as be considered for studying, using both HFM and IRT, on the walls of a school, located in the in Mesagne (Brindisi). In particular, the formulation described by Albatici & Tonelli [2] will be used to evaluate the U-value of the transmittance by thermography.

## Problem statement

Heat Flux Meter technique for the evaluation of transmittance, although it is regulated, shows a seasonal limitations because of the need to have a thermal gradient of at least 10-15K, above all in Mediterranean environment where this gradient is not often guaranteed.

Besides, the stationary conditions assumed by hypothesis in this context, necessarily involve long times for the data acquisition in situ, generally a minimum of 72 h, is required by regulations. If this condition it is not considered, it will induce a very high error in measuring, even higher than 30% from the theoretical evaluation.

The application of Thermography, in the building industry, is ruled by the standard 13187:2000 [6], on the thermal performance of buildings. It is considered a qualitative test method, that allows us to identify the ideal location for the placement of HFM instrumentation. The attempt of this experimental study is to overcome the critical issues highlighted above and so to reduce the acquisition time and to deseasonalize the measurements of transmittance validating thermography as a quantitative test.

## Approach and techniques

The measurements have been performed on the walls of a school, located in the in Mesagne (Brindisi). The wall object of this study was of 35 cm thickness, constituted by 2 cm of plaster on each side of an inner tufa of 30 cm. The theoretical U-value reported in bibliography is 1.305 W/m<sup>2</sup>K.[8]

In situ, U-values are measured using heat flux meter positioned in a representative area of the building element and away from the influence of heat sources (Fig.1). The selection of a representative area, where the heat flux meter has been installed, together with probes to measure both internal and external air and wall surface temperatures, has been made by thermography (ISO 9869) (Fig.4). Output from all sensors is measured and recorded at regular intervals using data-loggers.

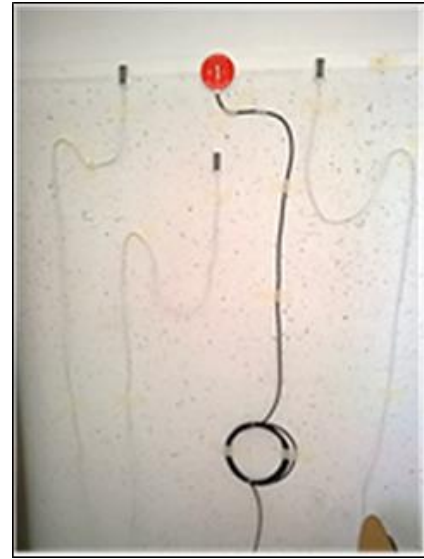


Fig. 1. HFM Instrumentation

Characteristics	Instrumentation HFM
Number of temperature sensors	6 sensors: 3 internal and 3 external
Dimension of heat flux plate	Diameter of 50 mm, thickness 5 mm
Substrate	Thermopile embedded in resin with high thermal conductivity

Table 1.Characteristics of the heat flow measurements instruments

In order to validate the thermography as a quantitative test in determining the U-value, on the same situ, the use of the artificial thermal radiation to induce the thermal flow has been considered to determine the experimental setup. The thermography set-up used (Fig.2,3), consists in an outdoor and in an indoor setup.

In the first one, two halogen lamps, with power of 1000 W, to induce thermal gradient, are positioned at 1.2 meters from the external wall.



Fig. 2. Outdoor setup of IRT measurements

In the indoor setup, simply, a camera Flir SC640 for measuring the temperature of internal wall is located at two meters from the examined wall. In the figure 5 are shown visible and thermal IR images of the indagated walls.

The thermal characteristics of the camera are reported in table 2.



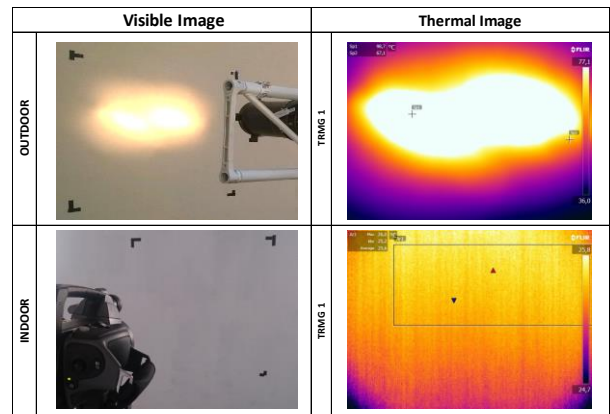
Fig. 3. Inner setup of IRT measurements

Characteristics	Flir SC640
Detector	Microbolometer
Resolution	640x480 pixels
Spectral range	7.8-14 $\mu\text{m}$
Thermal sensitivity	< 30 mK
Temperature range	-40-120°C; 0-500°C; 300-1500°C
Accuracy	$\pm 2\%$
Image frequency	30 Hz

Table 2. Characteristics of IR thermal camera



Fig. 4. Preliminary evaluation of thermal bridge for identify the ideal location for the placement of HFM instrumentation.



FFig. 5. Visible and thermal image of the indagated walls

## Results

HFM data are processed by using the average method for the calculation of the U-value, which results 1,33 W/m<sup>2</sup>K.

The results obtained using HFM are shown in figure 6.



Thermal data have been processed by Research-IR software in order to obtain the trend of temperature vs time.

Temperature data of the wall have been registered for a period of 82 hours, the same of the HFM measurements.

The mean value of the wall temperature has been calculated and used in the formulation described by Albatici & Tonelli, in substitution of  $T_i$ .

$T_{int}$  is the mean temperature of outdoor environment, while  $T_{out}$  is the mean temperature of indoor environment. These two temperatures have been measured with a thermohygrometer.

$$U = \{5.67\epsilon_{tot}[(T_i/100)^4 - (T_{out}/100)^4] + 3.8054v(T_i - T_{out})\} / (T_{int} - T_{out}) \quad [\text{W/m}^2\text{K}] \quad (1)$$

The second term of the formulation has been ignored because the velocity of wind has been set equal to zero.

The resulting U-value is 1,307 W/m<sup>2</sup>K.

If a period of 24 hours is considered for the evaluation of the wall temperature mean value, the U-value obtained is 1,241 W/m<sup>2</sup>K.

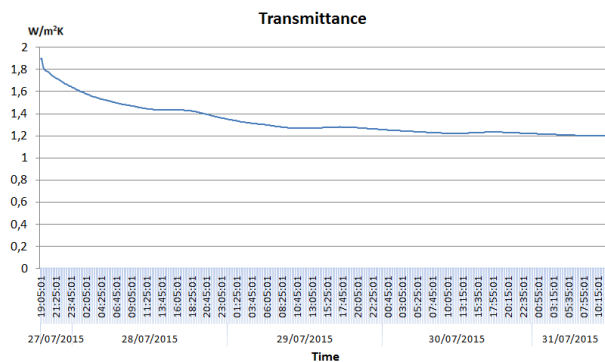


Fig.6 Transmittance calculated with the average method

## Conclusion

The advantage of methodology with IR measurements, imposing a thermal gradient, is to obtain the right range of temperature necessary to measure in any season the U-Value. Furthermore, this methodology is less time consuming than the HFM one, in fact it is possible the evaluation of U-value in only 24 hours, with a reasonable error.

## Acknowledgments

The describe study was performed throughout the course of the research and technological development project : PON02\_00323\_2938699, Soluzioni innovative per l'EFFicienza Energetica in eDILizia – EFFEDIL.

## References

1. European Parliament. Directive 2012/27/EU of the European Parliament and of the Council of 25 October 2012 on the energy efficiency. Off. J. Eur. Union 2012, L315, 1–56.
2. Albatici, R.; Tonelli, A.M. Infrared thermovision technique for the assessment of thermal transmittance value of opaque building elements on site. *Energy Build.* 2010, 42, 2177–2183.
3. Albatici, R.; Tonelli, A.M., Chiogna M. A comprehensive experimental approach for the validation of quantitative infrared thermography in the evaluation of building thermal transmittance. *Applied Energy.* 2015, 141, 218–228.
4. Hoyano, A.; Asano, K.; Kanamaru, T. Analysis of the sensible heat flux from the exterior surface of buildings using time sequential thermography. *Atmos. Environ.* 1999, 33, 3941–3951.
5. Fokaides, P.; Kalogirou, S. Application of infrared thermography for the determination of the overall heat transfer coefficient (U-Value) in building envelopes. *Appl. Energy* 2011, 88, 4358–4365.
6. UNI EN 13187:2000, Thermal Performance of Buildings Qualitative Detection of Thermal Irregularities in Building Envelopes Infrared Method;
7. ISO 9869, Thermal Insulation Building Elements In-situ Measurement of Thermal Resistance and Thermal Transmittance, 1994.
8. GL 102 – SG02 "Trasmittanza termica", Comitato Termotecnico Italiano Energia e Ambiente, 2011



# INFRARED THERMOGRAPHY APPLIED TO CHARACTERIZATION OF A PIPE INTERNALLY AND EXTERNALLY CORRODED

Mohamed EL AFI<sup>1</sup>, Sougrati BELATTAR<sup>2</sup>

<sup>1,2</sup> Department of Physics, Faculty of Science Semlalia, BP 2390, 40000 Marrakech, Morocco

<sup>1</sup> med.elafi@gmail.com

<sup>2</sup> s.belattar@uca.ma

Infrared thermography became a powerful thermal non-destructive testing technique that allows the study of the surface temperature variation of structures, when this latter is submitted to a given heat flux excitation. The obtained internal or external surface temperature can show the homogeneity or the non-homogeneity of the considered structure by analysis of the existence of a surface temperature contrast. The presence of an eventual internal or external defect will be translated at the surface by a task on the thermographical image. A healthy material will present a uniform surface temperature while the defective one will present a surface spot corresponding to the existing of an internal or external defect. This technique is often used in several areas of the industry (automotive, petroleum, shipbuilding, aerospace, etc.). The detection of possible anomalies in the object under examination is conditioned by a sufficient variation of thermal properties of defect compared to the healthy material to generate a significant contrast.

## 1. Introduction

Detection of hidden rust in pipes is of great importance in the field of maintenance and security of civil engineering works especially when trying to locate fluid leaks due to corrosion of these pipes [1] [2] or surface defects requiring repair. These abnormalities may lead to loss of money and valuable natural resources and sometimes a danger to public health. The presence of water or humidity on or in the vicinity of the pipe can cause rust areas that can be visible or hidden. Rust is strongly responsible for the damages produced in the walls and pipes in buildings all around the world [3] [4].

The adoption of the control of these structures by Infrared Camera is very important because of its flexibility as technic and is quick and simple to implement.

In this study, the model of oil or gas transportation type is adopted. This structure is supposed to be excited on the external face by a heat flow, the bottom face being maintained at a constant temperature and the other faces are assumed insulated. For different diameters, positions and different types of pipe materials

are studied. For modeling we adopted the finite element method combined to infrared thermography as an auscultation technic [5], since in the general context of the construction; thermography is most commonly used for investigating aspects of the building envelope, walls and roofs [5][6].

## 2. Description of the structure

### 2.1. Geometrical characteristics

The studied structure is a pipe having a length  $l = 1000$  mm, internal diameter = 108mm and external diameter = 127mm.

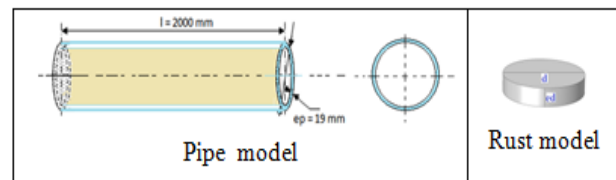


Figure1: Studied model

### 2.2 Thermophysical characteristics

Table1 shows the used thermophysical parameters in the study.

Table 1: Thermophysical parameters

	$\lambda$ : W/m.K thermal conductivity	$\rho$ : Kg/m <sup>3</sup> density of the material	$C_p$ : J/Kg.K heat capacity at constant pressure
Steel	44,5	7850	475
Corrosion	0.6	5242	648.7

### 3. Numerical Modelling

To solve the following thermal equation:

$$a \nabla^2 T = \frac{dT}{dt}$$

Where parameter  $a = \lambda / \rho c$  is called thermal diffusivity, we call upon the numerical method of the finite elements [4,5]. The analytical resolution is indeed impossible being given the geometry of the problem. The method consists in using an approximation by finite elements of the unknown functions T to discretize the variational form of the equation (1) and to transform it into system of algebraic equations of the form:

$$[A]. T = F$$

Where,

A: square matrix of dimension  $[N_h, N_h]$

F: a vector of  $N_h$  components

T: the vector of the temperatures to be calculated.

We start by building the variation form of equation (1). We carry out a spatial discretization which consists in calculating the elementary integrals by using the finite element and a temporal discretization.

There are many specialized software which enable implementation of the method of finite elements in a more or less simple and convivial way. They take care in particular of the grid of the studied object, of the automatic numbering of the elements and the nodes, of the calculation of a solution then of the chart of the results.

In this study, we used commercial software based on the finite element method and which makes it possible to calculate the evolution of temperature at any moment and in any point of material. The material is considered isotropic.

- A heat pulse applied to the external face of the pipe of a flux density  $Q = 50 \text{ W/m}^2$ .

- The section limits of the pipe are maintained at a constant temperature  $T_a = 25^\circ\text{C}$ .
- The internal face of the pipe is in convective heat exchange with air characterized by a heat transfer coefficient  $h = 10 \text{ W/K.m}^2$ .

The initial temperature of the subdomains is  $25^\circ\text{C}$ .

### 4. Results of Simulation

#### 4.1 Considered model

In order to detect the rust thermal effect on the thermal state of the steel pipe, many situations are considered. The study concerns the effect of the diameter of a circular rust stain, the effect of the depth of the rust in the steel layer and finally the effect of the pipe thickness on the surface temperature on the given structure for a given defect.

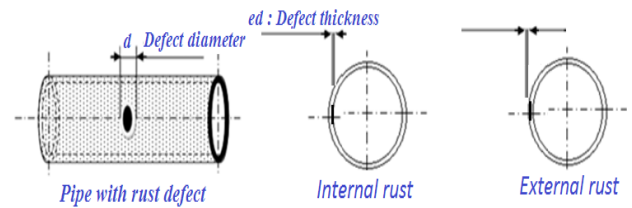


Figure2: Model steel

#### 4.2 Rust layer Diameter Effect

In this section a steel pipe, containing rust layers of circular forms having a thickness of  $e_d = 5 \text{ mm}$  and different values of diameter  $d = 20 \text{ mm}$ ,  $30 \text{ mm}$  and  $40 \text{ mm}$ , is considered. The thermographic image and the spatial evolution of the surface temperature of the pipe are calculated and presented.

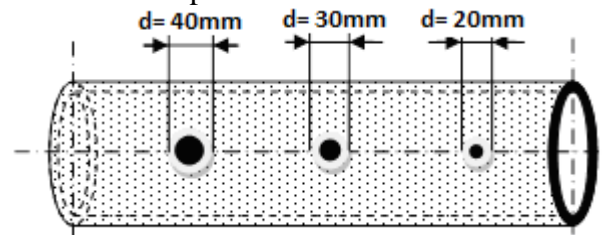


Figure 3: Steel pipe model

figures 4, 5 and 6 represent the thermal images and spatial evolution of the temperature of the entry of the rusted surface for three values of

diameters respectively  $d=20$  mm, 30 mm and 40 mm.

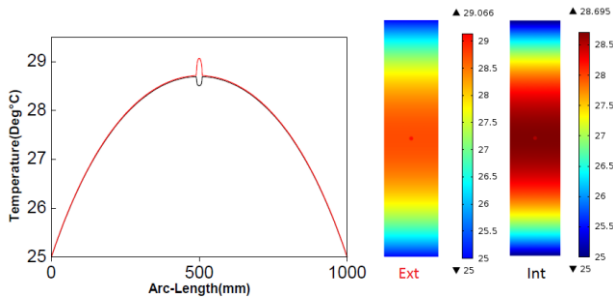


Figure 4: Thermographical image and spatial evolution of the temperature of the entry face ( $d=20$  mm)

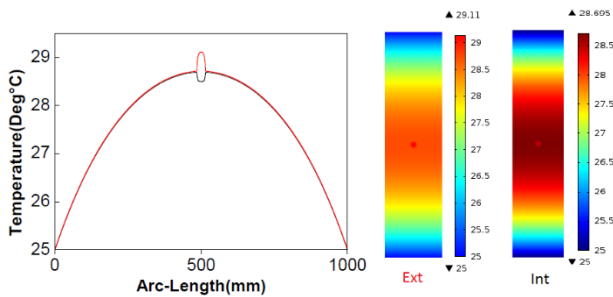


Figure 5: Thermographical image and spatial evolution of the temperature of the entry face ( $d=30$  mm)

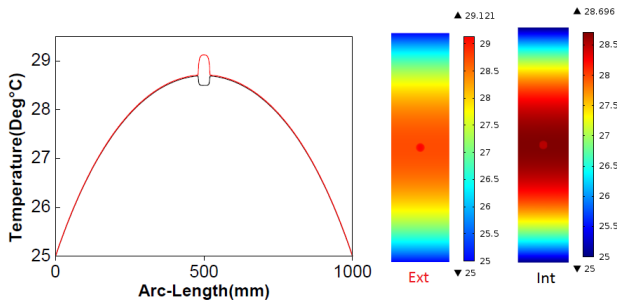


Figure 6: Thermographical image and spatial evolution of the temperature of the entry face ( $d=40$  mm)

The presence of the defect, rust, is much more visible in the case of the diameters of 30 and 40 mm. The thermographical images, particularly those of figures 5 and 6, clearly show the presence of rust inside the pipe. This presence is indicated by a different colored spot (colder) relative to its neighboring colors. That is to say, the presence of rust is accompanied by a surface temperature drop compared to adjacent areas. The curves of figure 4, 5 and 6 represent the temperature spatial variation along an axis passing above the rusted area.

We can note that in the case of the diameter of 20 mm the temperature change is barely visible,

but for diameters of 30 and 40 mm the effect of the presence of rust is marked.

In table 2 is summarized the surface temperature drops due to the presence of rust.

Table 2: Surface temperature fall in the above rusted regions

D(mm)	20	30	40
$\Delta T_{int}(^{\circ}C)$	-0.186	-0.195	-189
$\Delta T_{ext}(^{\circ}C)$	0.350	0.394	0.408

### 4.3 The effect of rust layer thickness

The pipe used before is considered and this time the defect thickness takes the following values: 3mm, 6mm and 9mm. The diameter of the rust stain is constant and equal to 40mm. The thermographical images of the three cases and the surface temperature curves (fig.8) obtained show that the more the rust layer thickness increases, the more the surface temperature of the entry face also increases and consequently the detectability of these defects becomes easier. In the same way, one can show that the changes of temperature due to the presence of the defect remain weak compared to the healthy state of control. Indeed the difference in temperature of the healthy region and that containing the defect, precise measurements are essential for such detections.

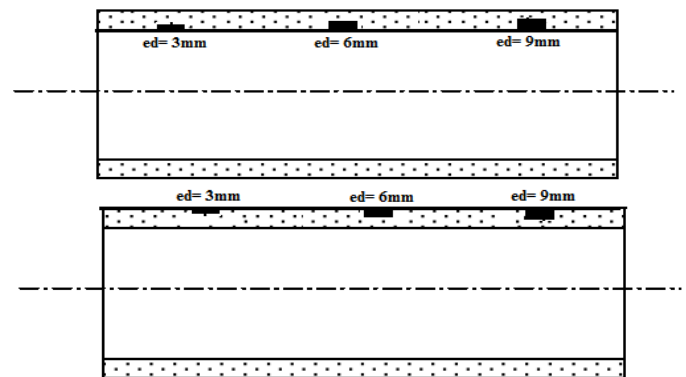


Figure7: Model of internal and external defect, variable rust thickness

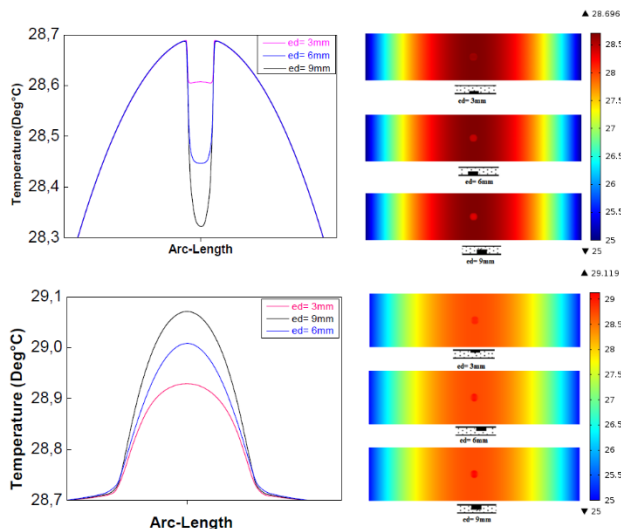


Figure 8: Thermographical image and spatial evolution (internal defect)

In the table 3 is summarized the surface temperature drops due to the presence of rust.

Table 3: Surface temperature fall in the above rusted regions

Ed(mm)	3	6	9
T <sub>int</sub> (°C)	-28.685	-28.685	-28.685
Δ T <sub>int</sub>	0.075	0.238	0.365
T <sub>ext</sub> (°C)	28.93	29.010	29.070
Δ T <sub>ext</sub>	0.251	0.290	0.350

The effect of the thickness of the rust is much more striking in view of the value of the temperature drop between the region containing rust and its vicinity without rust.

More rust spreads deep into the steel, more it becomes easily detectable.

#### 4.4 Effect of the variable thickness of pipe

In this last case of study, the variable parameter is the thickness of the pipe. The taken values of thickness for simulations are  $e_p = 12\text{mm}$ ,  $19\text{mm}$  and  $32\text{mm}$ , figure9.

The study is relative to the detectability of the circular rust layer having an arbitrary constant thickness  $e_d = 5\text{mm}$  and an arbitrary constant diameter of  $d = 40\text{mm}$ .

The thermograms in Figure 10 show that more the pipe thickness increases, more the temperature fall decreases in magnitude but in low maner.

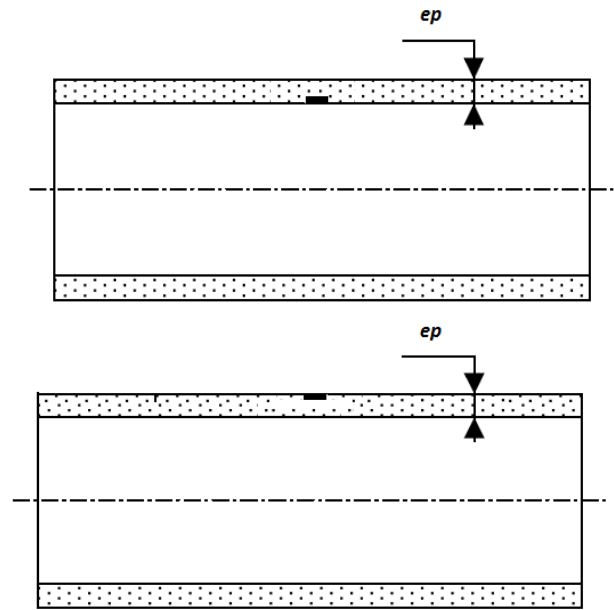


Figure9: Model of internal and external defect, variable pipe thickness

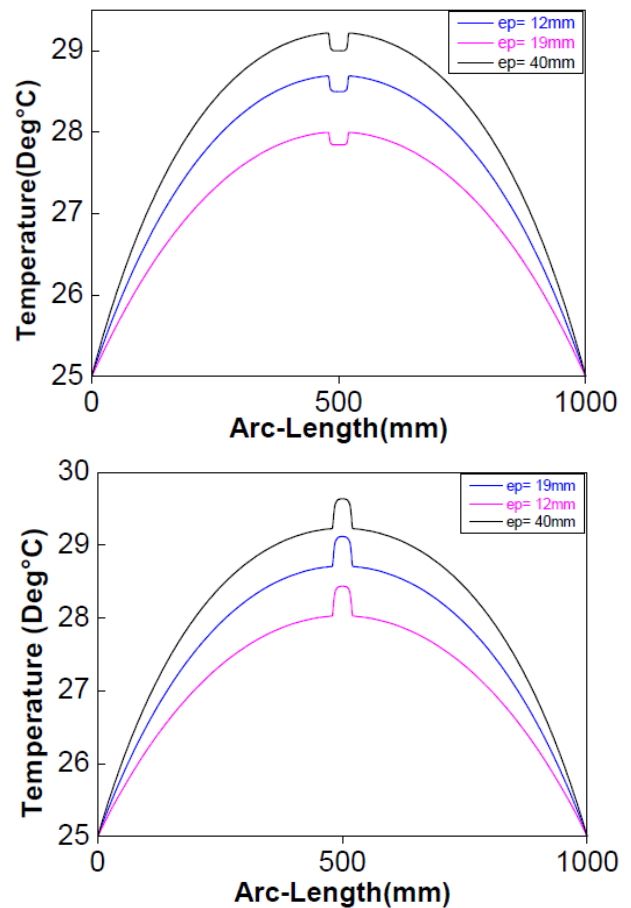


Figure 10: Thermographical image and spatial evolution (Internal defect)

From the curves it may be noted first that, although the initial and boundary conditions are

the same for all three thickness of the pipe, the temperature of region without rust is not the same depends on the thickness of the pipe. Falls temperatures generated by the presence of rust vary slightly depending on the thickness of the pipe as shown in the table 4 the thicker the wall increases, the amplitude of the fall temperature decreases.

In the table 3 is summarized the surface temperature drops due to the presence of rust.

Table 4: Surface temperature fall in the above rusted regions

$E_p(\text{mm})$	12	19	32
$T_{\text{int}}(^{\circ}\text{C})$	29.215	28.668	27.995
$\Delta T_{\text{int}}$	-0.218	-189	-0.154
$T_{\text{ext}}(^{\circ}\text{C})$	29.640	29.120	28.437
$\Delta T_{\text{ext}}$	0.408	0.408	0.407

## 5. Conclusion

In this section we studied the effect of the presence of a defect of rust type, located on the internal and external surface of a pipe. The results show that the effect of the diameter of the rust layer is more connected to the width of the temperature fall caused by the presence of rust and the thickness of the rust is more connected to the magnitude of the temperature fall.

More rust layer thickness, on the internal or external surface of the pipe, is large it is more easy to detect it and vice versa. The same applies to other case, more the diameter of the rust layer

is wide it is relatively easy to detect and vice versa.

The effect of the pipe thickness in the presence of rust is translated by a relative decrease of the internal surface temperature fall of the pipe when the pipe section increases and vice versa. This study showed that the detection of internal corrosion in a pipe from an internal image is possible with a precise infrared camera. The presented method is effective and simple to implement.

## 6. References

1. C Maierhofer, R Arndt, M Röllig, 'Influence of concrete properties on the detection of voids with impulse-thermography', *Infrared Physics & Technology*, No 49, pp 213– 217, 2007.
2. N. Laaidi, S. Belattar, Application of Thermal Nondestructive Testing Method to Oil Conduits Control, 11th International Conference on Quantitative InfraRed Thermography (QIRT 2012), Naples, Italy, 11-14 Jun 2012
3. M Milazzo, N Ludwig, V Redaelli, 'Evaluation of evaporation flux in building materials by infrared thermography', *Proceedings of QIRT02*, DubrovnikCroatia, pp. 150–155, 2002.
4. N. Laaidi, S. Belattar, A. Elballouti *Int. journal non-destructive testing and evaluation* , 158 – 163, 2011
5. A. Obbadi, S. Belattar, M. Beihaqi, A. Tmiri, A. Ballouti, IV International workshop- Advances in signal processing for Nondestructive Evaluation of Materials, 6 (2001) 195-200, Canada.
6. A.Obbadi, S. Belattar , *Revue marocaine de génie civil* 1 N° 105 (2004), 16-21 Maroc

# DETECTING DEFECTS IN MARINE STRUCTURES BY USING EDDY CURRENT INFRARED THERMOGRAPHY

W. Swiderski

Military Institute of Armament Technology, Poland, 05-220 Zielonka, Wyszynskiego Str., 7,  
waldemar.swiderski@wp.pl

Eddy current infrared (IR) thermography is a new nondestructive testing (NDT) technique used for the detection of cracks in electro-conductive materials. It combines the well-established inspection methods of eddy current NDT and IR thermography. This technique uses induced eddy currents to heat test samples. In this way, IR thermography allows visualization of eddy currents distribution which is subjected to distortion in defect sites. The paper discusses a numerical code used for modeling eddy current IR thermography procedures in application to marine structures.

## Introduction

One of the basic requirements for selecting materials in shipbuilding is their high resistance toward corrosion. Also, some economic factors, first of all, cost, determine designers' choice of materials to be used in specific types of watercraft. The main criterion for selecting materials to be used in marine structures is material strength. This is typically met by steels and high strength aluminum alloys. Structural steel is the traditional material used for 150 years in the shipbuilding industry because of its excellent mechanical properties and low manufacturing costs. Aluminum alloy as an alternative material began to be used in the 1930s.

Structural steels for ship construction must meet stringent requirements. Internal and external forces acting on ship hulls have to be taken into account during the designing process. There are other factors, such as wave strength, sea conditions, waves impact etc., that cause vibrations, thermal differences, load displacement, effects of fatigue, corrosion cracking, etc. The construction of vessel during operation is subjected to cyclic fatigue loads that are comparable to mutual bending loads.

## Eddy current IR thermographic NDT

Infrared thermography is a NDT technique allowing fast inspection of large surfaces [1, 2]. There are different implementations of NDT techniques depending on the stimulation source, basically: pulsed, step or modulated. Test objects are stimulated with a heat source, which can be of many types, such as optical, mechanical or electromagnetic [3-5]. In the inspection of metals, an effective heat source can be designed on the basis of eddy currents.

Distribution of eddy currents in test objects depends on a number of characteristics adhering to object material. The most important material parameters are [6]: electrical conductivity  $\gamma$ , magnetic permeability  $\mu$  and operating frequency of a transducer  $f$ . Structural elements of ships made of metal sheets represent convenient test objects for applying pulsed eddy current thermography in order to detect hidden defects.

The use of pulsed eddy current IR thermography in NDT of composite materials, metals and metal alloys has been described in a number of papers [7, 8]. In this paper the emphasis is made on testing marine structures, in particular, on numerical modeling of some practical tests cases.



## Modeling eddy current IR thermographic NDT

The ThermoEdCur computer program from Innovation, Ltd. has been used to optimize heating parameters in the inspection of metallic sheet-like samples containing subsurface defects [9].

A feature of ThermoEdCur is the heating option by means of eddy currents. In this case, the stimulating heat energy  $Q$  penetrates in-depth with attenuation being described by the following formula:

$$dQ = Q_0 e^{-\gamma \cdot dz} \quad (1)$$

where  $dQ$  is the energy absorbed within the  $dz$  distance, and  $\gamma$  is the eddy current absorption coefficient defined by:

$$\gamma = \frac{\sqrt{\pi f \sigma \mu_0 \mu}}{2} \quad (2)$$

Here  $f$  is the eddy current frequency,  $\sigma$  is the electrical conductivity [S/m],  $\mu_0 = 1.257 \cdot 10^{-6}$  N/m is the magnetic permeability of free space [H/m],  $\mu$  is the material relative magnetic permeability. Therefore, eddy current energy absorption is characterized by the following parameters:  $f, \sigma, \mu$ .

To verify possibilities of detecting cracks and corrosion areas in metal sheets by applying eddy current IR thermography, two models were used for computer simulation.

In Model 1 a metallic sheet sample having lateral size of 100x200 mm and thickness of 6 mm for steel and 3 mm for aluminum, contained three subsurface air-filled cracks (0.1 mm thickness each) located at various depths below the surface. In Model 2 metal sheet samples of the same size as in the case of Model 1 contained three corrosion areas of varying material loss.

Some examples of the results obtained in the inspection of Models 1 and 2 are presented in Table 1 and 2.

Material	Defect	$\Delta T$ [°C]	$\tau_m$ [s]	$C$ [%]
Steel	Defect1	12.83	3.35	100
Steel	Defect2	0.88	4.05	37
Steel	Defect3	0.12	4.45	5

Table 1. The simulation results – Model 1

Material	Defect	$\Delta T$ [°C]	$\tau_m$ [s]	$C$ [%]
Steel	Defect4	0.07	4.95	4
Steel	Defect5	0.17	4.8	8
Steel	Defect6	0.48	4.3	22

Table 2. The simulation results – Model 2

## Conclusion

The results of numerical modeling indicate that eddy current IR thermography method can be effectively used in the detection of subsurface defects (micro-cracks, delaminations) and corrosion areas in steel plates and aluminum sheets widely used in marine structures. The use of a line heat source moving across a test surface at a constant speed minimizes uneven heating phenomena which typically appear when using broad-area optical heaters thus facilitating detection of deeper defects.

## References

1. X. P. V. Maldague. Theory and Practice of Infrared Technology for NonDestructive Testing. John Wiley-Interscience, New York 2001.
2. K. Dragan, W. Swiderski. Multimode NDE approach for structure health assessment of composite elements in aerospace applications. Acta Physica Polonica A, Vol. 117, No 5. 2010
3. C. Ibarra-Castanedo, E. Grinzato, S. Marinetti, P. Bison, N. Avdelidis, M. Grenier, J-M. Piau, A. Bendada and X. Maldague. Quantitative assessment of aerospace materials by active thermography technique. 9th International Conference on Quantitative InfraRed Thermography, Kraków. 2008
4. W. Swiderski. Lock-in Thermography to rapid evaluation of destruction area in composite materials used in military applications. SPIE, Vol. 5132. 2003
5. V. Vavilov. Thermal/Infrared Testing.-NDT Handbooks series, Moscow, Spektr Publisher, 2008, 545 p.
6. Ch. B. Kiran Kumar, C. V. Krishnamurthy, B. W. Maxfield and K. Balasubramaniam. Tone Burst

- Eddy-Current Thermography (TBET). Review of Quantitative Nondestructive Evaluation Vol. 27, D. O. Thompson and D. E. Chimenti, American Institute of Physics. 2008
7. M. Pan et al. Defect characterisation using pulsed eddy current thermography under transmission mode and NDT applications. NDT & E International, Elsevier, Vol. 52, 2012
  8. L. Cheng, G. Y. Tian. Surface Crack Detection for Carbon Fiber Reinforced Plastic (CFRP) Materials Using Pulsed Eddy Current Thermography. Sensors Journal, IEEE, Vol. 11, Issue 12, 2011.
  9. ThermoEdCur Operation Manual.-Innovation, Ltd., Tomsk, Russia, 2014, 48 p.

# Towards thermal imaging based condition monitoring in offshore wind turbines

S. Van Hoecke<sup>1</sup>, O. Janssens<sup>1</sup>, R. Schulz<sup>1</sup>, K. Stockman<sup>2</sup>, M. Loccuffier<sup>2</sup>, R. Van de Walle<sup>1</sup>

<sup>1</sup> Multimedia Lab, Department of Electronics and Information Systems Ghent University-iMinds

<sup>3</sup> SYSTeMS, Department of Electrical Energy, Systems and Automation, Ghent University

This paper illustrates the potential of thermal imaging as a new sensor for condition monitoring in offshore wind turbines by monitoring fully covered and sealed rolling element bearings using a thermal camera. This potential is confirmed by the presented results, illustrating the suitability of thermal imaging to detect different lubrication levels as well as an outer raceway fault both with and without unbalance.

## Introduction

The significance of renewable energy has increased and will keep increasing over the coming decades as the European Union has set a 20% renewable energy target for 2020. With this goal in mind, the European Wind Energy Association (EWEA) proposed three possible growth scenarios for wind energy towards 2020. The three scenarios project an increase in installed wind turbine capacity of 41%, 64%, or 85% respectively compared to 2013 [1]. Offshore wind energy will play a major role as it profits from better wind conditions at sea than onshore. As, according to the EWEA, offshore wind is generally 8 m/s higher at European coastal waters compared to those onshore [2], offshore wind farms can easily outpace onshore farms in terms of installed capacity. However, exploitation of offshore wind farms is significantly more expensive than onshore wind farms as a result of the high construction costs, including foundation and cables, in order to withstand rough weather conditions. Furthermore, maintenance of offshore wind farms is more expensive and complex as logistics at sea are time intensive and costly, and access to the wind farms depends on the weather conditions. Offshore wind farms are sometimes not accessible for days or weeks, even when repairs are necessary. Therefore, in order to operate offshore wind turbines in an economic viable perspective, a reliable operation needs to be assured such that downtime and maintenance costs remain low and energy generation

guaranteed [3]. Unplanned, short-term maintenance on high sea is twice as expensive as planned interventions. Moreover, replacing broken components can take months [4]. Therefore, early and reliable fault detection is necessary to avoid more expensive consequential damage, or even a complete failure leading to a long loss of production [5].

## Condition Monitoring of the Drive Train

Figure 1 schematically presents the main components of a gearbox-based wind turbine drive train. Faults in this drive train are the main cause for downtime in offshore wind farms [6]. More specifically, because of their tribological nature, wind turbine drive train components such as gears and bearings are affected by friction and wear [7].

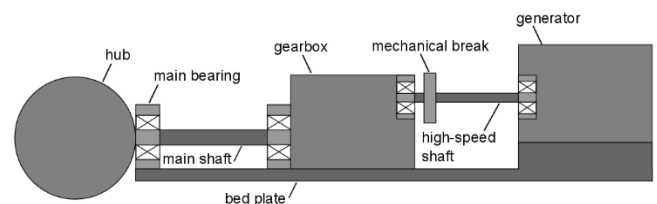


**Figure 20: Scheme of a wind turbine drive train with gearbox**

Additionally, bearings must deal with cyclic and transient loading as well as with alignment issues [8], making bearing faults one of the major issues regarding reliability of wind turbine drive trains.

Condition monitoring aims to detect degradation in an early stage, by continuously monitoring and interpreting well-chosen parameters. Combined with the knowledge of the expected evolution of the degradation and the remaining lifetime of components, intelligent planning and maintenance decisions can be made resulting in high performance. Additionally, condition monitoring can potentially even replace certain expensive and risky inspections by specialist staff.

Present condition monitoring techniques for industrial machinery includes vibration analysis, acoustic emissions and lubricant analysis. All present techniques show shortcomings for real-time measurements and data processing [9]. In particular, vibrations and acoustic emissions propagate through the structure which makes fault localization difficult. Different types of errors can result in similar vibration behavior, complicating fault classification. Other techniques such as lubricant analysis require onshore sample analysis in order to identify the faulty component, which itself is already costly in terms of time and financing. Furthermore, it requires the system to stop so that samples can be taken.

Besides noise and vibrations, faults will also cause specific temperature changes [10]. Contrary to vibrations, this elevated temperature is a local phenomenon and offers potential for thermal imaging to monitor drive-train components. Thermal imaging is a non-contact and non-intrusive technique, enabling condition monitoring without disrupting operation. Furthermore, thermal imaging allows spatial visualization of a monitored area and its heat propagation.

Thermal imaging is already commonly used on test rigs and in real environments such as pipelines, underground reservoirs and electric components. Huda et al. [11] and Jadin et al. [12] use machine learning algorithms applied on thermal images to detect faulty electrical components. Moreover, thermal imaging can

also be used for weld monitoring, corrosion detection, and gas/air flow monitoring.

### **Using Thermal Imaging on Rotating Machinery**

Despite its proven potential, thermal imaging has not yet received wide application for condition monitoring of rotating machinery, but receives increasing attention in research and industry. Younus [13], Widodo [14] and Lim [15] use thermal imaging to distinguish between misalignment, mass unbalance, bearing fault and normal operational conditions for rotating machinery, illustrating the potential of thermal imaging. However, previous work trains models on samples extracted from the same test run, risking overfitting and thus a memorized machine learning model instead of a generalized one, this way not being able to classify unseen data from other test runs correctly.

This paper analyses the potential of thermal imaging for monitoring rolling element bearings. The different tests of faults and conditions are done using a set of different bearings. After introducing the test setup, a methodology for analysing the thermal data is presented and applied on both healthy and faulty bearings. Afterwards, the results and major conclusions are presented.

### **Experimental Setup**

The presented test setup (see Figure 2) is used for monitoring completely covered and sealed FAG 22205-E1-K spherical roller bearings. These bearings consist of cylindrical rollers which manage high axial forces oscillating in both directions as well as radial forces. They are specifically designed to handle heavy loads similar to those in wind turbines. The close osculation between rollers and raceways supports uniform stress distribution, as it is usually the case in industrial applications such as in wind turbine drive trains.

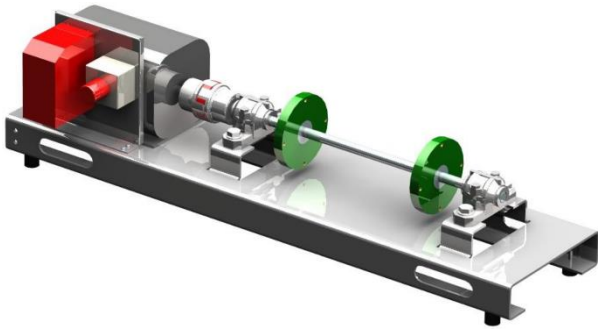


**Figure 21: Test setup**

In this particular setup, the bearings are mounted in a FAG SNV052-F-L plummer block housing. The used shaft has a diameter of 20 mm and is made of solid Cf53 with h6 tolerance rate.

Beside intact bearings, bearings with manually added pitting faults on the outer raceway have been monitored, as well as mildly inadequately lubricated and extremely inadequately lubricated bearings. All four conditions are also tested during mass imbalance, created by adding a 13 gram bolt to the disk located next to the monitored bearing housing at a radius of 5.4 cm, this way resulting in eight conditions. For every one of the eight conditions, five bearings are tested. Each test was run for one hour at a rotational speed of 1,500 rotations per minute, which is a standard rotational speed for high-speed components in European wind turbine drive trains. For monitoring the setup, the A655sc, an uncooled long-wave infrared (LWIR) camera by FLIR, has been used at a frame rate of 6.25 frames per second. Additionally, two thermocouples, located next to the setup, have been used to monitor the ambient temperature to provide reference temperatures for the data processing. Only the last 10 minutes of each hour (i.e. when the steady state is reached) are exported to AVI files for further processing and analysis. To reduce the size of the video files, lossless compression is applied using the H264 standard. The resulting videos consist of monochrome frames where the gray values correspond to temperatures in the range of [10°C 60°C]. Figure 3 presents an example of a frame, showing the shaft entering the bearing housing through the rubber seal as well as the

two thermocouples at the left back and right front side.

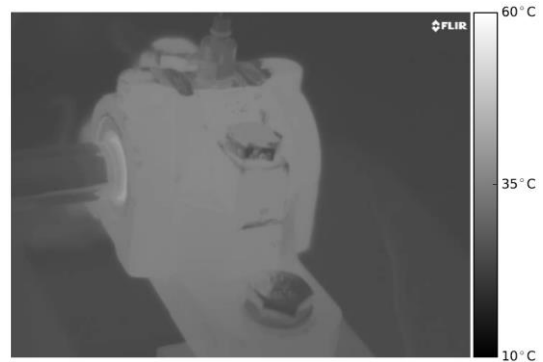


**Figure 22: One frame of an IR video of a healthy bearing**

## Methodology

A fault detection system automatically has to distinguish between conditions without human intervention for result interpretation. The automatic detection of a specific condition is regarded as a combination of a binary classification problem (pipeline 1) and a multi-class classification problem (pipeline 2). Hence, every 10-minute IR video has to be classified according to a certain machine condition, i.e. balance or imbalanced, and according to a suitable bearing condition, i.e. healthy, outer raceway fault, mildly inadequately or extremely inadequately lubricated. By using two pipelines, multiple labels are eventually assigned to a sample. For this research, a random decision forest (RDF) classifier is chosen for both pipelines as it has several advantages such as ease of use, human-interpretable decision rules of the individual decision trees and feature importance scores [16].

## Results

The first pipeline distinguishes between imbalance and balance, whereas the second pipeline distinguishes between healthy, outer raceway fault, mildly inadequately lubricated and extremely inadequately lubricated bearings. Classifying between balance and imbalance is a trivial task, as thermal imaging clearly indicates imbalance. As a result, the mean accuracy achieved by the RDF classifier during the leave-one-out cross-validation is 100% (+/- 0%).

Classifying the different bearing conditions is a more difficult task, resulting in an accuracy score of 87.5% (+/- 1.12%). Although the two pipelines work independently from one-another and have their own conditions to distinguish, in the end they need to be combined to get the most accurate fault diagnosis and distinguish between all eight possible combinations. As pipeline one has an accuracy of a 100% and pipeline two 87.5%, the eventual system is able to distinguish between the 8 conditions with an overall accuracy of 87.5%. For more details on feature selection for data mining on IR imaging, the reader is referred to [17].

## Conclusion

Fully covered and sealed rolling element bearings, similar to those in large size industrial applications and in wind turbines, have been monitored by a thermal camera. Whereas vibrations propagate through the drive train and fault localization requires high expertise, temperature increase is a more local phenomenon, supporting thermal imaging, a non-contact and non-intrusive technique, to enable condition monitoring without disrupting operation.

The presented results confirm the potential of thermal imaging as a new sensor for condition monitoring in offshore wind turbines and illustrate that by the use of IR imaging different levels of lubrication, with and without imbalance, or even an outer raceway fault can be detected. The different faults are classified by combining two random decision forest classifiers, resulting in 87.5% accuracy using leave-one-out cross-validation, illustrating that thermal cameras are a promising sensor for condition monitoring of wind turbine drive trains.

## References

thermal image, Expert Systems with Applications, 39, 2082-2091, 2012.

1. EWEA, "Wind energy scenarios for 2020; A report by the European Wind Energy Association," 2014.
2. World Energy Council, "World Energy Resources: Wind", url: [https://www.worldenergy.org/wp-content/uploads/2013/10/WER\\_2013\\_10\\_Wind.pdf](https://www.worldenergy.org/wp-content/uploads/2013/10/WER_2013_10_Wind.pdf)
3. Entezami M., Hillmansen S., Roberts C., "Distributed Fault Detection and Diagnosis for Wind Farms", Annual Conference of the Prognostics and Health Management Society, Portland (USA), 2010.
4. Daneshi-Far Z., Capolino G.A., Henao H., "Review of Failures and Condition Monitoring in Wind Turbine Generators". XIX International Conference on Electrical Machines, Rome (Italy) 2010.
5. Kusiak A., Verma A., "Prediction of Status Patterns of Wind Turbines: A Data Mining Approach". Journal of Solar Energy Engineering, vol. 133, American Society of Mechanical Engineers, New York (USA), 2011.
6. Sheng S., Veers P., "Wind Turbine Drivetrain Condition Monitoring" Applied Systems Health Conference, Virginia Beach (USA), 2011.
7. Hannon W.M., "Rolling Bearing Condition Monitoring", Encyclopedia of Tribology, pp. 2812-2820, Springer Science+Business Media, New York (USA), 2013.
8. Terrell E.J., Needelman W.M., Kyle J.P., "Wind Turbine Tribology". Green Tribology – Biomimetics, Energy Conservation and Sustainability, pp. 483-530, Springer International Publishing, Cham (Switzerland), 2012.
9. Zhang Z., Verma A., Kusiak A., 'Fault Analysis and Condition Monitoring of the Wind Turbine Gearbox', IEEE Transactions on Energy Conversion, Vol. 27, No. 2, 2012.
10. Schulz R., Verstockt S., Vermeiren J., Loccufier M., Stockman K., Van Hoecke S., Thermal Imaging for Monitoring Rolling Element Bearings, Quantitative InfraRed Thermography (QIRT) conference, Bordeaux, France, 2014.
11. Huda A.S.N., Taib S., Suitable feature selection for monitoring thermal conditions of electrical equipment using infrared thermography, Infrared Physics & Technology, 61, 184-191, 2013.
12. Jadin M.S., Taib S., Recent progress in diagnosing the reliability of electrical equipment by using infrared thermography, Infrared Physics & Technology, 55 (4), 236-245, 2012.
13. Younus A.M., Yang B.S., Intelligent fault diagnosis of rotating machinery using infrared
14. Widodo A., Satrijo D., Prahasto T., Lim G.M., Choi B.K., Confirmation of Thermal Images and Vibration Signals for Intelligent Machine Fault



- Diagnostics, International Journal of Rotating Machinery, 1-10, 2012.
15. Lim G.M., Bae D.M., Kim J.H., Fault diagnosis of rotating machine by thermography method on support vector machine, Journal of Mechanical Science and Technology, 28(8), 2948-2952, 2014.
  16. Breiman L., Bagging predictors, Mach. Learn. 24(2), 123-140, 1996.
  17. Janssens O., Schulz R., Slavkovikj V., Stockman K., Loccufier M, Van de Walle R., Van Hoecke S., Thermal Image based Fault Diagnosis for Rotating Machinery, submitted to Infrared Physics & Technology, 2015.

# AN EYE TO THE FUTURE, AN EYE TO THE PAST, THINKING TO A FULL-SCALE RESTORATION PROCESS: PHYSICAL AND CHEMICAL NDT ANALYSIS IN COOPERATION

S. Sfarra<sup>1</sup>, E. Cheilakou<sup>2</sup>, P. Theodorakeas<sup>2</sup>, D. Paoletti<sup>1</sup>, M. Kouï<sup>2</sup>

<sup>1</sup> Las.E.R. Laboratory, Department of Industrial and Information Engineering and Economics (DIIE), University of L'Aquila, Piazzale E. Pontieri no. 1, Loc. Monteluco di Roio, L'Aquila I-67100, Italy, stefano.sfarra@univaq.it

<sup>2</sup> NDT Laboratory, Department of Materials Science & Engineering, School of Chemical Engineering, National Technical University of Athens, Iroon Polytechniou no. 9, Zografou Campus, Athens GR-15780, Greece, elenheil@mail.ntua.gr

The case of the *S.S. Annunziata* Church (1178) located in Roio Colle (L'Aquila, Italy) is studied herein. The case offered the occasion for researchers coming from two Countries (Greece and Italy) to work both in person and in real-time, by using different techniques. In particular, chemical and physical NDT analysis were employed. Micro-samples were also collected and analyzed in a second time. The study started several years ago by the Las.E.R. Lab., *i.e.*, before that the cleaning process of the façade was conducted and completed in June 2015, *i.e.*, after 15 years from the first thermographic campaign, and 8 years from the second one. The second step follows the cleaning process, while the last follows the consolidation process by injection of mortar due to an earthquake. Qualitative and quantitative results have confirmed the alteration of the internal frescoes during the time.

## Introduction

The work is centered on a series of non-destructive inspections started in 2005 and ended in June of 2015. This started as a routine inspection on the cultural heritage of the city, conducted by the Las.E.R. Lab of UNIVAQ (L'Aquila, Italy), and it was concluded as a collaborative relationship with the NDT Lab of NTUA (Athens, Greece). This long term survey used passive thermography in order to inspect the façade and the internal walls of an ancient Church, built in 1178 [1]. The work could be considered as a unique case, since the most important phases of the restoration process, *i.e.*, cleaning and consolidation, have been monitored. In addition, the application of thermal imaging for the study of the interior walls permitted to confirm the historical supposition inherent to two different constructive steps, separated by the belfry. A first clue about the re-adaptation of the internal walls appeared after the 2009 earthquake that

caused the partial fall of the most recent decorative plaster, applied on the original frescoes. Probably, due to the plague that afflicted the Abruzzo region in 1464, 1484 and 1486, and the L'Aquila city in 1478, the local community, taking into account the health necessities, decided to renew the original decorative paintings by applying another layer, *i.e.*, by covering the original one and after that painting it.

The identification of the wall texture, at least for a small part, has been recovered using the active infrared thermography approach and by processing the thermograms, while the nature of the ancient pigments has been characterized by means of portable VIS-NIR Fiber Optics Diffuse Reflectance Spectroscopy (FORS) and laboratory methods including Environmental Scanning Electron Microscope (ESEM) coupled with an Energy Dispersive X-Ray Detector (EDX), and Attenuated Total Reflectance-Fourier Transform Infrared Spectrometer (ATR-FTIR).

## Main information of the SS. Annunziata Church

The Church having a rectangular structure and one nave, was built by stone walls of typical Romanesque craftsmanship and end products of Roman and early medieval ages. The date of consecration (1182) has been passed down by an epigraph engraved on a commemorative stone fixed within a wall. Inside the Church, two ogival recesses contain paintings dated between the fifteenth-century and sixteenth-century, while below the left recess, an Annunciation icon appeared after the 2009 earthquake.

The consolidation process of the stone walls started in 2011. Injections of mortar were pumped from the external wall inside the structure, thinking to an *opus incertum*, i.e., a double-skin concrete core. When the mortar appeared also on the internal wall, the point of injection was moved to another point. Fig. 1 clarifies the method applied.

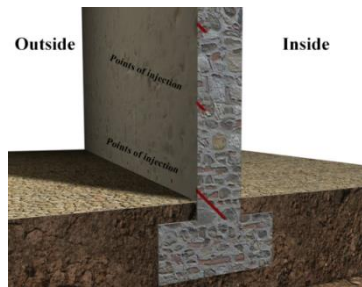


Fig. 1. Method of pumping the mortar in the wall as consolidation process

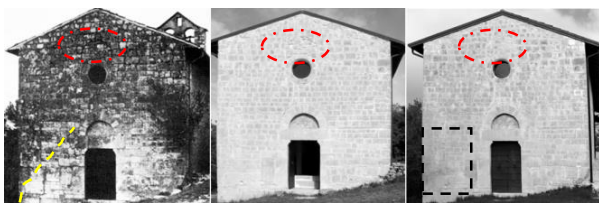


Fig. 2. SS. Annunziata Church: Photographs captured on June 17<sup>th</sup>, 2000 (left), June 17<sup>th</sup>, 2007 (middle) and June 17<sup>th</sup>, 2015 (right)

Fig. 2 summarises the evolution of the state of the façade from 2000, passing through 2007, and arriving to 2015, respectively. It is possible to note how the Church suffered in 2000 of biological attacks, lack of mortar between the

stones in 2015, as well as a curious aggregate of stones above the rose window (2000 – 2015).

## Results and Discussion

The different thermograms captured during this long term survey are reported in Figs. 3, 4 and 5. Here it shall be stated, that the different thermographic campaigns were performed taking into account the sun path, as these were conducted at 9:30 a.m. and they all have the same temperature scale. The above along with the monitoring of the climate conditions, which were quite similar to each individual campaign, enabled the relative comparisons. By observing the respective thermograms, the influence of the biological attack can be confirmed presented with increased temperature readings on the facade. The presence of black mould colonies (Fig. 2) is indicating the presence of moisture as well. Thus, considering the early time of inspection along with the low heat exchange coefficient of water, the zones of increased temperature can be correlated with the bio-deteriorated regions. It is also very interesting to note how the thermal imprints, signaled by a dotted line, follow the same trend of Fig. 2 (left – see the bottom left part).

Moreover, interesting results can be produced from Figs. 6 and 7, where the thermal behavior of the interior left and right wall sides is presented. In particular, the thermograms inside the white oval (Fig.7) reveal a layer of sub-superficial stones beneath the plaster surface. It is interesting the fact that these thermal imprints can be detected only in this part of the lateral wall, i.e., on the right side, while it is also interesting to note that, at the time in which the thermograms have been acquired, the sun did not directly irradiate the right side. On the other hand, at the respective external lowest wall part (Fig. 5) a high temperature reading is appeared, possibly due to the presence of moisture. Seeing from inside, it was confirmed that the lowest part of the wall is also affected by moisture from the ground, while the middle part has a different temperature, receiving slightly greater solar radiation, and similarly the upper part accumulates the greatest amount of sun heat.

However, based on the individual observations, it is possible to say that the thermograms out of the oval have two layers of plasters, *i.e.*, the old, that was revealed after the quake, and the new one, that covers the old fresco; on the contrary, the images inside the oval reveal only the new plaster that was applied upon the stone masonry, as in that case it was possible the detection of the sub-superficial stone masonry. Instead, the left side (Fig. 6) does not reveal the presence of the stone masonry; therefore, the realization of an oldest sub-superficial fresco as appears in Fig. 7 is highly probable.

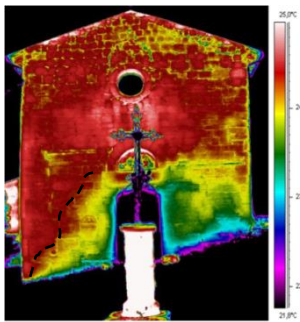


Fig. 3. S.S. Annunziata Church: Thermogram captured on June 17<sup>th</sup>, 2000

In order to detect the shape of the stone masonry and understand the quality of the consolidation process, a part of the ancient fresco (white rectangle – Fig. 7) was inspected by IRT technique; data coming from an active thermographic test (hot air stimulation) were processed thanks to the pulsed phase thermography (PPT) and principal component thermography (PCT) techniques [2] algorithms.

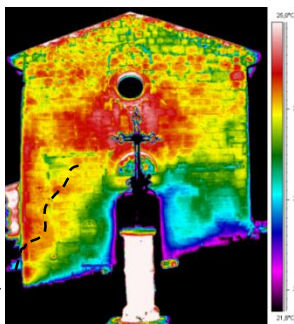


Fig. 4. S.S. Annunziata Church: Thermogram captured on June 17<sup>th</sup>, 2007

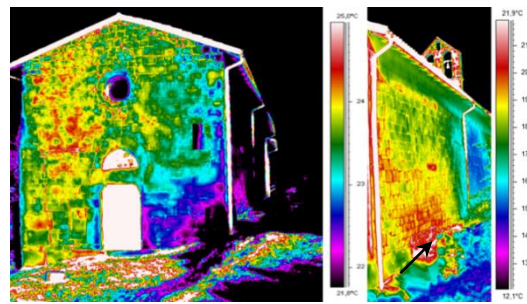


Fig. 5. S.S. Annunziata Church: Thermograms captured on June 17<sup>th</sup>, 2015 (façade and right wall)

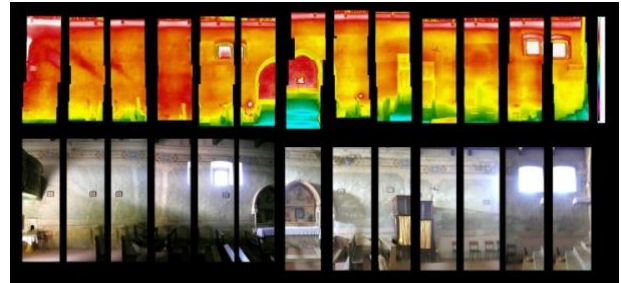


Fig. 6. S.S. Annunziata Church: Thermogram (top) and photograph (bottom) captured on June 15<sup>th</sup>, 2007 inherent to the left wall from the inside part



Fig. 7. S.S. Annunziata Church: Thermogram (top) and photograph (bottom) captured on June 15<sup>th</sup>, 2007 inherent to the right wall from the inside part

The inspected part is also pointed out in Fig. 8 by the red dotted rectangle. As can be seen from this Figure, PCT analysis revealed some regions of interest, signaled by arrows, also revealed by the PPT technique (Fig. 8). The differences indicated by the arrows can be possibly attributed to the presence of new mortar after the consolidation process by injections. It is interesting to notice that when working at 0.16 Hz instead of at 0.48 Hz, the aggregate marked by a yellow arrow appears with a greater

evidence. Along with the thermographic survey, the main pigments of the oldest fresco were analyzed *in-situ* by means of FORS technique. Pigments' identification was derived through comparative analysis between the acquired diffuse reflectance spectra and suitable spectral database of reference pigments, developed in the NDT Lab. [3]. The artist's color palette was found to comprise fresco pigments, *i.e.*, red (hematite) (Fig. 9) and yellow (goethite) ochre, green earth (glauconite) and blue glass pigment smalt suffering from discoloration.

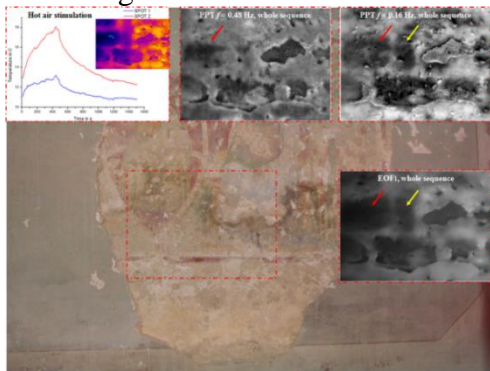


Fig. 8. S.S. Annunziata Church: The inspected part and the PPT and PCT results coming from an heat air stimulation

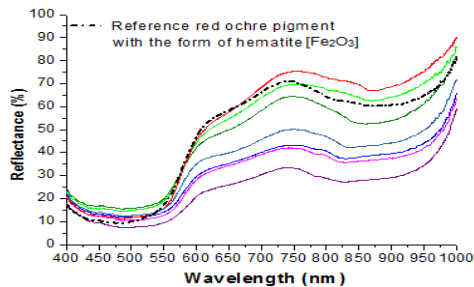


Fig. 9. Diffuse reflectance spectra of the red painted areas. The *in-situ* curves present similar spectral features with the reference pigment curve (dotted line) verifying the presence of red ochre (hematite)

The results obtained from the chemical elemental analysis (Fig. 10) and molecular structural characterization of the micro-samples through ESEM-EDX and ATR-FTIR methods established the reliability of the analytical information obtained by FORS technique [4]. Characteristic absorption bands of calcite and protein binding medium were recorded in all ATR-FTIR spectra, indicating the application of a *fresco-secco* wall painting technique.

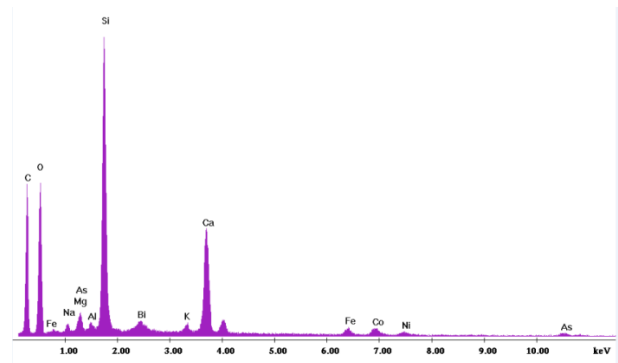


Fig. 10. EDX spectrum of blue micro-sample revealing high Si content along with lower K and Co amounts, indicating the presence of smalt. Impurities of Al, Fe, As, Ni and Bi are also detected coming from the silica source and the cobalt ore used to manufacture the pigment. The high Ca levels suggest the presence of CaCO<sub>3</sub> coming from the plaster.

## Conclusions

Seeing the results, it is possible to affirm that the joint use of chemical and physical NDT analysis is highly recommended when is needed solving both structural and artistic ambiguities. It is demonstrated that a smart procedure during the years can confirm or deny the assumptions on the technique of execution of the wall paintings, helping both the art historians and the restorers.

## References

1. D. Paoletti, D. Ambrosini, S. Sfarra, F. Bisegna. Preventive thermographic diagnosis of historical buildings for consolidation, *J. Cult. Herit.*, **14**, pp. 116-21, 2013.
2. P. Theodorakeas, C. Ibarra-Castanedo, S. Sfarra, N.P. Avdelidis, M. Kouli, X. Maldague, D. Paoletti, D. Ambrosini. NDT inspection of plastered mosaics by means of transient thermography and holographic interferometry, *NDT&E Int.*, **47**, pp. 150-6, 2012.
3. E. Cheilakou, M. Troullinos, M. Kouli. Identification of pigments on Byzantine wall paintings from Crete (14<sup>th</sup> century AD) using non-invasive Fiber Optics Diffuse Reflectance Spectroscopy (FORS). *J. Archaeol. Sci.*, **41**, pp. 541-55, 2014.
4. E. Cheilakou, M. Kartsonaki, M. Kouli, P.A. Callet. Non Destructive study of the identification of pigments on monuments by colorimetry. *Int. J. Microst. and Mater. Prop.*, **4**(1), pp. 112-127, 2009.



# APPLICATIONS OF THE INFRARED THERMOGRAPHY TO THE ASSESSMENT OF HISTORIC BUILDINGS: A CASE STUDY IN PISA

A. De Falco<sup>1</sup>, T. Santini<sup>2</sup> M. Sguazzino<sup>3</sup>

<sup>1</sup> Dept. of Energy, Systems, Territory and Construction Engineering, University of Pisa, Largo L. Lazzarino, 1 – Pisa - [a.defalco@ing.unipi.it](mailto:a.defalco@ing.unipi.it)

<sup>2</sup> Studio ThermoTech Sas, Via Bottaccio, 28 Massa - [t.santini@studiothermotech.it](mailto:t.santini@studiothermotech.it)

<sup>3</sup> Dept. of Civil and Industrial Engineering, University of Pisa, Largo L. Lazzarino, 1 – Pisa - [mizio82g@libero.it](mailto:mizio82g@libero.it)

Measuring the thermal response of materials in building assessment has a wide range of applications concerning not only the thermophysical aspects, but also the structural ones. The last topic is particularly interesting in the context of historic buildings, where the modern tools for surface temperature measurement are capable of providing many useful information: the masonry texture and the materials detection under the plaster are the fundamentals for the evaluation of the structural behavior and for the selection of the strengthening and restoration criteria. In this regard, the full-field, contactless and real time investigation makes the infrared thermography indispensable. The thermographic technique is taken here into consideration in an emblematic case study.

## Introduction

In the context of historic buildings, information on distributive and structural schemes is essential for the safety evaluation and for the identification of conservation criteria. This is achieved by the joint use of data from historical analysis, detailed geometric survey and non-destructive or minor-destructive investigations. The infrared thermography has clear advantages for the amount of the information provided and for its non-invasive nature which makes the technique particularly suitable to the assessment of historic and artistic buildings.

As demonstrated in [1] and [2], the ability of the technique to read the different thermal images released on the surfaces by different materials under the plaster is related to the percentage difference of the thermal diffusivity of the blocks to that of the mortar joints. This is reflected in the survey campaign herein presented, which is an emblematic case in the restoration field.

## Franchetti Palace in Pisa

Franchetti Palace is a “U”-shaped masonry building located in the historic center of Pisa and is currently the seat of the Reclamation Consortium. It is composed by a three story main body of 22 m x 38 m, which is part of the aggregate of via San Martino, with two lower wings fronting the Arno river (Fig.1).



Fig. 1. Franchetti palace.

As many buildings of the historic center, the palace has undergone an articulated evolution. The first phase takes place in the Middle Age (XII-XIII century) with a group of tower-houses separated by alleyways. These common medieval buildings were erected by powerful families and are characterized by the main facade made up of Verrucano (sedimentary siliceous-clastic rock)



blocks and monoliths [3], with wide openings and arches in the upper part.

In the late Renaissance phase, the ancient constructions are to form two adjacent buildings (Fig.2).



Fig. 2. The facade on via San Martino.

The third phase, which provides the current configuration, was fulfilled under the Jewish Franchetti family, which brought together the fractional ownership and operated the restructuring at the end of the XIX.

While the nineteenth century configuration is well known from historical documents, the evolution from the original situation is not so clear. In this context, thermographic survey has provided a significant contribution.

### The thermographic survey

The survey has been performed between March and June 2012, by means of a fully radiometric IR camera AVIO TVS 500 EX, with long-wave microbolometer FPA sensor (320x240), having thermal sensitivity of 0.05 °C and geometric resolution of 1.3 mrad. The camera high performances allowed obtaining high definition images. Furthermore, in order to optimize thermal image, the measurement campaign of the weather conditions and environmental hygrothermal quantities (ambient temperature and relative humidity) was carried out by using a psychrometric probe with forced ventilation. The value of the emissivity parameter  $\varepsilon$  of the target object has been evaluated through the “Contact Thermometer Method” procedure [4], by means of temperature probes. Furthermore, in order to obtain measurable temperature differences on the surface of the

observed elements, a previous heating of the surface was often necessary.

The acquisition of the IR images of the external surfaces was performed in passive mode, under normal environmental conditions. Instead, the internal surfaces were heated by using a LPG powered convector with 37 kcal maximum power; the measurements presented here were performed during both the heat absorption and the cooling down process.

The technique has provided information about:

- \_ different masonry textures;
- \_ ancient architectural details within the masonry walls;
- \_ cracking on walls and frescoed vaults;
- \_ anomalies like hidden chimneys and voids.

The IR images of the south west facade on via San Martino reveal the hidden structures of the ancient tower-houses made up of square stone blocks (Fig.3).

The higher thermal conductivity and a generally lower volumetric heat capacity of the stones in comparison with clay bricks and lime mortar produced a strong thermal contrast ( $T = 5\text{ °C}$ ) between the different materials. Six piles was detected, four of them corresponding to the transversal walls of the palace (Fig.3). In Fig.4 one can distinctly observe two central arches in the upper part of the façade, with the typical cantonal on the right side. This observation confirms the historical information of the existence of an adjacent alley. On the left side, however, the interruption of the structure at the arch springing is clearly visible. Putlog holes for the wooden beams of the medieval balconies are clearly visible at the top of the stone structure and at the underlying floor. The IR images taken from inside, showing the single stone blocks of the arches and piles, confirm the presence of the old structures on the entire wall thickness (Fig.5).

In this case, the materials under the plaster have been clearly detected, thanks to the 50% percentage variation between the thermal diffusivity of white-pink quartzite (Verrucano) ( $\alpha_s \approx 10^{-6}\text{ m}^2/\text{s}$ ) compared to the limestone mortar ( $\alpha_m \approx 5 \cdot 10^{-7}\text{ m}^2/\text{s}$ ), [1] and [5].

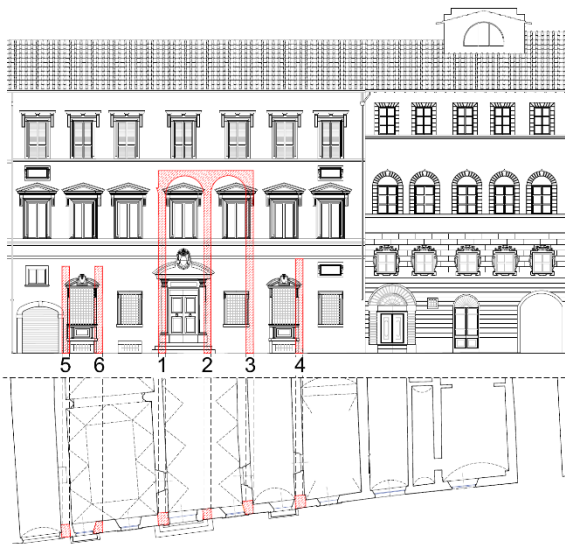


Fig. 3. The hidden structures on the facade along San Martino street with a part of the plan view.

Various types of infill walls between the masonry piers have been detected: those which are made up of clay brick masonry have been quite clearly identified, since they are characterized by a noticeable thermal uniformity, due to the low difference (not more than 10%) between the diffusivity value of the mortar and that of the clay bricks. However, there are also areas with chaotic texture, with irregular stone elements, as on the left of the pile 4 seen from inside (Fig.5).

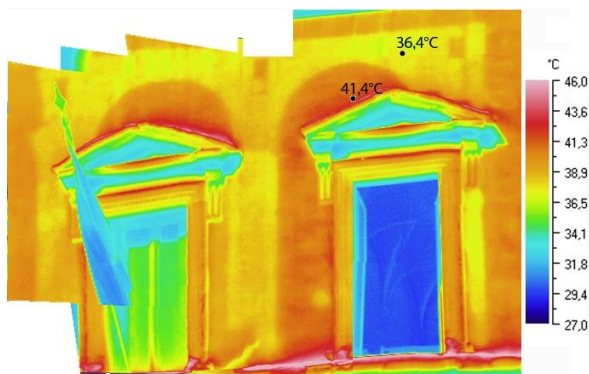


Fig. 4. Detail of the upper part of the facade on San Martino street.

From Fig.5, taken from the inside, the protrusion of pile 4 is recognizable from its surface temperature which reveals the presence of stone blocks. This discontinuity demonstrates that the walls incorporating the pile 4 are not in phase with it.

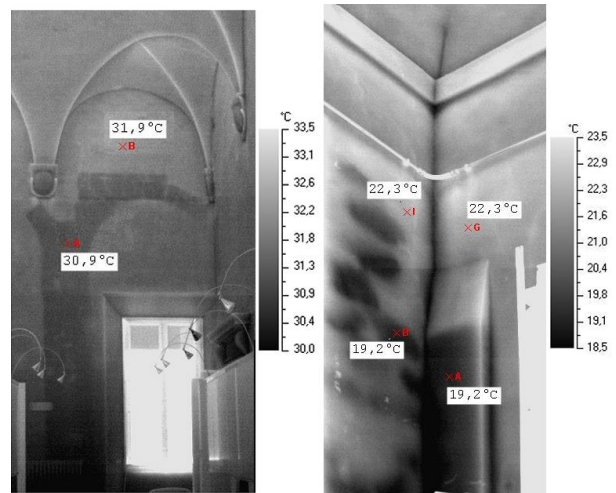


Fig. 5. Views from the inside: the image of the arches and the protrusion of the pillar 4.

The IR image of the facade towards the Arno highlights the Renaissance structure with three stone arches (Fig.6) which are currently filled with clay brick masonry. A vertical crack, which runs over the entire height of the palace, marks the change of masonry texture, which is characterized by stone elements on the left side (Fig.7). This discontinuity is located in correspondence of the transversal wall including the pile 4 (Fig.3 and 6).



Fig. 6. Superposition of IR and visible images of the facade fronting the Arno river.

A mosaicking of thermal images of the interior spaces is shown in Fig.8. One can observe the typical texture of in folio vaults, the trace of the brick ribs on the extrados and the level of the extrados filling. The wall with chaotic texture, that is characterized by stone elements, is crossed by a

chimney and is lined with in folio bricks at the lower part.

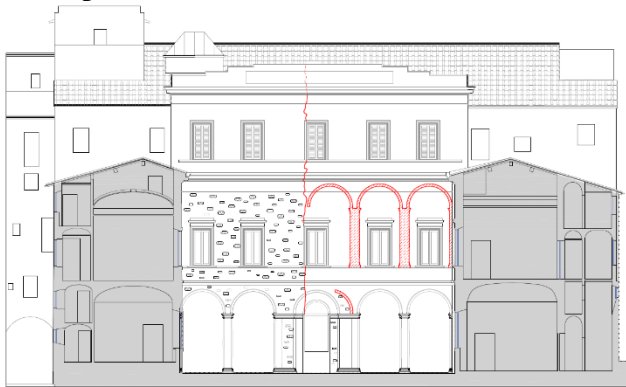


Fig. 7. The hidden texture on the facade fronting the Arno river.

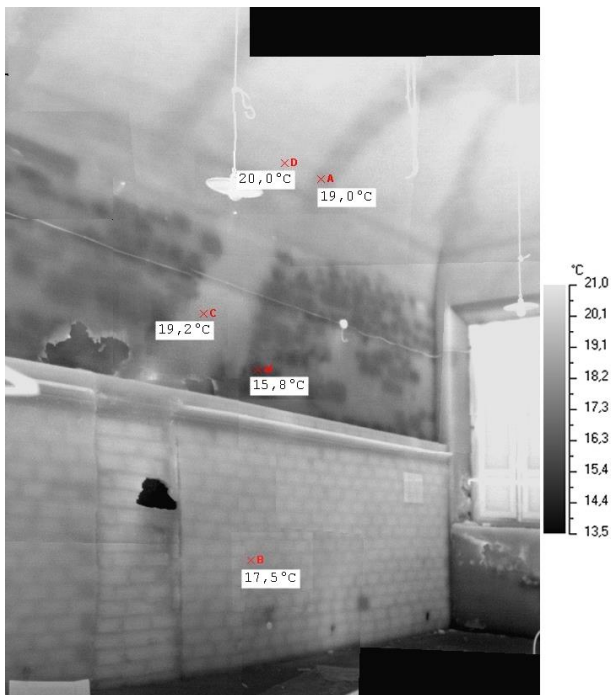


Fig. 8. IR image mosaic of the internal surfaces of a room at the ground floor.

### Results of the survey

The ability of infrared thermography to detect the masonry texture under the plaster is related to the different thermal properties of the blocks compared to the surrounding mortar: the best images have been obtained when the percentage variation of the thermal characteristics between nearby materials was higher than 50%.

In this emblematic case, the survey provides information that offer interesting insights regarding the building construction phases. A first synthesis

of the construction periods for the different parts of the structure is shown in Fig.9.

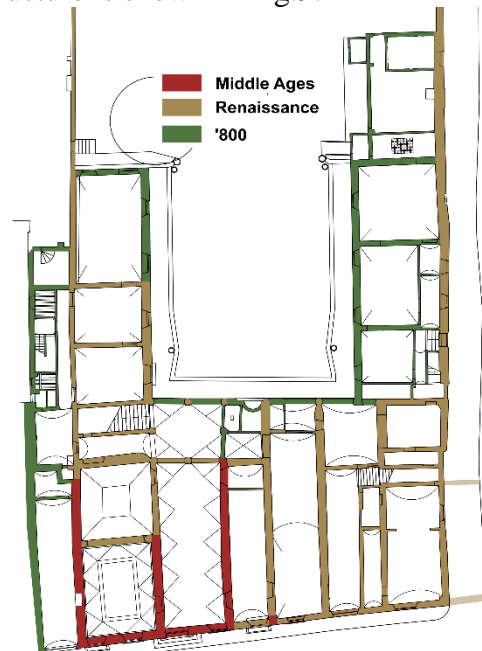


Fig. 9. Dating of current masonry structures.

### Conclusion

The IR thermography may provide an important contribution to the knowledge of the structural schemes and the construction phases of historical buildings. This paper presents an example of its potential in this regard.

### References

1. T. Santini. Summary of bachelor thesis in Civil Engineering: L'impiego della termografia nella diagnostica delle costruzioni murarie storiche: metodologie ed esempi. Bollettino Ingegneri, Vol. 12, pp. 17-20, 2008.
2. F. Fantozzi, S. Filippeschi, T. Santini. L'uso della termografia per una corretta diagnosi energetica. Proc. 7° CIRIAF - Sviluppo sostenibile, tutela dell'ambiente e della salute umana, Perugia, 30-31 Marzo, 2007.
3. M. Franzini, M. Lezzerini and L. Mannella. The stones of medieval buildings in Pisa and Lucca (western Tuscany, Italy). 3 – Green and white-pink quartzites from Mt. Pisano. Eur. J. Mineral, Vol. 13, pp. 187-195, 2001.
4. E 1933-97\_Standard Test Methods for Measuring and Compensating for Emissivity Using IR Imaging.
5. UNI 10351:1994 Materiali da costruzione. Conduttività termica e permeabilità al vapore.

# NON DESTRUCTIVE CHARACTERIZATION OF THERMAL AND OPTICAL PROPERTIES ON HIGH PERFORMANCES TEXTILES

M. Gargano<sup>1</sup>, N. Ludwig<sup>1</sup>, E. Rosina<sup>2</sup>

<sup>1</sup> Department of Physics, Università degli Studi di Milano, Italy, marco.gargano@unimi.it

<sup>2</sup> Department of Building Environment Science and Technology, Politecnico di Milano, elisabetta.rosina@polimi.it

Infrared thermography (IRT) is a method for temperature evaluation with a non-contact and non sampling approach that has an increasing popularity as application on Archaeological areas. IRT has also been widely used in the field of Cultural Heritage to study the thermal exchanges of open air sites in which shelters increase the internal temperature and can induce changes in local microclimate. Visible-IR spectroscopy and IRT can be used in an integrated approach to study the durability of the textile materials of shelters. This paper shows the results of tests on aged textiles at outdoor environmental conditions. The authors show also the simplified analytical models for the evolution of the optical properties due to ageing.

## Introduction

This paper shows the role of non-destructive testing (NDT) in the characterization of innovative materials for the protection of archaeological sites. In the last years several papers showed the change in the trend of designing shelters on archaeological areas: from mainly aesthetic issues to the effective protection and, especially, low impact on the site and environment. At present the compelling concern of conservators, scholars, designers, and the authorities for the protection of Archaeological area requires to test and adopt new solution that better meet the requirements of conservation. The authors analyzed any aspects in previous publications [1-4], highlighting how traditional covering solutions can often contribute to damage instead of offering protection. To overcome the limits of typical protective building systems, the project of new shelters needed to combine the requirements for preservation (compatibility and reversibility of new materials, as well as protection from environmental aggression) and new issues of their use (flexibility, feasibility, lowest maintenance and easy deconstruction to allow the reuse of the shelter in different locations and/or seasons). Recent researches [5-7] on high

performances textiles and ultra light structures are very promising, and they bring an important innovation for the realization of shelters, together with meeting most of the listed requirements. Nevertheless, scientific literature does not reports enough information regarding the durability and decreasing of performances of textiles, especially if exposed to polluted or aggressive environments. This paper describes the tests of a textile-based prototypes (PVC coated Polyester, mostly commonly used for many purposes shelters) proposed as an alternative solution to the provisional shelter, and the comparison of its characteristics and performances throughout six years of natural ageing in polluted environment.

## Materials and Methods

The authors measured both thermal and optical characteristics (in reflection and absorption set-up).

Thermal tests were performed using two simulations of external heating radiation. The first simulation is by reflection mode, using two halogen lamps (500W each, 1 meter distance, axis of lighting 45° from the surface of the sample). The lamps directly irradiate the external part of the textile. Thermal images were shot every 10 s, placing the thermocamera



(AVIO TVS700 micro bolometer uncooled detector) in front of the sample surface at 75 cm of distance. In the second test, one single halogen lamp provides the back heating at 80 cm from the textile, leaving the themocamera in front of the sample. Thermal images of the second test show the capability of the fabric to reduce and convey heat radiation from the direct irradiated surface toward the shaded side.

Optical property was measured using fiber optic reflectance spectrometry (FORS) equipped with optic fibers probe working in UV-Visible-Near Infrared band of electromagnetic spectrum (200-1050 nm). The Spectrometer (Ocean Optics HR4000) was used also in transmittance mode by using a diffusing neutral density glass (10%) as calibration reference instead of a BaSO4 99% reflectance standard with the aim to have comparable optical properties of the examined textiles which have an intrinsic high diffusivity. The authors measured the reflectance/transmittance on ten areas (4 mm<sup>2</sup>) and they calculated the average over the whole tests area.

Finally, the colorimetric measurement (Minolta CR-400 Chroma Meter) allowed the authors to evaluate the color changes in the samples.

## Results and Discussion

The researchers applied the main measurements campaigns on the brand new material, and samples taken after 15 and 65 months of ageing (in polluted environment). Data reported in figures 1 and 2 show the effect of aging on the heating of the textile by front (Fig. 1) and back-heating (Fig 2). In the following, figures 3 and 4 represent the value of the maximum heating reached after 5 minute of heating.

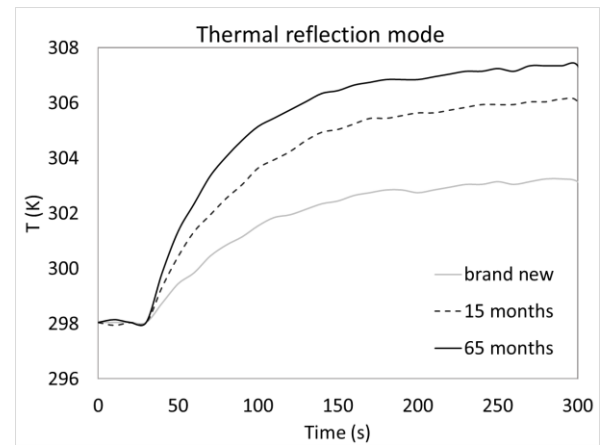


Fig. 1. Thermal trend of the surfaces of the textile samples at different condition of ageing by front heating.

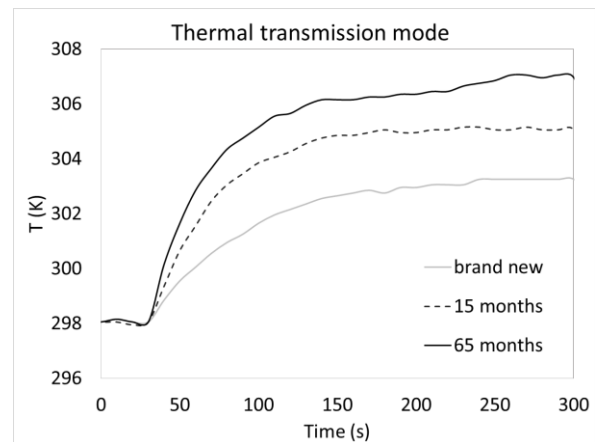


Fig. 2. Thermal trend of the surfaces of the textile samples at different condition of ageing by back heating.

Logarithmic and linear fits for the reflection and transmission modes are representative of the temperature increase during the heating.

After having measured the thermal properties, the authors measured the optical characteristic of the textile samples.

The test measured the spectral reflectance factor (Fig. 5), and the spectral transmission factor (Fig. 6) of the material. The graphics in figures 5 and 6 show the strong decrease of the reflectance in the green-blue regions of the spectrum, as well as the decrease of the transmittance. Has been very useful to find a logarithmic relation for both the spectra (Fig. 7 and 8) for these curves too. As reference wavelength was considered the 555 nm.



Fig. 3. Logarithmic of the maximum temperature reached after 5 minutes of heating in the reflection mode set up. This fit shows a correlation index of 0.99.

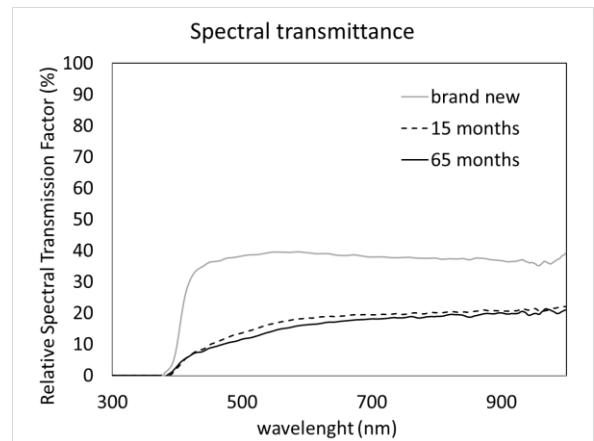


Fig. 6. Relative spectral transmission of the textile samples. Measurement were made using a 1% transmittance that diffuses the reference standard.



Fig. 4. Linear fit of the maximum temperature reached after 5 minutes of heating in the reflection mode set up.

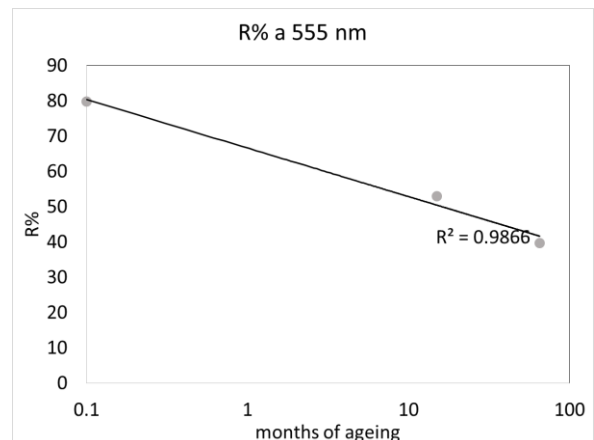


Fig. 7. Fit of the spectral reflection factor measured at 555 nm wavelength. Data show a logarithmic trend.

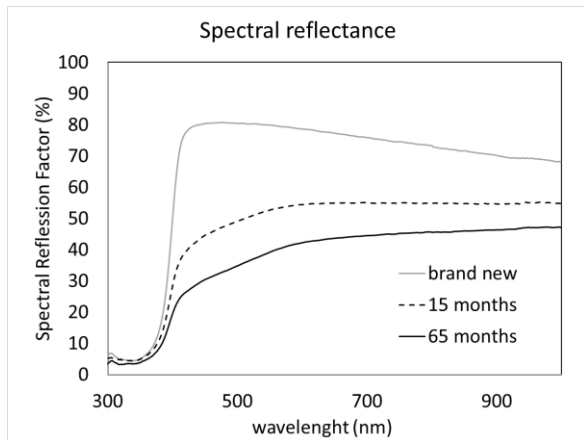


Fig. 5. Spectral reflectance factor of the textile samples.

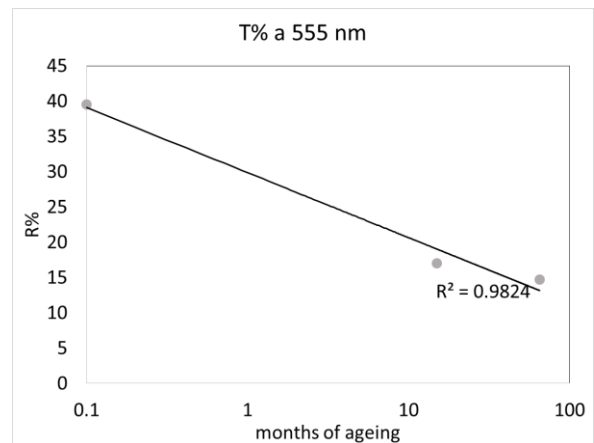


Fig. 8. Fit of the relative spectral transmission factor measured at 555 nm wavelength. Data show a logarithmic trend.



Beside the thermal and spectral variations, also colorimetric measurements were performed to evaluate the color change in the textile samples. Figure 7 shows the color data in CIEL\*a\*b\* color space, it is apparent that the color variations take place principally along the b\* axis (which represents the blue-yellow variations). Therefore, the main effect of ageing on the examined samples is the yellowing of the surface.

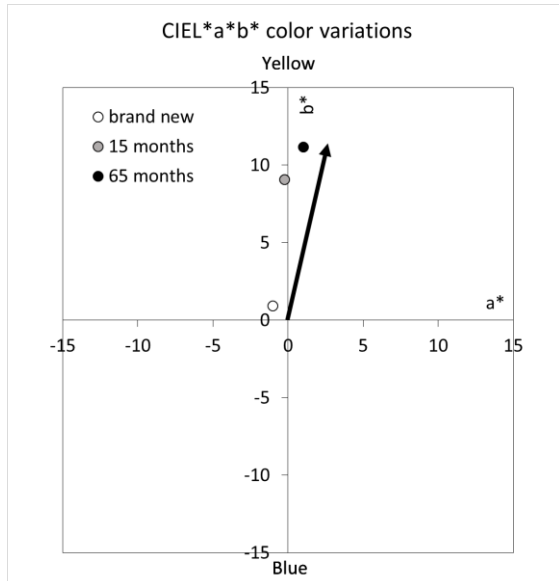


Fig. 9. Colorimetric data of the textile samples with the shift caused by the ageing.

## Conclusion

The use of textiles for sheltering archeological areas has recently achieved many approval from scientists and professionals, for its suitability and effectiveness. Nevertheless, its application can cause some damages to the fragile materials under the shelter, as well as for glass, steel, and even traditional materials like straws and timber.

With these multidisciplinary approach the authors propose an efficient methodology to evaluate the condition of the textiles also on site. The results of the present study indicate that the textiles do not show a linear decay, as many technical specifications from the producers seems to suggest, and the tests are mandatory to determine a more appropriate life time for these materials when installed in polluted or aggressive environment.

## References

1. P. Pesaresi, G. Rizzi, New and existing forms of protective shelter at Herculaneum: towards improving the continuous care of the site, *Conservation and Management of Archaeological Sites* 2006; 8(4), 237-252.
2. J. Ashurst, *Conservation of Ruins*, Routledge, 2007
3. Le coperture delle aree archeologiche: museo aperto. Istituto Centrale per il Restauro Gangemi Editori, Rome 2006.
4. M. Schmid, Protective shelters at the archaeological sites of Mallia (Crete) and Kalavassos-Tenta (Cyprus), *Conservation and Management of Archaeological Sites* 1998; 2(3), 143-153.
5. E. Rosina, A. Zanelli, P. Beccarelli, M. Gargano and E. Romoli, New procedures and materials for improving protection of Archeological areas. *Mat. Eva*, 69, 8, 979-989
6. A. Zanelli, E. Rosina, P. Beccarelli, R. Maffei, G. Carra: Innovative solutions for ultra-lightweight textile shelters covering archaeological sites. *Proceedings of ICSA 2013, Guimaraes, Portugal, 24-26 July, 2013*, pp 1-8
7. P. Beccarelli, E. Romoli, E. Rosina, A. Zanelli, Textile shelters for archaeological areas: a change in the preservation of Cultural Heritage, in *Tensile Architecture: Connecting Past and Future, Proceedings TensiNet Symposium, GSP 1900, Sofia 2010*, pp. 165-173.

# Non intrusive wall material recognition through active thermography and numerical modeling

F. Pietrarca<sup>a</sup>, M. Mameli<sup>a,b,\*</sup>, S. Filippeschi<sup>a</sup>, F. Fantozzi<sup>a</sup>

<sup>a</sup> Università di Pisa, DESTEC, Largo Lazzarino 2, 56122 Pisa, Italy.

<sup>b</sup> Università di Bergamo, Viale Marconi 5, 24044 Dalmine (BG), Italy.

\* *corresponding author*

## Abstract

In the framework of historical buildings, the wall thickness as well as the wall constituents are often not known a priori and active IR thermography can be exploited for detecting what kind of material lies beneath the external plaster layer. In the present work, the transient thermal response of walls made of different known materials underneath the plaster layer are simulated by validated numerical models. Meanwhile the surface temperature temporal trend of an unknown wall is recorded by an IR camera. The experimental data are finally compared with the simulations in order to identify what material lies under the unknown wall. An interesting qualitative accordance between the experimental results and the most common materials used in this zone has been observed.

## Introduction

The evaluation of the masonry building stability has to start from a detailed analysis of the wall that constitutes the building structure. Ideally, in order to have an adequate knowledge of the material characteristics of an existing building one should rely on documentation already available and on experimental investigations carried out in situ. If the building is listed as having historic or artistic value, destructive techniques are not applicable. The need to investigate the historic buildings with non-invasive methods in the case of plastered masonry is resolved right through the thermographic diagnosis. The passive thermography is already widely used and its capability to detect the architectural elements underneath the plaster is well-known. On the other hand the quantitative analysis of wall by using active thermography is matter of interest at the moment. Actually, active thermography has already been successfully applied in civil engineering as non destructive tool. For example, Theodorakeas et al. investigated the potential of active thermography based

on the cooling down procedures in order to test multilayered structures and identify hidden mosaic artefacts beneath layers of plaster [1]. A study reported in Fox et al. [2] also compared thermographic results and numerical simulation for investigating the transient behaviour of materials. The aim of the present work is to demonstrate the possibility of detecting the wall constituent materials by coupling a simple hybrid analytical/numerical tool to the use of active thermography in situ.

## In situ analysis

The in situ IR analysis consists in choosing an accessible historical building, perform a visual observation in order to detect the masonry texture below the plaster layer, and characterize the wall by means of infrared active thermography. Finally the recorded data can be compared, in a post processing time, with those coming from a numerical model. The reference case used in this paper is the “Ex Palazzo Littorio - Tribunale” at Lucca, , a building dating back to the early '900 where detachments of plaster allow to detect specifically the masonry texture. The masonry bearing walls (thickness from 65 cm to 30 cm) are composed of full brick and split stone hewn or irregularly shaped. The experimental

set-up (fig.1) consists of an infrared camera (AVIO TVS 600<sup>®</sup>) and an infrared oil heater (ISS 40<sup>®</sup>).

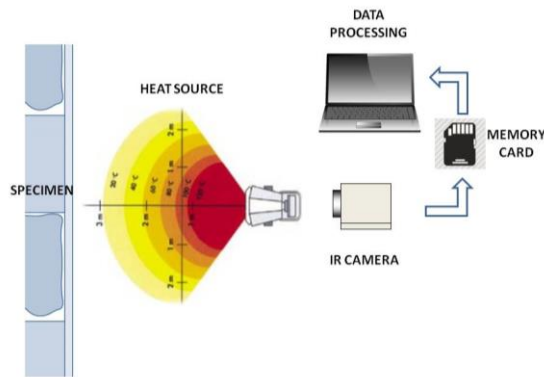


Figure 23 - Experimental set-up.

The thermographic system used for this study is made from focal plane array microbolometric sensors with an image resolution of 240x320 pixels. The camera detects the emitted radiation from the surface of the specimen in a wavelength region from 8 to 14  $\mu$  m. The camera optical characteristics are given by a 35 mm lens having a 25.8°x19.5° field of view and a 1.4  $\mu$  rad instantaneous field of view. The thermal resolution is 0.15 K and the temperature measurement accuracy is  $\pm 4\%$ . First, before switching on the heater, the room temperature (equal to 17.8 °C) was measured by means of a thermometer. The camera is placed on a tripod at a distance of 1.73 m from the wall, after evaluating appropriately focus and the area framed by the camera. For the monitoring of the heating process, thermal images are recorded sequentially with a time step of 10 s. The radiant heater was located at a distance of 1 m from the wall under investigation and switched on providing the external thermal stimulus necessary to identify the wall inhomogeneity.

### Hybrid Model

The aim is to develop a relatively easy numerical tool that may be used, in comparison with experimental data, in order to recognize the wall material under the plaster layer. If the model is simple it is also

more generic and can be applied to different walls at different environmental conditions. The novel idea is to couple a finite difference model for solving the outer plaster layer, with the semi-infinite wall analytical solution for the wall underneath. Such a model [3] is not only easy to implement but relies on fewer parameters with respect to the pure finite difference: since the transient solution is poorly affected by the convective condition on the other side of the wall (with this kind of heater), the heat transfer coefficient on this side is not needed. The model is developed in MATLAB environment. The wall is composed by the external plaster layer (grey control volume in fig. 2) and the internal wall (pink control volume in fig. 2). The hybrid model solves the transient heat conduction problem in the above control volumes with two different approaches: a forward (time) centred (space) explicit finite difference model for the plaster layer is coupled with the analytical solution for the semi-infinite solid for the internal wall. The main assumptions are:

- 1) The model is one dimensional (x is the direction perpendicular to the wall surface);
- 2) Convection on the external plaster layer is neglected;
- 3) Heat flux at the interface between the plaster layer and the semi-infinite solid is constant;

About point 2 some additional comments must be made. Convection can be neglected only if the heater is radiant, and the wall surface temperature does not grow very much. The plaster layer is discretized into n nodes, the first corresponding to the external surface receiving the radiative heat flux, the last corresponding to the contact point with the internal wall.

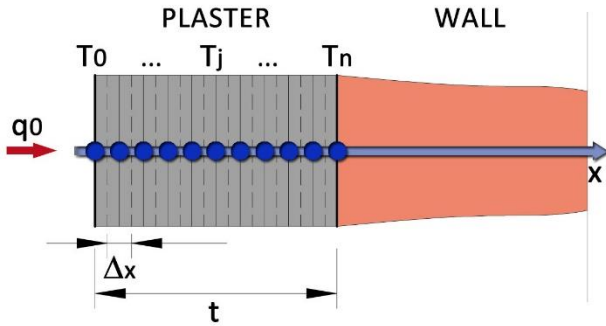


Figure 24 – Hybrid model layout: control volumes, nodes and boundary conditions.

At each time step, the heat flux evaluated at the last node with the finite difference model is utilized as boundary condition for the analytical solution of the semi-infinite solid, identified node, so as to evaluate the temperature at the interface between the two control volumes (eq.4). In the following set of equations, the index the apex refers to time instant while the subscript refers to the node. The initial and boundary conditions are:

$$T_n^0 = T_0 \quad 1)$$

$$T_0^{t+1} = 2F0 \cdot \left( \frac{q_0 \cdot \Delta x}{k} + T_1^t \right) + (1 - 2F0)T_0^t$$

Where  $k$  is the thermal conductivity;  $\Delta x$  is the spatial increment set to 0.02m;  $F0 = \alpha \cdot \Delta t / (\Delta x)^2$  is the Fourier number set to 0.25 for convergence purposes and  $q_0^t$  is the radiant heat flux in case of grey body calculated as follows:

$$q_0^t = \frac{5,67 \cdot 10^{-8} (T_i^4 - T_j^4)}{\frac{1}{F_{ij}} + \frac{1 - \varepsilon_j}{\varepsilon_j}} \quad 2)$$

Where:  $F_{ij} = 0,16$  is the view factor;  $\varepsilon_i = 0,99 \cong 1$  is the emissivity of the emitting body;  $\varepsilon_j = 0,87$  is the emissivity of the receiving body;  $T_i = 459 K$  is the temperature of the emitting body;  $T_j = 289,65 K$  is the temperature of the receiving body; The finite difference solution for the plaster layer is:

$$T_j^{t+1} = F0(T_{j+1}^t + T_{j-1}^t) + (1 - 2F0)T_j^t \quad 3)$$

The analytical solution at each time step for the semi-infinite solid domain is:

$$T_n^{t+1} = \frac{\frac{k}{\Delta x} (T_{n-1}^t - T_n^t) - q_s + \rho c \frac{\Delta x}{2} \frac{T_n^t}{\Delta t}}{\rho c \frac{\Delta x}{2} \frac{1}{\Delta t}} \quad 4)$$

Where  $q_s$  is the heat flux at the interface between the plaster layer and the inner wall, calculated as follows:

$$q_s = - \frac{k_{plaster} (T_n^t - T_0)}{\sqrt{\pi \alpha_{plaster} \Delta t}} \quad 5)$$

Where  $k_{plaster}$  and  $\alpha_{plaster}$  are relatively the thermal conductivity and the thermal diffusivity of the plaster layer. Notice that the model solution is independent on the wall thickness and this is a great advance since the overall wall thickness may not be known a priori.

## Results and validation

Figure 3 shows the wall surface temperature temporal trend for all the simulated materials. First of all the average temperature trend of points representing the block (Figure 3) is analysed. The comparison of the hybrid model with experimental data acquired shows an excellent accordance with the denser stones leading to exclude very likely that the analysed element is a brick. However, from the comparison between the experimental data and simulation, relevant information do not emerge on the exact material since the local stones are characterized by a very similar thermal response.

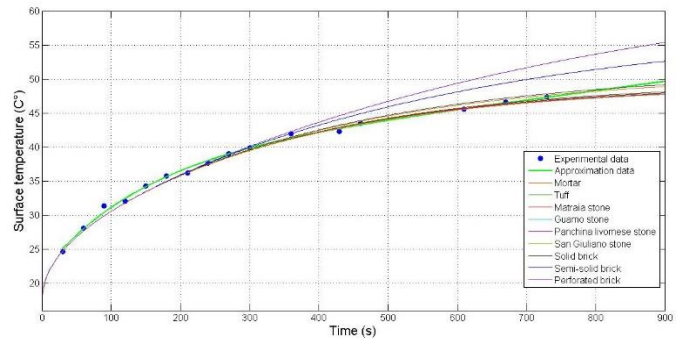


Figure 25 - Temperature trend of the block compared with the hybrid model.

In any case it is very interesting to notice that the model is able to reproduce the transient thermal behaviour pretty well in the first 300s. Furthermore, approaching to the steady state conditions the trends start diverging and it is easier to recognize what kind of material is more likely to be underneath the plaster layer

An additional comparison is made between the relative thermal contrasts resulting from the numerical model and the experimental to try to better characterize the type of stone framed by the camera. In particular the experimental absolute thermal contrast of the IR images was calculated as a function of time, starting from the average temperature of mortar and block areas. The absolute contrast is the absolute temperature rise of the defective area with respect to a reference region intact in a given time t:

$$C^a(t) = T_{\text{block}}(t) - T_{\text{mortar}}(t)$$

The relative contrast refers instead to the entire image returned by the camera and not to the individual area of study. The relative contrast is defined therefore as the ratio between the absolute contrast and the difference between the maximum temperature and the minimum that is found in the thermal image at a given instant of time t:

$$C^r(t) = \frac{C^a(t)}{T_{\text{max}}(t) - T_{\text{min}}(t)} \quad 7)$$

The blue spots in figure 5 represent the experimental thermal contrast while the vertical lines correspond to the numerical appearance time for each stone evaluated for a numerical thermal contrast of 0.01 which is considered the minimum value for the detection of the appearance time.

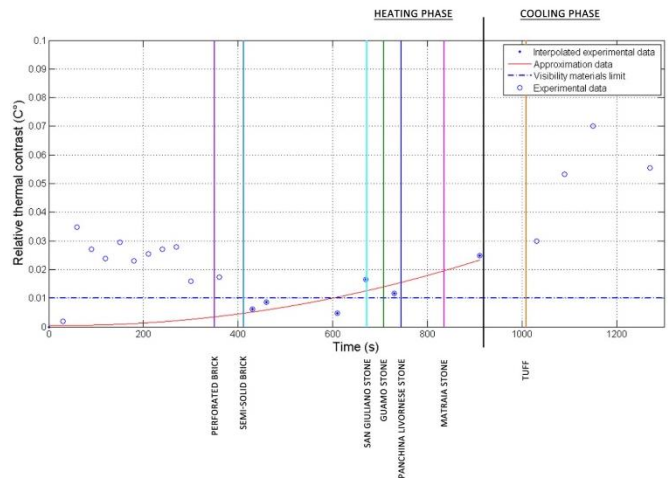


Figure 26 – Comparison between experimental and numerical appearance time detection.

This means that the blue spots which are just above the intersection between the vertical coloured lines and the horizontal blue dashed line (representing the above visibility limit on the thermal contrast) helps to identify the material underneath the plaster layer. In this case, San Giuliano stone and Panchina Livornese stone are the most suitable candidates. Further work must be done in order to validate the model on several different materials and make it a more reliable tool for the non-intrusive recognition tests.

## Conclusions

This paper analyses the feasibility of an innovative thermographic inspection method for the detection of the masonry wall material of historical buildings. This active method consists of monitoring the “appearance time” of the single stone under the plaster in the IR vision during the heating period. The transient evolution of the thermal contrast between the single stone and the mortar coming from the in-situ detection of a masonry wall has been compared with different known materials numerically simulated with a simple “hybrid model”. A cross comparison between the temperature trends and the thermal contrast/time of appearance allowed to identify the two materials that best matches with the experimental analysis. Further inspections must be carried out in the future to validate the method over a broader range of materials.

## References

- [1] Theodorakeas P., Avdelidis N. P., Cheilakou E., Kouli M., Quantitative analysis of plastered mosaics by means of active infrared thermography, *Construction and Building Materials*, 2014
- [2] Fox M., Coley D., Goodhew S., de Wilde P., Comparing transient simulation with thermography time series, in: *First Building Simulation and Optimization Conference*, Loughborough, UK, 10–11 September 2012.
- [3] Fantozzi F., Filippeschi S., Santini T., "L'uso della termografia per una corretta diagnosi energetica mirata a una riduzione dei consumi", Università di Pisa, CIRIAF, 2007.



# The use of IR-based techniques in the PRIMARTE project: an integrated approach to the diagnostics of the cultural heritage

L. Palombi<sup>1</sup>, M. Galeotti<sup>2</sup>, E. Massa<sup>3</sup>, R. Olmi<sup>1</sup>, M. Picollo<sup>1</sup>,  
A. Andreotti<sup>4</sup>, G. Bartolozzi<sup>1</sup>, M. Bini<sup>5</sup>, I. Bonaduce<sup>4</sup>, E. Cantisani<sup>6</sup>, M. Chimenti<sup>7</sup>, M.P. Colombini<sup>6</sup>,  
C. Cucci<sup>1</sup>, U. Dercks<sup>8</sup>, L. Fenelli<sup>8</sup>, I. Malesci<sup>6</sup>, A. Malquori<sup>9</sup>, M. Montanelli<sup>10</sup>, A. Morelli<sup>11</sup>, S. Penoni<sup>12</sup>,  
L.D. Pierelli<sup>13</sup>, C. Riminesi<sup>7</sup>, S. Rutigliano<sup>8</sup>, B. Sacchi<sup>7</sup>, S. Stella<sup>14</sup>, G. Tonini<sup>13</sup>, V. Raimondi<sup>14</sup>

<sup>1</sup> Applied Physics Institute “Nello Carrara” of the National Research Council of Italy (CNR-IFAC), Via Madonna del Piano 10, 50019 Sesto F.no (Italy), l.palombi@ifac.cnr.it

<sup>2</sup> Opificio delle Pietre Dure, Viale Strozzi 1, 50129 Firenze (Italy),  
monica.galeotti@beniculturali.it

<sup>3</sup> ART-TEST sas, Via del Ronco 12, 50125 Firenze (Italy), massa@art-test.com

<sup>4</sup> Department of Chemistry and Industrial Chemistry, University of Pisa, Via Risorgimento 35,  
56126 Pisa (Italy)

<sup>5</sup> ELAB SCIENTIFIC srl, Viale Giannotti 61, 50126 Firenze (Italy), info@elab-scientific.com

<sup>6</sup> Institute for the Conservation and Valorization of Cultural Heritage of the National Research Council of Italy (CNR-ICVBC), Via Madonna del Piano 10, Sesto Fiorentino – Firenze (Italy),  
b.sacchi@icvbc.cnr.it

<sup>7</sup> CULTURANUOVA srl, Via delle Conserve 25, 52100 Arezzo (Italy), chimenti@culturanuova.it

<sup>8</sup> Kunsthistorisches Institut in Florenz - Max-Planck-Institut, Via G. Giusti 44, 50121 Firenze  
(Italy), dercks@khi.fi.it

<sup>9</sup> Scuola di Studi Umanistici e della Formazione, University of Florence, Via Laura 48, 50121  
Firenze (Italy), laura.fenelli@gmail.com

<sup>10</sup> AK Innovation srl, Via Salvadori 26, Montaione - Firenze (Italy), marco@akinnovation.it

<sup>11</sup> SOING strutture e ambiente srl, Via Nicolodi 48, 57121 Livorno (Italy), alisamorelli@soing.eu

<sup>12</sup> FABERESTAURO snc, Piazza Ginori 13, 50019 Sesto Fiorentino - Firenze (Italy),  
faberestauro@libero.it

<sup>13</sup> NIKE Restauro di opere d'arte snc, Via del Ronco 12, 50125 Firenze (Italy),  
Nike.restauro@gmail.com

<sup>14</sup> BEL CHIMICA srl, Via San Michele 35, 51031 Agliana – Pistoia (Italy), crs@geal-chim.it

This paper presents an overview of the research carried out using IR-based techniques in frame of the PRIMARTE project aimed at introducing a highly multi-disciplinary, integrated approach in the documentation and diagnostics of the cultural heritage, with the main objective of developing an integrated methodology for the combined use of data acquired with diverse techniques. The latter have ranged from IR imaging to fluorescence lidar and UV fluorescence, from IR thermography to georadar, 3D electric tomography to microwave reflectometry, from analytical techniques (FORS, FT-IR, GC-MS) to high resolution photo-documentation and historical archive studies. All the data were integrated in a multimedia platform as a powerful tool for data storage, integration and management.

## Introduction

The PRIMARTE project, funded by the Region of Tuscany, was primarily focused on the documentation and diagnostics of

Cultural Heritage by using a highly multi-disciplinary, integrated approach. Its main goal was to develop an integrated methodology for the combined use of data, acquired on the site under investigation, by using diverse techniques. These included: hyperspectral fluorescence lidar imaging,

UV fluorescence and IR imaging, IR thermography, georadar, 3D electric tomography, microwave reflectometry, analytical on-site non-invasive spot techniques (FORS, FT-IR) and laboratory methodologies (FT-IR, GC-MS), high resolution photo-documentation and historical archive studies. The final stage of the project has yielded to the implementation of a multiplatform and multi-medial tool for the archiving, management, exploitation and dissemination of the collected information. This can be performed at different levels of complexity, starting from a low level where all scientific data are available as a tool for curators and conservators to a level suitable for the dissemination to the general public.

This paper presents an overview of the on-site research carried out within the PRIMARTE project, with particular reference to the IR-based techniques and their role in the project's activities. IR thermography, IR multispectral imaging, FT-IR and UV-Vis-NIR FORS spectroscopy were applied to a 'pilot site' and integrated with several other diagnostic and analytical techniques to study the chosen site in its entirety, from mural paintings to stone artifacts, to the architectural and archaeological structures.

### **The site and the integrated methodology**

A chapel dating back to the fourteenth century, located at 'Le Campora' site in the vicinity of Florence, was selected as the 'pilot site' for this research. The chapel is the remnant of a much larger structure, a major church and the adjacent monastery, which were destroyed in the past. The site, besides mural paintings and stone artifacts, featured also buried structures so that it offered a broad-spectrum test-bench for the project's team.

The first stage of the projects' activities at the site consisted in the application of imaging techniques so as to obtain an overall assessment of the status of the chapel's walls.

Thus, fluorescence lidar imaging, IR thermography were first applied to identify those areas that needed further in-depth investigation. These techniques provided false-colour coded maps on large areas of the chapel walls: the information gained from this first stage of research was exploited to identify specific areas of interest for in-depth investigation by means of high-spatial resolution techniques and, subsequently, non invasive spot measurement techniques. High spatial resolution techniques applied in situ included: multispectral imaging, UV fluorescence imaging, IR imaging and high resolution photography. The high spatially defined images acquired in the selected areas were exploited to choose the spots to study by means of in situ spot spectroscopic techniques, such as: Fiber-Optics Reflectance Spectroscopy (FORS) in the UV, visible and NIR ranges, integrated salinity and humidity measurements via dielectrometric measurements, colorimetry and *in situ* total reflectance (TR) FT-IR spectroscopy. The last stage of the integrated procedure consisted in the execution of analytical measurements based on micro-sampling: FT-IR spectroscopy, gas-chromatography-mass spectrometry (GS-MS), XRF, XRD and ionic chromatography were applied to provide analytical data on a selected set of microsamples.

Most of the above mentioned techniques were also applied to the stone artifacts in the chapel. The outdoor buried archaeological structures were studied by using the georadar and 3D electric tomography. All scientific data were complemented with exhaustive historical archive mining and art historic research. Finally, all data and information were integrated in the multimedia tool developed in the frame of the project for their full and synergetic exploitation.

### **IR thermography**

IR thermography has mainly been applied for investigating two issues: structural criticalities and conservation issues related to the presence of moisture and salts. The latter had caused the loss of part of the painting (detachment of the paint layer and a general discoloration process) over the centuries and one of the objective was to understand

if this process was still in progress. Fig.1 shows the low-resolution photo (Fig.1a) and (Fig.1b) the IR thermographic image acquired on the vault of the chapel, whose temperature appears quite uniform; the temperature difference between the right and left of the image can be ascribed to different structural setting of the building. The results of IR thermography analysis, used in conjunction with a novel prototype developed to produce integrated salt-humidity maps by means of microwave reflectometry [1], have shown that there were not substantial inputs of moisture in the upper part of the chapel and on the walls, whereas the measurements acquired in the areas of the walls in contact with soil were normal, except for the

reconstructed base of one of the wall. The results in their whole lead to assert a lack of ongoing degradation processes, while a critical issue has been identified as moisture infiltration from the roof in the past that caused consequential structural problems, plaster detaching and, in the end, the establishment of a highly humid microclimate that yielded to the formation of sulphate patinas. IR thermography has been also exploited to identify structural inhomogeneities in the walls. As an example, Fig.1c shows an area where an inhomogeneity was identified and possibly ascribed to a putlog hole for scaffolds. This result was also confirmed by the results of the 3D georadar measurements.

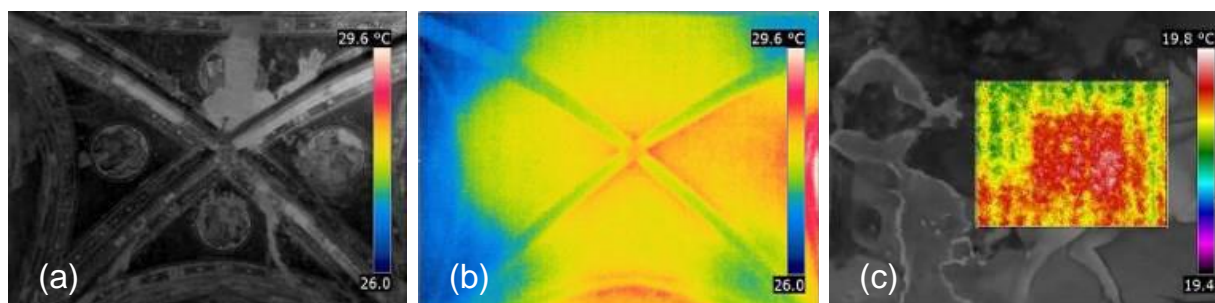


Fig. 1. IR thermography on sections of the Chapel. (a) Grey-scale image of the vault; (b) false-colour thermographic image of the vault; (c) IR thermography on the frescoed walls of the Chapel ascribed to a putlog hole.

## IR imaging

IR imaging has been used for the investigation of the frescoed walls of the Chapel. It has been useful to study inner paint layers where later refurbishments were applied in the past. As an example, Fig.3 shows the IR imaging acquisition on a section of the frescoed wall: the comparison between the image acquired in the 1050-nm spectral band and that acquired in the 600-nm band pointed out the presence of underlying details covered by later retouching.

## FORS and FT-IR spectroscopy

*In situ* UV-Vis-NIR FORS (Fiber Optics Reflectance Spectroscopy) and FT-IR

measurements were carried out to characterize the pigments used for the wall paintings, such as: azurite, green earths, yellow and red ochres, and to obtain information about some alteration processes and their by-products [2]. In many spots of the investigated surfaces the techniques pointed out the presence of gypsum with its typical absorption bands in the 1440 nm – 1540 nm interval. Fig.4 shows a typical FORS spectrum measured in an area affected by the presence of gypsum. On the basis of imaging techniques and *in situ* measurements, a limited number of micro-samples in selected spots were collected to carry out further investigation in the laboratory using several analytical techniques (FT-IR, GS-MS, XRF, XRD and ionic chromatography).

Several micro-samples from the wall paintings and from patinas on frescoes and stone



Fig. 3. IR imaging on wall paintings: (a) photo of the investigated area; (b) image acquired in the 600-nm spectral band and (c) image in the 1050-nm band. The area was 90 cm x 115 cm.

artifacts were analyzed using FT-IR spectroscopy to determine their composition and to obtain information about possible degradation processes.

## Conclusion

The PRIMARTE project has demonstrated the crucial role played by a multidisciplinary, integrated approach in facing the complex issues related to the diagnostics and documentation of the cultural heritage like a conservation yard. In this regard, the IR techniques offered a valuable tool for imaging diagnostics and documentation of the wall paintings as well as for the analytical investigation of the materials used and of possible by-products due to degradation processes. All data were also integrated with data acquired with other diagnostics techniques and with historical and

conservation notes and stored in a multimedia platform for consultation and management.

A demonstrator of the implemented multimedia tool available to the general public can be visited at: [www.primarte.eu](http://www.primarte.eu).

## References

1. R.Olmi, M.Bini, A.Ignesti, S.Priori, C.Riminesi and A.Felici, Diagnostics and monitoring of frescoes using evanescent-field dielectrometry, *Measurement Science and Technology*, Vol. 17, N. 8, pp. 2281-2288, 2006.
2. M. Bacci, L. Boselli, M. Picollo, B. Radicati, UV, VIS, NIR Fibre Optic Reflectance Spectroscopy (FORS), in: D. Pinna, M. Galeotti, R. Mazzeo (Eds.), *Practical handbook on diagnosis of paintings on movable support*, European Project ARTECH, Centro Di, Firenze, pp. 197-200, 2009.

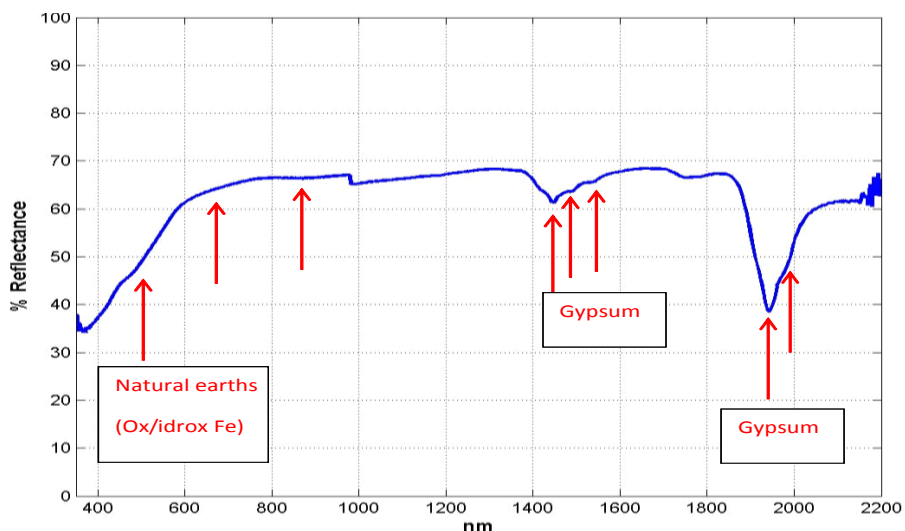


Fig. 4. *In situ* FORS measurements on selected points of the wall paintings

# **SATELLITE REMOTE SENSING OF EARTH THERMAL EMISSION FOR WEATHER, CLIMATE AND OCEAN OPERATIONAL APPLICATIONS**

**R. Bonsignori**

**EUMETSAT**

**Eumetsat-Allee 1, D64295 Darmstadt, Germany  
roberto.bonsignori@eumetsat.int**

An overview is given of the instruments observing the Earth and its atmosphere in the thermal emission bands from polar sun-synchronous and geostationary orbits owned and operated by EUMETSAT, along with their fields of application: weather forecasting and nowcasting, atmosphere and ocean monitoring, climate. Instrument characteristics and system aspects related to the operational use of such instruments are also addressed. Passive observations by infrared and microwave imagers and sounders constitute an important part of the organization's core business, as provider of meteorological and oceanographic data products to the user community for the benefit of the general public.

# TELESCOPE ARRAY FOR EXTRA-SOLAR PLANET DETECTION FROM FAR SIDE OF MOON

M. Strojnik and G. Paez

Optical Research Center, AP 1-948, CP 37000, Leon, Gto., Mexico  
mstrojnik@aol.com, gpaez@cio.mx

We propose that an array of 4 by 4 small-diameter telescopes, possibly 1 m in radius, be placed on the far side of Moon for continuous monitoring of nearby stars for the existence of a planetary companion. The advantages of this observatory location include long intervals of darkness, availability of a rigid platform in the form of a Moon body, and the absence of the atmosphere that allows the complete transmission of radiation in the spectral interval from visible to mm waves. The task is facilitated in that the telescopes would act as light “buckets” to collect photons during long integration periods. The technology has already been demonstrated, as humans in person delivered optical components to the Moon surface during the Apollo era. The disadvantages are primarily operational, requiring the establishment of a human habitat.

## 1. Planet Detection Problem

A planet in a solar system outside our own (an extra-solar system) is difficult to detect directly because the planet intensity is between  $10^{-6}$  to  $10^{-4}$  times lower than that of the star (see Fig. 1). Planet size is at least 100 times smaller than that of its star. Its distance from the Earth makes it appear as a point object.[1,2] There are currently no telescopes that can detect a planet using direct imaging techniques. However, discoveries of new planets are reported frequently, mostly with indirect techniques.

## 2. Sparse aperture array on the Moon surface

The need for the space system arises due to the opacity of the Earth atmosphere in many of the interesting spectral regions, the air turbulence, and scattering from the gases and particulates that constitute the atmosphere.

The incorporation of the sparsely filled aperture results in the absence of several spatial frequencies in the image that are present in the object.[3] Imperfect imaging would require rigid positioning and precise

control of apertures, at distances of at least 75 m.

The Rayleigh resolution criterion dictates this separation for the Estrella and the Tierra at 10 parsecs. (We denote as Estrella the nearby star with a planetary companion, called Tierra, as all nearby stars already have a name.) The star-planet separation would have to be increased even more to decrease the effects of the background diffracted and scattered radiation from the Estrella. This value needs to be lower than or comparable to that of the Tierra (for example,  $10^{-4}$  at  $100 \mu\text{m}$ ), in order that Tierra might be discernable against the background radiation.

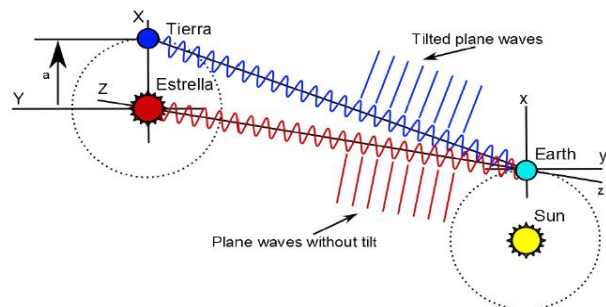


Fig. 1. Geometry for the detection of a planet outside our Solar system. The Estrella and the Tierra emit spherical waves. After free-space propagation, they become plane waves. They are tilted when they originate at an off-axis point, such as that on the Tierra.



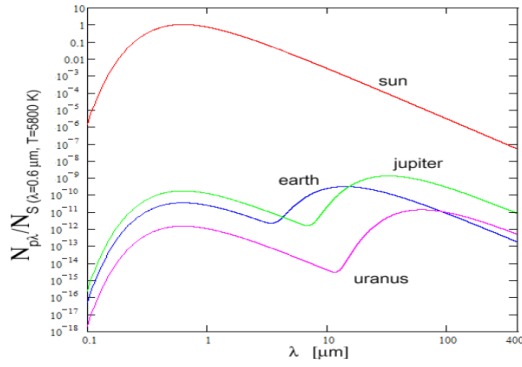


Fig. 2. Number of spectral photons emitted by the Sun and several planets as a function of wavelength, normalized against solar emission at Sun's maximum emission wavelength. The ratio of the number of planet spectral photons over the number of Sun's spectral photons may be considered the simplest signal-to-noise ratio.

Figure 2 presents the ratio of the number of planet spectral photons over the number of Sun's spectral photons. This may be considered the simplest signal-to-noise ratio. For the diffracted radiation from the Estrella to be less than the signal from the Tierra (under optimal observational conditions), two neighboring apertures may have to be separated by four times the resolution distance of 75 m (300 m).

Figure 3 displays the fringe separation as a function of wavelength. The angle subtended between the Estrella and the Tierra is a parameter. For the angular separation of 2  $\mu\text{rad}$ , the inter-fringe distance increases linearly from 5 m to 75 m as the detection wavelength ranges from 10  $\mu\text{m}$  to 150  $\mu\text{m}$ .

Then, with the Estrella at the origin and the Tierra in the orbit at 2  $\mu\text{rad}$ , ( $2 \times 10^{-6}$  rad), we evaluate the fringe separation to be  $\Delta x = 75$  m, using the wavelength of about 150 microns. This physically means that within the distance of 75 m, the incidence (the number of photons per unit area) will change from its maximum to its minimum and again to the maximum value. It will assume twice the same value within this sampling interval.

$$M(x, y, 0) = M_N + M_{\min} + 2M_{\text{amp}} \cos^2 \left[ \left( \frac{\pi}{\lambda} \right) (\theta_{Tx} x) + \partial \right] \quad (1)$$

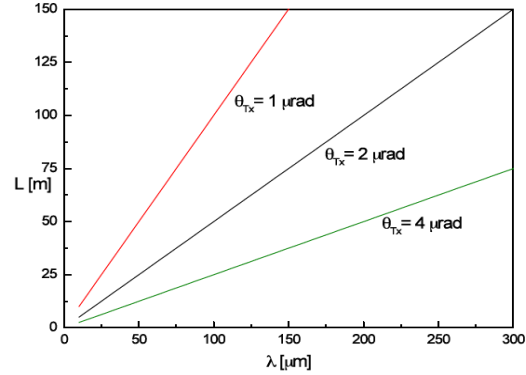


Fig. 3. Fringe separation  $L$  as a function of wavelength, with the angular separation between the Estrella and the Tierra  $\theta_{Tx}$  as a parameter. For the Tierra-Estrella angular separation of 2  $\mu\text{rad}$ , the distance between the adjacent incidence peaks increases linearly from 5 m to 75 m as the detection wavelength ranges from 10  $\mu\text{m}$  to 150  $\mu\text{m}$ .

This sinusoidal pattern riding on top of a large constant term is illustrated in Fig. 4, for 1.25 periods.  $M_N$  is the intrinsic noise level of the instrument configuration. The abscissa is marked in terms of the linear array dimension  $L$ , selected for the straw-man design parameters.

Thus,  $L$  might be equal to 75 m. We need at least four sampling apertures along each one of two perpendicular directions, to determine the period of the interference pattern and its modulation. The aperture would preferably be arranged non-redundantly.

### 3. Configuration of aperture array

The proposed minimum array to sample the incidence distribution is then 4 apertures along a selected  $x$ -direction, and another 4 along a perpendicular  $y$ -direction. We propose a complete 4 by 4 array, rather than two linear 4- aperture arrays in two perpendicular directions to increase the overall photon collecting area, to be discussed further below. The collecting area along each direction is quadrupled by increasing the number of apertures by 2 (from 8 to 16). This strategy permits the aperture diameters to be smaller, facilitating their fabrication, transport, and finally *in-situ* assembly.

Aperture centers may be separated equidistantly over the linear array length of 75 m.

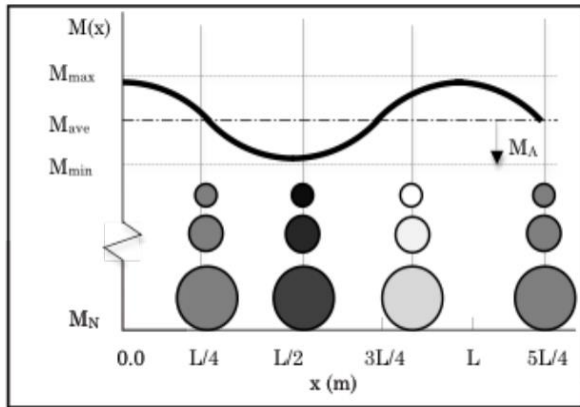


Fig. 4. The effect of the aperture diameter on its ability to sample accurately the value of the modulation term of the sinusoidal pattern. The smaller the aperture diameter, more closely the sampled value approaches to the actual value of the incidence at that position, except at the average modulation.

This would give array center coordinates at -37.50 m, -12.5 m, 12.5 m, and 37.50 m. It might be even better, and not significantly more difficult to implement, if the collecting apertures are located according to non-redundant scheme.

A non-redundant linear aperture configuration is such that in the list of all possible separations between the aperture centers, each one appears only once.[3] A potential nonredundant aperture layout would have centers at -35.5 m, -24.5 m, 19 m, and 35.5 m, measured from the linear array center of gravity at 0. There would be four lines of such linear arrays, similarly separated according to the proposed scheme, along perpendicular coordinate, at -35.5 m, -24.5 m, 19 m, and 35.5 m, measured from the linear array center of gravity at 0. This nonredundant array positioning allows for the following distinct inter-aperture distances, in each direction: 11 m, 20 m, 31 m, 44.5 m, 64.5 m, and 75.5 m.

The non-redundant configuration permits sampling the spatial frequency space with twice the number of samples compared to the redundant configuration, in each orthogonal

direction. Other non-redundant values for the centers of apertures may be chosen to facilitate their positioning and alignment. These positions may be determined during the engineering study.

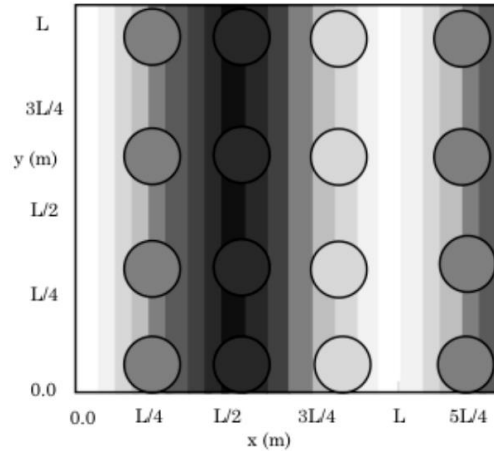


Fig. 5. An array of 4 by 4 apertures, arranged in nonredundant configuration along the x- and y-direction. The apertures are superimposed on the modulation of the radiation from the Estrella and Tierra when they (star and planet) are on a line parallel to the x-coordinate. Each aperture averages the radiation over its collecting area.

Figure 5 illustrates the sampling problem in further detail. The background shows the modulation for the incidence when the Estrella-Tierra line is parallel to x-axis. Then there is no modulation along the y-axis. The apertures are laid out in a non-redundant configuration both along the x- and y-direction, with parallel rows and parallel columns. The apertures at the same x coordinate contribute to the incidence for the same value of this coordinate.

An interesting observation may be drawn upon examining this figure in the case that two sets of apertures fall on the same incidence distribution. In this special case, the length of the array is exactly equal to the period of the modulation term: two aperture columns sample the same incidence; therefore, there are only three distinct sampling apertures per period. Furthermore, the apertures that sample the darkest part of the fringe actually measure the DC component of the incidence pattern. Therefore, as a minimum, four apertures along each coordinate are needed to determine unequivocally the modulation parameters.

Each aperture acts as a light collector (sometimes called light-bucket); thus, it only measures the amount of radiation incident on it. It actually

averages the radiation over its area. Figures 4 and 5 illustrate the effect of aperture diameter on its ability to sample accurately the modulation term of the interferometric pattern. The sampling process, in fact, favors apertures with small diameter, and arrays with large number of apertures along each perpendicular direction. Small diameter telescopes are also easy to fabricate, transport, assemble, and install. The total light-collecting area is the product of the number of apertures and the area of each aperture. Figure 6 depicts the number of photons collected from the Jupiter-like Tierra at 10 parsecs as a function of total light-collecting area, with integration time as a parameter. The relatively large integration time of 1 sec or more is a time interval difficult to maintain stable for a human hand or an instrument moving in space. It is easily accomplished for a telescope system attached to a solid rock, like Moon. According to the proposed configuration, the area of each telescope is  $3.14 \text{ m}^2$  and the total observatory area is nearly  $50 \text{ m}^2$ .

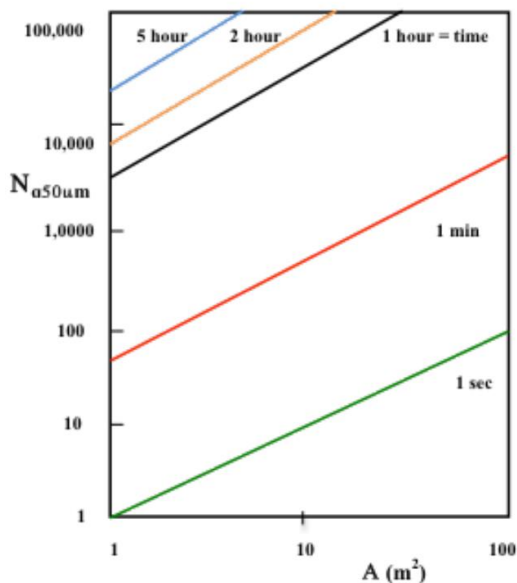


Fig. 6. Number of photons at  $50 \mu\text{m}$  emitted by the Tierra at 10 parsecs as a function of the area of the intercepting apertures on Earth, with the integration time as a parameter. A stable platform allows long integration times even when area of each individual telescope is small. A small integration time of a mobile platform requires a large signal-collecting area. Conversely, integration time of several hours on a rigid lunar surface permits small-area collectors.

Should it become desirable that each aperture collects 100 photons, the integration time could be increased to 1 minute. An observatory with 16 small telescopes could be placed on the far side of Moon for continuous monitoring of nearby stars for the existence of a planetary companion, similar to the Earth, and feasible for human colonization.[4] The minimum collecting area of about  $50 \text{ m}^2$ , proposed here, is expected to accumulate measurable signal of 100 photons at  $25 \mu\text{m}$  originating at the Tierra during a relatively short observation time of 4 seconds.

#### 4. Summary

Compared to other proposals for the Earth-based or orbiting facility, 1-m-radius telescope could be considered small, i.e., less than the diameter of the Hubble telescope, now for 25 years collecting data in space. This technology has been developed and proven in the eighties. There would be no need for assembly on the far side of Moon, facilitating significantly the logistics of the mission. With a 4 by 4 telescope array, the radiation-collecting area is about  $50 \text{ m}^2$ . The absence of atmosphere permits the search to extend from less than  $10 \mu\text{m}$  to  $300 \mu\text{m}$  to find Earth-like or even much colder planets.

#### References

1. C. Vasquez-Jacaud, M. Strojnik, G. Paez, "Effects of a star as an extended body in extra-solar planet search," *J. Mod. Optics*, **57** (18), 1808–1814 (2010); DOI:10.1080/09500340.2010.528564.
2. M. S. Scholl, "Signal detection by an extra-solar system planet detected by a rotating rotationally shearing interferometer," *J. Opt. Soc. Am. A*, **13** (7), 1584- 1592 (1996); <http://dx.doi.org/10.1364/JOSAA.13.001584>.
3. M. Strojnik, G. Paez, "Comparison of linear and rotationally shearing interferometric layouts for extrasolar planet detection from space," *Appl. Opt.*, **42** (29), 5897 - 5905 (2003); DOI:10.1364/AO.42.005897
4. M. Strojnik and M. K. Scholl, "Extrasolar planet observatory on the far side of the Moon," *J. Appl. Remote Sens.*, **8** (1), 084982 (2014); doi:10.1117/1.JRS.8.084982.

**AN INITIATIVE TO INCLUDE COHERENCE AND POLARIZATION IN EARTH SCENE  
CLASSIFICATION**

**Anum Barki<sup>1</sup>, Kory J. Priestley<sup>2</sup>, and J. R. Mahan<sup>3</sup>**

**<sup>1</sup>Optical Engineer, Remote Sensing Flight Systems Branch, NASA Langley Research Center,  
Hampton, VA 23682 USA  
anum.r.barki@nasa.gov**

**<sup>2</sup>CERES and RBI Project Scientist, Science Directorate, NASA Langley Research Center,  
Hampton, VA 23682 USA  
kory.j.priestley@nasa.gov**

**<sup>3</sup>Emeritus Professor, Department of Mechanical Engineering, Virginia Polytechnic Institute and  
State University, Blacksburg, VA 24060 USA  
jrmahan@vt.edu**

Thermal radiation emitted and reflected from the Earth and viewed from near-Earth orbit may be characterized by its spectral distribution, its degree of coherence, and its state of polarization. The current generation of Earth radiation budget instruments have been designed and calibrated to be sensitive to wavelength while minimizing the impact of polarization and diffraction on science products. This contribution explores the possibility of improving the performance of such instruments by including coherence and polarization in scene identification protocols. An instrument intended to measure the coherence and polarization of typical Earth scenes is introduced and modeled by treating individual rays as quasi-monochromatic, polarized entities.

### **Introduction**

A primary goal of Earth science is to monitor the planetary thermal radiation budget with sufficient accuracy and over a sufficiently long time period to identify and track global climate change. The current Earth radiation budget campaign, CERES, consists of a suite of three broadband scanners embarked on a series of near-Earth-orbit satellites [1]. Gaps in the CERES data are filled by narrow-band, high-resolution observations obtained from geostationary meteorological satellites [2]. Angular distribution models applied during data processing are based on geophysical scene-type identification.

Thermal radiation emitted and reflected from the Earth and viewed from near-Earth orbit may be characterized by its spectral distribution, its degree of coherence, and its state of polarization. The CERES instruments are sensitive to

wavelength within broad bands and have been designed to minimize the impact of polarization and diffraction on science products. However, an opportunity may exist for improving overall accuracy by including degree of coherence and state of polarization in the description of the various scene types. This additional information would then be included in the data processing protocol. For example, a scene that is moderately coherent in a given wavelength interval might experience sufficient diffraction as it passes through the instrument optics to affect the spatial distribution of power in the detector plane. Alternatively, if the state of polarization of the quasi-monochromatic radiation from a given scene differs significantly from that of the corresponding pre-launch or on-board calibration source, the difference in throughput of the optical train might be significant. The first step in assessing the potential for improving the accuracy of Earth

radiation budget measurements is to characterize the degree of coherence and state of polarization of the scene types used to establish the top-of-the-atmosphere angular distribution models.

## Measurement Approach

Michelson interferometers have long been used to measure the coherence of quasi-monochromatic radiation, especially in the infrared. More recently, Fourier Transform Spectroscopy (FTS) has assumed the dominant role in spectral characterization of infrared sources and surface optical properties. The initiative described in the current contribution is similar to but far less ambitious than GIFTS, an atmospheric sounder concept based on FTS technology originally developed for the NASA New Millennium Program (NMP) Earth Observing-3 (EO-3) mission [3].

The instrument under consideration consists of the miniature Michelson interferometer shown in Figure 1.

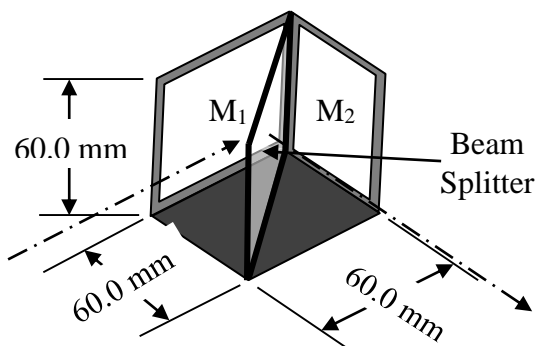


Fig. 1. Michelson interferometer concept.

Not shown are the beam-forming optics, a filter wheel, and a polarizer positioned on the entrance optical axis to the left, and the detector array centered on the exit optical axis. In Mode-I operation the flat mirror  $M_1$  may be displaced normal to its plane while the flat mirror  $M_2$  is fixed. Alternatively, in Mode-II operation mirror  $M_2$  may be slightly tilted to produce interference fringes on the focal plane array (FPA). Both operational modes are under active consideration.

Although the instrument could also be operated in the FTS mode, thus obviating the need for a filter wheel, the corresponding increase in complexity and data rate cannot be justified in view of the rather modest goal of the mission, which is to obtain a measure of coherence and polarization in a limited number of relatively broad wavelength bands. In Mode-I operation the displaceable mirror will be moved sequentially to a series of predetermined positions keyed to the filter wheel center frequency selection.

## Numerical Simulation

Operation is simulated by introducing a circular beam consisting of a large number—at least one million—of quasi-monochromatic, partially polarized rays into the entrance pupil with a random spatial distribution. The beam is split into two streams by the beam splitter and eventually reconstituted on a 100-by-100 pixel focal-plane array.

Each ray is characterized by (1) two mutually orthogonal polarization vectors, whose clock angle and magnitudes vary normally about mean values with a specified standard deviation, and (2) a phase angle (delay) whose value varies normally about a mean value with a specified standard deviation. The variations in polarization and phase are considered to be statistically stationary, which means that the intensity of rays arriving at a given pixel is computed as the sum of the squares of the electric fields for the two polarizations. In this way the coherence of the arriving quasi-monochromatic beam is known *a priori* from its statistics and thus can be compared with the value “measured” by the interferometer.

Figure 2 shows a simulated interferogram on the FPA with the interferometer operating in Mode II.

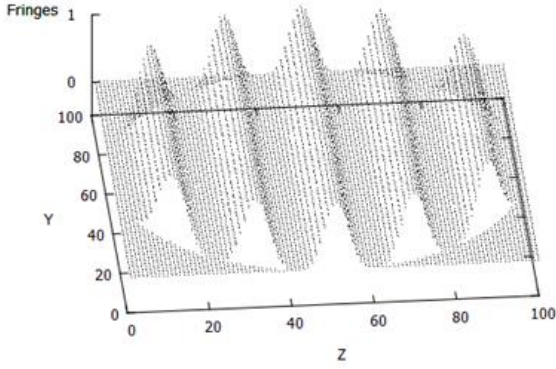


Fig. 2. Simulated fringe pattern during Mode-II operation (1.5 mm diameter linearly polarized, fully coherent, monochromatic beam at 1.0  $\mu\text{m}$ ).

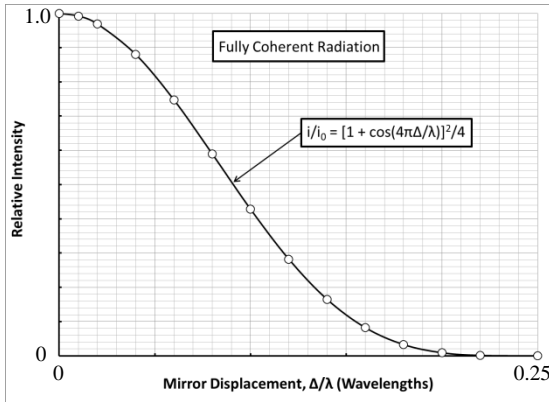


Fig. 3. Comparison of theory (curve) and simulated data (open circles) for a Michelson interferometer viewing fully coherent radiation while operating in Mode I.

Figure 3 is a comparison of Michelson interferometer theory (curve) with simulated data (open circles) for operation in Mode I. The horizontal axis is non-dimensional mirror  $M_1$  displacement  $\Delta$  divided by wavelength  $\lambda$ , so the result, which holds for all wavelengths, clearly reveals why the effectiveness of Michelson interferometers for measuring coherence increases with wavelength. Commercially available linear positioning stages are typically limited to a resolution of 1.0 nm, so it would be possible, though pushing the limits, to measure coherence in the 0.1-to- 0.2  $\mu\text{m}$  wavelength range, which is the lower limit required for Earth radiation budget applications.

Figure 4 shows the range of variation of relative intensity as a function of standard deviation  $\sigma_\delta$  of the randomly varying phase  $\delta$  of quasi-monochromatic radiation for two positions of mirror  $M_1$ : undisplaced and displaced one-quarter wavelength (Mode-I operation).

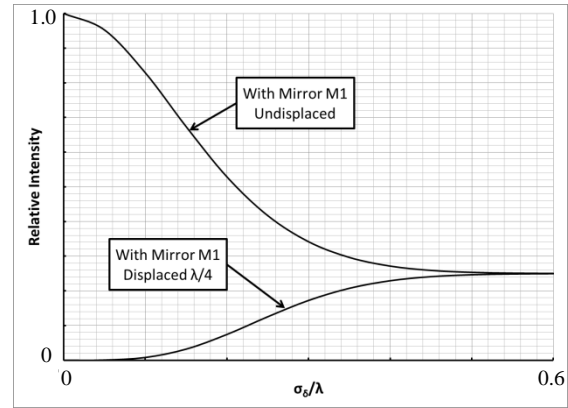


Fig. 4. Relative intensity as a function of standard deviation of phase delay for quasi-monochromatic radiation with randomly varying phase (from simulation of Mode-I operation).

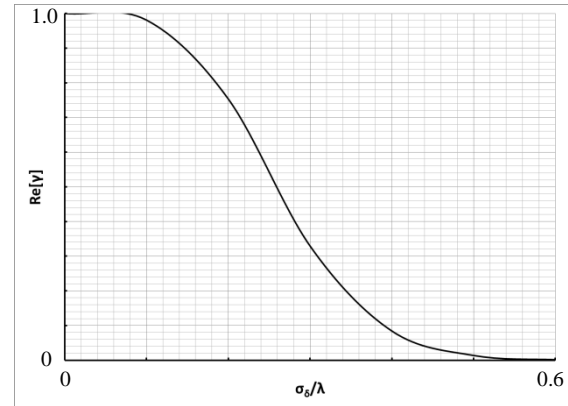


Fig. 5. Real part of coherence  $\text{Re}[\gamma]$  as a function of standard deviation of phase delay for quasi-monochromatic radiation with randomly varying phase (from simulation of Mode-I operation).

The real part of the coherence in this operating mode,  $\text{Re}[\gamma]$ , for a given value of standard deviation  $\sigma_\delta$  is known to be equal to the visibility,  $\mathcal{V}$ , of the relative intensities at the two mirror settings; that is,

$$\text{Re}[\gamma] = \mathcal{V} = \frac{(i/i_0)_{\max} - (i/i_0)_{\min}}{(i/i_0)_{\max} + (i/i_0)_{\min}} \quad (1)$$

where  $(i/i_0)_{\max}$  corresponds to a zero displacement of mirror  $M_1$  and  $(i/i_0)_{\min}$  corresponds to a one-quarter-wavelength displacement [4]. Figure 5 shows the variation of the real part of coherence  $\text{Re}[\gamma]$  as a function of standard deviation of phase delay for quasi-monochromatic radiation with randomly varying phase. Equation (1) may also be used in Mode-



II operation, in which case  $(i/i_0)_{\max}$  corresponds to the peak fringe intensity and  $(i/i_0)_{\min}$  corresponds to the minimum fringe intensity for adjacent fringes.

The polarization state of the incident beam at a given wavelength is obtained by alternating the polarizer between two pre-set quadrature orientations and recording the change in intensity of the transmitted beam.

## Conclusion

A compact and relatively simple instrument has been conceived for measuring the degree of coherence and state of polarization of typical Earth radiation scene types, and numerical simulation has been used to demonstrate its operation. Two operating modes have been identified and studied, both of which show promise for obtaining the required measurements. Because of its inherently small size and relatively low data rate, especially when operating in the nonscanning mode, we are

encouraged to pursue the concept into the prototype phase.

## References

1. Wielicki, B. A., R. D. Cess, M. D. King, D. A. Randall, and E. F. Harrison, Mission To Planet Earth: Role of Clouds and Radiation in Climate, Bulletin of the American Meteorological Society, Vol. 76, No. 11, November 1995, pp. 2125-215.
2. Doelling, D., N. Loeb, D. Keyes, M. Nordeen, D. Morstad, C. Nguyen, B. Wielicki, D. Young, and M. Sun (2013) Geostationary Enhanced Temporal Interpolation for CERES Flux Products. Journal of Atmospheric and Oceanic Technology. Vol. 30, No. 6, June 2013, pp. 1072-1090.
3. Bingham, G. E., R. J. Huppi, H. E. Revercomb, W. L. Smith, F. W. Harrison, A Geostationary Imaging Fourier Transform Spectrometer (GIFTS) for Hyperspectral Atmospheric Remote Sensing, SPIE Second International Asia-Pacific Symposium on Remote Sensing of the Atmosphere, Environment, and Space, Sendai, Japan, 9–12 October 2000.
4. Wolf, Emil, Introduction to the theory of coherence and polarization of light, Cambridge University Press, Cambridge, UK, 2007, 222 pp.

# The Potential and Challenges in the use of field-based Fourier Transform InfraRed Spectroscopy for geological applications

Graham Ferrier

Department of Geography, University of Hull, Hull, HU6 7RX, UK  
g.ferrier@hull.ac.uk;

Remote sensing data covering the Long-Wave-InfraRed (LWIR 8.0 to 14.0  $\mu\text{m}$ ) waverange can extend the capabilities of current solar reflective remote sensing methods both in terms of measurement sensitivity and acquisition of additional physical parameters. There are a number of challenges that need to be addressed in order for field-based FTIR spectroscopy to become a robust, operational methodology. Five measurement methods for acquiring FTIR measurements of solids, Transmission, Attenuated total reflection, Bi-directional reflection, Directional-hemispherical reflectance and emission, have been implemented. The capability of field based FTIR measurements discriminating geological environments are reviewed using results from a mineral exploration project on the Island of Milos, Greece.

## Introduction

Remote sensing in the solar reflective spectral range (visible, 0.4-0.7  $\mu\text{m}$  ; near infrared 0.7 – 1.1  $\mu\text{m}$ ; shortwave infrared 1.1 – 2.5  $\mu\text{m}$ ) has been widely demonstrated to be an invaluable methodology to assist geological analysis [1]. Although these reflectance-based datasets have been successful in a large number of applications there are significant limitations in the range and quality of the geological parameters that can be retrieved. The Long-Wave-InfraRed (LWIR 8.0 to 14.0  $\mu\text{m}$ ) waverange has the capability of retrieving additional physical parameters and resolving significantly more accurately the composition and physical condition of a material than solar reflected radiation [2-4]. Many common rock-forming minerals such as quartz, feldspars, olivines, pyroxenes, micas and clay minerals have spectral absorption features in the 8-14  $\mu\text{m}$  wavelength region [3]. For silicate minerals, a pronounced emittance minimum cause by fundamental Si-O stretching vibrations occurs near 10  $\mu\text{m}$  [2-4]. The vibrational frequency, and thus the wavelength of the

minimum, depends on the degree of coordination among the silicon-oxygen tetrahedral in the crystal lattice. The framework silicates, quartz and feldspar, have emittance minima at shorter wavelengths (9.3 and 10  $\mu\text{m}$ , respectively) than do sheet silicates such as muscovite (10.3  $\mu\text{m}$ ) and chain silicates such as the amphibole minerals (10.7  $\mu\text{m}$ ) [2-4]. Carbonates have strong absorption features associated with CO<sub>3</sub> internal vibrations both in the 6-8  $\mu\text{m}$  region [3] and also within the 8-14  $\mu\text{m}$  window. Carbonate minerals exhibit features at 11.4 and 14.3  $\mu\text{m}$  due to C-O bending modes, and sulphate minerals have an intense feature near 8.7  $\mu\text{m}$  caused by fundamental stretching motions [3]. FTIR spectroscopy has been successfully used to predict feldspar amounts and their mineralogical composition in igneous rocks [3].

However, the full exploitation of the LWIR is hampered by detector and instrumentation limitations combined with a lack of understanding of the influence of a wide range of compositional, morphological, topographical and environmental factors on the spectral emissivity signal received at-sensor. Without a complete, detailed understanding of the influence of these parameters on the spectral emissivity response from the range of rocks present an incomplete and even erroneous interpretation of the retrieved spectral emissivity is likely to occur.

FTIR spectroscopy is a technique based on the determination of the interaction between infrared radiation and a sample that can be solid, liquid or gaseous. It measures the wavelengths at which the sample absorbs, and also the intensities of these absorptions. The wavelengths are helpful for the identification of the sample's compositional make-up due to the fact that chemical functional groups are responsible for the absorption of radiation at different frequencies. The concentration of component can be determined based on the intensity of the absorption. The spectrum is a two-dimensional plot in which the axes are represented by intensity and frequency of sample absorption. Because all compounds show characteristic absorption/emission in the IR spectral region and based on this property they can be analysed both quantitatively and qualitatively using FTIR spectroscopy. FTIR spectroscopy therefore has the capability of providing quantitative information on the composition of a rock, sediment, soil, vegetation or atmosphere that cannot be achieved with reflectance spectroscopy. FTIR spectroscopy therefore has the potential to significantly advance the application of remote sensing in a wide range of applications. Although the potential applications for field-based emission spectroscopy are many and varied the utilisation of field-based FTIR spectroscopy by Earth Observation (EO) specialists in all sectors of the community has been limited by a number of challenges.

### Field-based FTIR measurements of solids

There are a wide range of sampling approaches that can be used to acquire field FTIR spectra depending on the nature of the material/object to be analysed, the temporal and spatial resolution of the sampling observation and the physical parameter being studied. FTIR instruments mainly differ by the measurement geometry they employ. These differences entail the size of the measurement spot on the sample, the angle of

the incoming and outgoing radiation on the sample and whether the reflected or the transmitted energy is measured. These measurement geometries can be categorized into a small number of groups (e.g., [4]) that are summarized in Figure 1.

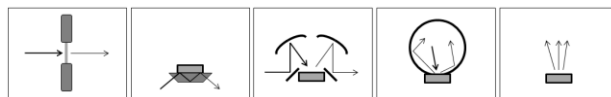


Fig. 1. Sketches illustrating examples of different measurement geometries for TIR spectroscopy: transmission, attenuated total reflectance, bi-conical reflectance, directional-hemispherical reflectance, emission (from left to right). Modified from [4].

FTIR measurements in the field are affected by a number of additional factors which can be classified into four types (i) instrumentation; (ii) surface; (iii) environmental and (iv) target effects. Without a good understanding of these effects the use of FTIR spectroscopy as a robust, operational observational methodology can be severely compromised.

### Challenges for field use

The incorrect use of an instrument can introduce a number of effects that can significantly degrade the quality of the acquired data. These effects can be minimised by gaining a sound understanding of the operational protocols and limitations of the instrument. A significant source of error is use of an instrument before its components have achieved thermal equilibrium. Every FTIR instrument has different requirements for this warming up period so it essential to determine the length of time of this period in the laboratory before carrying out any field-based studies. This can be accomplished by repeatedly measuring a known temperature blackbody over the course of many hours, being sure to calibrate before each measurement is taken. Any set of calibration factors can then be used to calibrate any future radiance measurement and determine how much drift occurred during that period. This process will provide the knowledge of how quickly the instrument's response drifts and what period of time should be allowed for stabilisation before commencing data collection. Another significant source of error is the changes (drift) in the response of an instrument as it

undergoes temperature changes in the field. To compensate for this instrument drift a blackbody calibration should be carried out with every sample measured. This minimises sensor drift effects on measurements since calibration is performed so close to the actual sample measurements. The cold blackbody temperature is typically set below that of the sample and conversely, the hot blackbody temperature is set just above the hottest object expected. Care must be taken to ensure that the temperature of the cold blackbody does not fall below the dew point temperature that would cause condensation or even frost to form on the blackbody surface and therefore affect the accuracy of the calibration. Most instruments can be considered linear over a limited range between temperature calibration points. Interpolation can be used successfully to arrive at intermediate temperatures derived from measured radiance without introducing significant error.

## Conclusion

The sources of remote sensing data covering the solar reflective spectral range is extensive with a wide array of sensors deployed on satellite, airborne, and Unmanned Aerial Vehicles platforms as well as on the ground. The utilisation of these datasets within environmental research projects is now at an operational level with standard data products being provided by a number of space research organisations. However, there are significant limitations with regard to the range of parameters and the accuracy of the measurements that can be retrieved using remote sensing data solely from the solar reflective spectral range. Use of remote sensing data covering the LWIR waverange offers many possibilities to extend the capabilities of current remote sensing methods in terms of both sensitivity and additional physical parameters.

There are however a considerable number of issues that can inhibit remote sensing scientists familiar with using solar reflective

spectral range from utilising FTIR spectroscopy-based measurements in their projects. The range of different measurement approaches, Transmission, Attenuated total reflection, Bi-directional reflection, Directional-hemispherical reflectance and emission can be confusing. What properties each method is measuring and the methods to compare and integrate measurements from these different approaches is often not readily apparent. The difficulty of acquiring high quality measurements of solids in the field is also daunting. The four factors, instrumentation, surface effects, environmental effects and target and measurement effects can significantly affect the field measurements and require that the researchers have an in-depth knowledge of the instruments being used and the physics of thermal remote sensing. The protocols for acquiring high quality field-based FTIR measurements of both solids and gases require care, time and effort. The processing of the raw datasets to meaningful, useable parameters requires a considerable level of effort and expertise. In the case of solids the extraction of spectral emissivity from temperature is a critical processing step requiring a significant amount of effort. In the case of retrieving gas composition the processing is significantly more complex requiring the implementation of radiative transfer modelling to extract the individual gas species compositions.

The range of new field portable FTIRs and supporting laboratory-based instruments coupled with the growing awareness of the essential data acquisition and processing protocols required to collect high quality field FTIR measurements means that the inhibitions that the general remote sensing community have had regarding using FTIR spectroscopy are now significantly reduced. It is envisaged that the use of FTIR spectroscopy in a wide range of environmentally related projects is likely to rapidly increase until it becomes a routine operational remote sensing methodology.

## References

1. Van der Meer, F. Spectral reflectance of carbonate mineral mixtures and bidirectional reflectance theory. *Remote Sensing Reviews*. 1995, 13(1-2): 67-94

2. Hook, S.J.; Dmochowski, J.E.; Howard, K.A.; Rowan, L.C.; Karlstrom, K.E.; Stock, J.M. Mapping variations in weight percent silica measured from multispectral thermal infrared imagery - Examples from the Hiller Mountains, Nevada, USA and Tres Virgenes-La Reforma, Baja California Sur, Mexico. *Remote Sens. Environ.* 2005, 95, 273-289.
3. Hunt, G.R.; Salisbury, J.W. Mid-Infrared Spectral behaviour of Sedimentary Rocks, *Environ. Res. Paper* 510-AFCRL-TR-74-0625. 1975, Air Force Cambridge Research Lab.
4. Salisbury, J.W.; Hapke, B.; Eastes, J.W.; Usefulness of weak bands in mid-infrared remote sensing of particulate planetary surfaces, *Journal of Geophysical Research.* 1987, 92, 702-710.

# WIDE & ACCURATE THERMAL CONTROL OF PLASMA FACING COMPONENT IN FUSION FACILITY

J. GASPAR<sup>2</sup>, M. HOURY<sup>1</sup>, JL. GARDAREIN<sup>2</sup>, Y. CORRE<sup>1</sup>, MH. AUMEUNIER<sup>1</sup>, X. COURTOIS<sup>1</sup>, JV. DAURELLE<sup>2</sup>, G. GIACOMETTI<sup>3</sup>, E. HUGOT<sup>4</sup>, M. JOUVE<sup>1</sup>, C. LE NILIOT<sup>2</sup>, C. MARTIN<sup>3</sup>, C. PARDANAUD<sup>3</sup>, C. POCHEAU<sup>1</sup>, F. RIGOLLET<sup>2</sup>, P. ROUBIN<sup>3</sup>, H. TORTEL<sup>5</sup>, J. VINCENTE<sup>2</sup>

<sup>1</sup>CEA, Institute for Research on Fusion by Magnetic confinement, 13108 Saint-Paul-Lez-Durance, France

<sup>2</sup>Aix-Marseille Université, CNRS, IUSTI UMR 7343, 13013 Marseille, France

<sup>3</sup>Aix-Marseille Université, CNRS, PIIM UMR 7345, 13397 Marseille, France

<sup>4</sup>Aix-Marseille Université, CNRS, LAM UMR 7326, 13388 Marseille, France

<sup>5</sup>Aix-Marseille Université, CNRS, Institut Fresnel UMR 7249, 13013 Marseille, France

Our work is aimed to address significant progress in understanding the different types of thermal behavior observed with IR thermography in fusion machines with full-metal walls. This involves both studying the behavior of the components which must withstand high flux densities (10 MW/m<sup>2</sup> in steady state) and improving our ability to guarantee their integrity. To do this, we develop a local and precise instrumentation of a component facing the plasma, and the development of numerical methods (data processing and modelisation) to help with understanding and interpreting of the measurement.

## Introduction

The walls of fusion machines constitute a major technological challenge. Experience gained over the last 30 years with various different fusion machines led to the selection of tungsten as the new material that complies with the operating requirements of such a machine. To date, only the JET (Great Britain) and ASDEX-U (Germany) machines use tungsten components, but their designs do not allow them to operate for significant periods (> 20 sec.) to be able to assess the behavior of the components under flux in steady state.

The Tore Supra Tokamak, supraconducting coils and active cooled by water circulation in the components, can operate for several minutes. Tore Supra is currently being converted to become a full-metal actively cooled machine, with components based on the same concept as that which is to be used for ITER. This change to Tore Supra, called the “WEST project” [1], will be a unique opportunity to test the actively cooled

tungsten components of the divertor with plasma conditions similar to that of ITER. This change is illustrated in the figure 1.

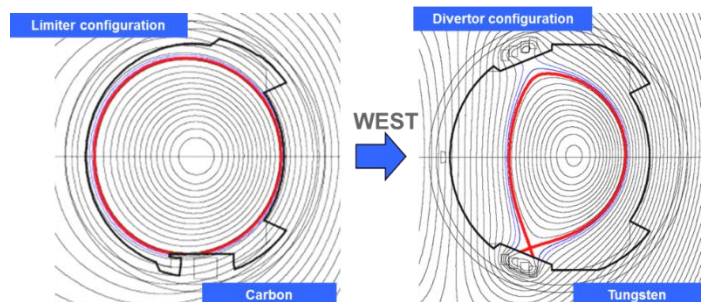


Fig. 1. Going from the limiter (left) to the WEST divertor (right) configuration of Tore Supra.

The main objective of WEST is to study the behavior of the ITER Plasma Facing Components (PFCs) and thus to limit the risks in the component manufacturing process and to test the resistance and ageing of these components during long and performant discharges. To achieve these objectives, innovative and ambitious instrumentation must be used.

IR thermography is the preferred technic for measuring surface temperatures in fusion machines, as the plasma produced in the vacuum



vessel does not disturb IR radiation transport. In addition, this temperature measurement method will be widely used in ITER. However, the introduction of metal walls for fusion machines gives rise to new problems, in particular in the interpretation of the measurements by IR technic.

Recovering the true surface temperature from the radiance collected by the camera is not a simple matter for complex thermal scenarios. Indeed, IR thermography detects the thermal radiation from all the objects in the observed scenario, i.e. both the thermal radiation emitted directly from the targets and that coming from other components and reflected by the targets. Moreover for the same surface temperature, the energy emitted and reflected by the objects changes with the thermal radiative properties of the materials. Misinterpretation of infrared measurements is critical in the operation of fusion facilities: indeed, if the evaluated surface temperature is lower than the true surface temperature, this represents a huge risk for the safety of the component, and then the machine operation. On the other hand, if the surface temperature is over-estimated, this will inhibit the possibility to reach high performance fusion experiment, and then reduce the capability of the machine operation.

To achieve the required level of control and accuracy for temperature measurements, our strategy is based on the combination of complementary and redundant measuring instruments, on a specific component that could be considered to be “super-instrumented”. This includes remote instruments (infrared cameras, microscopic display inter shots) and embedded sensors (thermocouples, fiber Bragg gratings [2], erosion markers). This is the framework of our work. On one hand a “super-instrumented” W-coated graphite PFC (with similar dimension and shaping than ITER PFU) is built for studying its thermal behavior, the instrumentation and the plasma-wall interaction physics. On the other hand, a

model (fully photonic model to predict the metallic PFCs behavior in reflective environment) and tools are developed for interpreting the measurements, in order to understand the source phenomena, solve the inverse problem and compare experiments and modelling.

### Approach and techniques

For heat flux characterizations, all the developed procedures of inversed calculation will be used to assess fluxes and temperatures at the surface of components in front of plasma from the measurements carried out in the material (TCs and Fibers) on the surface of the material (IR systems) or in the water (Pt100 probes). The TCs and fiber bragg gratings are embedded at 7.5mm from the surface, in order to maximize the heat flux sensitivity of the measurements, the distributions inside a plasma facing component for the TCs and fibers are shown in the figure 2. Figure 3 shows the locations of the TCs in a in the “super-instrumented” sector of the divertor.

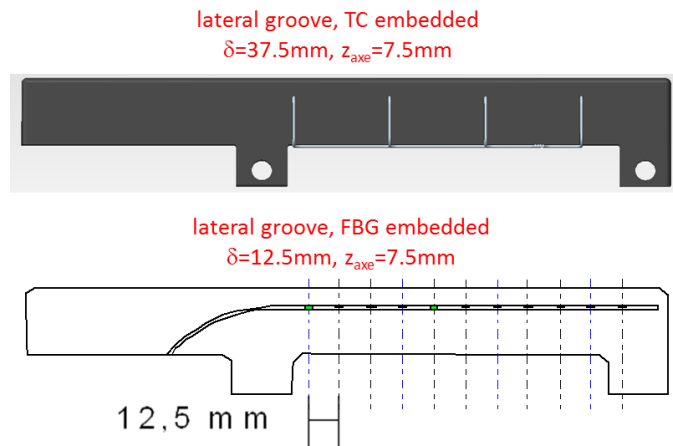


Fig. 2. Distributions inside a plasma facing component of the TCs (top) and the fiber bragg gratings (bottom).

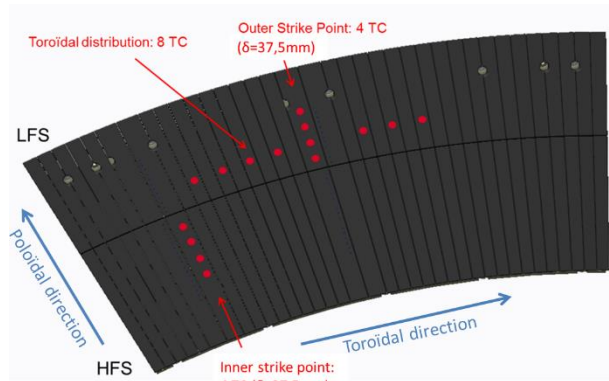


Fig. 3. Locations of the TCs in the “super-instrumented” sector of the WEST divertor.

The IR thermography system includes 7 standard divertor view (spectral range 1-5 $\mu$ m optimized @ 1.7 $\mu$ m) (fig 4), each endoscope has 2 lines-of-sight viewing two 30° sectors of divertor. It is also foreseen to have a view with a higher resolution (<1mm) on a reduced angular surface.

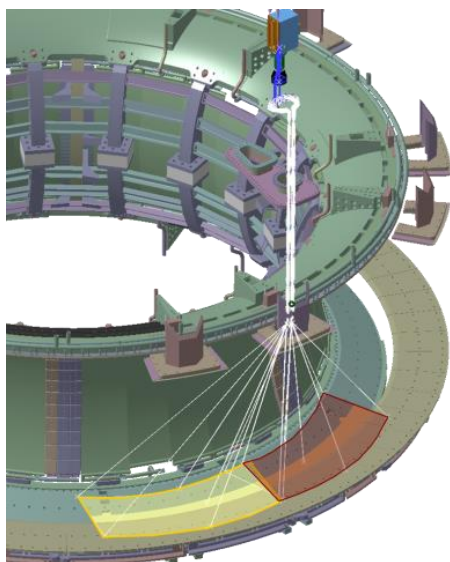


Fig. 4. Field of view of an IR endoscope

Two inverse methods will be developed using these thermal measurements. The first one is a linear method to identify the flux or the surface temperature of the material by deconvolution of the measurements, using the impulse response of the studied system. This last can be calculated [3] or measured [4] according to the complexity of the studied components. This method has the advantage

to be very fast (a few seconds to have a flux profile depending on time from TC measurements) but has the disadvantage takeoff no taking into account the variations of thermal properties with respect to temperature (non linear problem). The second method is the Conjugate Gradient Method coupled to the adjoint state [5] to obtain far more precise results (<5%) and to solve inverse problems more complex in geometry and/or non-linearity. This method is much slower (typically about ten hours to obtain a flux profile depending on time from TC measurements). These methods must be developed concurrently, as one is used during the experiment phase to obtain fast results between two shots (rather for operations), and the other is used for fine analyses of flux deposits on some shots (rather for physical studies).

About the measurements achieved by IR thermography, emissivity measurements of tungsten with respect to the wavelength, the temperature and the angle of view shall be performed in laboratory to be able to use measurements properly. Then, the tools and the inverse method developed for the embedded measurements will be adjusted to the surface measurements. Thus, the fundamental physical parameters of Plasma Wall interaction such as the heat flux density circulating along the field lines (parallel heat flux), and the spatial flux width in the Scrape Off Layer ( $\lambda_q$ ) will be determined more precisely. Finally, the total analyses should allow us to achieve a comprehensive energy balance of a component and to study heat transfer in the machine. The obtained results will then be compared to the predictions delivered by the PFC-Flux code [6] (modeling the heat fluxes deposited onto the components) that is used to design PFC for ITER and will help to validate and/or improve it. Figure 5 shows PFCFLUX calculations 2 standard magnetic configuration.

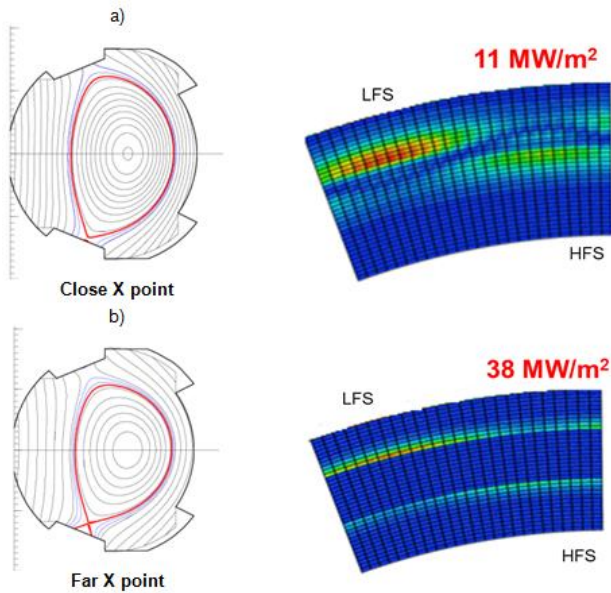


Fig. 5. PFCFLUX calculations of the heat load pattern on the WEST divertor for the 2 standard magnetic configuration, the close X point (a) and the far X point (b).

The comparison between fluxes or temperatures estimated with embedded measurements and with IR thermography will allow the test of various designs of material (geometry, shaping, material, technology) and the screening of possible defects. It is also possible to access to the thermophysical parameters of possible deposits or to the emissivities by reducing the difference between the data measured by IR thermography and the surface temperatures estimated from the embedded temperatures. This parameter estimation also based on the Conjugate Gradient Method has been tested successfully on the tokamak JET and has led to the production of cartographies of thermal resistance of carbon deposit with respect to the poloidal direction and time [7]. They will have to be adapted to access to other physical

parameters such as a possible contact resistance between two materials constituting the component, or the emissivity of the observed surface.

### Acknowledgments:

This work has been carried out thanks to the support of the A\*MIDEX project (n° ANR-11-IDEX-0001-02) funded by the « Investissements d’Avenir » French Government program, managed by the French National Research Agency (ANR)

### References

1. C. Bourdelle, J.F. Artaud, V. Basiuk, M. Bécoulet, S. Brémond, J. Bucalossi et al., WEST Physics Basis, Nuclear Fusion 55 (2015) 063017.
2. G. Laffont, R. Cotillard, P. Ferdinand, Multiplexed regenerated fiber Bragg grating for high-temperature measurement, Meas. Sci. Technol. 24 (2013) 094010.
3. J.-L. Gardarein, Y. Corre, F. Rigollet, C. Le Niliot, R. Reichle, P. Andrew, Thermal quadrupoles approach for two-dimensional heat flux estimation using infrared and thermocouple measurements on the JET tokamak, IJTS, Volume 48, Issue 1, January 2009, Pages 1-13.
4. S. Carpentier, Y. Corre, M. Chantant, R. Daviot, G. Dunand, J.-L. Gardarein et al., Study of heat flux deposition on the limiter of the Tore Supra tokamak JNM, Volumes 390-391, 15 June 2009, Pages 955-958.
5. J. Gaspar, J.-L. Gardarein, F. Rigollet, C. Le Niliot, Y. Corre, S. Devaux, Jet EFDA Contributors, Nonlinear heat flux estimation in the JET divertor with the ITER like wall IJTS 72 (2013) 82-91.
6. M. Firdaouss, T. Batal, J. Bucalossi, P. Languille, E. Nardon, M. Richou, Heat flux depositions on the WEST divertor and first wall components, Fusion Engineering and Design, Available online 7 January 2015, ISSN 0920-3796, <http://dx.doi.org/10.1016/j.fusengdes.2014.12.024>.
7. J. Gaspar, F. Rigollet, J.-L. Gardarein, C. Le Niliot Y. Corre, Two Successive Thermal Inverse Problems Solved for Plasma Facing Components Inside JET Tokamak: Estimation of Surface Heat Flux and Thermal Resistance of a Surface Carbon Layer, 15<sup>th</sup> IHTC, 2014, Japan

# **A NSCT-based infrared-visible image fusion approach using fast iterative-shrinking compressed sensing**

**Q. Zhang<sup>1</sup>, F. Ferrie<sup>2</sup>, X. Maldague<sup>3</sup>**

**<sup>1</sup> Computer Vision and Systems Laboratory, Laval University, Quebec, QC, Canada;  
Centre for Intelligent Machines, McGill University, Montreal, QC, Canada;  
q.z.ca@ieee.org**

**<sup>2</sup> Centre for Intelligent Machines, McGill University, Montreal, QC, Canada;  
ferrie@cim.mcgill.ca**

**<sup>3</sup> Computer Vision and Systems Laboratory, Laval University, Quebec, QC, Canada;  
maldagx@gel.ulaval.ca**

Infrared and visible image fusion has been a research hot topic in computer vision and image processing. Generally, the image fusion schemes consume a lot of data storage and resources, which leads to high computational complexity and more running time. Compressed sensing (CS) uses sparse sampling technique to represent a image, which reduces the cost and complexity in signal processing. In this paper, an advanced infrared-visible image fusion scheme has been proposed on the basis of the nonsubsampling contourlet transform (NSCT) and a fast iterative shrinkage compressed sensing (FISCS) algorithm. Both the numerical experiments and the human visual perception indicate that the presented approach achieves better quality of image fusion than the common fusion schemes.

## **Introduction**

Image fusion [1] is a technical process of combining several images or raw image data that are captured by different types of sensors or by a single sensor at different time periods. The fused image express more accurate and comprehensive information than any single image.

Infrared (IR) and visible image fusion [1] is an important technology brunch, which has been widely utilized in machine vision, computer surveillance, medical imaging and military imaging, etc. As for this variety of fusion issues, from the point of view of inherent image characteristics, the IR image contains less edge details, where its grayscale pixels distribute unevenly on account of the imaging principle, and people only focus on the interested target on it. Whereas, the visible image usually contains abundant texture and edge details, where its background information conforms to human visible perception characteristics.

Up until now, there have been various fusion algorithms proposed, which can be mainly classified into two categories [2]: multi-scale transform methods and sparse representation approaches.

The multi-resolution analysis transform solutions [2], such as discrete wavelet transform, Curvelet transform, and NSCT (nonsubsampling contourlet transform), etc., are usually comprised of three procedures, including decomposition of source images into multiscale coefficients, fusion of corresponding coefficients with certain rules, and image reconstruction using inverse transform methods.

The sparse representation image fusion methods [2] are built on the basis of thinking that image signals can be represented as a linear combination of only a few basis elements from learned dictionary, and the sparse coefficients can be considered as the salient features of the source images. The main procedures of sparse representation schemes are usually combined by dictionary learning, sparse

representation for source images, fusion of coefficients and image reconstruction.

However, for the IR and visible image fusion problems, most of the above fusion algorithms have their inborn advantages as well as disadvantages. In the common multi-scale transform strategies, some edges, contours or curves might be lost, or they have not enough translation invariance or produce a pseudo-Gibbs effects leading to distortion [3,4]. The NSCT, proposed by da Cunha *et al.* [3] in 2005, is a multi-scale, multi-directional and fully shift-invariant transform scheme, which can capture edges, textures and details of the input image, eliminating ringing effects and shaking phenomena. But, a NSCT-based algorithm needs suitable fusion rules to better obtain the fused image with enough image quality, while there are some issues existing, such as higher redundancy, computation complexity, etc. The sparse representation can effectively extract the underlying information from a source image, sparsely represent and finely fit to the data, and accurately reconstruct the image through solving linear inverse problem (LIP) [5].

In this paper, we attempt to utilize a fast iterative shrinkage compressed sensing (FISCS) algorithm into the NSCT-based infrared and visible image fusion issue, which can be named NSCT-FISCS. First, the source images are decomposed by NSCT to obtain high-pass subbands and low-pass subbands. Second, the FISCS method is mainly applied to the high-frequency coefficients, where the Fourier transform is implemented to generate measurements to obtain the projection measurement values of image coefficients, and a fast iterative shrinkage-thresholding algorithm, using the L-1 wavelet-based regularization, is used to recover the coefficients. Afterwards, all frequency coefficients are fused, employing corresponding fusion rules, and inversely transformed back to reconstruct the fusion image.

## Compressed Sensing

### 1. Principal theory

The compressed sensing (CS) is a theory illustrating that a signal can be reconstructed accurately if it can be sparsely represented far less than the number of its observations requested by traditional Nyquist theorem of signal sampling on the minimum sampling rate.

In the CS mechanism, consider the  $N$ -dimensional real signal  $\mathbf{x} \in \mathbf{R}^{N \times 1}$  expanded as a superposition of spikes of canonical bases in the orthonormal basis  $\Psi = \{\psi_i\}_{i=1}^N$ , we have the equation

$$\mathbf{x} = \Psi \mathbf{a} \quad (1)$$

Here,  $\Psi$  is the dictionary matrix and  $\mathbf{a}$  is the sparse coefficients vector of a digital image in a tight-frame under the dictionary matrix.

Assuming that  $\mathbf{a}$  is  $k$ -sparse, we can therefore compressively observe the signal using an observation matrix  $\Phi \in \mathbf{R}^{M \times N}$  incoherent with  $\Psi$  maintaining the relationship of  $k < M \ll N$ . Thus, the linear observed value  $\mathbf{y} \in \mathbf{R}^{M \times 1}$  can be written as

$$\mathbf{y} = \Phi \mathbf{x} = \Phi \Psi \mathbf{a} = \mathbf{M}_0 \mathbf{a} \quad (2)$$

where  $\mathbf{x}$  is the real signal, and  $\mathbf{M}_0$  is the sensing matrix.

The measurement of compressed sensing can be demonstrated as shown in Fig. 1, and the specific description of compressed sensing can be found at [4].

The solution of  $\mathbf{x}$  is the recovery of the source signal, which is usually a complicated non-linear inverse problem. On account of the size of measurement  $k < M \ll N$ , to obtain  $\mathbf{a}$  from  $\mathbf{y}$  is an issue of solving the under-determined equation, which is NP-hard problem and is usually solved by numerical iteration methods.



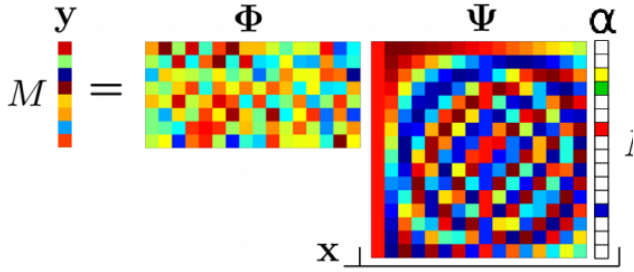


Fig. 1. Measurement of compressed sensing

## 2. Fast iterative shrinkage recovery

As is described in the work [5], the above CS solution can be pursued through solving a linear inverse problem (LIP) such as

$$\mathbf{Ax} = \mathbf{b} + \mathbf{w} \quad (3)$$

where,  $\mathbf{A} \in \mathbf{R}^{m \times n}$  and  $\mathbf{A}$  represents the blurring operator matrix,  $\mathbf{b} \in \mathbf{R}^m$  and  $\mathbf{b}$  represents the blurred image,  $\mathbf{w}$  is an unknown noise or perturbation.  $\mathbf{x}$  is the unknown signal to be estimated.

The solution of this LIP problem can be defined to be the solution of  $\mathbf{x}$  as a convex objective function written as:

$$\min_{\mathbf{x}} \left\{ f(\mathbf{x}) = \frac{1}{2} \|\mathbf{b} - \mathbf{Ax}\|^2 + \lambda \|\mathbf{x}\|_1 \right\} \quad (4)$$

where  $\lambda$  is the regularization parameter to control the weigh in the equation.

The solution can be converted to be the iterative shrinkage thresholding algorithm (ISTA), which can be converted to be

$$\mathbf{x}_{k+1} = \kappa_{\lambda t} \left[ \mathbf{x}_k - 2t\mathbf{A}^T (\mathbf{Ax}_k - \mathbf{b}) \right] \quad (5)$$

$$\kappa_{\alpha}(\mathbf{x})_i = (|x_i| - \alpha)_+ \text{sgn}(x_i) \quad (6)$$

This problem can be converted to be a numerical gradient method, considering the differentiable function  $f$ , which can be expressed as

$$\mathbf{x}_k = \kappa_{\lambda t_k} \left[ \mathbf{x}_{k-1} - t_k \nabla f(\mathbf{x}_{k-1}) \right] \quad (7)$$

where  $f(\mathbf{x}) := \|\mathbf{Ax} - \mathbf{b}\|^2$  and  $t_k \in (0, 1/\|\mathbf{A}^T \mathbf{A}\|)$ .

The estimated signal can be obtained by solving this equation.

## NSCT-based image fusion

### 1. Nonsampled contourlet transform

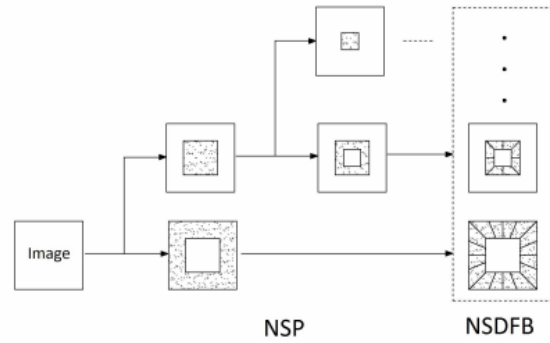


Fig. 2. Nonsampled filter bank structure

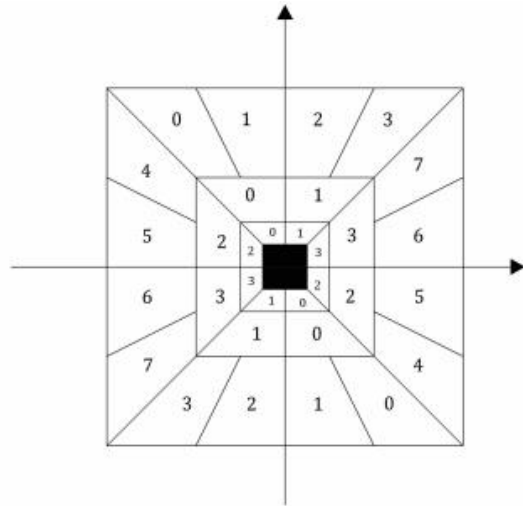


Fig. 3. Idealized frequency partition

The NSCT scheme, proposed by da Cunha *et al.* is developed on the basis of the structures of a nonsampled pyramid (NSP) and a nonsampled direction filter bank (NSDFB), which can illustrated as shown in Fig. 2 and Fig. 3.



NSP is used to obtain multiscale subbands to capture point discontinuities, and NSDFB is used to obtain directional decomposition to form linear structures.

## 2. IR image enhancement using S-function

Before fusing the IR image and visible image, we can apply S-function to enhance the contrast of IR image, in order that we can obtain much better fusion effect.

The adaptive contrast stretching S-function can be defined as:

$$S(i, j) = \frac{255}{k * \exp[-10 * A(i, j) / 255 - 5] + 1} \quad (8)$$

$$k = \frac{255 / \mu - 1}{\exp[-(10 * \mu / 255 - 5)]} \quad (9)$$

where  $A(i, j)$  denotes the pixel gray value of the IR image,  $\mu$  is the mean pixel gray value of the IR image.  $k$  is the inflection point parameter, and  $S(i, j)$  is the pixel value after contrast stretching.

## 3. Image fusion rules

For each NSCT image decomposition, the low-frequency coefficients stand for contour information which depicts an approximation of source image usually without useful sparsity, whereas, the high-frequency coefficients represent detail information having enough sparsity to be considered in compressive sampling and recovery.

### a). Low-frequency fusion rule

We use a simply adaptive weighting regional energy based fusion rule for the low-frequency coefficients fusion.

Similar to the aforementioned equations, the low-frequency regional energy for IR image **A** and **B** are denoted as follows:

$$E_{j_0}^A(x, y) = \sum_{m \in K, n \in L} w(m, n) [C_{j_0}^A(x + m, y + n)]^2 \quad (10)$$

$$E_{j_0}^B(x, y) = \sum_{m \in K, n \in L} w(m, n) [C_{j_0}^B(x + m, y + n)]^2$$

where we also choose  $K \times L$  as  $3 \times 3$  window mask, and the weight factors can be written as

$$W_{j_0}^A(x, y) = \frac{E_{j_0}^A(x, y)}{E_{j_0}^A(x, y) + k_{lowf} E_{j_0}^B(x, y)} \quad (11)$$

$$W_{j_0}^B(x, y) = 1 - W_{j_0}^A(x, y)$$

where  $k_{lowf}$  is a parameter to adjust the low-frequency coefficients energy on the visible image. The low-frequency coefficients after fusion will be

$$C_{j_0}^F(x, y) = W_{j_0}^A(x, y) C_{j_0}^A(x, y) + W_{j_0}^B(x, y) C_{j_0}^B(x, y) \quad (12)$$

### b). Highest-level high-frequency fusion rule

For the highest-level high-frequency coefficients fusion, we adopt the maximal selection rule, which can be written as follows:

$$C_{j,l}^F(x, y) = \begin{cases} C_{j,l}^A(x, y), & |C_{j,l}^A(x, y)| \geq |C_{j,l}^B(x, y)| \\ C_{j,l}^B(x, y), & |C_{j,l}^A(x, y)| < |C_{j,l}^B(x, y)| \end{cases} \quad (13)$$

### c). General-level high-frequency fusion rule

For the other high-frequency subband coefficients, we have developed an adaptive-Gaussian regional average gradient rule to proceed the fusion. The adaptive Gaussian membership functions can be defined as

$$\eta_B(x, y) = \exp \left[ -\frac{1}{2} \left( \frac{C_j^A(x, y) - \mu_G}{k_G \sigma} \right)^2 \right] \quad (14)$$

$$\eta_A(x, y) = 1 - \eta_B(x, y)$$

where  $\mu_G$  is the mean value of the coefficient image,  $\sigma_G$  is the variance of the coefficient image, and  $k_G$  is a parameter to adjust the membership function.

On the other side, the regional average gradient of an image can be defined as

$$G_t(x, y) = \frac{1}{MN} \sum_{x \in M} \sum_{y \in N} \sqrt{\frac{\Delta S_x^2(x, y) + \Delta S_y^2(x, y)}{2}} \quad (15)$$

where  $\Delta S_x$  and  $\Delta S_y$  are the variances on the  $x$  and  $y$  directions of the image.

Therefore, the weight factors and the final fused coefficients can be defined to be:

$$W_{j,l}^A(x,y) = \frac{\eta_A(x,y)G_t^A(x,y)}{\eta_A(x,y)G_t^A(x,y) + k_{highf}\eta_B(x,y)G_t^B(x,y)}$$

$$W_{j,l}^B(x,y) = 1 - W_{j,l}^A(x,y)$$

(16)

$$C_{j,l}^F(x,y) = W_{j,l}^A(x,y)C_{j,l}^A(x,y) + W_{j,l}^B(x,y)C_{j,l}^B(x,y)$$

(17)

where,  $k_{highf}$  is a parameter to adjust the adaptive regional average gradients for the high coefficients on the visible image.

### Experimental results and discussion

The experiments have been proceeded using a set of infrared and visible data. The NSCT directional decomposition is chosen as  $2^1 - 2^2 - 2^3$ . The result fusion images can be shown from Fig. 4 to Fig. 9. In addition, the performance results can be illustrated and compared as in Table 1.

Table 1: Performance of Different Fusion Rules

	IR Source	Visible Source	General Fusion	Proposed Fusion
<b><i>d</i></b>	33.1846	71.6673	64.1928	65.9579
<b><i>H</i></b>	6.9916	6.2951	6.9529	7.2843



Fig. 4. Original IR Image



Fig. 5. S-enhanced IR Image



Fig. 6. Visible Image



Fig. 7. Fused Image in Grayscale

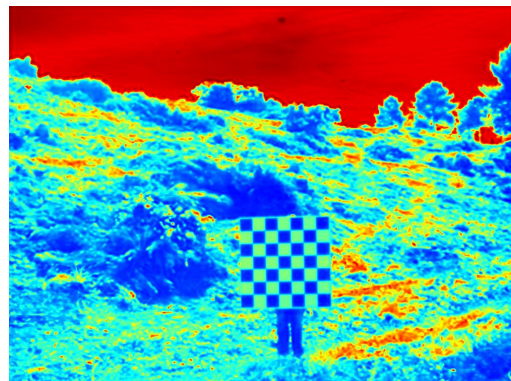


Fig. 8. Fused Image in HSV Space



Fig. 9. Fused image in RGB Space

From the Fig. 7, we can evidently see that the grayscale fusion image has already contained all the information inherited from both of the infrared and visible source images. Fig. 9 is the colorscale fusion image, which demonstrates the image clearer in RGB colorspace satisfying the human visual perception.

From the Table 1, we can obviously know that the proposed NSCT-FISCS algorithm receives much better results of performance in global standard deviation and Shannon information entropy.

## Conclusion

An advanced approach (NSCT-FISCS) for image fusion of infrared and visible images based on NSCT and FISCS has been

6.

proposed. The presented method can receive better fusion effects and speed up the convergence in the process of computation. Experimental results demonstrate the superiority of the proposed NSCT-FISCS fusion scheme via quantitative image quality and human visual perception.

## Acknowledgment

The authors would like to thank Mr. Tom Toulouse at University of Corsica, France for having provided the infrared and visible data set.

## References

1. C. Pohl, J. L. V. Genderen, Multisensor image fusion in remote sensing: concepts, methods and applications 19 (1998) 823–854.
2. Jun Wang ; Jinye Peng ; Xiaoyi Feng ; Guiqing He ; Jun Wu, et al. Image fusion with nonsubsampling contourlet transform and sparse representation, J. Electron. Imaging, 22(4), 043019 (Nov 19, 2013).
3. A. da Cunha, J. Zhou, M. Do, The nonsubsampling contourlet transform: Theory, design, and applications, Image Processing, IEEE Transactions on 15 (10) (2006) 3089–3101.
4. Qiong Zhang and Xavier Maldague. An infrared-visible image fusion scheme based on NSCT and compressed sensing, Proc. SPIE 9474, Signal Processing, Sensor/Information Fusion, and Target Recognition XXIV, 94740Y (May 21, 2015).
5. Bioucas-Dias, J.M.; Figueiredo, M.A.T., A New TwIST: Two-Step Iterative Shrinkage/Thresholding Algorithms for Image Restoration, Image Processing, IEEE Transactions on , vol.16, no.12, pp.2992,3004, Dec. 2007.

# Stationary Wavelet Transform denoising in Pulsed Thermography: influence of camera resolution on defect detection

G. M. Revel<sup>1</sup>, P. Chiariotti<sup>2</sup>, E. Copertaro<sup>3</sup>, G. Pandarese<sup>4</sup>

<sup>1</sup> Università Politecnica delle Marche, gm.revel@univpm.it

<sup>2</sup> Università Politecnica delle Marche, p.chiariotti@univpm.it

<sup>3</sup> Università Politecnica delle Marche, e.copertaro@pm.univpm.it

<sup>4</sup> Università Politecnica delle Marche, g.pandarese@univpm.it

Denoising filters are widely used in image enhancement. However, they might induce severe blurring effects the lower is the resolution of the original image. When applied to a thermal image in Non-Destructive Testing (NDT), blurring could entail wrong estimation of defect boundaries and an overall reduction in defect detection performances. This contribution discusses the application of a wavelet-based denoising technique to a thermographic sequence obtained from a Pulsed Thermography testing, when using a high-resolution 1024x768 FPA infrared camera. Influence of denoising approach on data post-processed by Principal Component Analysis is discussed. Results indicate marked enhancement in defect detection, especially when compared to those obtained with a standard-resolution 320x240 FPA infrared camera.

## Introduction

Pulsed Thermography (PT) has shown great potential in the field of Non-Destructive Testing (NDT), mainly because of its capability in inspecting wide surfaces in relatively short testing-time. This represents an advantage when compared to other NDT techniques as ultrasonic testing.

However, detection of thermal waves reflected by internal defects might become a difficult task. Indeed some difficulties in performing test might arise, mainly because of non-uniform heating, environmental reflections and low Contrast to Noise Ratio (CNR) for defects that are deep in the sample: all these aspects contribute in limiting both the maximum depth of inspection and the size of the minimum detectable defect. Different studies [1, 2] have shown how a denoising processing directly performed on the raw thermal images increases the defect detection probability. However, if on the one hand denoising surely decreases noise level, on the other hand it could generate blurring effects that might reduce defect's contrast, besides worsening the estimation of defect boundaries.

This paper discusses how a wavelet-based denoising pre-processing can influence Principal Component Analysis (PCA) when used on two sets of thermal sequences acquired with thermal cameras having different resolutions. The paper is organized as follows: the experimental set-up is presented at first in Section 1; Section 2 presents the wavelet-based denoising strategy used; impact of the denoising pre-processing and benefits achievable in terms of CNR in high and low-resolution thermal sequences are highlighted in Section 3, while Section 4 reports the main conclusions.

## Experimental setup

Pulsed Thermography tests were performed on a 280x280x4 mm carbon fiber reinforced polymer specimen with Teflon® insertions of different sizes (from 5 to 15 mm - x direction in Fig. 1a) and depths (from 0.3 to 2.0 mm - y direction of Fig. 1a). An ultrasonic C-scan was also performed on the same panel, in order to get reference data in terms of defects size and position (Fig. 1a).



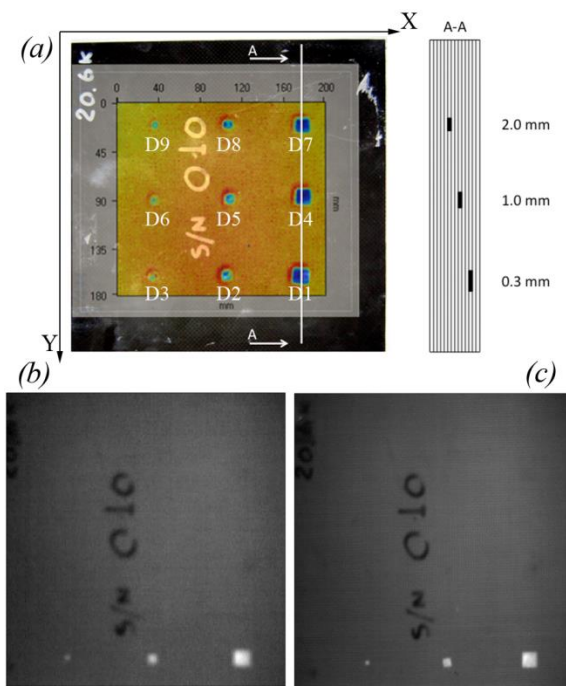


Fig. 26. Ultrasonic C-scan (a); thermal image acquired by 320x240 FPA at  $t=0.1$  s after heat pulse (b); thermal image acquired by 1024x768 FPA at  $t=0.1$  s after heat pulse (c).

The panel was placed 500 mm far from two flash lamps. Flash lamps provided a total load of 6 kJ in a 700  $\mu$ s time interval. Two uncooled microbolometric infrared cameras with different resolutions were used for monitoring temperature evolution of the panel's surface. The first camera is equipped with a 320x240 FPA sensor, which is a quite common resolution for infrared cameras, whilst the second, an Infratec Variocam® HD, disposes of a 1024x768 FPA. Apart from different resolutions, the two infrared cameras show same specifications as it concerns thermal sensitivity (better than 0.1 K) and measurement accuracy (better than  $\pm 2$  K). Acquisition rate and truncation time were set to 30 Hz and 20 s respectively for both infrared cameras.

Fig. 1b and 1c show thermal images (cold frame subtracted) respectively from the 320x240 FPA and the 1024x768 FPA.

## Proposed approach for enhancing defect identification

Interest of the scientific community in denoising techniques as pre-processing tools for enhancing PT results has gained relevance during the last years [1, 2]. It is widely accepted that the use of denoising filters on raw thermal images enhances the performances of well-known post-processing algorithms as Pulsed Phase Thermography, PCA, Signal Reconstruction, etc., making it possible to improve the defect detection task.

Among all denoising strategies, those based on wavelet processing do show interesting performances in terms of CNR improvement. Indeed, a trade-off between the removed noise and the blurring in an image always exists. However, wavelets capability to give detailed spatial-frequency information implies better discrimination between the noise and the real data, respect to what achievable with other filters like median or Gaussian ones, and such property might lessen the blurring effect or even overcome it completely.

The denoising approach used in this paper is based on the Stationary Wavelet Transform (SWT). Such transform has resulted in better performances respect to the Discrete Wavelet Transform (DWT), because more details can be preserved in approximation coefficients (see [3] for an application in image denoising). No further image enhancement methods are performed on the raw thermal sequences, even though some recent algorithms are available [4].

SWT has been applied to both high-resolution (HR) and low-resolution (LR) thermal sequences, using a *bior3.1* wavelet at decomposition level 2. PCA has been used in the subsequent post-processing.

## Results and comparison between HR and LR sequences

Fig. 2 and Fig. 3 show the first Principal Component (PC) (only small-depth defects area)

calculated respectively on the LR and on the HR thermal sequences. A comparison of PCs calculated when the sequences are/are not denoised is shown.

Denoising worsens PCA results when it is performed on the LR sequence (Fig. 2 a, b). Even though the pedestal of the PC profile (Fig. 2c) results smoother for the denoised sequence, the blurring effect leads to an evident lowering of the peaks corresponding to defects, thus resulting in a reduction of the CNRs. This happens especially on the smallest defect, as highlighted in Table 1.

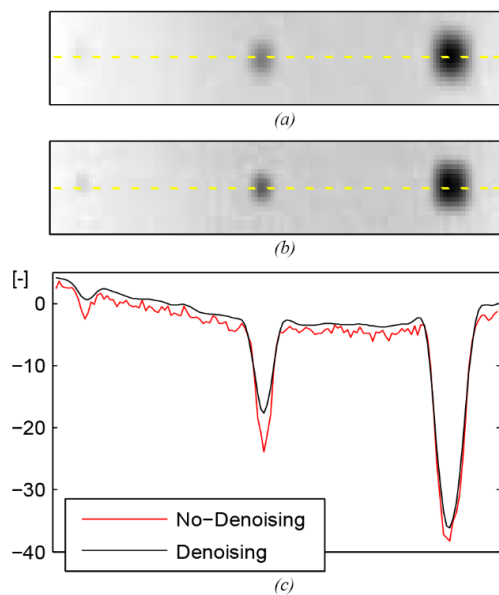


Fig. 2. First PC of thermal sequences from 320x240 FPA: with denoising (a); without denoising (b); profiles over defects line (c).

	CNR		
	No-Denoising	Denoising	% Difference
D1	4.4	4.2	-4 %
D2	7.0	5.7	-19 %
D3	3.8	2.4	-37 %

Table 1. CNRs for LR sequences. First PC.

Percentage difference is calculated according to Eq.1:

$$\% Diff = 100 \cdot \frac{CNR_{den} - CNR_{no\_den}}{CNR_{no\_den}} \quad [1]$$

On the other hand, the use of the same denoising approach on the HR sequence is effective in

reducing the noise content while keeping defect information, thus resulting in CNRs enhancement especially for the small defect (see Table 2).

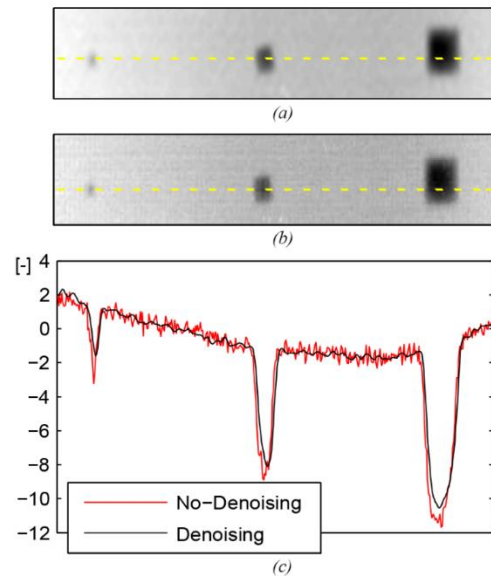


Fig. 3. First PC of thermal sequences from 1024x768 FPA: with denoising (a); without denoising (b); profiles over defects line (c).

	CNR		
	No-Denoising	Denoising	% Difference
D1	3.7	3.7	0 %
D2	3.5	3.9	+11 %
D3	3.4	4.4	+29 %

Table 2. CNRs for HR sequences. First PC.

Deeper defects, which are not enhanced in the first PC, can be detected at higher components: indeed, in both LR and HR thermal sequences, they show the maximum contrast on the fourth PC, which is analysed hereafter. Fig.4 shows the fourth PC for both denoised and non-denoised HR thermal sequences. The CNRs associated with defects D4-D7 (i.e. the ones that can be well appreciated) are reported in Table 3.

	CNR		
	No-Denoising	Denoising	% Difference
D4	2.4	3.2	+33 %
D5	1.3	2.8	+115 %
D6	1.4	2.5	+79 %
D7	0.8	1.9	+137 %

Table 3. CNRs for HR sequences. IV PC.



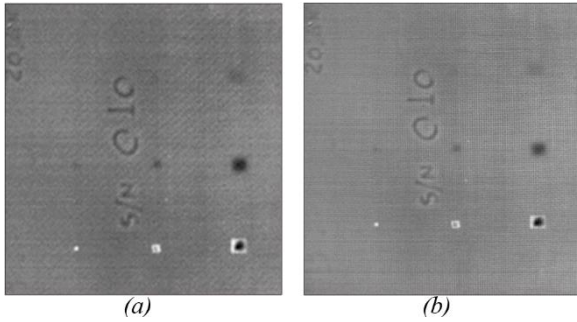


Fig. 4. Fourth PC of thermal sequences from 1024x768 FPA: with denoising (a); without denoising (b).

Again, when denoising is applied to the HR sequence it demonstrates its effectiveness in providing image enhancement. As a consequence, all the CNRs show a marked increase respect to the non-denoised case; percentage differences are more relevant respect to values obtained with small-depth defects on the first PC, where noise content is clearly less incident. Fig. 5 shows the fourth PC for both denoised and non-denoised LR sequences. CNRs associated with defects D4-D5 (i.e. those visible in Fig. 5) are reported in table 4.

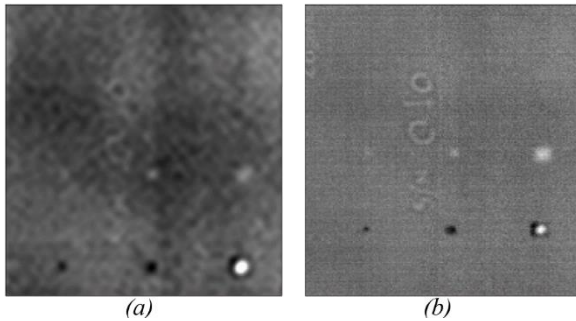


Fig. 5. Fourth PC of thermal sequences from 320x240 FPA: with denoising (a); without denoising (b).

	CNR		
	No-Denoising	Denoising	% Difference
D4	3.0	2.8	- 7 %
D5	3.4	2.1	- 38 %

Table 4. CNRs for LR sequences. IV PC.

As for small-depth defects, denoising applied to the LR sequence worsens PCA processing. Denoising makes the image more flattened, thus

decreasing the defect's contrast with respect to the image background (i.e. the area of the image not containing any defect) and therefore reducing the CNRs.

## Conclusions

The paper has discussed the influence of camera resolution on a wavelet-based denoising, in Pulsed Thermography. Influence of denoising on PCA results has been shown.

Impact of blurring effects on the LR sequence is strong: blurring, which inherently happens when performing denoising pre-processing, produces distortions and defocusing that might become so important to lessen defect detection capability, especially with the smallest defects.

Nevertheless, wavelet-based denoising has demonstrated to be a powerful tool if performed on a HR thermal sequence. When used in conjunction to PCA, CNRs increase and make it possible to highlight defects that are less evident if no denoising is performed.

## References

1. P. Hedayati Vahid, S. Hesabi, D. Lauredndeau, and X. Maldaque. A Defect Detection Approach in Thermal Images, proceedings of QUIRT 2014.
2. C. Ibarra-Castanedo, A. Bendada and X. Maldague. Thermographic Image Processing for NDT, proceedings of IV Conferencia Panamericana de END, Buenos Aires, 2007.
3. X.H. Wang, R.S. Istepanian, Y.H. Song, Micro array image enhancement by denoising using stationary wavelet transform, IEEE Trans. Nano Biosci. Vol. 2(4). pp. 184–189, 2003.
4. T. Liu, W. Zhang, S. Yan, A novel image enhancement algorithm based on stationary wavelet transform for infrared thermography to the de-bonding defect in solid rocket motors, Mechanical Systems and Signal Processing, Vol. 62–63, pp. 366-380, 2015. ISSN 0888-3270, <http://dx.doi.org/10.1016/j.ymsp.2015.03.01>

# FREQUENCY MODULATED HEATING SOURCE IN IR THERMOGRAPHY

P. Bison<sup>1\*</sup>, A. Bortolin<sup>1</sup>, G. Cadelano<sup>1</sup>, G. Ferrarini<sup>1</sup>, L. Finesso<sup>2</sup>, R. Mulaveesala<sup>3</sup>

<sup>1</sup> ITC-CNR, Corso Stati Uniti, 4; 35127 Padova, Italy. - paolo.bison@itc.cnr.it

<sup>2</sup> IEIIT-CNR, via Gradenigo 6/B - 35131, Padova, Italy. - lorenzo.finesso@ieiit.cnr.it

<sup>3</sup> INDIAN INSTITUTE OF TECHNOLOGY ROPAR, Rupnagar -140001, Punjab, India. - ravi@iitrpr.ac.in

Active Infrared Thermography is a technique widely used in assessing the conditions of parts of industrial components. The aim of this paper is that of comparing the pulse, the periodically modulated and the chirp methods of heating. The methods will be applied on a CFRP slab, prepared with teflon inserts of various dimensions and located at different depths, to simulate the presence of defects inside the material. The thermographic images of the experiments will be treated to produce eventually a binary map of the location of the defects.

## Introduction

Active Infrared Thermography is a technique widely used in assessing the conditions of parts of industrial components. It consists in the generation of heat in the component under test and in monitoring by InfraRed Thermography (IRT) the time evolution of the surface temperature. The heat generation can be done by several techniques (hot air, induction, acoustic waves etc.). Nonetheless the photothermal one is by far the most used consisting in the generation of heat as a consequence of the absorption of electromagnetic waves, typically (even though not necessarily) in the visible band. Lamps delivering either a flash pulse or a periodically modulated light are the most commonly used methods of heating. In both cases thermography records the time evolution of the surface temperature of the heated part. For pulse, data are successively treated according to various algorithms: among them Pulse Phase Thermography (PPT) [1], Principal Component Thermography (PCT) [2], Thermographic Signal Reconstruction (TSR) [3], Thermal Tomography (TT) [4] etc. For periodically modulated source the data processing follows in some way what is done by a lock-in amplifier [5,6]. In the past the scientific community

working in the field of IRT had been speculating on the best heating method to adopt (according to some optimum criteria) in such a way to increase as much as possible the detectability of inner defects [7,8]. More recently, a new heating method has been proposed independently by Mandelis and Mulaveesala [9-12]. It appears as a compromise between the pulse and periodic heating methods. It consists in the frequency modulation of the heating source by means of a chirp signal in one case, and in the application of suitable on-off sequence to a lamp according to the Barker code [13], the digital version of the chirp signal. Both heating schemes derive from the signal processing strategies adopted in the Radar technology.

The aim of this paper is that of comparing the pulse, the periodically modulated, the chirp and Barker code methods of heating. The four methods will be applied on a CFRP slab, prepared with teflon inserts of various dimensions and located at different depths, to simulate the presence of defects inside the material. The thermographic images of the experiments will be treated to produce eventually a binary map of the location of the defects. This map will be statistically evaluated in terms of sensitivity and specificity [14] by comparison with the 'true' map of the defects,

furnishing a rank of the four heating methods. Each heating method will be presented together with the description of the adopted signal processing algorithm.

## References

1. X. Maldague and S. Marinetti. Pulse phase infrared thermography. *Journal of Applied Physics*, 79(5):2694–2698, 1996.
2. N. Rajic. Principal component thermography for flaw contrast enhancement and flaw depth characterisation in composite structures. *Composite Structures*, 58(4):521–528, 2002.
3. S. Shepard, J. Lhota, B. Rubadeux, D. Wang, and T. Ahmed. Reconstruction and enhancement of active thermographic image sequences. *Opt. Eng.*, 42(5):1337–1342, May 2003.
4. Vavilov. Dynamic thermal tomography: Perspective field of thermal ndt. In S. A. Semanovich, editor, *THERMOSENSE XII*, volume 1313, pages 178–182. SPIE, 1990.
5. G. Busse, D. Wu, and W. Karpen. Thermal wave imaging with phase sensitive modulated thermography. *Journal of Applied Physics*, 71:3962–3965, 1992.
6. J. Krapez. Compared performances of four algorithms used for modulation thermography. In *QIRT-1998*, 1998.
7. W. Winfree and K. Cramer. Computational pulse shaping for thermographic inspection. In D. Burleigh and J. Spicer, editors, *Thermosense XVIII*, volume 2766, pages 228–235, 1996.
8. V. Vavilov and X. Maldague. Optimization of heating protocol in thermal ndt, short and long heating pulse: a discussion. *Research in Nondestructive Evaluation*, 6(1):1–18, 1994.
9. S. Tuli and R. Mulaveesala. Defect detection by pulse compression in frequency modulated thermal wave imaging. *QIRT Journal*, 2(1):41–54, 2005.
10. R. Mulaveesala and E. Tuli. Theory of frequency modulated thermal wave imaging for nondestructive subsurface defect detection. *Applied Physics Letters*, 89:191313–1 191313–3, 2006.
11. A. Mandelis. Frequency modulated (fm) time delay photoacoustic and photothermal wave spectroscopies. technique, instrumentation, and detection. part i: Theoretical. *Review of Scientific Instruments*, 57:617– 621, 1986.
12. A. Mandelis. Thermophotonic radar imaging: An emissivity-normalized modality with advantages over phase lock-in thermography. *Applied Physics Letters*, 98:163706–1 – 163706–3, 2011.
13. R. Barker. Group synchronizing of binary digital sequences. *Communication Theory*, pages 273–287, 1953.
14. T. Fawcett. An introduction to roc analysis. *Pattern Recognition Letters*, 27:861–874, 2006.

# COMPARISON OF FREQUENCIES VIBRATION FOR A BRIDGE OBTAINED FROM MEASUREMENTS WITH ACCELEROMETERS AND PIEZOELECTRIC SENSORS

N.Shimoi<sup>1</sup>, C. Cuadra<sup>2</sup>

<sup>1</sup> Akita Prefectural University , Dept.of Machine Intelligence and Systems Engineering, 84-4 Tsuchiya Aza Ebinokuchi, Yurihonjo, Akita 015-0055, Japan, Shimoi@akita-pu.ac.jp

<sup>2</sup> Akita Prefectural University , Dept. of Architecture and Environment Systems, 84-4 Tsuchiya Aza Ebinokuchi, Yurihonjo, Akita 015-0055, Japan, carlos@akita-pu.ac.jp

Deterioration or ageing of bridges structures and damages due to strong earthquakes may conduce to collapse of the bridge, sometimes with catastrophic consequences. Therefore investigation of structural condition of bridges is required for secure safe road operations. This paper presents a prototype of piezoelectric-cable sensor for vibration monitoring system that permits easy evaluation of integrity of a bridge structure. For this study a bridge located at Yurihonjo city, Japan was chosen as target structure. The structure is a continuous beam type bridge with steel beams of variable sections and reinforced concrete slabs to support the asphalt carpet. The bridge consists of seven spans with a total length of 256 m. The experimental measurements were performed on the first span near the left abutment.

## 1.Introduction

In Japan many bridges were constructed as a part of the reconstruction program after the Pacific War. Therefore old constructions of that date are now in danger due to the deterioration of their structures. On the other hand in the decade of 1980 of the last century constructions of large projects of building and bridges were initiated. Then high demand of materials, in special for reinforced concrete structures, induced the used of sea sand which contains salts that in reaction with water and cement originates the corrosion of steel reinforcement. Outside Japan an example of the necessity of health monitoring was evident in the collapse of the bridge I-35W on Mississippi river in USA. During the evening rush hour on August 1, 2007, the bridge suddenly collapsed, killing 13 people and injuring 145. In the case of Japan the Ministry of Land and Transportation has performed a study of vulnerability of bridges and 121 cases of bridges in danger have been reported. The risk of bridges is due to deterioration of

aged concrete bridges (weathering) and corrosion of steel bridges.



(a) Damage point for repair (b) damage point for repair (c) Damage point

Figure 1. Old damaged bridge and maintenance examples in Japan and the USA.

A continuous or real time structural health monitoring could help to prevent damages. Monitoring systems already exist however they are in general designed to be installed in new structures and are expensive. For existing old structures, simple and cheap sensor systems are required. In this research a new sensor that is based on piezoelectric cable inserted into a bolt shape is developed and its applicability to perform health monitoring of structures is verified by means of a series of measurement on vibration of a target bridge. The selected bridge is located at Yurihonjo city, Akita prefecture, Japan. The results obtained with this new simple smart sensor are comparable with those obtained with more sophisticated and

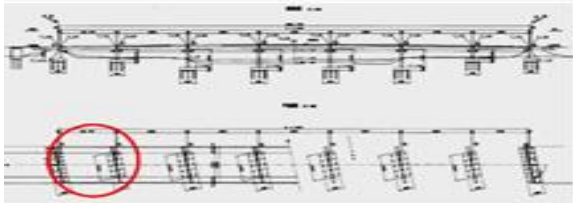
expensive commercial sensors. Fig.1 presents bridge damage in Japan and in the USA.

### 1.1 Target Bridge

A general view of selected structure for this study can be observed in Fig.2. This bridge is called Asuka Oohashi constructed in the year 1979 and spans over the Koyoshi river with a total length of 256 m. The target is a girder type bridge with 7 spans as is shown in Fig. 3(a). For measurements only the first span (encircled left span in Fig. 3(a)) was selected. The bridge structure is formed by steel beams which support a reinforced concrete slab as is shown in Fig. 3(b). The bridge has 2 abutments at both ends and 6 intermediate piers and therefore the selected span for measurements has an abutment at one end and a pier at other end, with a span length of 31 m.



(a) Elevation and plan views of bridge



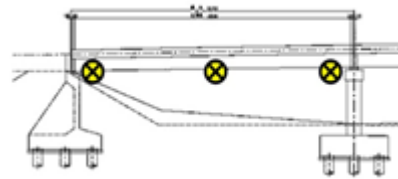
(b) The bridge in three dimensional an illustration

Figure 2. General scheme of target span

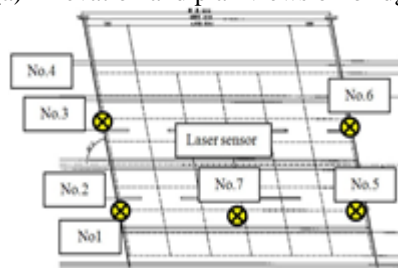
Points of vibration measurements on selected span are shown in Fig. 3. Bolt type sensors were located at seven points of measurements together with accelerometers to compare both results. In addition at middle of span a laser displacement transducer was setup near point No. 7.

Fig.4 shows some details of sensors setup. Basically, relative displacements between girders and support structure were measured at each point. For this purpose, sensors were fixed firmly to girder flange with its end in contact with support surface. Sensor 1, 2, 3, 4, 5 and 6 were setup in this way as can be observed in Fig. 4(a) and 4(b). Fig. 4(c) shows the detail of accelerometer and sensor

setup at point 7 which is the centre of span. Fig. 4(d) shows the wireless transmission unit (radio unit) and corresponding battery. This unit receives signal from sensor and sent it to the computer for data acquisition. Fig.4(e) Shown the setup of laser displacement transducer. Also vibration due to moving loads was measured and in Fig. 4(f) the truck of 19 t that was used for this test is shown.



(a) Elevation and plan views of bridge

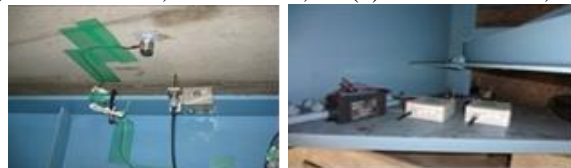


(b) The bridge in three dimensional an illustration

Figure 3. General scheme of target span



(a) Sensor Nos. 1, 3 and Nos.2,4 (b) Sensor Nos. 5 ,6



(c) Sensor Nos.7 and Accelerometer (d) Radio unit



(e) Laser sensor (f) The 19t truck for moving load

Figure 4. Details of sensor setup and measurements

### 3. Characteristics of proposed piezoelectric sensor

Basic scheme of measurement systems are shown in Fig. 5. Fig. 5(a) shows proposed system were signals from piezoelectric bolt sensors are transmitted to computer by means of a wireless module which contains a microcomputer board. As can be observed, the proposed system is simple and

it is easy to install in-situ. Former measurements systems require more equipment like energy generator, signal amplifiers, etcetera. The piezoelectric bolt sensor is shown in Fig. 5(b). Basically consists of a piezoelectric cable located in its inner core and external cover of urethane resin resulting in a nominal diameter of 15 mm.

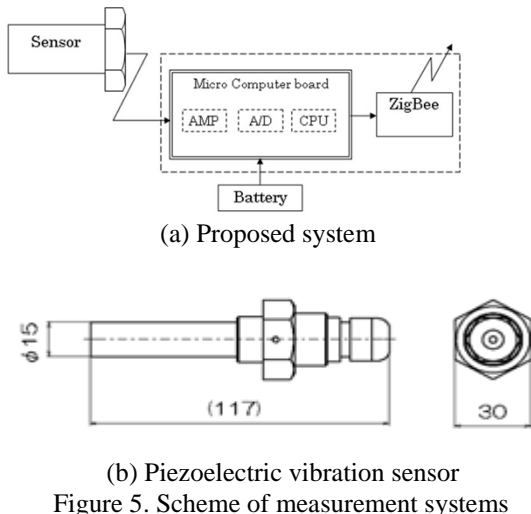


Figure 5. Scheme of measurement systems

#### 4. Estimation of predominant frequency of target bridge

As illustrative example of measurement results, responses at measurement point No.1 and No.2 are shown in Fig. 6. Upper part of the Fig. 6 shows acceleration responses obtained by means of accelerometers and bottom part of Figure shows the voltage output from the bolt sensors. From recorded signals, predominant frequencies were obtained by Fourier analysis. In Fig. 7 Fourier spectrum for signals from point No. 1 to No. 6 are shown. Upper part of each figure corresponds to accelerometers results and bottom part corresponds to proposed sensor results. Results for point No.1, No.2 and No.4 show good agreement between accelerometer results and proposed sensor results. The difference of results at point No.5 and at point No.6 it is believed that is due that proposed sensors and accelerometers are not set up at same location. However in the Fourier spectrum for proposed sensor a second peak

near 3.6 Hz is observed which is comparable with the predominant frequencies obtained from accelerometers.

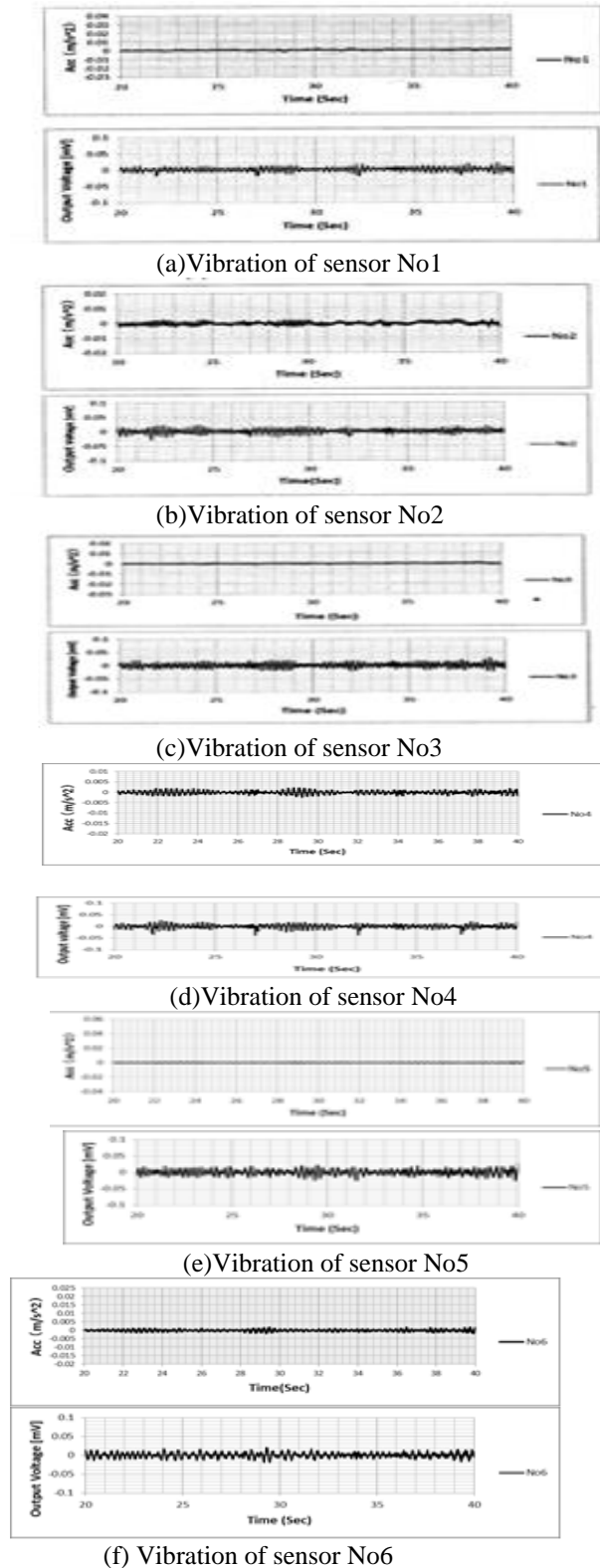


Figure 6. Measurements signals from accelerometers and from bolt sensors



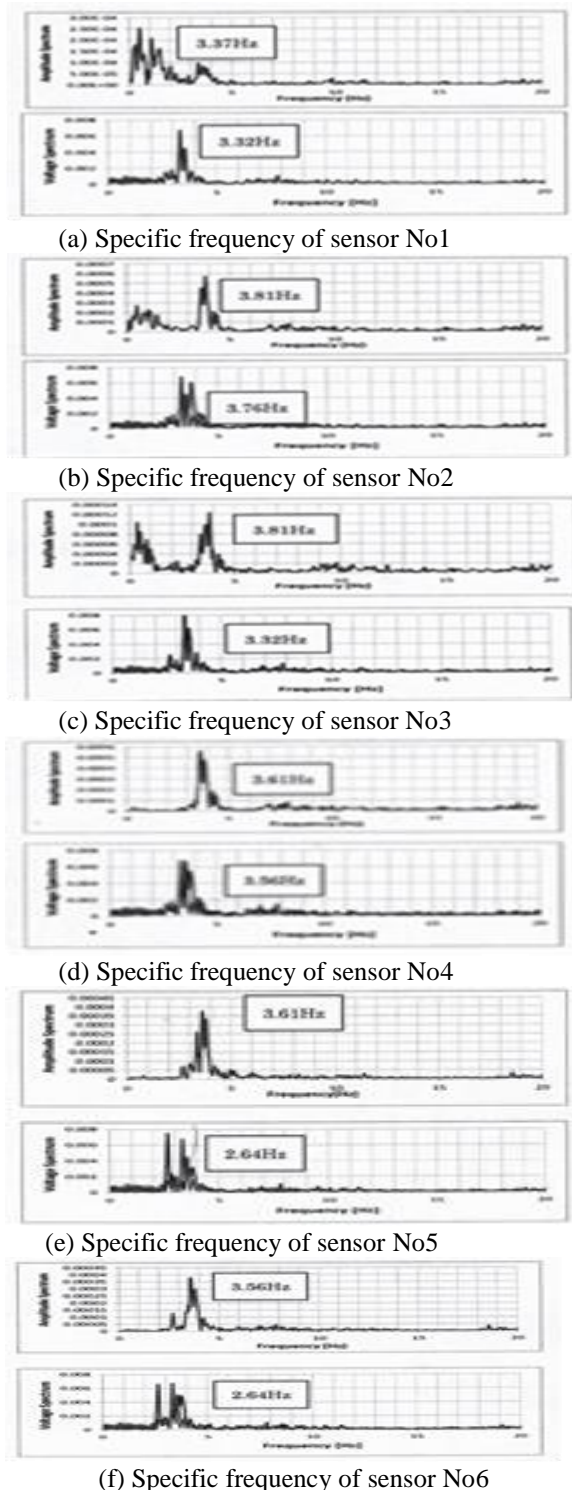


Figure 7 Predominant frequencies from Fourier analysis

## 5. Conclusion

In this research a new smart simple piezoelectric sensor and its corresponding data acquisition system were developed to be used for real time structural health monitoring of structures. Installation of the system in selected portion of selected bridge structure has permit to perform the monitoring of the structural response for free vibration and vibration in case of moving loads (vehicle loads). The applicability of this new bolt-type sensor for structural health monitoring and estimation of dynamic characteristics of a bridge structure was verified. Simultaneously commercial accelerometers were used for vibration measurements to compare with those measurements using proposed system. In general predominant frequencies obtained from in-situ measurements using accelerometers and proposed bolt sensors show good agreement. It was also verified that proposed sensor could be used also to detected impact loads acting on bridge structures. In this case verification was done by performing measurements using moving loads from a truck of 19 t. Measurements results from laser displacement transducer and proposed sensor are comparable

## Acknowledgements

This research was supported by The Japan Society for the Promotion of Science (JSPS KAKENHI Grand Number 25242033). Authors express their acknowledgments for that support.

# Perturbations of the heat transfer coefficient due to surface damages

G. Inglese<sup>1</sup>

<sup>1</sup> CNR IAC "M.Picone", via Madonna del Piano 10 50019 Sesto Fiorentino  
gabriele@fi.iac.cnr.it

Newton's cooling law is generally accepted as a good model for heat exchange from a conducting body and an aggressive environment at ordinary temperatures in presence of a significant current in the external fluid. Assume that the interface of the body has been damaged and that the corresponding anomaly consists mainly in a loss of matter. The fluid current is reasonably perturbed by the presence of such damage. For this reason a local change occurs also in the heat transfer coefficient. We conjecture that the size and the shape of the perturbation are related mainly to the non-smoothness of the damage and that the effects of such anomaly can be measured.

## Thermal model of a thin conductor

Consider a thin conducting plate  $\Omega = R^2 \times [0, a]$  ( $a > 0$ ). In fact, the plate separates an aggressive environment ( $z > a$ ) from our laboratory ( $z < 0$ ). From the laboratory side we are able to heat the plate with a lamp, a battery of lamps or a laser.

Let  $\Phi$  be the heat flux provided from the laboratory side to our specimen. We assume that it is a pulse and, at least in theory, it assumes the form

$$\Phi(x, y, t) = \Phi_0(x, y)\delta(t)$$

where

$$\Phi_0(x, y) = P_0 e^{-((x-x_1)^2 + (y-y_1)^2)/s^2}$$

We can record the surface temperature decay taking a sequence of maps of the bottom boundary  $z = 0$  by means of an infrared camera.

When the top boundary has been damaged, its geometry turns out to be modified. This fact gives rise to an abnormal behaviour of the

temperature decay that can be read on the side  $z = 0$  by means of our camera.

Assume that the damage is a conical (triangular in 2D models) thin hole on the top boundary. It is small but large enough to induce a measurable change of the temperature on the opposite side of the specimen.

The whole damaged top boundary is described by the function

$$z = a - \varepsilon\theta(x, y) \tag{1}$$

(where  $\varepsilon \ll a$ ) so that the damaged domain is  $\Omega_{\theta} = \bigcup_{x, y \in R} [0, a - \varepsilon\theta(x, y)]$ .

Here the function  $\theta(x, y)$  is assumed to be continuous but possibly non differentiable in a finite set of points of the domain.  $\theta(x, y)$  is zero out of a circular subset of the plane (i.e. the damage is localized inside this subset). The flux  $\Phi$  is concentrated around the center  $(x_1, y_1)$  of this circle.

The temperature of the specimen is a function  $u^\varepsilon(x, y, z, t)$ , defined in  $\Omega_{\theta} \times (0, T)$ , that satisfies the heat equation

$$\frac{\partial u}{\partial t} = \alpha \Delta u \quad (2)$$

with Robin boundary conditions derived directly from Newton's law of cooling

$$\begin{aligned} & \lambda \nabla u(x, y, z - \varepsilon \theta(x, y)) \cdot n + \\ & (\gamma_0 + \varepsilon \gamma_1(x, y))(u(x, y, z - \varepsilon \theta(x, y)) - U_{ext}) = \\ & \lambda u_x \theta_x + \lambda u_y \theta_y + \lambda u_z + (\gamma_0 + \varepsilon \gamma_1)(u - U_{ext}) + O(\varepsilon^2) = 0 \end{aligned} \quad (3.1)$$

and

$$\lambda u_z(x, y, 0, t) - \gamma_{lab}(u(x, y, 0, t) - U_{lab}) = \Phi(x, y, t). \quad (3.2)$$

Uniqueness of the solution of (2) requires also a complete information about the initial temperature all over  $\Omega_{\varepsilon\theta}$  :

$$u(x, y, z, 0) = U_0(x, y, z).$$

Mathematical results about existence, uniqueness and stability of classical and weak solutions of parabolic initial-boundary value problems like this can be found for example in [8]

Here,  $\alpha = \frac{\lambda}{\rho c}$  is the diffusivity of the material constituting our specimen ( $\lambda$  is the conductivity,  $\rho$  is the density and  $c$  is the specific heat).

We assume that the external fluid flows regularly over the undamaged surface and carries away heat. Hence, the heat transfer coefficient  $\gamma_0$  depends on the magnitude of the fluid current (see [11]). The term  $\varepsilon \gamma_1$  is supposed to appear since the geometrical perturbation of the interface modifies the fluid dynamics over the top surface of  $\Omega_{\varepsilon\theta}$  in the neighborhood of the damage. In fact, the fluid is trapped into the thin hole and heat transfer turns out to be reduced.

Observe that  $\varepsilon \theta(x, y)$  and  $\varepsilon \gamma_1(x, y)$  are assumed constant in time although they represent physical quantities in progress. In fact, the time scale of damage evolution is much larger than the time scale of our experiments.

Remark: *Can mathematics suggest models to Physics?* Newton's law of cooling would seem to be "... one of those empirical statements about natural phenomena that should not work but does" (O'Connell cited in [12]). Nevertheless, an old paper about elliptic PDEs (2) shows that, in presence of a vanishing coating with rapidly varying thickness, a Robin boundary condition is obtained as limit of a sequence of Dirichlet problems. The numerical value of the "transfer" coefficient is related to the frequency of the oscillating boundary. This result is mainly a model of rod reinforcement but it has been applied to corrosion detection via electrical impedance tomography which is based on equations that are essentially the same as the ones of thermal imaging [9].

The temperature  $u^0(x, y, z, t)$  is called background temperature. The difference

$$u^\varepsilon(x, y, 0, t) - u^0(x, y, 0, t)$$

is the *thermal contrast* measurable from the laboratory by means of an infrared camera.

### Position of the main inverse problem

We assume that  $\varepsilon \gamma_1$  is unknown. We recall that it has been supposed lower or equal to zero.

In this paper, we describe a procedure to evaluate it from the knowledge of  $u^0(x, y, z, t)$ ,  $\gamma_0$ ,  $\varepsilon \theta(x, y)$  and  $u^\varepsilon(x, y, 0, t) - u^0(x, y, 0, t)$  (thermal contrast).

Remark. In a more realistic framework, the damage on the top boundary is not known. In this case, we could pose an inverse problem in which both the functions  $\varepsilon \gamma_1(x, y)$  and  $\varepsilon \theta(x, y)$  must be identified. This problem has been addressed in [4] for Laplace's equation.

Conditions for the existence of solutions and stability estimates for this kind of inverse problems can be found, for example, in [6].

Although boundary conditions (3.1) (3.2) could be generalized including non linear terms (see for example [11]), we stress the fact that a linear the cooling law (see the introduction of [12]) is regarded as an appropriate model when we deal with low temperature-difference regime (less than 50 K). Nonlinear conditions, for example, are required in cooling of hot glass or steel (temperature difference from 100 to 1000 K). Identification of nonlinear cooling law from thermal data has been addressed, for example, in [3] and [5].

### Expansion of the problem in powers of $\varepsilon$ and reconstruction of the unknown term

In order to simplify the notation, here we deal with a 2D specimen. The variable  $y$  will be neglected and  $\mathcal{G}$  is zero out of the interval  $(x_{\min}, x_{\max})$ .

The domain derivative of  $u_\varepsilon$  is defined in  $\Omega$  as the Gateaux derivative of  $u_\varepsilon$  in zero with respect to the direction  $\theta$ :

$$u' = \lim_{\varepsilon \rightarrow 0} \frac{u^\varepsilon - u^0}{\varepsilon}.$$

It is known (see for example [10] and [1]) that  $u'$  fulfills equation (2) with boundary conditions

$$\lambda u'_{zz} + \gamma_0 u' = \theta(u'_{zz} - \frac{\gamma_0^2}{\lambda}(u^0 - U_{ext})) - \lambda u'_x \theta_x - \gamma_1(u^0 - U_{ext}) \quad (4)$$

for  $z = a$ , and

$$u'_z = 0$$

for  $z = 0$ .

Actually, the damage and the corresponding perturbation of the heat transfer coefficient

involved in our problem are scaled by  $\varepsilon$ . Moreover, the thermal contrast can be written as

$$\varepsilon u'(x, 0, t) + O(\varepsilon^2).$$

For this reason we introduce the scaled domain derivative  $w = \varepsilon u'$  which solves the heat equation (2) with boundary condition

$$\lambda w_z + \gamma_0 w = \varepsilon \theta(u''_{zz} - \frac{\gamma_0^2}{\lambda}(u^0 - U_{ext})) - \lambda u''_x \varepsilon \theta_x - \varepsilon \gamma_1(u^0 - U_{ext}).$$

Our method for identifying  $\varepsilon \gamma_1$  consists in the minimization of the penalized cost functional

$$\int (w(\varepsilon \gamma_1; x, 0, t) - (u^\varepsilon(x, 0, t) - u^0(x, 0, t)))^2 dx dt + \beta F(\gamma_1)$$

as a function of  $\varepsilon \gamma_1(x)$ .

Remark. We assumed  $\varepsilon \gamma_1(x) \leq 0$ . This is the only *a priori* information available. It means that the best choice of  $F$  should be (nonlinear) maximum entropy. Since at this stage we want to avoid nonlinear optimization, we will choose smoothing functionals related to the discretization imposed to  $\varepsilon \gamma_1(x)$ . As for the value of the regularization parameter we will use empiric methods or the L-curve.

In practice, we discretize  $\varepsilon \gamma_1$  in the following way

$$\varepsilon \gamma_1(x) = \varepsilon \sum_{k=0}^N \gamma_{1k} B_{kl}(x)$$

where  $B_{k,l}$  are the B-splines of order  $l \geq 2$  (“triangles” for  $l = 2$ ) built starting from the knots  $x_1 = x_m, \dots, x_N = x_M$  which have been chosen following the shape of  $\theta$ .

Thanks to linearity of our direct model based on the heat equation (2), we have

$$w(\varepsilon \gamma_1; x, 0, t) = \sum_{k=1}^N \varepsilon \gamma_{1k} w_k(x, 0, t)$$

where

$$w_k(x,0,t) = w(B_{k,l}; x,0,t)$$

We plug this expression into the cost functional. Straightforward calculations give us the Euler equations

$$(A^* A + \beta^2 F^* F) \varepsilon \gamma_1 = A^* \delta u$$

where the matrix elements are

$$(A^* A)_{ij} = \int w_i(x,0,t) w_j(x,0,t) dx dt$$

We assumed  $\varepsilon \gamma_1(x) \leq 0$ . This is the only *a priori* information available.

At this stage we limit ourselves to the single step function

$$\varepsilon \gamma_1(x) \approx g B_{1,1}(x)$$

where  $B_{1,1} = 1$  the interval  $x_{m \geq} \leq x \leq x_M$  and zero elsewhere. The numerical value of the parameter  $g$  is a kind of mean value. It is easy to see that in this very special case, we have

$$g = \frac{\int w_1(x,0,t) (u^\varepsilon(x,0,t) - u^0(x,0,t)) dx dt}{\int w_1^2(x,0,t) dx dt}$$

## References

1. P.Bison, M.Ceseri, D.Fasino and G.Inglese. Domain derivative approach to Active InfraRed Thermography, *Inverse Problems in Science and Engineering* 18:7, 873-889, 2010.
2. G.Buttazzo, R.V.Kohn. Reinforcement of a Thin layer with Oscillating Thickness, *Appl Math Optim* 16, 247-261, 1987.
3. H. W. Engl, P. Fusek and S. V. Pereverzev. Natural linearization for the identification of nonlinear heat transfer laws, *J. Inv. Ill-Posed Problems* 13 (6), 567-582, 2005.
4. D.Fasino and G. Inglese. Heuristic methods for the reconstruction of two corrosion parameters from incomplete boundary data in a thin rectangular domain, *J. Inv. Ill-Posed Problems* 13 (4), 339-351.
5. G. Inglese. Recovering the functional form of nonlinear heat transfer by means of thermal imaging, in *Engineering Optimization IV*, Rodrigues et al (Eds), (Londra: Taylor and Francis) 2015.
6. V. Isakov. *Inverse Problems for Partial Differential Equations* Appl Math Sciences 127 New York: Springer, 1998.
7. X.P.V. Maldague. *Theory and Paractice of Infrared Technology for Nondestructive Testing*, New York: Wiley and Sons, 2001.
8. Salsa S. *Partial Differential Equations in Action* Milano: Springer, 2008.
9. F.Santosa, M.Vogelius, J.M.Xu. An effective nonlinear boundary condition for a corroding surface. Identification of the damage nased on electrostatic data, *Z angew Math Phys* 49, 656-679, 1998.
10. Simon J. Differentiation with respect to the domain in boundary value problems, *Numer. Funct. Anal. Optim.* 2 649--687, 1980.
11. C.T. O'Sullivan. Newton's law of cooling - A critical assessment. *Am. J. of Phys.* 58 (10) 956-960, 1990.
12. M. Vollmer. Newton's law of cooling revisited, *European Journal of Physics* 30, 1063-1084, 2009.

# IMPROVEMENT OF PREDEFINED ELECTROOPTICAL SYSTEM PERFORMANCE BY A MATHEMATICAL MODEL FOR IMAGE INTENSIFIER TUBE

Dr. Nebi Gül<sup>1</sup>, Ali Berkol<sup>2</sup>

<sup>1</sup> Baskent University, Institute of Science and Engineering Ankara, Turkey  
nebigul@yahoo.com

<sup>2</sup> Baskent University, Institute of Science and Engineering Ankara, Turkey  
ali.berkol@yahoo.com

Electro-optical Night Vision systems have taken up rightfully its place in civilian and military applications. Being one of the most sophisticated devices, prolonged design, production, and test phases in electro-optical systems manufacturing would incur higher costs whereas modelling appears to be one of the significant cost drivers. This paper exemplifies a mathematical modelling for electro-optical Night Vision systems by a proposal that develops a model for Modulation Transfer Function (MTF) of Image Intensifier Tube (IIT) which is the crucial component in the Night Vision Devices (NVD). The model is based on MTF of IIT combined Gaussian Curve and Logarithmic Regulation methods. Obtained results point out the enhancement of prediction of MTF by Gaussian + logarithmic regulation formulas and mark a performance increase up to 95% from 70%. Hence this study gives a vision to related work in a way to state the next generation IIT performances via existing technology and so renders it possible to predict the performance levels to be reached in the upcoming 20 years.

## Introduction

One of the challenges that scientists faced through World War II was enabling it the warfighter operations in low visible theatre, primarily during nights, to safeguard more effective missions with minimized risk. First initiatives of night vision technology development have taken place since 1940s, based on the theory of how to view the objects or enhance the image visibility where low light conditions prevail.[1]

The key component of Passive Night Vision Systems is the IIT which is a device for amplifying the intensity of available light in an optical system to allow visibility under low light level (LLL) conditions. The quality and performance of IIT is defined by the widely used parameter designations (gain, resolution, noise, Modulation Transfer Function (MTF)) of military standards. [2]

As MTF value stands out as being the most distinctive performance indicator of IIT, it can be rated as a baseline to IIT performance modelling. This may hence lead to a conclusion that MTF value has proportion with image quality as higher the MTF value, higher the quality of image obtained.[3]

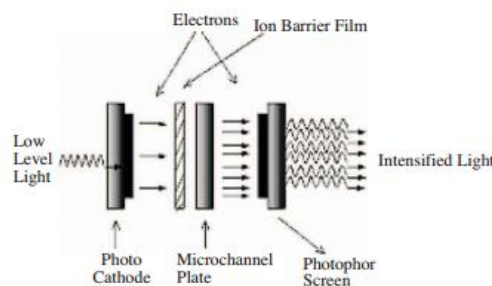


Fig. 1. Structure and operation of Image Intensifier Devices



As shown by Fig. 1, Photocathode converts the incoming photons into electrons and drives out these electrons towards the Micro Channel Plate (MCP). In this way, these photo-electrons induced by the instant level of light entering into each channel are amplified in geometrical proportion and form the electron beam which provides intensified light.[1][4]

### Modulation Transfer Function (MTF)

In general, the performance of an optical system is determined by its capability of resolving the smallest object at the farthest distance. On the other hand whilst these parameters are being obtained, MTF that designating the spatial frequency response in terms of line pair/mm or cycle/mm is utilized as the major factor of the performance measure. [3][5]

### MTFs for First, Second, Third and Fourth Generation Image Intensifier Tubes

Table 1 depicts the MTF values for 0, 2.5, 7.5, 15, 25 line pair/mm that sourced from the spatial frequency values of related military standards in terms of line pair/mm. Evidently, 1st and 2nd Generation IITs show no remarkable MTF differences at low frequencies (0, 2.5, 7.5 line pair/mm).[5] But variation of MTF value at the frequency 25 line pair/mm, points out the awareness through application area. Beyond dispute, other 3<sup>rd</sup> and 4<sup>th</sup> Generation transitions result in obvious MTF advancement. Thus, significant NVD improvements by means of MTF occur in 3<sup>rd</sup> and 4<sup>th</sup> generations. That's why 3<sup>rd</sup> generation IIT measured data are analyzed in detail.

Freq. Line Pair/mm	1st Gen. OMNI-I (%)	2nd Gen. OMNI-II (%)	3rd Gen. OMNI-III (%)	4th Gen. OMNI-IV (%)
0	100	100	100	100
2,5	83	83	83	92
7,5	58	58	60	60
15	20	20	38	61
25	3	10	20	38

Table-1: MTF measurements for 1st-4th Generation IIT

### MTF for 3<sup>rd</sup> Generation OMNI III

Owing the true MTF advancement occurred in 3<sup>rd</sup> Generation IITs, a mathematical model is generated for a 3<sup>rd</sup> Generation. [6]

$$MTF_{\text{reg.}}(f_x) = e^{-2\pi^2\sigma^2 m f_x^2} \quad (1)$$

The results obtained via varying spot widths (as given by Table 2) revealed that MTF value is closest to true measurement at the spot width of 0,015mm (15µm).[5]

σ(µm)	10	15	16	17	18	19	20	25
f <sub>x</sub> =0	1.0000	1.0000	1.0000	1.0000	1.0000	1.0000	1.0000	1.0000
f <sub>x</sub> =2,5	0.9877	0.9726	0.9689	0.9650	0.9608	0.9564	0.9518	0.9258
f <sub>x</sub> =7,5	0.8949	0.7789	0.7526	0.7255	0.6979	0.6698	0.6414	0.4996
f <sub>x</sub> =15	0.6414	0.3681	0.3208	0.2771	0.2372	0.2012	0.1692	0.0623
f <sub>x</sub> =25	0.2912	0.0623	0.0425	0.0283	0.0184	0.0116	0.0072	0.0004

Table-2: Unregulated MTF analysis for 3<sup>rd</sup> Generation IIT

This value, however, does not exactly tally with the true measurement value but the approximate one so as it may count as a reference in formulization of a mathematical model to be proposed. Figure 2 presents a comprehensive Picture of this approach.[5]

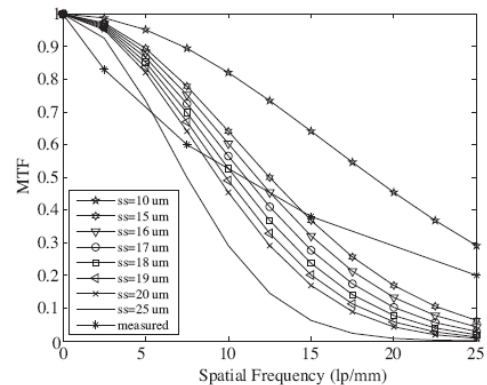


Fig. 2. MTF values for 3rd Generation IIT based on spot width

Since the Gaussian graphs of Figure 2 are obtained by Equation 1, this study anticipates that proposed mathematical model for real IIT would result in the most approximate measurement values. In Figure 2, real MTF

intersects to analytic MTF for 15 μm spot width. Basing this spatial frequency commonality, following logarithmic regulation coefficient is developed as given by the Equation 2.

$$K_3(f_x) = \begin{cases} \pi \cdot f_x \cdot \ln\left(\frac{f_x}{f_{co}}\right), 0,01 & (2) \\ f_x \cdot \ln\left(\frac{f_x}{f_{co}}\right), 0,01 \end{cases}$$

where;

$$f_x \leq f_{com} \text{ and } f_{com} < f_x \leq 25.$$

By adding this coefficient in Equation (1), Equation (3) is obtained as below: [5][6]

$$MTF_{g,yog3}(f_x) = \begin{cases} e^{-2\pi^2\sigma_m^2 f_x^2} + \pi \cdot f_x \cdot \ln\left(\frac{f_x}{f_{co}}\right), 0,01 & (3) \\ e^{-2\pi^2\sigma_m^2 f_x^2} + f_x \cdot \ln\left(\frac{f_x}{f_{co}}\right), 0,01 \end{cases}$$

Then Proposed Mathematical model by Equation 3 is used for the MTF analysis of 3<sup>rd</sup> Generation IIT and results are shown by Table 3 given hereunder:

σ(mm)	0,010	0,015	0,019	0,020	0,025
f <sub>x</sub> =0	1	1	1	1	1
f <sub>x</sub> =2,5	0.8470	<b>0.8319</b>	0.8157	0.8111	0.7851
f <sub>x</sub> =7,5	0.7316	<b>0.6156</b>	0.5064	0.4781	0.3363
f <sub>x</sub> =15	0.6414	<b>0.3681</b>	0.2012	0.1692	0.0623
f <sub>x</sub> =25	0.4189	<b>0.1900</b>	0.1393	0.1349	0.1282

Table-3: Regulated MTF Analysis for MX-10160 (per Equation 3)[5]

### MTF for 4<sup>th</sup> Generation IIT

Let K4 is the regulation coefficient for 4<sup>th</sup> Generation; Figure 3 shows the MTF value for 4<sup>th</sup> generation IIT drawn by the act of Equation 1.

$$MTF_{GYOG-OMNI-IV} = \left[ e^{-2\pi^2\sigma^2 f_x^2} + K_4(f_x) \right] \quad (4)$$

Here, K<sub>4</sub> (f<sub>x</sub>) is calculated as follows;

$$K_4(f_x) = \begin{cases} 0.055 \cdot \pi \cdot f_x \cdot \ln\left(\frac{f_x}{15}\right) & f_x \leq 15 \\ 0.01 \cdot f_x \cdot \ln\left(\frac{f_x}{15}\right) & 15 < f_x < 25 \\ 0 & f_x > 25 \end{cases} \quad (5)$$

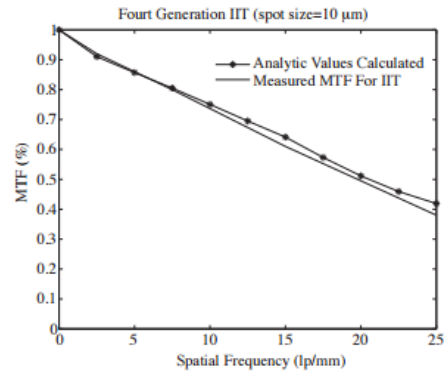


Fig.3. Measured MTF value for 4<sup>th</sup> Generation IIT and Regulated Analytic MTF corresponding to 10 micron spot width.

### Discussion for Results of the Developed Model (Next Generation)

It's shown that expressing MTF formula in terms of "Gaussian + Logarithmic" regulated formula yields more accurate results other than Gaussian formula in the development of IIT simulations.[6] The regulation additive to widely applied MTF formula in Literature is verified by checking with Boreman [3], as well as with expansion and phase of reverse Fourier transform. [7]

Here it's shown that the MTF values obtained for each night vision generations are used to calculate the MTF performance. Owing to this, interrelating the measurement values and employing from formula may lead to some futuristic inferences. For this purpose Table 4 is prepared to demonstrate the difference in MTF values corresponding to low and high spatial frequencies. Notably, the MTF differences during transformation from 3<sup>rd</sup> generation and 4<sup>th</sup> generation are encouraging for transforming to next generations.

Frequency lp/mm	1 <sup>st</sup> Gen. OMNI.-I (%)	2 <sup>nd</sup> Gen. OMNI.-II (%)	3 <sup>rd</sup> Gen. OMNI.-III (%)	4 <sup>th</sup> Gen. OMNI.-IV (%)	Next * Gen %
(A) 2,5	83	83	83	92	<b>99</b>
(B) 25	3	10	20	38	<b>55</b>
Max. (A-B)	80	73	63	54	<b>44</b>

Table-4: Inter-generations Low and High frequency MTF Differences (Four Columns data taken from Table-1)

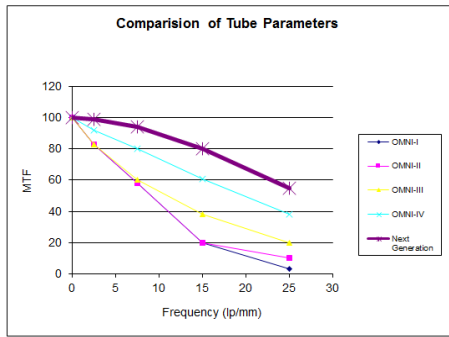


Fig.4. Comparison of tubes MTFs

Table 4 gives predictions regarding next generation MTF values but it still remains ambiguous that which means of physical effect prevails. Assuming the spot width would drop down below 10 microns, MTF equation is calculated for 1-9 micron spot widths and respective results are tabulated by Table 5. Note that developed model indicates the spot width as 7 microns.

$\sigma(\mu\text{m})$	1 $\mu\text{m}$	3 $\mu\text{m}$	5 $\mu\text{m}$	7 $\mu\text{m}$	9 $\mu\text{m}$
MTF (2,5) (lp/mm)	0,9998	0,9989	0,9969	0,9939	0,9900
MTF (7,5) (lp/mm)	0,9988	0,9901	0,9726	0,9470	0,9139
MTF (15) (lp/mm)	0,9956	0,9608	0,8949	0,8044	0,6978
MTF (25) (lp/mm)	0,9877	0,8949	0,7346	0,5463	0,3681

Table-5: MTF results based on Spot Width

## Conclusion

This study formulizes a mathematical model by utilizing the available data in an aim to predict the MTF value for Next Generation IIT and hence proposes the most approximate MTF value to measurements. Obtained MTF values

prove that as the generations advance, the spot width decreases and so the image quality of IIT increases provided that the equivalent spot width for Next Generation is 7 microns. Considering the 10 micron spot width gives the MTF for 4<sup>th</sup> Generation IIT, achieving the MTF value of 7  $\mu\text{m}$  spot width could take place within next 20 years. Furthermore, this mathematical model coupled with today's IIT technology ensures improvements by 10-20% in low frequencies and 30-40 % in high frequencies and encourages eliminating degradation effects of IIT's on NVDs.

## References

- [1] Biberman, L.M. (Editor) and Hall J.A 2000. "Ch.4: Early Image Intensifier Tube Structures" and "Ch.5: Present Image Intensifier Tube Structures" Electro-Optical Imaging: Systems Performance and Modeling SPIE Pres, ISBN 0-8194-3999-1.
- [2] US Military Standard, MIL-I-49453 (CR) 06 November 1989.
- [3] Boreman G.D, 2001 "Modulation Transfer Function in Optical and Electro Optical Systems" SPIE Pres ISBN: 0819441430 PP: 17
- [4] Holts G.C, 1996 "System MTF, CCD Array, Camera and Display" ICO Publishing, 2932 Cove Trail Winter Park, FL 32789.
- [5] Gul N., Efe M., " Improved Analytical Modulation Transfer Fonction for Image Intensifier CCD" TJEECS Turkish Journal of Electrical Engineering and Computer Sciences. Pp 71-81, Volume 18 Number 1, 2010.
- [6] Gul N, Efe M and Larochelle V, "Development of the Optical Transfer Function (OTF) for Image Intensifier Tube (IIT)" IEEE 25<sup>th</sup> Convention of Electrical and Electronics Engineers in Israel, pp 36-40, December 2008.
- [7] Gul N., 2010 "Image acquisition with IICD Camera at Ultra Low Light Level Through IR-Based Active Sensing and analytic calculations of ICCD MTF, Doctorate Thesis, April 2010 Ankara University

# Numerical method for the capacitance of HgCdTe MIS structure and band-to-band tunneling effect on the low frequency behavior in high frequency C-V characteristics

K. He<sup>1</sup>, X. Wang<sup>2</sup>, C. Lin<sup>3</sup>, Q. Y. Zhang<sup>4</sup>, R. J. Ding<sup>5</sup>

<sup>1</sup> Key Laboratory of Infrared Imaging Materials and Detectors, Shanghai Institute of Technical Physics, Chinese Academy of Sciences, Shanghai, China, 20083, hekai2206707@163.com

<sup>2</sup> Key Laboratory of Infrared Imaging Materials and Detectors, Shanghai Institute of Technical Physics, Chinese Academy of Sciences, Shanghai, China, 20083, wangxi88@foxmail.com

<sup>3</sup> Key Laboratory of Infrared Imaging Materials and Detectors, Shanghai Institute of Technical Physics, Chinese Academy of Sciences, Shanghai, China, 20083, chun\_lin@mail.sitp.ac.cn

<sup>4</sup> Key Laboratory of Infrared Imaging Materials and Detectors, Shanghai Institute of Technical Physics, Chinese Academy of Sciences, Shanghai, China, 20083, qinyao@mail.sitp.ac.cn

<sup>5</sup> Key Laboratory of Infrared Imaging Materials and Detectors, Shanghai Institute of Technical Physics, Chinese Academy of Sciences, Shanghai, China, 20083, dingrj@mail.sitp.ac.cn

Accurate relationship between the surface charge density  $Q_s$  and the surface potential  $\psi_s$  have been obtained by taking into account the effect of band non-parabolicity and carrier degeneracy. Based on this, a simple numerical method have been proposed to calculate low and high frequency capacitance-voltage characteristics of HgCdTe Metal-Insulator-Semiconductor (MIS) structure and the model of band-to-band tunneling capacitance have been improved which is responsible for the low frequency behavior in high frequency capacitance–voltage characteristics..

## Introduction

Mercury cadmium telluride (HgCdTe) infrared (IR) photodiode has been one of the most important types of advanced infrared detectors due to its performance advantage and technical maturity.<sup>1,2</sup> However, surface passivation has been a dominant factor in limiting device performance.<sup>3</sup> Therefore, there are many researches have been published in open literature about interface properties of passivation of HgCdTe infrared device using Metal-Insulator-Semiconductor (MIS) test method.<sup>4,5</sup> Although, the theory of MIS structure which are realized in HgCdTe should be modified to incorporate the unique features has been already been rigorously formulated,<sup>6</sup> many of works analyzed MIS capacitance-voltage data by non-degenerated MIS theory which isn't appropriate for HgCdTe.<sup>7,8</sup> In this paper, we propose a simple numerical method to calculate low and high

frequency capacitance-voltage (C-V) characteristics of HgCdTe MIS structure which can be used in experiment data processing. And depend on the method, the band-to-band tunneling effect on HgCdTe MIS C-V measurement has been investigated which cause the low frequency behavior in high frequency C-V characteristics.

## Physical Model

A. Surface Charge Density  $Q_s$  and Surface Potential  $\psi_s$

C-V curve of the MIS device is directly related to surface charge density  $Q_s$ . According to the theory of semiconductor, the relationship between the surface potential and surface charge density can be got by solving Poisson equation under the semiconductor surface. One-dimensional Poisson equation is given as,

$$\frac{d^2\psi_p(x)}{dx^2} = -\frac{q}{\epsilon_s\epsilon_0} (n_{p0} - p_{p0} + p_p(x) - n_p(x)) \quad (1)$$

Where,  $\psi_p(x)$  is potential,  $n_p(x)$  electron density,  $p_p(x)$  hole density, all be function of the position  $x$ ,  $n_{p0}$  is electron density and  $p_{p0}$  is hole density in the body of semiconductor at equilibrium condition.  $E_p = -\frac{d\psi_p}{dx}$  is defined as electric field intensity of surface charge area, that can be by multiplied Eq.(1) with  $2\frac{d\psi_p}{dx}$ , then integral from surface to body,

$$E_p^2 = 2\left(\frac{kT}{q}\right)^2 \left(\frac{q^2 p_{p0}}{\epsilon_s \epsilon_0 kT}\right) \int_0^{u_p} \frac{n_{p0} - p_{p0} + p_p - n_p}{p_{p0}} du_p \quad (2)$$

Using Gauss theorem, the surface charge density  $Q_s$  can be got,

$$Q_s = -\epsilon_s \epsilon_0 E_s = \mp \frac{\sqrt{2\epsilon_s \epsilon_0 kT}}{qL_D} F\left(u_s, \frac{n_{p0}}{p_{p0}}\right) \quad (3)$$

where,  $L_D = \sqrt{\frac{kT\epsilon_s \epsilon_0}{q^2 N_A}}$  is Debye length, and  $F\left(u_p, \frac{n_{p0}}{p_{p0}}\right) = \sqrt{\int_0^{u_p} \frac{n_{p0} - p_{p0} + p_p - n_p}{p_{p0}} du_p}$ .

It is intricate to solve the Eq. (3) when considering the effect of band non-parabolicity and carrier degeneracy of HgCdTe. In this paper, the Ariel's numerical model was used, corrected by Zhijue Quan<sup>9</sup>, that described the relationship between the Fermi level and the carrier density. Contracted Fermi level  $u_f = \frac{q\psi_{Bp}}{kT}$  ( $q\psi_{Bp} = E_i - E_{Fp}$ ) was used here.

Contracted Fermi level of electron

$$u_{fc} = \ln \frac{n}{B_0 N_c} + B_1 \left(\frac{n}{N_c}\right)^{\alpha_1} + B_2 \left(\frac{n}{N_c}\right)^{\alpha_2}$$

$$\alpha_1 = 0.526 + 0.236 \exp\left(-\frac{\alpha + 0.00211}{0.0279}\right)$$

$$\alpha_2 = 0.624 - 12.8\alpha + 128\alpha^2 - 541\alpha^3$$

$$B_0 = 1 + 3.75\alpha + 3.281\alpha^2 - 2.461\alpha^3$$

$$B_1 = 0.994 - 3.333\alpha$$

$$B_2 = -(0.577 - 7.93\alpha + 78.6\alpha^2 - 349\alpha^3) \quad (4)$$

Contracted Fermi level of hole

$$u_{vf} = \ln \frac{p}{B_{0v} N_v} + B_{1v} \left(\frac{p}{N_v}\right)^{\alpha_{1v}} + B_{2v} \left(\frac{p}{N_v}\right)^{\alpha_{2v}}$$

$$\alpha_{1v} = 0.745$$

$$\alpha_{2v} = 0.624$$

$$B_{0v} = 1$$

$$B_{1v} = 0.944$$

$$B_{2v} = -0.577$$

$$(5)$$

The Hg<sub>1-x</sub>Cd<sub>x</sub>Te used in this study was MW thin film material, with an average cadmium fraction  $x=0.3$ , acceptor concentration  $N_A=5\times 10^{15}\text{cm}^{-3}$ , at a temperature  $T=82\text{K}$ . Fig. 1. shows the relationship between surface potential and space-charge density considering the effect of conduction band non-parabolicity and carrier degeneracy: when  $\psi_s < 0$ ,  $Q_s$  is positive, corresponding to the accumulation case; when under flat-band condition  $\psi_s = 0$ ,  $Q_s=0$ ; when  $0 < \psi_s < 2\psi_{Bp}$ , it comes the cases of depletion and weak inversion; and  $\psi_s > 2\psi_{Bp}$  corresponds to strong inversion. In contrast to non-degenerated condition, there are much lower surface charge density in accumulation and strong inversion ranges.

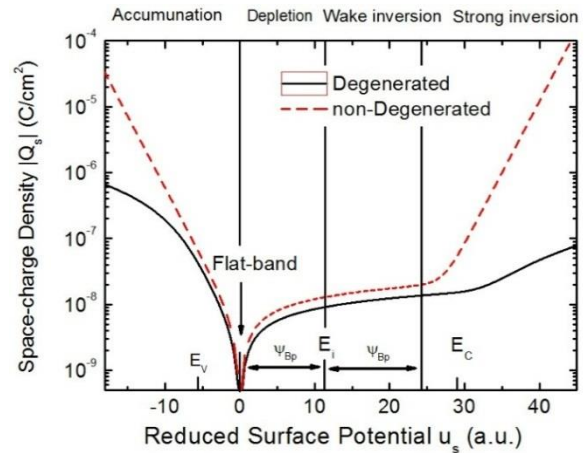


Fig. 1. Relationship between surface potential and space-charge density of p-type Hg<sub>0.7</sub>Cd<sub>0.3</sub>Te with  $N_A=5\times 10^{15}\text{cm}^{-3}$  at 82K. The dotted line is non-degeneracy, and the solid line with the effect of conduction band non-parabolicity and carrier degeneracy.



## B. Theoretical C-V Curve

The total capacitance of the MIS device is composed by the insulation layer capacitance  $C_i$  and semiconductor capacitance  $C_s$ , which defined as  $C_s(\psi_s) \equiv -\frac{dQ_s}{d\psi_s}$ . The relationship of  $Q_s$  and  $\psi_s$  can be got by numerical differentiation on the expression of  $Q_s$  and  $\psi_s$ .

$$C_{s,L} = -\frac{Q_s(u_s+du_s)-Q_s(u_s-du_s)}{2du_s} \cdot \frac{q}{kT} \Big|_{du_s \rightarrow 0} \quad (6)$$

$C_{s,L}$  is the capacitance of the semiconductor at low frequency.

For ideal C-V curve at high frequency, the effect of minority carrier redistribution is ignored, then  $F\left(u_s, \frac{n_{p0}}{p_{p0}}\right)$  is rewritten as

$$F_H\left(u_s, \frac{n_{p0}}{p_{p0}}\right) = \sqrt{\int_0^{u_s} \frac{p_s+n_{p0}}{p_{p0}} - 1} \quad (7)$$

The density of space-charge which can respond to high frequency signal is given by

$$Q_{s,H} = \mp \frac{\sqrt{2}\epsilon_s\epsilon_0kT}{qL_D} F_H\left(u_s, \frac{n_{p0}}{p_{p0}}\right) \quad (8)$$

Hence, High frequency capacitance of the semiconductor can be approximated as a piecewise function.

$$\begin{aligned} C_{s,H}(u_s) &= \frac{dQ_{s,H}}{du_s} \frac{q}{kT}; u_s < u_m \\ C_{s,H}(u_s) &= C_{s,H}(u_m); u_s \geq u_m \end{aligned} \quad (10)$$

Where,  $u_m = 2.10u_B + 1.33$ .

The gate voltage  $V_G$  of MIS device is given by

$$V_G = -\frac{Q_s(\psi_s)}{C_i} + \psi_s + V_{FB} \quad (11)$$

Where,  $V_{FB}$  is flat-band voltage. Fig. 2 demonstrates the relationship between

surface potential and gate bias when  $C_i = 1.5 \times 10^{-4} F/m^2$  and  $V_{FB}=0V$ .

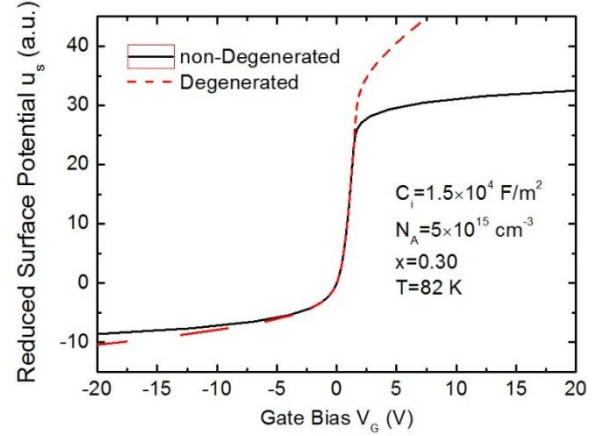


Fig. 2. Relationship between surface potential and gate bias.

Depend on the method, we can obtain the theoretical C-V characteristics of HgCdTe MIS device, in Fig. 3 ( a and b curve ). By contrast, non-degenerated result also be given in Fig. 3 ( c and d curve ).

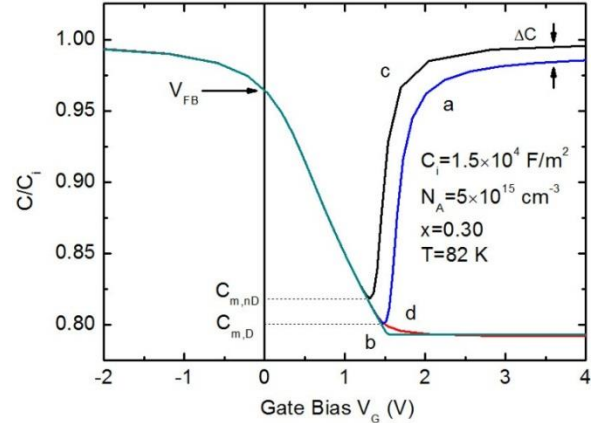


Fig. 3 Theoretical C-V curve of HgCdTe MIS device: the effect of band non-parabolicity and carrier degeneracy was considered in a and b, c and d were under non-degeneracy condition.

## C. Band-to-Band Tunnelling Effect

Low-frequency C-V curves were often obtained with high measurement frequency on LWIR HgCdTe device. R. K. Bhan<sup>10,11</sup> interprets this phenomenon by band-to-band tunnelling (BBT), BBT will introduce additional capacitance to narrow gap of LWIR HgCdTe. But we hold the point that the BBT current will be overestimated



without considering the effect of band non-parabolicity and carrier degeneracy which wasn't contained in Bhan's works. Here, the C-V curve with the influence of BBT is recalculated by using the equation between space-charge  $Q_s$  and surface potential  $\psi_s$  mentioned above. The space-charge generating as BBT is given by

$$Q_{\text{BBT}} = \frac{J_{\text{BBT}}(\psi_s)}{f} \quad (12)$$

where,  $f$  is the frequency of the test signal,  $J_{\text{BBT}}(\psi_s)$  the BBT current related to surface potential, can be written as

$$J_{\text{BBT}}(\psi_s) = \frac{q^3 \sqrt{2m_e^*} E \psi_s}{4\pi^3 \hbar^2 \sqrt{E_g}} \exp\left(-\frac{\pi \sqrt{\frac{m_e^*}{2}} E_g^{3/2}}{2qE\hbar}\right)$$

$$E = \frac{\psi_s}{W_s}$$

$$W_s = \sqrt{\frac{2\epsilon_s \epsilon_0 \psi_s}{qN_A}} \quad (13)$$

Where  $a$  and  $b$  stand for

$$a = \frac{q^3}{4\pi \hbar^2} \sqrt{\frac{qN_A m_e^*}{\epsilon_s \epsilon_0 E_g}}$$

$$b = -\frac{\pi E_g^{3/2}}{2\hbar q} \sqrt{\frac{\epsilon_s \epsilon_0 m_e^*}{qN_A}} \quad (14)$$

According to the definition of dynamic capacity, capacitance related to BBT current is given by

$$C_{\text{BBT}} = \frac{dQ_{\text{BBT}}}{d\psi_s} = \frac{1}{f} \frac{dJ_{\text{BBT}}}{d\psi_s} = \frac{1}{a \exp(b\psi_s^{-2}) (1.5\psi_s^{-1/2} - 0.5b)} \quad (15)$$

As  $C_{\text{BBT}}$  is in parallel with  $C_s$ , the total capacitance can be written as

$$\frac{1}{C} = \frac{1}{C_i} + \frac{1}{C_s + C_{\text{BBT}}} \quad (16)$$

Fig. 4 presents the calculated C-V curves to show the influence of BBT effect on high-

frequency ( $f=1\text{MHz}$ ) and low-frequency ( $f=1\text{kHz}$ ) C-V curve of LWIR ( $x=0.22$ ). As shown in Fig. 4(a), the BBT effect makes the C-V curve go from high-frequency to low-frequency behaviour though the measurement frequency as high as 1MHz. And in Fig. 4(b), the unsaturation capacitance in strong inversion range which is caused by carrier degeneracy is covered and rapidly increased to saturation.

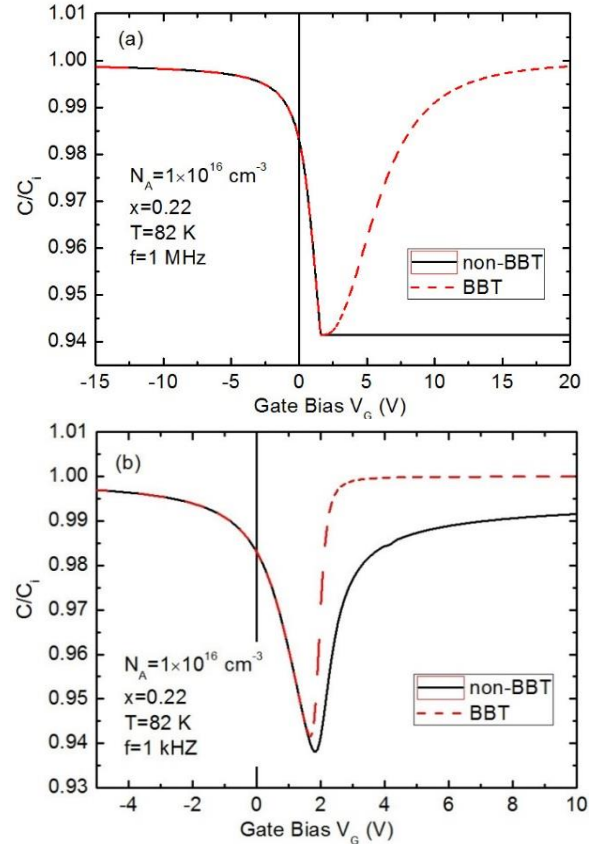


Fig. 4. The C-V curve of LWIR ( $x=0.22$ ) HgCdTe MIS device with the influence of BBT: (a) high-frequency C-V curve at  $f=1\text{MHz}$ , (b) low-frequency C-V curve at  $f=1\text{kHz}$

## Conclusion

In summary, to obtain the theoretical C-V characteristics of HgCdTe MIS device, we calculated the accurate relationship between the surface charge density  $Q_s$  and the surface potential  $\psi_s$  by taking into account the effect of band nonparabolicity and carrier degeneracy, and a simple numerical method have been proposed. Depend on this, the band-to-band tunneling effect on HgCdTe MIS capacitance-voltage measurement

also has been investigated which have influence on the C-V characteristics in strong inversion range.

## References

1. A. Rogalski, J. Antoszewski, L. Faraone. Third-generation infrared photodetector arrays, *Journal of Applied Physics*, Vol. 105: 091101, 2009.
2. Kai He, Yang Li, Xing Chen, et al. Numerical approach to generalized transmission line model and its application to Au/Sn/p-HgCdTe contact. *Journal of Applied Physics* by Annealing in a Cd/Hg Atmosphere. *Journal of Electronic Materials*, Vol. 31(7): 683-687, 2002.
3. V. A. Altschul, E. Finkman, G. Bahir. Approximations for Carrier Density in Nonparabolic Semiconductors. *IEEE Transactions on Electron Devices*, Vol. 39, 6, 1992.
4. Z. J. Quan, X. S. Chen, L. Z. Sun, et al. Effects of carrier degeneracy and conduction band non-parabolicity on the simulation of HgCdTe photovoltaic devices. *Infrared Physics & Technology*, Vol. 50(1), 1-7, 2007.
5. R. K. Bhan, V. Gopal, Analysis of surface leakage currents due to Zener tunnelling in HgCdTe photovoltaic diodes. *Semiconductor Science and Technology*, Vol. 9, 289-297, 1994.
6. R. K. Bhan, R. S. Saxena, N. K. Saini, et al. The low frequency behaviour in high frequency capacitance-voltage characteristics due to contribution of band-to-band tunnelling and generation-recombination in Hg<sub>0.75</sub>Cd<sub>0.25</sub>Te MIS capacitors. *Infrared Physics & Technology*, Vol. 54: 379-381, 2011.
7. Applied Physics. Vol. 115, 164506, 2014.
8. K. He, S. M. Zhou, Y. Li, et al. Effect of surface fields on the dynamic resistance of planar HgCdTe mid-wavelength infrared photodiodes, *Journal of Applied Physics*, Vol. 117, 204501, 2015
9. V. Voitsekhovskii, S. N. Nesmelov, et al. Capacitance-voltage characteristics of metal-insulator-semiconductor structures based on graded-gap HgCdTe with various insulators, *Thin Solid Films*, Vol. 522, 261-266, 2012.
10. J. S. Kim, J. H. Song, S. H. Su. Electrical Properties of ZnS, CdTe/HgCdTe Interface Evaporated from Effusion Cell in UHV Chamber, *SPIE*, Vol. 4130, 0277-786x, 2000.
11. Bloom, Y. Nemirowsky. Bulk levels and interface calculations for narrow band-gap semiconductors, *Solid-State Electronics*, Vol. 31(1): 17-25, 1988.
12. S. Y. An, J. S. Kim, D. W. Seo, et al. Passivation of HgCdTe p-n Diode Junction by Compositionally Graded HgCdTe Formes

## Author Index

- Atsushi **Akai** 36  
Giampietro **Alberti** 111  
Amin **Al-Habaibeh** 186  
Ana **Alves Pinto** 190  
A. **Amato** 119  
Dario **Ambrosini** 263  
Francesco **Ancona** 162  
Ole Kæseler **Andersen** 107  
Alessia **Andreotti** 313  
Saplontai **Aniela** 138  
Lars **Arendt-Nielsen** 107  
A.S. **Aricò** 119  
Maryam **Asrar** 186  
Patrizia **Aversa** 279  
Atilla **Aydinli** 123
- Amirreza **Baghbanpourasl** 214  
Zhizhong **Bai** 20  
Alessandro **Barducci** 32  
Gaia Dominique **Bariffi** 41  
Anum R. **Barki** 322  
Eva **Barreira** 242  
Giovanni **Bartolozzi** 313  
Elton **Bauer** 242  
Sougrati **Belattar** 283  
Alice **Bellazzi** 59  
Lorenzo **Belussi** 59  
Ali **Berkol** 354  
Marco **Bini** 313  
Paolo **Bison** 45, 255,259,267,344  
Stanca **Boboia** 142  
Simone **Boccardi** 206  
Ilaria **Bonaduce** 313  
Roberto **Bonsignori** 317  
Alessandro **Bortolin** 45,255,259,344  
Andrea **Bosio** 111  
Barbara **Bukowska-Belniak** 76  
Tinca **Buruiana** 147
- Gianluca **Cadelano** 45,255,259,344  
Emma **Cantisani** 313  
Natalia **Caparrini** 49  
Giovanni Maria **Carlomagno** 206
- Martin **Chamberland** 83  
Eleni **Cheilakou** 296  
Chung-Ming **Chen** 133  
Jianxin **Chen** 99  
Xingyou **Chen** 3  
Lu **Chen** 167,179  
Massimo **Chimenti** 313  
Fabrizio **Clarelli** 267  
Sarosi **Codruta** 138  
Loredana **Colceriu** 147  
Maria Perla **Colombini** 313  
Edoardo **Copertaro** 340  
Antonio **Cricenti** 103,127  
Carlos **Cuadra** 346  
Costanza **Cucci** 313
- Mario **D'Acunto** 103  
Dorin **Dadarlat** 142  
Ludovico **Danza** 53  
Anna **De Falco** 300  
Rosa **De Finis** 162  
Ute **Dercks** 313  
Ruijun **Ding** 6,167,179,358  
Prodan **Doina** 142  
Donatella **Dominici** 263  
Janice **Dulieu-Barton** 247  
Jean **Dumoulin** 24  
Marc **Duval** 83  
Mohamed **El Afi** 283  
Sezai **Elagoz** 123  
Yuksel **Ergun** 123  
Sediki **Ezeddine** 183
- Fabio **Fantozzi** 308  
Vincent **Farley** 83  
Laura **Fenelli** 313  
Henrique **Fernandes** 95,234  
Giovanni **Ferrarini** 45,255,259,344  
Frank **Ferrie** 334  
Graham **Ferrier** 326  
Sauro **Filippeschi** 308  
Lorenzo **Finesso** 344  
Julien **Fleuret** 152

Damiano **Formenti** 111  
Steffen **Frahm** 107  
Simon **Fréchet** 152  
Vasco P. **Freitas** 242

Marc-André **Gagnon** 83  
Monica **Galeotti** 313  
Umberto **Galietti** 279,162  
Jean-Laurent **Gardarein** 330  
Marco **Gargano** 111,304  
Jonathan **Gaspar** 330  
Waldemar **Gawron** 129  
Marc **Genest** 95  
Seyed Alireza **Ghaffari** 152  
Matteo **Ghellere** 59  
Yi **Gu** 3  
Nebi **Gül** 354  
Éric **Guyot** 83  
Donatella **Guzzi** 32

Valentina **Hartwig** 201  
Atsushi **Hashimoto** 72  
Ulf **Hassler** 95  
Shunichi **Hayashi** 115  
Li **He** 6,99  
Kai **He** 358  
Piotr **Hellstein** 210  
Takayuki **Hibino** 251,275  
Ioana **Hodisan** 142  
Wolfgang **Holub** 95  
Mustafa **Hostut** 123  
M. R. **Houda** 186  
Michael **Houry** 330  
David K. **Hsu** 224

Clemente **Ibarra-Castanedo** 234,259  
Kwang-Hee **Im** 224  
Zghal **Imen** 194  
Tsuyoshi **Inagawa** 36  
Gabriele **Inglese** 267,35  
Hiroki **Ito** 229  
Tatsuya **Iwama** 229  
Yui **Izumi** 251,275

Bushra **Jalil** 201  
Olivier **Janssens** 220,291  
Eric **Johnson** 28  
Simon **Joncas** 95  
Jeong-An **Jung** 224

Takaharu **Kameoka** 72  
Artur **Keblowski** 129  
Daniel **Kessler** 76  
S. P. **Khanna** 16  
Igor **Kharitonov** 171  
Fariba **Khodayar** 246  
Abidin **Kilic** 123  
Yong **Kim** 28  
Sun-Kyu **Kim** 224  
Matthieu **Klein** 152  
Malgorzata **Kopytko** 87,129  
Valeri **Kotelnikov** 175  
Maria **Koui** 296  
Katarzyna **Kowalczyk-Gajewska** 115  
Dominik **Kukla** 115

Antonio **L'Abbate** 201  
Félix Labrie **Larrivée** 152  
Susana **Lagüela** 49  
Philippe **Lagueux** 83  
Renée **Lampe** 190  
Yan-Feng **Lao** 16  
Cinzia **Lastri** 32  
Chi-En **Lee** 133  
Lei **Lei** 45  
Andrzej **Lesniak** 76  
Hsby **Li** 3  
Aizhen **Li** 3  
L. H. **Li** 16  
Hao **Li** 6  
Chun Lin 6,167,179,358  
E. H. **Linfield** 16  
Dan **Liu** 6  
M. Lo Faro 119  
Mia **Loccufier** 220,291  
Luján **López** 49  
Marco **Luce** 103,127  
Nicola **Ludwig** 111,304  
Vincenza **Luprano** 279  
Fabio **Luzi** 41

Yingjie **Ma** 3  
Marcelo Sung **Ma Jo** 152  
Pawel **Madejczyk** 129  
J. Robert **Mahan** 322  
Michal **Maj** 115  
Xavier **Maldague** 95,  
152,234,246,259,334  
Irene **Malesci** 313  
Alessandra **Malquori** 313  
Mauro **Mameli** 308  
Moldovan **Marioara** 138  
Piotr **Martyniuk** 129  
Emanuela **Massa** 313  
Silvia **Mazzola** 41  
Carosena **Meola** 206  
Erick **Merliot** 24  
Italo **Meroni** 53,59  
Marioara **Moldovan** 138  
Marco **Montanelli** 313  
R. **Montanini** 119  
Carsten **Mørch** 107  
Annalisa **Morelli** 313  
Akihisa **Moriguchi** 229  
Davide **Moroni** 103  
Abdul **Mouazen** 79  
Ravibabu **Mulaveesala** 344  
Niubis **Mustelier** 242  
Lukáš **Muzika** 11

Nobuaki **Nagatomo** 91  
Leonardo **Nanni Costa** 41  
Iole **Nardi** 263  
Vanni **Nardino** 32  
Slokom **Nesrine** 194  
Elkadri **Noomene** 183

Yoshifumi **Ohbuchi** 91  
Roberto **Olmi** 313  
Veerle **Ongena** 220

Gonzalo **Paez** 157,318  
Lorenzo **Palombi** 313  
Davide **Palumbo** 162,279  
Giuseppe **Pandarese** 340  
Domenica **Paoletti** 259,296

Je-Woung **Park** 224  
Elsa **Pastor** 63  
Jaroslaw **Pawluczyk** 129  
Sara **Penoni** 313  
Fabio **Peron** 259  
Konstantin **Petrosyants** 171  
S.A. **Piccolo** 119  
Marcello **Piccolo** 313  
Elzbieta **Pieczyska** 115  
Louis David **Pierelli** 313  
Francesca **Pietrarca** 308  
Jozef **Piotrowski** 129  
Ivan **Pippi** 32  
Eulàlia **Planas** 63  
Maria Cristina **Pollastro** 53  
Luca **Potì** 201  
Cristina **Prejmerean** 138,142  
Kory J. **Priestley** 322  
Doina **Prodan** 138,142  
Wioletta **Pusz** 129

A. **Quattrocchi** 119  
Simon **Quinn** 247  
Cristina **Racioppo** 279

Valentina **Raimondi** 32,313  
Ermanno **Rampinini** 111  
Veronica **Redaelli** 41  
Gian Marco **Revel** 340  
Cristiano **Riminesi** 313  
Oriol **Rios** 63  
Francois **Robitaille** 95  
Antoni **Rogalski** 87,129  
Elisa **Rosciano** 263  
Elisabetta **Rosina** 304  
Raffaella **Rossi** 41  
Sara **Rutigliano** 313  
Jaroslaw **Rutkowski** 129  
Elena **Ryazanova** 175

Barbara **Sacchi** 313  
Takahide **Sakagami** 36,229,251,275  
Hidetoshi **Sakamoto** 91  
Francesco **Salamone** 53  
Ovidio **Salveti** 103,201

Fabio **Sansivero** 68  
Tiziana **Santini** 300  
Simon **Savary** 83  
Raiko **Schulz** 220,291  
Kazuyoshi **Sekine** 229  
Stefano **Sfarra** 259,263,296  
Maurizio **Sguazzino** 300  
Changzhi **Shi** 167,179  
Nobuhiro **Shimoi** 346  
Teruya **Shiomi** 229  
Daiki **Shiozawa** 36,229  
Laura **Silaghi-Dumitrescu** 138  
Saeed **Sojasi** 246  
G. **Squadrito** 119  
Boboia **Stanca** 142  
Maria **Staszczak** 115  
Sergio **Stella** 313  
Kurt **Stockman** 220,291  
Mihaela **Streza** 142  
Marija **Strojn** 157,318  
Ken-Ichiro **Suehara** 72  
Quanzhi **Sun** 167  
Michal **Švantner** 11  
Waldemar **Swiderski** 288  
Mariusz **Szwedo** 210

Tohru **Takamatsu** 251, 275  
Yoshitaka **Tamaki** 229  
Rosanna **Tamborrino** 279  
Hirotaka **Tanabe** 251, 275  
Tunay **Tansel** 123  
Panagiotis **Theodorakeas** 296  
Louis-Daniel **Théroux** 24  
Rachael **Tighe** 247  
Paul **Toasa** 270  
Blumenstein **Tobias** 190  
Hisaaki **Tobushi** 115  
Gabriella **Tonini** 313  
Hedi **Trabelsi** 183,194  
Gerhard **Traxler** 214  
Athos **Trecroci** 111  
Alessandro **Tredicucci** 114  
Pierre **Tremblay** 83  
S. **Trocino** 119  
Varvara **Turova** 190

Thomas **Ummenhofer** 270  
A. G. **Unil Perera** 16  
M. Miguel **Valero** 63

Rik **Van de Walle** 220,291  
Sofie **Van Hoecke** 220,291  
Prejmerean **Vasile** 138  
Lothar **Verledens** 220  
Zdenek **Vesely** 11  
Giuseppe **Vilardo** 68  
Mihaela **Vlassa** 147

Toby **Waine** 79  
Fangfang **Wang** 99  
Xi **Wang** 358  
Raymon **Watts** 152  
Yanfeng **Wei** 6,167,179  
Bin **Weng** 6  
Rebecca **Whetton** 79

Suping **Xi** 3  
Zhicheng **Xu** 99  
Jiajia **Xu** 99

In-Young **Yang** 224  
Zhenghua **Ye** 6  
Bardia **Yousefi** 152  
Lingyao **Yu** 95

Hai **Zhang** 95,234  
Yonggang **Zhang** 3  
Qinyao **Zhang** 358  
Qiong **Zhang** 334  
Yi **Zhou** 20  
Li **Zhou** 3  
Songmin **Zhou** 6  
Mingxing **Zhu** 167,179  
S.C. **Zignani** 119